KESHRA SANGWAL

NUCLEATION AND CRYSTAL GROWTH

Metastability of Solutions and Melts

WILEY

Nucleation and Crystal Growth

Nucleation and Crystal Growth

Metastability of Solutions and Melts

Keshra Sangwal
Department of Applied Physics
Lublin University of Technology
Poland

WILEY

This edition first published 2018
© 2018 John Wiley & Sons, Inc.

All rights reserved. No part of this publication may be reproduced, stored in a retrieval system, or transmitted, in any form or by any means, electronic, mechanical, photocopying, recording or otherwise, except as permitted by law. Advice on how to obtain permission to reuse material from this title is available at http://www.wiley.com/go/permissions.

The right Keshra Sangwal to be identified as the author of this work has been asserted in accordance with law.

Registered Office
John Wiley & Sons, Inc., 111 River Street, Hoboken, NJ 07030, USA

Editorial Office
111 River Street, Hoboken, NJ 07030, USA

For details of our global editorial offices, customer services, and more information about Wiley products visit us at www.wiley.com.

Wiley also publishes its books in a variety of electronic formats and by print-on-demand. Some content that appears in standard print versions of this book may not be available in other formats.

Limit of Liability/Disclaimer of Warranty
In view of ongoing research, equipment modifications, changes in governmental regulations, and the constant flow of information relating to the use of experimental reagents, equipment, and devices, the reader is urged to review and evaluate the information provided in the package insert or instructions for each chemical, piece of equipment, reagent, or device for, among other things, any changes in the instructions or indication of usage and for added warnings and precautions. While the publisher and authors have used their best efforts in preparing this work, they make no representations or warranties with respect to the accuracy or completeness of the contents of this work and specifically disclaim all warranties, including without limitation any implied warranties of merchantability or fitness for a particular purpose. No warranty may be created or extended by sales representatives, written sales materials or promotional statements for this work. The fact that an organization, website, or product is referred to in this work as a citation and/or potential source of further information does not mean that the publisher and authors endorse the information or services the organization, website, or product may provide or recommendations it may make. This work is sold with the understanding that the publisher is not engaged in rendering professional services. The advice and strategies contained herein may not be suitable for your situation. You should consult with a specialist where appropriate. Further, readers should be aware that websites listed in this work may have changed or disappeared between when this work was written and when it is read. Neither the publisher nor authors shall be liable for any loss of profit or any other commercial damages, including but not limited to special, incidental, consequential, or other damages.

Library of Congress Cataloging-in-Publication Data

Names: Sangwal, Keshra, author.
Title: Nucleation and crystal growth: metastability of solutions and melts / by Keshra Sangwal.
Description: First edition. | Hoboken, NJ : John Wiley & Sons, 2018. | Includes bibliographical references and index. |
Identifiers: LCCN 2018008606 (print) | LCCN 2018013537 (ebook) | ISBN 9781119461586 (pdf) | ISBN 9781119461593 (epub) | ISBN 9781119461579 (cloth)
Subjects: LCSH: Crystal growth. | Nucleation.
Classification: LCC QD921 (ebook) | LCC QD921 .S255 2018 (print) | DDC 548/.5–dc23
LC record available at https://lccn.loc.gov/2018008606

Cover Design: Wiley
Cover Images: © Evgeny Sergeev/Getty Images; © Keshra Sangwal

Set in 10/12pt Warnock by SPi Global, Pondicherry, India

Printed in the United States of America

10 9 8 7 6 5 4 3 2 1

In memory
of those
I miss

From goodness arises knowledge
and from passion greed,
negligence and error from dullness,
as also ignorance.

The Bhagavadgita

Contents

Preface *xiii*
Acknowledgments *xix*
List of Frequently Used Symbols *xxi*

1 Structure and Properties of Liquids *1*
1.1 Different States of Matter *1*
1.2 Models of Liquid Structure *6*
1.3 Water and Other Common Solvents *12*
1.4 Properties of Solutions *15*
1.4.1 The Solvation Process *17*
1.4.2 The Concentration of Solutions *19*
1.4.3 Density and Thermal Expansivity of Solutions *21*
1.4.4 Viscosity of Solutions *27*
1.5 Saturated Solutions *35*
1.6 High-Temperature Solvents and Solutions *43*
References *46*

2 Three-dimensional Nucleation of Crystals and Solute Solubility *49*
2.1 Driving Force for Phase Transition *49*
2.2 3D Nucleation of Crystals *54*
2.2.1 Nucleation Barrier *55*
2.2.2 Nucleation Rate *56*
2.2.3 3D Heterogeneous Nucleation *60*
2.3 Ideal and Real Solubility *63*
2.3.1 Basic Concepts *63*
2.3.2 Examples of Experimental Data *68*
2.3.3 Mathematical Representation of Solute Solubility in Solvent Mixtures *76*
2.4 Solute Solubility as a Function of Solvent–Mixture Composition *78*
2.4.1 A Simple Practical Approach *78*
2.4.2 Physical Interpretation of the δ Factor and Solvent Activity *87*

2.4.3 Preferential Solvation of Solute by Solvents *89*
2.5 Solid–Solvent Interfacial Energy *92*
2.6 Solubility and Supersolubility *96*
References *101*

3 Kinetics and Mechanism of Crystallization *105*
3.1 Crystal Growth as a Kinetic Process *106*
3.2 Types of Crystal–Medium Interfaces *107*
3.3 Thermodynamic and Kinetic Roughening of Surfaces *108*
3.4 Growth Kinetics of Rough Faces *111*
3.5 Growth Kinetics of Perfect Smooth Faces *112*
3.6 Growth Kinetics of Imperfect Smooth Faces *116*
3.6.1 Surface Diffusion and Direct Integration Models *117*
3.6.2 Bulk Diffusion Models *119*
3.6.3 Growth at Edge Dislocations *120*
3.7 Simultaneous Bulk-Diffusion and Surface-Reaction Controlled Growth *121*
3.8 Effect of Impurities on Growth Kinetics *123*
3.9 Overall Crystallization *127*
3.9.1 Basic Theoretical Equations *129*
3.9.2 Polynuclear Crystallization *133*
3.9.2.1 Instantaneous Nucleation Mode *134*
3.9.2.2 Progressive Nucleation Mode *135*
3.9.2.3 Trends of Overall Crystallization Curves *136*
3.9.2.4 Some Comments on the KJMA Theory *138*
3.9.3 Mononuclear Crystallization *139*
3.9.4 Effect of Additives on Overall Crystallization *139*
References *140*

4 Phase Transformation and Isothermal Crystallization Kinetics *145*
4.1 Nucleation and Transformation of Metastable Phases *146*
4.1.1 Thermodynamics of Crystallization of Metastable Phases *147*
4.1.2 Transformation Kinetics of Metastable Phases *151*
4.1.3 Transformation of Metastable Phases According to KJMA Theory *158*
4.1.4 Effect of Solvent on Transformation of Metastable Phases *160*
4.2 Some Non-KJMA Models of Isothermal Crystallization Kinetics *170*
4.2.1 Approach Involving Formation of an Amorphous Precursor *170*
4.2.2 Model of Mazzanti, Marangoni, and Idziak *175*
4.2.3 Gompertz's Model *178*
4.2.4 Model of Foubert, Dewettinck, Jansen, and Vanrolleghem *179*
4.3 Comparison of Different Models of Isothermal Crystallization Kinetics *181*
References *186*

5 Nonisothermal Crystallization Kinetics and the Metastable Zone Width *189*
5.1 Theoretical Interpretations of MSZW *191*
5.1.1 Nývlt's Approach *192*
5.1.2 Kubota's Approach *194*
5.1.3 Self-Consistent Nývlt-Like Equation of MSZW *195*
5.1.4 Approach Based on the Classical Theory of 3D Nucleation *197*
5.1.5 Approach Based on Progressive 3D Nucleation *199*
5.1.6 Approach Based on Instantaneous 3D Nucleation *202*
5.2 Experimental Results on MSZW of Solute–Solvent Systems *202*
5.2.1 Dependence of Dimensionless Supercooling on Cooling Rate *204*
5.2.2 Effect of Detection Technique on MSZW *210*
5.2.3 Relationships between β and Z and between Φ and F *212*
5.2.4 Relationship between Dimensionless F_1 and Crystallization Temperature *220*
5.2.5 Dependence of Parameters Φ and F on Saturation Temperature T_0 *222*
5.2.6 Physical Significance of E_{sat} and Its Relationship with ΔH_s *225*
5.2.7 The Nucleation Order m *230*
5.3 Isothermal Crystallization *232*
5.4 Effect of Additives on MSZW of Solutions *232*
5.4.1 Some General Features *233*
5.4.2 Theoretical Considerations *236*
5.4.2.1 Approach Based on Classical Nucleation Theory *236*
5.4.2.2 Final Expressions for Analysis of Experimental Data *238*
5.4.3 Some Examples of Effect of Impurities on MSZW *239*
5.4.3.1 Boric Acid Aqueous Solutions *239*
5.4.3.2 KDP Aqueous Solutions *244*
5.4.3.3 POP-Acetone Solutions Containing PPP Additive *246*
5.4.4 Dependence of Maximum Supersaturation Ratio on Impurity Concentration *250*
5.4.5 Solute-Additive Binding Energies and MSZW of Systems *252*
5.5 Effects of Some Other Factors on MSZW of Solutions *255*
5.5.1 Effect of Stirring and Ultrasound on MSZW *255*
5.5.2 Effect of Solution Volume on MSZW *255*
5.6 Nonisothermal Crystallization Kinetics in Melts *259*
References *260*

6 Antisolvent Crystallization and the Metastable Zone Width *267*
6.1 Observation Techniques for Antisolvent Crystallization *268*
6.2 Light Intensity Measurements *270*
6.2.1 Some Experimental Data *270*
6.2.2 Processes Involved in Antisolvent Crystallization *274*

6.3 Temperature Measurements *276*
6.3.1 Some Experimental Data *276*
6.3.2 Kinetics of Temperature Increase *279*
6.3.3 Physical Interpretation of Temperature Changes of ADP Solutions with Antisolvent Feeding Time at Different Rates *286*
6.3.4 Origin of Two Minima and Maximum in Temperature Change ΔT During Antisolvent Crystallization *287*
6.3.5 Relationship Between Different Temperature Changes, Antisolvent Feeding Rate, and Antisolvent Content *288*
6.3.6 Comparison of Light-intensity and Temperature Measurements *291*
6.4 Effect of Antisolvent Composition on Nucleation Rate *296*
6.5 Different Approaches of MSZW *298*
6.5.1 Modified Nývlt-like Approach *298*
6.5.2 Kubota's Approach *299*
6.5.3 Another Derivation of Nývlt-like Equation *300*
6.5.4 Approach Based on Classical Theory of 3D Nucleation *302*
6.6 Experimental Data of MSZW in Antisolvent Crystallization *303*
6.6.1 Analysis of Experimental $\Delta x_{\max}(R_A)$ Data *304*
6.6.2 Effect of Detection Technique on MSZW *312*
6.6.3 Effect of Stirring on MSZW *315*
6.6.4 Threshold and Limiting Antisolvent Addition Rates *318*
6.7 Combined Antisolvent/Cooling Crystallization *319*
References *321*

7 Induction Period for Crystallization *325*
7.1 Theoretical Background *327*
7.1.1 Theoretical Interpretation of Induction Period *328*
7.1.2 Some Other Relations *331*
7.1.3 Basic Equations *333*
7.2 Induction Period for Isothermal Crystallization *333*
7.2.1 Crystallization from Solutions *333*
7.2.2 Crystallization from the Melt *338*
7.3 Induction Period in Antisolvent Crystallization *343*
7.4 Induction Period for Nonisothermal Crystallization *345*
7.4.1 Crystallization from Solutions *345*
7.4.2 Effect of Impurities on Crystallization from Solutions *349*
7.4.3 Crystallization from the Melt *354*
References *358*

8 Ostwald Ripening, Crystal Size Distribution, and Polymorph Selection *361*
8.1 Supersaturation Decay During Antisolvent Crystallization *362*
8.1.1 General Trends *362*
8.1.2 Kinetics of Supersaturation Decay *362*

8.1.3 Relationship between Constant K and Antisolvent Feeding Rate R_A *367*
8.2 Solvation and Desolvation Processes *372*
8.2.1 Origin of Minima in $\Delta T_{sw}(t)$ Plots *373*
8.2.2 Kinetics of Evolution of Minima in $\Delta T_{sw}(t)$ Plots *374*
8.3 Evolution of Desupersaturation Curves *383*
8.4 Crystal Morphology *388*
8.5 Growth Rate Dispersion *396*
8.6 Ostwald Ripening *398*
8.7 Crystal Size Distribution *403*
8.8 Control of Phase and Size of Crystallizing Particles *412*
References *417*

9 Glass Formation and Crystallization Processes *423*
9.1 Glass Formation by Cooling of Melts *424*
9.2 Temperature Dependence of Viscosity and the Glass Transition Temperature *426*
9.3 Composition Dependence of Glass Transition Temperature *431*
9.4 Relationship between Glass Transition Temperature and Metastable Zone Width of Solutions *435*
9.5 Metastable Zone Width of Melts and Glass Formation *438*
9.5.1 Derivation of Basic Equations *438*
9.5.2 Effect of Melt Viscosity and Additives on Z and F Parameters *441*
9.5.3 Calculations of R_{Llim}, Z, F, and T_N for Molten Elements and Electrolytes *444*
9.5.4 Relationship between T_g and T_m for Various Substances *446*
9.5.5 Comparison of Cooling Behavior of Melts and Electrolyte Solutions *449*
References *451*

Appendix A Volumetric Thermal Expansion Coefficient of Melts *453*
References *455*

Appendix B Relationship between α_V and Other Physical Properties *457*
B.1 Molten Elements *457*
B.2 Molten Halite-Type Electrolytes *457*
Reference *461*

Appendix C Relationship between Densities d_m of Molten Metals and Electrolytes and Atomic Mass M *463*
Reference *464*

Index *465*

Preface

Crystallization of various inorganic and organic substances from solutions and melts has drawn increasing interest during the last seven decades for different reasons. Investigations have been concentrated on the growth of good-quality large, single crystals for their application in the fabrication of electronic and optoelectronic devices and understanding the role of crystallization conditions in the formation of the desired end product in different industries. For example, in the fertilizer industry, important requirements that the crystallized solid-state product has to fulfill are its phase or polymorph, growth morphology, and size distribution, because they ultimately determine the product's solid-state properties such as separation, flow, compaction, dissolution, and packing. The product should be stable during its storage life and should have such a solubility that it is easily devoured by the earth and plants. In the pharmaceutical industry, the requirements are even more stringent, because the *in vivo* performance of a drug depends not only on the polymorph but also on its oral bioavailability. In the food industry, it is the overall quality of products, like chocolates, confectionary coatings, and dairy products such as butter and cream, which is determined by the crystallization of fats contained in them. Similarly, cessation of flow of biodiesels in fuel lines and filters at low temperature by their clogging due to the formation, growth, and agglomeration of crystals of saturated fatty compounds contained in the fuel is an important issue in the petroleum industry. Another closely related problem is the formation of mineral scales in oil-extraction pipelines, heat-exchangers, house appliances, water pipes, mining and mineral processing, and desalination plants.

It is well known that the solubility of some compounds either increases or decreases with an increase in temperature in the entire temperature interval used for solubility measurements, whereas that of others exhibits sharp or diffuse breaks at certain temperatures due to phase changes associated with changes in the crystallographic structure and chemical composition of the crystallizing compound. There are also compounds which show negligible change in the solubility with temperature. Therefore, depending on the nature of curves of the temperature dependence of the solubility compounds,

different ways are required to create excess solute concentration, which is a measure of supersaturation for the crystallization of the solute in its solution saturated at a particular temperature in a solvent. For compounds, which have a reasonable temperature dependence of solubility in a particular temperature interval and do not undergo phase changes, supersaturation can be created simply by changing the temperature of their saturated solution. In this case, if T_0 is the initial temperature of a saturated solution containing a given compound and T is the temperature of crystallization, the temperature difference $\Delta T = T_0 - T$ is a measure of supersaturation and is the basis of crystallization by *isothermal and polythermal methods*. In the polythermal method, also known as *cooling crystallization*, the saturated solution is cooled at a known rate R_L, whereas in the isothermal method the saturated solution is cooled very fast (i.e. $R_L \rightarrow \infty$) to a predefined temperature where crystallization is carried out.

For compounds whose solubility in a given solvent changes poorly with temperature, supersaturation in the solution cannot be achieved by changing solution temperature. In such cases, supersaturation in the solution at a given temperature can be created by adding another solvent, called antisolvent, in which the compound is poorly soluble. Supersaturation is generated by the antisolvent because of the solubility difference of the solute in the two solvents. If the solution temperature containing a solute saturated in a given solvent is T_0, the antisolvent content Δx is a measure of supersaturation. Crystallization in which supersaturation is created by adding an antisolvent to a saturated solution at a constant temperature is known as *antisolvent crystallization*. Antisolvent crystallization is traditionally carried out at a predefined constant temperature either by feeding an antisolvent at a constant rate R_A to a saturated solution of a solute in a solvent in which it is fairly soluble or by feeding a known volume of saturated solution of the solute prepared in a solvent in which it is fairly soluble to a known volume of another solvent (i.e. antisolvent) in which the solute is poorly soluble. The latter approach is usually called *drowning-out crystallization*.

Supersaturation control is an important parameter for optimizing product qualities like purity, crystal size, crystal size distribution, and crystal shape during crystallization processes. Crystallization is carried out at some optimum supersaturation level lower than the maximum value of supersaturation at which intense nucleation occurs. The maximum value of supersaturation that a solute–solvent system can support defines its metastable zone width.

Metastable zone width of substances depends on a variety of factors such as saturation temperature, solvent used for preparation of supersaturated solutions, the presence of impurities dissolved in the solution, the presence of crystalline seeds in the solution, solution stirring and cooling rate of solution from saturation temperature in the polythermal method, and solvent addition rate in antisolvent crystallization. Consequently, understanding of the effect of

various factors on the width of metastable zone of a solute–solvent system has been a topic of constant interest.

During the last five decades, voluminous literature has emerged on the subject of determination and prediction of metastable zone width of a variety of systems. The first systematic studies reported, using the conventional polythermal method, data of the maximum supercooling ΔT_{max} of solutions saturated at known temperatures as a function of cooling rate R_L. Nývlt et al. (1985) have reviewed the literature published prior to 1984 on the metastable zone width of various systems. The experimental data of maximum supercooling ΔT_{max} for solute–solvent systems have traditionally been analyzed until now as a function of cooling rate R_L using the so-called Nývlt's equation, proposed in 1968, which contains two empirical parameters (i.e. nucleation order m and nucleation constant k_m). However, the physical significance of these parameters in Nývlt's equation has remained obscure until now. Therefore, interpretation of metastable zone width in terms of parameters containing well-defined physical quantities has been of theoretical and technological importance.

Since 2008, several papers have been devoted to the understanding of the effect of various experimental factors on the metastable zone width. In these papers, two types of approaches have been followed to explain the dependence of metastable zone width on different factors. The first type of approaches assumes the formation of critically-sized three-dimensional (3D) nuclei during the cooling of a solution below its saturation temperature T_0, but they differ in the way the 3D nucleation rate J depends on the developed solution supersaturation ln S. The quantity S, known as supersaturation ratio, is the ratio c/c_0, where c and c_0 are the actual and equilibrium solute (solubility) concentrations, respectively, in the solution. Most of the approaches assume that the nucleation rate J is related to the maximum supersaturation ln S_{max} by simple power law, i.e. $J \propto (\ln S_{max})^m$, while an approach based on the dependence of nucleation rate J on the maximum supersaturation ln S_{max} according to the classical 3D nucleation theory has also been proposed. The second type of approach is based on the concept of overall crystallization involving progressive and instantaneous nucleation mechanisms.

Increasing interest in the determination and theoretical interpretation of metastable zone width in antisolvent crystallization started relatively recently after the publication of a paper by O'Grady et al. (2007). These authors carried out measurements of metastable zone width in antisolvent crystallization of benzoic acid in a water–ethanol mixture and, following the classical approach of Nývlt for crystallization from solution by cooling at a constant rate (Nývlt et al., 1985), first derived a relation, which they called modified Nývlt relation, between the maximum antisolvent composition Δx_{max} added to a solution saturated at a given temperature T, and the rate of addition of the antisolvent R_A. As in cooling crystallization, here also most relations were derived on the assumption that 3D

nucleation rate J during antisolvent crystallization follows an empirical power-law dependence on antisolvent content Δx.

The formation of crystalline nuclei and their subsequent development into large-sized crystals in the liquid phase, whether a supersaturated solution or a supercooled melt, determine the efficiency of crystallization processes. These processes are intimately connected with the metastable zone width of the liquid phase. Since crystallization is carried out at supersaturations lower than the maximum value of supersaturation corresponding to the metastable zone width, understanding of processes of crystallization of inorganic and organic compounds from solutions and melts is of immense importance. Some of the topics related to lower supersaturation levels are: Induction period for crystallization (i.e. the time required for the onset of 3D nucleation) of crystalline phase from a solution of a given supersaturation, the evolution of overall crystallization with time, crystallization of metastable phases and phase transformation, and size distribution of crystalline particles.

Description of metastable zone width and processes and phenomena associated with metastability of solutions and melts is the subject matter of this book. Main emphasis is on low-temperature solutions, which are usually involved in crystallization in different industries, but melts are considered in view of the fact that crystallization of fats usually occurs from melts. The contents of the book reflect my own choice and my own involvement in the field during the last two decades. Starting from the basic knowledge of solutions and fundamentals of crystallization processes, different topics are organized and discussed in a general and unified way with appropriate support of published literature and illustrative figures. The presentation of contents of different chapters has been kept at the elementary level, with emphasis on the interpretation of different observations using basic concepts of nucleation and growth of crystals and undergraduate-level mathematics. However, nowhere I have made an attempt to survey the entire literature published on different topics.

The contents of the book can roughly be divided into three parts. The first part is introductory where basic concepts of structure and properties of liquids (Chapter 1), thermodynamics of solutions, solute solubility, and 3D nucleation of crystals (Chapter 2), and kinetics and mechanism of crystallization (Chapter 3) are outlined. The second part consists of four chapters, and gives an overview of experimental and theoretical aspects of isothermal crystallization (Chapter 4), nonisothermal crystallization (Chapter 5), antisolvent crystallization (Chapter 6), and induction period for isothermal and nonisothermal crystallization (Chapter 7). The last part addresses problems associated with the size distribution of crystals (Chapter 8) and metastability of molten metals and salts (Chapter 9). Influence of additives on different processes is also discussed. I have made every effort to make the book not only self-contained but also to make the contents of different chapters practically independent of each other.

The book is primarily addressed to graduate students as well as specialists in the fields of industrial crystallization, chemical engineering, materials science, and condensed matter physics, who are interested in looking for an overview of the fundamentals of metastable zone width and processes and phenomena associated with metastability of solutions and melts. It can also be used as a text for teaching elements of crystal growth at the undergraduate level to students of different specializations.

I have received immense benefit of ideas and concepts from the published works of numerous authors during the writing of this book. I have also used in the text a number of graphs published by different authors in various journals. I express my profound sense of gratitude to the authors whose works I have used in the book. I am also grateful to various publishers for their permission to use and reproduce various figures from journals and books published by them. The relevant sources of such works are duly cited whenever they appear in the text.

Keshra Sangwal

Lublin, January 2018

References

Nývlt, J., Söhnel, O., Matuchova, M., and Broul, M. (1985). *The Kinetics of Industrial Crystallization*. Prague: Academia.

O'Grady, D., Barret, M., Casey, E., and Glennon, B. (2007). The effect of mixing on the metastable zone width and nucleation kinetics in the anti-solvent crystallization of benzoic acid. *Chem. Eng. Res. Des.* 85: 945–952.

Acknowledgments

I am grateful to Professor Jolanta Prywer for her comments on the first three chapters, to Professor Ewa Mielniczek-Brzóska for going through the contents of the first draft of the entire book, to my son, Sunil, for pointing out numerous linguistic corrections in the text, and to Dr Jarosław Borc, Dr Kazimierz Wójcik, and Mr Krzysztof Zabielski for their assistance with the preparation of figures. I also thank my wife, Marta, for her constant support and patience.

Finally, I would like to express my thanks to Dr Thomas A. Scrace Jr, Associate Commissioning Editor, John Wiley & Sons, for enthusiastic support to undertake the publication of the book and to Ms Shirly Samuel, Project Editor, for coordinating its publication.

List of Frequently Used Symbols

a	diameter (size) of growth units; activity of a component
a_1, a_2	constants
A	viscosity coefficient A; surface area; constant
A_1	constant
b	slope; constant
b_1, b_2, ...	constants
B	viscosity coefficient B; parameter related to interfacial energy
B_1	constant
c	solute concentration
c_i	impurity (additive) concentration
C_p	heat capacity of liquid at constant pressure p
C_V	heat capacity of liquid at constant volume V
d	density; dimensionality of growing crystallites
D	diffusion coefficient
E	activation energy
E_a	activation energy for jump of ions/molecules in solution
E_sat	activation energy related to solute diffusion in solution
f	force constant for displacement of molecule in a crystal lattice; activity coefficient related to solute concentration in a solution; factor denoting the effect of impurity particles; the number of particles/aggregates per unit volume in saturated solution
f^*	kinetic factor associated with attachment of monomers to stable nucleus
Δf_a	excess activity coefficient due to ion–solvent interactions
F	parameter in CNT-based approach; activation energy for hole formation
F_1	parameter in CNT-based approach
G	Gibbs free energy
ΔG	free activation enthalpy; Gibbs free energy change
h	thickness of step
h_P	Planck constant

ΔH	change in enthalpy associated with a phase change
ΔH_b	enthalpy of boiling
ΔH_m	enthalpy of melting
ΔH_{mix}	enthalpy of mixing
ΔH_s	enthalpy of dissolution
I_n	normalized transmitted laser-beam intensity
J	rate of nucleation
J_s	rate of stationary nucleation
J_0	preexponential factor in equation of 3D nucleation
J_0, J_1, J_2	constants
k	constant; rate constant of reaction; Avrami constant
k_0	Coulombian proportionality constant
k_1, k_2, …	constants
k_B	Boltzmann constant
k_d	mass transfer coefficient by bulk diffusion
k_m	nucleation constant in Nývlt's approach
k_r	mass transfer coefficient by surface reaction
K	packing coefficient of solute in solution; rate constant
K_1, K_2	constants
K_L	Langmuir constant
L	constant relating the rate of temperature increase R_T to antisolvent feeding rate R_A
m	solute concentration in molality, factor related to wetting angle θ; mass; nucleation order in Nývlt's approach; fragility index
m^*	exponent in Kubota's approach
M	molar mass
n, N	number
N_A	Avogadro number
p	pressure; exponent
q	kinetic exponent in KJMA theory; elementary charge
Q_{diff}	differential heat of adsorption of impurity
ΔQ_{sw}	change in heat in solution due to temperature change ΔT_{sw}
r	radius of ion, hole, or two- or three-dimensional nucleus; ratio
R	growth rate of a face
R^2	best-fit parameter; correlation coefficient; goodness-of-the-fit parameter
R_A	antisolvent feeding rate
R_g	growth constant
R_G	gas constant ($R_G = k_B N_A$)
R_L	cooling rate of Solution or melt
R_s	radius of impurity particle
S	supersaturation ratio defined as the ratio of activities a/a_0 or concentrations c/c_0; entropy

ΔS	free activation entropy; entropy change
t	time
t_f	total transformation time for stable phase
t_{in}	induction period for 3D nucleation or crystallization
T	temperature
T_b	boiling point
T_g	glass transition temperature
T_m	melting point; temperature of melting
ΔT	temperature difference ($T - T_0$)
u	normalized temperature difference defined as the ratio of temperature difference $\Delta T = (T - T_0)$ to initial reference temperature T_0
v	displacement rate of step on F face
V	volume
w	bond energy per pair of atoms, ions, or molecules
x	mole fraction; parameter defined as the ratio of radius R_s of impurity particle to radius r_{2D} of 2D stable nucleus
x_0	average distance between kinks in a step ledge
Δx	antisolvent volume fraction in solution
X	composition of mixture of two solvents
y_0	average distance between neighboring steps on F face
$y(t)$	fraction of crystalline phase of mass $m(t)$ at time t from maximum solute mass m_{max} in solution or melt
z	valency of ions; Zeldovich factor
Z	number of nearest neighbors; parameter in CNT-based approach

Greek Symbols

α	surface entropy factor; empirical constant; fragility parameter related to fragility index m
$\alpha_1, \alpha_2, \ldots$	constants
α_{eff}	impurity effectiveness factor
α_V	volumetric thermal expansion coefficient
β	compressibility; constant; kink retardation factor; parameter in self-consistent Nývlt-like equation; stretched exponent
$\beta_0, \beta_1, \beta_2$	constants
β_l	kinetic coefficient for step displacement on F face
β_{surf}	kinetic coefficient for growth of rough face
γ	interfacial tension; solid–fluid interfacial energy
δ	thickness of diffusion layer; parameter relating melting entropies of two phases
$\delta_D(t)$	Dirac-delta function
δ_{max}	displacement distance of molecule from equilibrium position

ε	dielectric constant of liquid or solution; dimensionless activation energy at glass transition
ζ	constant
η	viscosity of liquid or solution
θ	wetting angle; surface coverage
Θ	time constant in KJMA theory
κ	shape factor for 3D nuclei; capillary length
λ	heat of crystallization; empirical constant; average diffusion distance in liquid
λ_s	average diffusion distance for adsorbed atoms/molecules on F face; dimensionless heat of solution
Λ	step retardation factor
μ	chemical potential of a phase or component; dipole moment
$\Delta\mu$	chemical potential difference associated with a phase change
π^*	dipolar polarizability
σ	supersaturation; dispersion in activation energy
τ	time lag until the formation of 3D nuclei; relaxation time; average jump time in liquid
ϕ	volume fraction of particles in viscous flow
ϕ, ϕ', ϕ''	numerical factors related to wetting angles
ϕ_V	specific volume; inverse of density d
Φ	apparent molar volume; parameter in self-consistent Nývlt-like equation
Ψ	parameter describing the strength of mutual interaction between liquid constituents
ω	interface energy increase; dimensionless interfacial energy
ω_u	parameter related to dimensionless interfacial energy ω and normalized temperature difference u in progressive nucleation-based approach
Ω	molecular volume

Subscripts

b	boiling
D	diffusion
eff	effective
g	glass
h	hole
lim	limiting
m	melting, melt
max	maximum
MN	mononuclear mechanism
MSZW	metastable zone width

N	nucleation
p	pressure p
PN	polynuclear mechanism
s	stable phase; solution
u	metastable or unstable phase
V	volume V
η	viscous flow
2D	two-dimensional
3D	three-dimensional

1

Structure and Properties of Liquids

A solution is a homogeneous mixture of physically combined two or more substances, which may be gaseous, liquid, or solid. A solution exhibits the same properties throughout its volume. The component that is present in excess is usually referred to as the solvent, whereas the other component combining with the former in different proportions is termed the solute. Under normal temperature and pressure conditions, solid NaCl, for example, dissolves in water forming its aqueous solution. Here, the solvent water is in the liquid state and is molten form of ice with its melting point $T_m = 0\ ^\circ C$. It is a common solvent used in solutions of numerous compounds for their crystallization and purification. Similarly, compounds like NaCl, which are present in the solid state under normal temperature and pressure conditions, exist in the liquid state above their melting point T_m and serve as solvents in high-temperature solution growth.

In this chapter, general features of the structure and properties of solvents and solutions are briefly described. For more information on the topics discussed here, the reader is referred to the literature (for example, see: Atkins, 1998; Bockris and Reddy, 1970; Eggers et al., 1964; Horvath, 1985; Mortimore, 2008; Stokes and Mills, 1965; Wright, 2007).

1.1 Different States of Matter

Under appropriate temperature and pressure conditions all elements and compounds can exist in vapor, liquid, and solid states. These states are characterized by the mean distance between the atoms and molecules composing them, and the ratio of the average potential energy of atoms/molecules to their kinetic energy is a characteristic parameter of the state. In the vapor state the atoms/molecules move randomly undergoing elastic collisions among themselves in the entire space available to them and the average distance between them is much larger than their size. The attractive forces between

Nucleation and Crystal Growth: Metastability of Solutions and Melts, First Edition.
Keshra Sangwal.
© 2018 John Wiley & Sons, Inc. Published 2018 by John Wiley & Sons, Inc.

the atoms/molecules are too small to keep them close to each other. In the liquid state, the average distance between the atoms/molecules is decreased to the extent that mutual attractive forces hold them close to each other. There is short-range order between nearest neighbors and both the number and the positions of nearest neighbors are, on an average, the same for all. However, the atoms/molecules in the liquid state have sufficient kinetic energy to jump from one position to the next. In the solid state, the distance between the neighboring atoms/molecules in the entire volume is similar to the average distance between them in the liquid state. In this case, the attractive forces are strong enough to keep them in their equilibrium positions despite their thermal motion and are of long-range order.

At a given pressure p, with an increase in temperature T, every solidified material first transforms into the liquid form at a temperature T_m, and this liquid thereafter begins to boil at temperature T_b and transforms into the vapor phase. Conversely, with a slow decrease in temperature, a material initially existing in the vapor phase condenses into the liquid phase at the temperature T_b, and the cooling of the liquid later solidifies at the temperature T_m and remains in this phase. At a given pressure p, the densities d of the solid and liquid phases decrease with increasing temperature T according to the relation:

$$d(T) = d_m - k(T - T_m), \tag{1.1}$$

where T_m is the melting point of the material, d_m is the density of the solid and the liquid at the melting temperature T_m, and k is a constant characteristic of the phase. Note that the value of the density d_m of a solid at T_m is always different from the density d_m of the molten liquid at T_m. From Eq. (1.1) one obtains the expression for the volumetric thermal expansion coefficient (also called volume thermal expansivity):

$$\alpha_V = \frac{k}{d_m} = -\frac{d - d_m}{d_m(T - T_m)} = -\frac{1}{d_m}\left(\frac{\Delta d}{\Delta T}\right), \tag{1.2}$$

where the density difference is $\Delta d = (d - d_m)$ and the temperature difference is $\Delta T = (T - T_m)$. If m is the mass of the solid or liquid material of volume V, using the definition of density $d = m/V$, $\mathrm{d}d/\mathrm{d}V = -m/V^2$, and the differential form of Eq. (1.2) rewritten in the form

$$\alpha_V = -\frac{1}{d}\left(\frac{\mathrm{d}d}{\mathrm{d}T}\right) = -\frac{1}{d}\left(\frac{\mathrm{d}d}{\mathrm{d}V}\right)_p\left(\frac{\mathrm{d}V}{\mathrm{d}T}\right)_p = \frac{V}{m}\left(-\frac{m}{V^2}\right)\left(\frac{\mathrm{d}V}{\mathrm{d}T}\right) = \frac{1}{V}\left(\frac{\mathrm{d}V}{\mathrm{d}T}\right), \tag{1.3}$$

one obtains

$$\frac{\Delta V}{V_0} = \alpha_V \Delta T. \tag{1.4}$$

where V and dV are the volume and the change in the volume, respectively, of the solid and the liquid. According to Eq. (1.4), the volume V of a solid and a liquid increases linearly with an increase in temperature T in contrast to Eq. (1.1), which predicts that their density d decreases linearly with increasing T.

The physical properties of liquids differ from those of solids. For example, melting of solids leads to an increase in their volume insignificantly (about 10%). Consequently, the average distance between their atoms/molecules after melting remains practically unchanged. In contrast to this, the volume thermal expansion coefficient α_V of solids is one-order lower than that in the liquid state. These differences in the physical properties of materials in the solid and liquid states are associated with differences in the nature of interactions between the atoms/molecules in the two states.

In order to compare the thermal properties of solids and liquids, it is convenient to consider their temperature dependence of the specific volume ϕ_V and the volume thermal expansion coefficient α_V. The specific volume ϕ_V, defined as inverse of density d (i.e. $\phi_V = 1/d$), is the measure of V of Eq. (1.4), whereas the thermal expansion coefficient α_V of the compound is related to density d by Eq. (1.3). Figure 1.1 illustrates the dependence of specific volume ϕ_V on temperature T of the commonly used solvent water and its solid-phase ice. From the figure it may be noted that:

1) At 0 °C the specific volume ϕ_V of ice is about 10% higher than that of water, and its values for ice increases linearly with temperature, with slope

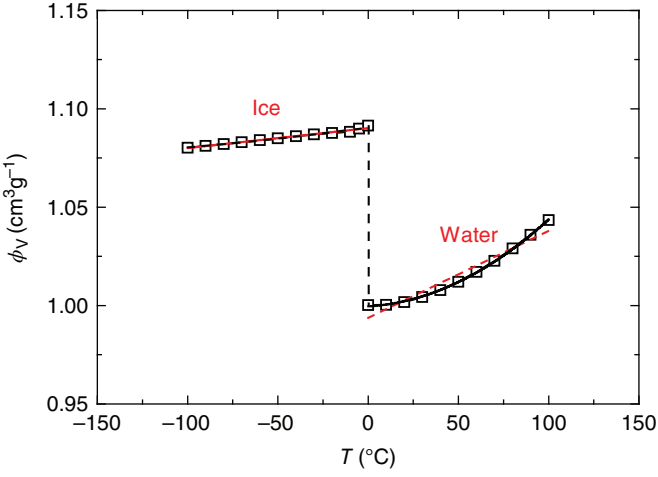

Figure 1.1 Dependence of specific volume ϕ_V on temperature T of water and ice. Data of density d for ice from www.EngineeringToolBox.com accessed 12 January 2017, and for water from Lide (1996/1997). For water solid, a curve is drawn according to Eq. (1.5), whereas the dashed curve shows a linear dependence.

$1.014 \cdot 10^{-4}$ $cm^3 \cdot g^{-1} \cdot K^{-1}$. Note that it is immaterial here whether the units of ϕ_V are $cm^3 \cdot g^{-1} \cdot K^{-1}$ or $cm^3 \cdot g^{-1} \cdot {}^\circ C^{-1}$ because we are concerned with temperature difference ΔT.

2) The value of ϕ_V for water increases up to about 30 °C practically linearly with temperature with a slope equal to that for ice, but beyond this temperature its value increases much rapidly practically following a second-order dependence:

$$\phi_V = \phi_{V0} + a_1(T - T_0) + a_2(T - T_0)^2, \tag{1.5}$$

where $T_0 = 273.15$ K, $\phi_{V0} = 0.9996(\pm 0.0003)$ $cm^3 \cdot g^{-1}$, $a_1 = 5.441(\pm 1.347) \cdot 10^{-5}$ $cm^3 \cdot g^{-1} \cdot K^{-1}$, $a_2 = 3.874(\pm 0.130) \cdot 10^{-6}$ $cm^3 \cdot g^{-1} \cdot K^{-2}$, and T is taken in K.

The above observations are associated with the difference in the structures of ice and water. An individual water molecule is nonlinear with the H—O—H angle of about 105° and the distribution of the four pairs of electrons of the six electrons from oxygen and the two electrons from hydrogen atoms is in four approximately equivalent directions. However, the oxygen atom is not situated at the center of the tetrahedron. Thus, a water molecule may be considered an electric dipole. This property of water molecules gives an open structure to ice lattice. The ice lattice consists of oxygen atoms lying in layers with each layer forming a network structure of open hexagonal rings composed of associated water molecules (see Figure 1.2). With an increase in temperature of network water, a molecule breaks its hydrogen bonds with the network and moves into interstitial regions. Thus, in liquid water there are networks of associated water molecules as well as certain fraction of free, unassociated water molecules. With increasing temperature more free, unassociated water molecules are broken from the associated network structure such that the fraction of unassociated water molecules increases at the expense of associated water molecules of the network structure. This results in increasing specific volume ϕ_V of liquid water where its value is determined by the ice and the free, unassociated water structures in the region below and above about 25 °C, respectively.

Figure 1.3 illustrates the dependence of volume thermal expansivity α_V on temperature T of ice and water. As expected from the nature of vibrations of water molecules in ice and liquid water, the expansion coefficient α_V is practically constant at $9.4 \cdot 10^{-5}$ K^{-1} up to −30 °C and then drops to the value of liquid water. For liquid water the value of α_V rapidly increases with temperature and approaches $7.5 \cdot 10^{-4}$ K^{-1} at 100 °C, following the binomial relation:

$$\alpha_V = \alpha_{V0} + \alpha_1(T - T_0) + \alpha_2(T - T_0)^2, \tag{1.6}$$

where $T_0 = 273.15$ K, $\alpha_{V0} = -3.13(\pm 1.23) \cdot 10^{-5}$ K^{-1}, $\alpha_1 = 1.207(\pm 0.057) \cdot 10^{-5}$ K^{-2}, $\alpha_2 = -4.49(\pm 0.55) \cdot 10^{-8}$ K^{-3}, and the temperature T is taken in K. The difference in the trends of the temperature dependence of α_V of ice and liquid water is obvious and is associated with their structures.

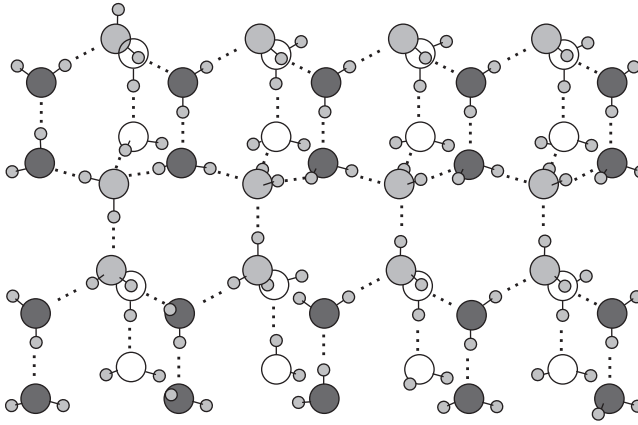

Figure 1.2 Network structure of ice with large interstitial spaces capable of free, unassociated water molecules. Structure of a free water molecule is also shown. Large and small circles denote oxygen and hydrogen atoms, respectively. Solid lines represent covalent bonds, whereas dotted lines represent hydrogen bonds. Dark, gray, and open oxygen atoms represent first, second, and third levels of water molecules parallel to the plane of the paper. Oxygen atoms lie in layers perpendicular to the plane of the paper in a direction parallel to the shorter edge (i.e. the *x* direction), with each layer forming a network structure of open hexagonal rings composed of water molecules joined by hydrogen bonds. Internet source of image file is unknown.

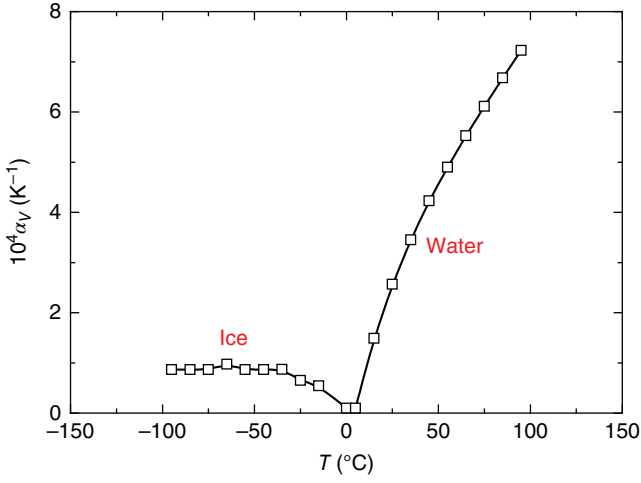

Figure 1.3 Dependence of volume thermal expansivity α_V on temperature T of water and ice. Sources of data of density d as given in Figure 1.1.

The formation of crystalline nuclei and the growth of these nuclei occur in the liquid phase. These processes of nucleation and growth are usually called crystallization processes. The liquid for crystallization can be a melt of an element or a compound itself or a solution prepared at a particular temperature by dissolving the element or the compound, called the solute, in a suitable nonreactive solvent. In this chapter, some general features of common solvents and solutions used for the crystallization of different inorganic and organic compounds are described, using typical examples of dilute, saturated, and supersaturated solutions of the compounds. Because of difficulties in finding appropriate solvents for the preparation of solutions of elements and lack of interest in their crystallization from solutions, they are not considered here.

1.2 Models of Liquid Structure

All solvents used in the preparation of solutions of different solutes for their crystallization are composed of molecules of various sizes. Some of the solvents used in crystallization from solutions of inorganic and organic compounds and their properties are listed in Table 1.1.

The simplest solvent is water composed of water molecules (molecular weight 18) while butanol, glycerol, and *N*-methyl-2-pyrrolidine (NMP), with molecular weights 74, 92, and 99, respectively, are solvents composed of relatively complex molecules. Some general trends of the different properties of these solvents may be noted:

1) Water has relatively high density d, high viscosity η, high dielectric constant ε, high melting point T_m, and high boiling point T_b than the corresponding properties of the lowest alcohols like methanol and ethanol.
2) Simple alcohols have roughly the same density d at 20 °C, whereas melting point T_m and dielectric constant ε decrease, and boiling point T_b and viscosity η increase with increasing molecular weight.
3) Normal alcohols like 1-proponol and 1-butanol have slightly higher density, higher dielectric constant ε, and higher boiling point T_b than those of iso-alcohols 2-propanol and 2-butanol. However, viscosity η and melting point T_m of normal alcohols are lower than those of iso-alcohols.
4) Other high carbon-containing solvents like ethylene glycol, glycerol, and NMP have high density d, high viscosity η, high dielectric constant ε, and relatively high melting point T_m and boiling point T_b than those of simple alcohols.

The aforementioned differences in the properties of the solvents are associated with the structure of their molecules. The structure of molecules determines not only the nature of interactions holding the molecules in the liquid

Table 1.1 Properties of some commonly used solvents.

Solvent	MW	d ($g \cdot cm^{-3}$)[a]	η (mPa s)[b]	ε (–)[a]	T_m (°C)	ΔH_m ($kJ \cdot mol^{-1}$)	T_b (°C)
Water (H_2O)	18.0	0.9982	0.890	80.1	0	6.01	100
Acetone (C_2H_6CO)	50.08	0.790	0.306	21.01	–95.0	26.53	56.3
MeOH (CH_3OH)	32.04	0.7914	0.544	33.3	–97.6	3.18	64.6
EtOH (C_2H_5OH)	46.07	0.7893	1.074	25.3	–114.1	5.02	78.2
1-PrOH (C_3H_7OH)	60.10	0.8035	1.945	20.8	–126.1	5.2	97.2
2-PrOH (C_3H_7OH)	60.10	0.7855	2.038	20.18	–89.5	5.37	82.3
1-BuOH (C_4H_9OH)	74.12	0.8098	2.544	17.84	–89.8	9.28	117.7
2-BuOH (C_4H_9OH)	74.12	0.8063	3.096	17.26	–114.7	—	99.5
Ethylene glycol ($C_2H_6O_2$)	62.07	1.1088	16.1	41.4	–13.0	—	197.3
Glycerol ($C_3H_8O_3$)	92.09	1.2613	18.2	46.53	18.2	8.48	290
NMP (C_5H_9NO)	99.13	1.0230	—	32.55	–24.0	202	—

BuOH, butanol; EtOH, ethyl alcohol; MeOH, methyl alcohol; MW, molecular weight; NMP, *N*-methyl-2pyrrolidine; PrOH, propanol. Other symbols are: density d, viscosity η, dielectric constant ε, boiling temperature T_b, melting temperature T_m, and enthalpy of melting ΔH_m.
[a] 20 °C.
[b] 25 °C.

state and their packing but also determines their motion in the liquid state and processes of solidification and evaporation.

Depending on the structure of molecules composing different liquids, the liquids may be classified as polar, nonpolar, and apolar. Molecules of a polar liquid are uncharged with an overall dipole moment, which may be the result of one individual polar bond within the molecule. Molecules of a nonpolar liquid are uncharged neutral with a zero dipole moment but contain bonds that are polar. Molecules of apolar liquids are neutral with an overall zero dipole moment. A measure of the polar or nonpolar nature of molecules composing a liquid is its dielectric constant ε (see Table 1.1).

Solidification and evaporation of liquids occur at their standard melting point T_m and boiling point T_b with corresponding changes in the heat energies ΔH_m and ΔH_b, respectively, under atmospheric pressure, and are associated with the entropy changes $\Delta H_m/T_m$ and $\Delta H_b/T_b$, respectively. At equal pressures the entropy of the phase stable at higher temperatures is always higher than that at lower temperatures. Therefore, vaporization of different liquids leads to an increase in their entropy at their normal boiling points and the value of this entropy is higher than that in solidification, i.e. $\Delta H_b/T_b > \Delta H_m/T_m$.

Vaporization entropy $\Delta H_b/T_b \approx 10.5R_G \approx 88$ kJ mol^{-1}·K^{-1} for many organic liquids is referred to as normal liquids and the above relationship is called *Trouton's rule*. Here, the gas constant $R_G = k_B N_A$, where k_B is the Boltzmann constant and N_A is the Avogadro number. However, this vaporization entropy $\Delta H_b/T_b$ is about $5R_G$ for simple monoatomic liquids, $7.5R_G$ for acetic acid, and up to about $15R_G$ for water, alcohols, and other hydrogen-bonded liquids, and several bivalent chlorides such as $PbCl_2$ and $ZnCl_2$, which behave as associated liquids. The trends of melting entropy $\Delta H_m/T_m$ of different substances are also similar to those of the vaporization entropy $\Delta H_b/T_b$, but their values are lower than those of $\Delta H_b/T_b$ for a given substance. For substances that behave as normal liquids, $\Delta H_m/T_m$ lies between about R_G and $2R_G$, but for associated liquids like water and bivalent chlorides, its value is up to $5R_G$. In the case of alkali halides and many organic compounds, $\Delta H_m/T_m$ is about $3R_G$ and $6R_G$, respectively (Sangwal, 1989; see Section 2.5).

There are also many organic liquids with $\Delta H_m/T_m < R_G$ but they have relatively a low number n of C atoms in their composition. Figure 1.4 shows the data of $\Delta H_m/R_G T_m$ as a function of the number n of carbon atoms in the chemical formula of some simple alcohols and alkanes, with $n \leq 5$ and $n \leq 10$, respectively. If the data for methane, butane, and nonane are excluded, the data for alkanes may be represented by the relation:

$$\frac{\Delta H_m}{R_G T_m} = 0.08 + 0.085n. \tag{1.7}$$

Except for pentanol, 2-propanol, and glycerol, the data for alcohols also follow this relation. The above relation holds for linear alcohols and alkanes, and deviations may be attributed to errors in the data and nonlinear nature of their chains. The linear dependence of $\Delta H_m/R_G T_m$ on the carbon number n of alkanes and alcohols suggests that, starting from methane and methanol, the melting entropy of these liquids is additive with entropy increment $(\Delta H_m/T_m)/n = 0.085R_G$ and energy increment $\Delta H_m/n = 0.085R_G T_m$ per CH_2— group. A constant $\Delta H_m/R_G T_m = 6$ for organic compounds suggests that melting of organic compounds involves strong association of their molecules.

In order to understand different properties of solvents, following the models for molten liquid electrolytes, discussed by Bockris and Reddy (1970), different models may be considered. Since a liquid can be obtained either by melting its

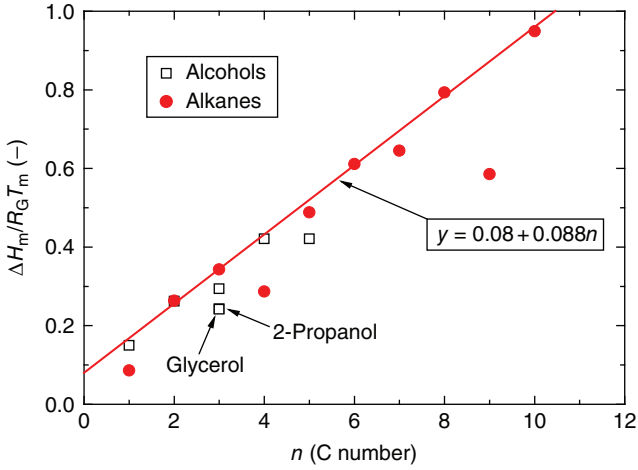

Figure 1.4 Relationship between $\Delta H_m/R_G T_m$ and number n of carbon atoms in the chemical formula of some simple alcohols and alkanes. Linear plot represents data according to relation (1.7). *Source:* Original data from Lide (1996/1997).

crystalline solid or by cooling its vapor, there are two ways of looking at the models of liquids. Thus, there are *lattice-based* and *gas-based models* for a liquid. The main observation that a model should explain is an increase in the volume upon melting and roughly the same distance between the molecules in the crystalline and liquid phases. The volume increase without a change in the mean distance between the neighboring molecules suggests that melting of the crystalline solid introduces empty space into the liquid. It is the mode of description of this empty space that differentiates one model from another.

The simplest model of a liquid is based on the concept of injection of vacancies known as Schottky defects in a crystalline lattice. Vacancies are produced in the lattice by removal of atoms/molecules from lattice sites in the interior to the crystal surface (Figure 1.5a). Vacancies are produced randomly inside the crystal with simultaneous volume increase through displacement of removed atoms/molecules from lattice sites to the crystal surface. As the temperature of the solid is increased, the number of vacancies increases as a result of the thermal motion of atoms/molecules of lattice sites and at the melting point they are so numerous in the lattice that the long-range order disappears. The vacancies are roughly of the size of displaced atoms/molecules. Since vacancies are produced at lattice sites, one refers to the *quasi-lattice model*.

When numerous vacancies are introduced in the crystalline lattice, the definition of crystalline lattice as a three-dimensional array of points no longer holds. Now, atoms/molecules and vacancies of the molten system may be considered to be distributed randomly. In other words, the vacancies form

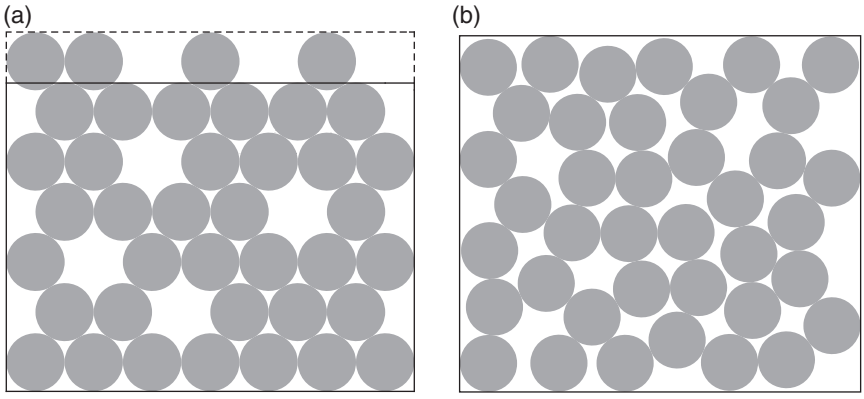

Figure 1.5 Schematic illustration of: (a) vacancies produced in crystal lattice and (b) randomly located holes in a liquid.

empty regions, called *holes*, of various sizes, and atoms/molecules and differently-sized empty spaces are randomly close-packed in the liquid volume (Figure 1.5b). This is the *hole* model. The process of formation of holes is somewhat similar to the formation of vacancies in the crystal lattice and is associated with the thermal motion of atoms/molecules constituting their clusters. However, in contrast to the creation of vacancies by removal of an atom/molecule from far away sites in the interior of the lattice to the crystal surface, ions of clusters are displaced relative to each other by amounts similar to their displacement. Since thermal motion is random and occurs everywhere in the liquid volume, holes are also produced randomly in the liquid. However, holes continuously appear and disappear, move, coalesce to form large holes, and disintegrate into smaller holes.

When a gas transforms into the liquid state, the freedom of motion of its atoms/molecules is restricted such that the motion of each of its atoms/molecules is confined within its cell of identical volumes (Figure 1.6). This is the basis of the *simple cell theory*. Every atom/molecule has a free volume available for its motion. If V is the volume of the liquid containing N atoms/particles and v_0 is the volume of each atom/molecule considered as a rigid sphere, the free volume v_f available to each atom/particle for its motion is

$$v_f = \frac{V}{N} - v_0, \tag{1.8}$$

where V/N is the average volume available to each atom/particle.

The restriction in the motion of atoms/molecules to their cells does not explain the transport properties of liquid, entropy of fusion, and volume expansion on melting. These difficulties are overcome in the *liquid free-volume*

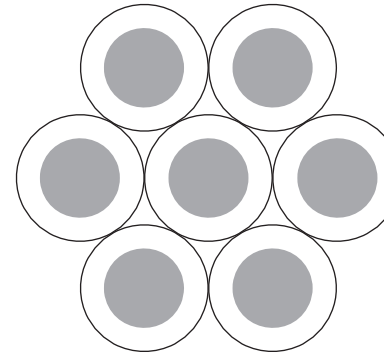

Figure 1.6 Free volume available for the motion of its atoms/molecules in a liquid.

theory. According to this theory, the liquid free volume is not distributed equally to each atom/molecule but there is a statistical distribution of free volumes among them and thermal forces are responsible for the statistical distribution of these free volumes.

The movement of an atom/molecule from one position to another not only results in the expansion of the cell of the moving atom/molecule and an increase in its energy but also leads to the contraction of the neighboring cell and a decrease in its energy. This explains the transport properties of liquids. An increase in the volume that occurs on melting implies an increase in the free volume. This means that, except for the free space in the liquid, the atoms/molecules have the same inter-neighbor distance.

The hole model explains most of the experimental observations. Some of the characteristics and predictions of this model are briefly described below.

The formation of holes in the liquid as a result of thermal fluctuations is due to an increase in the vibrations of the liquid molecules around their temporary equilibrium positions. According to the hole theory, the average hole radius r_h is given by (Bockris and Reddy, 1970)

$$r_h = 0.51\left(\frac{k_B T}{\gamma}\right)^{1/2}, \tag{1.9}$$

where k_B is the Boltzmann constant and γ is the surface tension of the melt. With the values of macroscopic surface tensions γ of different molten salts given in Eq. (1.9), estimates of the values of r_h show that a typical hole is roughly of the size of an ion.

The dependence of self-diffusion coefficient D and viscosity η of simple liquid electrolytes on temperature T follows an Arrhenius-type relation with activation energy E_D for diffusion and activation energy E_η for viscous flow, respectively, related to the melting point T_m by

$$E_D = E_\eta = 3.7 R_G T_m. \tag{1.10}$$

Relation (1.9) implies a relationship between the phenomena of diffusion and viscosity in liquids and is associated with the validity of the Stokes–Einstein relation:

$$D = \frac{k_B T}{6\pi r \eta}, \tag{1.11}$$

where r is the radius of moving particles.

Among the different models of liquids, it is found that the hole model is the most consistent model. In the case of ionic liquids, it satisfactorily explains the meaning of activation energy E_η for viscous flow as the work done in transferring a mole of particles from the surroundings of a hole into its interior, experimental compressibilities β and expansion coefficients α_V. It should be mentioned that relation (1.10) holds for nonassociated liquids in which transport processes, such as viscous flow, are determined by the enthalpy of hole formation. However, in associated liquids, such as water, with network structures, the transport process is determined by the energy required to rupture the bonds of the network.

1.3 Water and Other Common Solvents

Different properties of solvents are associated with the structure of particles (i.e. atoms, molecules, or ions) composing them and may broadly be grouped into three categories: (i) static properties, (ii) transport properties, and (iii) thermal properties. Density, refractive index, dielectric constant, and surface tension are essentially static properties and are connected with the statistical distribution of particles composing a liquid. Viscosity and electrical conductivity belong to the transport properties and are associated with the motion of particles in the bulk liquid. In contrast to the viscosity of a liquid that is determined by the relative motion of all particles in the liquid, electrical conductivity is associated with the transport of charged particles. Thermal conductivity, thermal expansivity, and freezing and evaporation of liquids fall in the category of thermal properties and are determined by the thermal motion of particles composing them. In fact, it is the structure of particles that ultimately interact with each other and decide their arrangement and instantaneous distribution in the liquid state and determine the properties of liquids.

Liquid water is commonly employed as a solvent for the crystallization of a wide range of inorganic and organic compounds and its structure and properties are relatively well known. Therefore, it is useful to compare the properties of liquid water with two other simple liquids: methanol and ethanol, which are used for preparing solutions. Some general trends of the behavior of these

solvents are briefly presented here from consideration of the temperature dependence of their density and viscosity under atmospheric conditions.

The temperature dependence of density d of solvents is usually expressed by the polynomial equation:

$$d = d_0 + b_1(T - T_0) + b_2(T - T_0)^2 + b_3(T - T_0)^3 + \cdots + b_n(T - T_0)^n, \tag{1.12}$$

where d_0 is the density of the solvent at temperature T_0, while b_1, b_2, b_3, and b_n are empirical constants, and T is usually taken in °C. In most cases a quadratic relation usually describes the $d(T)$ data satisfactorily, and the constants b_1 and b_2 are negative quantities. Note that the form of this equation is similar to the equation of the temperature dependence of volume thermal expansivity α_V (see Eq. (1.6)). Another equation relating density d of solvent water with its temperature T is of the form (Szewczyk and Sangwal, 1988):

$$d = d_0 \exp\left[\beta(T - T_c)^2\right], \tag{1.13}$$

where d_0 is the solvent density at T_c and β is a constant. Relation (1.13) was originally proposed for aqueous saturated electrolyte solutions (Sangwal, 1987) but has also been reported to hold for aqueous undersaturated solutions (Szewczyk and Sangwal, 1988). Since the density d of a solvent is the inverse of specific volume ϕ_V, it is expected that the dependence of specific volume ϕ_V of solvents, which reflects an expansion of their volume, on solvent temperature T also follows quadratic and exponential equations:

$$\phi_V = \phi_{V0} + \beta_1(T - T_0) + \beta_2(T - T_0)^2, \tag{1.14}$$

$$\phi_V = \phi_{V0} \exp\left[\beta^*(T - T_c)^2\right], \tag{1.15}$$

where β_1, β_2, and β^* are constants characteristic of the solvent, whereas ϕ_{V0} is the solution specific volume at T_0 in Eq. (1.14) and at T_c in Eq. (1.15).

Figure 1.7a and b shows the dependence of the specific volume ϕ_V and the volume thermal expansivity α_V of water, methanol, and ethanol on their temperature T. The data of Figure 1.7a may be represented by Eq. (1.14), with the parameters listed in Table 1.2, whereas those of Figure 1.7b by Eq. (1.4). Obviously, as seen from the values of the parameters ϕ_{V0} and β_1, the increase in ϕ_V with temperature is much higher for both alcohols than that for water. Similarly, the thermal expansivity α_V of methanol and ethanol is much higher than that of water. However, in contrast to a nonlinear increase in α_V with temperature for water, the temperature dependence of α_V for methanol and ethanol is linear. These observations of differences in the temperature dependence of specific volume ϕ_V and thermal expansivity α_V of the three solvents are directly associated with the bonds holding their molecules in the liquid state.

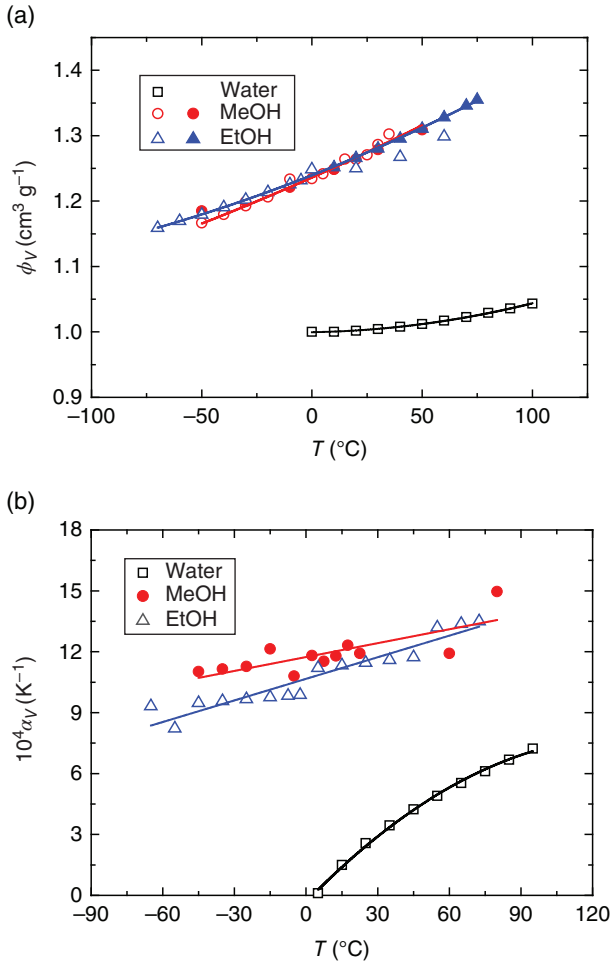

Figure 1.7 Dependence of (a) specific volume ϕ_V and (b) volume thermal expansivity α_V on temperature T of water, methanol, and ethanol. Sources of density data in (a): for water as in Figure 1.1, for methanol from (open circles) www.EngineeringToolBox.com and (filled circles) www.ddbst.com/en, and for ethanol from (open triangles) www.ddbst.com/en and (filled triangles) www.celcius.process.com. Data of (b) calculated from the above data. Data accessed 12 January 2017.

Table 1.2 Values of constants of Eq. (1.14).

Solvent	ϕ_{V0} (cm^3·g^{-1})	$10^3\beta_1$ (cm^3·g^{-1}·K^{-1})	$10^6\beta_2$ (cm^3·g^{-1}·K^{-2})
Water	0.9996	0.054	3.87
Methanol	1.2362	1.50	1.82
Ethanol	1.2395	1.33	2.58

The temperature dependence of viscosity η of solvents (and melts) may be represented by an Arrhenius-type relation (Bockris and Reddy, 1970; Stokes and Mills, 1965; also see Chapter 9):

$$\eta = \eta_0 \exp\left(\frac{E_\eta}{R_G T}\right), \tag{1.16}$$

where η_0 is the viscosity of the solvent at very high T when the exponential term approaches unity and E_η is the activation energy for viscous flow. Equation (1.16) is derived using the hole theory of liquids (Bockris and Reddy, 1970). Eyring's transition state theory also gives a similar temperature dependence of the viscosity η of solvents, written in the form (Horvath, 1985; Stokes and Mills, 1965):

$$\eta = \frac{h_P N_A}{V^0} \exp\left(\frac{\Delta G^0}{R_G T}\right), \tag{1.17}$$

where V^0 is the molar volume of the solvent, h_P is the Planck constant, and ΔG^0 is the free activation energy for viscous flow of the solvent. Since

$$\Delta G^0 = \Delta H^0 - T\Delta S^0, \tag{1.18}$$

where ΔH^0 and ΔS^0 are the heat and the entropy of activation, respectively, for constant values of ΔS^0 and V^0, Eq. (1.17) reduces to Eq. (1.16) with $\Delta H^0 = E_\eta$ and $h_P N_A / V^0 \exp(-\Delta S^0/R_G) = \eta_0$.

The main feature of Eq. (1.17) is that it provides the physical interpretation of the preexponential factor η_0 and the activation energy E_η. According to Eq. (1.16) the dependence of $\ln\eta$ against $1/T$ gives a linear plot with intercept $\ln\eta_0$ and slope E_η/R_G. Figure 1.8 shows plots of $\ln\eta$ against $1/T$ for water, methanol, and ethanol, with the corresponding intercepts $\ln\eta_0$ and slopes E_η/R_G, and the activation energy E_η and the constant $E_\eta/R_G T_m$ calculated therefrom given in Table 1.3.

Two features may be noted from Table 1.3. First, the value of the activation energy E_η for viscous flow is the highest for water, the lowest for methanol, and intermediate between these two values for ethanol. The difference in the values of E_η is due to the processes of creation of holes necessary for their subsequent motion in these solvents and are associated with the nature of chemical bonds in their structures. Second, the ratio $E_\eta/R_G T_m$ is much higher than the expected value of 3.7 of the hole theory of liquids. The high values of $E_\eta/R_G T_m$ are indicators of strong association of the molecules in these liquids. In fact, it is well known that liquid water is an associated liquid.

1.4 Properties of Solutions

A solution is obtained by adding a solute to an appropriate solvent at a given temperature and pressure conditions. A solute may be made up of (i) charged atoms or groups of atoms with negative or positive charges or

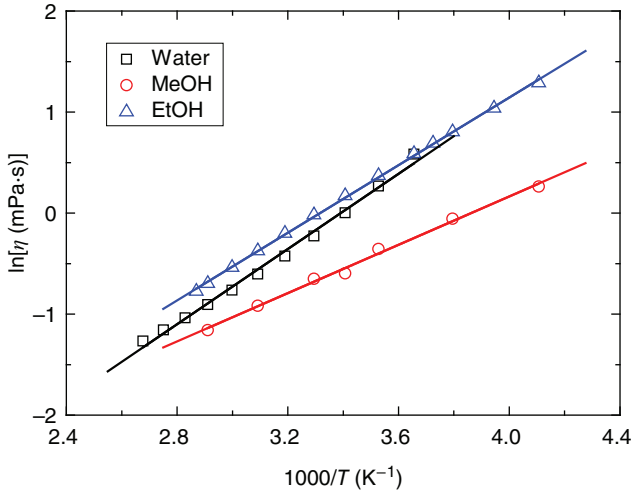

Figure 1.8 Dependence of lnη on 1/T for water, methanol, and ethanol. Sources of data: for water from Lide (1996/1997), for methanol from www.EngineeringToolBox.com and www.ddbst.com/en, and for ethanol from www.ddbst.com/en and www.celcius.process.com. Data for methanol and ethanol accessed 12 January 2017.

Table 1.3 Values of constants of Eq. (1.16).

Solvent	T_m (K)	$-\ln\eta_0$	$10^3 E_\eta/R_G$ (K^{-1})	$10^{-3}\eta_0$ (mPa·s)	E_η (kJ·mol^{-1})	E_η/R_G T_m (—)
Water	273.15	6.3108	1.86078	1.817	15.45	6.81
Methanol	175.55	4.6206	1.19616	9.847	9.95	6.81
Ethanol	159.05	5.5499	1.67339	3.888	13.91	10.52

(ii) uncharged neutral molecules. As in the case of liquids, molecular solutes may be composed of polar, nonpolar, or apolar molecules. Although water is the most common solvent and dissolves different types of substances, it is not a universal solvent. It easily dissolves ionic salts but there are many molecular substances that do not dissolve or poorly dissolve in water. The main requirement for the dissolution of a solute in water is that its ions or molecules interact with water molecules to liberate enough energy to break down the water structure. In nonionic solutes, these interactions occur between the O of H_2O molecules and the O and the N of molecular substances, forming hydrogen bonds. For example, in the case of methyl and ethyl alcohols,

hydrogen bonds occur between their O atoms and the O of H_2O. Sugars such as sucrose, $C_{12}H_{22}O_{11}$, dissolve in water mainly due to hydrogen bonds between their OH groups and O of H_2O molecules. In ionic solutes, however, their dissolution involves lattice breakup, followed by solvation of individual bare ions of splitted lattice.

Ionic solutes dissolved in water or dismantled on melting show conduction of electrical current through the migration of the ions present in the solution. Such ionic solutes and their solutions are known as *electrolytes* and *electrolyte solutions*, respectively. In contrast to these ionic solutes, there is a large number of organic substances dissolved in pure water, which show little conduction. Such solutes are composed of separate, neutral molecules and the bonding of atoms inside the neutral molecules is essentially nonionic. Such solutes and their solutions are known as *nonelectrolytes* and *nonelectrolyte solutions*, respectively.

The above comparative behavior of electrical conduction of solutions is based on water alone used as a solvent. However, when a nonaqueous solvent is chosen to prepare the solution of an electrolyte, the conduction in the solution is reduced tremendously due to the suppressed solvation of its ions by the solvent molecules.

1.4.1 The Solvation Process

In the case of an ionic solute dissolved in small concentrations in solvent water, the solute is dissociated into ions. Thus, the resulting solution consists of solvated ions and solvent water molecules in such a way that the dissociated ions acquire a particular time-averaged spatial distribution in the solution volume. The distance between the solvated ions is large and ion–ion interactions are insignificant in the solution. The process of solvation of ions is a consequence of ion–dipole interactions. Due to these interactions, some of the water molecules are trapped and oriented in the ionic field. The immobile water molecules in the immediate vicinity of the ions during their motion form the *primary solvation sheath*, but in the region between the primary solvation sheath and the bulk water there is also a *secondary region* of loosely-bound water molecules that influence their motion (see Figure 1.9a).

In order to describe the process of solvation of ions in a solvent S, the Born model for ion–solvent interactions may be applied. Following this model, we assume that: (i) one molecule of a solute dissociates into ions considered as rigid spheres of radius r_i and charge $z_i q$, where q is the elementary charge and z_i is the valency of the ion i, (ii) the solvent is a continuum of dielectric constant ε_s, and (iii) the interactions between the solvent and the ions are entirely electrostatic. Then the free energy ΔG_{I-S} of ion–solvent interactions per mole of ions is given by (Bockris and Reddy, 1970)

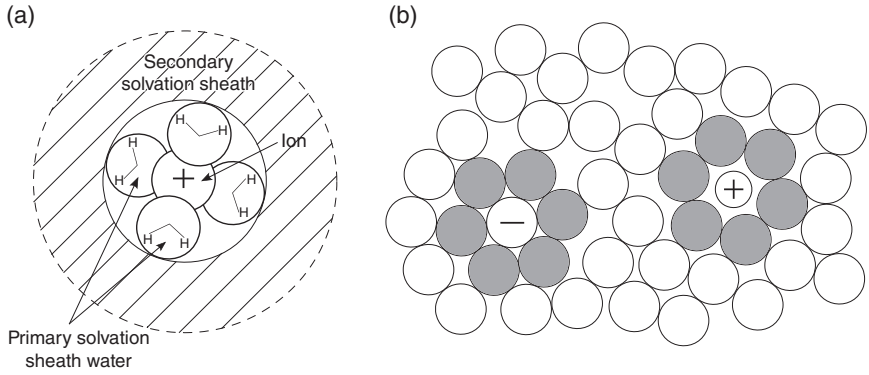

Figure 1.9 (a) Schematic illustration of primary and secondary regions of solvation of a monovalent cation. (b) Free water and immobile hydration water in primary solvation sheaths of ions shown as open and dark circles, respectively. Schematic (a) is based on an illustration in Bockris and Reddy (1970).

$$\Delta G_{\mathrm{I-S}} = -N_{\mathrm{A}} k_0 \frac{(z_{\mathrm{i}} q)^2}{2r_{\mathrm{i}}} \left(1 - \frac{1}{\varepsilon}\right), \tag{1.19}$$

where the Avogadro number $N_{\mathrm{A}} = 6{\cdot}10^{23}$ ions and the Coulombian proportionality constant $k_0 = 9{\cdot}10^9$ N·m^2·C^{-2}. Since $1 \gg 1/\varepsilon_{\mathrm{s}}$ (for example, $\varepsilon_{\mathrm{s}} = 80$ for water), $\Delta G_{\mathrm{I-S}}$ is negative, which means that the ions are more stable in the solvent than in a vacuum and the solute is soluble in the solvent of a high dielectric constant. However, when the solvent is replaced by another solvent A of dielectric constant ε_{a} such that $\varepsilon_{\mathrm{a}} < \varepsilon_{\mathrm{s}}$, the corresponding free energy $|\Delta G_{\mathrm{I-A}}| < |\Delta G_{\mathrm{I-S}}|$, the ions become relatively less stable and the solute is less soluble in this solvent. Obviously, solute ions more stable in solvent S are more solvated than in solvent A.

When the solute concentration is increased, the average distance between the ions decreases and ion–ion interactions become increasingly important. When the solute concentration is increased further, the water molecules bound to the solvated ions are not effective in dissolving ions further (Figure 1.9b). Then oppositely charged ions come close to form neutrally associated ion pairs. However, since the Coulombian attractive forces $z_+ z_- q^2/\varepsilon_{\mathrm{s}} r^2$ increase with decreasing dielectric constant ε_{s} of the solvent, for nonaqueous solvents of low dielectric constant ion-pair formation is favored. When the Coulombian attractive forces are still strong, ion-pair dipoles may attract ions and form triple ions. Triple-ion formation has been suggested in solvents of $\varepsilon_{\mathrm{s}} < 15$, while formation of even still larger clusters of four, five, or even more ions is possible in solvents of $\varepsilon_{\mathrm{s}} < 10$.

From the above picture of solvation of ions of an ionic solute immersed in a solvent, it follows that a solution is now composed of randomly distributed solute ions that are surrounded by regions of immobile, strongly trapped solvent molecules around them and randomly distributed molecules of solvents in its remaining volume around the solvated molecules. With increasing solute concentration c, the concentration of solvated ions of the solute increases, whereas the concentration of holes constituting the empty space in the solvent decreases. Therefore, the dependence of the properties of solutions of a solute on solute concentration c dissolved in a solvent is determined by the processes of solvation of solute ions and creation of holes.

Here, it should be remembered that the solvated ionic entities participating in the properties of solutions are larger than the bare, unsolvated ions because of the firmly trapped water molecules around them. Therefore, the radius of the kinetic entity participating in the transport properties of solutions is expected to change from one solvent to the other because of changes in the structure of the solvation sheath. Since solvent molecules constitute the firmly-trapped solvation sheath, the sizes of these firmly-trapped solvent molecules mainly contribute to the changes in the radii of the solvated ions. For example, in the case of solvents water, methanol, and ethanol, the size of the molecules increases in the order: water, methanol, and ethanol; the radius of the solvated ions also increases in this order.

Finally, it should be emphasized that in the solvation of a solute, normal extensive hydrogen-bonded structure of water, in general, responds to the presence of solute molecules and ions by spatial and orientational arrangements, which result in an overall increase in the order of the solution. Interactions of ions with the dipole of water molecules lead to their solvation but hydrophobic interactions are the predominant factor in the solvation of nonpolar or apolar molecules. In an aqueous solution of polar solutes, their molecules break down the hydrogen-bonded arrangement of water and replace it with a spherically symmetrical non-hydrogen-bonded shell of water molecules. In a nonelectrolyte, there is no dissociation of its molecules and the solute molecules retain their unbroken identity.

1.4.2 The Concentration of Solutions

Concentration of a solute dissolved in a solvent is expressed in different ways. Among the commonly used ways are: (i) mass composition or weight fraction concentration, usually given in percentage, relative to the solvent, which is the ratio of the mass of the solute dissolved to the mass of the solvent, (ii) weight fraction concentration, also given in percentage, relative to the solution, which is the ratio of the mass of the solute dissolved to the mass of the solution, (iii) molar concentration c, which is the ratio of the number of moles of the solute to the volume of the solution taken in moles per liter, i.e. $\text{mol}\cdot\text{dm}^{-3}$ denoted

by the symbol M, (iv) molal concentration m, which is the ratio of the number of moles of the solute contained in 1 kg of the solvent, and (v) mole fraction x, which is the ratio of the number of moles of the dissolved solute to the sum of the number of the moles of all components of the solution (symbol m). For preparing saturated solutions both individual solvents as well as mixtures of solvents are used. Molar and molal concentrations are frequently used to express solute concentration in aqueous solutions but weight percent concentration relative to the solvent are usually used to express concentration in different individual solvents and their mixtures. However, temperature dependence of solubility of various solutes in solutions is customarily expressed in mole fraction x, defined as

$$x\ (\text{mole fraction}) = \frac{\text{moles of solute in solution}}{\text{sum of moles of solute and solvent in solution}} = \frac{W_S/M_S}{W_S/M_S + W_F/M_F}, \tag{1.20}$$

where W_S and W_F are the masses and M_S and M_F are the molecular masses of solute S and solvent F (F for fluid), respectively. The commonly used units for solute concentration are given below:

$$M\ (\text{molarity}) = \frac{\text{moles of solute}}{1000\ \text{ml solution}} = \frac{W_S/M_S}{1000\ \text{ml solution}}, \tag{1.21}$$

$$m\ (\text{molality}) = \frac{\text{moles of solute}}{1000\ \text{g solvent}} = \frac{W_S/M_S}{1000\ \text{g solvent}}. \tag{1.22}$$

Apart from the above units, some other frequently used units are as follows:

$$c_W\ (\text{wt. fraction}) = \frac{\text{mass of solute}}{\text{mass of solvent}} = \frac{W_S}{W_F}, \tag{1.23}$$

$$c_W^s\ (\text{wt. fraction}) = \frac{\text{mass of solute}}{\text{mass of solution}} = \frac{W_S}{W_F^s} = \frac{W_S}{W_F + W_S} = c_W(1 + c_W)^{-1} < c_W, \tag{1.24}$$

$$c_m\ (\text{molar ratio}) = \frac{\text{moles of solute in solution}}{\text{moles of solvent in solution}} = c_W\frac{M_F}{M_S}. \tag{1.25}$$

In Eq. (1.24), W_F^S is the mass of the solution. In the case of a mixture of two miscible solvents 1 and 2, concentration x^* in mole fraction may be given by

$$x^*\ (\text{mole fraction}) = \frac{W_S/M_S}{W_S/M_S + (W_1/M_1)\{(1-X) + X(M_1W_2/M_2W_1)\}}, \tag{1.26}$$

where the composition of the solvent mixture is expressed in moles and X is the molar content of solvent 2. When $X = 0$ or $W_1/M_1 = W_2/M_2$, the above expression reduces to Eq. (1.21).

1.4.3 Density and Thermal Expansivity of Solutions

Dependence of density d of solutions on solute concentration c, expressed in moles, in their solutions in a solvent at a given temperature T is usually described by the relations:

$$d = d_0 + k_1 c + k_2 c^2, \tag{1.27}$$

$$d = d_0 + \frac{c}{k_3 + k_4 c}, \tag{1.28}$$

where k_1, k_2, k_3, and k_4 are empirical constants, and d_0 is the density of the solvent when $c = 0$. Usually, the change in solvent density d_0 with the addition of a solute is less than 10%. Therefore, Eq. (1.28) takes the form of Eq. (1.27), with $k_1 = 1/k_3$ and $k_2 = -k_4/k_3^2$. Using Eq. (1.27) one can also write the solute concentration dependence of solution specific volume in the form:

$$\phi_V = \phi_{V0} - k_5 c + k_6 c^2, \tag{1.29}$$

where $k_5 = \phi_{V0}/k_3 = k_1 \phi_{V0}$ and $k_6 = \phi_{V0} k_4 / k_3^2 = -k_2 \phi_{V0}$.

When the constant $k_2 = 0$ in Eq. (1.27), the solution density d increases and its specific volume ϕ_V, given by Eq. (1.29), decreases linearly with an increase in solute concentration c. The linear dependence of density d of a solution may be obtained from the additivity rule in the form:

$$d = d_0(1-x) + d^* x = d_0 + (d^* - d_0)x = d_0 + 10^3 c(M^* - KM_s), \tag{1.30}$$

where x and $(1 - x)$ are the mole fractions of the solute and the solvent in a solution, respectively, d_0 and $d^*$are their corresponding densities, M_s and M^* are their molar masses, respectively, and K is the packing coefficient of the solute. Application of the additivity rule to specific volumes ϕ_{V0} and ϕ_V^* of solvent and solute, respectively, also gives a similar relation, i.e.

$$\phi_V = \phi_{V0}(1-x) + \phi_V^* x = \phi_V^* - \left(\phi_{V0} - \phi_V^*\right)x = \phi_{V0} - 10^3 c(KM_s - M^*). \tag{1.31}$$

The packing coefficient K of the solute is defined as the ratio of apparent molar volume Φ of the solute to the molar volume V^0 of the solution, i.e. $K = \Phi/V^0$. The value of the packing coefficient K of a solute is practically a constant quantity and depends only on the solution temperature T. Its value is determined by the solvation process.

As in the case of the dependence of the density d and the specific volume ϕ_V of the solution of a solute in a given solvent at a given temperature T on the solute concentration c, the concentration dependence of the solution expansivity α_V at the given temperature also follows the quadratic equation:

$$\alpha_V = \alpha_{V0} + \alpha_3 c + \alpha_4 c^2, \tag{1.32}$$

where α_{V0} is the expansivity of the solvent at the temperature T and α_3 and α_4 are constants characterizing the solute concentration in the solution.

Figure 1.10 shows, as examples, the dependences of specific volume ϕ_V and volume thermal expansivity α_V on NaCl concentration in aqueous solutions at two selected temperatures of 25 and 80 °C. The dependences of ϕ_V and α_V on the solute concentration may be described by Eqs. (1.29) and (1.32), respectively, with the values of the constants given in Table 1.4.

It may be noted from the $\phi_V(c)$ plots that the constants k_5 and k_6 are practically temperature independent. As seen from Eq. (1.31), this is a result of the temperature independence of the packing coefficient K. From the $\alpha_V(c)$ plots, on the other hand, one observes changes in the signs of the constants α_3 and α_4, the transition taking place at a temperature of about 60 °C. This type of behavior is also observed for other electrolytes dissolved in water (see Horvath, 1985) and is associated with the adiabatic compressibility β_S of electrolyte solutions (see below), which go through minima between 50 and 70 °C for alkali metal chlorides.

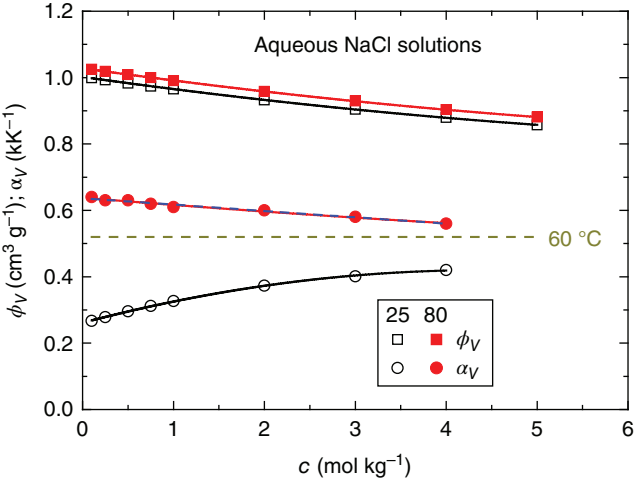

Figure 1.10 Dependence of specific volume ϕ_V and volume thermal expansivity α_V on NaCl concentration in aqueous solutions at 25 and 80 °C. Temperatures given in the inset is in °C. Dashed line shows a transition in $\alpha_V(c)$ dependence taking place at a temperature of about 60 °C. *Source:* Original data from Lide (1996/1997).

Table 1.4 Constants of Eqs. (1.29) and (1.32) for aqueous NaCl solutions.

	Eq. (1.29)			Eq. (1.32)		
T (°C)	ϕ_{V0} ($cm^3 \cdot g^{-1}$)	$-10^{-2}k_S$ ($l\ mol^{-1}$)	$10^{-3}k_6$ ($kg \cdot l \cdot mol^{-2}$)	$10^{-3}\alpha_{V0}$ (K^{-1})	$10^{-5}\alpha_3$ ($kg \cdot mol^{-1} \cdot K$)	$10^{-6}\alpha_3$ ($kg^2 \cdot mol^{-2} \cdot K$)
25	1.0021	3.866	1.92	0.261	7.22	−8.21
80	1.0282	3.866	1.85	0.628	−2.25	0.83

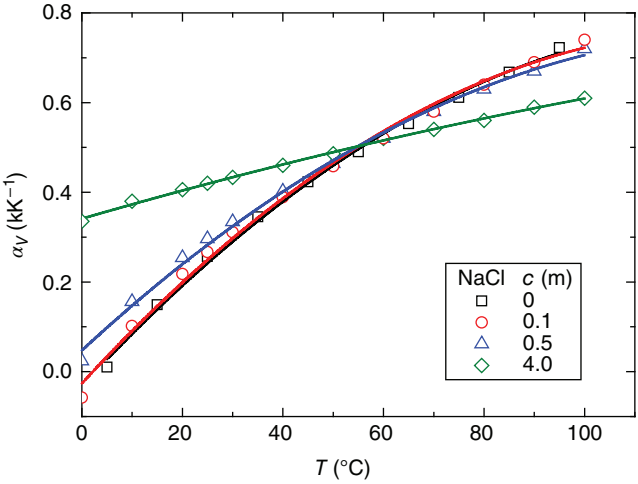

Figure 1.11 Dependence of volume thermal expansivity α_V on solution temperature T for three selected NaCl concentrations c in aqueous solutions. NaCl concentration c given in the inset is in molality. Original data from Lide (1996/1997). *Source:* Data for water from Figure 1.3.

The dependence of volume thermal expansivity α_V of solutions on their temperature T follows the same relation as relation (1.6) observed for solids and liquids. Figure 1.11 shows the experimental data of the volume thermal expansivity α_V of aqueous NaCl solutions of three selected concentrations c as a function of their temperature T, where the plots are drawn with the best-fit constants listed in Table 1.5. The data for water are from Figure 1.3. From the plots the following features may be noted:

1) The initial value of the expansivity α_{V0} at 0 °C increases with increasing concentration c.
2) The increase in the expansivity α_V with temperature is retarded by the addition of the solute to the solvent water.

Table 1.5 Constants of Eq. (1.6) for aqueous NaCl solutions.

c (m)	$10^{-5}\alpha_{V0}$ (K^{-1})	$10^{-5}\alpha_1$ (K^{-2})	$10^{-8}\alpha_2$ (K^{-3})
0	−3.13 ± 1.23	1.207 ± 0.057	−4.49 ± 0.55
0.1	−2.62 ± 1.27	1.220 ± 0.064	−4.72 ± 0.62
0.5	4.76 ± 1.07	1.036 ± 0.047	−3.77 ± 0.45
4.0	34.11 ± 0.31	0.327 ± 0.015	−0.57 ± 0.14

3) All plots intersect at a temperature of about 55 °C, suggesting a limiting value of temperature-independent α_V of about 0.48 kK^{-1}.

These features may be understood from the observed relationship between α_V of the solutions and isothermal and adiabatic compressibilities β_T and β_S, given by (see Horvath, 1985)

$$\alpha_V^2 = \left(\frac{\beta_T - \beta_S}{T}\right) C_p, \tag{1.33}$$

where C_p is the heat capacity at constant pressure per unit volume.

Figure 1.12a shows typical examples of the dependence of density d of aqueous ammonium oxalate (chemical formula: $(NH_4)_2C_2O_4$; abbreviation: Am2Ox) and sodium oxalate (chemical formula: $Na_2C_2O_4$; abbreviation: Na2Ox) solutions of selected concentrations on solution temperature T. The plots of the $d(T)$ data are drawn according to Eq. (1.12) with the best-fit parameters listed in Table 1.6. Figure 1.12b shows the specific volumes ϕ_V calculated from the above $d(T)$ data as a function of $(T - T_c)^2$ according to Eq. (1.15), whereas the plots are shown with the parameters included in Table 1.6. In the figure, concentration is given in mol· l^{-1}.

From Figure 1.12a it may be noted that in the case of ammonium oxalate solutions, the value of d_0 increases, whereas the values of both b_1 and b_2 decrease with an increase in solution concentration c. The values of d_0, b_1, and b_2 of Eq. (1.12) for 0.2 mol·l^{-1} sodium oxalate solution are different from those for 0.2 mol·l^{-1} ammonium oxalate solution. However, from Figure 1.12b it may be noted that in the range of concentration of ammonium oxalate solutions studied here, the value of ϕ_{V0} decreases with increasing solution concentration c, whereas those of β^* and T_c are independent of concentration c. The values of ϕ_{V0}, β^*, and T_c for 0.2 mol·l^{-1} sodium oxalate solution are different from those for 0.2 mol l^{-1} ammonium oxalate solution. These trends are associated with the solvation characteristics of the cations and anions of the salts and the effect of temperature on the solvation process. In comparison with ammonium oxalate, more changes are caused by sodium oxalate because of its smaller size, which results in more hydrated Na^+ ions than NH_4^+ ions.

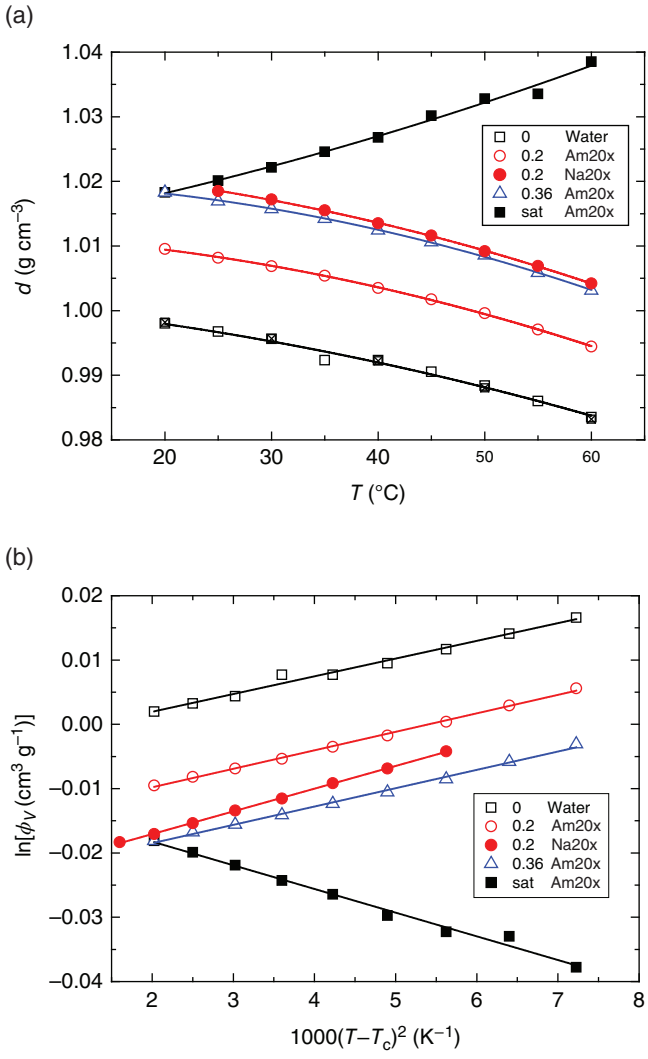

Figure 1.12 Dependence of (a) density d of aqueous ammonium oxalate (Am2Ox) and sodium oxalate (Na2Ox) solutions of selected concentrations on solution temperature T, with best-fit plots drawn according to Eq. (1.12) and (b) specific volume ϕ_V calculated from the above $d(T)$ data on $(T - T_c)^2$ according to Eq. (1.15). Concentration shown in the insets is given in mol·l^{-1}. For comparison, density d and specific volume ϕ_V of saturated Am2Ox solutions at different temperatures are also presented. *Source:* Original data of Am2Ox and Na2Ox from Frej et al. (2000) and Misztal (2004), respectively.

Table 1.6 Constants of Eqs. (1.12) and (1.15) for aqueous Am2Ox and Na2Ox solutions.

		Eq. (1.12)			Eq. (1.15)			
c (mol·l^{-1})	Salt	d_0 (g·cm^{-3})	$-10^{-4}b_1$ (g·cm^{-3}·K)	$-10^{-6}b_2$ (g·cm^{-3}·K^2)	$-10^{-2}\ln\phi_{V0}$	$10^{-6}\beta^*$ (K^{-2})	T_c (K)	$10^{-11}\beta^*/T_c^2(-)$
0		1.0017	1.2906	2.82	0.036	2.76	298	3.11
0.2	Am2Ox	1.0120	0.4585	4.09	1.554	2.87	298	3.23
0.2	Na2Ox	1.0229	0.7452	−39.5	2.413	3.53	288	4.25
0.36	Am2Ox	1.0201	0.0493	4.60	2.419	2.85	298	3.21
sat.	Am2Ox	1.0114	−2.8645	−2.59	1.087	−3.68	298	−4.14

Finally, it may be concluded that the above trends of $d(T)$ or $\phi_V(T)$ data of electrolyte solutions of particular concentrations are connected with the volume thermal expansivity α_V. However, although both equations describe the $d(T)$ and $\phi_V(T)$ data for solutions of different concentrations, Eq. (1.15) characterizes them for an electrolyte in terms of two constants d_0 (or $\phi_{V0} = 1/d_0$) and the dimensionless concentration-independent parameter β^*/T_c^2. Higher values of d_0 and β^*/T_c^2 represent more solvated ions.

1.4.4 Viscosity of Solutions

Figure 1.13 shows, as an example, the dependence of viscosity η of aqueous sucrose solutions at three selected temperatures on its concentration c. As is the general trend of the dependence of the viscosity η of solutions of different compounds, for the solution of a given concentration the viscosity η decreases with increasing temperature T, but at a given temperature the viscosity η of a solution initially increases practically linearly with concentration c up to about 35% and then increases rapidly. Obviously, in addition to solvent molecules, solvated entities participate in the viscous flow of solutions and both the composition of a solution in a solvent and the temperature of the solution determine its viscosity.

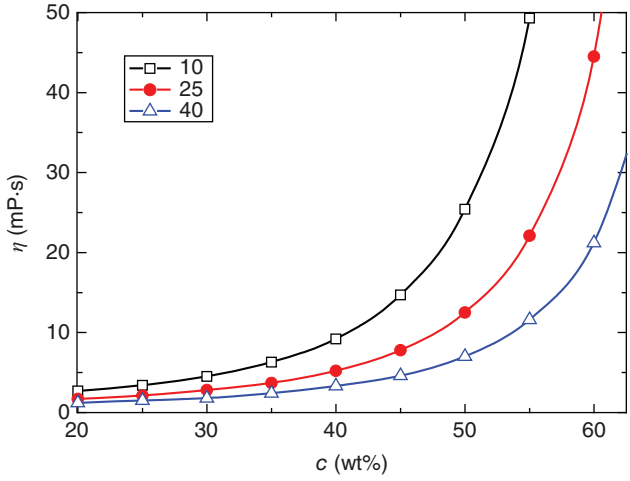

Figure 1.13 Dependence of viscosity η of aqueous sucrose solutions at three selected temperatures (°C) on its concentration c. Temperature in the inset is in °C. Original data from Asadi (2006).

To account for the effect of solute concentration in a solution, Jones and Dole gave the empirical relation (Horvath, 1985; Stokes and Mills, 1965):

$$\frac{\eta}{\eta^0} = 1 + Ac^{1/2} + Bc, \tag{1.34}$$

where η_0 is the viscosity of the solvent, and A and B are constants, which depend on solution temperature and are characteristic for an electrolyte. The ratio η/η_0 is the relative solution viscosity. However, this equation describes the viscosity data for relatively dilute electrolyte solutions. To describe concentrated solutions, a modified form of the above relation has been used (Horvath, 1985; Stokes and Mills, 1965), i.e.

$$\frac{\eta}{\eta^0} = 1 + Ac^{1/2} + Bc + Cc^2, \tag{1.35}$$

where C is an empirical constant.

The second term, with the constant A, on the right of Eq. (1.35) accounts for long-range Coulomb forces between the ions considered as point charges. The constant A is expected to be a positive quantity. However, this contribution from ion–ion interaction to the viscosity of electrolyte solutions is very small and explains the experimental $\eta(c)$ data only in very dilute solutions. At concentrations above about 0.002 M, a linear increase in viscosity with solute concentration is observed in strong electrolytes extending to 0.1 M and higher in aqueous solutions and to somewhat lower concentrations in some nonaqueous systems. In this concentration range, the B coefficient can be positive as well as negative, depending on the solute, the solvent, and the solution temperature. The origin of this B coefficient lies in ion–solvent interactions. Negative B coefficients are found for electrolytes composed of large ions in associated solvents such as water at relatively low temperatures. For example, at 25 °C, KCl and KI in aqueous solutions have negative B coefficients but NaCl in aqueous solutions has a positive B coefficient. However, KCl and KBr in methanol solutions have positive B coefficients.

The values of A and B parameters of Eq. (1.34) may be separated by plotting $[(\eta/\eta^0) - 1]/c^{1/2}$ against $c^{1/2}$ of the $\eta(c)$ data for a compound. The linear plot gives the intercept A and the slope B. Figure 1.14 shows, as an example, the dependence of $[(\eta/\eta^0) - 1]/c^{1/2}$ on $c^{1/2}$ of aqueous sodium oxalate (Na2Ox) solutions at three selected temperatures according to Eq. (1.34). The plots, drawn with the constants listed in Table 1.7, show that the value of parameter A decreases and that of B increases with an increase in solution temperature T. Some comments on these observations deserve attention.

The A parameter is a measure of ion–ion interaction involved in a salt dissolved in a given solvent and the temperature (Horvath, 1985; Stokes and Mills, 1965). Its value essentially depends on the valency of ions composing the salt and is a positive quantity. In contrast to the expected positive values of A, its

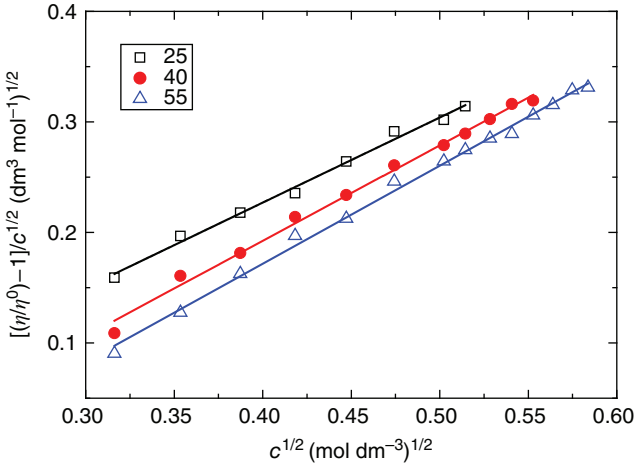

Figure 1.14 Dependence of viscosity $[(\eta/\eta^0) - 1]/c^{1/2}$ on $c^{1/2}$ of aqueous sodium oxalate (Na2Ox) solutions at three selected temperatures according to Eq. (1.34). Temperature in the inset is in °C. Original data from Misztal (2004).

observed negative values may be due to a large scatter in the values of η/η^0 at different concentrations and temperatures. This discrepancy may also due to the interaction of relatively large anions (i.e. $HC_2O_4^-$ or $C_2O_4^{2-}$ ions) and solvent molecules. The decrease in the value of A of the solutions with increasing temperature may be associated with weakening of ion–ion interactions in the solution, which leads to a diminution in the process of association of ions and solute molecules. In other words, when solvated ions form associates at low temperatures, the tendency of formation of molecular associates decreases with increasing temperature of the solution due to the decreasing ability of formation of bonds between the existing ions and the solvent molecules.

The value of the B parameter for electrolyte solutions is a sum of the values of contributions of cations and anions and depends on temperature (Horvath, 1985; Stokes and Mills, 1965). Assuming that dissolution of $Na_2C_2O_4$ in water results in the following ions:

$$\begin{aligned}(\mathrm{i})\ Na_2C_2O_4 + H_2O &\rightarrow Na^+ + OH^- + HC_2O_4^-;\ \text{and}\ (\mathrm{ii})\ Na_2C_2O_4 \\ &\rightarrow 2Na^+ + C_2O_4^{2-},\end{aligned} \tag{1.36}$$

where all ions are solvated, with the contributions of about 0.09 and 0.10 mol·dm^{-3} for Na^+ and OH^- ions, respectively, at 30 °C (Horvath, 1985), one finds the contribution of $HC_2O_4^-$ and $C_2O_4^{2-}$ ions to the B parameter, denoted by B_{2-} in Table 1.7, is practically the same and lies between 0.6 and

Table 1.7 Constants of Eq. (1.34) at different temperatures for aqueous Na2Ox solutions.

T (°C)	A ($dm^{3/2}·mol^{-1/2}$)	B ($dm^3·mol^{-1}$)	B_{2-} ($dm^3·mol^{-1}$)
25	−0.081 ± 0.011	0.770 ± 0.026	0.59
40	−0.153 ± 0.010	0.863± 0.022	0.68
55	−0.183 ± 0.008	0.887 ± 0.016	0.70

0.7 $mol·dm^{-3}$, which gives the average anionic volume $V_a = 2.56·10^{-27}$ m^3 and the radius $r_a = 0.85$ nm.

The B coefficients for various salts in aqueous and methanolic solutions are related to the molar entropy ΔS^0 of solution corrected for the so-called cratic contribution S^* of the solvent entropy, i.e. corrected solution molar entropy $= \Delta S^0 - S^*$, The solution molar entropy ΔS^0 is defined as the difference between the molar entropy S_c of the crystal and the partial molar entropy S_s in a hypothetical ideal 1 M solution, i.e. $\Delta S^0 = S_s - S_c$.

Depending on the strength or weakness of the bond between the ion and the solvent molecules in the primary solvation sheath, water molecules are strongly bound to the surface of some of the ions than the water molecules among themselves (structure-making ions), whereas they are weakly bound to the surface of other ions (structure-breaking ions). Because of higher charge density, ions having small size and high valency such as Li^+, Mg^{2+} and La^{3+}, bind the water molecules strongly and are structure makers while ions having relatively large size and low valency behave as structure breakers. The B coefficient of a solute-solvent system is usually considered as the sum of contributions made by the solute cations and anions, and these B_i coefficients of ions have been related to their other properties. For example, the ionic B_i coefficients for both monoatomic and polyatomic ions decrease with increasing partial molar entropies of hydration at 25 °C, and the ionic B_i coefficients increase with increasing hydrated ionic volumes V_H.

The viscosity of a liquid is the result of relative motion of its particles. Therefore, it is expected that electrolyte solutions containing large ions relative to the solvent molecules will have a viscosity higher than that of the solvent. Assuming that the ions behave as rigid spheres suspended in a continuum, the viscosity η of the suspension in a medium of viscosity η^0 may be given by the Einstein relation

$$\frac{\eta}{\eta^0} = 1 + 2.5\phi, \tag{1.37}$$

where ϕ is the volume fraction of the particle in the medium. This relation holds for solution of small ϕ. To deal with higher concentrations of particles, Vand proposed the relation

$$\ln\left(\frac{\eta}{\eta_0}\right) = \frac{2.5\phi}{1 - Q\phi}, \tag{1.38}$$

where Q is a parameter characterizing the mutual interaction between the liquid surface layers. For small volume fractions ϕ, this equation reduces to Eq. (1.37).

For small values of ϕ, $\phi = cV_m$, where c is the solute concentration in mol·l^{-1} and V_m is the molar volume in l·mol^{-1}. Then Eq. (1.38) takes the form

$$\ln\left(\frac{\eta}{\eta^0}\right) = \frac{B_2 c}{1 - Q'c}, \tag{1.39}$$

where $B_2 = 2.5V_m$ and $Q' = QV_m$. When $Q'c \ll 1$, Eq. (1.39) reduces to the form of Eq. (1.34), with $Ac^{1/2} \ll Bc$ and $B = 2.5\ V$.

Eyring's transition-state theory has extensively been used to explain the dependence of solution viscosity η on solute concentration c and solution temperature T (for example, see: Feakins et al., 1974, 1993; Goldsack and Franchetto, 1977, 1978; Horvath, 1985). A simplified version of this approach is presented below.

Using Eyring's transition-state theory, the solution viscosity η may be given by (Goldsack and Franchetto, 1977, 1978)

$$\eta = \frac{h_P N_A}{V} \exp\left(\frac{\Delta G}{R_G T}\right), \tag{1.40}$$

where V and ΔG are the molar volume and the free energies of activation for the solution, respectively. When the values of V and ΔG of the solution are the sums of contributions of solvent and solute, defined by

$$V = (1-x)V^0 + xV^S = V^0\left[1 + x\left(V^S - V^0\right)/V^0\right], \tag{1.41}$$

and

$$\Delta G = (1-x)\Delta G^0 + x\Delta G^S = \Delta G^0\left[1 + x\left(\Delta G^S - \Delta G^0\right)/\Delta G^0\right]. \tag{1.42}$$

Eq. (1.40) gives

$$\eta = \frac{h_P N_A}{V^0(1 + xV)} \exp\left(\frac{\Delta G^0(1 + xF)}{R_G T}\right), \tag{1.43}$$

and

$$\frac{\eta}{\eta^0} = \frac{1}{1 + xV} \exp\left(\frac{xF}{R_G T}\right), \tag{1.44}$$

where x is the solute concentration expressed in mole fraction, the solvent viscosity η^0 is given by Eq. (1.17), F is the activation energy required for the formation of a hole in the solution, and V and F are constants for different types of salts and depend on the solution temperature. Equation (1.43) takes the form of Eq. (1.17) when

$$\frac{1}{\eta_0} = \frac{V^0}{h_P N_A}(1 + xV) \tag{1.45}$$

$$E_\eta = \Delta G^0(1 + xF). \tag{1.46}$$

For an n : 1 salt the constants V and F are given by

$$V = \frac{V^S - V^0}{V^0} = \frac{nV_c + V_a}{V^0} - (n + 1), \tag{1.47}$$

$$F = \frac{\Delta G^S - \Delta G^0}{\Delta G^0} = n\Delta G_c + \Delta G_a - (n + 1)\Delta G^0. \tag{1.48}$$

In the above equations the superscripts S and 0 with the molar volume V and the free energy ΔG denote solute and solvent, respectively.

According to Eq. (1.43), addition of a solute to the solvent leads to a change in the viscosity η by changes in both the preexponential factor η_0 and the activation energy ΔG^0, and the B coefficient is related to the constants V and F. For aqueous electrolyte solutions the approximate relation is (Horvath, 1985)

$$B = \frac{(F/R_G T) - V}{55.51}, \tag{1.49}$$

with V and F given by Eqs. (1.47) and (1.48), respectively.

The above approach of the temperature dependence of the viscosity of solutions is useful in understanding the effect of solute concentration and obtaining the size of entities involved in viscous flow and crystallization of the solute. As an illustration, the experimental data of the temperature dependence of viscosity of aqueous ammonium oxalate solutions of different concentrations, reported by Frej et al. (2000), are considered. Figure 1.15 shows examples of the dependence of $\ln\eta$ of aqueous ammonium oxalate solutions of four selected concentrations and solvent water on $1/T$ according to Eq. (1.43). In the figure the plot for water represents the temperature interval between 15 and 50 °C. As seen from the figure, the plots of $\ln\eta$ against $1/T$ follow linear dependence with intercept $\ln\eta_0$ and slope E_η/R_G for different solute concentrations x (expressed in mole fraction) such that the linear plots of $\ln\eta$ against $1/T$ for the solutions are shifted upward relative to the plot for water and the shift increases with the solute concentration x in the solution. The various values of the intercept $\ln\eta_0$ and the slope E_η/R_G for different aqueous ammonium oxalate solutions obtained by Sangwal et al. (2004) are plotted as a function of concentration x according to Eqs. (1.45) and (1.46) in Figure 1.16. In Figure 1.16, two values of the intercept and the slope corresponding to $\eta(T)$ data for water in the temperature intervals between 15 and 50 °C and between 15 and 55 °C are presented to show that the extrapolated values of E_η/R_G and $\ln\eta_0$ for $x = 0$ can differ substantially from the values obtained from the experimental $\eta(T)$ data for water, depending on the temperature interval of the data considered as a

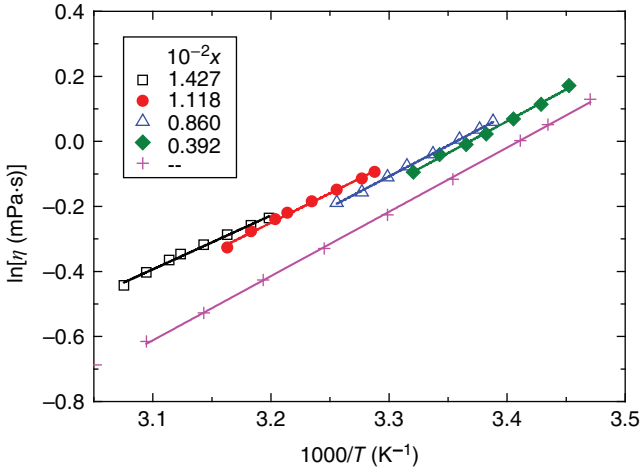

Figure 1.15 Dependence of lnη of aqueous ammonium oxalate (Am2Ox) solutions of four selected concentrations and water on 1/T according to Eq. (1.43). Solute concentration x shown in the inset is given in mole fraction. *Source:* Original data for ammonium oxalate solutions and water are from Frej et al. (2000) and Lide (1996/1997), respectively.

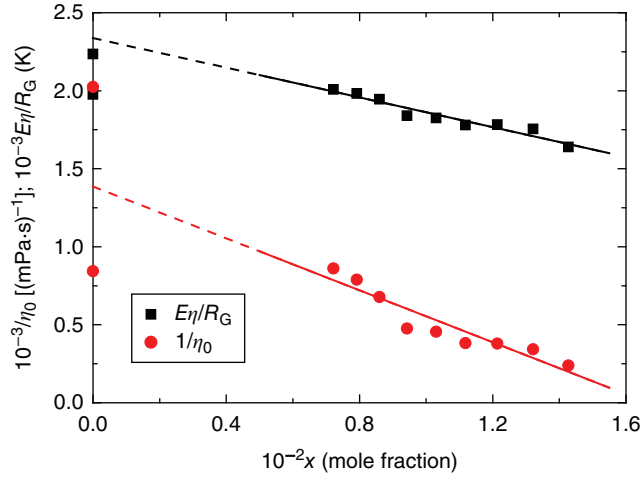

Figure 1.16 Relationship between $1/\eta_0$ and E_η/R_G on the concentration c of aqueous ammonium oxalate (Am2Ox) solutions according to Eq. (1.52). *Source:* Data from Sangwal et al. (2004).

Table 1.8 Estimated values of different constants from Eqs. (1.45) and (1.46).

Equation	Intercept			Slope	
(1.45)	$V^0/h_P N_A = 1386 \pm 120$ (mPa·s)$^{-1}$	$10^{-4}V^0 = 5.5 \pm 0.5$ m^3·mol^{-1}	$r^0 = 0.60 \pm 0.02$ nm	$-10^{-3}V^a = 1.09 \pm 0.15$ m^3·mol^{-1}	$r = 0.76 \pm 0.03$ nm
(1.46)	$10^3\Delta G^0/R_G = 2.338 \pm 0.051$ K	$\Delta G^0 = 19.4 \pm 0.5$ kJ·mol^{-1}		$-10^4F/R_G = 4.76 \pm 0.47$ K	$F = 396 \pm 39$ kJ·mol^{-1}

Source: After Sangwal et al. (2004).
[a] From plot original $V = -60 \pm 8$ (mole fraction)$^{-1}$.

reference. From the values of the intercept and the slope of the linear plots of Figure 1.16, the values of different quantities are given in Table 1.8.

It may be noted from Table 1.8 that both V and F are negative. This means that in the case of aqueous ammonium oxalate solution the following relations hold (cf. Eqs. (1.47) and (1.48)):

$$2V_c + V_a < 3V_0, \tag{1.50}$$

$$(2\Delta G_c + \Delta G_a) < 3\Delta G^0. \tag{1.51}$$

These relations indicate that the values of the activation energies are essentially determined by the size of ions and solvent molecules. The crystallographic radii of H_2O molecules, and NH_4^+ and $HC_2O_4^-$ ions are 0.138 nm, 0.148 nm, and about 0.20 nm. Therefore, it may be inferred that the average radius r_{H_2O} of holes due to water molecules in the solvent responsible for the viscous flow of water is greater than 0.168 nm.

Extrapolation of the plot of E_η/R_G against x to $x = 0$ gives the value of $\Delta G^0 = 19.4 \pm 0.5$ kJ·mol^{-1} (see Table 1.8). This value of ΔG^0 agrees well with the value of 18.6 kJ·mol^{-1} for viscous flow of water at high temperatures. Since both E_η and η_0 of solutions depend on solute concentration x, they are also mutually related (see Figure 1.20) and follow the expression (Sangwal et al., 2004):

$$\frac{E_\eta}{R_G} = A_1 - B_1 \ln \eta_0, \tag{1.52}$$

with constants: $A_1 = 97.5 \pm 23.7$ K and $B_1 = 282.9 \pm 3.8$ K. Rewriting this equation in the form of Eq. (1.17), one finds a new temperature $T^* = B_1 = 282.9 \pm 3.8$ K and a new preexponential factor $A_1/B_1 = \ln \eta_0{}^* = 0.344 \pm 0.08$ or $\eta_0{}^* = 1.406$ mPa·s, which gives the corresponding volume $V^* = h_P N_A/\eta_0{}^* = 4.71 \cdot 10^{-31}$ m^3. From the value of the solvent hole volume V^0 (see Table 1.8) and the above volume V^*, one obtains the solvent hole radius $r^0 = 0.604$ nm and the critical radius $r^* = 0.048$ nm. It is observed (see Figure 1.20b) that the data of $E_\eta(\eta_0)$ for water and aqueous ammonium oxalate solutions of various concentrations follow the same linear dependence (1.52). This observation suggests that the critical

volume V^* and the corresponding radius r^* are associated with the structure of the solvent water.

The estimated value of the hole radius r^0 is approximately four times the average radius $r_{H_2O} = 0.138$ nm of water molecules. This conclusion is consistent with relation (1.50), which predicts that the average radius r_{H_2O} of holes participating in viscous flow is greater than 0.168 nm. The value of the critical radius r^* is approximately twice the maximum displacement δ_{max} of a solvent molecule from its equilibrium position due to the thermal energy, i.e.

$$\delta_{max} = \left(\frac{2k_B T}{f}\right)^{1/2} \approx 0.022\,\text{nm}, \tag{1.53}$$

where $k_B T$ is the thermal energy of water molecules at its melting point T_m and $f \approx 15$ N/m is the force constant of ice lattice.

From the above discussion it follows that the value of the new temperature T^* is close to the melting point of ice, whereas the value of the critical radius r^* is related to the thermal vibrations of solvent molecules. Thus, it may be concluded that the values of the constants A_1 and B_1 of Eq. (1.52) are determined by the properties of solvent. In contrast to this, r^0 and r are the radii of holes in the solvent and the solution, respectively, and are associated with the viscous flow.

Finally, it should be emphasized that the values of the activation energies ΔG^0 and F for viscous flow of solvents and solutions decrease with increasing temperature. This is due to the fact that water and aqueous solutions behave as associated liquids with network structure. In associated liquids, the activation energy E_η for viscous flow is determined by the energy required to break the bonds of the network, whereas the fraction of the broken bonds increases with temperature (Bockris and Reddy, 1970).

1.5 Saturated Solutions

Saturated solutions are inherited by changes in solute concentration dissolved in suitable solvents with an increase in temperature. Therefore, a reasonable representation of the properties of saturated solutions by mathematical expressions is possible only through their dependence on temperature. In the case of solutions containing not very high solute concentrations, their properties such as density and viscosity increase practically linearly with solute concentration (see Section 1.4). However, for real solutions, the temperature dependence of the solubility of a solute in a given solvent is usually given by polynomial and Arrhenius-type relations (see Section 2.4). By combining these relationships with the linear dependence of solute concentration, one obtains equations similar to Eqs. (1.12), (1.13), and (1.17). In the case of density d, one obtains

$$d = d_0^* + a_1^*(T - T_0) + a_2^*(T - T_0)^2, \tag{1.54}$$

and

$$d = d_0^{**} \exp\left[\beta_0^*(T - T_c)^2\right]. \tag{1.55}$$

In Eq. (1.54), d_0^*, a_1^*, and a_2^* are new constants and d_0^* is the saturated solution density at T_0, whereas in Eq. (1.55), d_0^{**} and β_0^* are new constants and d_0^{**} is the density corresponding to T_c. Note that for saturated solutions $d^* > d_0$, $a_1^* > a_1$, and $a_2^* > a_2$. In the case of viscosity η, Eq. (1.44), which includes solution concentration, may be used. This relation predicts that an increase in solute concentration in the solution leads to an increase in the activation E_η and a decrease in the preexponential factor η_0. Some examples illustrating the validity of the above predictions are given below.

Figure 1.17a shows the dependence of the density d of saturated aqueous solutions of potassium bichromate (chemical formula $K_2Cr_2O_7$; abbreviation K bichromate or KBC) and sodium and ammonium oxalates on their temperature T according to Eq. (1.54), whereas Figure 1.17b presents the data as $\ln \phi_V = -\ln d$ of the above $d(T)$ data for saturated solutions against $(T - T_c)^2$ according to Eq. (1.55). The best-fit values of the plots are listed in Table 1.9, where the corresponding fitting parameters for water are also included for comparison.

From Table 1.9 and Figure 1.17, it may be seen that only saturated Na2Ox solutions show a trend similar to that of water. As in water, here both a_1^* and a_2^* are negative but the value of d_0^* increased. In contrast to the behavior of Na2Ox solutions, for KBC and Am2Ox saturated solutions, not only the values of the d_0^* are increased but also the values of the constants a_1^* and a_2^* are positive and their values for KBC solutions are much higher than those for Am2Ox solutions. Similarly, one notes from Table 1.9 that the specific volume $\phi_{V0} \approx 1/d_0^*$ for KBC solutions is lower than that for Am2Ox solutions but the parameter β^*/T_c^2 for different solute solutions is more informative. As in the case of water, this β^*/T_c^2 parameter is negative for Na2Ox solutions but is positive for KBC and Am2Ox solutions and its value is much higher for KBC solutions than that of Am2Ox solutions. These different trends of saturated solutions of different salts are associated with the differences in their solubilities in water with temperature and the solvation of solute ions.

Figure 1.18a and b shows typical examples of the dependence of the viscosity η of aqueous saturated solutions of potassium bichromate and sodium and ammonium oxalates, and three disaccharides on their temperature saturation T, respectively. Two different trends of the viscosity data are obvious. In the case of KBC, Am2Ox, Na2Ox, and sucrose, the viscosity η decreases with increasing saturation temperature of the solution, but an opposite trend of an increase in the viscosity η of the saturated solutions with increasing temperature of two other disaccharides (i.e. trehalose and maltitol) is observed. These different

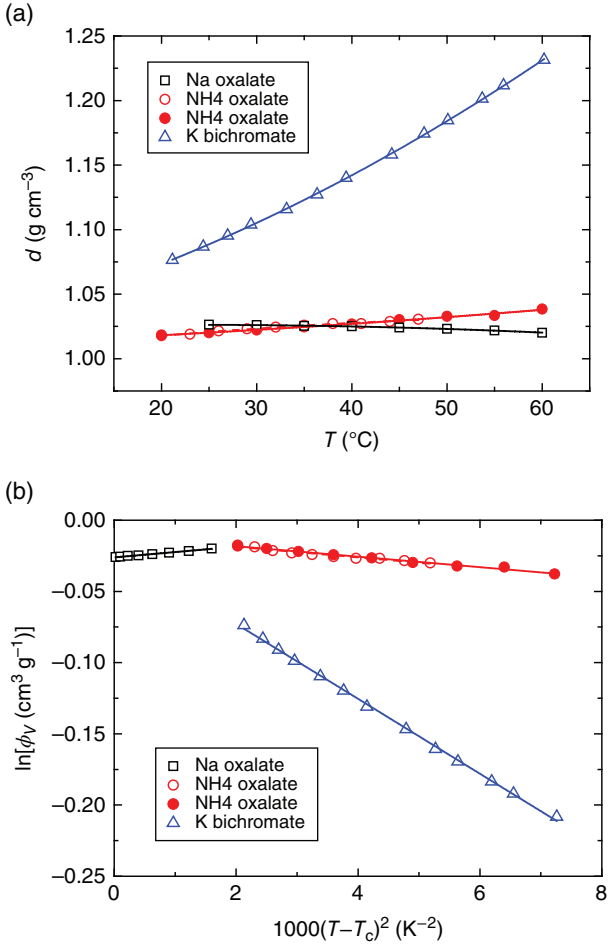

Figure 1.17 (a) Dependence of density d of saturated aqueous solutions of sodium and ammonium oxalates and potassium bichromate on their temperature T. (b) Plots of $\ln\phi_V$ of above saturated solutions against $(T - T_c)^2$ according to Eq. (1.13). Original data for sodium oxalate, ammonium oxalate, and potassium bichromate solutions are from Misztal (2004), Frej et al. (1998, 2000), and Szewczyk et al. (1985), respectively. *Source:* Data shown by open and filled circles for ammonium oxalate from Frej et al. (2000) and (1998), respectively.

trends of the temperature dependence of viscosity of saturation solutions are associated with the opposite effects of solution temperature and solute concentration (Gharsallaoui et al., 2008):

1) As is the usual situation, at a particular temperature the viscosity increases with increasing solute concentration.

Table 1.9 Constants of Eqs. (1.54) and (1.55) for aqueous saturated solutions.

	Eq. (1.54)			Eq. (1.55)			
Salt	d_0^*(g·cm^{-3})	$10^{-3}a_1^*$ (g·cm^{-3}·K)	$10^{-5}a_2^*$ (g·cm^{-3}·K^2)	$-10^{-2}\ln\phi_{V0}^{**}$	$-10^{-6}\beta_0^*$ (K^{-2})	T_c (K)	$10^{-11}\beta^*/T_c^2$ (–)
Water	1.00165	–0.129	–2.8247	0.356	–2.76	298	–3.10
KBC	1.0249	1.92	2.535	2.017	26.3	298	29.5
Na2Ox	1.0238	–0.210	–0.448	2.61	–3.74	253	–5.83
Am2Ox[a]	1.0114	0.286	0.259	1.120 dashed	0.373	298	4.19
Am2Ox[b]	1.0023	0.904	–0.674	1.087 solid	0.368	298	4.13

[a] Open circles and dashed line.
[b] Filled circles and solid line.

2) For the solution of a given solute concentration, the viscosity decreases with increasing solution temperature.

When factor (2) of the effect of temperature dominates factor (1) of solute concentration, the viscosity of the saturated solutions decreases with increasing temperature. This is the situation in the case of aqueous saturated solutions of KBC, Am2Ox, Na2Ox, and sucrose. Here, solute–solute interactions are stronger than solute–solvent interactions. However, when factor (1) of solute concentration dominates factor (2) of solution temperature, the saturated solution viscosity increases with increasing temperature. This is the situation for aqueous saturated solutions of maltitol and trehalose. In this case, solute–solvent interactions are stronger than solute–solute interactions.

The $\eta(T)$ data for the saturated solutions of different salts and disaccharides may be described reasonably well by a quadratic equation but the values of the parameters of the quadratic equation are not informative. Therefore, the $\eta(T)$ data for the saturated solutions of different solutes were analyzed using Eq. (1.44). Figure 1.19a and b shows the dependence of $\ln\eta$ of aqueous saturated solutions of potassium bichromate and sodium and ammonium oxalates, and of three disaccharides, respectively, on $1/T$, with the plots obtained with the best-fit parameters listed in Table 1.10. Values of E_η for concentrated aqueous solutions of the compounds are given in the parentheses in the last column.

The data of η_0 and E_η for aqueous saturated solutions follow relation (1.52), as shown in Figure 1.20a. However, the $E_\eta(\eta_0)$ data for saturated solutions of disaccharides and salts lie on two separate linear plots with the constants: A_1 = 1550.6 ± 218.2 K and B_1 = 352.1 ± 21.5 K, and A_1 = 86.2 ± 14.1 K and B_1 = 314.3 ± 2.9 K, and new preexponential factors $A_1/B_1 = \ln\eta_0^* = 4.4044$ or $\eta_0^* = 81.81$ mPa·s and $A_1/B_1 = \ln\eta_0^* = -0.27434$ or $\eta_0^* = 0.760$ mPa·s,

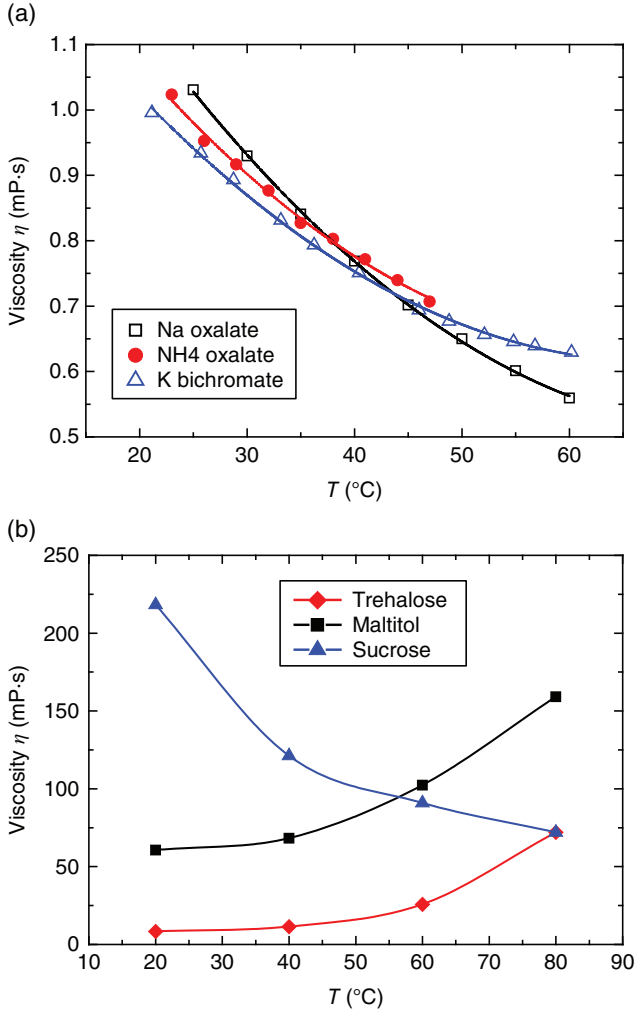

Figure 1.18 Dependence of viscosity η of aqueous saturated solutions of (a) sodium and ammonium oxalates and potassium bichromate, and (b) three disaccharides on their temperature saturation *T*. *Source:* Original data in (a) for sodium oxalate, ammonium oxalate, and potassium bichromate solutions are from Misztal (2004), Frej et al. (2000), and Szewczyk et al. (1985), respectively, but in (b) for disaccharides are from Gharsallaoui et al. (2008).

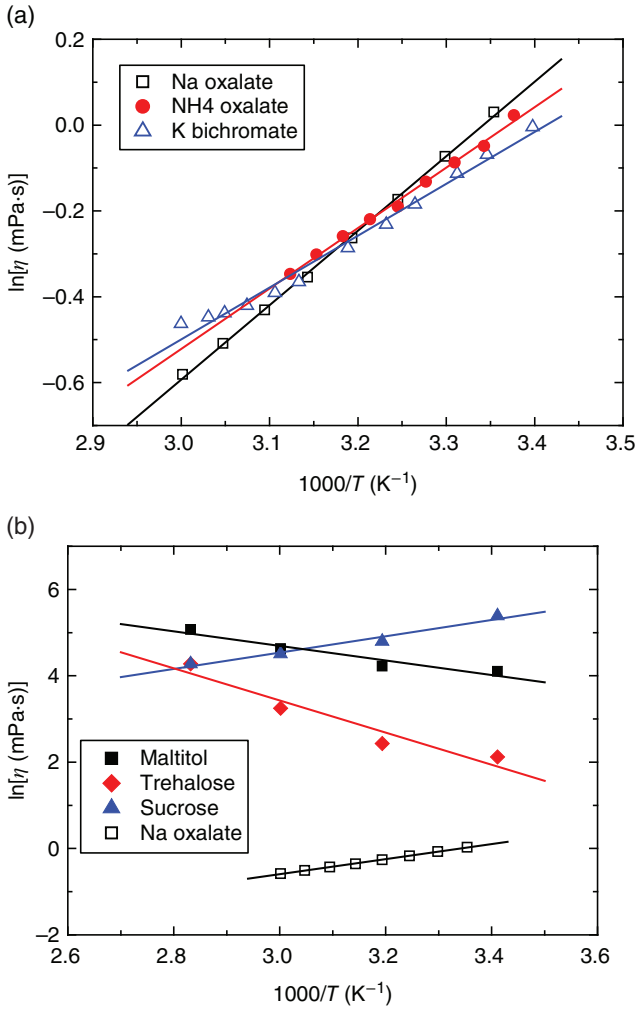

Figure 1.19 Dependence of lnη of aqueous solutions of (a) sodium and ammonium oxalates and potassium bichromate, and (b) three disaccharides on 1/*T*. *Source:* Original data is shown in Figure 1.18a and b, respectively.

respectively. As shown in Figure 1.20b, these linear dependences are similar to those observed for the data of η_0 and E_η for aqueous ammonium oxalate solutions of different concentrations. Differences in the $E_\eta(\eta_0)$ plots of these oxalate solutions and saturated aqueous solutions of different salts are clearly seen. The main effect of saturation of the solution is to increase the value of E_η of a compound.

Table 1.10 Values of constants of Eq. (1.16) for saturated solutions.

Solvent	T_m (K)	$-\ln\eta_0$	$10^3 E_\eta/R_G$ (K^{-1})	η_0 (mPa·s)	E_η (kJ·mol^{-1})	$E_\eta/R_G T_m$ (–)[a]
Water	273.15	6.3108	1.86078	$1.817\cdot10^{-3}$	15.47	6.81
$K_2Cr_2O_7$	671.15	4.1253	1.20858	$1.616\cdot10^{-2}$	10.04	4.42 (1.62)
$Na_2C_2O_4$	523.15	5.7986	1.73516	$3.032\cdot10^{-3}$	14.43	6.35 (3.31)
$(NH_4)_2C_2O_4$	406.15	4.7458	1.40807	$8.688\cdot10^{-3}$	11.71	5.15 (3.47)
Sucrose	459.15	1.1342	1.88985	0.322	15.71	6.92 (4.11)
Maltitol	419.15	–9.7409	–1.68356	$1.70\cdot10^{4}$	–14.0	–6.16 (–4.02)
Trehalose	488.15	–14.57556	–3.7159	$2.14\cdot10^{6}$	–30.90	–13.60 (–7.61)

[a] Values in parentheses refer to concentrated solutions.

The above values of η_0^* give the following threshold volumes $V^* = 8.1\cdot10^{-33}$ and $8.718\cdot10^{-31}$ m^3, and the threshold radii $r^* = 0.012$ and 0.059 nm for aqueous saturated solutions of disaccharides and salts, respectively. In comparison with the value of the threshold radius $r^* = 0.048$ nm for aqueous ammonium oxalate solutions of various concentrations, mentioned above, the value of this radius r^* for aqueous saturated solution of different salts is somewhat increased but that for disaccharide solutions is decreased enormously. These opposite effects of salts and disaccharides are due to their chemical nature. Moreover, as judged from the ratio $E_\eta/R_G T_m$ (with $T_m = 273.15$ K for water), aqueous solutions of salts and sucrose behave as associated systems, but this trend of associated systems is somewhat disrupted in aqueous potassium bichromate and ammonium oxalate solutions and is strongly disrupted in aqueous maltitol and trehalose solutions.

Crystallization always occurs in supersaturated solutions and occurs as a result of integration of entities present in them. Therefore, it is interesting to estimate the size of these entities from the data of viscosity of saturated solutions and supersaturated solutions. For this purpose, as an example, we use the viscosity data of concentrated ammonium oxalate solutions in the temperature range between 291.15 and 320.15 K and saturation concentrations c from 0.36 to 0.75 mol·dm^{-3} (Frej et al., 2000). Viscosity measurements were made for each saturated solution of concentration c_s starting from a temperature of 5 K above the saturation temperature T_s (undersaturation range) to the temperature T_N of onset of nucleation (supersaturation range). For constant selected temperatures T_N corresponding to known initial saturation concentrations c_s, viscosity data for supersaturated solutions of other c_s were considered for the analysis. Viscosity data for different c_s were also analyzed.

Figure 1.21 presents the dependence of relative viscosity η/η^0 of aqueous supersaturated and saturated solutions of ammonium oxalates on the original

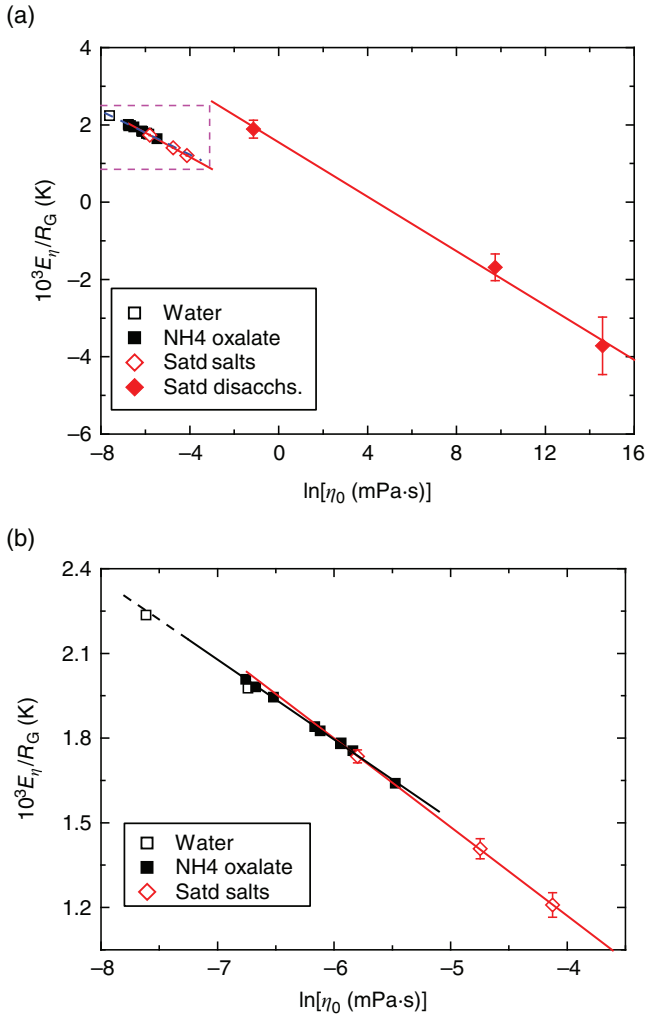

Figure 1.20 Plot of E_η/R_G against $\ln\eta_0$ for aqueous saturated solutions of different compounds and aqueous ammonium oxalate solutions of different concentrations according to Eq. (1.52). In (b) details of data of rectangular area. Former and latter data are from Table 1.10 and Figure 1.16.

saturation concentration c_s. Here, η^0 is the viscosity of water. Supersaturated solutions corresponding to different T_N are represented by different symbols, whereas saturated solutions are shown by asterisks. The data for supersaturated solutions were fitted according to Einstein's relation (1.37). The solid curve represents the data with an effective concentration $c_s(\text{eff}) = c_s - c_s^*$, where

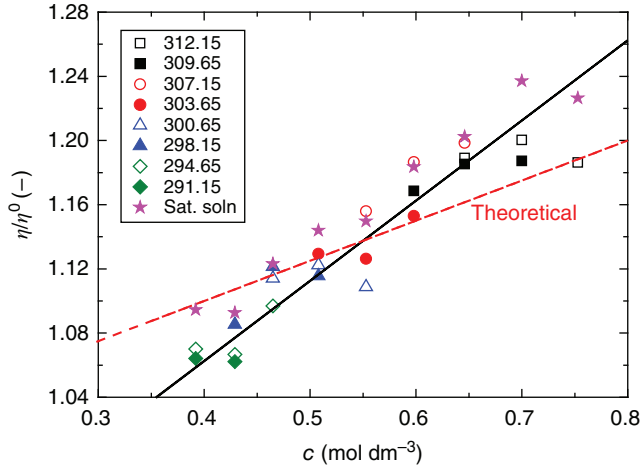

Figure 1.21 Dependence of relative viscosity η/η^0 of aqueous supersaturated and saturated solutions of ammonium oxalates on the original concentration c. Supersaturated solutions are represented by different symbols with saturation temperature given in K in the inset, whereas saturated solutions are shown by asterisks. *Source:* Original data from Frej et al. (2000). See text for details.

$c_s^* = 0.275$ mol·dm^{-3} is a threshold concentration beyond which relation (1.37) applies and has slope 0.5 dm^3·mol^{-1}. The data for saturated solutions also have a similar slope with a lower threshold of about 0.2 mol·dm^{-3}. However, in the entire concentration range the data may be described with a slope 0.25 dm^3·mol^{-1} (dashed curve). These slopes give $\phi = 0.2$ and 0.1 dm^3·mol^{-1}, from which one obtains the radius $r = 0.43$ and 0.34 nm of entities participating in viscous flow. These values are somewhat lower than the value given in Table 1.8 but are about twice larger than the crystallographic radii of 0.148 and 0.2 nm of individual NH_4^+ and $C_2O_4^{2-}$ ions, respectively. These results suggest that entities participating in crystallization from solution are solvated ions.

1.6 High-Temperature Solvents and Solutions

Some properties of solutions of ionic salts and molecular compounds dissolved in solvent water were described in the preceding sections. The role of the solvent here is to overcome forces between ions/molecules in the crystal to produce mobile entities in the form of ions/molecules in their solution by solvation processes. The solvent used here is in the liquid state at normal temperature and pressure conditions. Therefore, in the crystallization literature

such solvents and solutions are frequently referred to as low-temperature solvents and solutions.

There is another method of overcoming forces between ions/molecules in a crystal by heating it. The heat energy supplied to the solid increases the extent of vibrations of its ions/molecules until thermal forces prevail over long-range order leading to the melting of the solid. The molten material now has plentiful free space for the ceaseless motion of ions/molecules. Such molten liquids of particular materials dissolve other materials forming homogeneous solutions at high temperatures. In the crystallization literature the molten liquids obtained by heating materials, which are in the solid state under ordinary temperature and pressure conditions, and their homogeneous mixtures with other materials are called high-temperature solvents and solutions, respectively. High-temperature solvents are usually referred to as fluxes and, depending on the material to be crystallized, their composition may be quite complex.

Composition of the components of a flux determines not only its various properties but also the solubility of a substance in it and is associated with the formation of ions and complexes (Görnert and Sinn, 1985; Görnert and Voigt, 1984; Wanklyn, 1983). Volatility and viscosity of fluxes and solutions are important issues in high-temperature crystallization and it is frequently found that less viscous solutions are more volatile (Pritula and Sangwal, 2015). As in the case of different low-temperature solutions and solvents, the viscosity of high-temperature solutions decreases with an increase in temperature and follows Arrhenius-type relation (1.16). Values of best-fit parameters $\ln\eta_0$ and E_η/R_G for some systems are given in Table 1.11.

As in the case of aqueous saturated solutions of different compounds and aqueous ammonium oxalate solutions of different concentrations (see Figure 1.20), the data of E_η/R_G against $\ln\eta_0$ for these high-temperature systems also follows Eq. (1.52), as shown in Figure 1.22 with constants $A_1 = 4424 \pm 202$ K and $B_1 = 1404 \pm 34$ K, and new preexponential factor $A_1/B_1 = \ln\eta_0{}^* = 3.15$ or $\eta_0{}^* = 23.34$ mPa·s. This value of η_0^* gives the following threshold volume $V^* = 2.84{\cdot}10^{-33}$ m^3 and the threshold radius $r^* = 0.019$ nm. This value is comparable with the value of the maximum displacement δ_{max} of a solvent molecule from its equilibrium position due to the thermal energy (see Eq. (1.53)).

Taking the melting temperature $T_m = 722$ K for K_8 solution representative of all solutions, the values of E_η/R_GT_m were calculated using the data of E_η/R_G given in Table 1.11. It may be observed that the ratio $E_\eta/R_GT_m = 4.47$ for the solution used for the growth of $KLu(WO_4)_2$ crystals but its value exceeds 10 for the remaining solutions used for the growth of $KTiOPO_4$ and $CsLiB_6O_{11}$ crystals. This suggests that crystal growth from high-temperature solutions mainly occurs in associated solutions. The low value of the threshold radius r^* obtained above is connected with the associated nature of the solutions.

Table 1.11 Calculated values of parameters of Eq. (1.17) for some growth solutions.

Crystal[a]	Solution[b]	$-\ln \eta_0$	$10^3 E_\eta / R_G$ (K)	η_0 (mPa·s)	E_η (kJ·mol^{-1})
KTP	K_8	3.65 ± 0.35	9.89 ± 0.42	$2.6 \cdot 10^{-2}$	82.2 ± 3.5
	$K_8 + BaF_2$	4.28 ± 0.25	10.34 ± 0.30	$1.4 \cdot 10^{-2}$	86.0 ± 2.5
CLBO	$Cs_2CO_3 : Li_2CO_3 : H_3BO_3$ (1 : 1 : 11)	11.77 ± 1.11	21.20 ± 1.26	$7.7 \cdot 10^{-6}$	176.3 ± 10.5
	$Cs_2CO_3 : Li_2CO_3 : H_3BO_3$ (1 : 1 : 12)	10.40 ± 0.90	19.48 ± 1.02	$3.0 \cdot 10^{-5}$	162.0 ± 8.5
	$Cs_2CO_3 : Li_2CO_3 : H_3BO_3$: NaF (1 : 1 : 12 : 0.5)	9.22 ± 0.73	17.79 ± 0.83	$9.9 \cdot 10^{-5}$	147.9 ± 6.9
	$Cs_2CO_3 : Li_2CO_3 : H_3BO_3$: NaF (1 : 1 : 12 : 0.67)	9.69 ± 0.84	18.22 ± 0.95	$6.2 \cdot 10^{-5}$	151.5 ± 7.9
	$Cs_2CO_3 : Li_2CO_3 : H_3BO_3$: NaF (1 : 1 : 12 : 2)	9.07 ± 0.47	16.69 ± 0.53	$1.2 \cdot 10^{-4}$	138.3 ± 4.4
$KLu(WO_4)_2$	$KLu(WO_4)_2 : K_2W_2O_7$ (12 : 88)	0.68 ± 0.38	3.37 ± 0.48	1.96	28.0 ± 4.0

Source: Adapted from Pritula and Sangwal (2015).
[a] KTB – $KTiOPO_4$, CLBO – $CsLiB_6O_{11}$.
[b] K_8 ($K_8P_6O_{19}$).

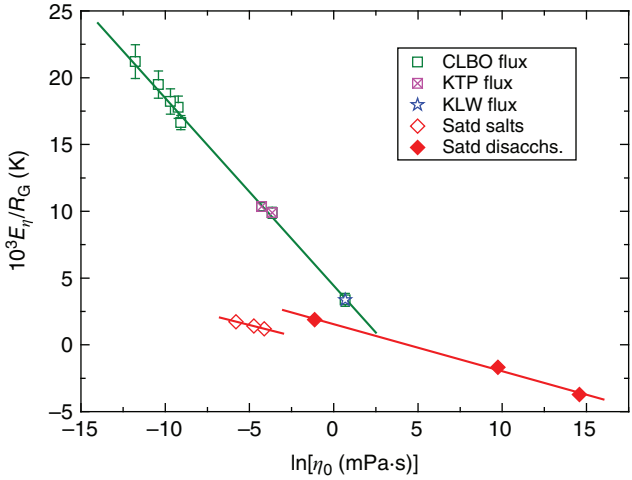

Figure 1.22 Linear relationship between E_η/R_G and $\ln\eta_0$ for some high-temperature systems according to Eq. (1.52). Data of E_η/R_G against $\ln\eta_0$ for aqueous saturated solutions of different compounds and aqueous ammonium oxalate solutions of different concentrations are also shown in the figure.

References

Asadi, M. (2006). *Beet-Sugar Handbook*. Hoboken, NJ: Wiley. Table A12.

Atkins, P.W. (1998). *Physical Chemistry*, 6e. Oxford: Oxford University Press.

Bockris, J.O.'.M. and Reddy, A.K.N. (1970). *Modern Electrochemistry*, vol. 1. New York: Plenum Press. Chap. 2.

Eggers, D.F., Gregory, N.W., Halsey, G.D., and Rabinovitch, B.S. (1964). *Physical Chemistry*. New York: Wiley.

Feakins, D., Freemantle, D.J., and Lawrence, K.G. (1974). Transition state treatment of the relative viscosity of electrolytic solutions. Applications to aqueous, non-aqueous and methanol + water systems. *J. Chem. Soc. Faraday Trans.* 70: 795–806.

Feakins, D.F.M.B., Waghorne, W.E., and Lawrence, K.G. (1993). Relative viscosities and quasi-thermodynamics of solutions of tert-butyl alcohol in the methanol-water system: a different view of the alkyl-water interaction. *J. Chem. Soc. Faraday Trans.* 89: 3381–3389.

Frej, H., Jakubczyk, M., and Sangwal, K. (1998). Density, surface tension, and refractive index of aqueous ammonium oxalate solutions from 293 K to 333 K. *J. Chem. Eng. Data* 43: 415–418.

Frej, H., Balińska, A., and Jakubczyk, M. (2000). Density and viscosity of undersaturated, saturated, and supersaturated aqueous ammonium oxalate solutions from 287 K to 325 K. *J. Chem. Eng. Data* 45: 415–418.

Gharsallaoui, A., Rogé, B., and Mathlouthi, M. (2008). Water-disaccharides interactions in saturated solution and the crystallisation conditions. *Food Chem.* 106: 1329–1339.

Goldsack, D.E. and Franchetto, R.C. (1977). The viscosity of concentrated electrolyte solutions. I. Concentration dependence at fixed temperature. *Can. J. Chem.* 55: 1062–1072.

Goldsack, D.E. and Franchetto, R.C. (1978). The viscosity of concentrated electrolyte solutions. II. Temperature dependence. *Can. J. Chem.* 56: 1442–1450.

Görnert, P. and Sinn, E. (1985). Fundamental aspects of flux growth. In: *Crystal Growth of Electronic Materials* (ed. E. Kaldis), 23–39. Amsterdam: Elsevier.

Görnert, P. and Voigt, F. (1984). High temperature solution growth of garnets: theoretical models and experimental results. In: *Current Topics in Materials Science*, vol. 11 (ed. E. Kaldis), 1–149. Amsterdam: North-Holland.

Horvath, A.L. (1985). *Handbook of Aqueous Electrolyte Solutions: Physical Properties, Estimation and Correlation Methods.* Chichester: Ellis Horwood. Chap. 2.

Lide, D.R. (1996/1997). *Handbook of Chemistry and Physics*, 77e. Boca Raton, FL: CRC Press.

Misztal, R. (2004). Badanie własności fizykochemicznych roztworów wodnych szczawianu sodu w obecności domieszek (Study of physico-chemical properties of aqueous sodium oxalate solutions in the presence of impurities). PhD thesis. Jagiellonian University, Kraków.

Mortimore, R.G. (2008). *Physical Chemistry*, 3e. Amsterdam: Elsevier. Chap. 23.

Pritula, I. and Sangwal, K. (2015). Fundamentals of crystal growth from solutions. In: *Handbook of Crystal Growth*, vol. II (ed. T. Nishinaga and P. Rudolph), 1185–1227. Elsevier.

Sangwal, K. (1987). A new equation for the temperature dependence of density of saturated aqueous solutions of electrolytes. *Cryst. Res. Technol.* 22: 789–792.

Sangwal, K. (1989). On the estimation of surface entropy factor, interfacial-tension, dissolution enthalpy and metastable zone-width for substances crystallizing from solution. *J. Cryst. Growth* 97: 393–405.

Sangwal, K., Frej, H., and Misztal, R. (2004). On the dimensions of species participating in the growth of ammonium oxalate monohydrate crystals from viscosity data of concentrated aqueous solutions. *Cryst. Res. Technol.* 39: 705–711.

Stokes, R.H. and Mills, R. (1965). *Viscosity of Electrolytes and Related Properies*. Oxford: Pergamon Press.

Szewczyk, J. and Sangwal, K. (1988). Density, refractive index, and specific refraction of aqueous lithium iodate solutions. *J. Chem. Eng. Data* 33: 418–423.

Szewczyk, J., Sokołowski, W., and Sangwal, K. (1985). Some physical properties of saturated, supersaturated, and undersaturated aqueous potassium bichromate solutions. *J. Chem. Eng. Data* 30: 243–246.

Wanklyn, B. (1983). The present status of flux growth. *J. Cryst. Growth* 65: 533–540.

Wright, M.R. (2007). *An Introduction to Electrolyte Solutions*. Chichester: Wiley.

2

Three-dimensional Nucleation of Crystals and Solute Solubility

Crystallization of a compound from its solution at a given temperature always occurs when it is in the supersaturated state. For the solution of a solute dissolved in a solvent, a measure of being in the supersaturated state is excess solute concentration with reference to its solubility. Crystallization of the compound from the supersaturated solution comprises the formation of stable three-dimensional (3D) nuclei and their subsequent growth into visible entities, whereas supersaturation is created by decreasing temperature of the saturated solution from a known temperature or by adding to the saturated solution another solvent in which the crystallizing solute is less soluble. A precise definition of supersaturation for the formation of these stable nuclei and their growth requires description of relationships between energy changes involved in these processes and the solute concentration in the solution, and between equilibrium solute concentration (solubility) and solution temperature.

The present chapter addresses different aspects of solutions with emphasis on basic concepts of supersaturation of solutions, occurrence of 3D nucleation in solutions, and solubility and supersolubility of solutions. Discussion of some of the topics presented here is based on the literature published before (Sangwal, 2007; Sangwal and Sato, 2012).

2.1 Driving Force for Phase Transition

At a given temperature, all physical (e.g. condensation, crystallization, phase transitions in the solid phase, etc.) and chemical processes (e.g. heterogeneous reactions) in the vapor, melt, or solution phases of every system take place through the formation of 3D nuclei of a new phase and occur only when the medium is supersaturated. In the case of crystallization of vapor, liquid, or solid phase, nuclei, which can attain a size greater than that of a critical nucleus, develop into crystals of visible size by the attachment of growth species (i.e. molecules, atoms, or ions). In order to understand the conditions when the

Nucleation and Crystal Growth: Metastability of Solutions and Melts, First Edition.
Keshra Sangwal.
© 2018 John Wiley & Sons, Inc. Published 2018 by John Wiley & Sons, Inc.

nuclei of phase II are formed from a homogeneous phase I such as vapor, melt, or solution, we refer to Figure 2.1. The solid curve in the figure shows the situation when the two phases are in equilibrium conditions. A vapor–crystal phase change is characterized by a p–T diagram, while a solution–crystal phase change by a c–T diagram. Here, p is the vapor pressure, c is the solute concentration, and p_0 and c_0 denote the saturation vapor pressure and the equilibrium solute concentration at temperature T_0, respectively.

We consider the change from vapor to crystalline phase during the cooling of the vapor, as shown by the line ABCD in the p–T diagram of Figure 2.1. Points B and D represent the equilibrium state in the two phases. At a constant vapor pressure p_1, a decrease in the temperature along the curve BC means passing through the equilibrium curve, with phase I becoming metastable (i.e. supersaturated). The supersaturation of the vapor phase is represented by the difference $\Delta p = p_1 - p_0$. At a constant temperature T_0, the change takes place along the curve CD as a result of decreasing supersaturation to the point D, where Δp becomes zero. Thus, the supersaturated state of the vapor phase may be represented either with reference to a constant temperature T_0 by the difference Δp or with reference to a constant vapor pressure p_1 by the difference $\Delta T = T_1 - T_0$.

In a c–T diagram, the supersaturation at a constant temperature T is represented by $\Delta c = c - c_0$, where c and c_0 denote the actual and equilibrium concentrations of solute in the solution. The supersaturation σ is defined by the quotients $\Delta p/p_0$ and $\Delta c/c_0$, while the supersaturation ratio $S = p/p_0$ or c/c_0.

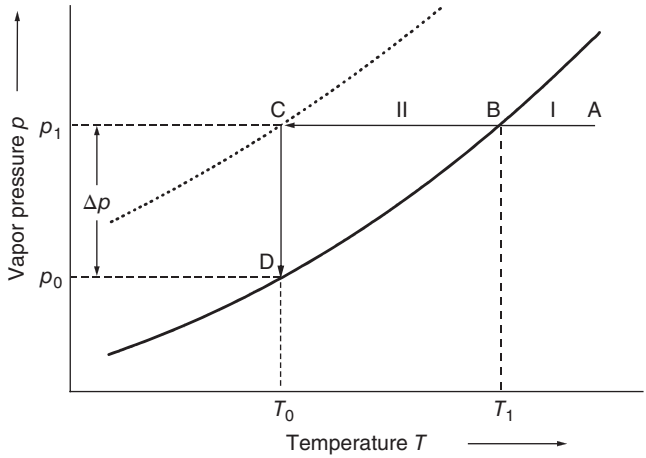

Figure 2.1 Schematic illustration of the dependence of vapor pressure p of a system on temperature. The solid curve shows the state when vapor phase I is in equilibrium with solid phase II, while the dotted curve shows the upper limit of the metastable zone when precipitation of phase II occurs in the system. See text for details.

In the case of a melt, its supercooling is defined by $\Delta T = T - T_0$, where T is the melting point T_m of the solute and T_0 is the temperature of the supercooled melt ($T_m > T_0$). It should be noted that the temperature difference ΔT is usually called undercooling in the literature on crystallization from the melt because the reference temperature there is the melting point T_m. However, the melt may be considered supercooled with reference to the crystallization temperature. We use this terminology in analogy with the definition of excess solute concentration Δc as a measure of supersaturation.

When $\Delta p = p - p_0$ or $\Delta c = c - c_0 > 0$, a system is said to be in the metastable state. Under these conditions only, nucleation, precipitation, deposition, and growth of new phase II is possible. Spontaneous nucleation (i.e. precipitation) of phase II occurs when Δp or Δc exceeds certain values Δp^* or Δc^*. These values of Δp^* or Δc^* characterize the width of the metastable zone and is shown by the dotted curve in Figure 2.1. When Δp or $\Delta c < 0$, the system is always stable. In this case, if phase II is present in the system, it undergoes evaporation or dissolution.

The driving force for the processes of crystallization (i.e. nucleation, precipitation, growth, deposition, etc.) is the difference in the Gibbs free energy G_I of supersaturated or supercooled mother phase I and the free energy G_{II} of the newly forming phase II. Under constant temperature and pressure conditions, any change in a system proceeds from a state of higher to a state of lower Gibbs free energy. Consequently, Gibbs function G is taken as a thermodynamic potential, and the change in the system as a passage from a state of higher to a state of lower potential. Thus, the reaction

$$aA + bB \rightarrow cC + dD, \tag{2.1}$$

is thermodynamically possible if the change in the free energy is

$$\Delta G = (cG_C + dG_D) - (aG_A + bG_B) < 0. \tag{2.2}$$

In the above equations, A and B are the reactants and C and D are the reaction products, while a, b, c, and d denote the number of moles of A, B, C, and D, respectively, participating in the reaction.

The change in the Gibbs free energy ΔG may be expressed by

$$\Delta G = G_{II} - G_I = \Delta H - T\Delta S, \tag{2.3}$$

where H and S denote the enthalpy and entropy of a phase, and $\Delta H = H_{II} - H_I$ and $\Delta S = S_{II} - S_I$. The dependencies of the free energy G_I of vapor, melt, or solution phase I, and G_{II} of solid phase II on temperature T and the free energy change ΔG with respect to temperature are schematically shown in Figure 2.2. Obviously, the formation of phase II is possible when $\Delta G > 0$ and occurs for $T < T_0$.

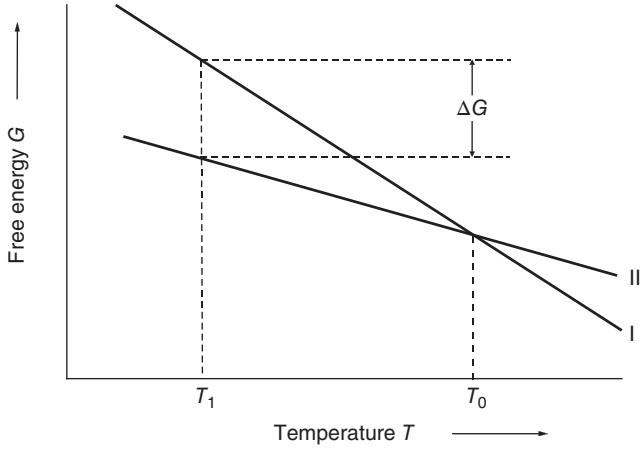

Figure 2.2 Change in Gibbs free energy G of vapor, melt, or solution (phase I) and solid (phase II) as a function of temperature of a system. Free energy change ΔG associated with phase change at T_0 is shown.

In crystallization from the melt and the solution, the free energy change may be expressed in terms of temperature difference ΔT. In the state of thermodynamic equilibrium when $\Delta G = 0$ (and $T = T_0$), from Eq. (2.3) one has

$$\Delta S = \frac{\Delta H}{T_0}, \tag{2.4}$$

which, for nonequilibrium conditions, gives

$$\Delta G = \Delta H - \frac{T\Delta H}{T_0} = \frac{\Delta H \Delta T}{T_0}, \tag{2.5}$$

where $\Delta T = T_0 - T$. Thus, the free energy change ΔG, given by Eq. (2.3), may be expressed in terms of temperature difference ΔT. During crystallization from the melt, the temperature difference ΔT is referred to as its supercooling and is denoted as $\Delta T = T_m - T$, where T is the temperature of the supercooled melt and T_m is the melting point of the solute (with $T < T_m$).

In order to understand the Gibbs free energy change ΔG associated with phase change or chemical change, it is necessary to consider the effect of composition of components present in the system. For a solution produced by adding n_i moles of its components, the free energy change ΔG may be given by

$$\Delta G = \sum_i n_i \Delta \mu_i, \tag{2.6}$$

where n_i is the number of moles of component i and $\Delta\mu_i$ is the change in the chemical potential of the component i associated with the phase change. Then from Eq. (2.5) one has

$$\Delta\mu = \frac{\Delta H \Delta T}{T_0 \nu}, \tag{2.7}$$

where ν is the number of particles produced by the dissociation of a solute molecule.

In the case of crystallization of molecular compounds, for which $\nu = 1$, with well-defined melting points T_m from the melt, Eq. (2.5) takes the form:

$$\Delta\mu = \left(\frac{\Delta H_m}{T_m}\right)\Delta T, \tag{2.8}$$

with $\Delta T = (T_m - T)$. For the crystallization of molecular compounds at temperature T_c from solutions saturated at temperature T_0, the chemical potential difference for crystallization is

$$\Delta\mu = \left(\frac{\Delta H_s}{T_0}\right)\Delta T, \tag{2.9}$$

where $\Delta T = (T_0 - T_c)$ and ΔH_s is the enthalpy of dissolution of the solute in the solution.

For an ideal mixture of gases when each gas component acts independently, the dependence of the chemical potential μ of a given component is given by

$$\mu - \mu^0 = k_B T \ln p, \tag{2.10}$$

where μ^0 is the standard chemical potential at a reference pressure, k_B is the Boltzmann constant, and T is the temperature in Kelvin. Similarly, in a solution the chemical potential μ of a given component may be given by

$$\mu - \mu^0 = k_B T \ln a, \tag{2.11}$$

where a is the activity of the component. From Eq. (2.10), one obtains the difference in the chemical potentials of a given phase corresponding to the vapor pressures p and p_0 as

$$\Delta\mu = k_B T \ln\left(\frac{p}{p_0}\right). \tag{2.12}$$

Similarly, in the case of solutions, one may write the chemical potential difference

$$\Delta\mu = k_B T \ln\left(\frac{a}{a_0}\right) = k_B T \left[\ln\left(\frac{f}{f_0}\right) + \ln\left(\frac{c}{c_0}\right)\right], \tag{2.13}$$

where a and a_0 are the activities of supersaturated and saturated solutions, respectively, f and f_0 are the corresponding activity coefficients, and c and c_0 are the concentrations of the solute in supersaturated and saturated solutions, respectively. For small values of supersaturations when $f/f_0 \approx 1$, Eq. (2.13) may be written in the form:

$$\Delta\mu = k_B T \ln\left(\frac{c}{c_0}\right). \tag{2.14}$$

Denoting the supersaturation ratio p/p_0 and c/c_0 by S and the supersaturation by $\sigma = (S - 1)$, Eqs. (2.12) and (2.14) may be written as

$$\Delta\mu = k_B T \ln S = k_B T \ln(1 + \sigma), \tag{2.15}$$

while for small values of σ when $\ln(1 + \sigma) \approx \sigma$,

$$\Delta\mu = k_B T \sigma. \tag{2.16}$$

For sparingly soluble salts, the supersaturation is given by

$$\frac{\Delta\mu}{k_B T} = S = \ln\left(\frac{a}{a_0}\right) = \ln\left[\frac{(a_{\text{cation}} a_{\text{anion}})}{K_{\text{sp}}}\right], \tag{2.17}$$

where a_{cation} and a_{anion} are the activities of free cations and anions, respectively, and $K_{\text{sp}} = (a_{0\text{cation}} a_{0\text{anion}})$ is the solubility product of the electrolyte. Thus, supersaturation here is defined as the ratio of formation product to solubility product.

The free energy change ΔG and the chemical potential difference $\Delta\mu$ of the above equations are the necessary driving force for crystallization, and the temperature difference ΔT and the supersaturation ratio S are measures of this driving force.

2.2 3D Nucleation of Crystals

The formation of 3D nuclei from atomic or molecular entities existing in the volume of a growth medium involves their aggregation in an ordered phase. The process is usually envisaged to occur as a result of collision of individual atoms or molecules C_1 in such a way that their collisions yield a sequence of aggregates of increasing size like dimers C_2, trimers C_3, … i-mers C_i, according to the general reversible reaction:

$$iC_1 \Leftrightarrow C_i, \tag{2.18}$$

where C_i is the resulting aggregate formed by the additions of i monomers C_1. Aggregates like C_2, C_3, …, C_i are usually called embryos, subnuclei, or clusters. The process of formation of subnuclei is in dynamic equilibrium, some of them

grow larger while the others simply disintegrate with time. However, the statistical addition of individual atoms/molecules to some of the subnuclei leads to their development into a size when they no longer disintegrate (see Section 2.2.2). Such nuclei are said to attain a critical size and are called 3D stable nuclei.

2.2.1 Nucleation Barrier

The surface tension of a sphere is the lowest. Therefore, it is usually assumed that the nuclei prefer to attain a round shape. The reduction in the Gibbs free energy of the system due to the formation of a spherical nucleus of radius r is equal to the sum of the surface excess free energy ΔG_S and the volume excess free energy ΔG_V. The surface free energy ΔG_S is associated with the creation of the surface of the solid phase in the growth medium and is equal to the product of the surface area of the developing nucleus and the interfacial tension γ between the surface of the nucleus and the supersaturated medium surrounding it. Similarly, the volume excess free energy ΔG_V is a result of creation of the volume of the nucleus in the medium and is equal to the product of the volume of nucleus and the chemical potential difference $\Delta\mu$ per unit volume. Then, one may write the free energy change as

$$\Delta G = \Delta G_S + \Delta G_V = 4\pi r^2\gamma - \frac{4}{3}\pi r^3 \Delta\mu. \tag{2.19}$$

Since the creation of the new phase II from a supersaturated medium is associated with a decrease in the chemical potential difference $\Delta\mu$, the ΔG_V term is a negative quantity. The two terms on the right-hand side of Eq. (2.19) depend differently on r. This behavior of ΔG associated with the formation of the nucleus is shown in Figure 2.3 as a function of nucleus radius r. As may be seen from the figure, ΔG passes through a maximum and the maximum value ΔG^*_{3D}

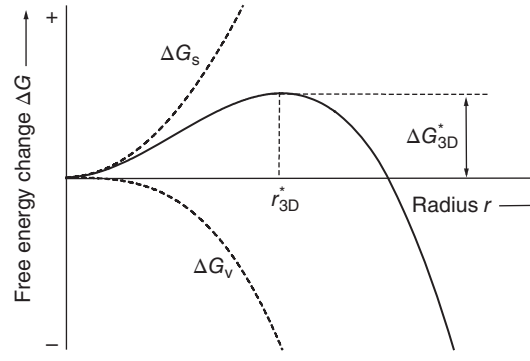

Figure 2.3 Change in Gibbs free energy ΔG as a function of radius r of nucleus formed in a supersaturated medium. Dashed curves show energy contributions ΔG_S and ΔG_V according to Eq. (2.19), whereas ΔG^*_{3D} is the activation barrier for the formation of 3D nucleus of radius r^*_{3D} according to Eq. (2.21).

corresponds to the critical radius r^*_{3D}. The value of r^*_{3D} may be obtained by maximizing Eq. (2.19), taking $d\Delta G/dr = 0$, i.e.

$$r^*_{3D} = \frac{2\gamma\Omega}{\Delta\mu}. \tag{2.20}$$

Upon substituting the value of r^*_{3D} from Eq. (2.20) into Eq. (2.19), one obtains

$$\Delta G^*_{3D} = \frac{16\pi}{3}\frac{\gamma^3\Omega^2}{(\Delta\mu)^2} = \frac{16\pi}{3}\frac{\gamma^3\Omega^2}{(k_B T \ln S)^2} = \frac{16\pi}{3}\frac{\gamma^3\Omega^2}{(\Delta T)^2}\left(\frac{T_m}{\Delta H_m}\right)^2 = \frac{4\pi}{3}\gamma r^{*2}_{3D}. \tag{2.21}$$

Note that Eqs. (2.20) and (2.21) contain $\Delta\mu$, which is given by different relations defined in Section 2.1, but Eq. (2.21) describes the dependence of ΔG^*_{3D} on supersaturation $\ln S$ and ΔT as applied during crystallization from supersaturated solutions and supercooled melts (cf. Eqs. (2.15) and (2.8)). The value of ΔG^*_{3D} is always a positive quantity because both γ and r^*_{3D} are positive quantities. Obviously, increasing supersaturation $\ln S$ and supercooling ΔT, and decreasing interfacial energy γ facilitate the formation of 3D nuclei.

In Eq. (2.21), the factor $16\pi/3$ is a result of the geometry of a spherical nucleus. For nuclei of other geometries, this geometrical factor has other appropriates values. For a cube, for example, this factor has a value of 32.

The occurrence of a crystalline phase in a supersaturated medium depends on the radius r of the nuclei forming in it. When the radius r of the nuclei is smaller than r^*_{3D}, the nuclei dissolve. However, when $r > r^*_{3D}$, the nuclei are stable and grow. The critical radius r^*_{3D} is the minimum size of a stable nucleus. As seen from Figure 2.3, only when the nucleus radius $r > r^*_{3D}$, the free energy ΔG for the formation of a nucleus decreases with an increase in r.

It should be noted that every phase transition is associated with two energy changes: the activation barrier ΔG^*_{3D} given by Eq. (2.21), and the overall change in the free energy ΔG, given by Eq. (2.3). The value of the activation barrier ΔG^*_{3D} is associated with the process of formation of 3D nuclei, whereas the overall change in the free energy ΔG determines whether the 3D nuclei formed in the growth system remain stable after their formation. The higher the activation barrier ΔG^*_{3D}, the more difficult it is to attain stable nuclei. Similarly, greater the change in ΔG, the higher is the stability of the phase formed (nuclei). As seen from Eq. (2.3), the stability of the crystallized phase in the growth system at a given temperature T is related to changes in its enthalpy and entropy (i.e. ΔH and ΔS).

2.2.2 Nucleation Rate

The formation of subnuclei of large size is a statistical process involving a particular free energy change $\Delta G(i)$ of cluster formation and the formation

of such subnuclei by the collision of a large number of atoms/molecules simultaneously is practically improbable. If C_0 is the concentration of possible sites for the formation of clusters of the new phase in the system, the equilibrium size distribution of the clusters of size i may be described by (Kashchiev, 2000)

$$C(i) = C_0 \exp\left[-\frac{\Delta G(i)}{k_B}\right], \tag{2.22}$$

where $C(i)$ denotes the concentration of C_i clusters containing i atoms/molecules C_1. The equilibrium size distribution between the C_i and C_1 clusters may also be given by

$$C(i) = C_1 \exp\left\{-\frac{[\Delta G(i) - \Delta G(1)]}{k_B T}\right\}, \tag{2.23}$$

where $C_1 = C(1)$. The monomer concentration C_1 is related to C_0 by

$$C_1 = C_0 \exp\left[-\frac{\Delta G(1)}{k_B T}\right]. \tag{2.24}$$

Since the equilibrium between C_i and C_1 clusters satisfies the Law of Mass Action, with the aid of Eqs. (2.23) and (2.24), Eq. (2.22) may be written in the form:

$$C(i) = C_0 \left(\frac{C_1}{C_0}\right)^i \exp\left\{-\frac{[\Delta G(i) - i\Delta G(1)]}{k_B T}\right\}. \tag{2.25}$$

In this equation. the preexponential term essentially denotes the equilibrium constant of the reaction of Eq. (2.18), whereas $[\Delta G(i) - i\Delta G(1)]$ is the net free energy change involved in the formation of i-sized cluster from individual atoms/molecules.

At constant temperature and supersaturation conditions, the occurrence of 3D nucleation is described by the so-called stationary nucleation rate J, given by (Kashchiev, 2000)

$$J = zf^* C^*, \tag{2.26}$$

where z is the Zeldovich factor lying between 0.01 and 1, f^* is a kinetic factor associated with the frequency of attachment of monomers to the stable nucleus, and C^* is given by Eqs. (2.22), (2.23), and (2.24) when the equilibrium concentration $C(i)$, the cluster formation free energy change $\Delta G(i)$, and the number i of atoms/molecules in the spherical critically-sized nucleus of radius r^* are

denoted by C^*, ΔG^*_{3D}, and i^*, respectively. Corresponding to the equilibrium concentration C^* given by Eq. (2.23), one obtains

$$\begin{aligned} J &= J_0 \exp\left(-\frac{\Delta G^*_{3D}}{k_B T}\right) = J_0 \exp\left(-\kappa \frac{\gamma^3 \Omega^2}{k_B T \Delta\mu^2}\right) \\ &= J_0 \exp\left(-\frac{B}{\ln^2 S}\right) = J_0 \exp\left(-\frac{B'}{T(\Delta T)^2}\right), \end{aligned} \tag{2.27}$$

where the kinetic factor

$$J_0 = z f^*_e C_0 S, \tag{2.28}$$

and the constants (cf. Eq. (2.21))

$$B = \kappa \left(\frac{\gamma \Omega^{2/3}}{k_B T}\right)^3, \tag{2.29}$$

$$B' = \kappa \left(\frac{\gamma \Omega^{2/3}}{k_B}\right)^3 \left[\frac{R_G T_m}{\Delta H_m}\right]^2. \tag{2.30}$$

In Eq. (2.30), the term in the square brackets is written in the form of a dimensionless quantity. Typically, $\Delta H_m / R_G T_m$ is about 2 for metals, 3 for anhydrous inorganic salts, and 6 for organic compounds (Sangwal, 1989; see below). Eq. (2.30) describes the nucleation rate J as a function of driving force for crystallization from supersaturated solutions and supercooled melts.

In the above expressions, f^*_e is the frequency of attachment of monomers to the nucleus at equilibrium, S is the supersaturation ratio (see Eqs. (2.9) and (2.15)), ΔG^*_{3D} is given by Eq. (2.21), and κ is the shape factor for the nuclei (for spherical nuclei $\kappa = 16\pi/3$). Typically, for melts and solutions, $0.01 < z < 1$, $C_0 \approx 10^{20}$ to $10^{29}\ m^{-3}$, $f^*_e \approx 1$ to $10^{12}\ s^{-1}$, and $1 < S < 10$, $J_0 = 10^{15}$ to $10^{40}\ m^{-3} \cdot s^{-1}$ (Kashchiev, 2000).

Equation (2.27) represents the temperature dependence of nucleation rate J and is usually referred to as the classical theory of 3D nucleation. Obviously, it is an Arrhenius-type relation where the activation barrier ΔG^*_{3D} is essentially a measure of the "difficulty" for embryos to attain the radius r^*_{3D} of the stable nuclei in a growth medium.

The behavior of nucleation rate J on supersaturation ratio S (and on the related chemical potential difference $\Delta\mu$ defined in Section 2.1) of systems is well described by Eq. (2.27). However, in the case of solutions at high concentrations and melts, the viscosity of the systems affects the nucleation rate J. The effect of viscosity η on J is due to its influence on the frequency f^*_e of attachment of monomers to the nucleus (Eq. (2.28)) associated with the diffusion of

monomers to the nucleus and their subsequent integration. In this case, the nucleation rate is given by

$$J = J_0^* \exp\left(-\frac{B}{\ln^2 S} + \frac{E_\eta}{k_B T} \right), \tag{2.31}$$

where J_0^* is a new kinetic factor such that $J_0^* < J_0$ and E_η is the activation energy for viscous flow.

In systems described by Eq. (2.31), the nucleation rate J initially increases with increasing supersaturation $\ln S$ but later it begins to decrease such that the nucleation rate J passes through a maximum at a particular value of $\ln S$. This is due to the fact that, at a given temperature, at low values of $\ln S$ when the B term dominates, the rate increases with an increase in $\ln S$. However, at very high values of $\ln S$ when the B term becomes negligibly small in comparison with the E_η term, the latter term begins to dominate. Consequently, at very high values of $\ln S$, the nucleation rate J is decreased. Absence of nucleation means that the system is in the glassy state.

The derivation of Eq. (2.27) using Eq. (2.22) assumes that the interfacial tension γ of a critically-sized nucleus is the same as that of a large bulk crystal. This assumption may hold in the case of large nuclei forming at low supersaturations, but is certainly violated at high supersaturations when the cluster size approaches atomic/molecular dimensions (cf. Eq. (2.20)). This may be understood better when the free energy change $\Delta G(i)$ for the formation of i-sized cluster is given by

$$\Delta G(i) = -i\Delta\mu + \kappa\gamma i^{2/3}, \tag{2.32}$$

where κ is the shape factor for the cluster. For $i = 1$, Eq. (2.32) gives the free energy change

$$\Delta G(1) = -\Delta\mu + \kappa\gamma. \tag{2.33}$$

From Eqs. (2.32) and (2.33), one obtains the net free energy change for the formation of the i-sized nucleus in the form:

$$\Delta G_{3D} - i\Delta G(1) = \kappa\gamma\left(i^{2/3} - i\right). \tag{2.34}$$

This equation describes the net free energy change $[\Delta G_{3D} - i\Delta G(1)]$ involved in the formation of i-sized cluster according to clustering reaction (2.18), and Eq. (2.25) of the equilibrium between C_i and C_1 clusters is said to be self-consistent because it reduces to Eq. (2.23) when $i = 1$.

When $i = i^*$, Eq. (2.34) represents the new activation barrier $\left[\Delta G_{3D}^* - i\Delta G(1)\right]$. The nucleation rate J in this case is also described by Eq. (2.27) with the kinetic factor J_0 given by Eq. (2.28). From Eq. (2.20), it may be noted that the interfacial energy γ of the stable nucleus is now size dependent and decreases with an increase in $\Delta\mu$, and the nucleation rate J strongly increases with $\Delta\mu$.

With the new activation barrier defined by Eq. (2.34), Eq. (2.27) holds when the nuclei are of large size and the size decreases smoothly with increasing $\Delta\mu$. However, at very high $\Delta\mu$ when the nuclei contain only very few atoms/molecules, change in the number of atoms/molecules by a new atom/molecule is possible in succession of $\Delta\mu$ intervals. This feature of nucleus formation is not accounted for by the classical nucleation theory. In the limit $i^* \rightarrow 1$, the atomistic theory of nucleation based on self-consistency in $C(i)$ as required by the Law of Mass Action (see Eq. (2.25)) provides a more adequate description of the nucleation rate (Kashchiev, 2000)

$$J = J_0 \exp\left(\frac{\Phi^*}{k_B T}\right) \exp\left(\frac{i^* \Delta\mu}{k_B T}\right), \tag{2.35}$$

where Φ^* is the effective excess energy of the nucleus and is $\Delta\mu$ independent.

2.2.3 3D Heterogeneous Nucleation

Homogeneous 3D nucleation is possible when there is no external source that alters either the value of the kinetic parameter J_0 or the interfacial energy γ. It is well known that foreign particles present in bulk supersaturated media as well as cracks and scratches on the walls of crystallizers frequently catalyze 3D nucleation. This type of nucleation is referred to as heterogeneous 3D nucleation.

Depending on the shape of embryos forming on the foreign substrate, the embryos develop in two or three dimensions. For example, a cap-shaped embryo changes its size in three dimensions, while a disk-shaped embryo grows laterally when its height remains unchanged. In the former case, the nucleation is 3D, while in the latter case it is two-dimensional. Therefore, in principle, nucleation on a foreign substrate can be both two- or three-dimensional.

We consider here 3D nucleation where the embryo forms on a flat substrate. In this case, the shape of the crystal embryo is essentially a spherical cap (see Figure 2.4a), with the equilibrium wetting (contact) angle θ defined from 0 and π by

$$\cos\theta = \frac{(\gamma_{sf} - \gamma_{cs})}{\gamma_{cf}} = m, \tag{2.36}$$

where γ_{cs}, γ_{sf}, and γ_{cf} denote the interfacial energy between crystalline solid phase (c) and foreign particle surface (s), foreign particle surface (s) and mother fluid phase (f), and crystalline solid phase (c) and mother fluid phase (f), respectively. For a sufficiently large nucleus, $\gamma_{cf} = \gamma$. The contact angle θ defines a numerical factor ϕ, given by

$$\phi = \frac{(2 + \cos\theta)(1 - \cos\theta)^2}{4}. \tag{2.37}$$

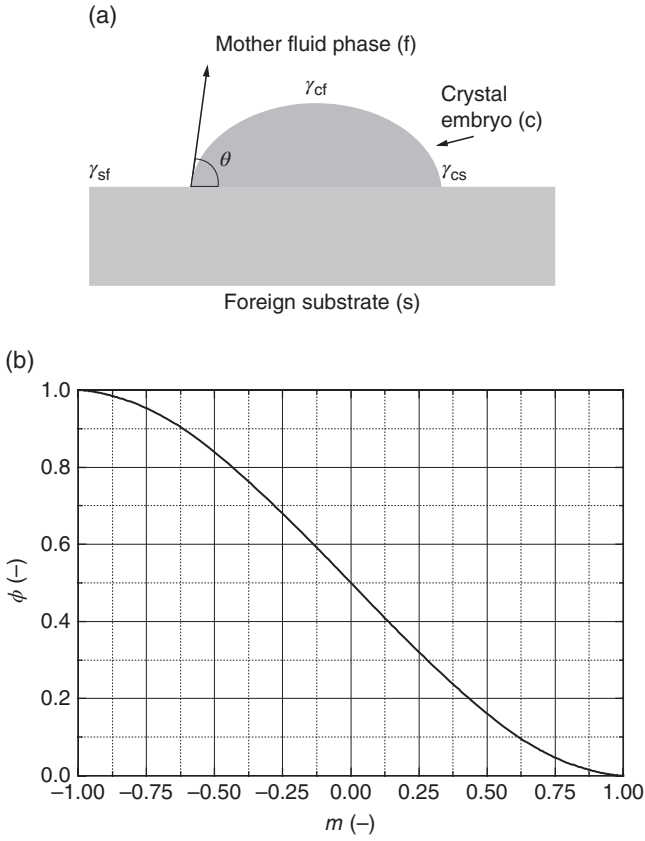

Figure 2.4 (a) Cross-section of a cap-shaped nucleus on the surface of a substrate; crystalline embryo (c), foreign substrate particle (s), and mother phase (f). (b) Dependence of the factor ϕ on $m = \cos\theta$ according to Eq. (2.37).

The value of ϕ lies between 0 and 1, depending on the value of $m = \cos\theta$, as shown in Figure 2.4b. Obviously, heterogeneous nucleation occurs when $-1 < m < 1$, and the situation $m = -1$ corresponds to homogeneous nucleation. When $\theta = 0$, $\phi = 0$; when $\theta = \pi/2$, $\phi = 1/2$; and when $\theta = \pi$, $\phi = 1$. The cases of $\theta = 0$ and $\theta = \pi$ are usually referred to as complete wetting and complete non-wetting, respectively.

Irrespective of whether nucleation is homogeneous or heterogeneous, the above treatment of 3D nucleation can be represented by unified formulae if the interfacial energy γ of nucleus formed by homogeneous nucleation is replaced by an effective interfacial energy γ_{eff}, given by

$$\gamma_{\text{eff}} = \Phi\gamma, \tag{2.38}$$

where the activity factor Φ is a number between 0 and 1, and is related to the numerical factor ϕ (see Eq. (2.38)). For cap-shaped nuclei, $\Phi = \phi^{1/3}$.

The above treatment of heterogeneous 3D nucleation considers only changes in the interfacial energy of the nucleus and does not take into account the process of integration of growth species into the embryos during nucleation on foreign particles. For example, it is easy to realize that nucleation on a foreign substrate body (s) of radius r_s reduces the effective surface of collision of embryos, where growth species are incorporated into embryos (cf. Figure 2.4a). This leads to a decrease in the value of the kinetic parameter J_0, thereby decreasing the nucleation rate J (see Eq. (2.27)). This effect is opposite to that of the predicted decrease in the nucleation barrier ΔG^*_{3D} due to a decrease in the interfacial energy γ (see Eqs. (2.27) and (2.38)). The decrease in the effective surface area for collision of embryos due to nucleation on foreign bodies is determined by the parameter (cf. Liu, 1999; Liu et al., 2000)

$$r' = \frac{r_s}{r^*_{3D}}, \tag{2.39}$$

where the radius of critical nucleus r^*_{3D} is given by Eq. (2.20). Since the nucleus radius r^*_{3D} decreases with an increase in supersaturation ln S, for the foreign particle of a particular r_s, the ratio r' of radii increases with increasing ln S. Therefore, the numerical factor ϕ now is a function of m and r'.

When the effective surface area for the collision of embryos is considered, the 3D nucleation is heterogeneous. Then the nucleation rate J_{het} may be given by an expression similar to Eq. (2.27) (cf. Liu, 1999; Liu et al., 2000)

$$J_{het} = J_{0(het)} \exp\left[-\frac{B_{het}}{\ln^2 S}\right] = J_{0(het)} \exp\left[-\frac{B'_{het}}{T(\Delta T)^2}\right], \tag{2.40}$$

where

$$J_{0(het)} = 4\pi a r_s^{\,2} N_0 \phi'(m,r')[\phi(m,r')]^{1/2} J_0, \tag{2.41}$$

$$B_{het} = \phi(m,r')B, \quad B'_{het} = \phi(m,r')B'. \tag{2.42}$$

In Eqs. (2.41) and (2.42), N_0 is the number of nuclei per unit area on the surface, a is the dimension of growth species, $\phi'(m,r')$ is a parameter that depends on r' similar to $\phi(m,r')$ and lies between 0 and 1, whereas B and B' are given by Eqs. (2.29) and (2.30), respectively. We note that, for heterogeneous nucleation, $0 < \phi(m,r') < 1$, $0 < \phi'(m,r') < 1$, and $4\pi a r_s^{\,2} N_0 < 1$. Consequently, $J_{0(het)} < J_0$, $B_{het} = \phi B < B$, and $B'_{het} = \phi B' < B'$. For homogeneous nucleation when $\phi(m,r') = \phi'(m,r') = 1$ and $4\pi a r_s^2 N_0 = 1$, Eq. (2.40) reduces to Eq. (2.27). In fact, when $r' >> 1$, and the nuclei may be considered to form on a planar substrate and Eq. (2.40) describes the nucleation rate J according to homogeneous 3D nucleation.

According to Eq. (2.40), the factors $\phi(m,r')$ and $\phi'(m,r')$ play different roles in different regimes of driving force. At low supersaturations $\ln S$, for example, when the nucleation barrier ΔG^*_{3D} is very high (see Eq. (2.27)), the exponential term associated with the nucleation barrier is dominant over contribution from collisions of embryos due to the available effective surface area on the substrate, represented by the factors $\phi(m,r') = \phi'(m,r')$. Thus, the nucleation rate is controlled by heterogeneous nucleation. However, with increasing supersaturation, the preexponential term involving factors associated with effective collisions becomes dominant over the exponential term. Consequently, for any two sets of m and $\phi(m,r')$ there is always a critical value of supersaturation when heterogeneous nucleation occurring at low supersaturation undergoes transition to homogeneous nucleation. Obviously, for a given system, different foreign particles having distinct surface properties and/or different sizes control nucleation in different supersaturation regimes. Homogeneous nucleation occurs only when $\phi(m,r') = \phi'(m,r') = 1$, and this occurs always at very high supersaturations.

Impurity particles present in the growth medium were considered above to act as active sites of heterogeneous nucleation. However, impurity particles present in the growth medium can also lead to a decrease in the value of the kinetic parameter J_0 by physically blocking the existing active sites (i.e. kinks) for the attachment of growth units on the 3D nuclei already formed before. If θ_i is the fraction of blocked active sites of a nucleus, then the kinetic factor becomes $J_0(1 - \theta_i)$. Assuming that the impurity adsorption on the active sites obeys the Langmuir adsorption isotherm, the relationship between heterogeneous nucleation rate J_{het} on impurity concentration c_i may be given by Eq. (2.40) with the preexponential factor $J_{0(het)} = J_0/(1 + K_L c_i)$, where K_L is the Langmuir constant.

2.3 Ideal and Real Solubility

2.3.1 Basic Concepts

As mentioned in Chapter 1, mixing of a solute with its solvent at given temperature and pressure conditions produces a mixture, which can be homogeneous as well as heterogeneous depending on the capability of the solvent to devour the solute. The limiting concentration of the solute that can be taken up by the solvent keeping homogeneity of the mixture is called its solubility and the solution is referred to as saturated. Addition of more solute to the saturated solution simply remains undissolved in it because the pure solute is in equilibrium with the dissolved solute. The free energy change for dissolving the solute in the solution approaches zero as the concentration approaches saturation.

The temperature dependence of the solute concentration of saturated solution (i.e. solubility) is predicted by the Le Chatelier principle, which states that

any change in the variables that characterize the state of a system in equilibrium causes a shift in the position of equilibrium in a direction that tends to counteract the change in the variable under consideration. Therefore, if dissolution is exothermic, solubility will decrease with an increase in temperature, and conversely, if dissolution is endothermic as is usually encountered, solubility will increase with temperature. Calcium hydroxide, $Ca(OH)_2$, is an example of a compound whose solubility decreases with an increase in temperature of solvent water. In the temperature range between 0 and 100 °C in water, the solubility of sodium chloride, NaCl, insignificantly increases with temperature, but the solubilities of KNO_3 and $PbCl_2$ at 100 °C are several times higher than those at 0 °C. Figure 2.5 illustrates typical examples of the temperature dependence of solubility x_s for some common inorganic compounds in water in the temperature interval 0–100 °C. As seen from the figure, the solubilities of all compounds neither increase nor decrease steadily in the entire temperature interval. There are different compounds whose solubility either increases or decreases in certain temperature intervals with an increase in temperature.

Smooth, continuous increase or decrease in solubility of a compound with temperature means that the same solid phase is in equilibrium in the solution at all temperatures. However, break in the curve of solubility x_s of a compound in a given solvent as a function of temperature T indicates that a change in the solid phase in equilibrium has occurred in the saturated solution at this temperature. In Figure 2.5, examples of well-defined breaks are Na_2SO_4, $KAl(SO_4)_2$, and $NH_4Al(SO_4)_2$. The breaks are caused by the formation of hydrates

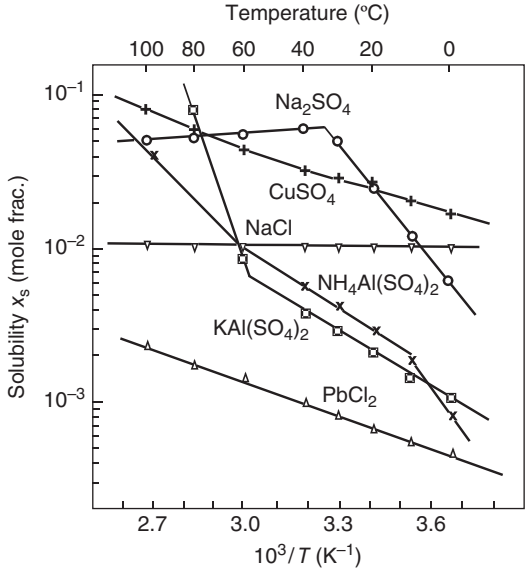

Figure 2.5 Typical examples of temperature dependence of solubility x_s for some common inorganic compounds in water in the temperature interval 0–100 °C. *Source:* Adapted from Sangwal et al. (1994).

containing different water molecules. A general trend of formation of hydrates of different salts in aqueous solutions is that the number of water molecules entering a compound decreases with increasing temperature. For example, $Na_2SO_4{\cdot}10H_2O$ is formed between 0 and 33 °C and the salt solubility increases with temperature, but anhydrous Na_2SO_4 is formed above 33 °C and the solubility decreases with increasing temperature. In contrast to only two phases of Na_2SO_4, with increasing solute concentration in the aqueous solution $MgSO_4$ forms dodecahydrate, heptahydrate, hexahydrate, and monohydrate in the temperature intervals between 0 and –2C, –2 and 52 °C, 52 and 73 °C, and 73 and 194 °C, respectively. Note that –2 °C is an eutectic point but 52 and 73 °C are peritectic points.

Increasing or decreasing trends of the dependence of solubility x_s on temperature T are usually discussed in terms of positive or negative temperature coefficient of solubility (i.e. $\partial x_s/\partial T$) in a particular temperature range. Depending on the nature of the solute–solvent system, the solubility coefficient can be high or low and can vary in different temperature intervals. It is the solute–solvent interaction that leads to the dissolution of the solute in the solution and decides the solubility.

The solubility of a solute in a solvent is expressed in different ways (see Section 1.4). Molar and molal concentrations are frequently used to express solute concentration in aqueous solutions but weight percent concentration relative to the solvent are usually used to express concentration in different individual solvents and their mixtures. However, the temperature dependence of solubility of various solutes in solutions is customarily expressed in mole fraction x. Here, we use x_s and x to denote solute solubility and concentration (frequently in mole fraction), respectively, but later in Section 2.5, we use the general notation c to denote solute concentration. For the sake of clarity, the concentration units are mentioned whenever required.

Dissolution of a solute to yield its saturation solution of concentration x_s is a case of phase change from solid to liquid phase and involves a free energy change ΔG^0, given by (cf. Eq. (2.11))

$$\Delta G^0 = -R_G T \ln x_s, \tag{2.43}$$

where the solute activity a of Section 2.1 is replaced by the concentration x_s. Using the Gibbs–Helmholtz equation

$$\frac{d\Delta G^0}{dT} = -\Delta S^0 = \frac{\Delta G^0 - \Delta H^0}{T}, \tag{2.44}$$

where ΔS^0 is the entropy of the solution and ΔH^0 is the change in the heat content, Eq. (2.43) may be written in the form of van't Hoff's equation:

$$\frac{d\ln x_s}{dT} = \frac{\Delta H^0}{R_G T^2}. \tag{2.45}$$

According to this relation the solubility of a solute is the same for all solutions and the enthalpy of dissolution $\Delta H^0 = \Delta H_m$. Eq. (2.44) is usually expressed in the form of an Arrhenius-type relation:

$$\ln x_s = \frac{\Delta H_m}{R_G T_m} - \frac{\Delta H_m}{R_G T}, \tag{2.46}$$

with $x_s = 1$ for $T = T_m$. Equation (2.46) holds when molecules of solute and solvent are similar and are miscible in the entire concentration range. Equation (2.46) describes the temperature dependence of solubility of *ideal solutions*.

Values of enthalpy of melting ΔH_m and melting point T_m are available in different handbooks (for example, see Lide, 1996/1997; Mullin, 2001), and follow the empirical relations (Sangwal, 1989; also see Section 1.2)

$$\frac{\Delta H_m}{R_G T_m} = 3 + \frac{6 n_h}{z_c^2}, \quad \text{for inorganic compounds}, \tag{2.47}$$

$$\frac{\Delta H_m}{R_G T_m} = 6, \quad \text{for organic compounds}, \tag{2.48}$$

where n_h is the hydration of water molecules and z_c is the charge of cation of a given salt.

Real solutions are rarely ideal but they follow a relation similar to Eq. (2.46), i.e.

$$\ln x_s = A - \frac{\Delta H_s}{R_G T}, \tag{2.49}$$

where A is a constant and the heat of dissolution

$$\Delta H_s = \Delta H_m + \Delta H_{mix}, \tag{2.50}$$

where ΔH_{mix} is the enthalpy of mixing. Solutions following Eq. (2.49) are called *regular solutions*. Regular solutions are similar to ideal solutions with the difference that thermal motion of its molecules leads to their association. Obviously, $\Delta H_{mix} \neq 0$ for regular solutions and $\Delta H_{mix} = 0$ for ideal solutions. In other words, in regular solutions $\Delta H_s \neq \Delta H_m$. Moreover, ideal solution relationship approximates the behavior of real systems only for mixtures of chemically similar substances and applies at low solute concentrations.

There are several different causes of nonideality in solutions such as differences in shapes of molecules and interactions between solute and solvent molecules (say c and f, respectively). Even when solute and solvent molecules are considered to be similar, one of the nonidealities originates from their random distribution in the solution volume. This is the model of regular solutions, which assumes that the solution volume is the sum of the volumes of N_c and N_f molecules of individual components and they pack the solution volume

simply by interchanging their positions. If w_{cc}, w_{ff}, and w_{cf} denote solid–solid, fluid–fluid, and solid–fluid bonds per pair of molecules/ions, respectively, the chemical potential per molecule of the solute may be given by (Eggers et al., 1964)

$$\mu_c - \mu_c^0 = k_B T \ln x_c + (1 - x_c)^2 w_{cf}, \tag{2.51}$$

and a similar expression for solvent molecules f; the energy of mixing

$$\Delta H_{mix} = \left(\frac{N_c N_f}{N_c + N_f}\right) w_{cf} = N_A x_c (1 - x_c) w_{cf}, \tag{2.52}$$

and entropy of mixing

$$\Delta S_{mix} = -k_B (N_c \ln x_c + N_f \ln x_f) = N_A k_B [x_c \ln x_c + (1 - x_c) \ln(1 - x_c)], \tag{2.53}$$

where N_A is the Avogadro number and x_c denotes the molar concentration of the solute.

Change in the bond energy w between solute and solution molecules in regular solution may be given by the relation:

$$\frac{Zw}{2} = \frac{Z(w_{cc} + w_{ff} - 2w_{cf})}{2}, \tag{2.54}$$

where Z is the number of nearest neighbors. Here, enthalpy of solution $\Delta H_s = Zw/2$ and enthalpy of melting $\Delta H_m = Z(w_{cc} - w_{ff})/2$. Therefore, the value of enthalpy of mixing $\Delta H_{mix} = Z(w_{ff} - w_{cf})$ of regular solutions may be used as an indicator of solid–solid, fluid–fluid, and solid–fluid interactions. When $\Delta H_{mix} > 0$, solid–fluid interactions are stronger than solid–solid and fluid–fluid interactions (i.e. $w_{cf} > w_{cc} + w_{ff}$). Then the ideal solubility is greater than the real one (cf. Eq. (2.50)). However, when $\Delta H_{mix} < 0$, solid–solid and fluid–fluid interactions are stronger than solid–fluid interactions (i.e. $w_{cf} < w_{cc} + w_{ff}$). Then the ideal solubility is lower than the real one. When $\Delta H_{mix} = 0$ (i.e. $w_{cf} = 0$), the solution behaves as an ideal solution. Thus, deviations from the ideal solubility behavior are due to the nature of interactions between solute and solvent molecules. Note that the second term on the right side of Eq. (2.51) is associated with the activity coefficient of a regular solution.

Equation (2.52) predicts a maximum and a minimum value of ΔH_{mix} at composition $x_c = 0.5$ for $w_{cf} > 0$ and $w_{cf} < 0$, respectively. This is a consequence of consideration of a two-component system of unassociated atoms/molecules. Association of atoms/molecules of components in the solution leads to a decrease in their motion such that the entropy of the system is lower than that of the ideal one. Consequently, one expects that the enthalpy of mixing ΔH_{mix} is negative and the entropy of mixing ΔS_{mix} is less positive than that for the ideal solution for systems in which association of their atoms/molecules takes place.

An opposite effect is encountered in systems composed of an associated component and a more or less passive component. In this case, mixing partially destroys association of atoms/molecules, which results in a positive enthalpy of mixing because rupturing of associated atoms/molecules requires consumption of heat. In such cases the value of the fraction x_c of the component of the system is also usually reduced below 0.5.

The above treatment of regular solutions is based on creating a mixture of two components: one of which is a solvent and the other is a solute and the dimensions of atoms or molecules composing them are the same. However, real solutions are not so simple regarding the dimensions of atoms/molecules of components, the physical nature of their composition as well as the total number of components present in them. In aqueous solutions of salts, for example, their molecules are dissociated into cations and anions, which exist as solvated entities of dimensions differing from that of water molecules. Therefore, Eqs. (2.52) and (2.53) of ΔH_{mix} and ΔS_{mix} should be considered as guidelines only.

The temperature dependence of solubility x_s of a solute in a saturated solution is also usually given by the empirical relation

$$x_s = a_1 + a_2 T + a_3 T^2 + \cdots, \tag{2.55}$$

where a_1, a_2, a_3, ..., are constants and T is taken in °C.

Apart from the effect of temperature, several factors are known to affect the solubilities of solutes. Among these, the effects of common ions, foreign ions, solution pH, and formation of complexes are well known (Berg, 1963; Charlot, 1976; Margolis, 1966; Pataki and Zapp, 1980). The presence of common ions always decreases the solubility of a solute, while foreign ions and complex formation lead to an increase in the solubility. Most of the observations of changes in the solutions of different solutes in their solvents can be interpreted in terms of changes in the values of ΔH_m or T_m caused by these factors. Since ΔH_m and T_m are mutually related (cf. Eqs. (2.47) and (2.48)), the ultimate consequence of the above factors may be explained from a consideration of changes in the enthalpy of mixing ΔH_{mix}, determined by the bond energy w_{cf} (see Eq. (2.52)).

2.3.2 Examples of Experimental Data

Real solutions composed of two components, one of which is a solvent and the other is a solute, were considered above. Equation (2.49) of the temperature dependence of the equilibrium concentration (solubility) of solutes deals with such two-component systems. However, depending on the practical requirement, real solutions may be composed of more than two components. For example, the solution may contain two or more solutes in a particular solvent or one solute in a mixture of two or more solvents.

At a given temperature, not only the solubility of different solutes in a particular solvent such as water is different but also the solubility of the same solute in different solvents is different. For example, at room temperature potassium dihydrogen phosphate (KH_2PO_4; popularly known as KDP) has a relatively high solubility in water but it is sparingly soluble in alcohols. Therefore, at a particular temperature the solubility of KDP in solvent water can be reduced by mixing it with alcohols in various proportions. Another miscible solvent, such as alcohols in the above case, in which the solute is insoluble or poorly soluble is usually called an *antisolvent* or *nonsolvent*. Addition of antisolvents to saturated solutions of solutes dissolved in fairly-soluble solvents is the basis of processes of salting-out and drowning-in (antisolvent crystallization).

Using the theoretical background of real solutions, some general features of the dependence of solubility of some inorganic and organic solutes on the temperature of mixtures of two solvents in different proportions and on the antisolvent content at different temperatures are presented below.

Figure 2.6 shows the experimental data of the temperature dependence of solubility x_s of ammonium oxalate [$(NH_4)_2C_2O_4$; abbreviated as AO] in water and water–acetone mixtures in the form of Arrhenius plots according to Eq. (2.49) with the best-fit values of the parameters A and $\Delta H_s/R_G$ shown in Figures 2.7a and 2.7b as a function of solvent mixture composition X (wt%), respectively. There are large errors in the estimated values of A and $\Delta H_s/R_G$ but definite

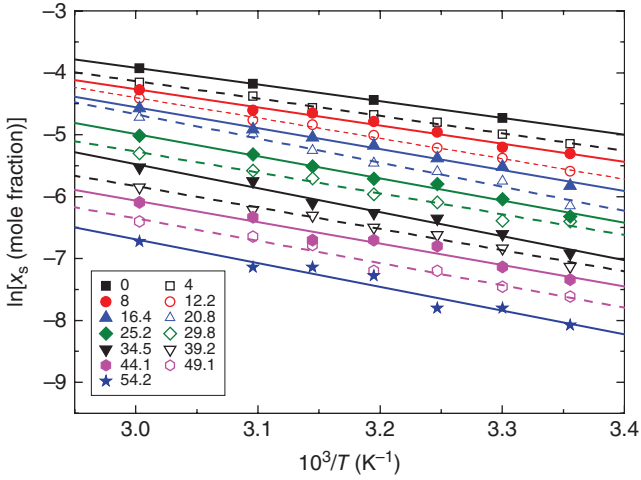

Figure 2.6 Dependence of solubility x_s of ammonium oxalate in water and water–acetone mixtures on temperature T in the form of Arrhenius plots. Linear plots are drawn according to Eq. (2.49) with the values of parameters of Figure 2.7. Composition X of water–acetone mixture is given in the inset as wt% of acetone. *Source:* After Sangwal et al. (2013). Copyright (2013), with permission from Elsevier.

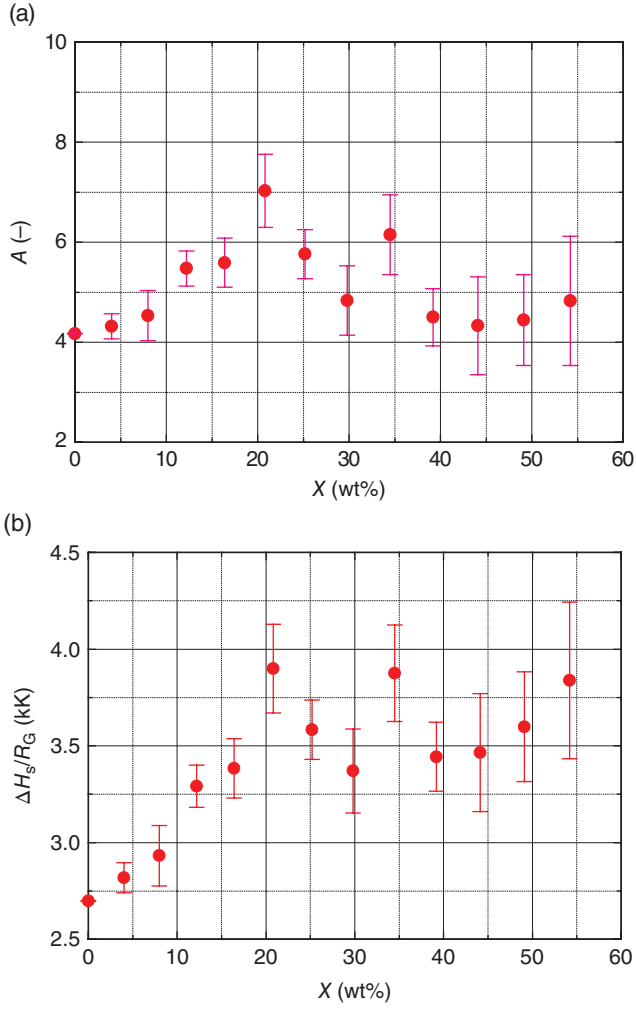

Figure 2.7 Plots of (a) preexponential factor A and (b) $\Delta H_s/R_G$ on composition X of acetone–water mixture. Standard deviation in the estimated values of A and $\Delta H_s/R_G$ is shown by vertical bars. *Source:* Adapted from Sangwal et al. (2013). Copyright (2013), with permission from Elsevier.

trends in their variation with X can be inferred. With an increase in X, the constant A increases from an initial value of 4.2, attains a maximum value of about 6 at X equal to about 25 wt%, and finally decreases and attains a constant value of about 4.5. However, $\Delta H_s/R_G$ slowly increases with an increase in X and finally attains a constant value of about 3.5 kK for X above about 25%. Since $\Delta H_s = \Delta H_m + \Delta H_{mix}$ (see Eq. (2.50)), from the increase in $\Delta H_s/R_G$ it follows that an increase in

acetone content in the water–acetone mixture leads to an increase in the enthalpy of mixing ΔH_{mix}.

Figure 2.8 shows the experimental data of the temperature dependence of solubility x_s of KDP in water and mixtures of water and ethanol, 1-propanol, and 2-propanol in different proportions as plots of $\ln x_s$ against $1/T$. The linear plots are drawn according to Eq. (2.49) with the values of constants A and $\Delta H_s/R_G$ listed in Table 2.1. It may be seen that the data are well described by

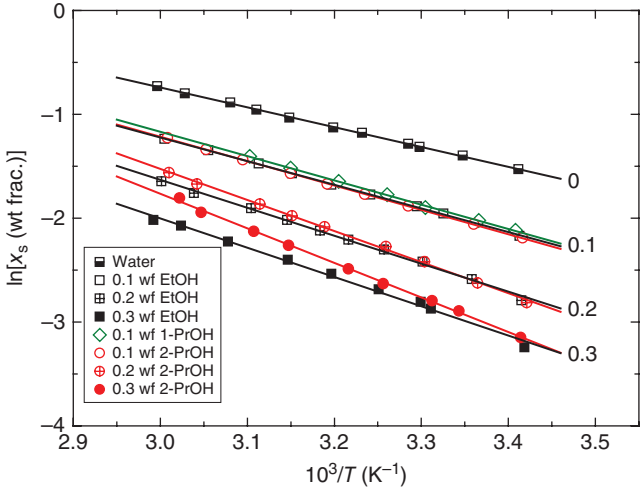

Figure 2.8 Plots of $\ln x_s$ of KDP in water and mixtures of water and ethanol, 1-propanol and 2-propanol in different proportions against $1/T$. Linear plots are drawn according to Eq. (2.49) with the values of constants A and ΔH_s listed in Table 2.1. *Source:* Original data from Barata and Serrano (1997).

Table 2.1 Values of constants A and $\Delta H_s/R_G$ of KDP+water+alcohol systems.

Compound	Solvent	X	A	$\Delta H_s/R_G$ (kK)	ΔH_s (kJ mol^{-1})
KDP	Water	0	4.992 ± 0.047	1.911 ± 0.015	15.89 ± 0.12
	Water + EtOH	0.1	5.620 ± 0.055	2.281 ± 0.017	18.96 ± 0.14
	Water + EtOH	0.2	6.442 ± 0.169	2.691 ± 0.053	22.38 ± 0.44
	Water + EtOH	0.3	6.447 ± 0.266	2.817 ± 0.083	23.42 ± 0.69
	Water + 1-PrOH	0.1	5.845 ± 0.096	2.338 ± 0.030	19.44 ± 0.24
	Water + 2-PrOH	0.1	5.826 ± 0.041	2.347 ± 0.013	19.51 ± 0.11
	Water + 2-PrOH	0.2	7.455 ± 0.144	2.994 ± 0.045	24.89 ± 0.37
	Water + 2-PrOH	0.3	8.211 ± 0.144	3.326 ± 0.045	27.65 ± 0.37

Eq. (2.49) and the values of the intercept A and the slope $\Delta H_s/R_G$ of the plots are determined by the solvent composition X. The data of the dependence of the heat of dissolution ΔH_s of KDP in different solvent-mixtures against their composition X is shown in Figure 2.9. The value of the heat of melting ΔH_m for KDP is also shown in the figure. It may be seen that ΔH_s increases with increasing solvent composition X and its value approaches that of ΔH_m at $X \approx 0.3$ weight fraction of ethanol and probably at a much higher value of X of 2-propanol. With reference to Eq. (2.51), it is easy to see that $\Delta H_{mix} < 0$ in this case.

Figure 2.10 presents two more examples of the temperature dependence of solubility x_s of vanillin (4-hydroxy-3-methoxybenzaldehyde) and ethyl vanillin (3-ethoxy-4-hydroxybenzaldehyde) in water and its mixtures with ethanol, 1- and 2-propanol, ethylene glycol (EGOH), and acetonitrile (ANT) in different proportions X against $1/T$. The entire data for the solubility x_s of vanillin in different solvent mixtures are shown in Figure 2.10a and b, whereas the data for the solubility x_s of vanillin (V) and ethyl vanillin (EV) in water and its mixtures with 2-propanol are compared in Figure 2.10c. The linear plots are drawn according to Eq. (2.49) with the values of constants A and $\Delta H_s/R_G$ listed in Table 2.2. From these plots it may be seen that: (i) the $x_s(T)$ data for the two compounds in different solvent mixtures may be described by regular solution relation (2.49), (ii) the solubility x_s of both vanillin and EV in water is the lowest and increases with the content of the three other solvents but an abrupt increase in the

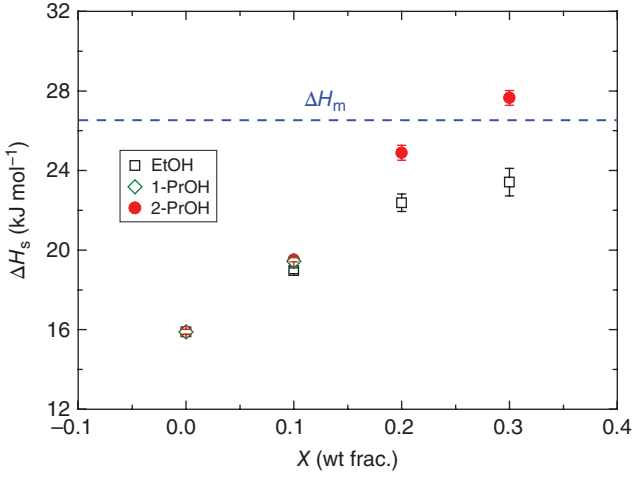

Figure 2.9 Dependence of heat of dissolution ΔH_s of KDP in water and mixtures of water and ethanol, 1-propanol and 2-propanol in different proportions against solvent composition X. Data from Table 2.1. Heat of melting ΔH_m for KDP is shown by a dashed line.

solubility occurs in ANT (see Figure 2.10a), and (iii) the solubility x_s of EV in mixtures of different solvents is lower than that of vanillin.

A better idea of the trends of the two compounds may be had from the plots of the dependence of heat of dissolution ΔH_s of vanillin and EV in water and its mixtures with ethanol, 1- and 2-propanol, EGOH, and ANT in different

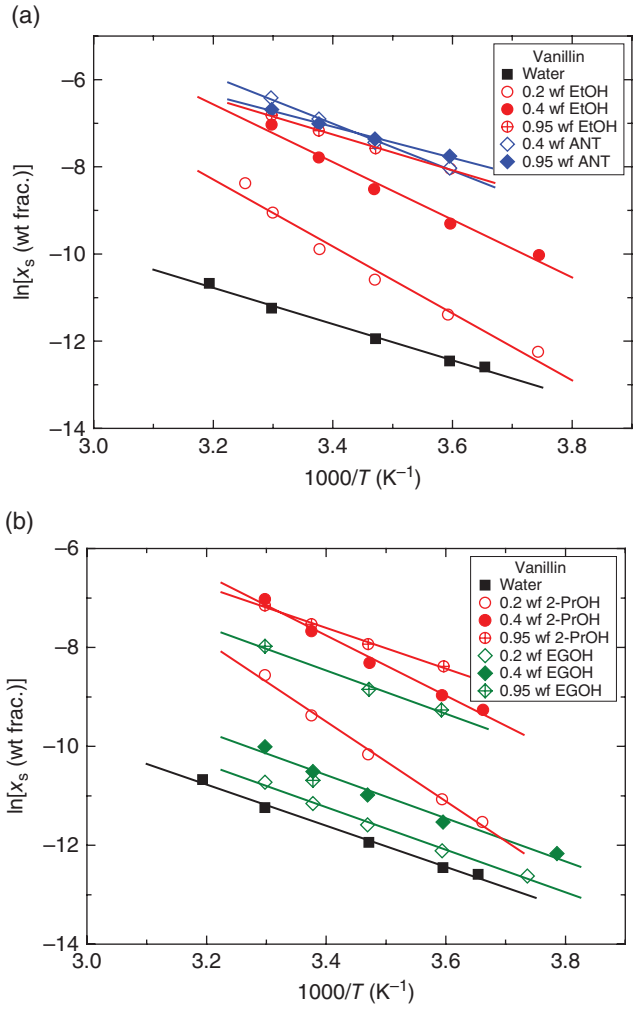

Figure 2.10 Plots of lnx_s of vanillin and ethyl vanillin in water and its mixtures with ethanol, 1- and 2-propanol, ethylene glycol (EGOH), and acetonitrile (ANT) in different proportions against 1/*T*. Linear plots are drawn according to Eq. (2.49) with the values of constants *A* and ΔH_s listed in Table 2.2. *Source:* Original data from Hussain et al. (2001).

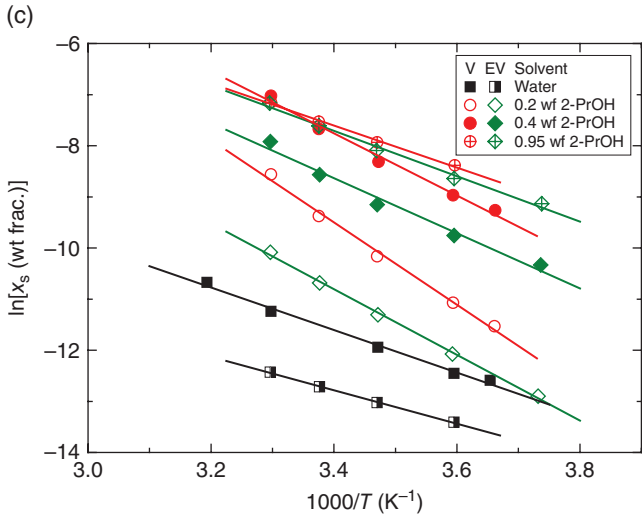

Figure 2.10 (Continued)

Table 2.2 Values of constants A and $\Delta H_s/R_G$ of vanillin and ethyl vanillin in different solvent mixtures.

Compound	Solvent	X	A	$\Delta H_s/R_G$ (kK)	ΔH_s (kJ mol^{-1})
Vanillin	Water	0	2.54 ± 0.67	4.160 ± 0.193	34.58 ± 1.60
	Water + EtOH	0.2	16.11 ± 2.14	7.685 ± 0.619	63.90 ± 5.14
	Water + EtOH	0.4	14.62 ± 1.75	6.621 ± 0.501	55.04 ± 4.16
	Water + EtOH	0.95	6.71 ± 0.39	4.107 ± 0.114	34.14 ± 0.94
	Water + 2-PrOH	0.2	17.91 ± 1.21	8.061 ± 0.348	67.02 ± 2.90
	Water + 2-PrOH	0.4	12.94 ± 1.31	6.087 ± 0.375	50.61 ± 3.10
	Water + 2-PrOH	0.95	6.38 ± 0.68	4.113 ± 0.196	34.20 ± 1.63
	Water + EGOH	0.2	3.41 ± 0.66	4.304 ± 0.190	35.38 ± 1.58
	Water + EGOH	0.4	4.27 ± 1.12	4.368 ± 0.320	36.32 ± 2.66
	Water + EGOH	0.95	6.44 ± 0.99	4.383 ± 0.289	36.44 ± 2.40
	Water + ANT	0.4	11.33 ± 0.77	5.393 ± 0.224	44.84 ± 1.86
	Water + ANT	0.95	5.07 ± 0.56	3.574 ± 0.162	29.72 ± 1.34
Ethyl vanillin	Water	0	−1.649 ± 0.279	3.274 ± 0.081	27.23 ± 0.68
	Water + EtOH	0.2	11.07 ± 0.53	6.433 ± 0.153	53.48 ± 1.27
	Water + EtOH	0.4	9.71 ± 1.47	5.396 ± 0.421	44.86 ± 3.50
	Water + EtOH	0.95	7.40 ± 0.84	4.443 ± 0.240	36.94 ± 1.99

proportions against solvent composition X. The melting points T_m of vanillin and EV are 81–83 and 76 °C, respectively. Using the empirical relation between ΔH_m and T_m, Eq. (2.48), the values of ΔH_m were found to be 17.7 and 17.4 kJ·mol^{-1} for vanillin and EV, respectively. The value of ΔH_m for vanillin is shown in Figure 2.11.

From Figure 2.11, one finds that ΔH_m is lower than ΔH_s for all solvent mixtures and the highest value of ΔH_s is observed at $X \approx 0.2$ weight fraction of solvent added to water. The fact that $\Delta H_s < \Delta H_m$ implies that $\Delta H_{mix} > 0$ in these cases.

The above increasing trend of ΔH_{mix} with second solvent content X may be understood from consideration of the bond energy w during dissolution given by Eq. (2.54). Since enthalpy of solution $\Delta H_s = Zw/2$ and enthalpy of melting $\Delta H_m = Z(w_{cc} - w_{ff})/2$ for a solute–solvent system, we assume that the enthalpy of mixing ΔH_{mix} for the solute in two miscible solvents A and B is given by the simple additivity rule. Then, corresponding to the composition X of B in the solvent mixture, one has

$$\begin{aligned}\Delta H_{mix} &= (1-X)\Delta H_{mixA} + X\Delta H_{mixB} \\ &= Z\left\{\left(w_{ff(A)} - w_{cf(A)}\right) + X\left[\left(w_{cf(A)} - w_{cf(B)}\right) - \left(w_{ff(A)} - w_{ff(B)}\right)\right]\right\},\end{aligned} \tag{2.56}$$

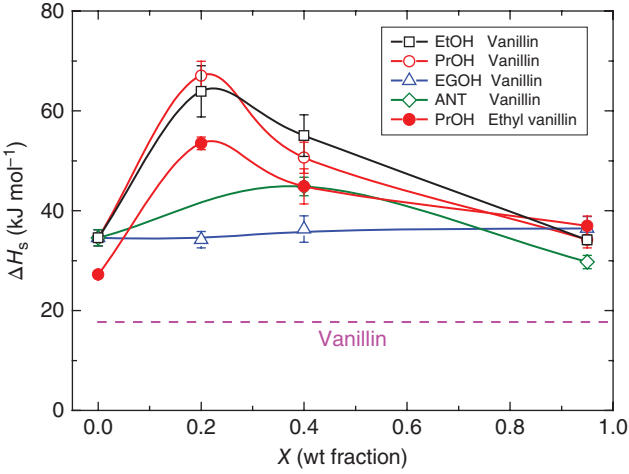

Figure 2.11 Dependence of heat of dissolution ΔH_s of vanillin and ethyl vanillin in water and its mixtures with ethanol, 1- and 2-propanol, ethylene glycol (EGOH), and acetonitrile (ANT) in different proportions against solvent composition X. Heat of melting ΔH_m for vanillin is shown by a dashed line. Data from Table 2.2.

where the subscripts A and B refer to the bond energies due to the solvents A and B, respectively. Relation (2.56) predicts the following situations:

1) For $X = 0$, $\Delta H_{mix} = Z(w_{ff(A)} - w_{cf(A)})$. Obviously, when $(w_{ff(A)} - w_{cf(A)}) > 0$, $\Delta H_{mix} > 0$. This situation deals with a solution of the solute in pure solvent A. A similar situation is possible for $X = 1$. Then the solution is in solvent B.
2) In the case of a solution of the solute in pure solvent A (i.e. for $X = 0$), the situation that $\Delta H_{mix} < 0$ is also possible when $(w_{ff(A)} - w_{cf(A)}) < 0$. A similar situation is possible for the solution in solvent B (i.e. when $X = 1$).
3) For $0 < X < 1$, depending on whether $(w_{ff(B)} - w_{cf(B)}) > (w_{ff(A)} - w_{cf(A)})$ or $(w_{ff(A)} - w_{cf(A)}) > (w_{ff(B)} - w_{cf(B)})$, ΔH_{mix} increases or decreases with an increase in X.

Former two predictions refer to solute solubility in individual solvents. A theoretical expression relating enthalpy of mixing ΔH_{mix} as a function of solute concentration x_c for such solutions was discussed above (Eq. (2.52)). Prediction (3) represents different situations of the dependence of enthalpy of mixing ΔH_{mix} on solvent mixture X for different systems. Physically, ΔH_{mix} can increase when interactions between the molecules of solvent B are stronger than those between the molecules of solvent A, and interactions between the solute ions and solvent B molecules are weaker than those between the solute ions and solvent A molecules. In contrast to this, ΔH_{mix} decreases when interactions between the molecules of solvent A are stronger than those between the molecules of solvent B, and interactions between the solute ions and solvent A molecules are weaker than those between the solute ions and solvent B molecules.

The former situation of $(w_{ff(A)} - w_{cf(A)}) < (w_{ff(B)} - w_{cf(B)})$, i.e $(w_{ff(B)} - w_{ff(A)}) > (w_{cf(B)} - w_{cf(A)})$, appears to hold in the case of an increase in the solubility of vanillin and EV upon the addition of solvent B. Physically, this means that addition of ethanol, 2-propanol, EGOH, and ANT favors increasing solid–fluid interactions due to solvents B, thereby leading to higher solubility of vanillin and EV. The latter situation holds in the case of the solubility of salts like AO and KDP in water to which another miscible solvent in which they have a low solubility is added. Physically, this means that addition of ethanol, 1-propanol, and 2-propanol to water results in the weakening of solid–fluid interactions by the cosolvent. However, this simple additivity-law approach does not explain nonlinear variation in solubility with increasing content of solvent B. This behavior may be explained using mutual solubility of two solvents.

2.3.3 Mathematical Representation of Solute Solubility in Solvent Mixtures

Several cosolvency models describing the solubility of solutes in mixed solvents have been reported in the literature (Jouyban-Gharamaleki and Acree, 1998;

Jouyban-Gharamaleki et al., 1999). In order to represent both effects of temperature and solvent mixture composition on the solute solubility, the following equation based on combination of van't Hoff and Jouyban–Acree models has been used (Jouyban et al., 2012, 2016; Muñoz et al., 2016):

$$\ln x_{m,T} = m_1\left(A_1 + \frac{B_1}{T}\right) + m_2\left(A_2 + \frac{B_2}{T}\right) + \frac{m_1 m_2}{T}\sum_{i=0}^{n} J_i (m_1 - m_2)^i, \tag{2.57}$$

where $x_{m,T}$ is the solubility of the solute in the solvent mixture at T, the first two terms represent the solute solubility in individual pure solvents 1 and 2 of fractions m_1 and m_2, respectively, A's and B's are constants of van't Hoff relation (2.49), J_i terms are constants of the model, and i is the number of solvents. The J_i terms may be calculated for $n = 2$ using a no-intercept least square analysis of $[\ln x_{m,T} - m_1(A_1 + B_1/T) - m_2(A_2 + B_2/T)]$ against $m_1 m_2/T$, $m_1 m_2(m_1 - m_2)/T$, and $m_1 m_2(m_1 - m_2)^2/T$. Obviously, for a two-solvent mixture from the solubility data the constants obtained are: A_1, B_1, A_2, B_2, J_0, J_1, and J_2. Then taking $m_2 = 1 - m_1$, from Eq. (2.57), one obtains

$$\ln x_{m,T} = \left(A_1 + \frac{B_1}{T}\right) + m_2\left((A_2 - A_1) + \frac{(B_2 - B_1)}{T}\right) + \frac{(J_0 - J_1 + J_2)m_2}{T} + \\ + \frac{(-J_0 + 3J_1 - 5J_2)\, m_2^2}{T} + \frac{(-2J_1 + 8J_2)\, m_2^3}{T} + \frac{(-4J2)\, m_2^4}{T}. \tag{2.58}$$

Equation (2.58) upon rearrangement gives

$$T(\ln x_{m,T} - A_1) = B_1 + C_1 T m_2 + C_2 m_2 + C_3 m_2^2 + C_4 m_2^3 + C_5 m_2^4, \tag{2.59}$$

where C's are parameters of the model, which may be calculated by regressing $T(\ln x_{m,T} - A_1)$ against Tm_2. m_2, m_2^2, m_2^3 and m_2^4.

It should be mentioned that the temperature dependence of the solubility x_m of different solutes in solvent mixtures has also been represented by the Apelblat equation (Dali et al., 2016; Liu et al., 2014; Zhou et al., 2013):

$$\ln x_m = A_m - \frac{B_m}{T} + C_m \ln T, \tag{2.60}$$

where A_m, B_m, and C_m are model constants. However, for binary solvent mixtures the Apelblat model does not enable to reproduce the solubility data at any composition and temperature of interest (Jouyban et al., 2016).

2.4 Solute Solubility as a Function of Solvent–Mixture Composition

2.4.1 A Simple Practical Approach

In contrast to the above dependences of solubility x_s of AO on temperature T for different solvent compositions X, mathematical description of the solubility data in different solvent mixtures as a function of solvent composition X at different temperatures T is of practical interest in antisolvent crystallization. For example, in their models of antisolvent crystallization, Kubota (2008) and O'Grady et al. (2007) assumed that the amount of excess solute associated with the creation of supersaturation for the onset of its crystallization in its saturated solution by the addition of an antisolvent increases linearly with the feeding rate of the antisolvent, whereas Sangwal (2010b) argued that it is the logarithm of the excess solute that increases linearly with the antisolvent feeding rate.

If one denotes the solubility of a solute in a solvent producing an ideal solution by x_s^* whereas that in another solvent giving regular solution by x_s, then from Eqs. (2.46) and (2.49), one obtains the solubility x_s of the solute in the latter solvent in the form (Sangwal, 2010b; Sangwal et al., 2013):

$$\ln x_s = \alpha_1 - \alpha_2 X, \tag{2.61}$$

with the constants

$$\alpha_1 = \ln x_s^* + (A - A^*), \tag{2.62}$$

and

$$\alpha_2 X = \frac{(\Delta H_s - \Delta H_m)}{R_G T}, \tag{2.63}$$

where $A^* = \Delta H_m / R_G T_m$ and $\Delta H_s - \Delta H_m = \Delta H_{mix}$. The constant α_2 is essentially a constant relating real solvent content X with a change in the mixing enthalpy ΔH_{mix} of the solution associated with the interactions of solute molecules/ions with those of two solvents in their mixtures, and is a measure of solute–solvent interactions at temperature T. Its value decreases with an increase in temperature T (cf. Eq. (2.63)). This situation holds when simple additivity rule holds for the mixtures of two solvents, but there are no preferred interactions between solute and either of the two solvents (Hildebrand and Scott, 1962). This means that the last term in Eq. (2.57) is omitted here. The value of α_1, on the other hand, is mainly associated with the difference $(A - A^*)$. Note that both α_1 and α_2 are dimensionless constants.

Figure 2.12a presents the data of the solubility x_s of AO in solutions of acetone –water mixtures as a function of their composition X at different temperatures T. Figure 2.12b shows the above data as plots of $\ln x_s$ against composition X of

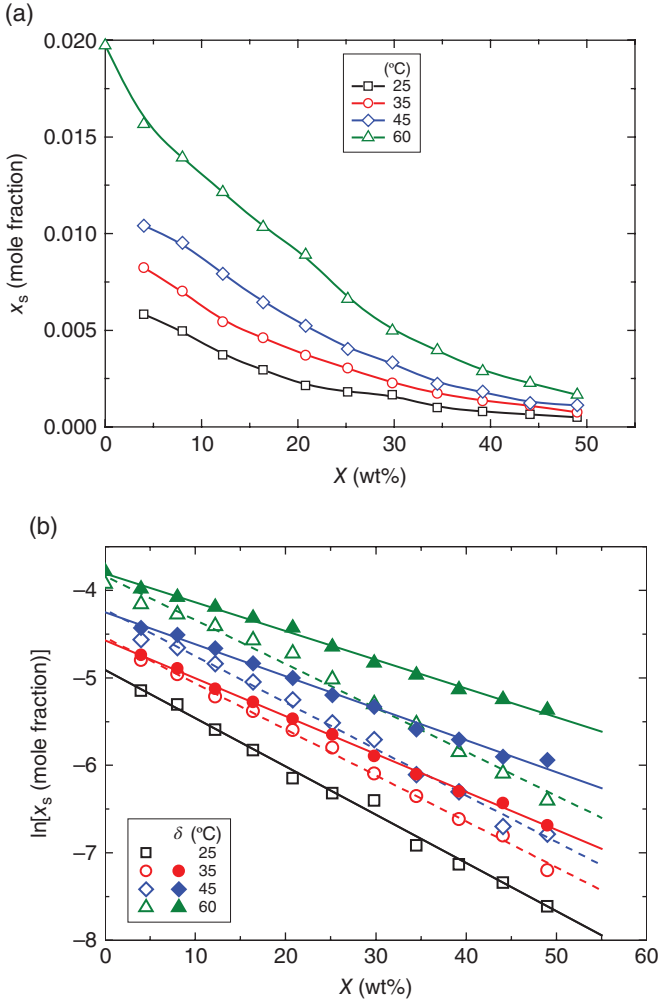

Figure 2.12 (a) Plots of x_s of AO in solutions of acetone–water mixtures against their composition X at different temperatures T. (b) Data of (a) shown as plots of $\ln x_s$ against X without (dashed lines) and with correction factor δ (solid lines) according to Eq. (2.64). Linear plots are drawn with best-fit parameters given in Table 2.3. *Source:* Adapted from Sangwal et al. (2013). Copyright (2013), with permission from Elsevier.

acetone in water. A careful examination of the plots reveals that the dependence of $\ln x_s$ of X is not strictly linear (dashed curves). In reality, the slope of the plot slowly increases with an increase in X, thereby showing a positive deviation from the linearity. The deviation from the best-fit linear dependence may be removed

by introducing a small correction term δ in the solubility x_s, such that the relationship between x_s and X may be expressed by the empirical relation:

$$\ln(x_s + \delta) = \alpha_1 - \alpha_2 X, \tag{2.64}$$

where the effective or corrected solute concentration $x_s' = x_s + \delta$. The values of the best-fit parameters of Eq. (2.64) are given in Table 2.3. Equation (2.64) is a modified version of Eq. (2.61), and has been proposed before (Sangwal, 2010b).

As seen from Table 2.3, the values of the parameters $-\alpha_1$ and α_2 decrease with an increase in saturation temperature T for both uncorrected and corrected $c(X)$ data, but this decrease is relatively weak in the values of the parameter α_2 obtained from the uncorrected data. Recalling that $\alpha_2 X = \Delta H_{mix}/R_G T$ (see Eq. (2.63)), one may anticipate that $\alpha_2 T = \alpha_T = \Delta H_{mix}/R_G X$ is related to T. Figure 2.13a and b illustrates the dependencies of parameters α_1 and α_T on solution saturation temperature T, respectively. The plots show the data of α_1 and α_T obtained by using Eq. (2.64) from the $c(X)$ data without and with the correction factor δ in the solubility c. In Figure 2.13a, the linear plot is drawn according to the empirical relation:

$$\alpha_1 = \alpha_{10} + \alpha_{11} T, \tag{2.65}$$

where the best-fit constants are: $\alpha_{10} = -14.056 \pm 0.031$ and $\alpha_{11} = 0.0308 \pm 0.0001$ K^{-1}. These values of α_{10} and α_{11} refer to the corrected data, but their values for the uncorrected data do not differ significantly from the above values. The linear increase in α_1 with temperature T is connected with an increase in the value of A in Eq. (2.62) with temperature T of saturated solutions. In Figure 2.13b, the linear plot is for the uncorrected data whereas the plot for the corrected data is drawn according to the empirical exponential function:

$$\alpha_T = \alpha_{T0} + \alpha_{T1} \exp\left[-\frac{(T - T_0)}{\Theta}\right], \tag{2.66}$$

where the best-fit values of the constants are: $\alpha_{T0} = 1.010 \pm 0.047$ kK, $\alpha_{T1} = 0.638 \pm 0.045$ kK, $T_0 = 298.15$ K, and $\Theta = 15.0 \pm 2.6$ K. In the case of uncorrected data, the value of the parameter α_T is practically independent of saturation temperature T and its average value, denoted by α_{Tav}, is 1.657 ± 0.036 K. Note that $\alpha_{Tav} = \alpha_{T0} + \alpha_{T1}$. The important point here is that in the investigated temperature range the fit for the data of solubility of AO in water–acetone mixtures improves significantly in the case of the corrected data obtained by Eq. (2.64) with the correction factor δ and dependence of the value of α_2 on temperature T is associated with the correction factor δ. This observation of best fit of the data with this correction factor δ is not confined to the above system alone. Some more examples corroborating this observation are presented below.

Table 2.3 Values of constants of Eq. (2.64) for different systems.

Solute[a]	Mixture	T (K)	δ	$-\alpha_1$	α_2	R^2
AO	Water/acetone	298.15	—	4.911	5.507	0.9966
		303.15	—	4.709	5.480	0.9979
			0.00025	4.726	4.863	0.9986
		308.15	—	4.539	5.257	0.9984
			0.0005	4.573	4.332	0.9991
		313.15	—	4.371	5.454	0.9966
			0.002	4.345	3.306	0.9957
		318.15	—	4.222	5.308	0.9952
			0.002	4.239	3.328	0.9955
		323.15	—	4.107	4.981	0.9943
			0.002	4.104	3.398	0.9963
		333.15	—	3.837	5.019	0.9944
			0.002	3.807	3.283	0.9977
KDP	Water/EtOH	303	—	1.351	12.571	0.9946
		323	—	0.974	10.758	0.990
	Water/1-PrOH	303	—	1.356	18.097	0.9908
		323	—	0.940	15.965	0.9938
	Water/2-PrOH	303	—	1.449	13.311	0.9825
			−0.044	1.515	24.275	0.9996
		323	—	1.046	10.133	0.9799
			−0.098	1.237	24.275	0.9992
K_2SO_4	Water/1-PrOH	303	—	2.367	6.316	0.9965
			−0.0028	2.277	7.907	0.9998
NTO	NMP/water	323	—	1.145	3.994	0.9954
			+0.0058	1.213	3.354	0.9990
Benzoic acid	EtOH/water	298.15	—	0.810	1.409	0.9920
			+0.29	0.349	0.592	0.9998
DHA	Water/EtOH	283.15	—	−0.926	3.130	0.9897
			+0.325	−0.883	1.947	0.9981
		313.15	—	−1.954	1.074	0.9834

1-PrOH, 1-propanol; 2-PrOH, 2-propanol; EtOH, ethanol.

[a] Data for AO from Sangwal et al. (2013) but for other compounds from Sangwal (2010a).

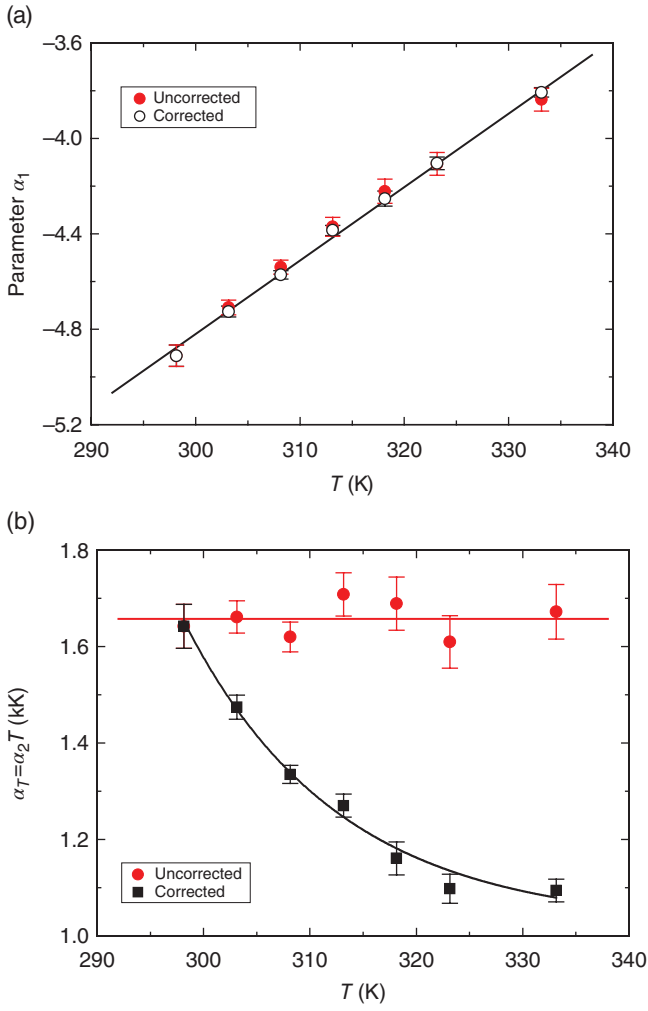

Figure 2.13 Dependence of parameters (a) α_1 and (b) $\alpha_2 T = \alpha_T$ on solution saturation temperature T. In (a) linear plot is drawn according to Eq. (2.65) with $\alpha_1(T)$ data without (solid circles) and with correction δ (open circles), whereas in (b) plots representing α_T data without (solid circles) and with correction δ (solid squares) are drawn with average α_T (i.e. $\alpha_{T\text{av}}$) and exponential function (2.66), respectively. *Source:* Adapted from Sangwal et al. (2013). Copyright (2013), with permission from Elsevier.

Figure 2.14a presents the dependence of ln$c$ for KDP on composition X of water containing different proportions of 2-propanol, 1-propanol, and ethanol. The data were recovered from the figures published by Barata and Serrano (1997). In this case, one observes that the plots of lnx_s on X of water–ethanol

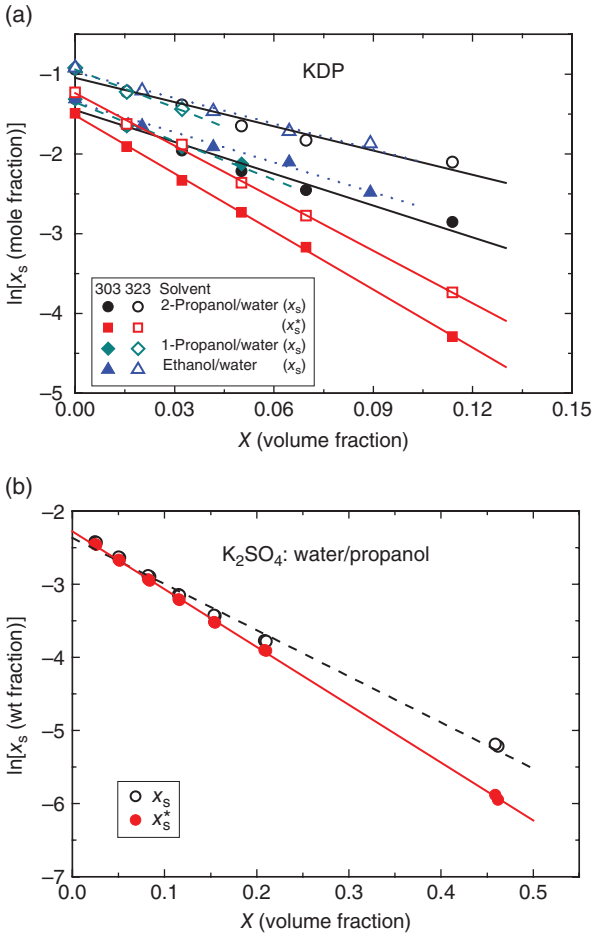

Figure 2.14 Dependence of lnx_s for (a) KDP on composition X of solvent water and antisolvents 2-propanol, 1-propanol, and ethanol at two different temperatures and (b) K_2SO_4 on composition X of water and antisolvent 1-propanol. In (a) circles and squares represent ln$x_s(X)$ data for 2-propanol/water mixture without and with correction δ, respectively. In (b) dashed and solid lines represent data without and with correction δ, respectively. Original data from: (a) Barata and Serrano (1997), and (b) Taboada et al. (2003). *Source:* Adapted from Sangwal (2010b). Copyright (2010), with permission from Wiley.

and water–1-propanol mixtures in the investigated X range are essentially linear, but the plots of lnx_s on X of water–2-propanol mixture show a decrease in the slope with an increase in X (i.e. negative curvatures). Figure 2.14b shows another example of the negative curvature in the plot of lnx_s for potassium

sulfate on X of water–1-propanol mixture. The experimental data of solubility of potassium sulfate are from Taboada et al. (2003).

Figure 2.15a shows another example of this type of behavior of solubility of 3-tro-1,2,4-triazol-5-one (NTO) at 323 K in (N-methylpyrrolidone (NMP))

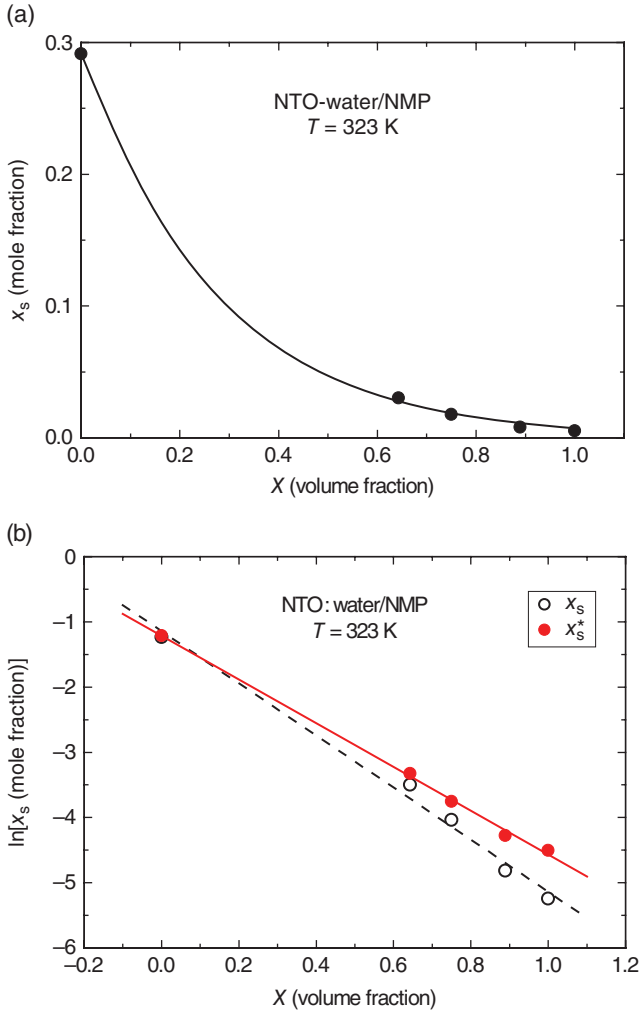

Figure 2.15 (a) Example of typical behavior of solubility x_s of NTO at 323 K as a function of composition X of solvent NMP containing water as antisolvent. (b) Data of (a) shown as a plot of lnx_s against composition X of solvent NMP and antisolvent water. In (b) open and solid lines represent data without and with correction δ, respectively. Original data from Kim and Kim (2001). *Source:* Adapted from Sangwal (2010b). Copyright (2010), with permission from Wiley.

containing water as an antisolvent. The data are reproduced from the Arrhenius-type plots for the solubility x_s of NTO, reported by Kim and Kim (2001). Figure 2.15b shows the data of Figure 2.15a as a plot of $\ln x_s$ against composition X of solvent NMP and antisolvent water. A careful examination of the plot reveals that the dependence of $\ln x_s$ of X is not strictly linear. In reality, the slope of the plot slowly increases with an increase in X, thereby showing a positive deviation from the linearity.

Figure 2.16 shows two other examples of the above behavior in the case of benzoic acid in solvent ethanol and antisolvent water at 298.15 K, and 1,3-dihydroxyacetone (DHA) in solvent water and antisolvent ethanol at two different temperatures: 283.15 and 313.15 K. The data for benzoic acid have been reported by O'Grady et al. (2007), while those for DHA are recovered from the plots of solubility x_s against temperature in different compositions X of mixtures of water and ethanol, reported by Zhu et al. (2003). The dependence appears linear in the investigated X range for benzoic acid at 313.15 K and for DHA in the range $X \leq 0.8$ at 283.15 K. A careful inspection of the $\ln x_s(X)$ data reveals that the plots for the data of benzoic acid and DHA at 283.15 K also exhibit positive deviations from linearity. In fact, with $\delta > 0$ for both benzoic acid and DHA, one obtains a linear dependence with much improved values of the correlation coefficient.

The best-fit values of constants α_1 and α_2 of Eq. (2.64) and the correlation coefficient R^2 for the fit for as-measured solubility x_s and effective solubility x_s^* for the above systems are listed in Table 2.3. From Table 2.3, the following features may be noted:

1) The values of α_2 strongly depend on the chemical nature of solute and antisolvent as well as on solution temperature. For example, the values of α_2 are much lower for NTO and DHA than those for KDP, while the best-fit value of α_2, as seen from the same solute KDP, increases with an increase in the complexity of antisolvent molecules.
2) The correction term δ can be positive as well as negative. The positive values of δ appear in solutes like NTO, benzoic acid, and DHA composed of complex organic molecules, while the negative values of δ in solutes like KDP and K_2SO_4 composed of simple ions. Exception here from this trend is AO in water/acetone systems, where $\delta > 0$, but this deviation is very low.
3) The value of the correction term δ is also related to the chemical nature of the antisolvent molecules. For example, for KDP solutions δ appears in antisolvent 2-propanol composed of nonlinear molecules, but δ is essentially zero in antisolvent ethanol.

Irrespective of the form of the dependence of α_1 and α_T on T, from the above dependencies, one can conclude that introduction of the correction factor δ improves the fit of the linear relationship between $\ln x_s$ on X according to

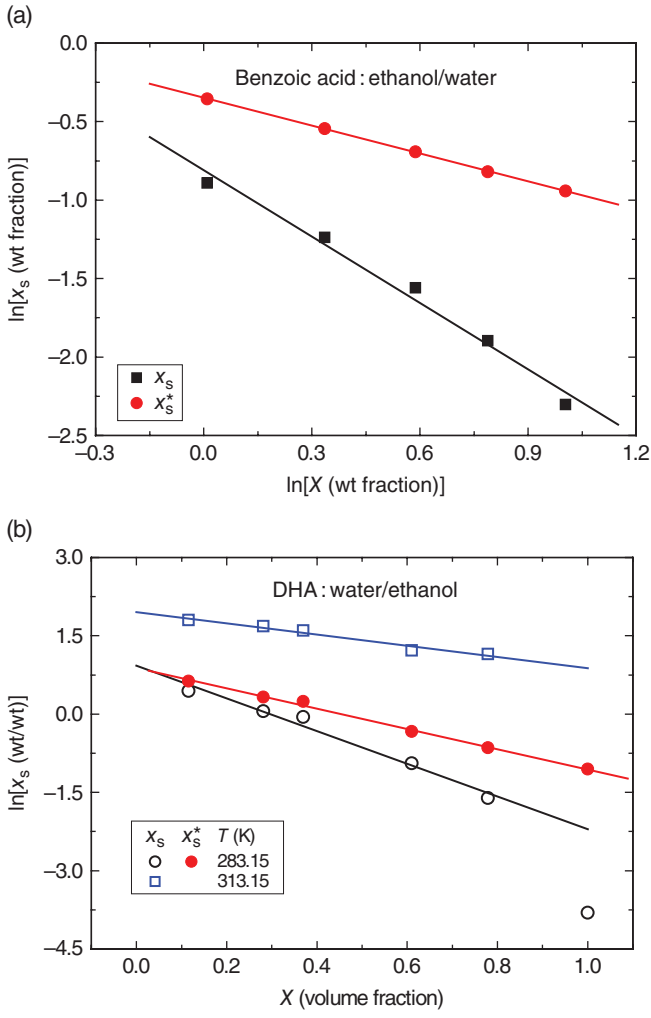

Figure 2.16 Plots of lnx_s for (a) benzoic acid against composition X of solvent ethanol and antisolvent water at 298.15 K and (b) DHA against composition X of solvent water and antisolvent ethanol at two different temperatures T. Original data from: (a) O'Grady et al. (2007) and (b) Zhu et al. (2003). *Source:* Adapted from Sangwal (2010b). Copyright (2010), with permission from Wiley.

Eq. (2.64). This implies that Eq. (2.61) applies when simple additivity rule holds for mixing entropies in the two solvents and the deviations accounted for by the correction factor $\delta \neq 0$ of Eq. (2.64) are caused by preferred interactions between solute and either of the two solvents.

2.4.2 Physical Interpretation of the δ Factor and Solvent Activity

The role of the correction factor δ in explaining the deviation in the $\ln x_s(X)$ plots may be understood easily in the case of aqueous solutions of ionic salts (Sangwal et al., 2013). Rewriting the term $(x_s + \delta)$ as $x_s(1 + \delta/x_s) = x_s f_a$, where f_a is an activity coefficient, one finds that deviations from the linearity between $\ln x_s$ and X are associated with the coefficient f_a. Since δ is a constant for solutions at a particular temperature T, the relation $f_a = (1 + \delta/x_s)$ implies that the activity coefficient f_a decreases with an increase in x_s. However, for solutions of different temperatures T, where δ increases with temperature T, f_a also increases with increasing T.

It is well known (Barata and Serrano, 1997; Bockris and Reddy, 1970) that the activity coefficients f_a of ionic solutions decrease from its highest value of unity as the concentration x of the solute increases. This situation is observed at low solute concentrations x when ion–ion (long range) interactions are predominant. However, with further increase in concentration the activity coefficient begins to increase after passing through a minimum at certain concentrations. At sufficiently high concentrations, the activity coefficient not only approaches but also exceeds the value of unity characteristic of limiting dilute solutions. These values of $f_a > 1$ are due to increasing role of ion–solvent (short range) interactions. The contribution of excess activity coefficient $\Delta f_a > 0$ due to ion–solvent interactions is given by (Bockris and Reddy, 1970)

$$\Delta f_a = -\frac{n_h}{n}\ln a_W + \ln\frac{n_W + n}{n_W + n - n_h}, \tag{2.67}$$

where n, n_W, and n_h are the number of moles of solute, free water, and bound water in the primary sheath of ions, respectively, and a_W is the activity of water. The first term is related to a change in the free energy due to the removal of water in the sheath of ions, whereas the second term is related to the change in the free energy due to change in the concentration of the solute ions due to the removal of water in their sheath. In solutions of limiting dilutions, $n_h \to 0$ and $a_W \to 1$. Consequently, both terms vanish. However, as the solute concentration increases, a_W decreases and n_h increases, resulting in an increase in Δf_a, which can be equal as well as exceed ion–ion interactions, such that $\Delta f_a > 0$. In fact, all factors resulting in an increase in the concentration of solute concentration (i.e. an increase in the number of n of solute) lead to an increase in Δf_a, and, conversely, factors that decrease solubility lead to a decrease in Δf_a. An increase in the temperature T of the saturated solutions of a given solvent and an increase in antisolvent concentration X in saturated solutions are typical examples of the former and latter effects, respectively. In the latter case, the dependence of correction factor δ on solute concentration x_s, as seen from Table 2.3, can also be explained in this manner.

Investigation of activity behavior of supersaturated solutions is important for understanding processes of crystallization. Data of measurements of the activity of aqueous solutions of different solutes are available (Stokes and Mills, 1965). However, most of these data are on undersaturated solutions in contrast to supersaturated solutions used in crystallization. Therefore, techniques capable of measuring the properties of supersaturated solutions have drawn enormous interest.

One of the measurement techniques is the electrodynamic balance technique that enables to measure water activity data for aqueous supersaturated solutions of different solutes far into the metastable region (for example, see: Bohenek et al., 1997; Cohen et al., 1987a, b, c; Mohan and Myerson, 1999; Na et al., 1995; Tang et al., 1986). The experimental setup is an improved version of the traditional Millikan oil-drop setup used for the determination of the charge of an electron and Avogadro's number. In the technique, a single charged solution droplet, which is trapped by the fields created by the electrodes of the apparatus, is continuously weighed. The levitation of the small droplet in the electric field enables to attain a very high supersaturation before crystallization because of suppression of heterogeneous nucleation. The small solution particle also responds rapidly to the ambient vapor pressure allowing control of concentration. The relative humidity RH of the vapor phase is a measure of the water activity a_w. The activities a and a_w of the crystallizing solute and solvent are related by the Gibbs–Duhem equation:

$$-\frac{1000}{M_w}\mathrm{d}\ln a_w = \nu m \mathrm{d}\ln a, \tag{2.68}$$

where ν is the number of ions from a dissociated molecule, m is the molality of the solute, and M_w is the molecular weight of water. The solute activity may be computed by integrating Eq. (2.68):

$$\ln\left(\frac{a}{a^*}\right) = -\frac{1000}{\nu M_w}\int_{m*}^{m}\left(\frac{\mathrm{d}\ln(a_w)}{\mathrm{d}m}\right). \tag{2.69}$$

The left-hand side of this equation is proportional to the chemical potential difference between the supersaturated and the saturated state (see Eq. (2.13)).

It is found that the water activity a_w as a rule decreases with increasing solute concentration m in the solution and the decrease is nonlinear. The water activity a_w decreases linearly with increasing solute concentration m only at low concentrations m, but the water activity a_w increasingly deviates linearly with increasing m. The relation between water activity a_w and solute concentration m is usually represented by empirical and semiempirical relations: polynomials (Cohen et al., 1987a, b; Mohan and Myerson, 1999; Na et al., 1995) and exponential functions (Bohenek et al., 1997). Figure 2.17 presents an example of the dependence of the water activity a_w on the molality m of KDP. Obviously, the

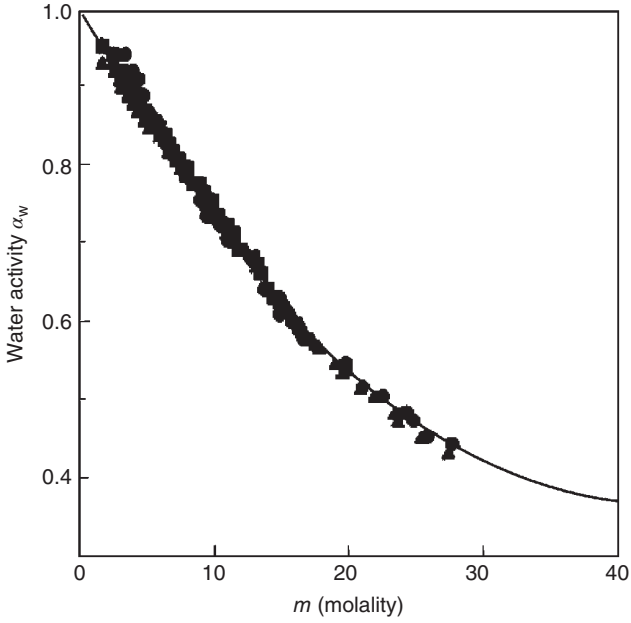

Figure 2.17 Example of the dependence of the water activity a_w on the molality m of KDP. Curve is drawn according to the empirical relation: $a_w = \exp[-0.018m(1 + 0.409m^{1/2} - 0.056m)]$. *Source:* After Bohenek et al. (1997). Copyright (1997), with permission from Elsevier.

dependence of water activity a_w on solute concentration m is not linear. This type of nonlinear behavior of the $a_w(m)$ data gives nonlinear dependence of solute activity-based supersaturation on molality-based supersaturation such that the slope of the curve is less than unity for an ideal solution (for example, see: Bohenek et al., 1997; Na et al., 1995). The data of water activity a_w for different solute solutions also enables to estimate the critical size of crystalline nuclei and solute–water interfacial energy using the classical theory of 3D nucleation (Bohenek et al., 1997; Cohen et al., 1987c).

2.4.3 Preferential Solvation of Solute by Solvents

In antisolvent crystallization the solute has a high solubility in the main solvent and relatively poor solubility in the cosolvent usually called antisolvent. Therefore, it is desired to obtain information on processes of preferential solvation of a solute by two solvents in saturated mixtures in terms of some thermodynamic quantities. Denoting the main solvent and the cosolvent as 1 and 2, respectively, and the solute as 3, the preferential solvation behavior of the solute is described

by the parameter defined as (Jouyban et al., 2016; Marcus, 2002, 2008; Martinez et al., 2016):

$$\delta x_{1,3} = x_{1,3}^{\mathrm{L}} - x_1 = -\delta x_{2,3}, \tag{2.70}$$

where $x_{1,3}^{\mathrm{L}}$ is the local mole fraction of main solvent 1 in the environment near to the solute 3 and x_1 is the bulk mole fraction composition of main solvent 1 in the initial binary solvent. If $\delta x_{1,3} > 0$, the solute is preferentially solvated by solvent 1. However, if $\delta x_{1,3} < 0$, the solute is preferentially solvated by solvent 2. Values of $\delta x_{1,3}$ are obtained from the inverse Kirkwood–Buff integrals for the individual solvent components in terms of the thermodynamic quantities (Marcus, 2002, 2008):

$$G_{1,3} = R_{\mathrm{G}} T \kappa_T - V_3 + x_2 V_2 D/Q, \tag{2.71}$$

$$G_{2,3} = R_{\mathrm{G}} T \kappa_T - V_3 + x_1 V_1 D/Q, \tag{2.72}$$

where κ_T is the isothermal compressibility of the solvent mixtures (GPa^{-1}), V_1 and V_2 are the partial molar volumes of the solvents 1 and 2, respectively, and V_3 is the partial molar volume of the solute. The function D is the derivative of the standard molar Gibbs energies of transfer of solute from neat cosolvent 2 to the binary mixtures, with respect to the solvent composition. The function Q involves the second derivative of the excess molar Gibbs energy of mixing of the two solvents with respect to the water proportion in the mixtures. These functions are given by

$$D = \left(\frac{\partial \Delta\, G_{3,2\to 1+2}^{0}}{\partial x_1} \right)_{T,p}, \tag{2.73}$$

$$Q = R_{\mathrm{G}} T + x_1 x_2 \left(\frac{\partial^2 \Delta\, G_{1+2}^{\mathrm{excess}}}{\partial\, x_2^2} \right)_{T,p}, \tag{2.74}$$

whereas the preferential solvation parameter is given by

$$\delta x_{1,3} = \frac{x_1 x_2 (G_{1,3} - G_{2,3})}{x_1 G_{1,3} + x_2 G_{2,3} + V_{\mathrm{cor}}}, \tag{2.75}$$

with the correlation volume V_{cor} obtained by

$$V_{\mathrm{cor}} = 2522.5 \left(r_3 + 0.1363 \left[x_{1,3} V_1 + x_{2,3}^{\mathrm{L}} V_2 \right]^{1/3} - 0.085 \right)^3, \tag{2.76}$$

where the radius r_3 of the solute is

$$r_3 = \left(\frac{3 \cdot 10^{21} V_3}{4\pi N_{\mathrm{A}}} \right)^{1/3}. \tag{2.77}$$

The Gibbs energy of transfer of solute from neat solvent 2 to solvent mixtures is given by

$$\Delta G^0_{3,2\to 1+2} = RGT \ln\left(\frac{x_{3,2}}{x_{3,1+2}}\right). \tag{2.78}$$

The value of $\Delta G^0_{3,2\to 1+2}$ is usually correlated according to a polynomial such as:

$$\Delta G^0_{3,2\to 1+2} = z_0 + z_1 x_1 + z_2 x_1^2 + z_3 x_1^3, \tag{2.79}$$

where z's are empirical constants. Based on the work of Martinez et al. (2016), an example of the analysis of the solvation behavior deduced from experimental solubility data of vanillin (solute 3) in cosolvent mixtures of propylene glycol (main solvent 1) + water (cosolvent 2) at two different temperatures is presented below.

It was found (Martinez et al., 2016) that the values of the standard Gibbs energies $G_{1,3}$ and $G_{2,3}$ are negative in all solution mixtures indicating that this compound shows affinity for both solvents in the mixtures. The parameters used in the calculations were: molar volume of vanillin V_3 = 103.0 $cm^3 \cdot mol^{-1}$, r^3 = 0.344 nm. Figure 2.18 shows the Gibbs energy ΔG^0 of transfer behavior of vanillin (3) from neat water (2) to propylene glycol (1) + water (2) cosolvent mixtures as a function of propylene glycol content x_1 at 298 and 313 K. Obviously, the Gibbs energy ΔG^0 smoothly decreases with increasing propylene glycol content x_1.

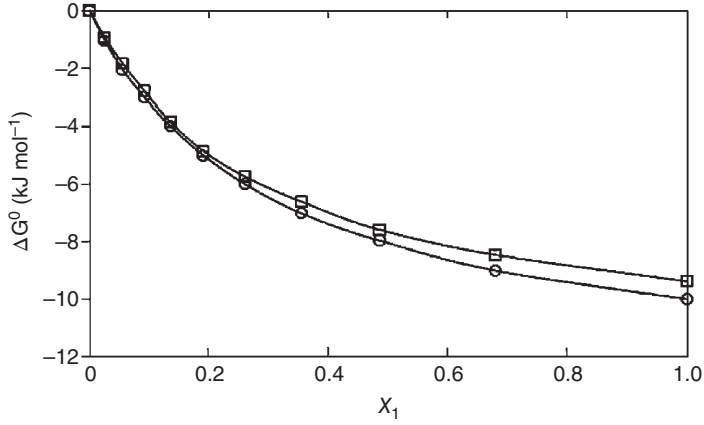

Figure 2.18 Gibbs energy ΔG^0 of transfer of vanillin (solute 3) from neat water (cosolvent 2) to cosolvent mixtures of propylene glycol (main solvent 1) + water (cosolvent 2) as a function of propylene glycol content X_1 at two temperatures: (circles) 298 K and (squares) 313 K. *Source:* After Martinez et al. (2016). Copyright (2016), with permission from Elsevier.

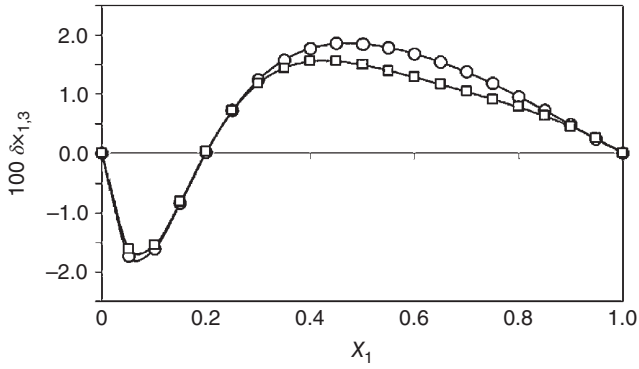

Figure 2.19 Dependence of preferential solvation parameter $\delta x_{1,3}$ on propylene glycol content X_1 in propylene glycol + water cosolvent mixtures at two temperatures: (circles) 298 K and (squares) 313 K. *Source:* After Martinez et al. (2016). Copyright (2016), with permission from Elsevier.

Figure 2.19 shows the dependence of preferential solvation parameter $\delta x_{1,3}$ on propylene glycol content x_1 in propylene glycol (1) + water (2) cosolvent mixtures at 298 and 313 K. Here, the dependence is nonlinear with the propylene glycol content x_1 in the cosolvent mixture. Addition of propylene glycol to water leads to make the parameter $\delta x_{1,3}$ negative initially approaching a minimum value at $x_1 = 0.05$ in the mixture. In these water-rich mixtures, the lowering of the net $\delta x_{1,3}$ to negative values is probably associated with the hydrophobic hydration around the nonpolar groups of vanillin. In the mixture composition $0.20 < x_1 < 1.0$, the local mole fraction of propylene glycol is higher than that of water. In this range of solvent mixture composition the increase in the solubility of solute vanillin is likely to be associated with the breaking of the ordered structure (hydrogen bonds) of water around the nonpolar moieties of solute, which increases the solvation of vanillin and exhibits a maximum value at $x_1 = 0.45$. From the figure, one also notes that the magnitude of preferential solvation by propylene glycol and water diminishes with an increase in temperature.

2.5 Solid–Solvent Interfacial Energy

The formation of liquid drops from the vapor and solid crystallites from supersaturated solution or melt is associated with the aggregation of molecules and ions in which their movement is restricted due to liberation of a certain quantity of energy. The transition from the gaseous to the liquid phase and subsequently from the liquid to the solid phase is a stepwise decrease in the molecular/ionic mobility and a decrease in the free energy of the system. During this process,

new clearly defined surface separating a liquid drop from the gaseous phase and a solid aggregate from the liquid is created. In the interior of the liquid drop and the solid crystallite the average distance between the molecules/ions composing them in different directions is maintained by an equilibrium between attractive and repulsive forces. The molecules/ions in the surface, where there is a disruption of equal attractive and repulsive forces, are held by surface forces in the liquid and the solid. These forces act perpendicular to the surface and are described in terms of expenditure of a certain quantity of energy as work done in the creation of the liquid or solid surface. The work done in the creation of the area of the surface of liquid–vapor or solid–solvent system at its different points is called the *interfacial energy* or, briefly, *surface energy* γ, usually with $mJ \cdot m^{-2}$ as its units. Since the molecules/ions in the surface layer are subjected to deformation tension, the work associated with its creation is also called *interfacial* or *surface tension*. As discussed in Section 2.2, note that the total work done W (or the change in the energy required) in the formation of liquid drop or solid crystallite is the sum of contributions due to the work W_S required to form the surface S (a positive quantity) and the work W_V required to form the bulk liquid or solid of volume V.

Interfacial energy γ is an important parameter in the theories of nucleation and crystal growth. This quantity is usually determined experimentally from data on 3D nucleation and growth kinetics and from contact-angle measurements. However, such a determination is time-consuming and laborious. Consequently, estimation of interfacial energy γ from physico-chemical data has drawn considerable attention (see: Nývlt et al., 1985; Söhnel and Garside, 1992). Using the values of γ, determined experimentally from 3D nucleation and growth measurements, of various sparingly- and readily-soluble electrolytes obtained from aqueous solution, its relationships with solubility and enthalpy of solution have been reported.

Nielsen and Söhnel (1971) observed that γ is related to the solubility c_0 $(mol \cdot l^{-1})$ by

$$\gamma = \frac{k_B T}{ha^2} \ln \frac{c_x}{c_0}, \tag{2.80}$$

where $c_x = d_x/M_x$ is the concentration of the solute x in the solid state (d_x and M_x are the density and the molecular mass of the solute), a is the interionic or interplanar distance, and h is average hydration number per ion. If h, a, and c_x are considered constants independent of the solute, Eq. (2.80) takes the linear form:

$$\gamma = A \ln c_0 + B, \tag{2.81}$$

with the empirical constants $A = -k_B T/ha^2$ and $B = (k_B T/ha^2)\ln c_x$. By correlating values of γ obtained from nucleation and growth experiments for different compounds, Söhnel (1982) observed that: $A = -7.95$ and $B = 34.5$, with a correlation coefficient of 0.93. From the above values of A and B with an average hydration

number h = 3, k_B = $1.38 \cdot 10^{-20}$ mJ·K^{-1} and T = 303 K, one obtains $a = 4.17 \cdot 10^{-10}$ m and $c_x = d_x/M_x = 76.7$ mol·l^{-1}. This value of a is reasonable, but apart from several deviations from the linear dependence, the value of c_x is relatively high. Moreover, relation (2.80) is empirical.

The surfaces of 3D nuclei are rough but as they grow larger, their surfaces become smooth and may be described by the surface entropy factor α (see Section 3.3). The α factor is related to the enthalpy of melting ΔH_m by (cf. Eq. (3.2))

$$\alpha = \xi\left(\frac{\Delta H_m}{R_G T}\right), \tag{2.82}$$

where ξ is a crystallographic anisotropy factor with a value of 1/2 for a Kossel crystal. In the case of regular solutions, this α factor is related to the solubility x_s, expressed in mole fraction, by (cf. Eq. (3.4))

$$\alpha = \xi(A - \ln x_s), \tag{2.83}$$

where the constant

$$A = \frac{\Delta H_m}{R_G T_m} + \frac{\Delta H_{mix}}{R_G T}. \tag{2.84}$$

For a Kossel crystal, the α factor is also related to the edge free energy $\gamma' = \gamma a^2$ by (Bennema et al., 1973)

$$\alpha = 4\gamma a^2/k_B T + 4\Delta S_{cn}, \tag{2.85}$$

where ΔS_{cn} is configurational entropy of critically-sized 3D nucleus. From Eqs. (2.84) and (2.85), one obtains

$$\gamma = \frac{k_B T(A^* - \ln x_s)}{8a^2}, \tag{2.86}$$

where $A^* = (A - 8\Delta S_{cn})$ and we have taken ξ = 1/2.

Equation (2.86) is similar to Eq. (2.81) with the difference that now the solubility is taken in mole fraction. Figure 2.20 shows the data of interfacial energy γ for various compounds as a function of their solubility x_s for three different values of $k_B T/8a^2$ according to Eq. (2.86) assuming that the constant $A^* = \Delta H_m/R_G T_m = 3$ for different compounds (Sangwal, 1989). In the figure the data considered by Söhnel (1982) for his relation (2.80) are replotted. The straight lines (1) and (3) cover the experimental data with the constant $k_B T/8a^2$ equal to 9.07 and 3.266 mJ·m^{-2}, respectively, which give physically sensible values of a as $2.4 \cdot 10^{-10}$ and $4.0 \cdot 10^{-10}$ m. Comparison of the values of the interfacial energy γ according to Eq. (2.86) for curve 2, represented by $a = 2.8 \cdot 10^{-10}$ m, with those from Eq. (2.81) reveals that the two relations give similar results for sparingly soluble salts but the predicted values are always higher for fairly soluble salts.

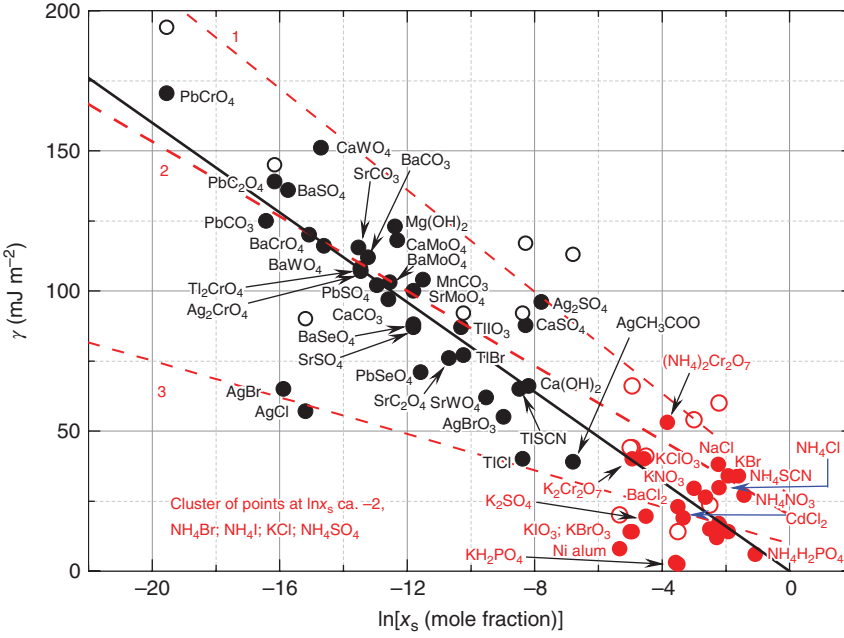

Figure 2.20 Dependence of experimental interfacial energy γ on $\ln x_s$ for various substances. Curves (1), (2), and (3) are the predicted dependencies according to Eq. (2.86) with $A^* = \Delta H_m/R_G T_m = 3$ and different values of $k_B T/8a^2$: (1) 9.07, (2) 6.665, and (3) 3.2665 mJ·m^{-2} corresponding to the following interionic distances a: (1) $2.4\cdot10^{-10}$, (2) $2.8\cdot10^{-10}$, and (3) $4.0\cdot10^{-10}$ m. Solid curve is drawn with $A^* = 0$ and slope $k_B T/8a^2 = -8$ mJ·m^{-2}, giving $a = 2.5\cdot10^{-10}$ m. *Source:* Adapted from Sangwal (1989). Copyright (1989), with permission from Elsevier.

It is easy to see that the relatively high predicted values of the interfacial energy γ for fairly soluble compounds are due to the terms $\ln c_x$ and A^* in Eqs. (2.81) and (2.86), respectively. In Eq. (2.86), these higher values of fairly soluble salts are due to our assumption that $A^* = 3$, which holds when $\Delta H_{mix}/R_G T = 8\Delta S_{cn}$. When one assumes that $A^* = 0$, Eq. (2.86) also covers the data for fairly soluble salts, as shown by the solid curve in Figure 2.20 with slope $-k_B T/8a^2 = 8$ mJ·m^{-2}, giving $a = 2.5\cdot10^{-10}$ m, and, corresponding to $A^* = 0$, a limiting value of solute concentration $x_x = 1$.

When the term $\ln x_s = -\Delta H_s/k_B T$, Eq. (2.86) is of the form of the relation given by Kahlweit (1975):

$$\gamma = \frac{190\Delta H_s}{\left(V_m^2 N_A\right)^{1/3}}, \tag{2.87}$$

with γ in mJ·m^{-2}, ΔH_s in J·mol^{-1}, and the molar volume V_m in m^3·mol^{-1} of different compounds. Based on the thermodynamics of regular solutions, Bennema and Söhnel (1990) gave the relation:

$$\gamma = \frac{251\Delta H_s}{\left(\nu\, V_m^2 N_A\right)^{1/3}}, \tag{2.88}$$

where ν denotes the number of ions in a dissociated molecule of electrolyte. On the basis of Gibbs adsorption isotherm, Mersmann (1990) proposed the relation:

$$\gamma = 0.414 k_B T \Omega^{-2/3} \ln\left(\frac{c_s}{c_0}\right), \tag{2.89}$$

where the solute concentration $c_s = d_s/M_s$, with d_s as the density of the crystal (kg·m^{-3}) and M_s as its molar mass (kg·kmol^{-1}), and $\Omega = M_s/d_s \nu N_A$ is the molecular volume of the solute. Equation (2.89) is essentially similar to relation (2.80) given by Nielsen and Söhnel (1971).

2.6 Solubility and Supersolubility

Crystallization of a compound always occurs from its supersaturated solutions in the metastable zone. Metastable zone is the region between curves representing solubility (solid curve) and supersolubility (dashed curve) shown schematically in Figure 2.21, which shows phase change from solution to crystalline phase during the cooling of the solution, as indicated by the line ABCD. In this figure, which is a modified version of Figure 2.1, we have used the same symbols as in Figure 2.1. Supersolubility curve in the figure indicates the limiting value of solute concentration when instantaneous 3D nucleation (i.e. precipitation) occurs in the solution.

In Figure 2.21, three areas can be distinguished: (i) stable undersaturated zone, (ii) metastable zone, and (iii) unstable supersaturated area. In area (i), which lies below the solubility curve, the actual concentration c of a solute in the solution at a given temperature, say T_0, is lower than the corresponding equilibrium concentration c_0 represented by the solubility for the solute–solvent system. In an undersaturated solution, more solute will dissolve. In areas (ii) and (iii) lying above the solubility curve, the actual solute concentration c at the temperature T_0 is higher than the solubility c_0 corresponding to the temperature T_0. In these areas the solution is supersaturated. However, processes of 3D spontaneous nucleation and crystal growth occur in the region lying between the solubility and supersolubility curves. This region is called the *metastable zone*. Obviously, the supersolubility curve represents the solute concentration when 3D nucleation occurs instantaneously.

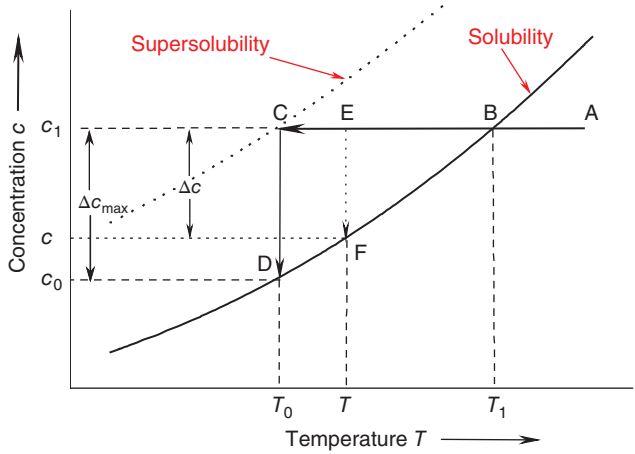

Figure 2.21 Schematic illustration of the dependence of solute concentration in a solute–solvent system on solution temperature. Solid and dashed curves represent solubility and supersolubility curves, respectively. See text for details. *Source:* Sangwal (2009). Copyright (2009), with permission from Wiley.

Deviation in the concentration c_1 of a dissolved salt from its equilibrium value c at a given temperature T (Point F) or deviation in the temperature of the solute–solvent system of a given equilibrium concentration c_1 from a saturation temperature T_1 (Point E) is a measure of the driving force for crystallization. In Figure 2.21, it is the concentration difference $\Delta c = c_1 - c$ corresponding to the saturation concentration c at temperature T or the temperature difference $\Delta T = T_1 - T$ corresponding to the saturation concentration c_1 at temperature T_1. In terms of solute concentrations in the solution at temperature T, the driving force for crystallization is the dimensionless supersaturation ratio $S = c_1/c$, and the degree of supersaturation or simply supersaturation $\sigma = \ln S \approx \Delta c/c$. Obviously, at temperature T, $S < 1$, $S > 1$, and $S = 1$ for undersaturated, supersaturated, and saturated solutions, respectively. In terms of the solubility of a solute, when 3D nucleation of the new phase occurs instantaneously, as shown schematically by the dashed curve in Figure 2.21 (Point C), the driving force for crystallization is the limiting value of metastable zone width represented by temperature T_0 and solute concentration c_1.

The metastable zone width can be achieved by a polythermal or isothermal method. In the polythermal (also called nonisothermal) method, the metastable zone width is measured as the maximum supercooling $\Delta T_{max} = (T_1 - T_0)$, with reference to a constant concentration c_0 corresponding to the saturation temperature T_0 (Point D), by cooling the solution at a constant cooling rate R_L from a temperature somewhat above T_1 (Point A in Figure 2.21) to the temperature

T_0 at which first crystals are detected in the solution (Point D). With reference to the temperature T_0 corresponding to the maximum solute concentration c_1, this metastable zone width is the maximum concentration difference $\Delta c_{max} = (c_1 - c_0)$. The isothermal method, on the other hand, consists of attaining solution supersaturation as fast as possible, followed by the measurement of time period for the appearance of first detectable nuclei in the solution. When the appearance of detectable nuclei occurs immediately after attaining the

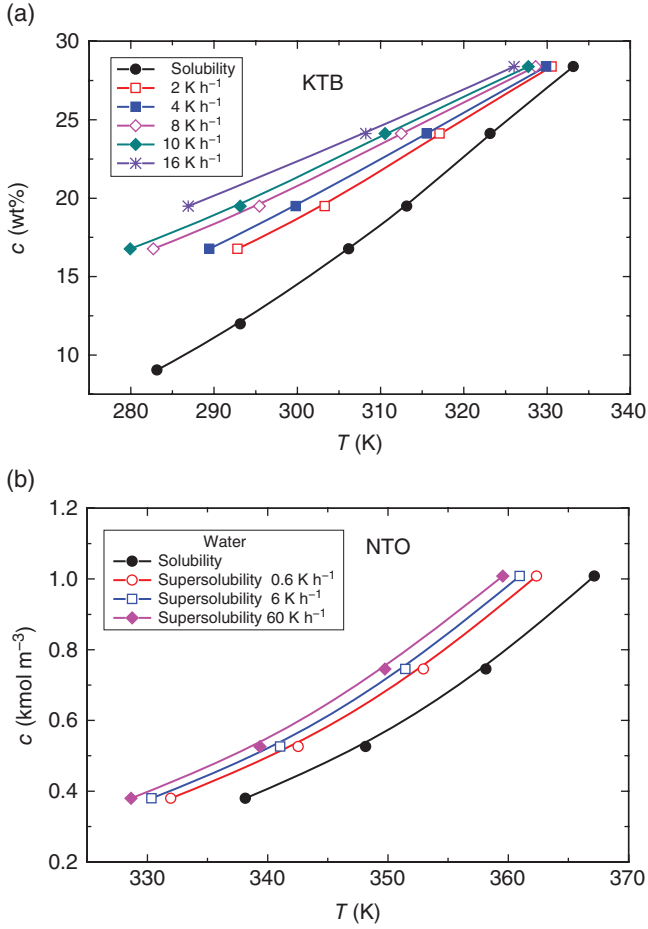

Figure 2.22 Typical examples of solubility and supersolubility curves for different systems: (a) KTB (potassium tetraborate tetrahydrate)–water, (b) NTO (3-nitro-1,2,4-triazol-5-one)–water, and (c) H_3PO_4–water. Supersolubility curves are for various cooling rates. (a and b) *Source:* From Sangwal (2011). Copyright (2011), with permission from Royal Chemical Society; (c) From Sangwal (2010a). Copyright (2010), with permission from Elsevier.

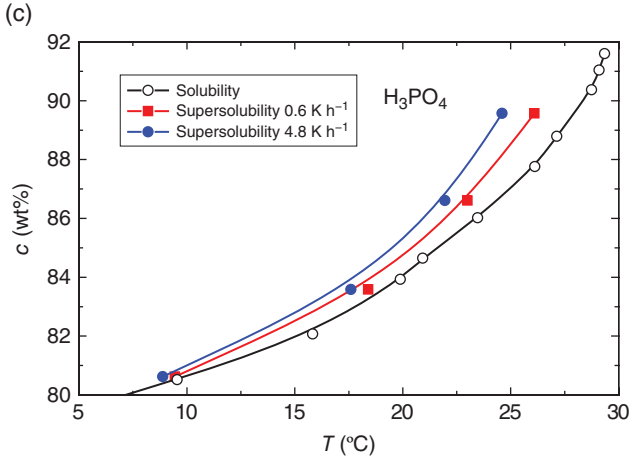

Figure 2.22 (Continued)

predefined supersaturation corresponding to the limiting temperature T_0, one defines the maximum supersaturation ratio $S_{max} = (c_1/c_0)$ and the maximum supersaturation $\ln S_{max} = \ln(c_1/c_0) = \Delta c_{max}/c_0$ as the width of the metastable zone width with reference to T_0.

In the polythermal method, it is observed that, irrespective of the cooling rate R_L, with an increase in saturation temperature T, the value of maximum supercooling $\Delta T_{max} = T - T_0$ decreases for some solute–solvent systems, it remains practically constant for some others, whereas it increases for the remaining solute–solvent systems. Typical examples showing such trends are shown in Figure 2.22. This means that the supercooling ratio $\Delta T_{max}/T$ decreases, increases, or remains constant with increasing saturation temperature T.

The nature of supersolubility curves in Figure 2.22 is similar to that of solubility curves, with the difference that they either diverge, converge, or run parallel to the solubility curve for a given system with increasing temperature T. This suggests that supersolubility curves may be described by an empirical equation similar to that for regular solutions. Figure 2.23 compares solubility curve (curve 1) predicted by real-solution relation (2.49) with the different trends of supersolubility curves 2 and 3 by changing the values of the parameters A and $\Delta H_s/R_G$ of this relation. Figure 2.23a shows the supersolubility curves by changing the values of A alone, whereas Figure 2.23b shows the supersolubility curves by changing the values of A and ΔH_s simultaneously. Obviously, the diverging trends of supersolubility curves may be reproduced by changing the parameter A, but their converging trend requires changes in both A and ΔH_s. Supersolubility curves running parallel to the solubility curve also requires changes in the values of both A and ΔH_s.

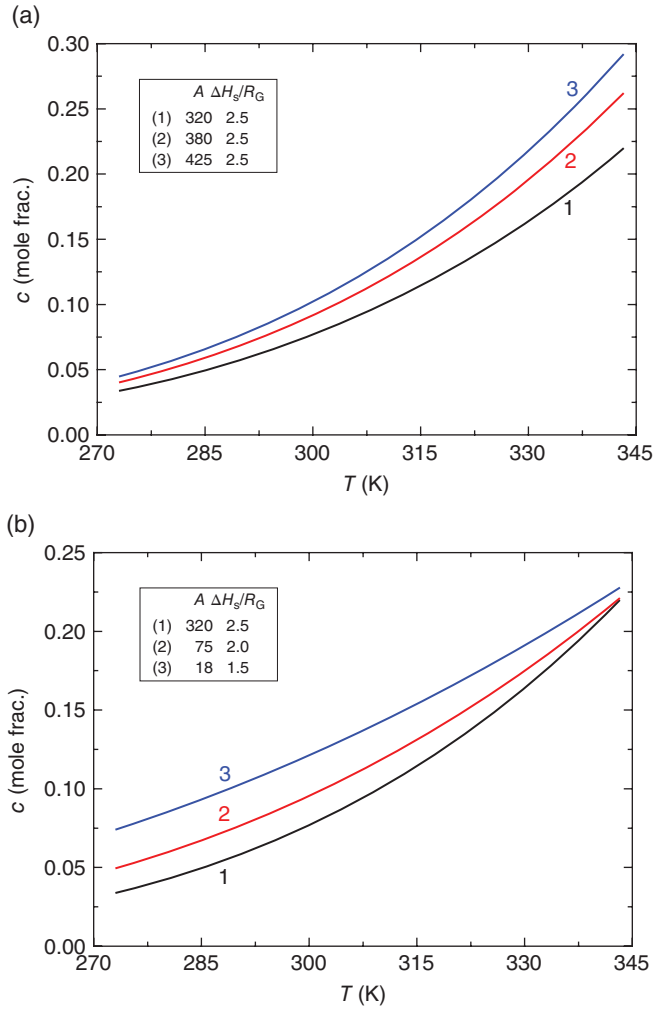

Figure 2.23 Reproduction of different trends of supersolubility curves 2 and 3 by real-solution relation (2.49) by changing values of (a) A and (b) A and ΔH_s. Curve 1 represents solubility curve.

Finally, it should be mentioned that it is difficult to assign any physical interpretation to changes involved in the values of A and ΔH_s in the above description of metastability zone width. Physical basis of the nature of the different types of curves of the metastability zone width is discussed in Chapter 5.

References

Barata, P.A. and Serrano, M.L. (1997). Thermodynamic representation of the solubility of potassium dihydrogen phosphate (KDP) + water + alcohol systems. *Fluid Phase Equilib.* 141: 247–263.

Bennema, P., Boon, J., van Leeuwen, and Gilmer, G.H. (1973). Confrontation of the BCF theory and computer simulation experiments with measured (R,σ) curves. *Krist. Tech.* 8: 659–678.

Bennema, P. and Söhnel, O. (1990). Interfacial surface tension for crystallization and precipitation from aqueous solutions. *J. Cryst. Growth* 102: 547–556.

Berg, E.W. (1963). *Physical and Chemical Methods of Separation*. New York: McGraw Hill.

Bockris, J.O.'.M. and Reddy, A.K.N. (1970). *Modern Electrochemistry*, vol. 1. New York: Plenum Press.

Bohenek, M., Myerson, A.S., and Sun, W.M. (1997). Thermodynamics, cluster formation and crystal growth in highly supersaturated solutions of KDP, ADP and TGS. *J. Cryst. Growth* 179: 213–225.

Charlot, G. (1976). *Analiza Nieorganiczna Jakościowa* [Qualitative Inorganic Analysis]. Warsaw: PWN.

Cohen, M.D., Flagen, R.C., and Seinfeld, J.H. (1987a). Studies of concentrated electrolyte solutions using the electrodynamic balance. 1. Water activities for single-electrolyte solutions. *J. Phys. Chem.* 91: 4563–4574.

Cohen, M.D., Flagen, R.C., and Seinfeld, J.H. (1987b). Studies of concentrated electrolyte solutions using the electrodynamic balance. 2. Water activities for mixed-electrolyte solutions. *J. Phys. Chem.* 91: 4575–4582.

Cohen, M.D., Flagen, R.C., and Seinfeld, J.H. (1987c). Studies of concentrated electrolyte solutions using the electrodynamic balance. 3. Solute nucleation. *J. Phys. Chem.* 91: 4583–4590.

Dali, I., Aydi, A., Alberto, C.C. et al. (2016). Correlation and semi-empirical modeling of solubility of galic acid in different pure solvents and in binary solvent mixtures of propan-1-ol + water, propan-2-ol + water and acetonitrile + water from 293.2 to 318.2 K. *J. Mol. Liq.* 322: 503–519.

Eggers, D.F., Gregory, N.W., Halsey, G.D., and Rabinovitch, B.S. (1964). *Physical Chemistry*. New York: Wiley.

Hildebrand, J.H. and Scott, R.L. (1962). *Regular Solutions*. Englewood Cliffs: Prentice-Hall.

Hussain, K., Thorsen, G., and Malthe-Sorenssen, D. (2001). Nucleation and metastability in crystallization of vanillin and ethyl vanillin. *Chem. Eng. Sci.* 56: 2295–2304.

Jouyban, A., Acree Jr, W.E., and Martinez, F. (2016). Modeling the solubility and preferential solvation of gallic acid in cosolvent + water mixtures. *J. Mol. Liq.* 224: 502–506.

Jouyban, A., Fakhree, M.A.A., and Acree, W.E. Jr. (2012). Comments on "measurement and correlation of solubility of (Z)-2-(2-Aminothiazol-4-yl)-2-methoxyaminoacetic acid in different pure solvents and binary mixtures of water + (ethanol, methanol, or glycol)". *J. Chem. Eng. Data* 57: 1344–1345.

Jouyban-Gharamaleki, A. and Acree, W.E. (1998). Comparison of models for describing multiple peaks in solubility profiles. *Int. J. Pharm.* 167: 177–182.

Jouyban-Gharamaleki, A., Valee, L., Barzegar-Jalali, M. et al. (1999). Comparison of various cosolvency models for calculating solubility in water-cosolvent mixtures. *Int. J. Pharm.* 177: 93–101.

Kahlweit, M. (1975). Ostwald ripening of precipitates. *Adv. Colloid Interface Sci.* 5: 1–35.

Kashchiev, D. (2000). *Nucleation: Basic Theory with Applications*. Oxford: Butterworth-Heinemann.

Kim, K.-J. and Kim, K.-M. (2001). Nucleation kinetics in spherulitic crystallization of explosive comppound: 3-nitro-1,2,4-triazol-5-one. *Powder Technol.* 119: 109–116.

Kubota, N. (2008). A new interpretation of metastable zone widths measured for unseeded solutions. *J. Cryst. Growth* 310: 629–634.

Lide, D.R. (1996/1997). *Handbook of Chemistry and Physics*, 77. Boca Raton: CRC Press.

Liu, B., Sun, H., Wang, J., and Yin, Q. (2014). Thermodynamic analysis and correlation of solubility of disodium 5'-guanylate heptahydrate in aqueous ethanol mixtures. *Fluid Phase Equilib.* 370: 58–64.

Liu, X.Y. (1999). A new kinetic model for three-dimensional heterogeneous nucleation. *J. Chem. Phys.* 111: 1628–1635.

Liu, X.Y., Tsukamoto, K., and Sorai, M. (2000). New kinetics of $CaCO_3$ nucleation and microgravity effect. *Langmuir* 16: 5499–5502.

Marcus, Y. (2002). *Solvent Mixtures: Properties and Selective Solvation*. New York: Marcel Dekker.

Marcus, Y. (2008). On the preferential solvation of drugs and PAH in binary solvent mixtures. *J. Mol. Liq.* 140: 61–67.

Margolis, E.J. (1966). *Chemical Principles in Calculations of Ionic Equilibria*. New York: MacMillan.

Martinez, F., Jouyban, A., and Acree Jr, W.E. (2016). Further comments on "solubility and thermodynamic behavior of vanillin in propane-1,2-diol + water mixtures at different temperatures". *Food Chem.* 196: 757–759.

Mersmann, A. (1990). Calculation of interfacial tensions. *J. Cryst. Growth* 102: 841–847.

Mohan, R. and Myerson, A.S. (1999). The effect of additives on the water activity of supersaturated solutions of β-succinic acid. *J. Cryst. Growth* 206: 99–108.

Mullin, J.W. (2001). *Crystallization*, 4e. Oxford: Butterworth-Heinemann. Chap. 5.

Muñoz, M.M., Peña, M.A., Almanza, O.A. et al. (2016). Solubility and apparent specific volume at saturation of some pharmaceutical salts in methanol + water mixtures at 298.15 K. *J. Mol. Liq.* 220: 842–847.

Na, H.-S., Arnold, S., and Myerson, A.S. (1995). Water activity in supersaturated solutions of organic solutes. *J. Cryst. Growth* 149: 229–235.

Nielsen, A.E. and Söhnel, O. (1971). Interfacial tensions of electrolyte crystal-aqueous solution, from nucleation data. *J. Cryst. Growth* 11: 233–242.

Nývlt, J., Söhnel, O., Matuchova, M., and Broul, M. (1985). *The Kinetics of Industrial Crystallization*. Prague: Academia.

O'Grady, D., Barret, M., Casey, E., and Glennon, B. (2007). The effect of mixing on the metastable zone width and nucleation kinetics in the anti-solvent crystallization of benzoic acid. *Chem. Eng. Res. Des.* 85: 945–952.

Pataki, L. and Zapp, E. (1980). *Basic Analytical Chemistry*. Budapest: Akademiai Kiado.

Sangwal, K. (1989). On the estimation of surface entropy factor, interfacial tension, dissolution enthalpy and metastable zone width for substances crystallizing from solution. *J. Cryst. Growth* 97: 393–405.

Sangwal, K. (2007). *Additives and Crystallization Processes: From Fundamentals to Applications*. Chichester: Wiley. Chap. 2.

Sangwal, K. (2009). A novel self-consistent Nývlt-like equation for metastable zone width determined by the polythermal method. *Cryst. Res. Technol.* 44: 231–247.

Sangwal, K. (2010a). On the effect of impurities on the metastable zone width of phosphoric acid. *J. Cryst. Growth* 312: 3316–3325.

Sangwal, K. (2010b). On the interpretation of metastable zone width in anti-solvent crystallization. *Cryst. Res. Technol.* 45: 909–919.

Sangwal, K. (2011). Some features of metastable zone width of various systems determined by polythermal method. *Cryst. Eng. Comm.* 13: 489–501.

Sangwal, K., Mieniczek-Brzóska, E., and Barylska, S. (2013). Solubility of ammonium oxalate in water-acetone mixtures and metastable zone width of their solutions. *Chem. Eng. Res. Des.* 92: 491–499.

Sangwal, K. and Sato, K. (2012). Nucleation and crystallization kinetics of fats. In: *Structure-Function Analysis of Edible Fats* (ed. A.G. Marangoni), 25–78. Urbana: AOCS Press.

Sangwal, K., Wiktorowska, B., and Sokolowska, T. (1994). Crystal growth from low-temperature from solutions. In: *Elementary Crystal Growth* (ed. K. Sangwal), 255–301. Lublin: Saan Publishers. Chapter 8.

Söhnel, O. (1982). Electrolyte crystal-aqueous solution interfacial tensions from crystallization data. *J. Cryst. Growth* 57: 101–108.

Söhnel, O. and Garside, J. (1992). *Precipitation: Basic Principles and Industrial Applications*. London: Butterworth-Heinemann.

Stokes, R.H. and Mills, R. (1965). *Viscosity of Electrolytes and Related Properies*. Oxford: Pergamon Press.

Taboada, M.E., Palma, P.A., and Graber, T.A. (2003). Crystallization of potassium sulfate by cooling and salting-out using 1-propanol in a calorimetric reactor. *Cryst. Res. Technol.* 38: 21–29.

Tang, I.N., Munkelwitz, H.R., and Wang, N. (1986). Water activity measurements with single suspended droplets: the NaCl-H_2O and KCl-H_2O systems. *J. Colloid Interface Sci.* 114: 409–415.

Zhou, J., Fu, H., Cao, H. et al. (2013). Measurement and correlation of the solubility of florfenicol in binary 1,2-propanediol + water mixtures from 293.15 K to 316.25 K. *Fluid Phase Equilib.* 360: 118–123.

Zhu, Y., Youssef, D., Porte, C. et al. (2003). Study of the solubility and the metastable zone of 1,3-dihydroxyacetone for the drowning-out process. *J. Cryst. Growth* 257: 370–377.

3

Kinetics and Mechanism of Crystallization

Crystalline solids are composed of molecules or atoms arranged in a periodic manner in three dimensions. If the location of a single molecule or an atom in a crystal is known, the location of all other molecules or atoms in the crystal can be described in terms of lattice parameters given by unit vectors and angles between them. These lattice parameters define the fundamental *building blocks* in a crystal referred to as *unit cells*. An infinite array of a particular type of unit cells arranged side by side in space is thus the definition of the so-called *perfect crystal* in contrast to real crystals where the periodic arrangement is interrupted by some planes. When the periodicity of structure extends throughout a certain piece of material, one speaks of a single crystal. However, when the periodicity of structure is interrupted at the boundaries of adjoining single-crystal grains (i.e. at grain boundaries), one speaks of polycrystalline materials. The growth of individual stable three-dimensional (3D) nuclei results in single-crystal grains during crystallization from melts.

Real crystals contain various types of defects due to nonideal conditions of their growth and subsequent treatments. Depending on their geometrical dimensions, the crystal lattice defects are usually classified as follows: (i) point defects, (ii) line defects such as dislocations, (iii) planar defects such as grain boundaries and stacking faults, and (iv) volume defects such as voids and inclusions of secondary phases. Among the various defects, dislocations are known to serve as sources of steps for crystal growth. The reader is referred to the literature to acquire basic concepts of properties of dislocations in crystals (for example, Hull, 1975).

In a supersaturated or supercooled medium, 3D crystalline nuclei are formed by the aggregation of solute atoms or molecules and only those nuclei that exceed critical dimensions can grow larger into visible entities by the attachment of solute atoms or molecules at suitable sites available on their surfaces. If the growth of a nucleus occurs unimpeded, for example, in the supersaturated medium, the grown crystal ultimately acquires a shape, called *growth habit* or *growth morphology*, composed of well-defined planes. Examination of these as-grown planes of the morphology, usually referred to as *surface micromorphology*, reveals different types of spirals and steps on them. It is these steps

Nucleation and Crystal Growth: Metastability of Solutions and Melts, First Edition.
Keshra Sangwal.
© 2018 John Wiley & Sons, Inc. Published 2018 by John Wiley & Sons, Inc.

and their configuration in terms of the concentration of kinks on the surfaces of growing crystals that serve as favorable sites for the attachment of atoms or molecules available from the surrounding supersaturated medium and determine the kinetics of growth of individual faces of crystals and overall crystallization. The present chapter is devoted to the theories of crystal growth and overall crystallization. However, in view of the vast literature existing on these topics, only the basic ideas of these theories are presented. The contents of the chapter are largely based on the reviews published before by the author (Sangwal, 1994, 1998, 2007). For more details on the topics discussed here the reader is referred, among others, to Brice (1973), Chernov (1984), Kashchiev (2000), and van der Eerden (1993).

3.1 Crystal Growth as a Kinetic Process

The development of 3D stable nuclei by the attachment of growth species leads to the formation of macroscopic entities with well-developed surfaces. However, the growth species arriving on a crystal surface from the bulk supersaturated medium do not enter the lattice immediately. The growth species present in the bulk medium first diffuse to the crystal surface (*bulk* or *volume diffusion*) and, after landing on the surface, they lose one degree of freedom and are free to migrate on the surface (*surface diffusion*); see Section 3.7. These growth units constitute a loosely adsorbed layer, at the maximum a few interplanar spacings thick. Figure 3.1 shows different positions for the attachment of growth units at a flat crystal–medium interface of a simple cubic lattice. A growth unit attached at the surface terrace, a smooth step ledge (usually called *step ledge* or *step*), and a kink site has 1, 2, and 3 out of the 6 nearest neighbors, respectively. Therefore, a growth unit arriving on the surface terrace, at the terrace ledge, and at the kink simply loses one, two, and three degrees of freedom. If w is the binding energy per pair, the corresponding binding energy of a growth unit attached at these sites is w, $2w$, and $3w$, respectively.

The probability of capture of a growth unit at a given site depends through terms $\exp(nw/k_BT)$ (where n is the number of bonds formed, k_B is the

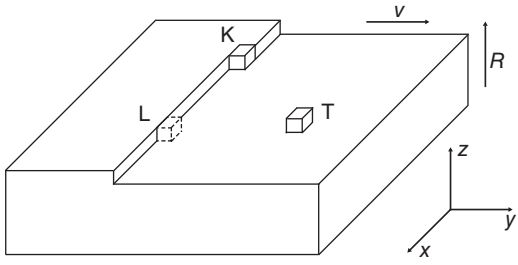

Figure 3.1 Different positions for the attachment of growth units at a flat crystal–medium interface of a simple cubic lattice. Growth unit may be attached at the surface terrace T, a smooth step ledge L, and a kink site K.

Boltzmann constant, and T is the temperature in Kelvin). Therefore, the growth unit has a much higher probability of becoming a part of the crystal at the kink site rather than at the ledge or at the surface terrace. Consequently, in contrast to ledges, the contribution of kinks is overwhelmingly high in the rate v of displacement of a step along the surface and in the rate R of displacement of the surface normal to it. Similarly, the contribution to the face growth rate R by the direct attachment of growth units at the terrace is negligible.

The kinetics of crystal growth may, in general, occur in the following stages:

1) Transport of growth units to the growing surface by bulk diffusion and their capture onto the surface terrace.
2) Migration of growth units adsorbed onto the terrace to the step by surface diffusion and their capture at the step.
3) Migration of growth units adsorbed onto the step to the kink site and their integration into the kink.
4) Transport of the released heat of the reaction and solvent molecules from the solvated atoms/molecules.

One or more of the above steps may control the growth rate, but it is always the slowest step that determines the growth rate.

Growth kinetics, as characterized by rates v and R, depends on the crystal structure, structure of crystal–medium interface (i.e. rough or smooth), the presence of dislocations emerging on the growing face, supersaturation of the growth medium, growth temperature, stirring, and impurities present in the growth medium. Difference in the growth rates R of different faces of a crystal determines its external shape (macromorphology). Growth kinetics also influences the topography of a growing surface and the stability of a growth interface. Using the above background of crystal growth processes, various models for the growth of smooth flat (i.e. singular) faces are described.

3.2 Types of Crystal–Medium Interfaces

Faces bounding a crystal are different regarding the density of steps and kinks present on them at a particular temperature. From a consideration of the surface free energy per unit area, as shown by the Gibbs–Wulff plot, Burton et al. (1951) divided faces into singular and nonsingular ones. According to this classification, singular faces correspond to cusps (i.e. minimum surface free energy per unit area) while nonsingular faces show maxima on the Wulff plots. There are also the so-called vicinal faces, which are misoriented by a small angle from singular faces. Hartman and Perdok (1955a, b) classify the faces of a crystal into F (flat), S (stepped), and K (kinked) faces, as shown Figure 3.2. F-type faces possess at least two sets of chains of periodically bonded atoms, molecules, or radicals (called Periodic Bond Chains, PBCs), S faces have one such PBC while

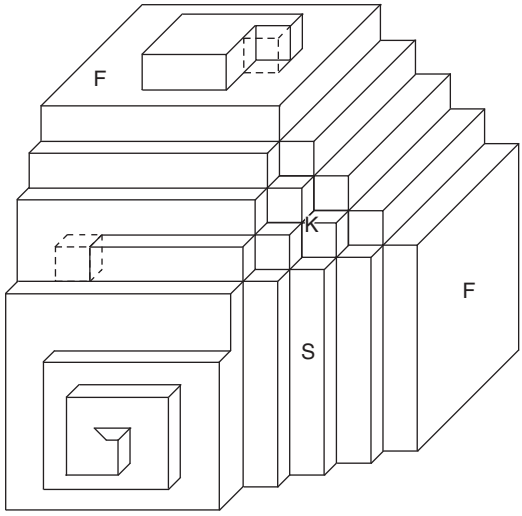

Figure 3.2 Classification of different types of faces of a simple cubic crystal according to the Periodic Bond Chains (PBCs): F (flat), S (stepped), and K (kinked). Three F faces representing examples of ideally smooth morphology, 2D nucleation, and spiral steps due to a screw dislocation in *y*, *z*, and *x* directions, respectively, are shown. Spiral originates at the emergence point of screw dislocation on the surface. *Source:* Adapted from Boistelle and Astier (1988). Copyright (1988), with permission from Elsevier.

K faces do not have any PBC. Thus, F, S, and K faces correspond to singular, vicinal, and nonsingular faces, respectively. Cahn (1960) considers the solid–fluid interface as sharp and diffuse from consideration of successive atomic layers during transition from the solid phase to the fluid phase. When this transition between the solid and fluid layers is abrupt, the interface is sharp. However, when it is difficult to define precisely the boundary between the solid and fluid layers, the interface is diffuse.

F faces may also be classified in terms of their smoothness. They can be ideally smooth or rough on the atomic scale. Growth on an ideally smooth F face is possible if two-dimensional (2D) nucleation (perfect interface) or the presence of dislocations emerging on the surface (imperfect interface) supply kinks necessary for the attachment of growth units. These two situations are illustrated in Figure 3.2. In the case of a rough face, a large number of kinks are always present on the surface and statistical addition of individual atoms/molecules to these kinks leads to its growth in a direction normal to the face.

3.3 Thermodynamic and Kinetic Roughening of Surfaces

As mentioned above, atoms/molecules adsorbed on a surface terrace may migrate to the step ledges and ultimately join it at the kink sites. The question is how these kinks are formed in the step ledges and when an entire surface is composed of kinks.

Perfect surface terrace of a crystal is devoid of step ledges and a perfect ledge on the surface terrace is devoid of kinks. This situation is indeed possible at

0 K when the building units (i.e. atoms or molecules) composing the crystal do not undergo thermal vibrations around their equilibrium positions in the lattice. At temperatures above 0 K, all building units oscillate in the crystal lattice and the amplitude of these vibrations increases with increasing temperature. Because of the statistical nature of the distribution of these thermal vibrations, some of the building units forming a perfect step ledge are driven out of their lattice positions, forming "gaps" in them, i.e. pairs of adjoining kinks of opposite sign, which ultimately rearrange to attain a minimum energy configuration. Thus, a straight step no longer remains straight and possesses a certain number of kinks. In other words, an otherwise smooth step becomes rough due to the escape of building units from it to the surface and the joining of migrating building units from the surface to the step. The degree of roughness increases with increasing temperature, and is accompanied by a decrease in the specific free linear energy γ_1 of the step. When the roughening of F faces is associated with temperature, one speaks of *thermodynamic roughening* of surfaces.

The above discussion of the roughness of a step is for a crystal–vapor system, but the arguments are equally valid for the case of crystal–melt and crystal –solution interfaces. In these cases, normally the so-called lattice gas model is used. In this model, it is assumed that the fluid atoms are packed in the same lattice as in the crystal, but the binding energies in the two phases are different. The increase in the interface energy ω associated with an increase in the step energy due to the formation of a kink in the step is given by (Bennema and Gilmer, 1973; Chernov, 1984)

$$\omega = \frac{w_{cc} - w_{ff}}{2} - w_{cf}, \tag{3.1}$$

where w_{cc}, w_{ff}, and w_{cf} are the bond energies between neighboring solid–solid, fluid–fluid, and solid–fluid atoms (cells), respectively, and there is a particular value of the dimensionless increase in step energy $\omega/k_B T_R$, with T_R as a critical temperature, called *roughening temperature*, when the step ceases to exist and the face is not smooth. When one considers the free linear energy γ_1 of a step with kinks of monoatomic height, $\omega/k_B T_R \approx 0.69$. However, in the absence of this restriction, $\omega/k_B T_R = 0.88$. According to Burton et al. (1951), thermal roughening for solid–vapor interfaces takes place above the melting point of a solid and is rarely encountered in practice.

Considering an initially plane interface on which adatoms in a single layer are allowed to occupy randomly lattice sites (single layer model), Jackson (1958) calculated the change in the free energy on adding atoms (molecules) to a fraction x of the N possible sites at equilibrium temperature T and defined the so-called surface entropy factor α as

$$\alpha = \frac{Z\omega}{k_B T} = \frac{\xi \Delta H_m}{k_B T}, \tag{3.2}$$

where Z is the possible number of bonds with the first nearest neighbors in a plane parallel to the surface under consideration, ξ is the ratio of the binding

energy of an atom in the slice to the total crystallization energy being defined with reference to vacuum, and ΔH_m is the latent heat of melting.

From an analysis of Relation (3.2) for different values of α, Jackson showed that surfaces with $\alpha < 2$ are rough while those with $\alpha > 2$ are smooth. When applied to the solid–vapor interface, this model predicts atomically smooth interfaces.

In the language of the lattice gas model, the surface entropy factor α is defined by (cf. Eqs. (3.1) and (3.2))

$$\alpha = \frac{4\omega}{k_B T} = \frac{2(w_{cc} + w_{ff}) - 4w_{cf}}{k_B T}. \tag{3.3}$$

In the case when complete wetting is assumed (i.e. when $w_{ff} = w_{cc}$), this equation reduces to Eq. (3.2) because $\Delta H_m = (w_{cc} - w_{ff})/2$. However, depending on whether $w_{cf} > w_{ff}$ or $w_{cf} < w_{ff}$, deviations in the values of α predicted by Eq. (3.3) may be expected. In terms of solubility x_s (expressed as mole fraction), α is given by (Bennema and van der Eerden, 1987; Elwenspoek, 1986a)

$$\alpha = \xi\left(\frac{\Delta H_m}{k_B T_m} - \ln x_s\right), \tag{3.4}$$

where T_m is the melting point of the crystal. This equation is valid for growth from ideal and regular solutions containing two or more components. Equation (3.4) reveals that the lower the saturation concentration x_s, the higher is the value of α. In other words, α decreases for substances with a positive temperature coefficient of solubility and increases for substances with a negative one.

For the (001) face of a Kossel crystal, computer simulation showed (Gilmer and Bennema, 1972; van der Eerden et al., 1978) that when $\alpha < 3$ the solid–fluid interface is rough, and a linear (continuous) growth takes place. In this case, growth rate R of the face increases linearly with the driving force (i.e. supersaturation or supercooling). However, when α rises above 3 the interface becomes smoother on a molecular level, so that for $3 < \alpha < 4$ growth by surface nucleation is possible in the absence of steps, while for $\alpha > 4$ observable growth requires the presence of dislocations. In the former case when $3 < \alpha < 4$, the growth rate R follows an exponential dependence on supersaturation or supercooling; in the latter case when $\alpha > 4$, the growth rate R follows a quadratic dependence on supersaturation or supercooling.

Apart from thermodynamic roughening of surfaces associated with temperature, surface roughening can also take place as a result of an increase in the value of the driving force (i.e. supersaturation or supercooling) for growth. This type of roughening of a surface is called *kinetic roughening*. Kinetic roughening is often observed in organic crystals and, above a critical supersaturation at an equilibrium temperature, the growth rate of a face depends linearly on the

supersaturation σ and the face becomes round. Kinetic roughening is connected with the size of the critical 2D nucleus, which approaches the size of an atom or molecule on the surface. This is possible for a small value of linear free energy γ_l of a step when the supersaturation is increased to a critical value σ (see Eq. (3.19)). The critical value of supersaturation, σ_{cr}, above which kinetic roughening takes place, is related to a dimensionless free energy per growth unit in a step on crystal surfaces (Elwenspoek, 1986b; Elwenspoek and van der Eerden, 1987). In this case, there is no activation barrier for 2D growth and every atom landing on the surface may become a part of the surface without surface diffusion processes (continuous growth).

3.4 Growth Kinetics of Rough Faces

Rough faces are characterized by a large number of inherent kink sites and, therefore, there is no need of 2D nucleation on them. Following Brice (1973), we consider that atoms or molecules initially present in the liquid state are added to the faces randomly after overcoming an activation barrier ΔG_I (Figure 3.3). If ΔG is the energy difference associated with their transfer from the liquid to the solid phase, the linear growth rate of the face may be given by

$$R = \left(\frac{a}{x_0}\right)^2 aJ = \beta_{surf}\sigma, \tag{3.5}$$

where a is the diameter of the depositing atoms/molecules, x_0 is the average distance between kinks on the surface, J is the net number of atoms/molecules entering these kinks per unit time, i.e.

$$J \approx \frac{k_B T}{h_P}\frac{\Delta G}{k_B T}\exp\left(-\frac{\Delta G_I}{k_B T}\right), \tag{3.6}$$

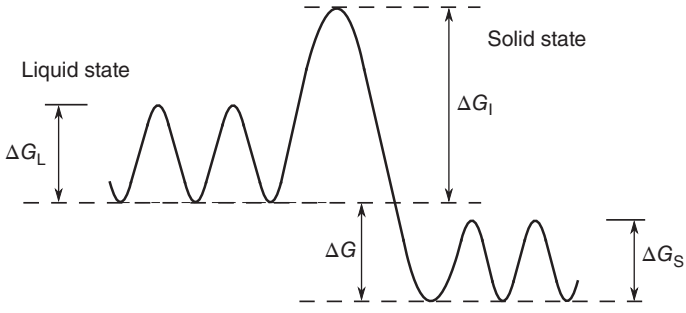

Figure 3.3 Change in free energy associated with the growth of a rough crystal interface. Different energy changes are shown. *Source:* Adapted from Brice (1973).

the supersaturation is defined in terms of the free energy change ΔG by (see Section 2.1)

$$\sigma = \frac{\Delta G}{R_G T}, \tag{3.7}$$

and the kinetic coefficient β_{surf} for growth of the rough face by

$$\beta_{surf} = a\frac{k_B T}{h_P}\exp\left(-\frac{\Delta G_I}{k_B T}\right), \tag{3.8}$$

where h_P is the Planck constant. In the case of growth from viscous liquids, the growth rate Eq. (3.5) is divided by the diffusion coefficient D of atoms in the liquid, and is given by

$$R = \frac{\beta_{surf}\sigma}{D} = \eta'\sigma\exp\left(-\frac{\Delta G_I - \Delta G_L}{k_B T}\right), \tag{3.9}$$

where ΔG_L is the activation energy for diffusion and η' is the dynamic viscosity of the liquid.

According to Eq. (3.5), the growth rate R of a crystal face growing by the continuous growth mechanism exhibits a linear dependence on supersaturation σ. The linear dependence of the interface growth rate on supersaturation was presented independently by Wilson in 1900 and by Frenkel in 1932, and is usually referred to as the Wilson–Frenkel law for normal growth.

3.5 Growth Kinetics of Perfect Smooth Faces

The growth of perfect faces devoid of dislocations is possible by the incorporation of growth units at the kinks of steps supplied by 2D nucleation. Suppose that 2D nucleation occurs on the surface at a rate J_{2D} ($m^{-2}\cdot s^{-1}$), L (m) is the linear diameter of the face under consideration and v is the rate of displacement of steps on the surface terrace, the average time required for the nucleation of successive layers on the surface is L/v and the number n of nuclei formed on the surface during this time is $J_{2D}L^3/v$, i.e. $L = A^{1/2} = (nv/J_{2D})^{1/3}$. Therefore, depending on the rate v of displacement of steps of the 2D nuclei on the surface, three versions of growth by 2D nucleation are possible. When $A^{1/2} < (v/J_{2D})^{1/3}$, a 2D nucleus is formed only after the spreading of the layer formed by the preceding nucleus over the entire surface with $v = \infty$. This is the *mononuclear model*. However, when $A^{1/2} > (v/J_{2D})^{1/3}$, many stable nuclei are formed on the surface and meet the layers initiated by other nuclei. This is the *polynuclear model*. In the extreme case of this model, $v = 0$ (Figure 3.4a). However, to account for the fact that $0 < v < \infty$ is also possible, a model involving simultaneous birth and spread of nuclei (*B+S model*), also called the *multiple*

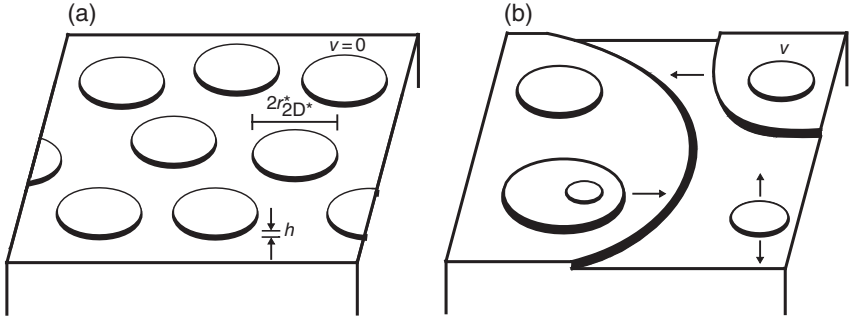

Figure 3.4 Two-dimensional nucleation models of growth based on finite step velocity *v*: (a) polynuclear model and (b) multiple nucleation model. In (b) lateral displacement of different steps are shown by arrows.

nucleation model, is frequently used (Figure 3.4b). Obviously, surface nucleation is discrete in the mononuclear model, but nucleation is continuous in the polynuclear and multiple nucleation models.

The normal growth rate R of a face of area A due to the formation of 2D nuclei at a rate J_{2D} may be given by

$$R = hAJ_{2D}, \tag{3.10}$$

where h is the height of steps of the nuclei. In the case of multiple nucleation model when $0 < v < \infty$, on replacing the face are A by $(v/J_{2D})^2$, one obtains

$$R = hJ_{2D}{}^{1/3}v^{2/3}. \tag{3.11}$$

It may be noted that Eq. (3.10) applies to mononuclear and polynuclear models. In the mononuclear model, the rate-limiting step is the formation of a critically-sized 2D nucleus and the average frequency of nucleation is AJ_{2D}, where the total area A available for 2D nucleation is πL^2. However, in the polynuclear model, the rate-limiting step is the filling-up of the area A by the formation of 2D nuclei and the available area A for 2D nucleation is $\pi r_{2D}^{*\,2}$. In contrast to the mononuclear and polynuclear models, in the multiple nucleation model the rate-limiting step is the displacement velocity v of steps formed by stable 2D nuclei.

Integration of atoms/molecules adsorbed on the surface into kinks in the steps can occur either by their migration over the surface terrace at an average distance λ_s or by their direct exchange at the step edge (see Figure 3.5). The former mechanism, called the *surface diffusion mechanism*, holds when the surface diffusion distance λ_s for the adsorbed atoms/molecules is relatively large and is at least comparable with the average distance y_0 between growth steps containing the kinks (i.e. $\lambda_s \geq y_0$). However, when the adsorbed atoms/molecules

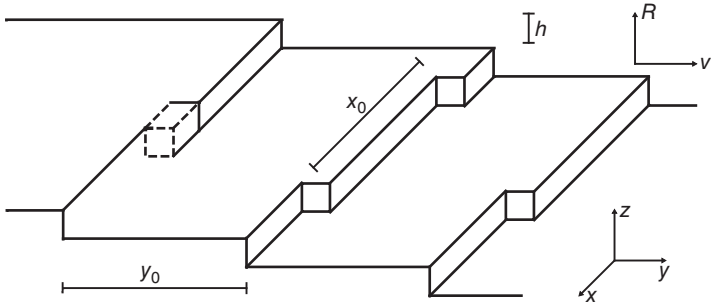

Figure 3.5 Explanation of average distance y_0 between growth steps, average distance x_0 between kinks, step height h, and directions of displacement of step ledges and face with rates v and R, respectively. An atom/molecule adsorbed on the surface terrace between two step ledges has an average diffusion distance λ_s for its movement on the surface.

are relatively immobile (i.e. $\lambda_s \ll y_0$), their diffusion over the surface will not contribute significantly to growth. Instead, due to their high concentration in the liquid mother phase, the growth units landing on the surface will be captured directly at kinks in the steps. This is the *direct integration mechanism*. However, in both of these mechanisms, the transport of the growth atoms/molecules in the liquid phase is faster than their surface diffusion or direct integration.

The difference between the equations of face growth rate R based on surface diffusion and direct integration of growth units lies in the expressions for the step displacement velocity v. In the case of surface diffusion, the velocity v of a straight step is given by (Burton et al., 1951; Sangwal, 1994)

$$v = 2\sigma\left(\frac{\lambda_s}{a}\right)\beta_l, \tag{3.12}$$

where the kinetic coefficient β_l for the step is given by

$$\beta_l = a\nu \exp\left(-\frac{\Delta G_{att}}{k_B T}\right), \tag{3.13}$$

λ_s is the diffusion distance on the surface, a is the size of the growth unit, $\nu = k_B T/h_P$ is the frequency of vibration of molecules/atoms on the surface, ΔG_{att} is the energy required for the integration of atoms/molecules into the crystal, and the supersaturation (see Section 2.1) is

$$\ln S \approx \sigma = \frac{(c - c_0)}{c_0}, \tag{3.14}$$

where c and c_0 denote, respectively, the actual and equilibrium solute concentrations expressed in mole fraction. The kinetic coefficient β_l for the step is essentially the same as β_{surf} of Eq. (3.8) when $\Delta G_{att} = \Delta G_I$.

Equation (3.12) is the extreme case of Eq. (3.30) when both retardation factors β and Λ, related to the density of kinks in the steps and the density of steps on the surface, respectively, are unity, and only a part of the adsorbed atoms/molecules reach the kinks in the steps of the 2D nuclei. Equation (3.12) represents the maximum velocity corresponding to the capture of all atoms/molecules arriving by surface diffusion into the kinks in the steps. In solution growth, ΔG_{att} is equal to the energy ΔG_{dehyd} required for the dehydration of atoms/molecules during its integration into the crystal.

In the case of growth by the direct integration of growth units, for not very concentrated solutions when $\Omega c_0 \leq 0.2$, the step velocity may be given by (Chernov, 1961, 1984; Chernov et al., 1986b)

$$v = \beta_l \frac{c - c_0}{d - c} = \beta_l \Omega c_0 \sigma, \tag{3.15}$$

where d is the crystal density and has units of c and c_0, Ω is the specific molecular volume of atoms/molecules, and the kinetic coefficient β_l for steps is given by Eq. (3.13) in which the activation energy ΔG_{att} is now equal to the activation energy for the integration of atoms/molecules into the kinks and is usually denoted by W.

The rate of 2D nucleation is given by (Chernov, 1984; Ohara and Reid, 1973; Sangwal, 1994)

$$J_{2\text{D}} = C_1 \sigma^{1/2} \exp\left(- \frac{\Delta G^*_{2\text{D}}}{k_{\text{B}} T} \right), \tag{3.16}$$

where

$$C_1 = \pi h n_1 c_0 \beta_l, \tag{3.17}$$

the free energy change $\Delta G^*_{2\text{D}}$ corresponding to the formation of a stable disc-shaped 2D nucleus of critical radius $r^*_{2\text{D}}$ of height h on the perfect surface is

$$\Delta G^*_{2\text{D}} = \frac{\pi h \gamma^2 \Omega}{k_{\text{B}} T \sigma} = \pi h \gamma r^*_{2\text{D}}, \tag{3.18}$$

and the critical radius $r^*_{2\text{D}}$ of the 2D nucleus is

$$r^*_{2\text{D}} = \frac{\gamma \Omega}{k_{\text{B}} T \sigma}. \tag{3.19}$$

In Eqs. (3.17) and (3.18), γ is the surface free energy, and the concentration of adsorbed atoms/molecules (i.e. the number of atoms/molecules per unit area) on the surface is given by

$$n_1 = h c_0 \exp\left(- \frac{E_{\text{ad}}}{k_{\text{B}} T} \right), \tag{3.20}$$

where E_{ad} is the energy of adsorption of the atoms/molecules on the surface. Equations (3.18) and (3.19), for $\Delta G^*_{2\text{D}}$ and $r^*_{2\text{D}}$, for the formation of a stable

disc-shaped 2D nucleus are obtained by following a procedure similar to that for a spherical 3D nucleus (see Section 2.2.1) with $k_B T\sigma = \Delta\mu$ (cf. Eq. (2.16)).

The forms of the finite velocity v of movement of steps involving surface diffusion and direct integration are essentially the same (see Eqs. (3.12) and (3.15)). Using the expression for step velocity v and Eq. (3.16) for nucleation rate J_{2D}, the face growth rate R according to different models may be given as follows:

1) *Mononuclear model:*

$$R = hAJ_{2D} = hAC_1\sigma^{1/2}\exp\left(-\frac{\Delta G^*_{2D}}{k_B T}\right). \tag{3.21}$$

2) *Polynuclear model:*

$$R = hAJ_{2D} = \pi r^{*2}_{2D} hC_1\sigma^{1/2}\exp\left(-\frac{\Delta G^*_{2D}}{k_B T}\right). \tag{3.22}$$

3) *Multiple nucleation model:*

$$R = hv^{2/3}J_{2D}{}^{1/3} = hC_2^{2/3}C_1^{1/3}\sigma^{5/6}\exp\left(-\frac{\Delta G^*_{2D}}{3k_B T}\right), \tag{3.23}$$

where the constants $C_2 = 2\lambda_s/a$ and $C_1 = \Omega c_0$ are for growth by surface diffusion and direct integration mechanisms, respectively.

All of the three models predict an exponential dependence on supersaturation σ at low σ and $R \propto \sigma^{1/2}$ or $R \propto \sigma^{5/6}$ at high σ. Since supersaturation σ increases the nucleation rate J and decreases the critical nucleus radius r^*_{2D}, all of them predict a maximum in R at some value of supersaturation σ. However, they differ from each other in the dependence of R on the area A of the growing crystal and the supersaturation σ for growth. According to the mononuclear model the growth rate R increases with the area A of the growing crystal, whereas no dependence of R on A is predicted by the polynuclear and multiple nucleation models. All these models predict observable growth rates at supersaturations exceeding 25–50%.

3.6 Growth Kinetics of Imperfect Smooth Faces

The main postulate of different models of growth kinetics of imperfect smooth faces is that the presence of a screw dislocation, because of its geometry, ensures a continuous source of steps (kinks) for the integration of growth entities on a

growing surface and that there is no need for 2D nucleation involving an activation barrier ΔG^*_{2D} (see Eq. (3.18)). If an array of steps of height h and interstep distance y_0, forming a spiral hillock of inclination $p = h/y_0$, traverses across a growing surface at a rate v, then the normal growth rate R is given by (see Figure 3.5)

$$R = \frac{hv}{y_0} = pv, \tag{3.24}$$

where the interstep distance y_0 is related to the radius r^*_{2D} of the critically-sized circular nucleus corresponding to activation barrier ΔG^*_{2D} (see Eq. (3.18)) by (cf. Eq. (3.19))

$$y_0 = 19r^*_{2D} = \frac{19\gamma\Omega}{k_B T\sigma}. \tag{3.25}$$

In this relation it is assumed that the hillock inclination p is constant and the supersaturation σ_s available on the surface is equal to the supersaturation σ_b in the bulk solution.

It is frequently observed that growth steps on the F faces of crystals have thickness mh, which is a multiple of the height h of elementary steps (where $m \geq 1$). However, the above equations are also valid for such multiple-height steps.

3.6.1 Surface Diffusion and Direct Integration Models

According to the surface diffusion model (Bennema and Gilmer, 1973; Burton et al., 1951), advanced by Burton, Cabrera and Frank, referred to as the BCF model hereafter, the step velocity v and the face growth rate R are given by

$$v = 2\sigma\left(\frac{\lambda_s}{a}\right)\beta\Lambda\beta_l \tanh\left(\frac{y_0}{2\lambda_s}\right), \tag{3.26}$$

and

$$R = C^*\frac{\sigma^2}{\sigma_1}\tanh\left(\frac{\sigma_1}{\sigma}\right), \tag{3.27}$$

where

$$C^* = \frac{\beta\Lambda\Omega N_0}{a}\beta_l, \tag{3.28}$$

and

$$\sigma_1 = \frac{\gamma\Omega}{2k_B T\lambda_s}, \tag{3.29}$$

In the above equations, N_0 is the concentration of growth units on the surface, while β is the kink retardation factor related to the density of kinks in the steps

and Λ is the step retardation factor related to the density of steps on the surface terrace.

Equation (3.26) represents the general expression for v for a situation in which the average kink distance $x_0 \ll \lambda_s$. The step kinetic coefficient β_l is given by Eq. (3.13). When the average step distance $y_0 \gg \lambda_s$ (i.e. $\sigma \ll \sigma_1$),

$$v = 2\sigma\left(\frac{\lambda_s}{a}\right)\beta\Lambda\beta_l, \tag{3.30}$$

and the face growth rate

$$R = C^*\frac{\sigma^2}{\sigma_1}. \tag{3.31}$$

However, when $y_0 \ll \lambda_s$ (i.e. $\sigma \gg \sigma_1$),

$$v = \sigma\left(\frac{y_0}{a}\right)\beta\Lambda\beta_l, \tag{3.32}$$

and

$$R = C^*\sigma. \tag{3.33}$$

Equations (3.31) and (3.33) represent the ideal parabolic and linear laws, respectively.

According to Eqs. (3.31) and (3.33), $\beta_l = v/\sigma$ when $2\lambda_s/a = 1$ and $\Omega c_0 = 1$, i.e. the constant $C_2 = 1$ in Eq. (3.23). Equation (3.26) thus implies that $(2\lambda_s/a)\beta\Lambda \tanh(y_0/2\lambda_s) = 1$. This condition means that the step velocity v depends on σ through β, Λ, and y_0 at low σ while only through β and Λ at high σ. However, the values of the kink retardation factor β and the step retardation factor Λ depend on σ but their relationships with σ are complicated.

According to Eqs. (3.30) and (3.32), two distinct relationships between v and σ may be distinguished for β and Λ equal to unity. At low σ when y_0 is very large and the condition $y_0 \gg \lambda_s$ holds, Eq. (3.30) reduces to Eq. (3.12) and $v \propto \sigma$. At high σ when the condition $y_0 \ll \lambda_s$ holds, Eq. (3.32) predicts a supersaturation-independent v, because $y_0 \propto 1/\sigma$.

The factor β is determined by the exchange between the kinks and the adsorbed molecules. When this exchange is slow such that the surface supersaturation near the kinks exceeds zero ($\sigma_s > 0$), $\beta < 1$. However, when the exchange between them is rapid, $\beta = 1$. The value of Λ is determined by the relation between the surface diffusion distance λ_s and the mean interkink distance x_0. When $\lambda_s \gg x_0$, $\Lambda = 1$. In contrast to this, when $\lambda_s \leq x_0$, $\Lambda < 1$. These cases correspond to low σ when $y_0 > \lambda_s$. At high supersaturations, on the other hand, when $y_0 \ll \lambda_s$, both $\beta \approx 1$ and $\Lambda \approx 1$ for $\lambda_s \gg x_0$ and $\sigma_s \geq 0$. The distances y_0 and x_0 are explained in Figure 3.5.

According to the direct integration model (Chernov, 1961, 1984; Chernov et al., 1986a, b), usually called the Chernov model, the step velocity v is given by Eq. (3.15) while the face growth rate

$$R = C\sigma^2, \tag{3.34}$$

where the constant

$$C = \frac{k_B T}{19\gamma} h c_0 \beta_l, \tag{3.35}$$

with β_l given by Eq. (3.13). According to Eq. (3.34), the face growth rate $R \propto h/\gamma$. However, at high supersaturations, the steps become sufficiently rough such that the interstep distance y_0 is practically independent of supersaturation σ. This ultimately leads to a linear dependence of the face growth rate R on σ.

Finally, it should be noted that the form of Eqs. (3.31) and (3.34) for R is essentially the same at low σ when $\sigma \ll \sigma_1$ and $\tanh(\sigma_1/\sigma) = 1$. However, for supersaturations σ lying between the interval between parabolic and linear dependence of face growth rate R, one expects $R \propto \sigma^n$ with $1 < n < 2$. From a comparison of the plots of Eqs. (3.23) and (3.27) of multiple nucleation model and the BCF theory expressed in the following forms:

$$Y = X^{5/6} \exp\left(-\frac{1}{X}\right), \tag{3.36}$$

$$Y = X^2 \tanh\left(\frac{1}{X}\right), \tag{3.37}$$

where Y and X are R- and σ-related parameters, Garside et al. (1975) showed that the two equations can be fitted over a limited range of σ by the empirical power-law equation:

$$R = C_n \sigma^n, \tag{3.38}$$

where $5/6 < n \leq 5$ and C_n is a constant. Therefore, if $n > 2$, it can safely be assumed that the multiple nucleation model is likely to hold. Values of the exponent n between 1 and 2 can also result when a group of screw dislocations participates in the growth of an F face (Bennema and Gilmer, 1973; Burton et al., 1951; Chernov et al., 1986a, b).

3.6.2 Bulk Diffusion Models

In these models, it is assumed that an unstirred diffusion layer of thickness δ is developed at the surface of a growing crystal and that diffusion of growth units in the bulk medium is slower than their diffusion on the surface and integration into kinks. Considering low or high density of kinks in the steps, two models have been developed. The BCF model (Burton et al., 1951) considers the

situation when the distance between kinks in a step is large such that diffusion fields develop around the kinks and on the surface. On the other hand, the Chernov model (Chernov, 1961) treats the case when the distance between kinks is so small that a step can be considered as a line sink.

In the BCF model, the displacement rate v of a step in a set of parallel steps is related to the bulk diffusion constant D of the solute and the supersaturation $\sigma(x_0)$ available at the kinks of average distance x_0. However, in the Chernov model, the rate of motion of steps is related to the supersaturation $\sigma(y_0)$ available at the steps of average distance y_0 and the kinetic coefficient β_l for step motion (see Eq. (3.36)). The linear growth rate R of a face is given by

$$R = \left(\frac{h}{y_0}\right) v = C_3 \sigma \sigma(x_0, y_0), \tag{3.39}$$

where $\sigma(x_0,y_0)$ denotes $\sigma(x_0)$ and $\sigma(y_0)$ of the two models and C_3 represents a constant in the models.

Both models define a typical critical supersaturation σ_c such that $R \propto \sigma^2$ and $R \propto \sigma$ for $\sigma \ll \sigma_c$ and $\sigma \gg \sigma_c$, respectively. However, the predictions of the two models somewhat differ from each other. The BCF model predicts that the face growth rate R is practically independent of δ for $\sigma \ll \sigma_c$ but R is inversely proportional to δ for $\sigma \gg \sigma_c$. In contrast to this, the Chernov model predicts that the dependence of R on supersaturation σ is inversely proportional to δ both at low and high σ.

It should be noted that according to these bulk diffusion models the step velocity v continuously decreases with decreasing interstep spacing y_0, and no impurity is required for this process.

3.6.3 Growth at Edge Dislocations

The role of screw dislocations in the growth of F faces of crystals is well established from the observation of growth spirals on them as well as from studies of growth kinetics (Chernov, 1984; Sangwal, 2007; Verma, 1953). However, after 1962 several workers reported (see Bauser and Strunk, 1981, 1984; Keller, 1986) that edge dislocations act as persistent sources of monomolecular steps in the form of concentric closed-loop patterns. It was also reported (Sherwood and Shripathi, 1988) that, at a given supersaturation, the growth rate R of F faces of potash alum crystals increases with an increase in the density of edge dislocations.

An edge dislocation may be visualized as the termination of atoms/molecules of an "extra half-plane" inserted in a perfect crystal lattice such that the terminal edge of the extra half-plane, representing the dislocation line, lies in a direction perpendicular to the plane under consideration. For geometrical reasons, therefore, the termination of an edge dislocation in the plane is not expected to

provide sources of steps for crystal growth. The origin of activity of edge dislocations has been explained in terms of Coulomb interactions, impurity segregation at dislocations, dissociation of edge dislocation into partial dislocations, and surface relaxation. According to the surface relaxation mechanism advanced by Frank (1981), crystals have surface stresses of the order of their surface free energies, but these stresses can be either tensile or compressive. Due to its geometry, an edge dislocation always has a region compressed on one side and dilated on the other side of the site of its emergence on the surface, leading to compressive and tensile surface stresses in its vicinity. Irrespective of whether the surface stress is compressive or tensile, they decrease the energy of a surface nucleus. Therefore, the region near the emergence point of a dislocation is always more favorable than the unstrained surface for the formation of a 2D nucleus on the surface.

Assuming that changes in surface stresses due to edge dislocations emerging on a growing surface and due to externally applied stresses on a crystal facilitate 2D nucleation on a surface through changes in surface energy γ, from the multiple nucleation model one may write (see Eq. (3.23))

$$\ln\left(\frac{R}{\sigma^{5/6}}\right) = K_1 - \frac{K_2 \Delta\gamma^2}{\sigma}, \tag{3.40}$$

$$\frac{R}{R_0} = \exp\left[B'\left(\gamma^2 - \gamma_0^2\right)\right], \tag{3.41}$$

respectively. In Eq. (3.40), $\Delta\gamma$ is the change in the surface energy γ caused by an edge dislocation, while K_1 and K_2 are constants. In Eq. (3.41), γ and γ_0 are the values of the surface energy in the presence and absence of externally applied stresses, respectively, and B' is a constant. The experimental results obtained by Sherwood and Shripathi (1988) can be explained by using the above expressions.

3.7 Simultaneous Bulk-Diffusion and Surface-Reaction Controlled Growth

As described in Section 3.1, crystal growth involves various steps, which may be grouped into two stages. Solute molecules are transported from the bulk medium of uniform concentration to the solid surface and then they are captured by the crystal lattice. These two stages involve different concentration gradients covering: (i) a rigid, stagnant layer, with a thickness of a few molecular dimensions, composed of adsorbed molecules/ions in the immediate vicinity of the crystal and (ii) a diffuse layer, extending from the rigid layer deep into the bulk medium, formed as a result of mutual attractive and repulsive interactions between different charged entities. These stages are illustrated schematically in

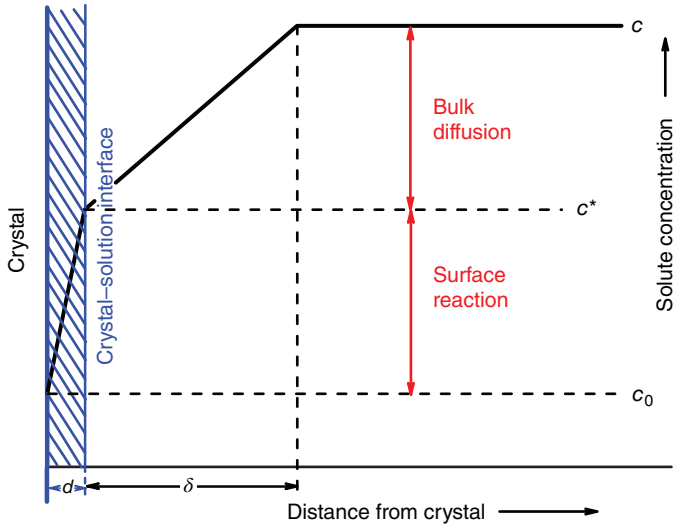

Figure 3.6 Schematic illustration of concentration gradient in different regions away from crystal–medium interface. Stagnant and diffuse layers of thicknesses d and δ, respectively, and different concentrations are shown.

Figure 3.6, whereas the mass transfer rate in the two stages are given by the relations

$$\frac{\mathrm{d}m}{\mathrm{d}t} = k_{\mathrm{d}} A(c - c^*), \quad \text{(bulk diffusion)}, \tag{3.42}$$

$$\frac{\mathrm{d}m}{\mathrm{d}t} = k_{\mathrm{r}} A(c^* - c_0), \quad \text{(surface reaction)}, \tag{3.43}$$

where m is the mass of the solid deposited in time t, c and c^* denote solute concentration in the bulk medium and crystal–medium interface, respectively, c_0 is the crystal solubility, A is the surface area of the growing crystal, and k_{d} and k_{r} are mass transfer coefficients by bulk diffusion and surface reaction, respectively. The coefficient k_{d} is related to the thickness δ of the diffuse layer and the coefficient D of solute diffusion in the bulk medium by: $k_{\mathrm{d}} = D/\delta$.

It is not simple to apply Eqs. (3.42) and (3.43) directly because they contain the interfacial concentration c^*, which is difficult to measure. Therefore, the interfacial concentration c^* is usually eliminated by considering an overall concentration difference $c - c_0$, which can be measured easily. The general equation relating the overall growth rate with the concentration difference $c - c_0$ is usually written in the form:

$$\frac{\mathrm{d}m}{\mathrm{d}t} = K_{\mathrm{G}} A(c - c_0)^n, \tag{3.44}$$

where K_G is the overall crystal growth coefficient, and the exponent n, frequently referred to as the growth order, lies between 1 and 2. When $n = 1$, the interfacial concentration c^* may be eliminated from Eqs. (3.42) and (3.43) to have the relation:

$$\frac{1}{K_G} = \frac{1}{k_d} + \frac{1}{k_r}, \tag{3.45}$$

or

$$K_G = \frac{k_d k_r}{k_d + k_r}. \tag{3.46}$$

When the surface reaction is very fast such that $k_r \gg k_d$, $K_G \approx k_d$, and crystal growth is controlled by bulk diffusion. However, when diffusion is very fast (i.e. $k_d \gg k_r$), $K_G \approx k_r$; then growth is controlled by surface reaction. For other relative values of k_d and k_r, both diffusion and surface reaction contribute to crystal growth.

Finally, it should be mentioned that the linear dependence in Eq. (3.43) assumes that the growing surface is relatively rough and contains a high density of kinks on it.

3.8 Effect of Impurities on Growth Kinetics

Impurities contained in the growth medium can lead to dramatic changes in the growth kinetics of crystals. Impurities may affect crystal growth rates in different ways. They can change the properties of the growth medium, whereby the equilibrium saturation concentration (i.e. solubility) of the solute and, hence, the supersaturation available for nucleation and growth, are altered. Impurities can also affect the kinetic and thermodynamic terms involved in different growth models. The kinetic parameters in the growth models for the F faces are associated with the density of kinks and obstructions provided in the movement of steps on the surface by impurity particles whereas the thermodynamic parameter in the growth models is the interfacial energy γ.

The kinetic effect of impurities in the growth theories is directly associated with a change in the density of kinks by impurity particles in competing with the integration of growth units into them. When impurity particles are strongly adsorbed at the kink sites such that they physically block the accessibility of growth units to the kinks, the impurity leads to a decrease in the velocity v of movement of steps on the crystal surface and the face growth rate R. Adsorption of impurities can also change the properties of the crystal–medium interface such that the interfacial energy γ of the growing crystal is changed. The change in the value of γ results in a change in the nucleation rate J in the 2D

nucleation models (the exponential terms in Eq. (3.16)) and the radius r^*_{2D} of critical 2D nucleus and hence the spacing y_0 between the spiral steps in the BCF theory (Eq. (3.25)). Therefore, the growth rate R based on these theories is changed (see Section 3.6).

The commonly observed effect of impurities is to retard growth rates. Therefore, it is usually assumed that adsorption of an impurity increases the value of γ. However, consideration of the adsorption process in terms of adsorption isotherms and reversible adsorption equilibrium shows that impurity adsorption decreases the value of γ (Davey, 1979; Kern, 1967). This decrease in γ will, consequently, cause an increase in R (Ohara and Reid, 1973).

Kinetic and thermodynamic effects of an impurity may be included in the equations of the 2D nucleation barrier ΔG^*_{2D}, the 2D stable nucleus radius r^*_{2D}, and the 2D nucleation rate J_{2D} using the model of heterogeneous nucleation for a perfect F face, advanced by Liu et al. (1997). In their model, the authors made the following assumptions: (i) the impurity particles adsorbed on the crystal surface are cylindrical with an average radius R_s and an average density N_s, and (ii) R_s and N_s remain constant during growth. The schematic illustration of the mechanism of heterogeneous 2D nucleation on such impurity cylindrical particles is similar to that shown in Figure 2.4a; see Chapter 2. As in the case of 3D nucleation, when the impurity particles are present on the surface, they serve as substrates for 2D nucleation and decrease the nucleation barrier, given by

$$\Delta G^*_{2D(het)} = \Delta G^*_{2D(hom)} \phi'(m,x), \tag{3.47}$$

whereas the nucleation rate is given by (Liu et al., 1997)

$$J_{2D} = C_1 \sigma^{1/2} f(m,x,R_s,N_s) \exp\left(- \frac{\Delta G^*_{2D(hom)} \phi'(m,x)}{k_B T} \right). \tag{3.48}$$

In the above equations, the factor $\phi'(m, x)$ has values from 0 and 1, the factor m is related to the contact angle θ (i.e. $m = \cos\theta$), the parameter $x = R_s/r^*_{2D}$, the factor $f(m,x,R_s,N_s)$ lies between 0 and 1, and the nucleation barrier $\Delta G^*_{2D(hom)}$ for homogeneous nucleation is given by Eq. (3.18).

It may be seen from Eq. (3.48) that the factor $\phi'(m,x)$ included in the exponential term lowers the energy barrier ΔG^*_{2D} for heterogeneous nucleation, thereby increasing the nucleation rate J_{2D}, while the factor $f(m,x,R_s,N_s)$ in the preexponential term leads to a decrease in J_{2D}. Therefore, the ultimate nucleation rate J_{2D} is determined by these two factors. One can calculate the growth rate R of a perfect smooth face using Eqs. (3.10) and (3.11) for polynuclear and multiple nucleation models, respectively. Note that adsorption of impurity molecules also results in a decrease in the critical radius r^*_{2D} of 2D nucleus.

It is well known that at a particular supersaturation σ the steps produced by 2D nuclei and screw dislocations move with a certain velocity v, which is related

to the kinetic coefficient β_l for their displacement. This β_l coefficient is determined by the average density of available kinks in the steps and associated with the energy ΔG_{att} required for the integration of atoms/molecules into the crystal (see Eq. (3.13)). Therefore, impurity molecules adsorbed at kinks are expected to decrease the step velocity v. Another consequence of adsorption of impurity molecules is to decrease the average distance y_0 between steps as a consequence of decrease in the critical radius r^*_{2D} of 2D nuclei by the impurity.

Step ledges produced by 2D nuclei and screw dislocations move with a certain velocity v at a particular supersaturation σ. Therefore, in the case of multiple nucleation model, which is close to reality, we consider growth of an F face controlled by surface diffusion. For growth of a perfect smooth surface, substitution of the values of J_{2D} from Eq. (3.48) and step velocity v from Eq. (3.15) in Eq. (3.11) gives the face growth rate

$$R = hC_2^{2/3}C_1^{1/3}\sigma^{5/6}f(m,x,R_s,N_s)^{1/3}\exp\left(-\frac{C_5\phi'(m,x)}{T^2\sigma}\right), \tag{3.49}$$

where the constant

$$C_5 = \frac{\pi h\,\gamma_{cf}^2\Omega}{3\,k_B^2}. \tag{3.50}$$

For simplicity, we consider BCF theory of growth controlled by surface diffusion. Then, for growth in the presence of an impurity, from Eqs. (3.24), (3.25), and (3.26), one obtains the face growth rate

$$R = C^* f(m,x,R_s,N_s)\frac{\sigma^2}{\sigma_1\phi''(m,x)}\tanh\left(\frac{\sigma_1\phi''(m,x)}{\sigma}\right), \tag{3.51}$$

where C^* and σ_1 are given by Eqs. (3.26) and (3.29), respectively, whereas the parameter $\phi''(m,x)$ behaves like $\phi'(m,x)$ and lies between 0 and 1.

The above general considerations show that, at relatively low impurity concentration, the theoretical models of growth predict opposite effects of impurities on growth kinetics. The thermodynamic parameter associated with the effective interfacial energy γ tends to increase face growth rate R, whereas the kinetic effect connected with the integration of growth units to the growing steps and face tends to decrease them. At relatively high supersaturations when a high density of kinks is available at the ledges, additive adsorption always decreases R for all values of impurity concentrations. However, at low supersaturations, which ensure a low density of kinks at the ledges, the rates increase for small additive concentrations and decrease as the additive concentration is increased. This type of behavior was first observed by Bliznakov and Kirkova (1956) for the linear growth rates of the (100) and (111) faces of $Pb(NO_3)_2$ grown from aqueous solutions in the presence of methyl blue (Figure 3.7).

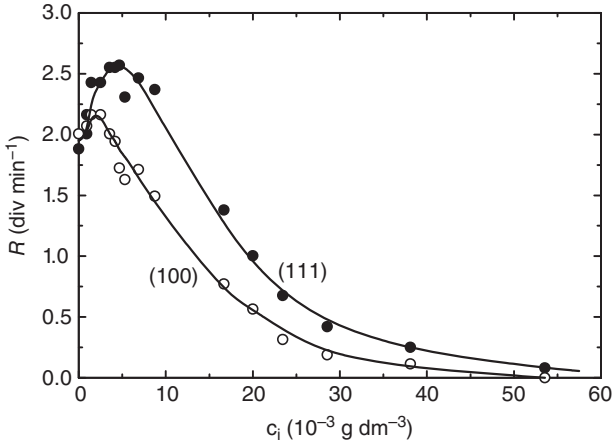

Figure 3.7 Dependence of linear growth rates R of (100) and (111) faces of $Pb(NO_3)_2$ grown from aqueous supersaturated solutions on concentration c_i of methyl blue. *Source:* Adapted from Bliznakov and Kirkova (1956).

Impurities can adsorb on the surface terrace nonselectively and can diffuse over large distances between the neighboring ledges on the surface. These impurities are called as mobile impurities. They can adsorb preferentially at kinks in the ledges. There are also impurities that adsorb selectively on the surface terrace and remain immobile there for long durations. Such impurities are called as immobile impurities. However, the above considerations of the simultaneous effects of thermodynamic and kinetic parameters are valid for any impurity, which is capable of adsorbing at kinks as well as at the surface terrace.

The value of the impurity concentration, at which a peak in the $v(c_i)$ and $R(c_i)$ curves is observed, depends on the supersaturation used for growth, the temperature of growth, the nature of the adsorbing impurity, and on the nature of the crystal face. The experimental results on growth kinetics show that the maxima in the curves of growth rate R against impurity concentration c_i are usually observed at relatively low impurity concentrations in the case of inorganic salts growing in the presence of impurities adsorbing nonselectively on the surface (Bliznakov and Kirkova, 1956; Kirkova and Nikolaeva, 1973). However, such maxima are not observed in the $R(c_i)$ curves in the case of impurities adsorbing selectively on the surface (Black et al., 1986; Chu et al., 1989; Davey et al., 1986; Ristić et al., 1994).

In contrast to the growth of F faces by the displacement of ledges on the surface terrace, the growth of S and K faces takes place by the so-called normal growth involving statistical deposition of growth molecules at growth sites (i.e. kinks) without their diffusion on the surface (see Section 3.4). Therefore,

adsorption of impurity particles at kinks on S and K decreases the density of kinks and hinders the access of solute molecules to them, thereby leading to a decrease in the growth rates of these faces. The displacement of these faces occurs in a direction normal to it and sometimes they behave as F faces (Li et al., 1990).

3.9 Overall Crystallization

The process of transformation of solute from supersaturated solution or supercooled melt (phase A) of initial concentration c_A at a given temperature to the final equilibrium concentration c_B (phase B) representing the cessation of crystallization with time is represented schematically in Figure 3.8a. The solute concentration may be divided into three stages. In stage A, the concentration of solute practically remains constant up to a certain time t_B in the liquid medium. At time t_B the solute present in the liquid begins to crystallize by the formation and growth of 3D nuclei. Time up to t_B is known as the *induction period* for crystallization of phase B. Crystallization of phase B continues until time t_f when transformation of phase A into phase B ultimately ceases (i.e. solute crystallization ceases). In the time interval between t_B and t_f, the rate of crystallization initially increases and subsequently approaches a zero value asymptotically after approaching a maximum value at some time t^*. Between t_B and t^* lies the intermediate stage (A + B) where 3D stable nuclei are formed and, once formed from the dissolved solute, they grow larger into detectable entities. At time t^* the formation of 3D nuclei ceases to occur. Stage B represents exclusively the growth of crystallites of phase B and lies between times t^* and t_f. Beyond time t_f, solute crystallites alone are present in the system. In this stage, the solute appears as crystalline mass in equilibrium with the dissolved solute in the solution or in the solidified melt.

The process of transformation of solute dissolved in a supersaturated solution into the solid phase involving a decrease in solute concentration c_A to c_B in Figure 3.8a may be described from consideration of values of supersaturation ratio S^*_{3D} and S^*_{2D} for the formation of critically-sized 3D and 2D nuclei, respectively; see Eqs. (2.20) and (3.19). We assume that the interfacial energy γ of the crystallizing solid is independent of its size, the volume Ω of the crystallizing molecules in these nucleations remain unchanged, and the growing critical 3D nucleus retains its spherical shape. From Eqs. (2.20) and (3.19), one notes that the value of $\ln S^*_{3D}$ for the formation of critical 3D nucleus is twice the value of $\ln S^*_{2D}$ for the formation of critical 2D nucleus. With the crystal size $L = 2r_{3D}$, from Eq. (2.20) the relationship between crystal size L and supersaturation ratio S may be given in the form:

$$\ln S = \left(\frac{4\gamma\Omega}{k_B T}\right)\frac{1}{L(S)}. \tag{3.19a}$$

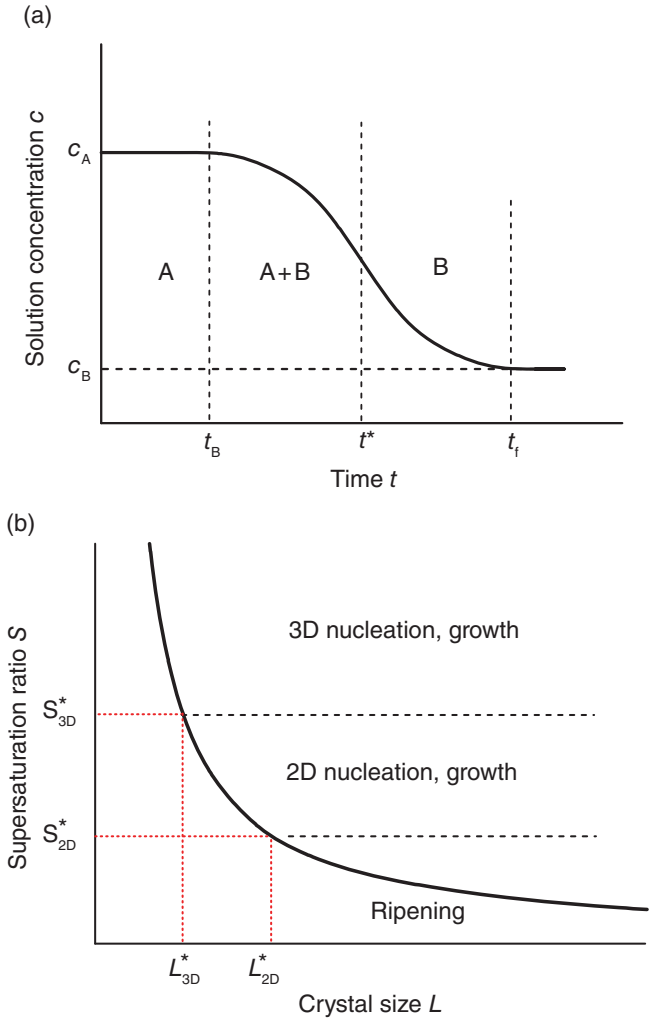

Figure 3.8 (a) Evolution of solution (phase A) of initial solute concentration c_A during the crystallization of solute B with time *t*. (b) Relationship between supersaturation ratio *S* and crystal size *L* according to Eq. (3.19a) and three supersaturation regions. See text for details.

Figure 3.8b shows the above dependence with an arbitrary $4\gamma\Omega/k_BT$, where the values of S^*_{3D} and S^*_{2D} and the corresponding crystal sizes L^*_{3D} and $L^*_{2D} = 2L^*_{3D}$ are presented schematically. The three supersaturation regions $S > S^*_{3D}$, $S^*_{3D} > S > S^*_{2D}$ and $S > S^*_{2D}$ define regions of occurrence of 3D nucleation and growth, 2D nucleation and growth of 3D nuclei, and ripening of 3D crystals, respectively. However, it should be noted that when the growth of 3D crystals is facilitated by dislocations, the limit of supersaturation for growth is lower than S^*_{2D} indicated in Figure 3.8b.

3D nucleation and growth of crystals of a material from its solution or melt in a closed system can occur only in the metastable region where the liquid phase is supersaturated or supercooled. Continued nucleation and growth of crystallites of the material from the liquid phase in the metastable zone at a particular temperature leads to the crystallization of the entire mass of the material until the system reaches the equilibrium state. This type of crystallization is known as *overall crystallization* of a phase in a closed system.

It is easy to realize that solute crystallization begins from the supersaturated solution of concentration c_A and the maximum crystallization is attained at concentration c_B with the corresponding times t_B and t_f, respectively. Therefore, it is convenient to consider the concentrations of crystallized solute (or overall crystallization) taking c_A and c_B as the lowest and the highest crystallized masses, respectively. If m_{max} is the maximum mass of the crystallizing phase, in terms of crystallized mass $m(t)$ at time t the fraction $y(t)$ of crystalline phase in the closed system may be defined as

$$y(t) = \frac{m(t)}{m_{max}}. \tag{3.52}$$

Alternatively, for the same system the fraction of the uncrystallized phase may also be described as $1 - y(t)$. However, in the discussion of solid fraction $y(t)$, instead of masses $m(t)$ and m_{max}, the volume V_c(t) of the crystallized solid at time t from the maximum volume V of the solute in the melt or in the supersaturated solution is usually used.

Theoretical description of the kinetics of overall crystallization was developed mainly between 1937 and 1941 by A.N. Kolmogorov, W.A. Johnson, and R.F. Mehl, and M. Avrami, and is frequently referred to as the *Kolmogorov–Johnson–Mehl–Avrami (KJMA) theory*. The theory has found interesting applications in the interpretation of kinetics of crystallization of different types of materials from melts and solutions. Here, the KJMA theory is briefly presented following mainly Kashchiev (2000). Some other approaches are given by Foubert et al. (2003), Marangoni (2005), and Padar et al. (2008). Foubert et al. (2003) and Padar et al. (2008) give relatively simple derivations of the final equations without consideration of diffusion processes in the system.

3.9.1 Basic Theoretical Equations

We consider a supersaturated phase of volume V and the total of N_m nucleation centers for the crystallizing phase. If $N(t)$ is the number of nuclei at time t and J_s (s^{-1}) is the time-independent nucleation rate per active center, the decrease in the number of nuclei formed with time t may be given by

$$\frac{dN(t)}{dt} = -J_s[N_m - N(t)], \tag{3.53}$$

with the solution

$$N(t) = N_{\mathrm{m}}[1 - \exp(-J_{\mathrm{s}}t)]. \tag{3.54}$$

For instantaneous nucleation when $J_{\mathrm{s}}t << 1$, we have

$$N(t) = N_{\mathrm{m}}J_{\mathrm{s}}t, \tag{3.55}$$

where the stationary, time-independent nucleation rate J_{s} is given by Eq. (2.27). When $J_{\mathrm{s}}t >> 1$, the number $N(t)$ of nuclei increases exponentially with time t (progressive nucleation). In other words, the number $(N_{\mathrm{m}} - N(t))$ of available centers for nucleation per unit volume decreases exponentially, i.e.

$$[N_{\mathrm{m}} - N(t)] = VJ_{\mathrm{a}}(t') = N_{\mathrm{m}} \exp(-J_{\mathrm{a}}t). \tag{3.56}$$

The time dependence of the number $N(t)$ of nuclei is related to the time-dependent nucleation rate $J_{\mathrm{a}}(t)$ by the relation:

$$J(t) = \frac{N_{\mathrm{m}}J_{\mathrm{a}}(t)}{V}. \tag{3.57}$$

For nonstationary nucleation at constant supersaturation and without preexisting clusters on the active centers, the time-dependent nucleation rate J_{a} per active center is given by (cf. Kashchiev, 2000; Toschev, 1973)

$$J_{\mathrm{a}} = J_{\mathrm{s}}\left[1 + 2\sum_{n=1}^{\infty}(-1)^n \exp\left(-\frac{n^2 t}{\tau}\right)\right], \tag{3.58}$$

with τ as the *induction period* or *nonstationary time lag* for nucleation given by

$$\tau = \frac{4}{\pi^3 z^2 f^*}, \tag{3.59}$$

where z is the Zeldovich factor lying between 0.01 and 1, and f^* is the attachment frequency of monomers to the nucleus. For a typical value of $z = 0.1$, $\tau \approx 10/f^*$. The time lag τ characterizes the ability of a system to reorganize itself until a steady flow of nuclei is formed in it, i.e. the number of nuclei increases linearly with time t. Since the process of reorganization of the system involves diffusion of the i-sized nuclei, the time lag τ may be given by

$$\tau = \frac{4k_{\mathrm{B}}T}{\lambda D}, \tag{3.60}$$

where D is the diffusion coefficient and the parameter $\lambda = 2\Delta G^*_{2\mathrm{D}}/3i^{*2}$, with $\Delta G^*_{3\mathrm{D}}$ as the activation energy required for the formation of stable i^*-sized nucleus.

If $V_n(t,t')$ is the volume of any individual n-sized crystallite, which depends on the earlier moment $t' \le t$, we assume that the crystallites are isomorphic and do

not contact with each other during their growth. Then the crystalline volume dV_c formed between t' and t may be given by

$$dV_c = V_n(t', t)J_a(t')(V - V_c)dt', \tag{3.61}$$

where V_c is the total crystallized volume. Under the initial condition $V_c = 0$, integration of Eq. (3.61) gives

$$V_c(t) = V\left[1 - \exp\left\{-\frac{V_{ex}}{(t)V}\right\}\right]. \tag{3.62}$$

where the extended volume V_{ex} is given by

$$V_{ex} = V\int_0^t J_a(t')V_n(t', t)dt'. \tag{3.63}$$

Equation (3.62) is the KJMA formula. Physically, V_{ex} is the total crystalline volume that would have been formed from the crystallizing phase during time t if the initial volume V would not have been exhausted by the growing crystallites and there were no contacts between these crystallites. Consequently, initially V_c is practically equal to V_{ex}, and for the duration when $V_c < 0.2V$, Eq. (3.62) takes the form:

$$V_c = V\int_0^t J_a(t')V_n(t', t)dt'. \tag{3.64}$$

Substitution of $VJ_a(t')$ from Eq. (3.57) in Eq. (3.63) gives

$$V_{ex} = N_m\int_0^t V_n(t', t)\exp(-J_a t)dt'. \tag{3.65}$$

To determine the kinetics of crystallization, one has to take into account the time-dependent growth of the crystallites.

The crystallites can grow in one, two, or three directions, usually referred to as lineal (rod-like), plate-like, or polyhedral shapes, respectively. Assuming that the radius r of a crystalline cluster grows according to the power law

$$r(t) = \left(R_g t\right)^{\nu}, \tag{3.66}$$

the time dependence of crystallite growth rate $R(t)$ may be written in the form:

$$R(t) = \nu R_g{}^{\nu} t^{\nu-1}, \tag{3.67}$$

where R_g is a growth constant and ν is a number characterizing the supply of growth entities to the growing crystallites. The values of ν are 1/2 and 1 for

growth controlled by volume diffusion and interface transfer, respectively. The value of the growth constant R_g is determined by monomer attachment frequencies.

Assuming that a crystallite of effective radius r retains its geometrical shape during growth at time t, the volume of the growing crystallite may be given by

$$V_n(t) = \kappa r^d = \kappa \left[\int_0^t R(t) \mathrm{d}t \right]^d , \tag{3.68}$$

where $d = 1, 2, 3$ is the dimensionality of the growing crystallite, κ is the shape factor (for example, $\kappa = 4\pi/3$ for a sphere), t is the growth time, and the crystallite growth rate $R(t) = \mathrm{d}r(t)/\mathrm{d}t$.

Combination of Eqs. (3.62), (3.63), and (3.68) gives the KJMA formula:

$$y(t) = \frac{V_c(t)}{V} = 1 - \exp\left\{ -\kappa \int_0^t J(t') \left[\int_0^{t-t'} R(t'') \mathrm{d}t'' \right] \mathrm{d}t' \right\}. \tag{3.69}$$

This equation shows that the evolution of the fraction of the crystallized volume is controlled by two parameters: nucleation rate J and growth rate R.

It should be noted that physically $y(t)$ is the probability of crystallization of the entire volume until time t after the onset of the overall crystallization process. This means that there is an average time t_{av} for crystallization from the supersaturated system, given by

$$t_{av} = \int_0^\infty t \mathrm{d}y(t) = \int_0^\infty \exp\left\{ -\frac{V_{ex}(t)}{V} \right\} \mathrm{d}t. \tag{3.70}$$

The number $N(t)$ of nucleating crystallites in the system at time t is related to $y(t)$ by

$$N(t) = V \int_0^t J(t')[1 - y(t)] \mathrm{d}t' = V \int_0^t J(t') \exp\left\{ -\frac{V_{ex}(t')}{V} \right\} \mathrm{d}t'. \tag{3.71}$$

Under the condition that crystallites do not grow into each other when they come in mutual contact, a maximum number N_m of crystallites is produced finally in the system. This number is characterized by the limiting value of $N(t)$ when $t = \infty$, given by

$$N_m = V \int_0^\infty J(t) \exp\left\{ -\frac{V_{ex}(t)}{V} \right\} \mathrm{d}t. \tag{3.72}$$

From Eq. (3.72), one obtains the average volume V_{av} of the crystallites at the end of overall crystallization:

$$V_{av} = \frac{V}{N_m} = \left[\int_0^\infty J(t)\exp\left\{-\frac{V_{ex}(t)}{V}\right\}dt\right]^{-1}. \tag{3.73}$$

Obviously, for a particular solute volume V, the number $N(t)$ of nucleating crystallites at time t, and the maximum number N_m of crystallites and the average volume V_{av} of the crystallites at the end of crystallization depend on the nucleation rate J and the extended volume V_{ex}.

Overall crystallization of a phase may occur by the formation of one or many stable nuclei in the volume and their subsequent growth. In these cases, the process is said to take place by *mononuclear* and *polynuclear* mechanisms, respectively. In the polynuclear mechanism, several nuclei in the volume can form in two ways. In the first case, the number N of nuclei per unit volume forms continuously during the crystallization process. In the second case, the N nuclei per unit volume may be formed in the system at the initial moment $t = 0$. This is equivalent to crystallization on seeds added to a supersaturated solution or supercooled melt. After their formation, the nuclei grow at a constant rate until the completion of crystallization in the entire volume. These two types of nucleation are known as progressive (or sporadic) and instantaneous nucleation modes, respectively. However, during progressive nucleation the nucleation rate can be time independent (stationary nucleation) as well as time dependent (nonstationary nucleation). In contrast to the polynuclear mechanism, when crystallization in the entire volume occurs as a result of the appearance of only one stable nucleus, one talks of mononuclear mechanism.

Irrespective of whether nucleation is homogeneous or heterogeneous, nucleation always occurs on nucleation centers. The total number N_m of nuclei in the system cannot exceed the total number N_a of these active nucleation centers present in it. The active centers thus determine both the maximum number of nuclei formed in the system and the duration of nucleation. During the nucleation process, the number of active centers is exhausted progressively during crystallization. Therefore, the time dependence of the kinetics of nucleation on active centers determines the overall crystallization kinetics. The theoretical expressions for mononuclear or polynuclear mechanism and for instantaneous or progressive nucleation are different from each other.

3.9.2 Polynuclear Crystallization

Equation (3.63) applies to systems in which phase transformation occurs under conditions when statistically many nuclei are formed in the volume. As mentioned above, these nuclei can form by instantaneous and progressive nucleation modes. We describe them below.

3.9.2.1 Instantaneous Nucleation Mode

In this case, all crystallites in a system are nucleated essentially at the initial moment $t = 0$ so that these nuclei grow larger until the entire old phase transforms into a new phase. Nucleation on N_a active centers such as impurity particles or tiny seeds added to the system are typical examples of this process when the number N_a is equal to the maximum number N_m of crystallites in the volume V. Then the $J(t)$ dependence is of the form:

$$J(t) = \left(\frac{N_m}{V}\right)\delta_D(t), \tag{3.74}$$

where $\delta_D(t)$ is the Dirac-delta function. Remembering the fact that the following result holds for the product of the Dirac-delta function $\delta_D(t)$ with an arbitrary function $y_1(t',t)$:

$$\int_0^t \delta_D(t')y_1(t',t)\mathrm{d}t' = y_1(0,t), \tag{3.75}$$

and using this relation for $J(t)$ in Eq. (3.73), one obtains

$$y(t) = \frac{V_c(t)}{V} = 1 - \exp\left\{-\frac{\kappa N_m}{V}\left[\int_0^{t-t'} R(t'')\mathrm{d}t''\right]^d \mathrm{d}t'\right\}. \tag{3.76}$$

Substituting the value of $R(t'')$ from Eq. (3.67) in Eqs. (3.76) and (3.70) and taking integration, one obtains

$$y(t) = \frac{V_c(t)}{V} = 1 - \exp\left\{-\left(\frac{t}{\Theta}\right)^{\nu d}\right\}, \tag{3.77}$$

$$t_{av} = \Gamma\left(1 + \frac{1}{\nu d}\right)\Theta, \tag{3.78}$$

where the time constant

$$\Theta = \left(\frac{V}{\kappa N_m}\right)^{1/\nu d}\frac{1}{R_g}, \tag{3.79}$$

the gamma function

$$\Gamma(x) = \int_0^\infty y_1{}^{x-1}\mathrm{e}^{-y_1}\mathrm{d}y_1, \tag{3.80}$$

the maximum number of crystallites

$$N_m = VJ_s t_{av} = \Gamma\left(1 + \frac{1}{\nu d}\right)VJ_s\Theta, \tag{3.81}$$

and R_g is given by Eq. (3.67).

From the above relations it may be seen that the time constant Θ, the average crystallization time t_{av}, and the maximum number of crystallites N_m decrease by increasing the growth constant R_g and/or the average concentration N_m/V of crystallites.

3.9.2.2 Progressive Nucleation Mode

After substituting the values of $J(t)$ for nonstationary nucleation from Eq. (3.58) and $R(t)$ from Eq. (3.67) in Eq. (3.69), its integration gives

$$y(t) = \frac{V_c(t)}{V} = 1 - \exp\left\{ -\frac{\kappa J_s (R_g t)^{\nu d}}{1+\nu d} t \left[1 - \left(\frac{\pi^2 x}{6} \right) - (2x) \sum_{n=1}^{\infty} (-1)^n \exp\left(-\frac{n^2}{x} \right) \right] \right\}, \tag{3.82}$$

where $x = \tau/t$, with the time lag of nucleation τ given by Eqs. (3.59) and (3.60). For $x \to 0$, Eq. (3.82) reduces to the simple form:

$$y(t) = \frac{V_c(t)}{V} = 1 - \exp\left\{ -\left(\frac{t}{\Theta} \right)^{1+\nu d} \right\}, \tag{3.83}$$

with the average crystallization time

$$t_{av} = \Gamma\left[\frac{2+\nu d}{1+\nu d} \right] \Theta, \tag{3.84}$$

and the maximum number of crystallites

$$N_m = V J_s t_{av} = \Gamma\left[\frac{2+\nu d}{1+\nu d} \right] V J_s \Theta, \tag{3.85}$$

where the time constant

$$\Theta = \left(\frac{1+\nu d}{\kappa R_g^{\nu d} J_s} \right)^{1/(1+\nu d)}. \tag{3.86}$$

From the above equations it follows that accelerated overall crystallization associated with higher nucleation and growth rates (J and R_g, respectively) leads to lower time constant Θ, average crystallization time t_{av}, and maximum number N_m of crystallites.

It should be noted that, except for the value of the exponent in Eqs. (3.77) and (3.83), the form of the two equations is the same and may be given by the unified formula:

$$y(t) = \frac{V_c(t)}{V} = 1 - \exp\left[-\left(\frac{t}{\Theta} \right)^q \right], \tag{3.87}$$

provided that growth occurs by the power law (3.66) and nucleation is either instantaneous or occurs progressively in the stationary regime. The kinetic

exponent $q = \nu d$ is for instant nucleation and $q = 1 + \nu d$ for progressive nucleation. Obviously, depending on the dimensionality d of crystallites, for bulk diffusion when $\nu = 1/2$, the exponent lies between 0 and 1.5 and between 1 and 2.5 when crystallization occurs by instantaneous and progressive nucleation modes, respectively. However, for interface transfer when $\nu = 1$, the exponent lies between 0 and 3 and between 1 and 4 when crystallization occurs by instantaneous and progressive nucleation modes, respectively.

Finally, it should be emphasized that the time constant Θ of Eqs. (3.79) and (3.86) is intimately connected with the time lag τ for nucleation given by Eqs. (3.59) and (3.60).

3.9.2.3 Trends of Overall Crystallization Curves

The united formula (3.87) of the KJMA theory contains two parameters, the time constant Θ and the exponent q, which describe isothermal crystallization in terms of stationary nucleation and growth processes. It is instructive to assess the effect of these parameters on the behavior of plots of overall crystallization $y(t)$ as a function of crystallization time t. Figure 3.9 illustrates the effect of these parameters on the trends of $y(t)$ plots according to Eq. (3.87). The following features may be observed from these plots:

1) For a given value of the time constant Θ when the exponent $q \leq 1$, the initial curvature of the plot is convex and attains a maximum value at high t. However, when $q > 1$, the duration of detectable crystallization is delayed and the shape of the plot attains S-shape such that the initial curvature is concave and then, after a practically linear region of crystallization representing constant growth rate, the curvature becomes convex (see Figure 3.9a).
2) For a given value of the exponent $q > 1$, with an increase in the value of the time constant Θ the duration of detectable crystallization increases and the value of constant growth rate decreases (curves 2 and 3 in Figure 3.9a).
3) Same values of constant growth rate in $y(t)$ plots may be obtained for different combinations of values of q and Θ but the initial duration of detectable crystallization is determined by the value of Θ (curves 1 and 2 in Figure 3.9b).
4) Delayed onset of crystallization by a certain time t_0 with the same values of q and Θ due to impurities and additives results in an increase in the initial duration of detectable crystallization without a change in the growth rate (solid curves 2 and 3 in Figure 3.9b). However, the $y(t)$ data due to delayed onset of crystallization by a certain time t_0 may be reproduced by increased values of q and Θ, as shown by comparing solid curve 3 with dashed curve 4 in Figure 3.9b.

The above features are associated with physical quantities and processes involved in overall crystallization of the system. The effect of impurities is discussed in Section 3.9.4.

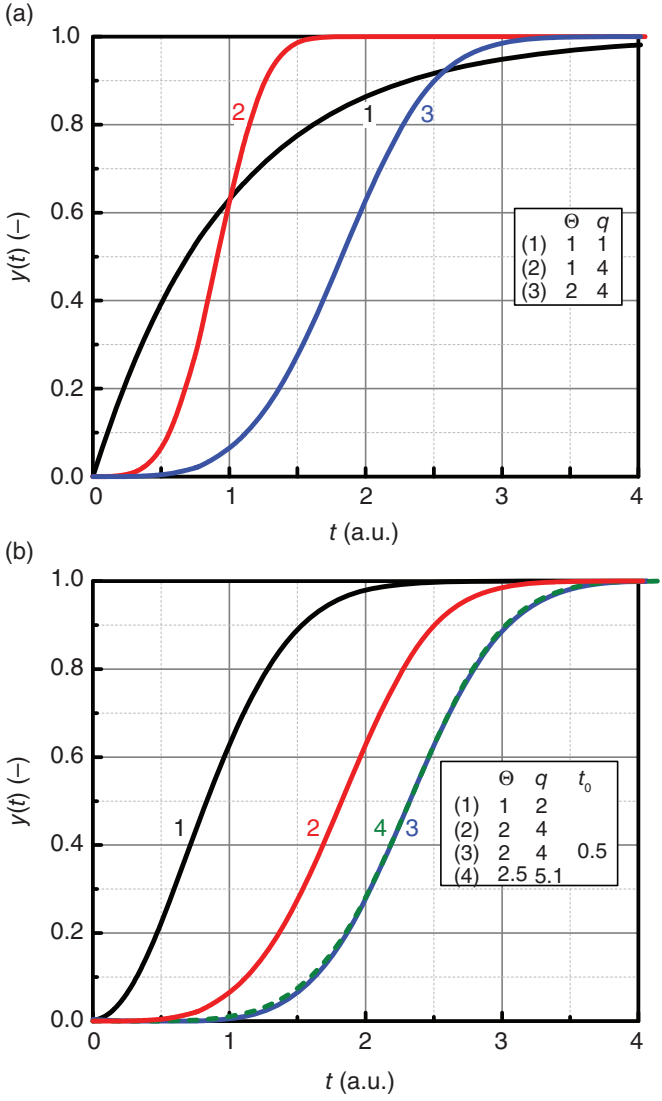

Figure 3.9 Overall crystallization $y(t)$ as a function of crystallization time t for different values of time constant Θ and exponent q according to Eq. (3.87): (a) effect of q and Θ on $y(t)$ plots and (b) effect of delay time t_0 in crystallization for known values of q and Θ on initial duration of detectable crystallization and growth rate. In (b) solid curve 3 of the $y(t)$ plot due to delayed onset of crystallization by a certain time t_0 is compared with dashed curve 4 drawn with increased values of q and Θ.

3.9.2.4 Some Comments on the KJMA Theory

In the literature on overall crystallization of fats, Eq. (3.87) is usually presented in the following forms:

$$y(t) = \frac{V_c(t)}{V} = [1 - \exp(-kt^q)], \tag{3.88}$$

$$y(t) = \frac{V_c(t)}{V} = \left\{1 - \exp\left[-(k't)^q\right]\right\}, \tag{3.89}$$

where the constants $k = \Theta^{-1/q}$ and $k' = \Theta^{-1}$. Equations (3.88) and (3.89) are generally known as the Avrami (or approximate Avrami) and the modified Avrami equations, respectively (Foubert et al., 2003; Padar et al., 2008). The difference between the two equations lies in the values of k and k'. In the former case, the constant k is a function of q; but in the latter case, k' is apparently independent of q. In fact, the modified Avrami equation is a reparameterized form of the original Avarami equation such that $k' = k^{1/q}$.

The "precise" form of the KJMA equation (3.82) for progressive nucleation contains the term in the square brackets. This term, say $Y(x)$, is a complicated function of the time lag τ-related parameter $x = \tau/t$, and its value determines the nature of the $y(t)$ dependence. Equation (3.88) is derived on the assumption that the nucleation time lag $\tau = 0$ when the term $Y(x) = 1$. However, it has been argued (Kashchiev, 2000; Toschev, 1973) that

$$Y(x) = 1 - \left(\frac{\pi^2 x}{6}\right) - (2x)\sum_{n=1}^{\infty}(-1)^n \exp\left(-\frac{n^2}{x}\right) \approx 1 - \left(\frac{\pi^2 x}{6}\right), \tag{3.90}$$

which holds for $x \leq 1/5$. Therefore, for $t << \tau$ the process of overall crystallization is delayed and the delay is mainly determined by the value of τ and is associated with nonstationary nucleation. Note that the approximate and the modified Avrami equations, represented by Eqs. (3.88) and (3.89), are based on the assumption that $Y(x) = 1$ in Eq. (3.90).

The above treatment predicts that the exponent q in Eq. (3.87) is an integer, but analysis of isothermal crystallization data often reveals that q is a non-integer. This non-integer value of q can result when: (i) growth of crystallites is controlled by diffusion of atoms/molecules in the volume and (ii) the dimensionality d of crystallites does not remain constant during overall crystallization.

The merits and demerits of the modified Avrami equation (3.87) have been discussed by several authors (Foubert et al., 2006; Khanna and Taylor, 1988; Marangoni, 1998; Padar et al., 2008). As pointed out by Marangoni (1998), the reparameterization of the original Avrami equation is arbitrary and has no theoretical justification. This is due to the fact that the time constant Θ, which is inverse of the new parameter k', is a complicated function, for example, during crystallization occurring by progressive nucleation, of nucleation rate

J_s, growth constant R_g as well as exponent q (see Eq. (3.86)). However, the independence of k' on q or dependence of k' or k on crystallization temperature T_c is indeed physically possible in a narrow range of crystallization temperature T_c because the parameters J_s and R_g are temperature dependent.

3.9.3 Mononuclear Crystallization

The above treatment of overall crystallization involves nucleation and growth of statistically a large number of crystallites when $N_m > 1$. However, when the nucleation rate J_s is sluggish and the growth rate constant R_g is sufficiently fast, it is possible that only one nucleation center leads to the crystallization of the entire volume V. In this case, crystallization occurs by the mononuclear mechanism, which applies when $N_m < 1$. Assuming that nucleation is stationary and crystallites grow following the power-law relation (3.66) and using the condition that $N_m < 1$ and the gamma function is unity, from Eqs. (3.85) and (3.86) for the maximum number N_m of crystallites, one may write

$$V < \left[\frac{\kappa}{1+\nu d}\left(\frac{R_g}{J_s}\right)^{\nu d}\right]^{1/(1+\nu d)}. \tag{3.91}$$

This inequality means that the mononuclear mechanism applies when at a given volume V and nucleation rate J, the growth rate R of crystallite is so high that no new nuclei are formed until the entire volume of the supersaturated system is crystallized after the formation of the first nucleus. High growth rate R of a stable nucleus after its formation implies that physically crystallization by the mononuclear mechanism occurs in the entire supersaturated system volume V and is controlled by the nucleation rate J alone. When crystallization occurs by stationary nucleation, from Eq. (3.69), one obtains

$$y(t) = \frac{V_c(t)}{V} = 1 - \exp(-J_s V t), \tag{3.92}$$

with $t_{av} = 1/J_s V$, $N_m = 1$, and $V_{av} = V$.

Comparison of Eq. (3.92) with (3.83) shows that the $y(t)$ dependence of crystallization by the monomolecular mechanism may be described by the latter with $q = 1$ and $\Theta = 1/J_s V$. The value of $q = 1$ corresponds to $d = 0$, and the relation for Θ follows from Eq. (3.86) when $d = 0$ and $\kappa = V$.

3.9.4 Effect of Additives on Overall Crystallization

As seen from Eq. (3.87), overall crystallization $y(t)$ depends on the values of two parameters: the exponent q and the time constant Θ. Therefore, the effect of additives on the $y(t)$ dependence may be interpreted in terms of changes caused by them in different parameters contained in the equations of the values of q and Θ.

If it is assumed that during crystallization the process of supply of atoms/molecules to the growing nuclei remains unaltered, from Eq. (3.81), one can identify the concentration of nucleation centers N_m/V, the dimensionality d of growing crystallites, and the growth rate constant R_g as the parameters are likely to be affected by additives during instantaneous nucleation. Similarly, from Eq. (3.86), the parameters likely to be affected by additives are the dimensionality d of growing crystallites, the nucleation rate J_s, and the growth rate constant R_g. Since the concentration of nucleation centers N_m/V in instantaneous nucleation and the nucleation rate J_s are determined by processes associated with the formation of stable nuclei by the attachment and detachment of atoms/molecules present in the supersaturated system, one can conclude that the processes involved in the effect of additives on overall crystallization are essentially the same in both types of nucleation modes.

According to the above equations, changes in J_s (or N_m/V) and R_g show similar trends of the $y(t)$ dependence. Increase in the values of J_s (or N_m/V) and R_g leads to an increase in the value of y, whereas decrease in their values lead to a decrease in y. However, the real effects of different impurities on the J_s and R_g are not similar and are associated with the chemical nature of additive particles. For example, soluble di- and triphosphates, which show a tendency to adsorb on the surface of $SrSO_4$ and $CaCO_3$ particles, not only lead to a decrease in the nucleation rate and the number of $SrSO_4$ and $CaCO_3$ crystallites formed but also inhibit their growth (Söhnel and Garside, 1992). Soluble organic polymers and surface-active agents also show a similar effect (Füredi-Milhofer and Sarig, 1996). Trivalent cations like Fe^{3+} and Cr^{3+}, on the other hand, lead to an increase in the nucleation rate J_s and a inhibition of growth rate R in the crystallization of KDP from aqueous solutions (Mullin, 2001). As discussed below, these differences are associated with different effects of an impurity on the processes of 3D nucleation and growth of crystallites.

Effects of impurities on 3D nucleation rate J_s and growth rate R were discussed in Sections 2.2.3 and 3.8, respectively. As described in Section 2.2.2, the presence of an impurity in a supersaturated solution may affect the nucleation rate J_s by causing changes in the solid–liquid interfacial energy γ_{eff} and/or the kinetic factor J_0. Similarly, the presence of an impurity can affect the face growth rate R by changes caused in the interfacial energy γ_{eff} and inhibition of advancing steps (see Section 3.8).

References

Bauser, E. and Strunk, H. (1981). Analysis of dislocations creating monomolecular growth steps. *J. Cryst. Growth* 51: 362–366.

Bauser, E. and Strunk, H. (1984). Microscopic growth mechanisms of semiconductors: experiments and models. *J. Cryst. Growth* 69: 561–580.

Bennema, P. and van der Eerden, J.P. (1987). Crystal graphs, connected nets, roughness transition and the morphology of crystals. In: *Morphology of Crystals* (ed. I. Sunagawa), 1–75. Terrapub, Tokyo.

Bennema, P. and Gilmer, G.H. (1973). Kinetics of crystal growth. In: *Crystal Growth: An Introduction* (ed. P. Hartman), 263–325. Amsterdam: North-Holand, Chap. 10.

Black, S.N., Davey, R.J., and Halcrow, M. (1986). The kinetics of crystal growth in the presence of tailor-made additives. *J. Cryst. Growth* 79: 765–774.

Bliznakov, G.M. and Kirkova, E.K. (1956). Der Einfluß der Adsorption auf das Kristallwachstum. *Z. Phys. Chem.* 206: 271–280.

Boistelle, R. and Astier, J.P. (1988). Crystallization mechanisms in solution. *J. Cryst. Growth* 90: 14–30.

Brice, J.C. (1973). *The Growth of Crystals from Liquids*. Amsterdam: North-Holland.

Burton, W.K., Cabrera, N., and Frank, F.C. (1951). The growth of crystals and the equilibrium structure of their surfaces. *Phil. Trans. R. Soc.* 243 (866): 299–358.

Cahn, J.W. (1960). Theory of crystal growth and interface motion in crystalline materials. *Acta Metall.* 8: 556–562.

Chernov, A.A. (1961). Sloisto-spiral'nyi rost kristallov. *Uspekhi Fiz. Nauk* 73, 277–331. (Engl. Transl.): The spiral growth of crystals. Sov. Phys. *Uspekhi* 4: 116–148.

Chernov, A.A. (1984). *Modern Crystallography III: Crystal Growth*. Berlin: Springer.

Chernov, A.A., Rashkovich, L.N., and Mkrtchyan, A.A. (1986a). Solution growth kinetics and mechanism: prismatic face of ADP. *J. Cryst. Growth* 74: 101–114.

Chernov, A.A., Rashkovich, L.N., Smol'ski, I.L. et al. (1986b). Processy rosta kristallov iz vodnych rostvorov (gruppa KDP) [Crystal growth processes from aqueous solutions (KDP group)]. *Rost Kristallov (Growth of Crystals)* 15: 43–88.

Chu, Y.D., Shiau, L.D., and Berglund, K.A. (1989). Effects of impurities on crystal growth in fructose crystallization. *J. Cryst. Growth* 97: 689–696.

Davey, R.J. (1979). The control of crystal growth. In: *Industrial Crystallization 78* (ed. E.J. de Jong and S.J. Jančić), 169. Amsterdam: North-Holland.

Davey, R.J., Fila, W., and Garside, J. (1986). The influence of biuret on the growth kinetics of urea crystals from aqueous solutions. *J. Cryst. Growth* 79: 607–613.

van der Eerden, J.P. (1993). Crystal growth mechanisms. In: *Handbook of Crystal Growth*, Vol. 1 (ed. D.T.J. Hurle), 307–475. Amsterdam: Elsevier, Chap. 6.

van der Eerden, J.P., Bennema, P., and Cherpanova, T.A. (1978). Survey of Monte Carlo simulations of crystal surfaces and crystal growth. *Prog. Cryst. Growth Charact.* 1: 219–254.

Elwenspoek, M. (1986a). Comment on the α-factor of Jackson for crystal growth from solution. *J. Cryst. Growth* 78: 353–356.

Elwenspoek, M. (1986b). Kinetics of a rough crystal face: temperature dependence of the growth rate. *Appl. Phys.* A41: 123–125.

Elwenspoek, M. and van der Eerden, J.P. (1987). Kinetic roughening and step free energy in the solid-on-solid model and on naphthalene crystals. *J. Phys. A: Math. Gen.* 20: 669–678.

Foubert, I., Dewittinck, K., and Vanrolleghem, P.A. (2003). Modelling of the crystallization kinetics of fats. *Trends Food Sci. Technol.* 14: 79–92.

Foubert, I., Dewittinck, K., Janssen, G., and Vanrolleghem, P.A. (2006). Modelling two-step isothermal fat crystallization. *J. Food Eng.* 75: 551–559.

Frank, F.C. (1981). Edge dislocations as crystal growth sources. *J. Cryst. Growth* 51: 367–368.

Füredi-Milhofer, H. and Sarig, S. (1996). Interactions between polyelectrolytes and sparingly soluble salts. *Prog. Cryst. Growth Charact Mater.* 32: 45–74.

Garside, J., Janssen-van Rosmalen, R., and Bennema, P. (1975). Verification of crystal growth rate equations. *J. Cryst. Growth* 29: 353–366.

Gilmer, G.H. and Bennema, P. (1972). Computer simulation of crystal surface structure and growth kinetics. *J. Cryst. Growth* 13/14: 148–153.

Hartman, P. and Perdok, W.G. (1955a). On the relations between structure and morphology of crystals. I. *Acta Crystallogr.* 8: 49–52.

Hartman, P. and Perdok, W.G. (1955b). On the relations between structure and morphology of crystals. II. *Acta Crystallogr.* 8: 521–524.

Hull, D. (1975). *Introduction to Dislocations*, 2e. Oxford: Pergamon.

Jackson, K.A. (1958). *Liquid Metals and Solidification*. Cleveland: ASM.

Kashchiev, D. (2000). *Nucleation: Basic Theory with Applications*. Oxford: Butterworth-Heinemann.

Keller, K.W. (1986). Hill formation by two-dimensional nucleation as one mode of crystal growth. *J. Cryst. Growth* 78: 509–518.

Kern, R. (1967). Rost kristalla i adsorbtsii (crystal growth and adsorption), In: *Rost Kristallov (Growth of Crystals)* Vol. 8, (ed. N.N. Sheftal), 5. Nauka: Moscow.

Khanna, Y.P. and Taylor, T.J. (1988). Comments and recommendations on the use of the Avrami equation for physico-chemical kinetics. *Polym. Eng. Sci.* 28: 1042–1045.

Kirkova, E.K. and Nikolaeva, R.D. (1973). Investigation of the crystallization of the system KAl(Cr)$(SO_4)_2$12 H_2O under various conditions. *Krist. Tech.* 8: 463–470.

Li, L., Tsukamoto, K., and Sunagawa, I. (1990). Impurity adsorption and habit changes in aqueous solution grown KCl crystal. *J. Cryst. Growth* 99: 150–155.

Liu, X.Y., Maiwa, K., and Tsukamoto, K. (1997). Heterogeneous two-dimensional nucleation and growth kinetics. *J. Chem. Phys.* 106: 1870–1879.

Marangoni, A.G. (1998). On the use and misuse of the Avrami equation in the characterization of the kinetics of fat crystallization. *J. Am. Oil Chem. Soc.* 75: 1465–1467.

Marangoni, A.G. (2005). Crystallization kinetics. In: *Fat Crystal Networks* (ed. A.G. Marangoni), 21–82. New York: Marcel Dekker.

Mullin, J.W. (2001). *Crystallization*, 4e. Oxford: Butterworth-Heinemann.

Ohara, M. and Reid, R.C. (1973). *Modeling Crystal Growth Rates from Solutions*. Englewood Cliffs: Prentice-Hall.

Padar, S., Jeelani, S.A.K., and Windhab, E.J. (2008). Crystallization kinetics of cocoa fat systems: experiments and modeling. *J. Am. Oil Chem. Soc.* 85: 1115–1126.

Ristić, R., Shekunov, B.Y., and Sherwood, J.N. (1994). Growth of the tetrahedral faces of sodium chlorate crystals in the presence of dithionate impurity. *J. Cryst. Growth* 139: 336–343.

Sangwal, K. (1994). Kinetics and mechanisms of crystal growth. In: *Elementary Crystal Growth* (ed. K. Sangwal), 83–176. Lublin: Saan, Chap. 4.

Sangwal, K. (1998). Growth kinetics and surface morphology of crystals grown from solutions: recent observations and their interpretations. *Prog. Cryst. Growth Charact. Mater.* 36: 163–248.

Sangwal, K. (2007). *Additives and Crystallization Processes: From Fundamentals to Applications*. Chichester: Wiley.

Sherwood, J.N. and Shripathi, T. (1988). Evidence for the role of pure edge dislocations in crystal growth. *J. Cryst. Growth* 88: 358–364.

Söhnel, O. and Garside, J. (1992). *Precipitation: Basic Principles and Industrial Applications*. London: Butterworth-Heinemann.

Toschev, S. (1973). Homogeneous nucleation. In: *Crystal Growth: An Introduction* (ed. P. Hartman), 1–49. Amsterdam: North-Holland.

Verma, A.R. (1953). *Crystal Growth and Dislocations*. London: Butterworth.

4

Phase Transformation and Isothermal Crystallization Kinetics

Crystallization in the metastable zone of a solute–solvent system or molten phase can occur when some amount of supersaturation or supercooling is created in the system experimentally either by a polythermal (nonisothermal) or an isothermal method. In the polythermal method, supersaturation in the system is generated by cooling it from a temperature higher than saturation temperature T_0 at a constant cooling rate R_L down to the limiting temperature T_{lim} when spontaneous nucleation occurs. Constant cooling of the system results in increasing supersaturation (or supercooling), accompanied by steadily increasing formation of three-dimensional (3D) nuclei and their subsequent growth with the time of cooling. In the isothermal method, on the other hand, the system is cooled from the saturation temperature T_0 (or melting point T_m) to a temperature T lying above T_{lim} so that a certain supersaturation (or supercooling) in the solution/melt is attained as fast as possible to observe the processes of formation and growth of 3D nuclei. This method provides a means of measurements of time period for the appearance of first detectable nuclei (i.e. induction period for crystallization) in the system and kinetics of crystallization as a function of crystallization time and initially defined supersaturation/supercooling. When the appearance of detectable nuclei occurs immediately after attaining the predefined supersaturation/supercooling corresponding to the limiting temperature T_{lim}, one considers the excess solute concentration Δc_{max} and the temperature difference $\Delta T_{max} = (T_m - T_{lim})$ as the width of the metastable zone width with reference to solute concentration c_{lim} (corresponding T_{lim}) and melt temperature T_m, respectively.

Practically every solid crystallizing from solutions and melts is known to exist in different forms. During crystallization from solutions, one encounters amorphous phases, solvates, and polymorphs. Solvates are chemical compounds for which the ratio between solvent and solute molecules is constant. Usually, they crystallize in different structures. Different solids with the same chemical composition are called polymorphs or polymorphic modifications. Polymorphs are known to crystallize from solutions as well as melts. In contrast

Nucleation and Crystal Growth: Metastability of Solutions and Melts, First Edition.
Keshra Sangwal.
© 2018 John Wiley & Sons, Inc. Published 2018 by John Wiley & Sons, Inc.

to polymorphism, there is also a phenomenon called isomerism, where the atoms are arranged in different ways, giving rise to different molecules. In the solid state, polymorphs and isomers have different properties, but in the solution, only the isomers have different properties.

The present chapter deals with the processes of crystallization of solids from solutions and melts at predefined temperatures. In the first part, processes associated with the crystallization of polymorphs, whereas in the second part, various approaches advanced to explain the kinetics of crystallization are described.

4.1 Nucleation and Transformation of Metastable Phases

Calcium carbonate is a typical example of a substance that exists in different phases. In the order of increasing stability, the calcium carbonate phases are: calcium carbonate hexahydrate ($CaCO_3 \cdot 6H_2O$; CCH), calcium carbonate monohydrate ($CaCO_3 \cdot H_2O$; CCM), amorphous calcium carbonate ($CaCO_3$, ACC), vaterite, aragonite, and calcite. Most experimental work on calcium carbonate deals with anhydrous crystalline polymorphs (vaterite, aragonite, and calcite), because they are stable in a large temperature range between 0 and 90 °C. However, hydrate forms and anhydrous calcium carbonate have been poorly investigated, mainly because of their low stability and narrow temperature range of stability; CCH is stable between 0 and 25 °C, CCM between 10 and 50 °C, and ACC between 10 and 55 °C. These unstable phases act as precursors for calcium carbonate precipitation at low temperature (Clarkson et al., 1992; Elfil and Rogues, 2001; Kawano et al., 2002).

Another example of a substance that exists in different phases is calcium oxalate. In the order of increasing stability (and decreasing solubility), calcium oxalate shows the following phases (Ouyang et al., 2005): calcium oxalate trihydrate ($CaC_2O_4 \cdot 3H_2O$; COT), calcium oxalate dihydrate ($CaC_2O_4 \cdot (2 + x)$ H_2O, with $x < 0.5$; COD), and calcium oxalate monohydrate ($CaC_2O_4 \cdot H_2O$; COM). From supersaturated solutions of calcium oxalate, obtained by mixing reactants, without additives COM and COT are usually formed, but under different experimental conditions COD is also formed. The form that prevails depends on the experimental conditions (Brecević et al., 1989; Jung et al., 2004; Nancollas, 1982; Skritić et al., 1987).

There are numerous studies on the overall crystallization of important sparingly soluble salts. For a short review on the subject the reader is referred to Füredi-Milhofer and Sarig (1996). A general feature of the crystallization of these salts is that the solution pH, the supersaturation available for growth, the ratio of reactants, the experimental temperature, and the nature and

concentration of additive determine the type of crystallizing polymorph and its growth rate. For example, in the case of calcium carbonate both vaterite and calcite grow at pH ≥ 9.3, while only vaterite is produced at pH ≤ 9.2.

Complex fats containing different fatty acid groups also usually exhibit polymorphic transformation. For example, tripalmitoylglycerol (PPP), composed of three identical palmitic acid groups, shows three polymorphic forms: α, β′, and β (Sato, 2001). They have different molecular structures characterized by the packing of their chains: disordered aliphatic chain conformation in the α polymorph, intermediate packing in the β′ polymorph, and most dense packing in the β form. Therefore, the Gibbs free energy is the highest in the α form, intermediate in the β′ form, and the lowest in the β polymorph. In other words, the α form is unstable, the β form is stable, whereas the β′ form has intermediate stability.

4.1.1 Thermodynamics of Crystallization of Metastable Phases

Apart from difference in the molecular structures, polymorphic forms and phases of a substance are also characterized by differences in their enthalpies of melting ΔH_m and melting points T_m. Figure 4.1 illustrates the dependence of the ratio $\Delta H_m/T_m$ on T_m for polymorphs of different fatty acid groups. There are two features of these polymorphs: (i) their melting points T_m and melting enthalpies ΔH_m increase with increasing stability of a polymorph, and (ii) the ratio $\Delta H_m/T_m$ increases with increasing T_m (i.e. stability) of a polymorph. The increase in the ratio $\Delta H_m/T_m$ slowly decreases with increasing T_m of the polymorphs.

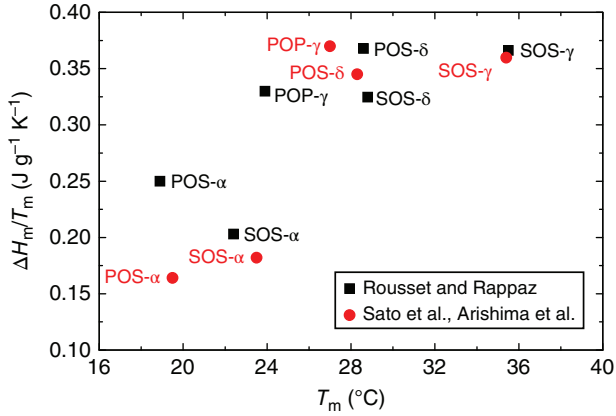

Figure 4.1 Dependence of the ratio $\Delta H_m/T_m$ on the melting point T_m for the polymorphs of various fatty acids. *Source:* Reproduced from Sangwal and Sato (2012). Copyright (2012), with permission from AOCS Press..

Under the same conditions several phases can coexist, but at constant volume and temperature conditions the phase characterized by the lowest free energy $G = H - TS$ at a given temperature T is the stable one. Here, H and S denote the enthalpy and entropy of a phase. The ability of formation of two forms, say A and B, from the melt may be explained in terms of the relative changes in their corresponding Gibbs free energy ΔG_A and ΔG_B. Figure 4.2 shows schematically the temperature dependence of the Gibbs free energy G for two phases A and B, crystallizing from, for example, the same melt or supersaturated solution. Figure 4.2 is an extension of Figure 2.2. The difference in the Gibbs free energy change for the formation of two polymorphic forms at a given temperature T may be given by (cf. Eq. (2.5))

$$\begin{aligned}\Delta G_B - \Delta G_A &= \left(\frac{\Delta H_{m(B)}}{T_{m(B)}}\right)\left(T_{m(B)} - T\right) - \left(\frac{\Delta H_{m(A)}}{T_{m(A)}}\right)\left(T_{m(A)} - T\right) \\ &= \left(\frac{\Delta H_{m(B)}}{T_{m(B)}}\right)\left\{T_{m(B)}\left[1 - \delta\left(\frac{T_{m(A)}}{T_{m(B)}}\right)\right] - T(1-\delta)\right\},\end{aligned} \tag{4.1}$$

where the enthalpy of melting ΔH_m and the melting temperature T_m refer to a given polymorphic phase, the subscripts A and B refer to the values of $(\Delta H_m/T_m)$ and T_m of A and B forms, $(T_{m(A)}/T_{m(B)}) < 1$, and $\delta = (\Delta H_{m(A)}/T_{m(A)})/(\Delta H_{m(B)}/T_{m(B)}) < 1$. Obviously, since the term in the curly brackets of Eq. (4.1) is always positive, $\Delta G_B - \Delta G_A > 0$, implying that the formation of the stable B form is always favorable at $T < T_{m(B)}$.

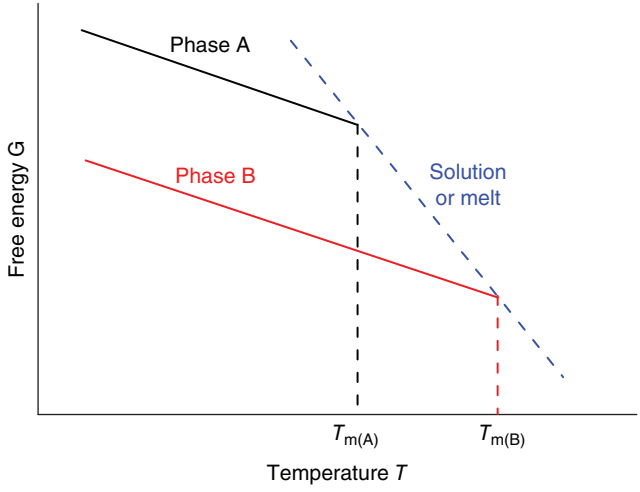

Figure 4.2 Dependence of Gibbs free energy G for two phases A and B, crystallizing from melt on temperature T. Dashed line passing through $T_{m(A)}$ and $T_{m(B)}$ represents the $G(T)$ dependence for the liquid–solid equilibrium.

At temperatures below $T_{m(B)}$, the higher stability of phase B does not mean that this should nucleate first. This may be explained by the dependence of nucleation rate J on the nucleation barrier ΔG^*_{3D} of each phase and the preexponential factor J_0 associated with the kinetics of attachment of atoms/molecules to the developing embryos of the two phases (see Eqs. (2.27) and (2.35)). The higher stability of phase B than that of phase A implies that: (i) at a particular temperature T, the nucleation barrier ΔG^*_{3D} for the nucleation of phase B is higher than that for phase A due to the fact that the interfacial tension γ of phase B is higher than that of phase A and (ii) the concentration of atoms/molecules available for their attachment to developing nuclei is lower for phase B than that for phase A. Both of these factors lead to a lower nucleation rate of phase B than that of phase A. Consequently, less stable phase A crystallizes first in contrast to phase B.

The dominating effect of the interfacial energy γ of phase A for crystallization is easy to understand in the case of supersaturated solutions of the two phases. We recall here that the solubility of different compounds, including polymorphs of a particular compound, increases with a decrease in their melting points T_m and that the interfacial energy γ of different compounds decreases with their increasing solubility (see Section 2.5). Consequently, the solubility of phase A corresponding to the temperature T_m(A) is lower than that of phase B corresponding to the temperature T_m(B), and the interfacial energy γ of phase A is lower than that of phase B. Since the interfacial energy γ appears in the exponential terms of Eqs. (2.27) and (2.35), its effect is much pronounced at low supersaturations ln S when the exponential term dominates over the preexponential term. This explains why during the crystallization of various substances one frequently observes that the newly formed phase in the supersaturated mother phase is the metastable one rather than the thermodynamically most stable one.

After its formation, the metastable phase A undergoes transformation into the stable phase B because the system tends to attain the minimum free energy state by transformation of the metastable phase into the thermodynamically stable phase (Section 2.4). The transformation can occur both in the solid state and in the solution or melt. The former occurs when the two phases nucleate in the solid state, but in the *solution-* or *melt-mediated transformation*, the kinetics depend on the dissolution rates of the metastable phase and on the nucleation and growth rates of the stable phase. Crystal free energies associated with the two types of transformations are shown schematically in Figure 4.3.

Solid-state transformation takes place when the metastable form A is stored below its melting point T_m(A) (Figure 4.3a). In this case, the rate of transformation is essentially determined by the magnitude of the activation free energy barrier $\Delta G^{\#}_{ss}$. The energy barrier $\Delta G^{\#}_{ss}$ involves all types of energies associated with structural changes that are required for the phase transformation.

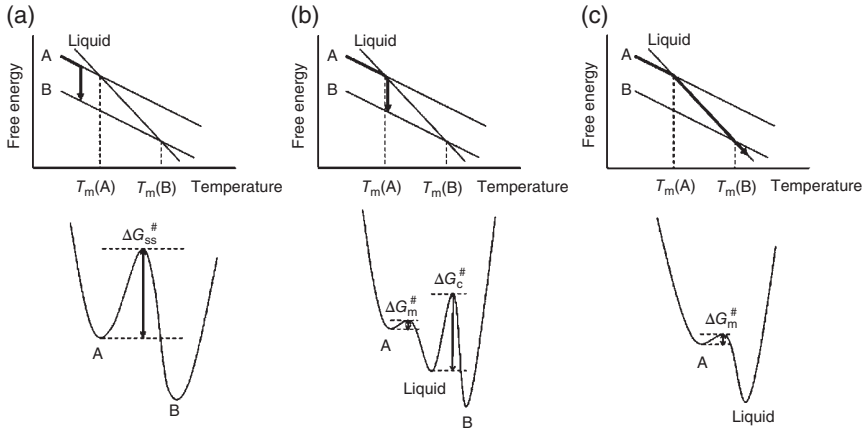

Figure 4.3 Schematic illustration of different transformation routes and corresponding activation energies $\Delta G^{\#}$ for transformation. (a) Solid-state transformation of A to B form occurs when $T < T_m$(A), (b) melt- or solution-mediated transformation of A to B form occurs when $T > T_m$(A) or T_s(A), but (c) this process requires that $\Delta G_m{}^{\#} > \Delta G_c{}^{\#}$. See text for details. *Source:* After Bayés-Garcia et al. (2013). Copyright (2013), with permission from Royal Chemical Society.

Melt- or solution-mediated transformation of phase A to phase B occurs at temperature above the melting point T_m(A) or the saturation temperature (see Figure 4.3b) when crystallization of phase B follows. Here, the rate of transformation is determined by the value of the activation energy barriers $\Delta G_m^{\#}$ and $\Delta G_c^{\#}$ for the melting or dissolution of phase A and for the nucleation and growth of phase B, respectively. The rate of transformation of phase A to phase B is governed by the condition that $\Delta G_m^{\#}$ of phase A is lower than $\Delta G_c^{\#}$ of phase B. This means that when direct formation of the stable phase B is not possible, the overall crystallization becomes a two-stage process in which the formation of phase A in the first stage precedes the appearance of the second stage. In simple melting or dissolution the form A does not undergo phase transformation to B phase because $\Delta G_m^{\#} > \Delta G_c^{\#}$ (Figure 4.3c).

Whether a transformation is solid–solid or melt- or solution-mediated is determined by the induction time t_{in} necessary for the transformation and is related to the temperature difference $\Delta T = T_m - T_c$ or concentration difference $\Delta c = c_0 - c_c$, where T_c and c_c refer to the melt temperature T and supersaturated solution concentration c at the time of crystallization. The induction time t_{in} for solid–solid and melt- or solution-mediated transformation and simple melting, denoted as t_{in}(ss), t_{in}(mm), and t_{in}(m), respectively, may be given by (Bayés-Garcia et al., 2013)

$$t_{\text{in}}(\text{ss}) = A_{\text{ss}} \exp\left(\frac{\Delta G_{\text{ss}}^{\#}}{R_{\text{G}} T}\right), \tag{4.2}$$

$$t_{\text{in}}(\text{mm}) = A_{\text{mm}} \exp\left(\frac{\Delta G_{\text{mm}}^{\#}}{R_{\text{G}} T}\right) = A_{\text{mm}} \exp\left[\frac{\left(\Delta G_{\text{m}}^{\#} + \Delta G_{\text{c}}^{\#}\right)}{R_{\text{G}} T}\right], \tag{4.3}$$

$$t_{\text{in}}(\text{m}) = A_{\text{m}} \exp\left(-\frac{\Delta G_{\text{m}}^{\#}}{R_{\text{G}} T}\right), \tag{4.4}$$

where A_{ss}, A_{mm}, and A_{m} are constants related to the net resident time for atoms/molecules to be a part of the transforming solid. Obviously, the induction time for a transformation increases with an increase in the activation energy $\Delta G^{\#}$.

Preferential formation of a less stable phase followed by successively more stable phases of different compounds during crystallization from solutions and melts is expected from the *Ostwald rule of stages*. According to this rule, the phase with the highest solubility of a compound in a solvent forms preferentially during a sequential precipitation. In the case of compounds crystallizing from aqueous solutions, the Ostwald sequence of stages is the sequence of decreasing hydration. The formation of highly hydrated phase first may result from either a low interfacial energy of this phase during the nucleation stage or a decreased dehydration of ions required in the formation of more highly hydrated phases. These two factors ultimately determine the kinetics of phase transformation. The former factor is associated with the thermodynamics while the latter is related to the composition and lattice structure of the crystallizing phase. Preferential formation of less stable phases during the crystallization of compounds from the melt is also determined by thermodynamics and lattice structure.

4.1.2 Transformation Kinetics of Metastable Phases

Transformation of less stable phase A into more stable phase B in the metastable region of the liquid state (melt or solution) at a particular crystallization temperature T is a common observation of various compounds. Various factors such that solvents, additives, and interfaces are known to influence the crystallization behavior of different polymorphic phases. To understand the crystallization behavior of different phases we refer to Figure 4.4, which presents the dependence of initial concentration c_{in} of different solutions, corresponding to concentration c at time $t = 0$, on crystallization time t at 298 K, of methyl- and *i*-butyl esters of BPT [BPT: 2-(3-cyano-4-(2-methylpropoxy)-

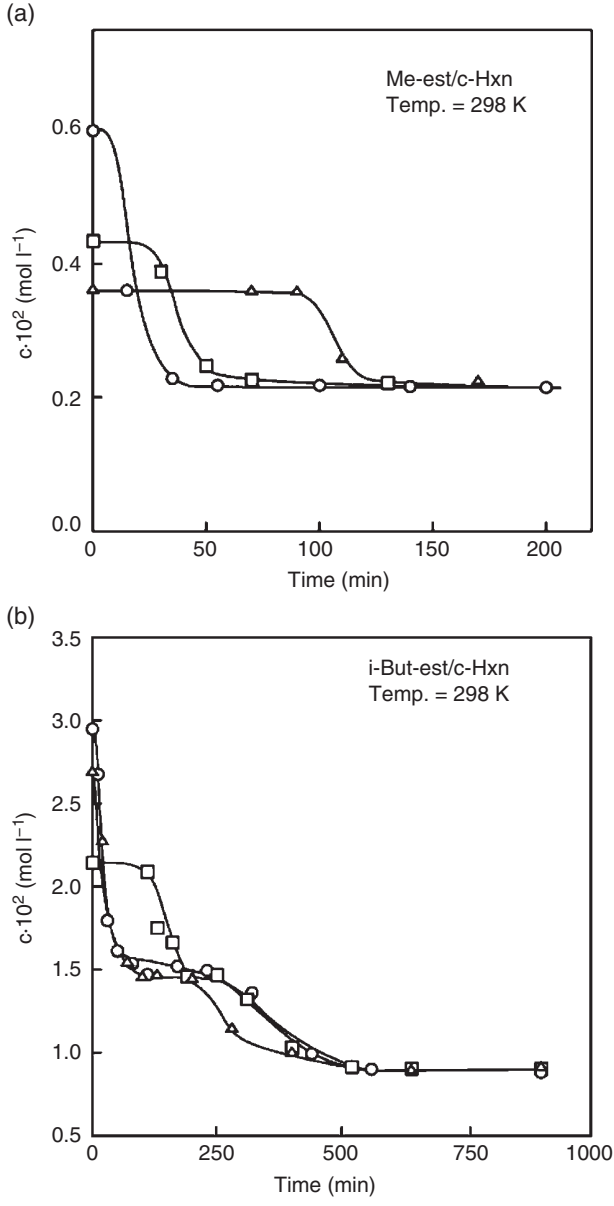

Figure 4.4 Change in the concentration *c* of solutions of (a) Me-est and (b) i-But-est in c-Hxn with time *t* at 298 K. *Source:* Adapted from Kitamura et al. (2008). Copyright (2008), with permission from Elsevier.

phenyl)-4-methyl-thiazole-5-carboxylic acid], abbreviated as Me-est and i-But-est, respectively, dissolved in cyclohexane (c-Hxn) solvent at 323 K rapidly cooled down to 298 K (Kitamura et al., 2008). The crystallized polymorphic phase was identified from the slurry sampled and filtered to separate the crystals after different durations.

In Figure 4.4a, rapid cooling crystallization was carried out in c-Hxn at initial concentration c_{in} between 0.36 and 0.60 cmol·l^{-1}. After a decrease in the concentration due to crystallization one observes in each run a constant value of concentration $c = 0.212$ cmol·l^{-1} corresponding to the solubility of the crystallizing phase in the solvent c-Hxn. In this case, polymorphic phase A of Me-est was observed in the entire crystallization duration. Note that the plots of this figure are similar to the schematic illustration of Figure 3.8 of crystallization of solute phase B from the liquid phase A.

In contrast to the crystallization of Me-est in c-Hxn, the rapid cooling crystallization of i-Bu-est from solutions in c-Hxn at initial concentrations c_{in} between 2.1 and 3.0 cmol·l^{-1}, shown in Figure 4.4b, reveals two steps of concentration change occurring as concentration plateaus at 1.48 and 0.9 cmol·l^{-1} corresponding to the solubility of A and B polymorphs, respectively. Because of its higher solubility, the less stable polymorphic phase A undergoes transformation to more stable polymorph B of lower solubility. In this transformation process the initially crystallizing less stable polymorph A dissolves and results in the simultaneous nucleation of growth of polymorph B until the entire crystallized mass of phase A is exhausted and phase B alone is formed in the solution.

Transformations involving crystallization of stable phases from metastable phases in the solutions or melts are known as *solution-* or *melt-mediated transformations*. Transformation of metastable phases to stable phases also occurs in the solid state but *solid-mediated transformations* are relatively sluggish because of high-energy barriers involved in the process. The transformation process involves dissolution or melting of the metastable phase A in contact with solution or melt and the formation of 3D nuclei of stable phase B and growth of these nuclei into crystallites until the stable form alone remains in the solution or melt.

The process of crystallization of stable phase B via the formation of metastable phase A from solution or melt as a function of time may be divided into two stages. The parameter changing with time is the concentration c of crystallizing phase above its equilibrium concentration c_0. The process of crystallization of this phase of concentration c in the solution with respect to c_0 at a given temperature is determined by the available supersaturation ratio $S = c/c_0$ and the supersaturation $\ln S$. In the case of crystallization of a phase from its melt, the time-dependent parameter is the temperature decrease $\Delta T = (T_m - T_c)$ of the crystallizing phase at T_c from its melting point T_m. Figure 4.5 shows, as

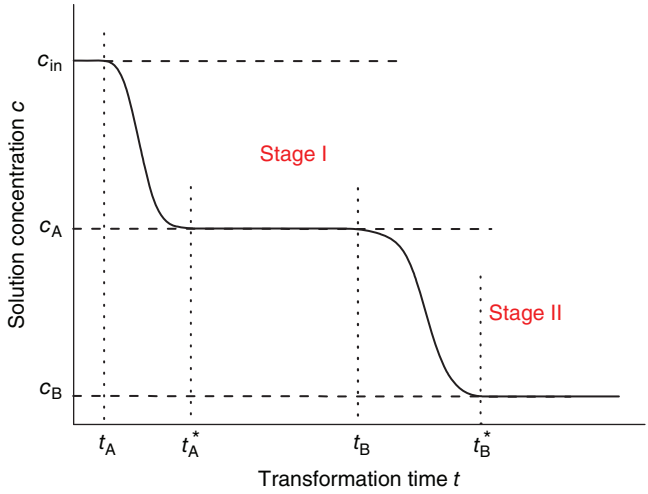

Figure 4.5 Schematic illustration of evolution of solution concentration involving different stages during the transformation process of crystallization of a stable phase B from metastable phase A from solution or melt.

an illustration, these two-stage crystallization of solution-mediated phase transformation.

As shown in Figure 4.5, the first stage is associated with the beginning of formation of 3D nuclei of metastable state A from an initial concentration c_{in} at a certain time t_A, followed by the formation of more 3D nuclei successively and their subsequent growth until the solute concentration approaches the equilibrium concentration c_A of the metastable phase A at time t_A^*. Beyond t_A^*, the concentration of crystallites of phase A in the solution continuously increases until time t_B when 3D stable nuclei of stable phase B begins to form. This is the beginning of the second stage which lasts up to time t_B^* when the entire solute concentration again attains another equilibrium concentration c_B at time t_B. Initially, the equilibrium concentration c_A of the metastable phase A is maintained by its formation from the initial concentration c_{in} and by the nucleation and growth of crystallites of the stable phase B with reference to the concentration c_B. In this stage, the mass of crystallized metastable phase A remains constant whereas the mass of the crystallizing phase B increases. In other words, a dynamic equilibrium is set up between the rate of dissolution of the crystallizing unstable phase A and the rate of crystallization of the stable phase B. However, with an increase in time when the entire mass of the crystallized metastable phase A is dissolved, the available solute concentration asymptotically approaches the equilibrium concentration of the stable phase B when the

transformation of the metastable phase A is complete. In this second stage beyond time t_B, initially overall crystallization of the stable phase B is relatively fast as a result of high supersaturation available for the formation of 3D nuclei progressively and their subsequent growth but later, after attaining a maximum growth rate, crystallization ceases to occur at time t_B^*.

A solution- or melt-mediated phase transformation process is characterized by transformation time, induction time, and active phase transformation time. Phase transformation refers to the entire process of transformation of the stable phase from the beginning of an experimental run, the initial period during which no phase transformation is observed is the induction period, whereas the time period from the appearance of stable phase in a sample until its complete transformation is called the active transformation time. If one assumes that a metastable phase occurs instantaneously (i.e. $t_A^* - t_A = 0$) in Figure 4.5, the duration $t_B^* - t_A^*$ involving an overall decrease in the equilibrium concentration from c_A to c_B is the entire transformation time, the duration $t_B - t_A^*$ of dynamic equilibrium between the dissolution of phase A and crystallization of phase B is the induction period for the crystallization of stable phase B, whereas the duration $t_B^* - t_B$ is the active phase transformation time. However, when the formation of metastable phase A occurs from some other highly unstable phase analogously as the phase transformation of B from A, one encounters another phase transformation process. It may be noted that the excess concentration differences $c_{in}-c_A$, c_A-c_B, and $c_{in}-c_B$ are the values of the driving force involved in the crystallization of phase A, phase B from metastable phase A, and phase B from the beginning, respectively. The transformation process may be determined either by the dissolution of the metastable phase A or by the crystallization of the stable phase B.

Figure 4.6 presents a typical example of the relationship between (filled circles) solution concentration c in acetone at 22 °C and weight fraction y_s (open circles) of stable β polymorph of tegafur in the solid phase during the solution-mediated phase transformation of its metastable α polymorph (Bobrovs et al., 2014). Tegafur is a pharmaceutically active compound, is an antitumor agent, with the chemical formula: 5-fluoro-1-(tetrahydrofuran-2-yl)pyrimidine-2,4 (1*H*,3*H*)-dione. The tegafur concentration in the solution and the amount of the crystallized solid phase were determined by evaporating the solute at room temperature, whereas the crystallized polymorphs were identified from the crystallographic structure of the crystallized filtrates using ex situ power X-ray diffraction analysis.

From Figure 4.6 it may be noted that the solution concentration remains at the level of the solubility of the α phase but starts to decay when the entire α phase transforms into the stable β phase. This is a consequence of the fact that the overall rate of dissolution of the α phase is higher than the rate of crystallization of the stable β phase. Physically, this means that the polymorphic

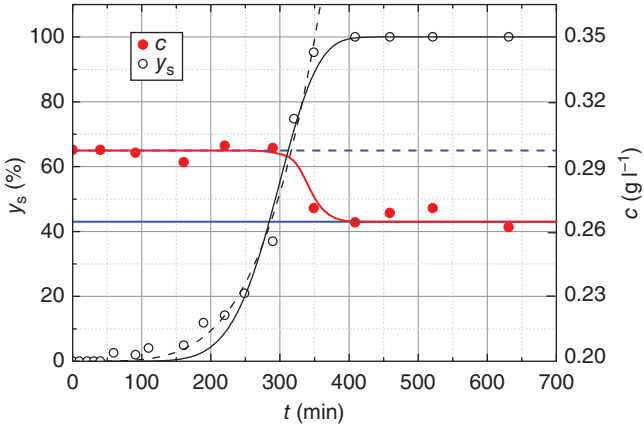

Figure 4.6 Relationship between solution concentration c (filled circles) in acetone at 22 °C and weight fraction y_s (open circles) of stable β polymorph of tegafur in the solid phase during the solution-mediated phase transformation of its metastable α polymorph. Continuous and dashed horizontal lines represent solubilities of α and β phases, respectively, but the continuous line between these horizontal lines is added as a guide. Continuous and dashed curves representing the dependence of weight fraction y_s on crystallization time t are drawn according to Eq. (4.5) and power-law relation (4.6). See text for detail. *Source:* Adapted from Bobrovs et al. (2014). Copyright (2014), with permission from Royal Chemical Society.

transformation in this case is controlled by the nucleation and growth of the β phase. In the other case when the conditions for the phase transformation are such that the dissolution rate of the unstable α phase is lower than the rate of nucleation and growth of the β phase, polymorphic transformation is anticipated to be controlled by the dissolution of the unstable α phase. Diffusion of the solute resulting from dissolution of unstable α phase in the bulk liquid can equally control the process of polymorphic transformation when the nucleation and growth of stable phase occurs on foreign substrates. During diffusion-controlled polymorphic transformation the solubility level of the metastable phase becomes undistinguishable from the solubility level of the stable phase.

The fraction $y(t)$ of a crystalline phase (frequently called *overall crystallization* of a phase) in a closed system of total solute volume V from the melt or supersaturated solution involving the formation of many nuclei may be described by instantaneous nucleation and progressive nucleation mechanism (Kashchiev, 2000). As discussed in Section 3.8, in terms of mass $m(t)$ crystallized at time t in volume V, the overall crystallization may be given by the Kolmogorov–Johnson–Mehl–Avrami (KJMA) theory in the form

$$y(t) = \frac{m(t)}{m_{\max}} = 1 - \exp\left[-\left(\frac{t}{\Theta}\right)^q\right], \tag{4.5}$$

where m_{max} is the maximum mass of the crystallizing phase, the exponent $q = \nu d$ and $1 + \nu d$ for instantaneous and progressive nucleation mechanisms, respectively (see Eqs. (3.77) and (3.83)), and Θ is a time constant, the value of which is different in the two mechanisms (see Eqs. (3.79) and (3.86)). Equation (4.5) follows from Eq. (3.87) where we have replaced the volume $V_c(t)$ of the crystallized at time t from the total volume V of the solute in the melt or its supersaturated solution at a given temperature. When $(t/\Theta)^q \ll 1$, Eq. (4.5) simplifies to the power law:

$$y(t) = At^p, \tag{4.6}$$

where the constant $A = 1/\Theta^p$, the time constant $\Theta = (1/A)^{1/p}$ and q is replaced by p to distinguish it from the power-law exponent.

The experimental data of overall crystallization $y_s(t)$ of stable tegafur polymorph, shown in Figure 4.6, may be analyzed using Eqs. (4.5) and (4.6). The plots are drawn in the figure with the following best-fit values of different parameters: $q = 7.2$ and $\Theta = 306$ min, and $A = 2.92 \cdot 10^{-6}$ min^{-p} and $p = 2.5$. One observes that the data are better described by power-law relation (4.6) than the original KJMA equation (4.5), which predicts much lower crystallization for durations $t < 250$ min. However, both relations reproduce the data well in the region of steep linear increase for t between 250 and 350 min. One also finds that there is an induction period of about 50 min when crystallization of the stable phase does not occur. This value of induction period is much lower than the crystallization duration above which KJMA relation holds.

Figure 4.6 presents an example of phase transformation in which the growth of stable phase B is observed with a negligible amount of crystallized metastable phase A involved in its transformation such that the time interval $\left(t_A^* - t_A\right)$ is negligible (see Figure 4.5). However, both metastable and stable phases are also frequently encountered during solution- and melt-mediated phase transformation. Figure 4.7 illustrates schematically this type of two-stage process of crystallization of a stable form occurring in the bulk melt or supersaturated phase. This figure is another presentation of Figure 4.5 and shows the evolution of total crystallized mass of both metastable and stable phases with time. The first stage is associated with the crystallization of the metastable A polymorph of mass m_A, while the second stage involves the transformation of the metastable A polymorph into the stable B polymorph of mass m_B. Then the total crystallized mass

$$m_{total} = m_A + m_B = m_{A(max)} y_A + m_{B(max)} y_B, \tag{4.7}$$

where m_A and m_B are the amounts of metastable A and stable B forms, respectively, $y_{A,B}$ is the fraction of the crystallized mass of the crystallized A or B form, and $m_{A,B(max)}$ denotes the maximum masses of the two forms (cf. Eqs. (4.5) and (4.6)). When the crystallized fraction y_A of the metastable form A is negligible,

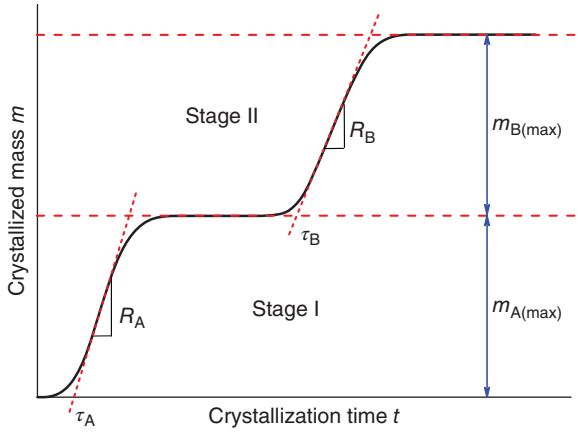

Figure 4.7 Schematic illustration of evolution of crystallized mass m of both metastable and stable phases with time t during solution- or melt-mediated transformation of metastable phase A into stable phase B. Growth rates $R_{A,B}$, time constants $\tau_{A,B}$, and maximum crystallized mass $m_{A,B(max)}$ are indicated.

one observes only the second stage in the crystallization experiment. Physically, this situation is possible when the crystallizing unstable A phase transforms simultaneously into the more stable B phase. The crystallization behavior in this one-step mechanism is given by

$$m_{\text{total}} = m_{\text{B(max)}} y_{\text{B}}. \tag{4.8}$$

The quantities $y_{A,B}$ and $m_{A,B(max)}$ of a crystallizing phase A or B are related by Eq. (4.5). The quantity $y_{A,B}$ in Eqs. (4.6) and (4.7) is the fraction of crystalline phase A or B in a closed system.

4.1.3 Transformation of Metastable Phases According to KJMA Theory

The nucleation and growth of a stable phase s within a metastable phase u makes the kinetics of formation of the former depend on those of the latter, and may be described by (Kashchiev, 2000)

$$y_{\text{s}}(t) = y_{\text{u}}(t)\left\{1 - \exp\left[-\left(\frac{\Theta_{\text{u}}}{\Theta_{\text{s}}}\right)^{s}\left(\frac{t}{\Theta_u} - b'\right)\right]^{s}\right\}, \tag{4.9}$$

or, alternatively, in the form

$$y_{\text{s}}(t) = y_{\text{u}}(t)\left(1 - \exp\left\{-\left[\frac{(t - \Theta_{\text{u}} b')}{\Theta_{\text{s}}}\right]^{s}\right\}\right), \tag{4.10}$$

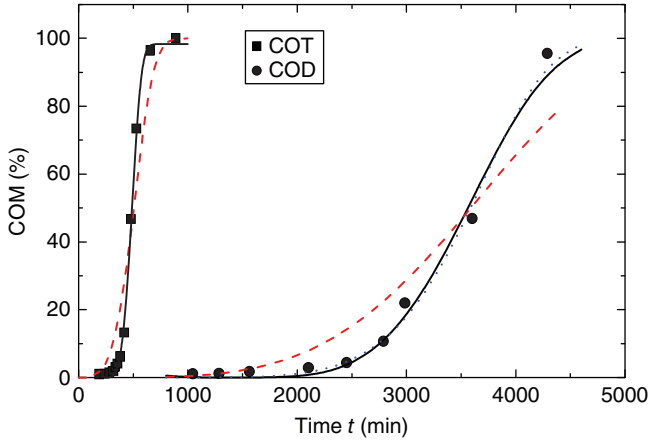

Figure 4.8 Transformation *y* of COM from COT and COD at 37 °C as a function of time *t*, and best-fit plots of the data according to different relations: (solid curve) Eq. (4.10) with exponent $q = 4 = u = s = 4$, (dashed curve) Eq. (4.5) with the exponents $q = 4$, and (dotted curve) Eq. (4.5) with exponent $q = 7.1$ and 9.2 for COD and COT, respectively. *Source:* Original data from Nancollas (1982).

where $b = (u - 1/u)^{1/u}$, $y_u(t)$ is given by Eq. (4.5), u and s denote the value of q for the crystallization of metastable and stable phases, respectively, while Θ_u and Θ_s are the corresponding time constants. We recall that $q = \nu d$ and $1 + \nu d$ for instantaneous and progressive nucleation mechanisms, respectively. Obviously, Eq. (4.10) is of the same form as Eq. (4.5), but crystallization of the stable phase s occurs after a time period $\Theta_u b'$ and a time constant different from Θ_u. In fact, when the quantity $\Theta_u b' = 0$, Eq. (4.10) reduces to Eq. (4.5). However, as shown by Kashchiev (2000), for the ratio $\Theta_u/\Theta_s > 0$ and the constant $b' > 0$, the dependence predicted by Eq. (4.9) or (4.10) differs significantly from that of Eq. (4.5).

Figure 4.8 shows an interesting example of two-stage transformation of trihydrate (COT) and dihydrate (COD) of calcium oxalate metastable phases to stable calcium oxalate monohydrate (COM) at 37 °C as a function of time. It may be seen from the figure that transformation of COT occurs much faster than that of COD and the induction period for the onset of crystallization of COT is much shorter than that of COD. These differences are associated with the higher solubility of COT and COD and their dissolution rates. The above data of transformation of the two metastable phases were analyzed using general and extended KJMA equations (4.5) and (4.10), respectively. Solid curves represent the best fit of the data according to Eq. (4.10) with exponent $q = 4 = u = s = 4$, whereas dashed and dotted curves describe the data according to Eq. (4.5) with $q = 4$ and a new exponent $q' > 4$, respectively, i.e.

$$y_s = 1 - \exp\left[-\left(\frac{t}{\Theta_s'}\right)^{q'}\right], \tag{4.11}$$

where Θ'_s is a new time constant. As shown by dotted curves, the data could be represented well with the exponent $q' = 7.1$ and 9.2 for COD and COT, respectively. This implies that direct crystallization of a stable phase from melt or supersaturated solution without negligible presence of metastable form occurs when the time constant Θ_u is relatively small for the metastable phase when $y_u = 1$.

Description of the experimental data according to Eqs. (4.10) and (4.11) implies that

$$\left(\frac{\Theta_u}{\Theta_s}\right)^s \left[\left(\frac{t}{\Theta_u}\right) - b'\right]^s = \left[\frac{(t - \Theta_u b')}{\Theta_s}\right]^s = \left(\frac{t}{\Theta'_s}\right)^{q'}. \tag{4.12}$$

From this equality one finds

$$b' = \left(\frac{t}{\Theta_u}\right)\left[1 - \left(\frac{t}{\Theta'_s}\right)\right]^{(q'-s)/s}, \tag{4.13}$$

where $q' > s$.

In the extended KJMA equation (4.10), the second time-lag $\Theta_u b'$ term is related to the time constant Θ_u and the exponent u represents crystallization of the metastable form. Therefore, it is not an independent parameter and Eq. (4.10), in fact, contains six parameters that determine the shape of the two-step crystallization curve. The parameters $m_{u(max)}$ and $m_{s(max)}$ in Figure 4.7 determine the heights of the plateau of the first and the second steps, respectively. The higher the values of $m_{u(max)}$ and $m_{s(max)}$, the more are the heights of the plateau of the first and the second steps. The time constant $\Theta_{u,s}$ determines the moment when the curve abruptly departs from the time axis. The higher the value of $\Theta_{u,s}$, the more is the delay when the curve leaves the time axis. The exponents u and s determine the slope of the straight-line part of the curve and its curvatures. The higher the values of these exponents, the higher is the steepness of the crystallization curves.

4.1.4 Effect of Solvent on Transformation of Metastable Phases

Transformation of a metastable phase into the next stable one may be described by Eq. (4.10) of the overall crystallization. This relation compares with the KJMA equation when $\Theta'_s \approx \Theta_s^{4/q'}$ and $y_u = 1$. When $\left(t/\Theta'_s\right) \ll 1$, Eq. (4.11) reduced to the linear form

$$y_s = \left(\frac{t}{\Theta'_s}\right)^q \approx y_{s0} + y't, \tag{4.14}$$

where $y_{s0} = \left(\Theta'_s\right)^{-q} - q'$ and $y' = \left(q' - q'^2\Theta'_s\right)^{q'}$.

It is convenient to analyze experimental $y_s(t)$ data using Eq. (4.11) rewritten in the form

$$\ln[-\ln(1-y_s)] = -q\ln\Theta_s + q\ln t, \tag{4.15}$$

where we have omitted primes with q and Θ_s to maintain the similarity of Eq. (4.11) with the KJMA relation (4.5). From the plots of $\ln[-\ln(1 - y_s)]$ of fraction y_s of the crystallized phase as a function of time $\ln t$, the values of q and Θ_s can be obtained. Plots of $\ln[-\ln(1 - y_s)]$ against $\ln t$ are frequently known as *Avrami plots*. Note that when the approximation $(t/\Theta_s) \ll 1$ holds, Eq. (4.15) also predicts a simple linear relationship between y_s and t.

Data on the time dependence of overall crystallization y may be obtained in terms of crystallized mass m per unit volume or surface area. Then for the analysis of the $m(t)$ data one has $y = m(t)/m_{max}$ (see Eq. (4.8)) in Eqs. (4.10), (4.11), and (4.14). From the values of different constants thus obtained, the nature of processes can be discussed for different systems in various solvents. The constants Θ_m/Θ_s, Θ_m, Θ_s, u, s, and q' include the effects of both nucleation and growth of the crystallizing phase. However, when crystallization is determined as $m(t)$ dependence, the value of m_{max} almost exclusively gives information about the processes involved in the nucleation stage. Some experimental data of evolution of phase transformation of metastable phases to stable ones in different solvents are described and discussed below.

Figure 4.9 presents two typical examples of solution-mediated phase transformation of tegafur and prasugrel hydrochloride where experimental data of weight fraction y_s of stable β polymorph of tegafur from its metastable α polymorph (Figure 4.9a) and stable polymorph I of prasugrel hydrochloride from its metastable polymorph II (Figure 4.9b) in the solid phase in different solvents as a function of time t are presented. One observes that there is an induction period t_{in} for the detectable crystallization of the stable phase of both compounds and the value of t_{in} increases with increasing total transformation time t_f. However, the value of t_{in} for prasugrel hydrochloride in different solvents is more distinctly defined than that for tegafur, and all of the $y_s(t)$ plots of prasugrel hydrochloride exhibit S-shaped trend in contrast to those of tegafur, which approach the maximum yield abruptly.

Bobrovs et al. (2014) concluded that the induction time t_{in} in all of the solvents used in the phase transformation of stable β polymorph of tegafur from its metastable α polymorph was about 0.1 of the phase transformation time t_f, where t_f is the transformation time when y_s approaches unity. To compare the reaction rate and reaction path in all of the solvent used since the beginning of phase transformation, these authors plotted the data of weight fraction y_s of the stable phase as a function of normalized time t/t_f, as shown in Figure 4.10a. From a similarity in the trend of the data in different solvents the authors concluded that the best correlation for the data is observed according to the power

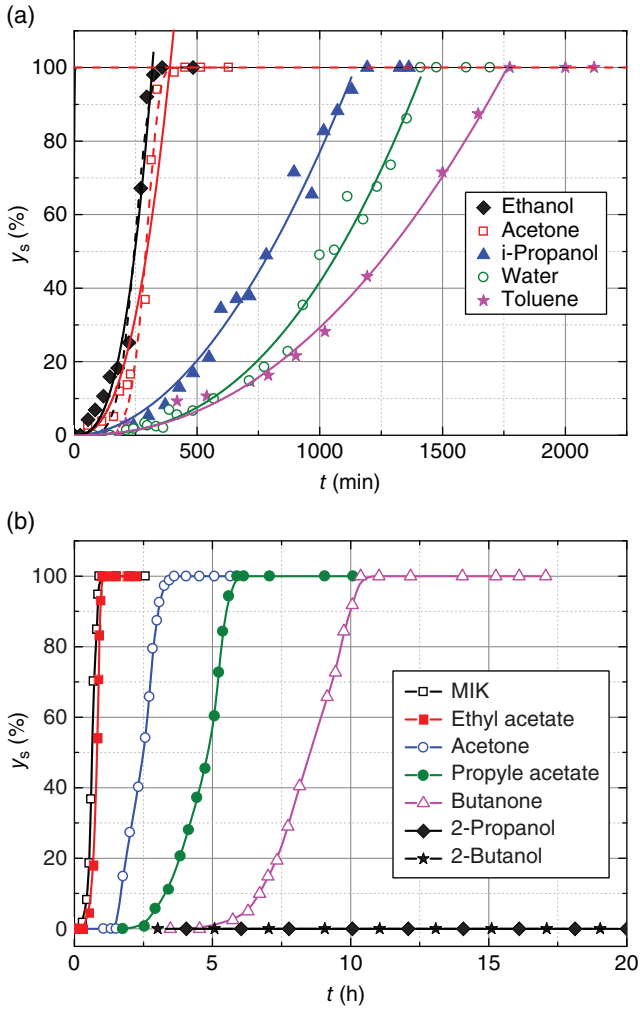

Figure 4.9 Weight fraction y_s of (a) stable β polymorph of tegafur from its metastable α polymorph and (b) stable polymorph I of prasugrel hydrochloride from its metastable polymorph II in the solid phase in different solvents as a function of time t during solution-mediated phase transformation. *Source:* Adapted from: (a) Bobrovs et al. (2014) and (b) Du et al. (2014). (a) Copyright (2014), with permission from Royal Chemical Society and (b) Copyright (2014), with permission from American Society of Chemistry.

law: $y = (kt)^2$, where k is the phase transition rate constant. A plot similar to that of Figure 4.10a is shown in Figure 4.10b for the data of weight fraction y_s of stable polymorph I of prasugrel hydrochloride from its metastable polymorph II in the solid phase in different solvents as a function of normalized transformation

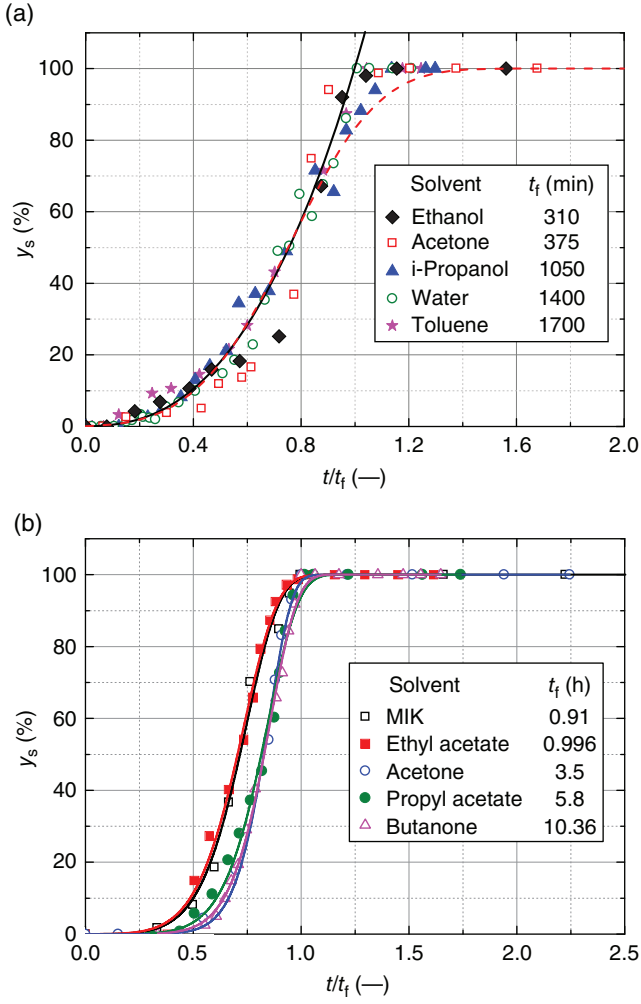

Figure 4.10 Weight fraction y_s of (a) stable β polymorph of tegafur from its metastable α polymorph and (b) stable polymorph I of prasugrel hydrochloride from its metastable polymorph II in the solid phase in different solvents as a function of normalized transformation time t/t_f with respect to time t_f when transition is complete. Values of t_f estimated from the original plots are given in insets. *Source:* Original data from (a) Bobrovs et al. (2014) and (b) Du et al. (2014).

time t/t_f. In contrast to the practically overlapping data $y_s(t/t_f)$ of Figure 4.10a for different solvents, the $y_s(t/t_f)$ data of Figure 4.10b appear to be displaced from each other. Moreover, except for *i*-propanol most of the data in Figure 4.10a appear to follow power law, but all of the data in Figure 4.10b exhibit a clearly

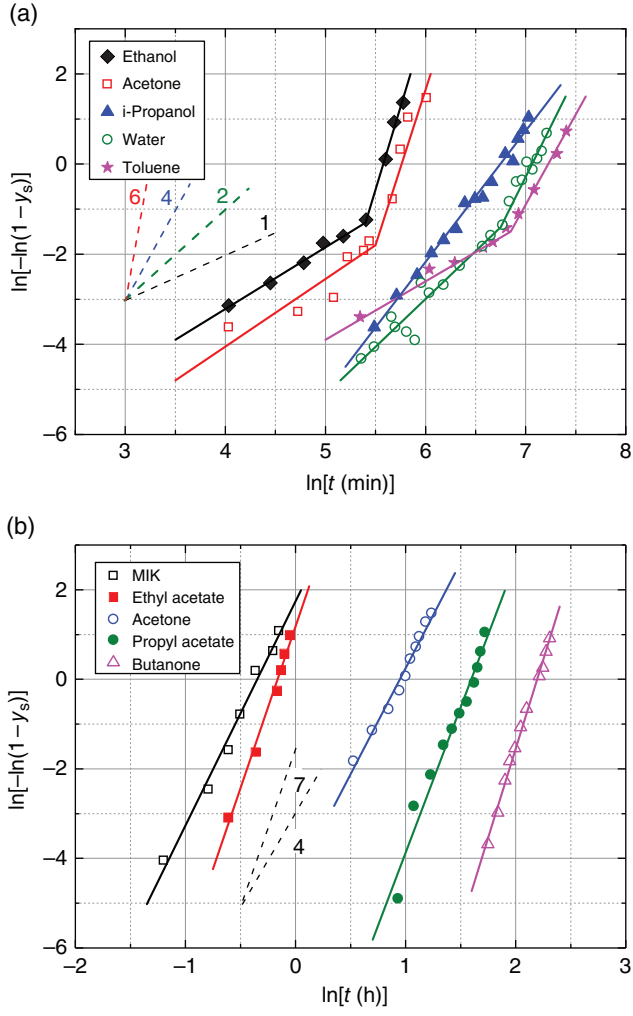

Figure 4.11 Plots of ln[–ln(1 – y_s)] against ln$t$ for (a) stable β polymorph of tegafur from its metastable α polymorph and (b) stable polymorph I of prasugrel hydrochloride from its metastable polymorph II in the solid phase in different solvents. Solvents are given in insets. Different values of exponent q are shown as a guide. *Source:* Original data from (a) Bobrovs et al. (2014) and (b) Du et al. (2014).

seen S-shaped trend. However, one also observes an initial induction period t_{in} of about $0.1t_f$ and $0.3t_f$ for the crystallization of stable polymorphs of tegafur (Figure 4.10a) and prasugrel hydrochloride (Figure 4.10b), respectively.

The $y_s(t)$ data of Figure 4.9 of transformation y_s of stable β polymorph of tegafur and stable polymorph I of prasugrel hydrochloride from corresponding metastable polymorphs in different solvents are shown in Figure 4.11 as plots of ln

Table 4.1 Constants A, p, and Θ, and other parameters for tegafur transformation in different solvents.

Solvent	A (min^{-p})	p	R^2	Θ (min)	t_f (min)	k^{-1} (min)[a]	$10^2\Delta c_{AB}$ (g·l^{-1})[a]
Ethanol	$1.31{\cdot}10^{-5}$	2.75	0.968	60	310	35.7	3.33
Acetone	$2.92{\cdot}10^{-5}$	2.52	0.902	63	375	43.5	2.05
i-Propanol	$1.30{\cdot}10^{-4}$	1.92	0.985	105	1050	111.1	0.6
Water	$1.69{\cdot}10^{-6}$	2.46	0.987	220	1400	153.8	0.3
Toluene	$7.36{\cdot}10^{-6}$	2.20	0.996	210	1700	178.6	0.06

[a] From Bobrovs et al. (2014).

$[-\ln(1 - y_s)]$ against $\ln t$. As seen from the plots, the two compounds show different trends in different solvents. In the case of prasugrel hydrochloride, the exponent q remains constant in the entire transformation of the stable phase and its value lies between about 4 and 7 (Figure 4.11b). In contrast to this, except for transformation of stable phase in *i*-propanol solution where the exponent q is about 3, transformation in solutions of other solvents occurs in two periods. In these cases, the value of the exponent q is lower in the initial period and lies between about 1 and 2 for different solvents, whereas q lies between about 4 and 6 in the latter period. The latter values of q are similar to those for prasugrel hydrochloride.

In view of two different values of q for the transformation of tegafur in most of the solvents, analysis of the original $y(t)$ data of Figure 4.9a according to the power law (4.5) gave the values of A and p listed in Table 4.1. In the table the calculated values of the time constant Θ, the values of transformation time t_f from the original $y(t)$ data, and the values of the inverse of rate constant k and difference Δc_{AB} in the solubilities of metastable α and β polymorphs from the paper of Bobrovs et al. (2014) are also listed. Table 4.2 contains data of constants $-q\ln\Theta$ and q for the transformation of prasugrel hydrochloride obtained in different solvents from the $y(t)$ data according to Eq. (4.15). The calculated values of the time constant $\Theta = A^{-1/p}$, the values of transformation time t_f from metastable polymorph II to stable polymorph I from the original $y(t)$ data, and the values of induction period t_{in} and solubility c_0 of stable polymorph I from the paper of Du et al. (2014) are also included in the table.

From Table 4.1 it may be noted that the values of Θ and k^{-1} for tegafur transformation are comparable for different solvents, the value of transformation time t_f is about 10 times k^{-1}, and the value of t_f increases with a decrease in the solubility difference Δc_{AB} between unstable and stable forms. The possible value of the induction time t_{in} in different solvents is roughly equal to that of k^{-1}. This inference is in agreement with the observation of Bobrovs et al. (2014). The

Table 4.2 Constants $-q\ln\Theta$, q, and other parameters Θ for prasugrel hydrochloride transformation in different solvents.

Solvent	$-q\ln\Theta$	q	R^2	Θ (h)	t_f (h)	t_{in} (h)[a]	$10^4 c_0$ (mole frac.)[a]
MIK	1.736	5.00	0.984	0.71	0.91	0.38	1.66
Ethyl acetate	1.177	7.22	0.966	0.85	0.996	0.66	1.04
Acetone	−4.485	4.73	0.986	2.58	3.50	1.46	9.98
Propyl acetate	−10.364	6.49	0.965	4.93	5.80	2.11	1.92
Butanone	−17.429	7.94	0.994	8.98	10.36	5.28	3.71

[a] From Du et al. (2014).

comparable values of Θ and k^{-1} are a consequence of the fact that the term $t/\Theta \ll 1$ in the KJMA relation (4.5). However, values of p (or q) do not appear strictly 2, as argued by Bobrovs et al. (2014), for crystallization from different solvents. Table 4.2 for prasugrel hydrochloride, on the other hand, shows that the transformation time t_f is about twice the value of induction time t_{in} and is lower than the time constant Θ by a factor of about 0.8 in different solvents. These observations are associated with the fact that the KJMA relation (4.5), with a high value of the exponent q, applies in this case. However, no relationship appears between these crystallization parameters and the solubility c_0 of the stable phase.

The effect of solvent on the kinetics of crystallization of a given phase is associated with the processes of its nucleation and growth in the solution. The nuclei are formed by solute molecules existing as solvated associates in the solution, which undergo partial desolvation before their integration into the crystal lattice. The solvated molecules are adsorbed on the surfaces of growing nuclei and crystals. Therefore, every solvated solute associate has to shed some of its solvent molecules before integration into the crystal. These processes are related to solute–solvent interactions involving van der Waals force and hydrogen bonding. Measure of the strength of solute–solvent van der Waals interactions is the dipolar polarizability π^*, whereas measures of the strength of hydrogen bonding between the solvent and the solute are hydrogen-bond donor ability α or hydrogen-bond donor ability β. Du et al. (2014) analyzed the effect of these measures in the formation of prasugrel hydrochloride polymorphs in different solvents and concluded that hydrogen-bond donor ability α mainly determines the formation of different polymorphs. The authors observed that form I is formed in solvents with α close to zero, whereas form II or solvates is formed in solvents with α exceeding 20. These authors also observed that solubility of form I alone is not the factor determining the transformation rate, and speculated

that phase transformation from the metastable II phase to the stable phase I occurs in solvents where hydrogen-bond donor ability α and van der Waals interaction between the solute and solvent molecules are dominant.

Bobrovs et al. (2014) found that the rate constant k of solution-mediated transition of metastable α phase of tegafur to its stable β form is linearly related to the difference Δc_{AB} between the equilibrium solubilities in different solvents. The authors attributed this observation to the solvent-independent driving force for phase transition and is related to the free energy difference $\Delta G^{\#}$ between the polymorphs (see Figure 4.3b).

The possible relationship between the solution-mediated transformation time t_f for tegafur and prasugrel hydrochloride in different solvents and the solvent parameters may be analyzed. Figure 4.12a shows plots of the time constant Θ for crystallization and other parameters, such as the dipole moment μ, the dielectric constant ε, and the dipolar polarizability π^*, related to the nature of the solvent, against the total transformation time t_f for the stable β polymorph of tegafur from its metastable α polymorph in different solvents, whereas Figure 4.12b presents plots of the time constant Θ for crystallization, the solubility c_0 of the stable polymorph, the dipole moment μ, and the dipolar polarizability π^* against the total transformation time t_f for the polymorph I of prasugrel hydrochloride from its metastable polymorph II in the solid phase in different solvents. In the plots the values of dipole moment μ and dielectric constant ε of different solvents are taken from Lide (1996/1997), those of dipolar polarizability π^* of solvent molecules are taken from Du et al. (2014) but those of solubility difference Δc_{AB} (Table 4.1) and solubility c_0 (Table 4.2) are from Bobrovs et al. (2014) and Du et al. (2014), respectively.

From the above figures one observes a linear increase in time constant Θ with increasing transformation time t_f in different solvents but Θ/t_f is about 1/7 and 5/6 for the transformation of tegafur and prasugrel hydrochloride, respectively. These different values of Θ/t_f are associated with different trends of 3D nucleation and growth in the two cases. As inferred from Eq. (3.86), a relatively low value Θ for the transformation of tegafur is due to a high nucleation rate J_s and a low growth rate R, whereas a relatively high value of Θ for the transformation of prasugrel hydrochloride is due to a low nucleation rate J_s and a high growth rate R. These differences appear to be associated with the trends of the dipolar polarizability π^* of molecules in different solvents with t_f. For example, the value of π^* in different solvents is practically constant in the case of tegafur but its value shows a weak decrease with increasing t_f.

Increase in the value of total transformation time t_f with a decrease in the solubility difference Δc_{AB} between unstable and stable forms of tegafur appears to follow the power-law dependence: $z = z_0(\Delta c_{AB})^{-n}$, where z denotes t_f, k, and Θ, and n is a constant. Figure 4.13 shows plots of $\ln z$ against $\ln(\Delta c_{AB})$. If the data for toluene are neglected, the exponent $n \approx 0.6$ for all of the parameters.

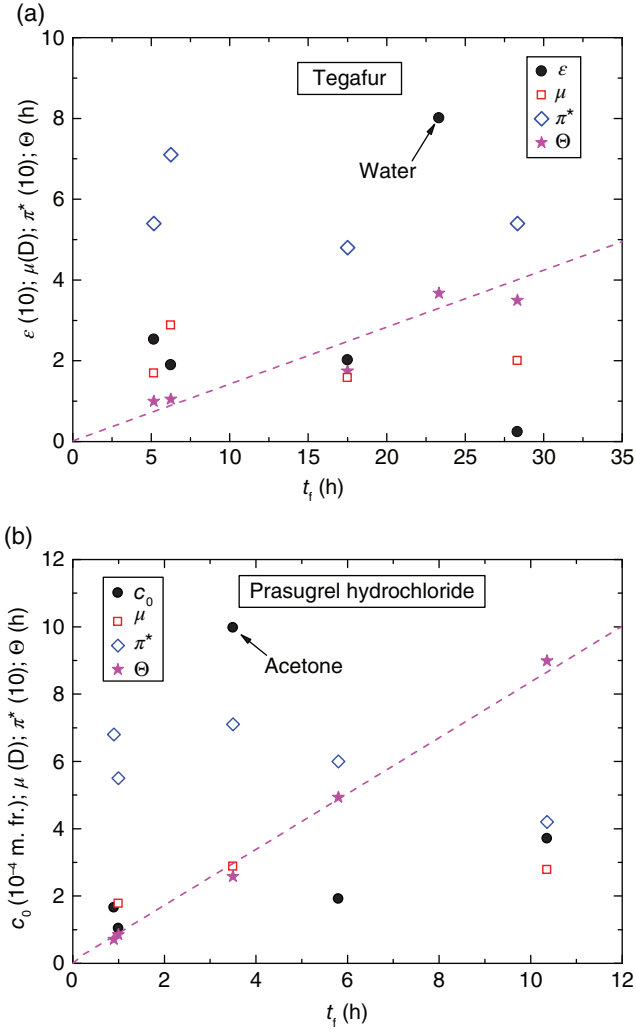

Figure 4.12 Plots of dipole moment μ, dielectric constant ε or solubility c_0 of stable polymorph, dipolar polarizability π^*, and time constant Θ against total transformation time t_f for (a) stable β polymorph of tegafur from its metastable α polymorph and (b) stable polymorph I of prasugrel hydrochloride from its metastable polymorph II in the solid phase in different solvents. See text for details.

However, for the values of Θ of all solvents, $n = 0.31 \pm 0.9$. Since t_f and k are related to Θ, one can attribute the value of the exponent n to the processes of 3D nucleation and growth of crystallites, as represented by the nucleation rate J_s (see Eq. (3.86)).

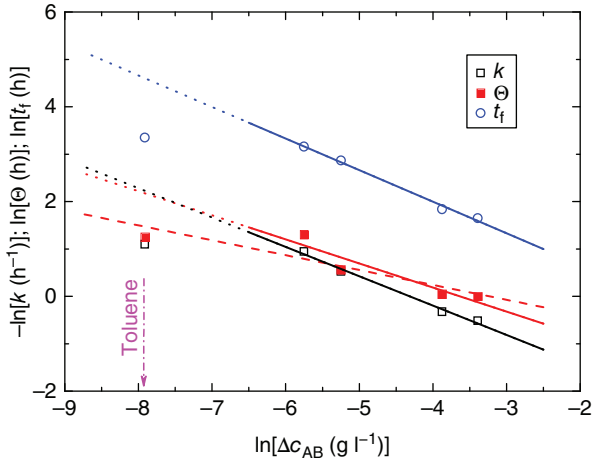

Figure 4.13 Plots of transformation time t_f, reaction constant k, and time constant Θ as a function of solubility difference Δc_{AB}, shown as ln–ln dependences, for transformation of stable β polymorph of tegafur from its metastable α polymorph. Data from Table 4.1.

The question in solid- and solution-mediated phase transformation is where the 3D nuclei of the stable form are formed and once formed how they subsequently grow to crystallites. Among the preferred sites are edges of crystals of unstable form and some of their planes that can act as a substrate for the nucleation and growth of crystals of the stable phase. In such cases, it is the nature of solute aggregates present in the solution that determines the crystallization kinetics of the stable phase. To discuss whether aggregates present in solution have some influence on phase transformation, we consider the results of experiments, carried out by Bobrovs et al. (2015), using a 90 : 10 mixture (wt fraction) of theophylline form II and IV phases in methanol solutions saturated at 23 °C with stable phase IV and metastable phase II, and commercial theophylline form II in methanol solutions saturated at 23 °C. Figure 4.14 shows the above data in the form of plots of $\ln[-\ln(1 - y_s)]$ against $\ln t$. These experiments exclude induction periods and represent phase transformation alone in the three cases.

The plots of the $y_s(t)$ data follow two distinct time periods for solution-mediated phase transformation. In the case of transformation in the 90 : 10 mixture of theophylline form II and IV phases in methanol solutions, transformation shows the constant q equal to about 1 and 4 below and above $\ln t = -1$ (i.e. $t \approx 0.4$ h). This implies that the transformation is relatively fast at a later stage. In the case of transformation in commercial theophylline phase II in methanol solutions, the first period is relatively long but later the transformation is also fast ($q \approx 3$). The former period is probably associated with secondary nucleation of new stable IV phase by the already existing nuclei, whereas the

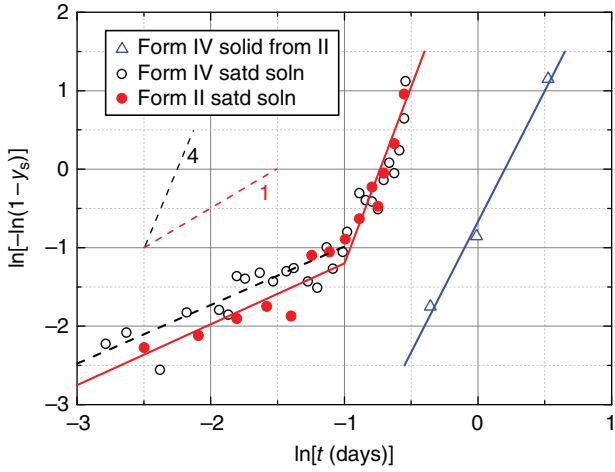

Figure 4.14 Plots of ln[−ln(1 − y_s)] against ln$t$ for stable form IV of theophylline in solution-mediated phase transformation from: (1) 90 : 10 mixture (wt fraction) of theophylline form II and IV forms in methanol solutions saturated at 23 °C with (open circles) form IV and (filled circles) form II, and (2) commercial theophylline form II in methanol solutions saturated at 23 °C. *Source:* Bobrovs http://pubs.rsc.org/-/content/articlehtml/2015/ce/c4ce02484b. Licensed Under CC BY 3.0.

latter is due to the nucleation and growth of stable IV phase. A somewhat higher value of y_s in the solution saturated with phase IV than that saturated with phase II is due to difference in the original concentration in the solution.

4.2 Some Non-KJMA Models of Isothermal Crystallization Kinetics

4.2.1 Approach Involving Formation of an Amorphous Precursor

This approach is based on the formation of an initial amorphous precursor of very low stability, which subsequently dissolves and transforms, depending on operational conditions, with time to increasingly more stable forms of different crystalline structures following Ostwald rule of stages. The process of each transformation occurs in two steps. In the first step, metastable and stable crystalline phases grow simultaneously at random sites in the solution volume by forming precipitate-free zones around them where, as expected by solution-mediated transformation mechanism, the metastable precursor phase slowly disappears with time. In the second step, the metastable phase dissolves and the dissolved mass is transported to the stable phase. As in the case of combined diffusion- and surface-controlled growth, the transformation process may also be considered as a two-stage process in which the transformation is controlled

either by the dissolution of the metastable phase or by the growth of the stable phase (Davey et al., 1986). If the concentration of the metastable phase stays constant at its solubility level during its transformation into the stable form, the transformation is controlled by the growth kinetics of the stable phase. However, if the entire dissolved mass of the metastable phase is simultaneously transformed to the stable phase, the transformation is likely to be dissolution controlled. Many examples of such transformations are known during the crystallization of various compounds by mixing two or more reactants (*reactive crystallization*). Figure 4.4b represents an example of transformation controlled by the growth of a stable phase.

A typical example in support of this approach are the experimental results of crystallization of calcium carbonate by mixing sodium carbonate solution at different feeding rates F to $CaCl_2$ solution containing different concentrations c_{Mg} of $MgCl_2$ and the effect of feeding rate and feed concentration on: (i) the lifetime of amorphous calcium carbonate and (ii) the crystallization fraction of metastable vaterite phase and its transformation to stable calcite phase (Kawano et al., 2002; Kitamura, 2001). Evolution of calcium carbonate precipitation with time in a crystallizer was carried out by feeding 150 ml aqueous solution of 0.05 or 0.2 M concentration (c_0) of Na_2CO_3 with a pump to the same concentration of $CaCl_2$ solution, without or with Mg^{2+} ions as an additive (Kitamura, 2001). The solution was stirred and the temperature was held constant at 298 K. After mixing, the solution was neutral and the pH remained constant in an experiment. The feeding rate F of Na_2CO_3 solution was changed between 0.05 and 5 ml·s^{-1}, and the concentration of Mg^{2+} additive was 5 or 10 mM. The main findings of the investigation are discussed below.

Figure 4.15 shows typical plots of change in the concentration c_{Ca} of Ca^{2+} ions with time t from the start of mixing of solutions of 0.05 mol·l^{-1} calcium chloride without and with the addition of two concentrations c_{Mg} of $MgCl_2$ for different feed rates F of 0.05 mol·l^{-1} $CaCO_3$ solutions. The values of c_C^e and c_V^e denote the solubility of calcite and vaterite, respectively. The resulting values of the concentration c_{Ca} are intermediate between the solubilities of calcite and vaterite. The figure shows that for the different feeding rates F the Ca^{2+} ion concentration rapidly decreases initially, and then attains a constant value, both in the pure system and in systems containing Mg^{2+} ions, when the amorphous precursor phase practically disappears in the solution. A similar behavior of $Ca^{2+}(t)$ plots was found for $c_0 = 0.2$ mol·l^{-1} solutions, but the constant value of Ca^{2+} ion concentration attained after the initial period is higher than in $c_0 = 0.05$ mol·l^{-1}. In the presence of Mg^{2+} ions the concentration of Ca^{2+} ions is increased in comparison with that in the pure system. The Ca^{2+} ion concentration is somewhat altered with a change in the feeding rate F of $NaCO_3$ solutions.

The composition of the polymorphs was found to depend on the concentration c_0 of the solutions, the feeding rate F of sodium carbonate solution, and the crystallization time t. Figure 4.16 shows the change in the composition y_C of calcite on time t from pure solutions of 0.2 mol·l^{-1} concentration c_0. The

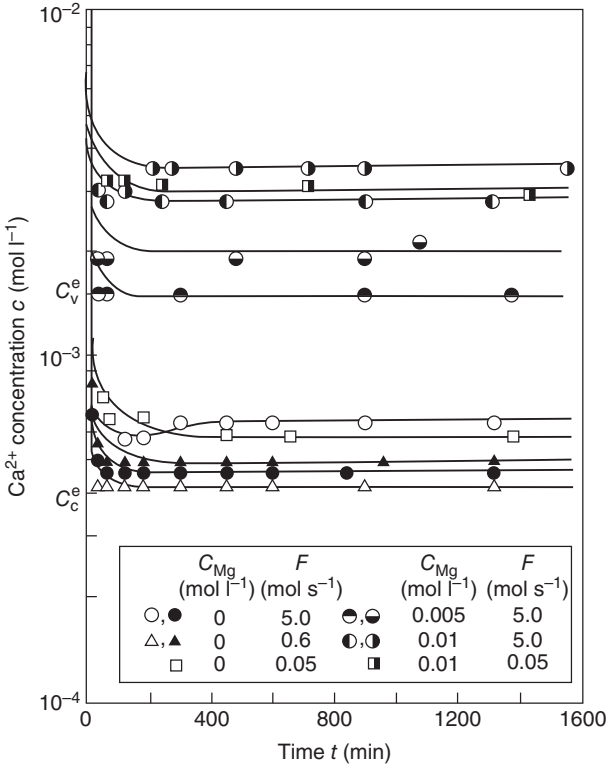

Figure 4.15 Change in concentration c of Ca^{2+} with time t after the start of mixing of solutions of 0.05 mol·l^{-1} calcium chloride containing different concentrations c_{Mg} of $MgCl_2$ with the addition of 0.05 mol·l^{-1} sodium carbonate at different feeding rates F. *Source:* Adapted from Kitamura (2001). Copyright (2001), with permission from Elsevier.

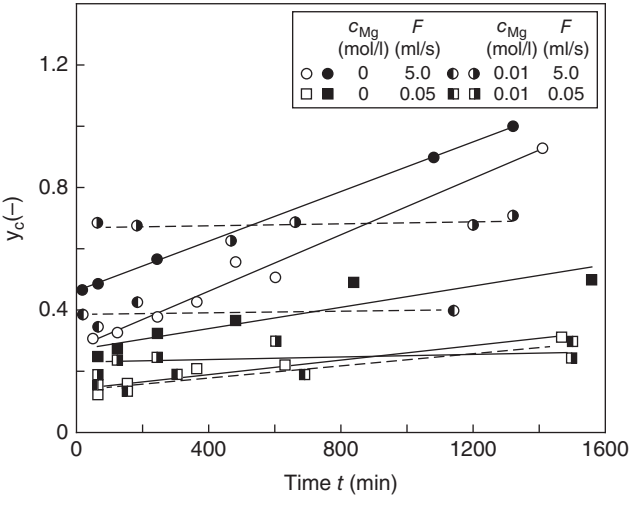

Figure 4.16 Dependence of composition y_C of calcite on time t for 0.2 mol/l solutions. *Source:* Adapted from Kitamura (2001). Copyright (2001), with permission from Elsevier.

$y_C(t)$ dependence is linear with a constant slope y'. The linear dependence is expected from the KJMA-type relation (4.14) for the transformation of metastable phase. Note that calcite composition y_C for $c_0 = 0.2$ mol·l^{-1} is lower than that for $c_0 = 0.05$ mol·l^{-1}, implying that the crystallization of vaterite is higher with increasing c_0. Addition of Mg^{2+} ions leads to an increase in the initial values of y_C, but the slope of the $y_C(t)$ plots is drastically decreased. The slope approaches a value equal to zero, especially at high feed rates F. The decrease in the slope of $y_C(t)$ plots implies that the transformation rate of vaterite to calcite is suppressed by the Mg^{2+} ions.

Kitamura (2001) argued that the initial decreasing concentration of Ca^{2+} ions before attaining a constant value is due to the presence of the precursor amorphous calcium carbonate in the form of globular and fibrous particles. The nucleation of polymorphous crystals occurs in the vicinity of the precursor and the polymorphous crystals grow by devouring the precursor particles surrounding the crystals, implying that the solubility of the precursor is higher than that of the polymorphous crystals. The lifetime of the precursor is relatively long and when it disappears, both polymorphous phases nucleate and grow as a result of dissolution of the precursor particles. The disappearance of the precursor with simultaneous precipitation of vaterite and calcite is an evidence of solution-mediated transformation. After the precursor has disappeared completely, the metastable vaterite phase dissolves and transforms into the stable calcite phase by solution-mediated transformation.

Using the ideas of combined diffusion- and surface-controlled growth, solution-mediated transformation of unstable phase u to stable phase s may be described as a result of dissolution of phase u and growth of phase s (Kitamura, 2001):

$$\frac{dm_u}{dt} = k_u m_u^{2/3}\left(c_u^e - c'\right), \tag{4.16}$$

$$\frac{dm_s}{dt} = k_s m_s^{2/3}\left(c' - c_s^e\right), \tag{4.17}$$

where m_u and m_s are the masses of metastable and stable phases, respectively, c_u^e and c_s^e are their corresponding solubilities, and k_u and k_s are the rate constants of dissolution and growth of the metastable and the stable phases, respectively. The concentration c' is determined by the relative rates of Eqs. (4.16) and (4.17). During transformation, the initial solution concentration c_u^e decreases with time and finally approaches the solubility c_s^e of the stable form. In general, the overall growth rate of the stable phase may be given by

$$\frac{dm_s}{dt} = k_G m_s^{2/3}\left(c_u^e - c_s^e\right), \tag{4.18}$$

where k_G is the overall growth rate constant. Elimination of c' from Eqs. (4.16) and (4.17) gives

$$\frac{1}{k_G} = \frac{1}{k_u} + \frac{1}{k_s}\left(\frac{m_s}{m_u}\right)^{2/3}. \tag{4.19}$$

When the growth constant $k_s \gg k_u$, $k_G \approx k_u$ and the transformation is dissolution controlled (Eq. (4.16)). However, when $k_u \gg k_s$, $k_G \approx k_s$ and the transformation is controlled by the growth of the stable phase (Eq. (4.17)). In Figure 4.15, the concentration remains practically constant despite the progress of transformation, implying that the transformation process is dissolution controlled, and the transformation may be described by Eq. (4.16).

The concentrations of solutions increase with an increase in the feed concentration and decrease with an increase in the feed rate, while the concentration attains a value c' intermediate between the solubility of metastable (vaterite) and stable (calcite) phases (see Figure 4.15). These results are a consequence of the competition of the two processes described by Eqs. (4.16) and (4.17). Assuming that the solubility difference between metastable and stable phases and the total amount ($m_u + m_s$) of the crystals remains constant, the fraction of the metastable and stable phases may be given by

$$y_u = \frac{m_u}{(m_u + m_s)}, \quad y_s = \frac{m_s}{(m_u + m_s)}. \tag{4.20}$$

Then from Eqs. (4.16) and (4.20), one obtains

$$y_u{}^{1/3}(t) = y_u{}^{1/3}(0) - k_u' t, \tag{4.21}$$

where k_u' is a rate constant of transformation of the metastable phase. However, noting that growth constant k_s of the stable phase is relatively large, the term on the right-hand side of Eq. (4.17) may be considered constant. Then Eqs. (4.17) and (4.20) give

$$y_s(t) = y_s(0) + k_s' t, \tag{4.22}$$

where k_s' is a rate constant of transformation of the stable phase.

According to Eqs. (4.21) and (4.22), the mass fraction y_u of dissolved vaterite decreases as $y_u^{1/3}$ whereas that of y_s of crystallized calcite increases linearly with the transformation time t. In fact, Kitamura (2001) observed such dependences from his experimental data.

Instead of studying mass-based changes in solution concentrations of metastable and stable crystalline forms with time during phase transformation, another procedure involves the investigation of processes of nucleation, growth, and dissolution of the solid-state forms and modeling of the entire transformation process using population balance equation (for example, see Cornel et al., 2009). The experimental setup for these studies usually consists of supersaturated solution contained in a temperature-controlled glass

reactor equipped with an ATR-FTIR probe, an FBRM probe, a glass impeller, and a temperature recorder. The ATR-FTIR probe is used to measure the liquid-phase concentration, which enables to estimate the growth rate of the stable phase. The FBRM probe enables in situ measurements of the chord length distribution of the crystallized solid phase for monitoring the particle size distribution (PSD). The PSD of the metastable phase is carried out offline using a Coulter device. Nucleation kinetics of the metastable phase is determined from induction time measurements using ATR-FTIR and FBRM, whereas growth and dissolution rates of the metastable form and growth rate of the stable form are assumed to occur following the well-known equations described in Chapters 2 and 3. In the case of dissolution, it is assumed that the dissolution rate linearly changes with the available supersaturation ($S_u - 1$). However, since the stable form results from the transformation of the metastable phase, the growth rate of the stable form has to be estimated from seeded batch experiments without the formation of new particles during desupersaturation of solutions of known initial supersaturations. The time dependence of desupersaturation behavior of seeded and unseeded supersaturated solutions is discussed in Chapter 8.

4.2.2 Model of Mazzanti, Marangoni, and Idziak

This model was advanced by Mazzanti, Marangoni, and Idziak (2005) and later modified by them (2008). They called the model as the ordinary diffusion equations (ODEs) model. It deals with the modeling of individual contributions of unstable and stable forms of a crystallizing material. The model is based on the following postulates: (i) there are regions of liquid fractions A^* and B^* from which unstable u and stable s forms can be crystallized directly, but crystallization of the stable phase s can also occur from the region of fraction A^* by the transformation of the unstable phase u, (ii) the transformation of the metastable form u into the stable form s is controlled by bulk diffusion, (iii) the crystallization kinetics of both metastable and stable forms can be described by Eq. (4.5) of the KJMA theory, and (iv) supersaturation $\ln S$ or undercooling ΔT available for crystallization is defined as the ratio of the uncrystallized mass in the liquid phase (melt or supersaturated solution) to the mass of the material that could crystallize. If m is the mass of a crystallized solid and m_0 is the value of m at equilibrium, the supersaturation is

$$\ln S \approx \frac{(m_0 - m)}{m_0} = 1 - \frac{m}{m_0}. \tag{4.23}$$

Denoting the untransformed material in the liquid phase by $L = m_0 - m$ and assuming that KJMA theory applies, the untransformed mass can be described by the differential form of Eq. (4.5) in the form:

$$\frac{\partial L}{\partial t} = -qkL\left[-\ln\left(\frac{L}{m_0}\right)\right]^{(q-1)/q}, \tag{4.24}$$

where k is the Avrami constant related to the time constant Θ ($k = \Theta^{-1/q}$; see Eqs. (3.79) and (3.86)) and q is the growth mode exponent (see Eq. (3.87)). Thus, the rate of phase transition is a function of the mass of the material left in the phase undergoing transformation. This phase can be the melt of the crystallizing material itself or its crystallized unstable α form.

During crystallization at a given temperature, if the material fraction m_0 that can crystallize into unstable form u is A^* and the additional liquid fraction B^* that can crystallize into stable form s, the total amount of the liquid fraction that can crystallize into the stable form s is $A^* + B^*$. As the unstable α phase grows, the material available from the region A^* becomes depleted, leaving behind an uncrystallized fraction A. This means that the amount of crystallized form u is: $m_u = A^* - A$. In the case of growth of the stable phase s for which the crystallized material is from both of the regions A^* and B^*, the uncrystallized portions of both A and B are reduced. The fractions of the stable phase s from A and B regions are $A/(A + B)$ and $B/(A + B)$, respectively. Following Mazzanti et al. (2008), the above concepts are used to obtain the equations given below.

The consumption of the liquid fraction A, as it is converted into unstable phase u and then into stable phase s, after the occurrence of its formation at time t_{us}, is given by

$$\frac{\partial A}{\partial t} = -q_u k_u A\left[-\ln\left(\frac{A}{A^*}\right)\right]^{(q_u-1)/q_u} - \left\{q_s k_s (A+B)\left[-\ln\left(\frac{A+B}{A^*+B^*}\right)\right]^{(q_s-1)/q_s}\frac{A}{A+B}\right\}_{t>t_{us}}, \tag{4.25}$$

where q_u and k_u are the Avrami constants describing the transformation of A to form u, whereas q_s and k_s refer to the constants describing that the form s is formed from the liquid ($A + B$). The formation of unstable phase u from the liquid fraction A and its consumption due to transformation into s form is given by

$$\frac{\partial m_u}{\partial t} = -q_u k_u A\left[-\ln\left(\frac{A}{A^*}\right)\right]^{(q_u-1)/q_u} - \left\{q_c k_c m_u\left[-\ln\left(\frac{m_u}{m_u(\max)-m_u(\min)}\right)\right]^{(q_c-1)/q_c}\right\}_{t>t_{us}}, \tag{4.26}$$

where the constants q_c and k_c refer to the solid–solid transformation of form u into form s. The crystallization of the liquid fraction B into phase s is given by

$$\frac{\partial B}{\partial t} = -\left\{q_s k_s (A+B)\left[-\ln\left(\frac{A+B}{A^*+B^*}\right)\right]^{(q_s-1)/q_s}\frac{B}{A+B}\right\}_{t>t_{us}}. \tag{4.27}$$

The amount of s phase at time t can be computed from the mass balance equation

$$m_s = (A^* + B^*) - (A + B) - m_u, \tag{4.28}$$

with the initial conditions: $A(t = 0) = A^*$, $B(t = 0) = B,^*$ and $m_u(t = 0) = 0$. The value of $m_u(\min)$ is obtained from the procedure, such as integrated X-ray intensity profile from small-angle two-dimensional X-ray diffraction pattern of the material, differential scanning calorimetry, or pulse nuclear magnetic resonance, followed to register the crystallized material content.

Using the above system of equations, their parameters are obtained by fitting the experimental time dependence of crystallization of unstable and stable phases. Figure 4.17 shows plots of solid fat content (SFC) of anhydrous milk fat (AMF) crystallized at 17 °C and 90 s^{-1} shear as a function of time. The lines represent the fit obtained by using the model. The dashed line denotes the time t_{us} when the growth of the s phase becomes diffusion controlled, described by the relation:

$$\frac{\partial m_s}{\partial t} = \frac{k_s}{2(t - t_{us})^{1/2}}, \tag{4.29}$$

where k_s is a kinetic constant (in $\min^{-0.5}$), which is a function of temperature. In the figure, unstable u and stable s phases are denoted by α and β′ phases, respectively, whereas the time t_{us} is indicated by $t_{\alpha\beta}$.

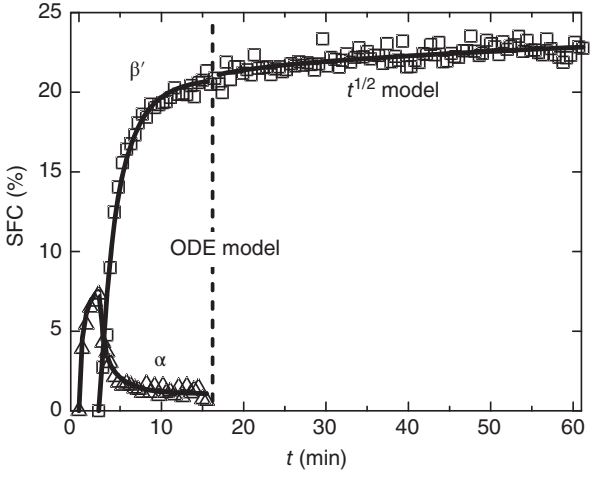

Figure 4.17 Plots of solid fat content (SFC) of α and β′ polymorphs of anhydrous milk fat (AMF) crystallized at 17 °C and 90 s^{-1} shear as a function of time. Solid lines represent the fit obtained by using the model. Dashed line denotes the time $t_{\alpha\beta}$ when the growth of the β′ phase becomes diffusion controlled. *Source:* Reproduced from Mazzanti et al. (2008). Copyright (2008), with permission from The European Physical Journal (EPJ).

4.2.3 Gompertz's Model

Gompertz function and its modifications are used in diverse areas such as various bacterial growth in different media, population growth of individual biological species, and germination of seeds (for example, see Sangwal, 2015). However, Kloek et al. (2000) were the first to use Gompertz's empirical equation to describe the experimentally observed curves of isothermal fat crystallization. They were subsequently followed by Vanhoute et al. (2002) and Foubert et al. (2003). Following Foubert et al. (2003), we describe below the essential features of Gombertz's model.

In its original form Gompertz's equation is given in the form:

$$Y = Y_0 \exp[-\exp(Y_1 - Y_2 t)], \tag{4.30}$$

where Y is the logarithm of the relative population size, and Y_0, Y_1, and Y_2 are empirical constants. To give specific meaning to the empirical parameters, they should be defined in terms of parameter $m_{\max}$ (the maximum value of Y), the growth rate R (tangent at the inflection point), and time lag τ (time-axis intercept of the tangent), as illustrated schematically in Figure 4.7, where unstable u and stable s phases are denoted as A and B phases, respectively. To find the inflection point at $t = t_{\text{infl}}$, one sets the second derivative of Eq. (4.30) to zero, which gives

$$t_{\text{infl}} = \frac{Y_1}{Y_2}. \tag{4.31}$$

The first derivative at t_{infl} gives the growth rate

$$R = \frac{(Y_0 - Y_2)}{e}, \tag{4.32}$$

where $e = 2.718$. The time lag τ may be calculated from the tangent line through the inflection point, i.e.

$$\tau = \frac{(Y_1 - 1)}{Y_2}. \tag{4.33}$$

From Eqs. (4.32) and (4.33), one finds

$$Y_1 = \frac{Re}{Y_0}\tau + 1. \tag{4.34}$$

When $t \to \infty$, $Y \to Y_0$ and $Y_0 \to m_{\max}$. Then for the crystallization of stable s form from melt or supersaturated solution, Gompertz's empirical equation (4.30) may be written as

$$m_{\text{total}} = m_{\text{s(max)}} \exp\left\{-\exp\left[\frac{2.718R_{\text{s}}}{m_{\text{s(max)}}}(\tau_{\text{s}} - t) + 1\right]\right\}, \tag{4.35}$$

where m_{total} (= Y) is the amount of the crystallized stable s form at time t, $m_{\text{s(max)}}$ is the maximum mass of the s form, and τ_{s} and R_{s} are, respectively, the time lag and growth rate of the stable s form. When crystallization of the stable s form is accompanied by simultaneous crystallization of metastable u form, the crystallization kinetics may be given by

$$m_{\text{total}} = m_{u(\text{max})} \exp\left\{ - \exp\left(\frac{2.718R_{\text{u}}}{m_{\text{u(max)}}}(\tau_{\text{u}} - t) + 1 \right) \right\} + m_{\text{s(max)}} \exp\left\{ - \exp\left[\frac{2.718R_{\text{s}}}{m_{\text{s(max)}}}(\tau_{\text{s}} - t) + 1 \right] \right\}, \tag{4.36}$$

where τ_{u} and R_{u} are, respectively, the time lag and growth rate of the metastable u form, and $m_{\text{u(max)}}$ is the maximum mass of the u form.

As in the case of KJMA theory, Eq. (4.36) contains six parameters. The parameters $m_{\text{u(max)}}$ and $m_{\text{s(max)}}$ determine the heights of the plateau of the first and the second steps, respectively, whereas the time constants τ_{u} and τ_{s} determine the moment when the curve abruptly departs from the time axis. The growth rates R_{u} and R_{s} determine the slopes of the straight-line parts of the curve.

4.2.4 Model of Foubert, Dewettinck, Jansen, and Vanrolleghem

This approach was proposed by Foubert et al. (2006) and is an extension of their previous model (Foubert et al., 2003). This model, called Foubert model hereafter, is based on consideration of (i) uncrystallized phase left in the crystallizing medium and (ii) transformation of crystallized metastable phase u into stable phase s. The relative crystallizable phase $h(t)$ remaining in the medium is given by

$$h(t) = \frac{m_{\max} - m(t)}{m_{\max}} = 1 - y(t), \tag{4.37}$$

where $m_{\max}$ (% solid phase) is the maximum amount of crystallizing phase (i.e. solid phase) from that of the initial amount contained in the melt or supersaturated solution (see Figure 4.7). Assuming that crystallization of the solid phase is a first-order forward reaction and a reverse reaction of order n, the rate of relative crystallizable phase is given in the form:

$$\frac{\mathrm{d}h(t)}{\mathrm{d}t} = K(h^n - h), \tag{4.38}$$

with

$$h(0) = \frac{m_{\max} - m(0)}{m_{\max}}, \tag{4.39}$$

where K is the rate constant (defined as inverse of time t) and $m(0)$ is the amount of crystalline mass initially present in the melt or supersaturated solution, which is related to the induction time t_{in} of crystallization. In view of difficulty in measuring $h(0)$ experimentally from the plots of crystallized mass x as a function of time t, Eq. (4.37) is represented in terms of induction period t_{in} in the form:

$$h(t) = \left\{1 + \left[(1-x)^{1-n} - 1\right]\exp\left[-(1-n)K(t - t_{in}(x))\right]\right\}^{1/1-n}, \tag{4.40}$$

where $t_{in}(x)$ is the induction period required for the crystallization of x. In Eq. (4.40), the induction period $t_{in}(x)$ is related to the reference crystallized mass x by

$$t_{in}(x) = \frac{1}{(1-n)K}\left(-\ln\left\{\frac{(1-x)^{1-n} - 1}{[1 - m(0)/m_{max}]^{1-n} - 1}\right\}\right). \tag{4.41}$$

Using Eqs. (4.37) and (4.38), the absolute amount $m(t)$ of crystallization at time t may be given by

$$\frac{dm(t)}{dt} = K(m_{max} - m) - Km_{max}\left(\frac{m_{max} - m}{m_{max}}\right)^{n}. \tag{4.42}$$

Eq. (4.42) is the starting equation of the two-step model involving the transformation of metastable u phase into the stable s phase such that one u crystal is transformed into one s crystal.

If R_u is the rate of formation of metastable u phase from the supersaturated solution or supercooled melt and R_s is the rate of transformation of the u phase into s phase, one may write

$$\frac{dy_u(t)}{dt} = R_u - R_s, \tag{4.43}$$

$$\frac{dy_s(t)}{dt} = R_s. \tag{4.44}$$

The rate R_s of formation of stable s phase may be given by

$$R_s = K_s(1 - y_s) - K_s(1 - y_s)^{n_s}, \tag{4.45}$$

where K_s is the rate constant of s phase and n_s is the order of the reverse reaction. Similarly, the rate R_u of formation of u phase may be given by

$$R_u = K_u[1 - (y_u + y_s)] - K_u[1 - (y_u + y_s)]^{n_u}, \tag{4.46}$$

where K_u is the rate constant of u phase and n_u is the order of the reverse reaction. The initial values of $y_u(0)$ and $y_s(0)$ at $t = 0$ may be calculated from Eq. (4.46), i.e.

$$y_u(0) = 1 - \left[1 + \frac{(1-x)^{1-n_u} - 1}{\exp(n_u - 1)K_u t_{in(u)}}\right]^{1/(1-n_u)}, \tag{4.47}$$

$$y_s(0) = 1 - \left[1 + \frac{(1-x)^{1-n_s} - 1}{\exp(n_s - 1)K_s t_{in(s)}}\right]^{1/(1-n_s)}, \tag{4.48}$$

where $t_{in(u)}$ and $t_{in(s)}$ are the periods needed to reach x (taken arbitrarily as 1%) of crystallization of u and s phases, respectively.

To account for the fact that crystallization fractions y_u and y_s lead to different maximum values, the expressions for y_u and y_s are multiplied by the corresponding maximum values of $m_{u(max)}$ and $m_{s(max)}$, observed as % solid or released heat as $J \cdot g^{-1}$. Then,

$$m_u = m_{u(max)} y_u, \tag{4.49}$$

$$m_s = m_{s(max)} y_s, \tag{4.50}$$

where m_u and m_s are the amounts of crystallized u and s phases, respectively. The total amount m_{total} of crystallization is then given as the sum of m_u and m_s, i.e. $m_{total} = m_u + m_s$; see Eq. (4.7). The experimental data on m_{total} and m_s are fitted simultaneously.

The fitting procedure involves eight parameters. Foubert et al. (2006) examined the influence of these parameters on the overall crystallization curves. It was shown that the parameters $m_{u(max)}$ and $m_{s(max)}$ determine the heights of the plateau of the first and the second steps, respectively, The time constants $t_{in(u)}$ and $t_{in(s)}$ determine the moment when the curve abruptly departs from the time axis. The higher the value of $t_{in(u)}$ and $t_{in(s)}$, the more is the delay when the curve leaves the time axis. However, the rate constants K_u and K_s as well as n_u and n_s determine the slopes of the straight-line parts of the curve and their curvatures. The higher the values of these parameters, the higher is the steepness of the crystallization curves.

4.3 Comparison of Different Models of Isothermal Crystallization Kinetics

As mentioned in Section 4.2, the KJMA theory provides information on the dimensionality d of growing crystallites as well as on the nucleation and growth processes. Therefore, it is not surprising that this theory, as presented by Eq. (4.5), has been most widely used in the isothermal crystallization kinetics of fats. The main advantage of this theory is that all of its parameters have well-defined physical significance. Gompertz's empirical equation, on the other hand, contains empirically fitting parameters, which have no physical significance. In the Foubert model, although the physical meaning can be assigned

to practically all of the parameters, yet the weakest point is the arbitrary choice of the induction period $t_{in}(x)$ required for the crystallization of $x = 1\%$.

Two typical examples of the influence of temperature and time on the overall crystallization of different materials from melts are illustrated in Figures 4.18 and 4.19. Figures 4.18 and 4.19 show the experimental data obtained at different

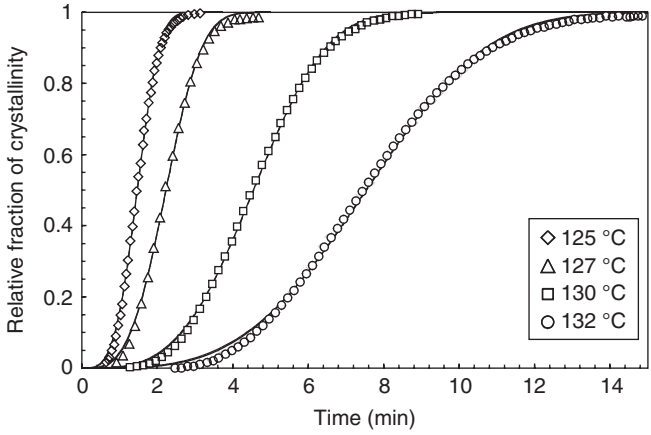

Figure 4.18 Dependence of overall crystallization fraction *y* of polypropylene on time *t* at different temperature T_c. The data, shown by symbols, are from Lopez-Manchado et al. (2000). Solid curves are drawn by using Avrami's "precise" equation, whereas dotted curves are drawn by using Eq. (4.7). *Source:* Adapted from Padar et al. (2008). Copyright (2008), with permission from Springer.

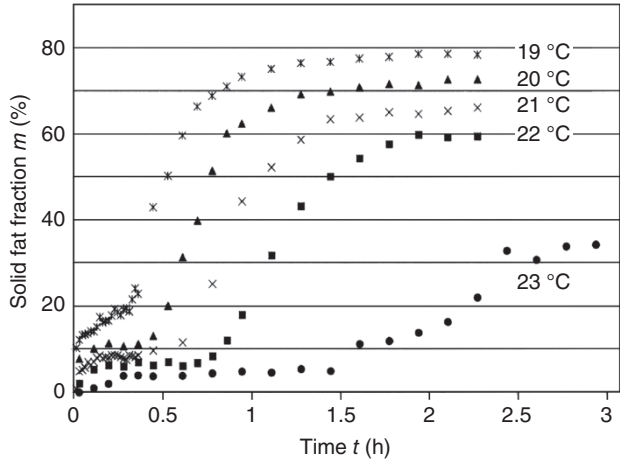

Figure 4.19 Dependence of solid fat fraction (%) of cocoa butter on time *t* at different crystallizing temperature T_c. *Source:* Adapted from Foubert et al. (2005). Copyright (2005), with permission from Wiley.

temperatures T_c on isothermal crystallization of polypropylene and cocoa butter, respectively. The data on polypropylene were reported by Lopez-Manchado et al. (2000) and later analyzed by Padar et al. (2008) using the "precise" Avrami equation, with dimensionality $d = 3$, based on Eq. (3.90) (i.e. Eq. (4.5)) and approximate Avrami equation (3.88). The crystallization kinetics of polypropylene was investigated by differential scanning calorimetry. The data on cocoa butter were reported by Foubert et al. (2005), and were obtained by the pulsed nuclear magnetic resonance (pNMR) method.

The following general features of the overall isothermal crystallization may be summarized from Figure 4.18:

1) Crystallization of polypropylene is a single-stage process.
2) During the single-stage crystallization of polypropylene, there is a small time lag, or induction period $t_{in(\beta)}$, when detectable fraction of the crystallizing phase is formed. This time lag increases with an increase in crystallizing temperature T_c.
3) The slope R_β of the linear parts of the crystallization curves of polypropylene involving single stage decreases with an increase in crystallization temperature T_c.
4) Both the "precise" and the "approximate" Avrami equations describe the experimental data on polypropylene reasonably well and there is practically insignificant difference between the best fit of the experimental data by the two equations. The best-fit curves by the two equations are indistinguishable in the crystallized fraction between about 0.2 and 0.8, and the deviation between the experimental data and the best-fit curves increases with increasing T_c.

In contrast to the above case, from Figure 4.19 the following features may be noted:

1) Crystallization of cocoa butter occurs in two stages. During the two-stage crystallization of cocoa butter, there is practically no induction period $t_{in(\alpha)}$ for the onset of crystallization of the metastable α phase but the induction period $t_{in(\beta)}$ for the crystallization of the stable β phase, as defined by extrapolating the linear parts of the curves to the time axis, increases with decreasing T_c.
2) The slopes R_α and R_β of the linear parts of the crystallization curves in the region of crystallization of the metastable and stable forms decrease with an increase in T_c.
3) Between the two linear parts defining R_α and R_β, there is a plateau region along the time axis. The width of this plateau region increases with an increase in T_c.

Most of the above features may be explained by the models described above, but features (2) and (4) concerning crystallization of polypropylene and feature (3) concerning crystallization of cocoa butter deserve particular attention. In

order to interpret the dependence of the width of the plateau region on crystallization temperature T_c, we define the plateau region as $\Delta t_{in} = [t_{in(\beta)} - t_{f(\alpha)}]$, where $t_{f(\alpha)}$ is the value of the finish time up to $m_{\alpha(max)}$ of α form and $t_{in(\beta)}$ is the time when β form appears in the overall crystallization curve (see Figure 4.7). Then from Figure 4.18 we consider the trajectories of $t_{f(\alpha)}$ and $t_{in(\beta)}$ obtained by joining their values corresponding to various T_c. If the solid fraction scale is represented by crystallization temperature T_c, it is easy to recognize that this procedure yields two linear plots of temperature T_c against time t such that there are two extreme temperatures T_0 and T_{max} when the plateau width Δt_{in} is zero and maximum, respectively, as shown in Figure 4.20. Here, T_0 is the crystallization temperature when plateau is not observed. Denoting the time corresponding to T_0 by t_0, from Figure 4.20, one obtains

$$\frac{T_c - T_0}{t_{in(\beta)} - t_0} = -b_\beta, \quad \frac{T_c - T_0}{t_{f(\alpha)} - t_0} = -b_\alpha, \tag{4.51}$$

where b_α and b_β are the slopes of $T(t)$ plots corresponding to the end and beginning of crystallization of unstable α and stable β forms, respectively, $T_c < T_0$ and $b_\beta < b_\alpha$. From these relations, one finds the relationship between plateau width Δt_{in} and crystallization temperature T_c:

$$\Delta t_{in} = t_{in(\beta)} - t_{f(\alpha)} = (T_c - T_0)\left(\frac{1}{b_\beta} - \frac{1}{b_\alpha}\right). \tag{4.52}$$

According to Eq. (4.52), Δt_{in} increases with an increase in T_c, as observed in the case of cocoa butter (Figure 4.19). When $b_\alpha \to \infty$, crystallization of the β phase occurs in single stage. Crystallization of polypropylene is an example of this special case (Figure 4.18). However, instead of intermediate plateau regions in the time dependence of crystallization curves, accelerated

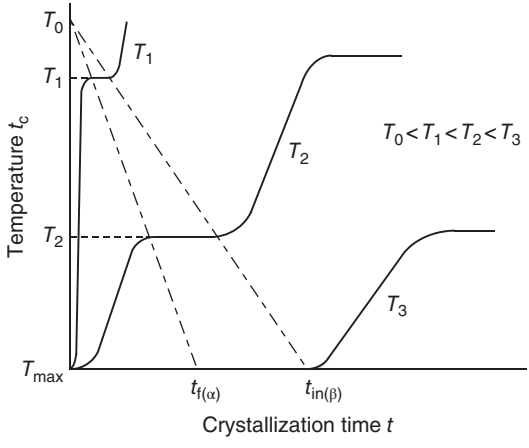

Figure 4.20 Schematic illustration of dependence of crystallization temperature T_c on $t_{f(\alpha)}$ and $t_{in(\beta)}$. It is assumed that T_c decreases linearly with increasing both $t_{f(\alpha)}$ and $t_{in(\beta)}$ with slopes b_α and b_β, respectively. *Source:* Reproduced from Sangwal and Sato (2012). Copyright (2012), with permission from AOCS Press.

transformation regions have also been observed (see Padar et al., 2008). The above explanation can equally be applied to such cases.

Now we consider feature (4) of crystallization of polypropylene. For this purpose, we reexamine, as an example, the experimental data on the crystallization kinetics of cocoa butter (Figure 4.21) followed by differential scanning calorimetry (Foubert et al., 2003).

Foubert et al. (2003) compared the quality of fit of Avrami equation (4.5), Compertz equation (4.36), and Foubert equations (4.47) and (4.48) for the above data. These authors concluded that the Gompertz equation provides a better fit than the Avrami equation, but Foubert equation gives the best fit. However, it may be noted that when one makes an allowance for the time t_0 needed by a system to attain the crystallization temperature T_c, the fit of Avrami equation for the data of crystallization kinetics improves remarkably. Figure 4.21 illustrates an example of this type of fit with corrected time for the data on cocoa butter analyzed by Foubert et al. (2003). The dashed curve represents the crystallized mass, measured as crystallization heat ΔH_c, as a function of recorded time t. This curve shows the original fit reported by Foubert et al. (2003). The dotted and continuous curves are drawn for the fit with the rescaled time $t^* = t - t_0$, where $t_0 = 0.20$ and 0.31 h are the corrections used. Obviously, the fit improves upon the introduction of the correction time t_0 and the best fit in the entire time interval is obtained when $t_0 = 0.31$ h in the case of the analyzed data. This aspect of the fit of experimental data of

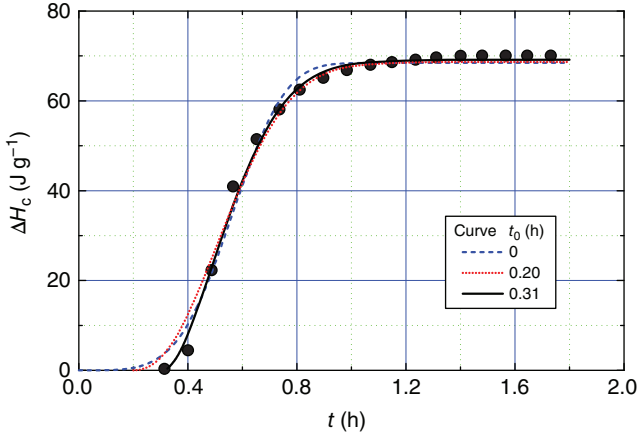

Figure 4.21 Example of fit of Avrami equation (4.5) to the crystallization kinetics of cocoa butter with corrections t_0 in time. Dashed curve is for $t = 0$, but dotted and continuous curves are drawn with $t_0 = 0.20$ and 0.31 h, respectively. *Source:* Original data from Foubert et al. (2003).

crystallization kinetics according to Avrami equation was also discussed in Section 3.9.2.3.

Measurement of the time period t_{in} required for the detection of crystallization by different techniques is based on the cooling of a saturated medium to a predefined crystallization temperature T_c as rapidly as possible, followed by continuous monitoring of the crystallization process. However, it is well known (Wright et al., 2000) that the detection of the initial stages of crystallization depends on the sensitivity of experimental techniques and the rapidness with which the preset isothermal crystallization temperature T_c of the sample in the experimental setup is reached. The latter factor mainly depends on the heat transfer between the sample and its surroundings used for cooling, whereas the former is related to the time t_g required for the growth of stable critically-sized 3D nuclei to achieve sizes for the detection of the crystallites by the measurement technique. Consequently, the time period recorded by different techniques for the occurrence of crystallization is always more than that required for the induction period t_{in}, which is the period required for the formation of stable nuclei in a system supersaturated at apparent T_c. In fact, these are main errors that lead to erroneous conclusion about the validity of crystallization models.

Finally, it should be mentioned that another period not accounted for in the measured induction period t_{in} is the time t_{reorg} required for the reorganization and orientation of growth species before the formation of stable 3D nuclei, but this period is also included in the definition of the induction period t_{in}, given by

$$t_{in} = t_{reorg} + t_N + t_g, \tag{4.53}$$

where t_N is the actual time required for the formation of critically-sized nucleus at a given value of the driving force as determined by supersaturation $\ln S$ or supercooling ΔT. The classical 3D nucleation theory accounts for this t_N alone. This means that, strictly spoken, the relationship between induction period t_{in} and driving force for 3D nucleation predicted by the classical nucleation theory hold when t_{reorg} and t_g are negligibly small in comparison with t_N.

References

Bayés-Garcia, L., Calvet, T., Cuevas-Diarte, M.A. et al. (2013). In situ observation of transformation pathways of polymorphic forms of 1,3-dipalmitoyl-2-oleoyl glycerol (POP) examined with synchrotron radiation X-ray diffraction and DSC. *Cryst. Eng. Comm.* 15: 302–314.

Bobrovs, R., Seton, L., and Actiņš, A. (2014). Solvent-mediated phase transformation between two tegafur polymorphs in several solvents. *Cryst. Eng. Comm.* 16: 10581–10591.

Bobrovs, R., Seton, L., and Dempster, N. (2015). Reluctant polymorph: investigation into the effect of self-association on the solvent mediated phase transformation and nucleation of theophylline. *Cryst. Eng. Comm.* 17: 5237–5251.

Brecević, L., Kralj, D., and Garside, J. (1989). Factors influencing the distribution of hydrates in calcium oxalate precipitation. *J. Cryst. Growth* 97: 460–468.

Clarkson, J.R., Price, T., and Adams, C. (1992). Role of metastable phases in the spontaneous precipitation of calcium-carbonate. *J. Chem. Soc. Faraday Trans.* 88: 243–249.

Cornel, J., Lindenberg, C., and Mazzotti, M. (2009). Experimental characterization and population balance modeling of the polymorph transformation of L-glutamic acid. *Cryst. Growth Des.* 9: 243–252.

Davey, R.J., Cardew, P.T., McEwan, D., and Sadler, D.E. (1986). Rate-controlling processes in solvent-mediated phase transformations. *J. Cryst. Growth* 79: 648–653.

Du, W., Yin, Q., Gong, J. et al. (2014). Effect of solvent on polymorph formation and nucleation of prasugrel hydrochloride. *Cryst. Growth Des.* 14: 4519–4525.

Elfil, H. and Rogues, H. (2001). Role of hydrate phases of calcium carbonate on the scaling phenomenon. *Desalination* 137: 177–186.

Foubert, I., Dewittinck, K., and Vanrolleghem, P.A. (2003). Modelling of the crystallization kinetics of fats. *Trends Food Sci. Technol.* 14: 79–92.

Foubert, I., Vanrolleghem, P.A., and Dewittinck, K. (2005). Insight in model parameters by studying temperature influence on isothermal cocoa butter crystallization. *Eur. J. Lipid Sci. Technol.* 107: 660–672.

Foubert, I., Dewittinck, K., Janssen, G., and Vanrolleghem, P.A. (2006). Modelling two-step isothermal fat crystallization. *J. Food Eng.* 75: 551–559.

Füredi-Milhofer, H. and Sarig, S. (1996). Interactions between polyelectrolytes and sparingly soluble salts. *Prog. Cryst. Growth Charact. Mater.* 32: 45–74.

Jung, T., Kim, W.-S., and Choi, C.K. (2004). Biomineralization of calcium oxalate for controlling crystal structure and morphology. *Mater. Sci. Eng.* C24: 31–33.

Kashchiev, D. (2000). *Nucleation: Basic Theory with Applications*. Oxford: Butterworth-Heinemann.

Kawano, J., Shimobayashi, N., Kitamura, M. et al. (2002). Formation process of calcium carbonate from highly supersaturated solution. *J. Cryst. Growth* 237 (239): 419–423.

Kitamura, M. (2001). Crystallization and transformation mechanism of calcium carbonate polymorphs and the effect of magnesium ion. *J. Colloid Interface Sci.* 236: 318–327.

Kitamura, M., Hayashi, Y., and Hara, T. (2008). Effect of solvent and molecular structure on the crystallization of polymorphs of BPT esters. *J. Cryst. Growth* 310: 3067–3071.

Kloek, W., Walstra, P., and van Vliet, T. (2000). Crystallization kinetics of fully hydrogenated palm oil in sunflower oil mixtures. *J. Am. Oil Chem. Soc.* 77: 389–398.

Lide, D.R. (1996/1997). *Handbook of Chemistry and Physics*, 77e. Boca Raton, FL: CRC Press.

Lopez-Manchado, M.A., Blaglotti, J., Torre, L., and Kenny, J.M. (2000). Effects of reinforcing fibers on the crystallization of polypropylene. *Polym. Eng. Sci.* 40: 2194–2204.

Mazzanti, G., Marangoni, A.G., and Idziak, S.H.J. (2005). Modelling phase transitions during the crystallization of a multicomponent fat under shear. *Phys. Rev. E* 74: 041607.

Mazzanti, G., Marangoni, A.G., and Idziak, S.H.J. (2008). Modelling of two-regime crystallization in a multicomponent lipid system under shear flow. *Eur. Phys. J. E* 27: 135–141.

Nancollas, G.H. (1982). Phase transformation during precipitation of calcium salts. In: *Biological Mineralization and Demineralization* (ed. G.H. Nancollas), 79–99. Berlin: Springer.

Ouyang, J.-M., Deng, F., and Duan, L. (2005). Effect of concentrations of lecithin, calcium and oxalate on crystal growth of calcium oxalate in vesicles. *Collids Surf. A* 257/258: 215–220.

Padar, S., Jeelani, S.A.K., and Windhab, E.J. (2008). Crystallization kinetics of cocoa fat systems: experiments and modeling. *J. Am. Oil Chem. Soc.* 85: 1115–1126.

Sangwal, K. (2015). Comparison of selected mathematical functions for the analysis of growth behavior of items and physical interpretation of Avrami-Weibull function. https://www.researchgate.net/publication/282075546 (accessed 13 March 2018); doi: 10.13140/rg.2.1.3852.3367.

Sangwal, K. and Sato, K. (2012). Nucleation and crystallization kinetics of fats. In: *Structure–Function Analysis of Edible Fats* (ed. A.G. Marangoni), 25–78. Urbana: AOCS Press.

Sato, K. (2001). Crystallization behaviour of fats and lipids: a review. *Chem. Eng. Sci.* 56: 2255–2265.

Skritić, M., Füredi-Milhofer, H., and Marković, M. (1987). Precipitation of calcium oxalates from high ionic strength solutions. V. The influence of precipitation conditions and some additives on the nucleating phase. *J. Cryst. Growth* 80: 113–120.

Vanhoute, B., Dewettinck, K., Foubert, I. et al. (2002). The effect of phospholipids and water on the isothermal crystallization of milk fat. *Eur. J. Lipid Sci. Technol.* 104: 490–495.

Wright, A.J., Narine, S.S., and Marangoni, A.G. (2000). Comparison of experimental techniques used in lipid crystallization studies. *J. Am. Oil Chem. Soc.* 77: 1239–1242.

5

Nonisothermal Crystallization Kinetics and the Metastable Zone Width

Cooling of a saturated solution of a solute in a solvent from the saturation temperature T_0 leads to the creation of supersaturation, which ultimately leads to the formation of three-dimensional (3D) nuclei and the growth of these nuclei into visible crystallites with increasing cooling duration. For a constant rate R_L of cooling of the liquid, the temperature decrease ΔT from T_0 to T occurs in the duration Δt of cooling according to the relation:

$$R_L = \frac{\Delta T}{\Delta t} = \frac{\Delta T_{max}}{\Delta t_{max}}, \tag{5.1}$$

where $\Delta t = (t_0 - t)$ and t_0 and t are the times corresponding to T_0 and T, respectively. If t_{lim} is the time and T_{lim} is the temperature when visible crystallites are detected in the solution, one may define the maximum duration $\Delta t_{max} = (t_0 - t_{lim})$ and the maximum temperature decrease $\Delta T_{max} = (T_0 - T_{lim})$. The maximum temperature difference ΔT_{max} defines the metastable zone width (MSZW) of the saturated solution for the cooling rate R_L. Analogously, one may define Δt_{max} and ΔT_{max} for the cooling of a molten homogeneous phase. Determination of MSZW from measurement of the maximum supercooling ΔT_{max} experimentally by controlled cooling of saturated solutions is usually known as the *polythermal method* of MSZW or *controlled cooling crystallization*.

Determination of MSZW by the polythermal method is illustrated schematically in Figure 5.1. A solution of known concentration c_0 of solute at the saturation temperature T_0 (Point B) is cooled at a constant cooling rate R_L, from a temperature a few K above T_0 (Point A) to a temperature T_{lim} at which first crystallites are detected in the solution (Point C). The maximum supercooling $\Delta T_{max} = (T_0 - T_{lim})$ and the maximum concentration difference $\Delta c_{max} = (c_0 - c_{lim})$ are measures of MSZW. The supersaturation ln S created in the solution during cooling is defined in terms of supersaturation ratio $S = c_0/c$ and the maximum supersaturation ratio $S_{max} = c_0/c_{lim}$. During its cooling at a given rate

Nucleation and Crystal Growth: Metastability of Solutions and Melts, First Edition.
Keshra Sangwal.
© 2018 John Wiley & Sons, Inc. Published 2018 by John Wiley & Sons, Inc.

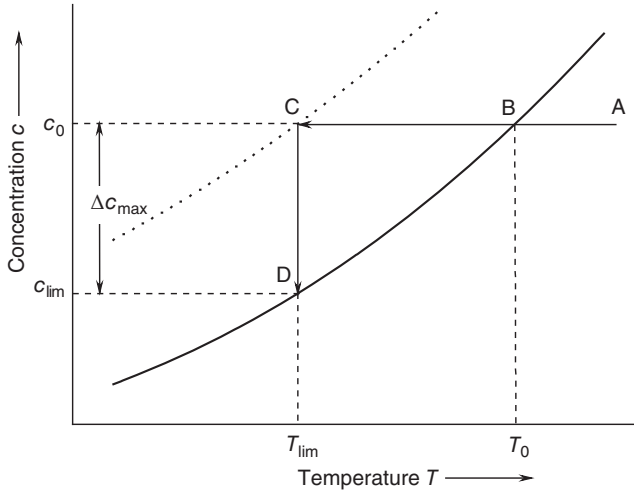

Figure 5.1 Schematic illustration of the basis of determination of the maximum supercooling ΔT_{max} in the polythermal method of metastable zone width. See text for details.

R_L from the saturation temperature T_0, the temperature T_{lim} of occurrence of crystallization is recorded by visual observation of appearance of crystallites in the solution (Akrap et al., 2010; Anuar et al., 2009; Haja Hameed et al., 2003; Kim, 2000; Li et al., 2005; Nývlt et al., 1985; Omar and Ulrich, 2007; Rajesh et al., 2001; Sahin et al., 2007; Sangwal and Wójcik, 2009; Sayan and Ulrich, 2001; Wohlgemuth et al., 2010) or sudden discontinuity in the temperature dependence of some property of the solution such as its electrical conductivity (Graber et al., 1999; Lyczko et al., 2002), ultrasonic velocity (Gürbüz and Özdemir, 2003; Marciniak, 2002; Titiz-Sargut and Ulrich, 2002), density (Marciniak, 2002; Sangwal and Wójcik, 2009), or turbidity of the solution (Graber et al., 1999; Marciniak, 2002; Poornachary et al., 2008; Taboada et al., 2003; Wierzbowska et al., 2007; Zhang et al., 2012), latent heat of crystallization using differential scanning calorimetry (DSC) (Myerson and Jang, 1995; Wierzbowska et al., 2007), and other sophisticated techniques based on measuring crystal size and its distribution like in-line video microscopy (Qu et al., 2006), focused beam reflectance measurements (FBRM) (Barrett and Glennon, 2002; Dang et al., 2007; Wang and Ching, 2006; Wang et al., 2008), and attenuated total reflectance Fourier-transform infrared (ATR FTIR) spectroscopy (Barrett et al., 2010; Danuwila et al., 1994, 1997; Groen and Roberts, 2004; Lewiner et al., 2001). From these studies it has been found that MSZW for a substance depends on a variety of factors such as saturation temperature, solvent used for the preparation of supersaturated solutions, the presence of impurities dissolved in the

solution, the presence of crystalline seeds in the solution, solution stirring, the cooling rate of solution from saturation temperature, and detection technique.

The techniques used for the study of cooling crystallization from melts are similar to those from solutions. Among the commonly used techniques for monitoring, the crystallization of fats, for example, is based on the measurement of crystallizing solid fat content and transmittance or absorbance of light. Pulsed nuclear magnetic resonance and latent heat of crystallization serve as measures of solid phase content, whereas turbidimetry and imaging of crystallites microscopically using polarized light serve as light scattering centers in the melt volume. Marangoni (2005) has surveyed the advantages and disadvantages of different techniques used in the crystallization of fats.

During the last five decades, voluminous literature has emerged on the determination of MSZW of various compounds in different solvents from measurements of the maximum supercooling ΔT_{max} using the polythermal method (Nývlt et al., 1985; Sangwal, 2011b). The experimental data of the maximum supercooling ΔT_{max} for solute–solvent systems have traditionally been analyzed until now as a function of cooling rate R_L using Nývlt's equation (5.6), proposed in 1968. Nývlt's equation contains two empirical parameters (i.e. nucleation order m and nucleation constant k_m), the physical significance of which has remained obscure until now. However, since 2008, several papers have been devoted to the understanding of the physical meaning of these empirical constants as well as explaining the effect of various experimental factors on the MSZW of different compounds from solutions.

In this chapter different approaches of interpretation of MSZW of solute –solvent systems are reviewed first and then the effect of impurities on the MSZW and some features of crystallization from melts are described and discussed. For a survey of the literature prior to 1985 on the MSZW of various solute–solvent systems and the effects of different individual factors such as solution saturation temperature, thermal history, crystallization detection method, mechanical stirring, additives, and solution volume, the reader is referred to the book by Nývlt et al. (1985). Brief reviews on the subject were published recently by Sangwal (2011a, b) and Sangwal and Sato (2012).

5.1 Theoretical Interpretations of MSZW

There are two types of approaches to explain the dependence of MSZW on various factors. The first type of approach assumes the formation of critically-sized 3D nuclei during the cooling of a solution below saturation temperature T_0 (Kubota, 2008; Nývlt, 1968; Sangwal, 2009a, b) but they differ in the way the nucleation rate J depends on the developed solution supersaturation ln S. Most of these approaches (Kubota, 2008; Nývlt, 1968; Sangwal, 2009b) assume that

the nucleation rate J is related to the maximum supersaturation $\ln S_{max}$ by simple power law (see Eq. (5.3)), while a recent approach (Sangwal 2009a, c, 2010) assumes that the nucleation rate J is described by the classical 3D nucleation theory. The second type of approach is based on the concept of overall crystallization involving progressive and instantaneous nucleation mechanisms (Kashchiev et al., 2010a, b).

5.1.1 Nývlt's Approach

Nývlt (1968) assumed that an excess solute concentration Δc is generated in the solution during its cooling by the supercooling ΔT according to the relation:

$$\Delta c = \left(\frac{dc}{dT}\right)_T \Delta T, \tag{5.2}$$

and that, in the vicinity of metastability, the nucleation rate J is related to the excess solute concentration Δc by the power-law relation:

$$J = k_m(\Delta c)^m, \tag{5.3}$$

where m is the apparent nucleation order, $(dc/dT)_T$ is the temperature coefficient of solubility at temperature T, and k_m is the nucleation constant, the value of which depends on the processes of formation and growth of stable 3D nuclei into visible entities and the experimental method used for the measurement of MSZW. From Eq. (5.2), one may express the rate of creation of excess solute concentration Δc as a function of cooling rate $R_L = \Delta T/\Delta t$ in the form:

$$J = \frac{\Delta c}{\Delta t} = \left(\frac{dc}{dT}\right)_T R_L. \tag{5.4}$$

The processes of creation of excess solute concentration Δc with cooling time (Curve 1) and detectable 3D nucleation in the vicinity of the maximum solute concentration Δc_{max} (Curve 2) are shown schematically in Figure 5.2. Schematic illustration of these processes has been given before by Nývlt et al. (1985) and Kim and Mersmann (2001). In the original version of Nývlt, the change in solute concentration is considered on mass basis, but Kim and Mersmann considered change in solute concentration in terms of the number of nuclei formed in the supersaturated solution of volume V.

It should be mentioned that Figure 5.2 also shows schematically a decay in Δc after attaining its maximum value Δc_{max} at time t_{in} (see Curve 1) and overall crystallization of solute by the formation of 3D nuclei and their subsequent growth (Curve 2). In the figure t_N and t_{in} indicate the moments of the onset and observation of 3D nuclei, respectively, whereas t_f denotes the time when the entire solute is crystallized. The detection limit of the crystallized mass at t_{in} is denoted by y^*.

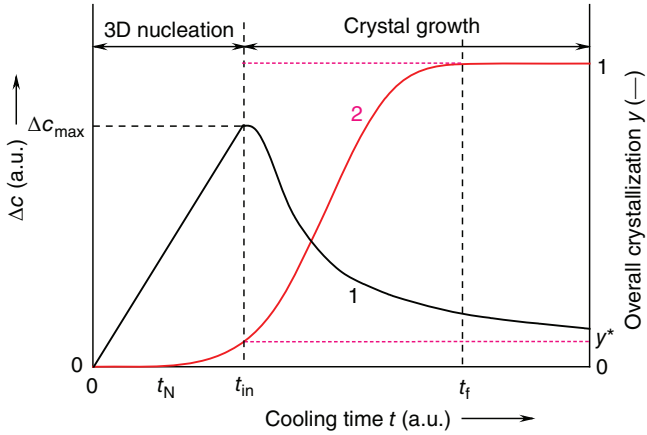

Figure 5.2 Schematic illustration of evolution of excess solute concentration Δc with cooling time (Curve 1) and overall crystallization of solute by the formation of 3D nuclei and their subsequent growth (Curve 2). Note an initial increase in excess solute concentration Δc and occurrence of 3D nucleation in the vicinity of metastability, followed by a decay in Δc. Times t_N and t_{in} show the moments of the onset and observation of 3D nuclei, respectively, whereas t_f denotes the time when the entire solute is crystallized. Detection limit of the crystallized mass is denoted by y^*.

Upon substituting the value of Δc from Eq. (5.2) in Eq. (5.3) and equating the nucleation rate J corresponding to the maximum excess solute concentration Δc_{max} given by the power-law relation (5.3) with that due to the rate of creation of excess solute concentration $\Delta c = \Delta c_{max}$ according to Eq. (5.4), one obtains

$$\Delta T_{max} = \left(\frac{dc}{dT}\right)_T^{(1-m)/m} \left(\frac{R_L}{k_m}\right)^{1/m}. \tag{5.5}$$

Taking logarithms on both sides of Eq. (5.5), upon rearrangement, one obtains

$$\ln \Delta T_{max} = \frac{1-m}{m} \ln\left(\frac{dc}{dT}\right)_T - \frac{1}{m} \ln k_m + \frac{1}{m} \ln R_L. \tag{5.6}$$

Equation (5.6) predicts a linear dependence of $\ln \Delta T_{max}$ on $\ln R_L$. This linear dependence enables to calculate the values of m and k_m because $(dc/dT)_T$ can be determined from solubility data.

It should be mentioned that Eq. (5.3) describes the dependence of nucleation rate J on the maximum concentration difference Δc_{max} at constant temperature T_{lim}, whereas Eq. (5.4) describes the relationship between J and linear cooling rate R_L from T_0 to T_{lim}, which results in a linear increase in the concentration difference Δc with time. Both of these equations refer to the situation when Δc_{max} and ΔT_{max} are attained during cooling at a constant cooling rate R_L.

However, in reality, nucleation occurs continuously even before $\Delta c_{\max}$ and $\Delta T_{\max}$ are reached.

5.1.2 Kubota's Approach

The MSZW of a system depends on the method of detection of the first nucleation events. Consequently, even for the same system the value of MSZW determined by different techniques is different. The above Nývlt model does not consider this feature of MSZW. To include this feature in the MSZW determined by cooling crystallization, Kubota (2008) proposed a model, which takes into account the number of detectable nuclei N_{det} in volume V after some time t:

$$\frac{N_{\text{det}}}{V} = \int_0^t J(t)\mathrm{d}t. \tag{5.7}$$

Assuming that the nucleation rate is given by (cf. Eq. (5.3))

$$J(t) = k_1(\Delta T)^{m^*}, \tag{5.8}$$

where $k_1 = k[(\mathrm{d}c_0/\mathrm{d}T)_T]^{m^*}$ with m^* as a constant, and the cooling rate $R_{\text{L}} = \mathrm{d}(\Delta T)/\mathrm{d}t$ (i.e. $\mathrm{d}t = \mathrm{d}(\Delta T)/R_{\text{L}}$), from Eq. (5.8), one obtains

$$\frac{N_{\text{det}}}{V} = \frac{k_1}{R_{\text{L}}}\int_0^{\Delta T_{\max}} (\Delta T)^{m^*} d(\Delta T) = \frac{k_1}{(m^*+1)R_{\text{L}}}(\Delta T_{\max})^{m^*+1}. \tag{5.9}$$

Taking logarithm on both sides and upon rearrangement, one gets

$$\ln(\Delta T_{\max}) = \frac{1}{m^*+1}\ln\left(\frac{N_{\text{det}}}{V}\right) - \frac{1}{m^*+1}\ln\left(\frac{k_1}{m^*+1}\right) + \frac{1}{m^*+1}\ln R_{\text{L}}. \tag{5.10}$$

According to this equation the plot of $\ln(\Delta T_{\max})$ against $\ln R_{\text{L}}$ is again a straight line with a slope $1/(m^*+1)$ and an intercept represented by the first two terms on the right-hand side of Eq. (5.10). However, the slope $1/(m^*+1)$ remains constant irrespective of the method of measurement of MSZW but delayed detection of onset of crystallization, represented by the first term on the right-hand side of Eq. (5.10), leads to a higher value of the intercept of the plot.

There is a close similarity in the forms of relations (5.6) and (5.10), which are derived on the assumption of the validity of power-law relations (5.3) and (5.8) between nucleation rate J and concentration difference Δc or temperature difference ΔT from the equilibrium state. In reality, there is poor justification of this assumption, especially when the so-called embryos reach the size of critically-sized nuclei according to the classical theory of 3D nucleation.

5.1.3 Self-Consistent Nývlt-Like Equation of MSZW

It is usually found that the quantity $(dc_0/dT)_T$ strongly depends on temperature T, but the quantity $(dc_0/dT)/T$ is practically temperature independent. Therefore, it is expected that, in contrast to the original Nývlt's equation (5.6), an expression relating dimensionless maximum supercooling $\Delta T_{max}/T_0$ with the cooling rate R_L describes the experimental $\Delta T_{max}(R_L)$ data better. Then from Eq. (5.5), one gets the relation (Sangwal, 2009b):

$$\ln\left(\frac{\Delta T_{max}}{T_0}\right) = \left[\frac{1-m}{m}\ln\left(\frac{dc_0}{T_0\,dT}\right) - \frac{1}{m}\{\ln k_m + (2m-1)\ln T_0\}\right] + \frac{1}{m}\ln R_L. \tag{5.11}$$

This expression is similar to the original Nývlt's equation (5.6). According to this equation, plots of $\ln(\Delta T_{max}/T_0)$ against $\ln R$ give slope $1/m$ and intercept equal to the term contained in the square brackets.

Sangwal (2009b) developed a self-consistent Nývlt-like equation, abbreviated as self-consistent approach (SCA), such that the logarithm term on the left-hand side of the final equation contains dimensionless parameter $\Delta T_{max}/T_0$. The key points in the derivation of the final equation of this approach are: (i) to redefine nucleation rate J as a power-law function of dimensionless supersaturation ratio S and (ii) to employ the theory of regular solutions to describe the temperature dependence of solubility.

Using the theory of regular solutions (see Section 2.3.1), one may write the relationship between the ratio of solution concentrations c_0 and c_{lim} corresponding to temperatures T_0 and T_{lim}, respectively, and supercooling ΔT in the form (cf. Figure 5.1):

$$\frac{c_0}{c_{lim}} = S_{max} = \exp\left(\frac{\Delta H_s}{R_G T_0}\frac{\Delta T_{max}}{T_{lim}}\right) = \exp\left(\frac{\lambda_s u_{max}}{1-u_{max}}\right), \tag{5.12}$$

where $\Delta T_{max} = (T_0 - T_{lim})$ such that $T_0 > T_{lim}$ and $c_0 > c_{lim}$, ΔH_s is the heat of solution, R_G is the gas constant, and the dimensionless maximum temperature difference u_{max} and the dimensionless heat of solution λ_s are defined as

$$u_{max} = \frac{\Delta T_{max}}{T_0}, \quad \lambda_s = \frac{\Delta H_s}{R_G T_0}. \tag{5.13}$$

Upon taking logarithm on both sides of Eq. (5.12), one obtains

$$\ln S_{max} = \frac{\Delta c_{max}}{c_0} = \left(\frac{\lambda_s u_{max}}{1-u_{max}}\right), \tag{5.14}$$

where $\Delta c_{max} = (c_0 - c_{lim})$. Assuming that the nucleation rate J is related to solution supersaturation $\Delta c/c_0$ and cooling rate $R_L = \Delta T/\Delta t = \Delta T_{max}/\Delta t_{max}$ (cf. Eq. (5.1)), from Eq. (5.14), one may write

$$J = f\frac{\Delta c_{max}}{c_0 \Delta t} = f\frac{\Delta c_{max}}{c_0 \Delta T}\frac{\Delta T}{\Delta t} = f\left(\frac{\Delta H_s}{R_G T_0}\right)\left(\frac{R_L}{T_{lim}}\right) = \frac{f\lambda_s}{T_0(1-u_{max})}R_L, \qquad (5.15)$$

where the constant f has units as nuclei/volume. The value of f is governed by aggregation and diffusion processes in the solution. Following Nývlt we assume that, in the vicinity of metastability, the nucleation rate J may be given by a power-law relation in the form:

$$J = K(\ln S_{max})^m, \qquad (5.16)$$

where the new constant $K = k_m/c_0^m$. Upon substituting the value of $\ln S_{max}$ from Eq. (5.14) in (5.16), one obtains

$$J = K\left(\frac{\lambda_s u_{max}}{1-u_{max}}\right)^m. \qquad (5.17)$$

Upon equating Eqs. (5.15) and (5.17), one gets

$$u_{max} = \left(\frac{f}{KT_0}\right)^{1/m}\left(\frac{\lambda_s}{1-u_{max}}\right)^{(1-m)/m} R_L^{1/m}, \qquad (5.18)$$

which, upon taking logarithms on both sides, gives

$$\ln u_{max} = \frac{1-m}{m}\ln\left(\frac{\lambda_s}{1-u_{max}}\right) + \frac{1}{m}\ln\left(\frac{f}{KT_0}\right) + \frac{1}{m}\ln R_L. \qquad (5.19)$$

Equation (5.19) may be written in the simplified form:

$$\ln u_{max} = \Phi + \beta \ln R, \qquad (5.20)$$

where Φ is the value of $\ln(\Delta T_{max}/T_0)$ when $\ln R_L = 0$, and is given by

$$\Phi = (\beta - 1)\ln\left(\frac{\lambda_s}{1-u_{max}}\right) + \beta\ln\left(\frac{f}{KT_0}\right). \qquad (5.21)$$

Equation (5.20) predicts a linear dependence of $\ln u_{max}$ on $\ln R_L$, with slope $\beta = 1/m$ and intercept Φ. The linear dependence (5.20) enables to calculate values of nucleation order m from the slope β and the term $\ln(f/KT_0)$ from the intercept because usually $\lambda_s/(1 - u_{max}) \approx \lambda_s$ and may be calculated from the solubility data of the investigated compound. The factor f may be calculated independently from the equilibrium solute concentration at temperature T_0, while the value of K depends on the supersaturation range where Eq. (5.16) holds.

Equation (5.20) is similar to the modified Nývlt's equation (5.11) based on the dimensionless quantity u_{max}, where the term $\ln(dc/dT)_T/T_0$ is replaced

by $\ln[\lambda_s/(1 - u_{max})]$ and the term $[\ln k_1 + (2m - 1)\ln T_0)] = \ln(f/KT_0)$. The term $\lambda_s/(1 - u_{max})$ has an additional advantage over the term $(dc/dT)_T/T_0$ in that it excludes the effect of saturation temperature T_0 on $(dc/dT)_T$.

For substances fairly-soluble in water, the typical value of $\lambda_s/(1 - u_{max}) = \Delta H_s/R_G T_{lim}$ lies between 2 and 5, and K is related to the preexponential factor J_0 of Eq. (2.27) of the classical theory of 3D nucleation, where J_0 is about 10^{26} molecules·m^{-3}·s^{-1} (see Kashchiev, 2000). The value of $\ln(K/J_0)$ decreases from about 18.4 at $\ln S = 0.1$ to 10 at $\ln S = 0.3$ (i.e. K decreases from 10^{34} to 10^{30} m^{-3}·s^{-1}); see Sangwal (2009b). This implies that the value of K significantly decreases with increasing supersaturation $\ln S$. Assuming that each molecule is incorporated into the growing crystallite, the upper limit of the factor f may be estimated from solute concentration c_0 in the saturated solution, i.e. $f \approx c_0 N_A$ (N_A is the Avogadro number equal to $6{\cdot}10^{23}$ mol^{-1}). For fairly-soluble substances in water, the typical equilibrium solution concentration c_0 at 303 K lies between 0.2 and 0.5 mol·dm^{-3}, which gives f equal to about 10^{29} molecules·m^{-3}.

The quantities $\lambda_s/(1 - u_{max})$ and f/KT_0 of Eq. (5.21) appear in logarithm terms. Therefore, contributions of $\ln[\lambda_s/(1 - u_{max})]$ and $\ln(f/KT_0)$ to the term Φ of Eq. (5.21) may be considered to be insensitive to the nature of solute, saturation temperature T_0, and type of nucleation during metastability. Thus, it may be concluded that the value of the term Φ of Eq. (5.21) for a system at saturation temperature T_0 is essentially determined by nucleation order $m = 1/\beta$ and nucleation constant K. The value of the nucleation constant K for a solute–solvent system at saturation temperature T_0, in its turn, is determined by solute concentration c_{max} and mutual interactions between ions/molecules leading to the formation of associates and aggregates in the solution.

5.1.4 Approach Based on the Classical Theory of 3D Nucleation

In this approach (Sangwal, 2009a), referred to as the approach based on the classical nucleation theory (CNT), the derivation of the relation between dimensionless maximum temperature decrease $u_{max} = \Delta T_{max}/T_0$ and cooling rate R_L is similar to the SCA described above and also employs the theory of regular solutions to describe the temperature dependence of solubility. However, instead of the power-law function of dimensionless supersaturation ratio S to define the 3D nucleation rate J, the classical theory of 3D nucleation is used. According to the classical theory, the rate J of formation of stable 3D spherical nuclei corresponding to the supersaturation ratio S_{max} may be given by (see Section 2.2)

$$J = J_0 \exp\left(-\frac{B}{\ln^2 S_{max}}\right), \tag{5.22}$$

where the preexponential factor J_0 is determined by the processes of association of molecules or ions present in the growth medium with the nuclei and their dissociation from these nuclei and the thermodynamic parameter B is given by

$$B = \kappa \left(\frac{\gamma \Omega^{2/3}}{k_B T_{lim}} \right)^3, \tag{5.23}$$

where κ is a numerical shape factor for the nuclei (e.g. $\kappa = 16\pi/3$ for spherical nuclei), γ is the effective solid–liquid interfacial energy, Ω is the volume of a solute molecule (i.e. molecular volume), k_B is the Boltzmann constant equal to R_G/N_A (N_A is the Avogadro number), and T_{lim} is the solution temperature when 3D nucleation occurs. Using Eq. (5.23) for B and Eq. (5.14) for $\ln S_{max}$ in Eq. (5.22), one obtains

$$J = J_0 \exp\left\{ -\left[\frac{\kappa \omega^3}{u_{max}^2 \lambda_s^2 (1 - u_{max})} \right] \right\}, \tag{5.24}$$

where we have defined the dimensionless interfacial energy as

$$\omega = \frac{\gamma \Omega^{2/3}}{k_B T_0}. \tag{5.25}$$

On equating Eqs. (5.15) and (5.24), one obtains

$$\exp\left\{ -\left[\frac{\kappa \omega^3}{u_{max}^2 \lambda_s^2 (1 - u_{max})} \right] \right\} = f \left(\frac{\lambda_s}{1 - u_{max}} \right) \frac{R_L}{J_0 T_0}, \tag{5.26}$$

which, upon taking logarithm on both sides and rearrangement, gives

$$\frac{1}{u_{max}^2 (1 - u_{max})} \approx u_{max}^{-2} = F - F_1 \ln R_L = F(1 - Z \ln R_L), \tag{5.27}$$

where $F = F_1/Z$, with

$$F_1 = \frac{\lambda_s^2}{\kappa \omega^3}, \tag{5.28}$$

$$Z = \frac{F_1}{F} = \ln \left[\frac{f \lambda_s}{J_0 T_0 (1 - u_{max})} \right] \approx \ln \left(\frac{f \lambda_s}{J_0 T_0} \right), \tag{5.29}$$

with dimensionless heat of dissolution λ_s and dimensionless interfacial energy ω given by Eqs. (5.13) and (5.25), respectively. According to Eq. (5.27), at a given constant saturation temperature T_0, the quantity $u_{max} = \Delta T_{max}/T_0$ increases with an increase in cooling rate R_L. This behavior has been observed for all of the systems investigated so far. Equation (5.27) predicts that the quantity $u_{max} = \Delta T_{max}/T_0$ decreases with an increase in saturation temperature T_0 and a decrease in cooling rate R_L. This general trend is also observed.

The main advantage of this approach is that the two parameters, i.e. the parameter J_0 associated with the kinetics of formation of nuclei in growth medium and the effective solid–liquid interfacial energy γ, of the CNT (see Eq. (5.22)) account for both homogeneous nucleation and heterogeneous nucleation caused by impurities or by existing seeds. In the case of heterogeneous nucleation, the value of the effective interfacial energy γ is lower than that in homogeneous nucleation, but in both cases the value of the effective interfacial energy γ has a well-defined physical background.

Equation (5.27) predicts that, at a given saturation temperature T_0, the quantity $u_{\max}^{-2}$ decreases linearly with an increase in $\ln R_L$, with slope F_1 and intercept F. It may be noted that the value of the slope F_1 depends on the dimensionless interfacial energy ω and the dimensionless heat of dissolution λ_s, while the intercept F depends on ω, λ_s, the kinetic factor J_0 associated with the integration of growth units to the growing nuclei, and on the factor f determined by aggregation and diffusion processes in the solution. Obviously, F_1 is determined by thermodynamic and solvation processes, while F is governed by thermodynamic and kinetic parameters as well as processes associated with the solvation of solute ions/molecules and their transport in the solution. However, it should be noted that the constant Z is not a dimensionless quantity. Instead, its value depends on the units of cooling rate R_L, but the term $Z\ln R_{L\infty}$, where $\ln R_{L\infty}$ refers to the extrapolated value of $\ln R_L$ when $u_{\max}^{-2} = 0$, is a constant quantity for a crystallizing system.

The order of the values of F_1 and F may be estimated independently. For substances fairly-soluble in water, the typical value of $\lambda_s = (\Delta H_s/R_G T_0)$ lies between 2 and 5, that of $\omega = (\gamma_{eff}\Omega^{2/3}/k_B T_0)$ between 0.2 and 0.7, the parameter $f \le 10^{29}$ molecules·m^{-3} (see Section 5.1.3), and $J_0 \approx 10^{26}$ m^{-3}·s^{-1} (cf. Kashchiev, 2000). If one takes $\omega = 0.2$, $\lambda_s = 5$, and $f = 10^{27}$ m^{-3}, one finds $F_1 \approx 200$, $F = 360$, and $Z = 0.6$.

5.1.5 Approach Based on Progressive 3D Nucleation

Kashchiev et al. (2010a) considered the early stages of crystallization occurring by the formation of stable 3D nuclei progressively and their subsequent growth during the cooling of solution at a constant rate (see Curve 2 in Figure 5.2) and derived the relation for volume fraction $y = V_c/V$ of crystallites (where V_c is the total volume of crystallites in the volume V of the solution when the crystallites do not contact each other) in the form:

$$y(u) = K_{\nu,d}\left(\frac{u^3}{2\omega_0}\right)^{(n+1)\nu d+1} \exp\left[-\frac{\omega_u}{(1-u)u^2}\right], \tag{5.30}$$

with the dimensionless constant

$$K_{\nu,d} = \frac{\Gamma[(n+1)\nu d+1]}{(n+1)^d}\kappa\lambda^{n\nu d} J_0 K_G^{\nu d}\left(\frac{T_0}{R_L}\right)^{\nu d+1}, \tag{5.31}$$

$$\omega_u = \kappa\omega^3 u = \kappa\left(\frac{\gamma\Omega^{2/3}}{k_B T_0}\right)^3 \frac{\Delta T}{T_0}, \tag{5.32}$$

where λ is the heat of crystallization ($\lambda = \Delta H_s = k_B T_0 \lambda_s$; see Eq. (5.13)), the dimensionless temperature difference $u = \Delta T/T_0$, Γ is the gamma function, $K_G^{\nu d}$ is the kinetic constant for growth, the exponent ν is equal to 0.5 and 1 for nucleation occurring by volume diffusion and surface reactions, respectively, n is the growth exponent lying between 1 and 2 when crystallites grow by normal- or spiral-growth mechanism, and d is the dimensionality of growing crystallites (see Section 3.9). Equation (5.30) is valid when

$$u < 0.1, \quad \lambda u < 1, \quad 0 < \left(\frac{2\omega_u}{3}\right)^{1/2}. \tag{5.33}$$

In the case of 3D crystallites with $d = 3$ and $\nu = 1$, from Eqs. (5.30) and (5.31), one gets

$$y(u) = K_{1,3}\left(\frac{u^3}{2b}\right)^{3n+4} \exp\left[-\frac{b}{(1-u)u^2}\right], \tag{5.34}$$

$$K_{1,3} = \frac{\Gamma(3n+4)}{(n+1)^3}\kappa\lambda^{3n} J_0 K_G^3 \left(\frac{T_0}{R_L}\right)^4. \tag{5.35}$$

However, in the case when $d = 0$, Eq. (5.30) describes the total number N of crystallites in the form:

$$N(u) = K_N\left(\frac{u^3}{2\omega_u}\right) \exp\left[-\frac{\omega_u}{(1-u)u^2}\right], \tag{5.36}$$

where the constant

$$K_N = \frac{V J_0 T_0}{R_L}, \tag{5.37}$$

with the crystallite volume $V = \kappa$.

In the case of maximum supercooling when $u = u_{max}$, from Eqs. (5.36) and (5.37), one obtains

$$\ln u_{max} - \frac{a_2}{a_1(1-u_{max})\,u_{max}^2} = \frac{1}{a_1}\ln R_L - \frac{1}{a_1}\ln R_0^*, \tag{5.38}$$

where the constants $a_1 > 0$, $a_2 > 0$, and $R_0^* > 0$. For u_{max} determined by y, they are given by

$$a_1 = 3 + \frac{3n\nu d}{\nu d + 1}, \quad a_2 = \frac{\omega_u}{\nu d + 1}, \tag{5.39}$$

$$R_0^* = T_0 \left\{ \frac{\Gamma[(n+1)\nu d + 1]}{(n+1)^d} \frac{\kappa \lambda^{n\nu d} J_0 K_G^{\nu d}}{(2\omega_u)^{(n+1)\nu d + 1} y^*} \right\}^{1/(\nu d + 1)}, \tag{5.40}$$

where y^* is the detection limit for the volume fraction y of crystallites by a particular experimental technique. However, for $u_{\max}$ determined by N when $d = 0$, they are given by

$$a_1 = 3, \quad a_2 = \omega_u, \tag{5.41}$$

$$R_0^* = T_0 \frac{VJ_0}{2\omega_u N_{\det}}. \tag{5.42}$$

In the initial stages of crystallization when the crystallites are expected to possess a high density of growth sites (kinks) on their surfaces and the supply of solute ions/molecules to the growing nuclei occurs by bulk diffusion, it is reasonable to take $n = 1$, $\nu = ½$, and $d = 3$ for 3D crystallites. Then

$$a_1 = 4.8, \quad a_2 = \frac{\omega_u}{4}. \tag{5.43}$$

When the crystallites attain visible dimensions (for example, by coagulation) without growth such that $u_{\max}$ is determined by N when $n = 0$, $d = 3$, and $\nu = 1/2$, Eq. (5.39) gives

$$a_1 = 3, \quad a_2 = \frac{\omega_u}{2.5}. \tag{5.44}$$

From the above considerations it may be concluded that the progressive nucleation approach predicts $3 \le a_1 \le 7.5$ when crystallites grow by the normal- and spiral growth mechanisms and that the lowest value equal to 3 corresponds to the situation when the crystallites or aggregates of nuclei do not grow. However, when crystallites grow by a two-dimensional (2D) nucleation mechanism, the growth exponent n can attain much higher values (see Section 3.6.1). Then, a_1 can have values exceeding 7.5. From Eq. (5.39) it also follows that, irrespective of the mechanism by which crystallites attain visible dimensions, a_1 increases at the expense of a decrease in a_2.

Depending on whether the first or the second term on the left-hand side of Eq. (5.38) is constant in a particular range of cooling rate R_L, two cases arise. When the second term is constant, Eq. (5.38) takes the form:

$$\ln u_{\max} = \left[\frac{a_2}{a_1 (1 - u_{\max})\, u_{\max}^2} - \frac{1}{a_1} \ln R_0^* \right] + \frac{1}{a_1} \ln R_L, \tag{5.45}$$

which is similar to self-consistent Nývlt-like Eq. (5.20) with $a_1 = m$. However, when the first term is constant, one finds

$$\frac{1}{(1 - u_{\max})\, u_{\max}^2} \approx \frac{1}{u_{\max}^2} = \frac{1}{a_2} \left[\left(a_1 \ln u_{\max} + \ln R_0^* \right) \right] - \frac{1}{a_2} \ln R_L. \tag{5.46}$$

This equation is similar to Eq. (5.27) of the approach based on the classical theory of 3D nucleation, with $a_2 = m$. In this case, m is related to the interfacial energy γ and the dimensionless maximum temperature difference $u_{\max} = \Delta T_{\max}/T_0$ (cf. Eq. (5.32)).

5.1.6 Approach Based on Instantaneous 3D Nucleation

Kashchiev et al. (2010b) also considered the case of instantaneous nucleation in which all crystallites appear at a particular time and subsequently grow in the absence of newly developing nuclei. These authors derived the relation for volume fraction of crystallites in the form:

$$y(u) = K^*_{\nu,d}\left[u^{(n+1)\nu} - u_0^{(n+1)\nu}\right]^d, \tag{5.47}$$

where the dimensionless parameter is

$$K^*_{\nu,d} = \frac{\kappa c_0 (\lambda^n K_G T_0/R_L)^{\nu d}}{4(n+1)^d}, \tag{5.48}$$

where κ is a shape factor for the crystallites, c_0 is the solute concentration, u_0 is a critical relative supercooling for crystallization at time $t_0 < t_{\max}$ corresponding to $u_{\max}$, and K_G is the kinetic constant for growth. When $y(u) = y(u_{\max})$ and $u_{\max} \gg u_0$ such that $u_{\max}^{(n+1)\nu} \gg u_0^{(n+1)\nu}$, Eq. (5.47) reduces to the form:

$$\ln u_{\max} = \frac{1}{n+1}\ln R_L - \frac{1}{n+1}\ln R_0^{**}, \tag{5.49}$$

where the constant

$$R_0^{**} = \left[\frac{\kappa c_0}{(n+1)^d y^*}\right]^{1/\nu d} \lambda^n K_G T_0. \tag{5.50}$$

Since $1 < n < 2$ when crystallites grow by normal- and spiral-growth mechanisms, one obtains the traditional m in Nývlt's equation to lie between 2 and 3.

5.2 Experimental Results on MSZW of Solute–Solvent Systems

Some typical examples of solubility and supersolubility curves for different compounds in water solvent were presented before in Figure 2.22. It was mentioned there that the trends of different supersolubility curves are similar to those of solubility curves, with the difference that they either diverge, converge, or run parallel to the solubility curve for a given system with increasing

temperature T, which suggests that supersolubility curves may be described by an empirical equation similar to that of regular solutions. In fact, it was shown that the diverse trends of supersolubility curves may be reproduced by changing the parameter A but their diverging trend requires changes in both A and ΔH_s, and that the supersolubility curves running parallel to the solubility curve also require changes in the values of both A and ΔH_s. However, the reproduction of different trends in terms of the parameters A and ΔH_s is not based on any sound theoretical interpretation.

In this section the data of MSZW of different compounds are examined from the standpoint of different theoretical approaches presented above. For the analysis the published experimental data of maximum temperature difference ΔT_{max} as a function of cooling rate R_L of different solute–solvent systems, the following 12 compounds in appropriate solvents were selected (see Table 5.1): Potassium tetraborate tetrahydrate (KTB) (Sahin et al., 2007), ammonium sulfate in the presence and absence of seeds (ASF+ and ASF–, respectively) (Nývlt et al., 1985), sodium bichromate dihydrate (NaBC) (Wang et al., 2016), L(+)-ascorbic acid (LAA) (Wierzbowska et al., 2007), keto-1,2,3,4-tetrahydro-6-methylcarbazole (KTMC) (Correla et al., 2006), phosphoric acid (Ma et al., 2009), 3-nitro-1,2,4-triazol-5-one (NTO) (Kim, 2000; Kim and Kim, 2001; Kim and Mersmann, 2001), 1,3-dipalmitoyl-2-oleoylglycerol (POP) (Smith et al., 2005), tripalmitoylglycerol (PPP) (Smith et al., 2005), *RS*-tartaric acid (*RS*-TA) (Zhang et al., 2012), and *R*- and *RS*-4-hydroxy-2-pyrolidone (*R*-HPD and *RS*-HPD) (Wang and Ching, 2006; Wang et al., 2008). KTB is used in lubrication oil, disinfectant, and detergent industries

Table 5.1 Selected solute–solvent systems and values of their heat of solution.

Compound	Solvent	ΔH_s (kJ·mol^{-1})	Compound	Solvent	ΔH_s (kJ·mol^{-1})
KTB	Water	18.1	KTMC	Acetone	22.4
ASF	Water	6.3	*R*-HPD	Isopropanol	23.0
NaBC	Water	7.54	*RS*-HPD	Isopropanol	28.5
H_3PO_4	Water	5.90	NTO	Water	31.6
DL-TA	Water	25.8		Water/NMP (0.125)	13.63
LAA	Water/MeOH/ EtOH	13.2		Water/NMP (0.333)	10.80
PPP	Acetone	194.2		Water/NMP (0.556)	9.67
POP	Acetone	133.0			

(Sahin et al., 2007), NaBC is a strong oxidizing agent and is used as a corrosion inhibitor and in the manufacture of other chemicals, LAA is the popular vitamin C, *RS*-TA is an important and versatile organic acid used, among others, in carbonated beverages and effervescent tablets, KTMC is a useful starting material for the synthesis of antibacterial and antifungal agents and antidepressant drug (Correla et al., 2006), NTO is an explosive (Kim, 2000; Kim and Kim, 2001), PPP and POP are popular fats contained in palm oil (Smith et al., 2005), while HPD is a versatile chiral intermediate for the synthesis of several biologically active compounds (Wang et al., 2008).

The following topics are discussed: (i) Relationship between dimensionless cooling $u_{max} = \Delta T_{max}/T_0$ and cooling rate R_L, (ii) discussion of relationships between $-\Phi$ and $\ln F/2$ and between β and Z, (iii) comments on the temperature dependence of the dimensionless parameter F_1 of the approach based on the classical theory of 3D nucleation and the role of heat of dissolution ΔH_s and crystal–solvent interfacial energy γ, (iv) analysis of the temperature dependence of parameters F and Φ, and (iv) nature of the nucleation order m reported for different systems.

5.2.1 Dependence of Dimensionless Supercooling on Cooling Rate

Figure 5.3 presents examples of the dependence of dimensionless maximum supercooling $u_{max} = \Delta T_{max}/T_0$ with cooling rate R_L for potassium tetraborate (KTB), 3-nitro-1,2,4-triazol-5-one (NTO), and H_3PO_4 aqueous solutions saturated at different temperatures. It may be noted that u_{max} increases practically linearly with increasing R_L in the case of KTB–water system (Figure 5.3a), but u_{max} increases steeply first, followed by a progressively slow increase with an increase in R_L in the case of NTO–water and H_3PO_4–water systems (Figure 5.3b and c). Trends of plots of u_{max} against R_L similar to those of Figure 5.3 are observed for all solute–solvent systems in which crystallization of a particular phase takes place. A linear dependence of u_{max} on R_L occurs in a narrow range of R_L. The highest value of u_{max} is about 0.08 for the KTB–water system, about 0.03 for the NTO–water system, and about 0.01 for the H_3PO_4–water system. In most of the cases $u_{max} < 0.1$, but u_{max} reaching about 0.2 has also been observed for some systems such as NTO–water/NMP, where NMP denotes *N*-methyl-2-pyrrolidone (Sangwal, 2011a). From the plots of u_{max} against R_L of Figure 5.3, it may be noted that for a given cooling rate R_L the value of u_{max} decreases for KTB–water and NTO–water systems and that for the H_3PO_4–water system increases with an increase in the saturation temperature T_0.

It is found that the plots of $\ln u_{max}$ against $\ln R_L$ indeed show a linear dependence for the entire data of different systems, as predicted by Eq. (5.20). Figure 5.4 shows examples of plots of $\ln u_{max}$ against $\ln R_L$ for KTB–water, NTO–water, and H_3PO_4–water systems for solutions saturated at different temperatures. The best-fit values of the constants Φ and β of the plots are listed in

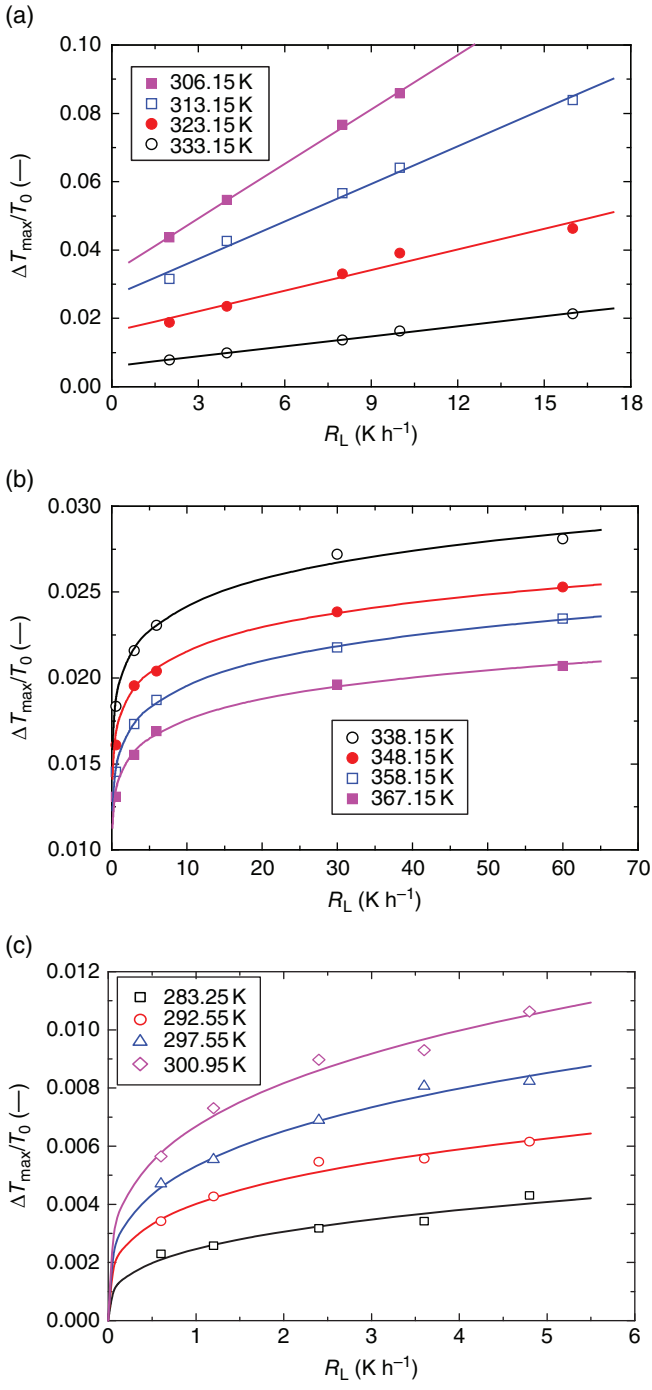

Figure 5.3 Examples of the dependence of dimensionless maximum supercooling $u_{max} = \Delta T_{max}/T_0$ with cooling rate R_L for different systems: (a) KTB–water, (b) NTO–water, and (c) H_3PO_4–water. *Source:* Original data from (a) Sahin et al. (2007), (b) Kim and Mersmann (2001), and (c) Ma et al. (2009).

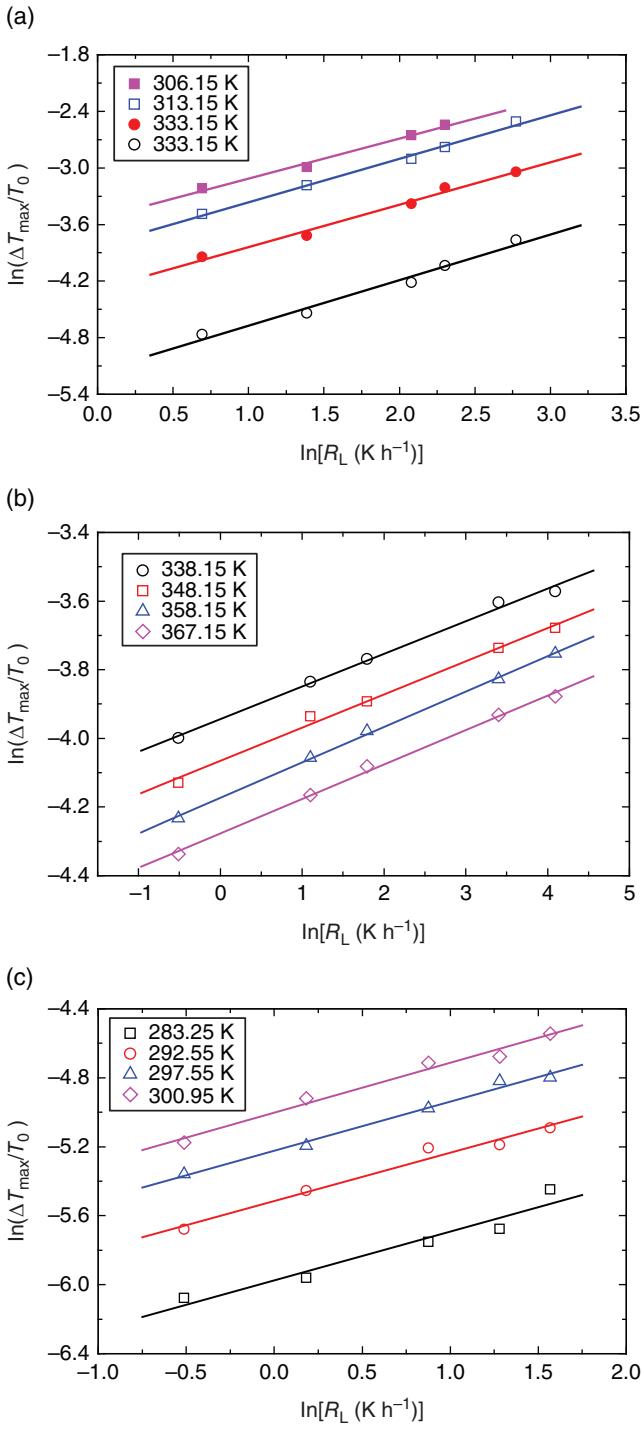

Figure 5.4 Plots of ln u_{max} against ln R_L for (a) KTB–water, (b) NTO–water, and (c) H_3PO_4–water systems of different saturation temperatures T_0 according to Eq. (5.20). *Source:* Adapted from (a and b) Sangwal (2009b) and (c) Sangwal (2010). (a and b) Copyright (2009), with permission from Wiley, and (c) Copyright (2010), with permission from Elsevier.

Table 5.2. Figure 5.5 presents plots of u_{max}^{-2} against $\ln R_L$ for the above three systems, according to Eq. (5.27). The plots of u_{max}^{-2} at various saturation temperatures T_0 against $\ln R_L$ also reveal the predicted linear dependence for many solute–solvent systems, as seen for KTB–water and H_3PO_4–water systems (Figure 5.5a and c). However, in some systems the $u_{max}^{-2}(\ln R_L)$ data show negative curvatures (i.e. have lower values) from the linear dependence in the central parts of the plots. Figure 5.5b illustrates a typical example of this behavior from the experimental $u_{max}(R_L)$ data for the NTO–water system for different temperatures as a function of as-applied cooling rate R_L but the fit is improved when a corrected cooling rate R_L^*, such that $R_L^* = (R_L - \Delta R_L)$ with a threshold cooling rate $\Delta R_L > 0$, is used in the plots. In the case of the NTO–water system, the threshold cooling rate $\Delta R_L \approx 0.5\ \mathrm{K{\cdot}h^{-1}}$. The best-fit parameters of the plots are included in Table 5.2. Physically, ΔR_L corresponds to the situation when a system

Table 5.2 Values of constants of Eqs. (5.20) and (5.27) for three selected systems.

		Eq. (5.20)				Eq. (5.27)			
System	T_0 **(K)**	$-\Phi$	β	m	R^2	F **(10^3)**	F_1 **(10^2)**	Z	R^2
KTB–water[a,b]	306.15	3.54	0.424	2.38	0.995	0.686	0.224	0.356	0.997
	313.15	3.83	0.461	2.17	0.997	1.217	0.414	0.340	0.976
	323.15	4.29	0.449	2.22	0.994	3.527	1.186	0.336	0.985
	333.15	5.16	0.483	2.08	0.989	20.54	6.994	0.341	0.991
NTO–water[a,b]	338.15	3.94	0.095	10.5	0.997	2.656	0.371	0.140	0.984
	—	—	—	—	—	(2.353)[c]	(0.276)	(0.117)	(0.998)
	348.15	4.07	0.097	10.3	0.997	3.397	0.483	0.142	0.977
	—	—	—	—	—	(3.007)	(0.362)	(0.120)	(0.999)
	358.15	4.17	0.103	9.7	0.999	4.199	0.621	0.148	0.985
	—	—	—	—	—	(3.693)	(0.462)	(0.125)	(0.999)
	367.15	4.27	0.100	10.0	0.998	5.176	0.753	0.146	0.982
	—	—	—	—	—	(4.563)	(0.562)	(0.123)	(0.998)
H_3PO_4–water[d]	283.25	5.97	0.283	3.53	0.969	15.91	6.381	0.401	0.994
	292.55	5.51	0.280	3.57	0.987	6.544	2.790	0.426	0.967
	297.55	5.22	0.286	3.50	0.994	3.611	1.521	0.421	0.990
	300.95	5.00	0.289	3.46	0.989	2.356	1.028	0.436	0.964

[a] From Sangwal (2009a).
[b] From Sangwal (2009b).
[c] Values in parentheses refer to best fit for corrected cooling rate R_L^*.
[d] From Sangwal (2010).

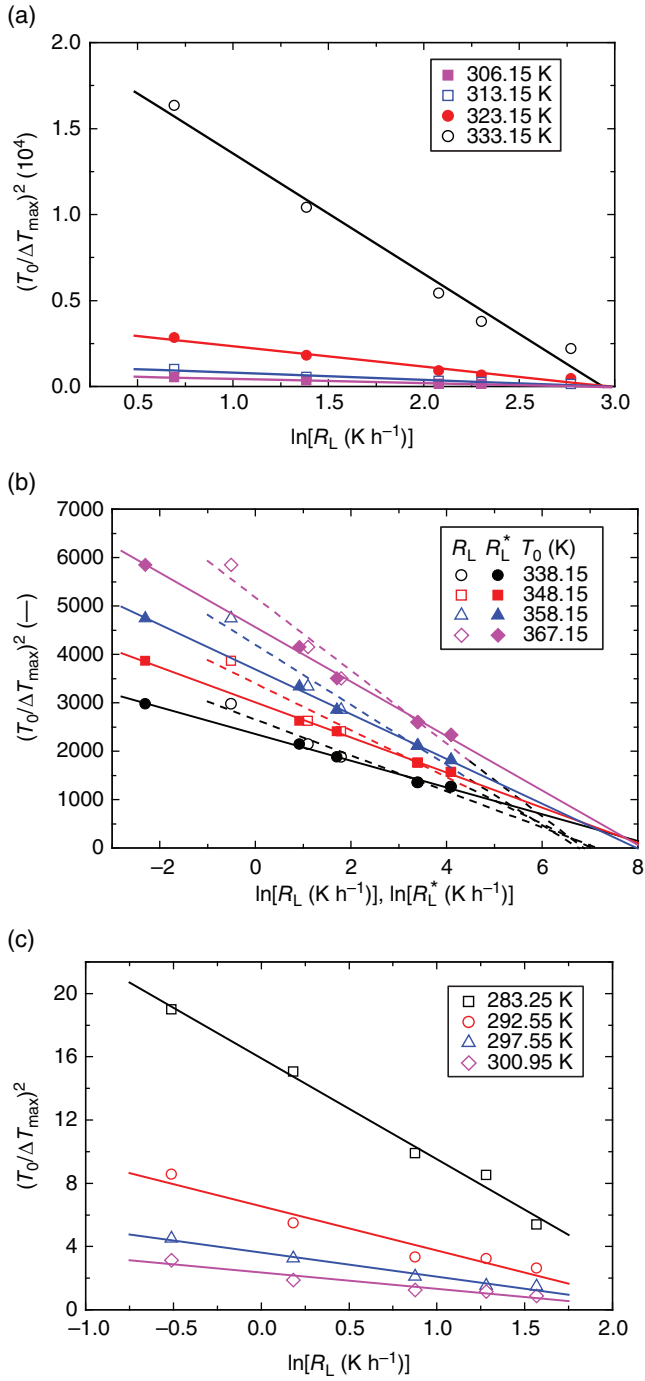

Figure 5.5 Plots of (a) u_{max}^{-2} against ln R_L for (a) KTB–water, (b) NTO–water, and (c) H_3PO_4–water systems of different saturated temperatures T_0 according to Eq. (5.27). In (b) dashed and solid lines present data for uncorrected R_L and corrected R_L^*, respectively. *Source:* Reproduced from (a and b) Sangwal (2009a) and (c) Sangwal (2010). (a and b) Copyright (2009), with permission from American Chemical Society, and (c) Copyright (2010), with permission from Elsevier.

begins to respond to the cooling procedure and is associated with the setting up of a thermal equilibrium between the solution and the environment.

From Table 5.2, the following features may be noted:

1) The slope β of the $\ln u_{max}$ against $\ln R_L$ plots according to Eq. (5.20) for a particular compound is practically independent of saturation temperature T_0 but the values of β for different compounds are different. Similarly, the parameter Z of the plots of u_{max}^{-2} against $\ln R_L$ according to Eq. (5.27) for a particular compound is practically independent of T_0 but the values of Z for different compounds are different.
2) The parameter $-\Phi$ for different compounds depends on solution temperature T_0 but the trends of increase in its value on solution temperature T_0 for different compounds are different. Dependence of the parameter F on T_0 for different compounds also shows trends similar to those of $-\Phi$. Among the different systems mentioned above, the values of $-\Phi$ and F were observed to decrease with increasing T_0 for most of the compounds (see Figure 5.3a and b) but their values increase with increasing T_0 for H_3PO_4–water and *RS*-TA–isopropanol systems (Figure 5.3c).

It should be noted that the value of F obtained from plots of u_{max}^{-2} against $\ln R_L$ for a given solute–solvent system according to Eq. (5.27) is not uniquely defined because of the approximation $\left[u_{max}^2(1-u_{max})\right]^{-1} = u_{max}^{-2}$, which in fact gives the slope $(1 - u_{max})F_1 < F_1$ determined by Eq. (5.28). The constant Z also contains the $(1 - u_{max})$ term but small variations in its value do not change Z because all quantities defining it are contained in the logarithm term. Therefore, the value of the intercept F is mainly affected by changes in F_1. Since usually the ratio $u_{max} < 0.1$, the approximation $\left[u_{max}^2(1-u_{max})\right]^{-1} \approx u_{max}^{-2}$ leads to a decrease in the value of u_{max}^{-2} and an increase in the value of F_1 by less than 10%. Therefore, for practical purposes it is sufficient to use Eq. (5.27) for the analysis of the experimental $u_{max}(R_L)$ data.

It is well known (see Section 2.5) that the solubility of different compounds increases with a decrease in the solid–liquid interfacial energy γ. Therefore, a decrease in γ also means a decrease in the dimensionless interfacial energy ω of Eqs. (5.28) and (5.25) and an increase in the values of β and Z. The higher the solubility of different compounds in a given solvent, the lower are the values of β and Z. Thus, the values of β and Z for a compound are intimately connected with its solubility in a solvent.

It is a general observation that the value of m obtained from the experimental $u_{max}(R_L)$ data for different solute–solvent systems usually exceeds 3. The observed value of m exceeding about 3 for different systems indicates that crystallization in these systems occurs by the progressive nucleation mode (see Section 5.2.7).

5.2.2 Effect of Detection Technique on MSZW

It was observed above that intercepts Φ and F and slopes β and Z of Eqs. (5.20) and (5.27) have characteristic values for a given system of known saturation temperature T_0. However, it is frequently observed that the values of the above quantities depend on the detection technique. Figure 5.6 shows a typical

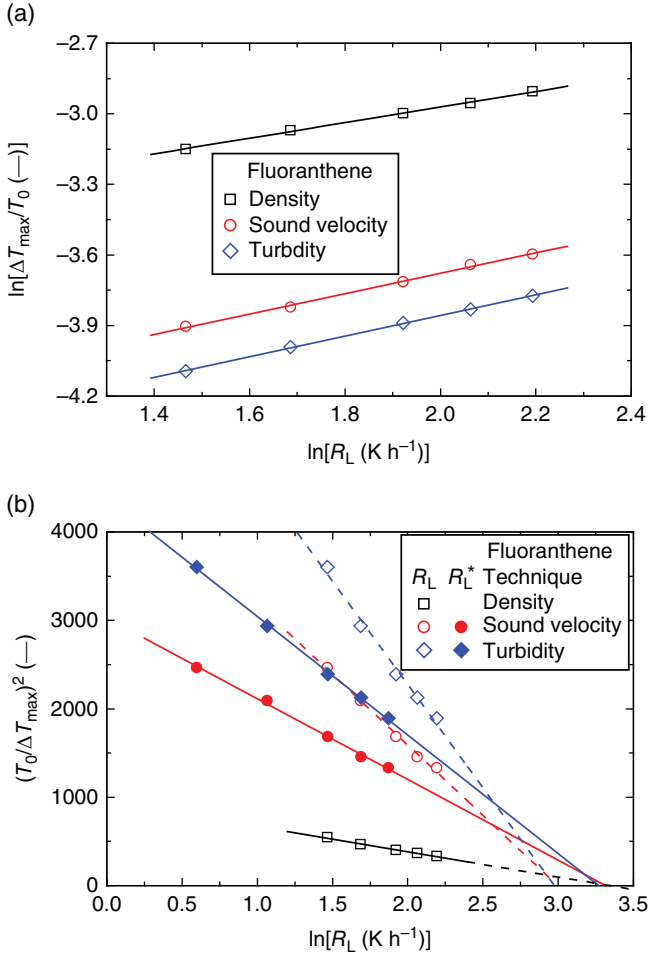

Figure 5.6 Plots of (a) $\ln u_{max}$ and (b) u_{max}^{-2} against $\ln R_L$ for the crystallization of fluoranthene–trichloroethylene system detected by density, ultrasound velocity, and turbidity measurements. Solution saturation temperature $T_0 = 306.57 \pm 2.16$ K and cooling rate R_L between 4.32 and 9 K·h^{-1}. In (b) filled points represent data with corrected $R_L^* = R_L - \Delta R_L$ ($\Delta R_L = 2.5$ K·h^{-1}), whereas dashed and solid lines represent best fit of the data. *Source:* Original data from Marciniak (2002).

example of plots of (a) $\ln u_{max}$ and (b) u_{max}^{-2} against $\ln R_L$, drawn from the data of maximum temperature difference ΔT_{max} as a function of cooling rate R_L, reported by Marciniak (2002), according to Eqs. (5.20) and (5.27), respectively, for the crystallization of a fluoranthene–trichloroethylene system detected by density, ultrasound velocity, and turbidity measurements. It may be seen from Figure 5.6a that the largest MSZW, as reflected by the value of Φ, is observed by the density measurement and the lowest by the turbidity method, but the slope β is the lowest from density measurements and the highest from the turbidity measurements, with the values of β differing by about 10%. Obviously, the values of the intercept Φ of the plots are affected relatively more than β by the MSZW detection technique. The same inference may be made from Figure 5.6b, which shows roughly the same $Z \approx 0.30$ independent of the detection technique.

The study of MSZW of POP solutions in acetone saturated at three different temperatures T_0 by turbidimetry and growth exotherms by Smith et al. (2005) revealed that ΔT_{max} recorded by growth exotherms was always greater than that obtained by turbidimetry. Analysis of these data showed (Sangwal and Smith, 2010) that the values of $\beta = 1/m$ and Z, although relatively insensitive to saturation temperature T_0, depend on the technique used for the measurement of maximum supercooling ΔT_{max} for a solute–solvent system of a particular saturation temperature T_0. For POP, the value of β calculated from data obtained using turbidimetry is 0.062 (i.e. $m = 16.2$) but its value calculated from data obtained by growth exotherms is 0.069 (i.e. $m = 14.5$).

According to Eqs. (5.6) of Nývlt's approach, (5.10) of Kubota's approach, and (5.20) of the self-consistent Nývlt-like equation, the value of the nucleation order m or $m^* + 1$, as determined from the slopes of the plots of $\ln(\Delta T_{max})$ or $\ln(\Delta T_{max}/T_0)$ against $\ln R_L$, is independent of the method of detection of crystallization event for a system. The above relations contain the quantities k_m, N_{det}, and k_1, and $(1 - u_{max})$ and K, which are affected by the detection method. One expects that a technique that detects delayed crystallization event (i.e. higher ΔT_{max}) should lead to changes in the above quantities such that the intercept of the plots is increased. However, since all of these quantities in the above equations appear in the logarithm terms, the changes in the intercept, represented by cooling-rate independent quantity Φ, are likely to be relatively small. As discussed in the next section, this cooling-rate independent quantity Φ is related to cooling-rate independent quantity $(u_{max})_0 = (\Delta T_{max}/T_0)_0 = \exp\Phi = F^{-1/2}$. Therefore, the above arguments can also be employed to explain the effect of detection technique from consideration of Eq. (5.27) and to find a connection between $\beta = 1/m$ and Z.

The main limitation of the above approaches is that they do not take into account the influence of growth of 3D nuclei into crystallites detectable by a detection technique. This aspect is included in the approach involving the formation of 3D nuclei progressively and their simultaneous growth into

crystallites of different dimensionalities d by diffusion or mass transfer of solute molecules (Section 5.1.5). As noted before, the value of m for a solute–solvent system is relatively insensitive to saturation temperature T_0. This is indeed predicted by Eq. (5.38) of the approach based on progressive nucleation when the crystallites of a substance have the same dimensionality and grow by the same mechanism (i.e. n, ν, and d) and the interfacial energy γ of the system remains unchanged; see Eq. (5.39). Equation (5.38) also predicts the effect of detection technique through the R_0^* term. The lowest value of m predicted by this equation is 3 when $d = 0$. However, when nuclei grow into crystallites, the parameters a_1 and a_2 of Eq. (5.38) determine the values of $a_1 = m$ and $a_2 = 1/Z$, depending on whether the first or the second term on the right-hand side of Eq. (5.38) is dominant.

5.2.3 Relationships between β and Z and between Φ and F

Figure 5.7 shows plots of parameter β of Eq. (5.20) against T_0^{-1} for different compound–solvent systems, whereas Figure 5.7b shows the $\beta\left(T_0^{-1}\right)$ data for NTO in water/NMP mixtures. Figure 5.8 shows plots of parameter Z of Eq. (5.27) against T_0^{-1} for different compound–solvent systems but in Figure 5.8b the $Z\left(T_0^{-1}\right)$ data for NTO in water–NMP mixtures are presented. From these figures it may be noted that: (i) the parameter β has different values between 0.03 and 0.8 and Z between 0.06 and 0.45 for different solute–solvent systems but $\beta \neq Z$ for a particular system and (ii) the parameters β and Z are independent of T for most of the systems but in the case of NTO in water/NMP mixtures, their values slowly decrease with increasing T_0^{-1}.

Figure 5.9a and b shows plots of the experimental data of β/Z against T_0^{-1} for different compounds and NTO in water/NMP mixtures, respectively, whereas the different trends are summarized in Table 5.3. It may be noted from the plots that: (i) the value of the ratio β/Z for NTO–water/NMP mixtures decreases with increasing T_0^{-1}, and (ii) the value of the ratio β/Z for other systems practically remains independent of T_0^{-1} and is characteristic for an individual system.

Figure 5.10a and b shows plots of $-2\Phi/\ln F$ against T_0^{-1} for different compounds and NTO in water–NMP mixtures, respectively, whereas the different trends are summarized in Table 5.4. From the plots and Table 5.4 it may be noted that: (i) the value of the ratio $-2\Phi/\ln F$ lies between 1 and 1.8 for different compounds, (ii) the value of the ratio $-2\Phi/\ln F$ essentially remains unity and independent of T_0^{-1} for some systems while it increases with increasing T_0^{-1} for others, and (iii) in the latter case, the slope $(-2\Phi/\ln F)/T_0^{-1}$ increases with increasing value of the ratio $-2\Phi/\ln F > 1$, the maximum increase in the slope taking place for KTB–water and *R*-HPD–isoproponol systems.

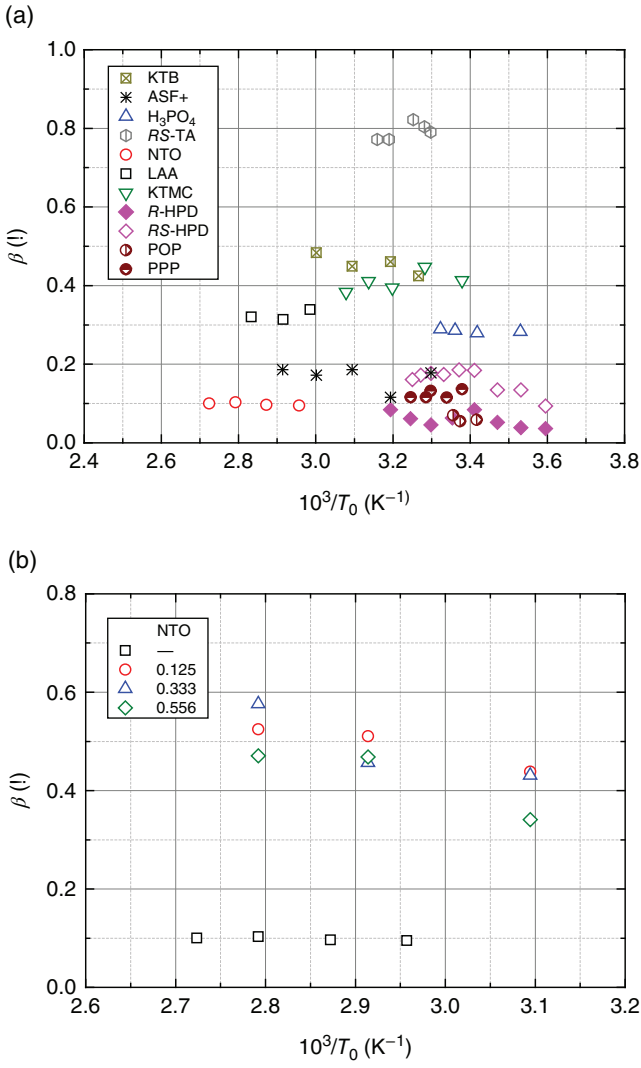

Figure 5.7 Plots of parameter β of Eq. (5.20) against T_0^{-1} for (a) different compound–solvent systems and (b) NTO in water/NMP mixtures. In (b) NMP content in the water/NMP mixture is given in the inset.

In order to explain the above features, we refer to Eqs. (5.20) and (5.27), which appear entirely different from each other. However, this apparently different appearance may be understood by taking the logarithm of Eq. (5.27) written in the form of Eq. (5.20), i.e.

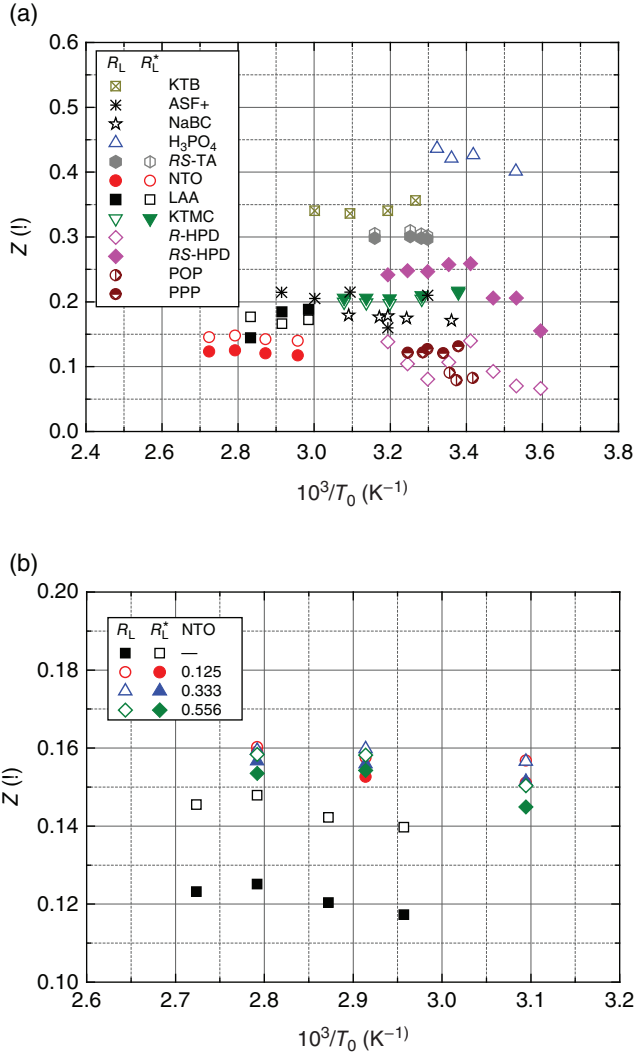

Figure 5.8 Plots of parameter Z of Eq. (5.27) against T_0^{-1} for (a) different compound–solvent systems and (b) NTO in water/NMP mixtures. In (b) NMP content in the water/NMP mixture is given in the inset.

$$\ln u_{\max} = -\frac{1}{2}\ln F - \frac{1}{2}\ln(1 - Z\ln R_L). \tag{5.51}$$

Comparison of this equation with Eq. (5.20) suggests the following equalities:

$$\Phi = -\frac{\ln F}{2}, \tag{5.52}$$

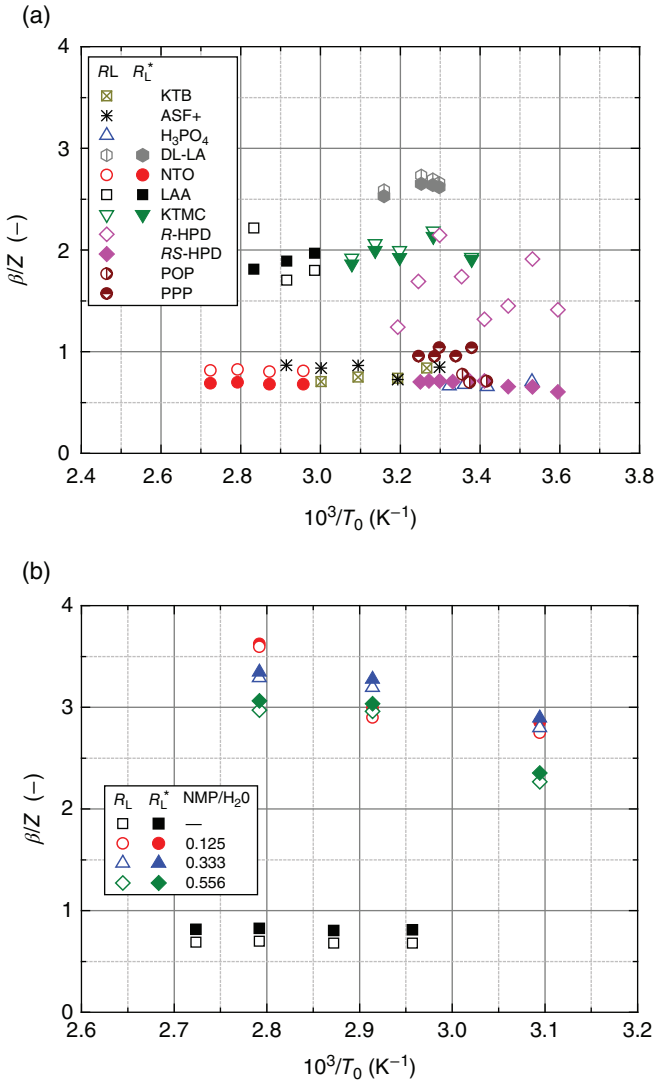

Figure 5.9 Plots of β/Z against T_0^{-1} for (a) different compounds and (b) NTO in water–NMP mixtures. In (b) NMP content in the water/NMP mixture is given in the inset.

$$\beta = -\frac{\ln(1 - Z\ln R_L)}{2\ln R_L}, \tag{5.53}$$

where $F = F_1 Z$ and F_1 and Z are given by Eqs. (5.28) and (5.29), respectively. Relation (5.53) applies when $\ln R_L \geq 1/Z$ and implies that the term in the

Table 5.3 Value of β/Z for different compounds.

β/Z	Compounds[a]
0.7–0.8	NTO (0.14), *RS*-HPD (0.25), H_3PO_4 (0.42) POP (0.09)
0.9	ASF+ (0.17), KTB (0.33)
1.0	PPP (0.12)
1.6	*R*-HPD (0.1)
1.9–2.0	KTMC (0.2), LAA (0.18)
2.6	*RS*-TA (0.3)
>2.5	β/Z decreases with increasing $1/T$ for NTO-NMP/water systems (0.14–0.16)

[a] Values of Z are given in parentheses.

parentheses of Eq. (5.27) exceeds unity such that $Z > 0$. For small $(1 - Z\ln R_L)$ when $\ln(1 - Z\ln R_L) \approx -Z\ln R_L$, Eq. (5.53) gives $\beta \approx Z/2$. Obviously, the parameter β is related to constant Z and its value depends on the applied cooling rate R_L.

As seen from Eq. (5.29), the parameter Z is related to different constants like f, $T_{0,}$ and J_0, which are determined by the temperature dependence of solute solubility x_0 and λ_s, and is practically a temperature-independent constant for a particular solute–solvent system. Therefore, for a given solute–solvent system, one expects the temperature dependence of Z mainly through variations in the values of constants f, T_0, and J_0. For small variations in the values of constants f and J_0 with temperature T_0, one expects Z essentially to remain temperature independent because different constants are contained in the logarithm term. However, for compounds whose solubility increases rapidly with temperature T_0 and the term f/J_0T_0 increases significantly with increasing temperature, the parameter Z is expected to show a noticeable increase with increasing T_0. This explains the observations of Figures 5.8 and 5.9. A similar trend is expected for the temperature dependence of β for small $(1 - Z\ln R_L)$ in Eq. (5.53) when the approximation $\beta \approx Z/2$ holds but other trends are likely to appear in situations when this approximation does not apply. The trends of the dependence of β on T_0 presented in Figure 5.7 may be explained in this way.

In order to understand different trends of the experimental β and β/Z data for different systems, we consider the predictions of Eq. (5.53) for different values of $\ln R_L$ in the observed highest value of $Z = 0.45$. The dependencies of β and β/Z, respectively, for different values of $\ln R_L$ on the parameter Z drawn according to Eq. (5.53) are shown in Figure 5.11a and b, respectively.

As seen from Figure 5.11a, the value of β increases linearly with Z only for $\ln R_L$ close to zero in its entire range. The lowest value of β of 0.03 is obtained for all values of $\ln R_L$ when $Z \leq 0.06$ (Figure 5.11a) and is possible for systems endowed

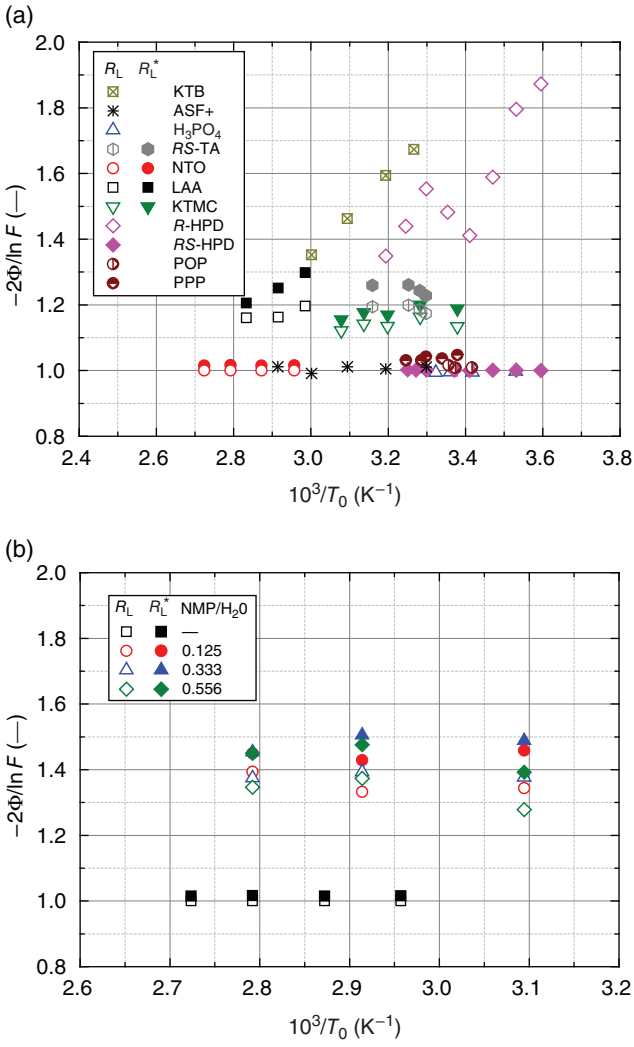

Figure 5.10 Plots of $-2\Phi/\ln F$ against T_0^{-1} for (a) different compounds and (b) NTO in water–NMP mixtures. In (b) NMP content in the water/NMP mixture is given in the inset.

Table 5.4 Values of $-2\Phi/\ln F$ for different compounds.

$-2\Phi/\ln F$	Compounds[a]
1	NTO (0.14), *RS*-HPD (0.25), ASF+ (0.17), H_3PO_4 (0.42), PPP (0.12), POP (0.09)
1.15	KTMC (0.2), LAA (0.18), *RS*-TA (0.3)
>1.35	$-2\Phi/\ln F$ increases with increasing $1/T$ for KTB (0.33), *R*-HPD (0.1)
Abnormal	$-2\Phi/\ln F$ decreases with increasing $1/T$ for NTO–NMP/water systems (0.14–0.16)

[a] Values of Z are given in parentheses.

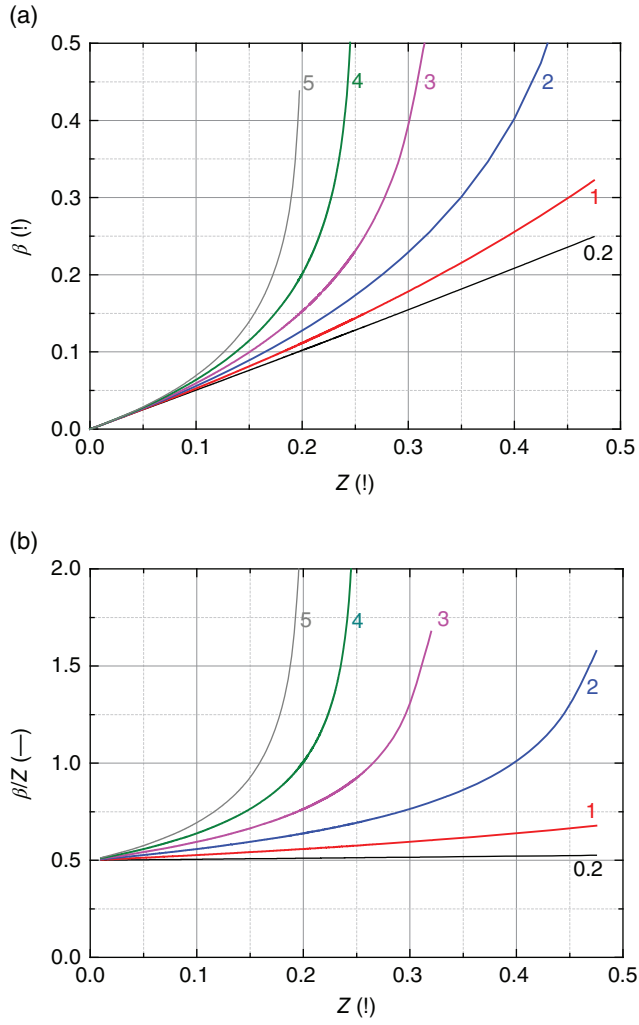

Figure 5.11 Predicted dependence of (a) β from approximation (5.31) and (b) β/Z on Z for different ln R_L.

with low values of f/J_0T_0 and $\lambda_s/(1 - u_{max}) = \Delta H_s/R_G T_{lim}$ (see Eq. (5.29)). After the initial linear increase, the value of β steadily increases for different values of ln R_L and finally follows a steep increase with increasing Z. The value of $\beta < 0.1$ for $Z < 0.2$ in the entire range of ln R_L, but its value attains a higher value up to a higher Z in the range of ln $R_L > 2$. Figure 5.11b shows that the plots of the ratio β/Z against the parameter Z also reveal trends similar to those of β against Z of

Figure 5.11a but the increase in the value of β/Z is much pronounced with increasing Z for $\ln R_L > 2$.

It is interesting to note from Figure 5.11b that the anticipated value of β/Z is close to 0.5 for all values of $\ln R_L$ when $Z \approx 0.06$ but its value corresponding to the observed Z range is determined by the range of the limiting $\ln R_L$. For example, $\beta/Z = 0.7$ with $Z = 0.45$ for $\ln R_L < 1$, $\beta/Z = 1.7$ with $Z = 0.315$ for $\ln R_L < 3$, $\beta/Z = 2$ with $Z = 0.25$ for $\ln R_L = 4$, and $\beta/Z = 2.5$ with $Z = 0.2$ for $\ln R_L < 5$. From Figure 5.11b, the following features may be noted:

1) The limiting values of Z and $\ln R_L$ are mutually related; the higher the value of Z, the lower is the value of $\ln R_L$.
2) The lower limiting value of Z and the higher limiting $\ln R_L$ associated with it lead to the higher value of β/Z.

The above predictions are consistent with the experimental data presented in Figure 5.9. Slow decrease in the value of Z and β/Z with increasing saturation temperature T_0 of different solute–solvents is also expected from Eq. (5.29). As seen from Eq. (5.29), this decrease is expected to be pronounced in the case of high solubility of solute–solvent systems, such as NTO in water/NMP mixtures, involving low values of $\lambda_s/(1 - u_{max}) = \Delta H_s/R_G T_{lim}$.

The trends of the plots of the ratio $-2\Phi/\ln F$ against $1/T_0$ for most of the solute–solvent systems are very similar to the trends of the plots of β/Z against $1/T_0$. The value of the ratio $-2\Phi/\ln F$ against $1/T_0$ is unity for NTO –water, ASF–water, *RS*-HPD-isopropanol, POP-acetone, PPP-acetone, and H_3PO_4–water systems, and is about 1.2 for KTMC–acetone, *RS*-TA–water, and LAA–water/MeOH/EtOH systems, and are independent of T_0. The constant value of $-2\Phi/\ln F = 1$ is obtained when $0.7 < \beta/Z < 1$, and is associated with relatively low values of $\ln R_L$. However, the value of $-2\Phi/\ln F$ lies between about 1.1 and 1.2 when $\beta/Z > 1$, and is associated with relatively high values of limiting $\ln R_L$. These trends are related to the experimental values of $u_{max} = \Delta T_{max}/T_0$ at different cooling rates R_L. The equality $\Phi = -\ln (F^{1/2})$ is observed when u_{max} is low, but relatively high u_{max} leads to deviations from the equality. In the case of seeded phosphoric acid aqueous solutions, for example, where $u_{max} \approx 0.011$, $\Phi \approx -\ln(F^{1/2})$ at different T_0 (Sangwal, 2010). The increasing values of $-2\Phi/\ln F$ with increasing $1/T_0$ for KTB–water and *R*-HPD–isopropanol systems are exceptions to the above trend. This anomalous behavior is probably associated with the dependence of Z on saturation temperature T_0 (see Eq. (5.29)).

Finally, it should be mentioned that the widely different values of parameter $\beta = 1/m$ between 0.03 and 0.8 correspond to the values of m between 33 and 1.25. As argued above, $m = 33$ is associated with low values of $f/J_0 T_0$ and $\lambda_s = \Delta H_s/R_G T_0$, whereas the lowest value of $m = 1$ is caused by a rapid increase in β and β/Z with limiting values of Z for various $\ln R_L$. These observations are associated with relatively slow and rapid increase, respectively, in the creation of supersaturation by solution cooling. Slow creation of

supersaturation leads to the occurrence of 2D nucleation on the surfaces of nuclei forming progressively, whereas rapid development of supersaturation favors instantaneous 3D nucleation in the cooling solution. These inferences are consistent with the theoretical considerations involving progressive and instantaneous nucleation modes (see Sections 5.2.5 and 5.2.6) and analysis of distribution of nucleation order m for different systems (see Section 5.5).

5.2.4 Relationship between Dimensionless F_1 and Crystallization Temperature

As seen from Table 5.2, the parameters F and F_1 strongly depend on the saturation temperature T_0 of the investigated solute–solvent system. The parameter $F = F_1/Z$ and both F_1 and Z are related, among others, to the saturation temperature T_0. Therefore, the temperature dependence of F is not simple in comparison with that of F_1. However, in contrast to the F parameter, which contains the units of time used for cooling rate R_L, the parameter F_1 is a dimensionless quantity and involves two unknown parameters: (i) the dimensionless solid–solution interfacial energy ω and (ii) the dimensionless heat of dissolution λ_s. Therefore, we consider here the temperature dependence of F_1 for different systems.

From Eq. (5.28), the dependence of the dimensionless parameter F_1 on temperature T_0 may be given in the form:

$$F_1 = \frac{k_B(\Delta H_s)^2}{\kappa\left(\gamma\Omega^{2/3}\right)^3} T_0(1-u_{max}), \tag{5.54}$$

where we have substituted the values of the dimensionless heat of dissolution λ_s and the dimensionless interfacial energy ω using Eqs. (5.13) and (5.25), respectively. Assuming that the values of the heat of dissolution ΔH_s and the interfacial energy γ for a given solute–solvent system are independent of temperature T_0, one expects that F_1 increases linearly with $T_0(1 - u_{max})$. The quantity F_1 increases practically linearly with T_0 for several systems as seen from Figure 5.12a. However, this change in F_1 becomes increasingly steep with T_0 for NTO in NMP/water mixtures for which u_{max} decreases with an increasing T_0 and even steeply decreases with an increase in T_0 for H_3PO_4–water and *RS*-TA–water systems or for which u_{max} increases with an increase in T_0 (Figure 5.12b and c). As seen from Figure 5.12c, the trends of changes in F_1 with T_0 for different systems are associated with the dependence of u_{max} on T_0 and the transition from increase to decrease in the value of F_1 occurs at $F_1 \approx 10^4$. Obviously, F_1 increases and decreases with an increase in T_0 for $F_1 < 10^4$ and $F_1 > 10^4$, respectively. The latter situation is encountered in systems of relatively low values of MSZW due to heterogeneous and secondary nucleation occurring in them.

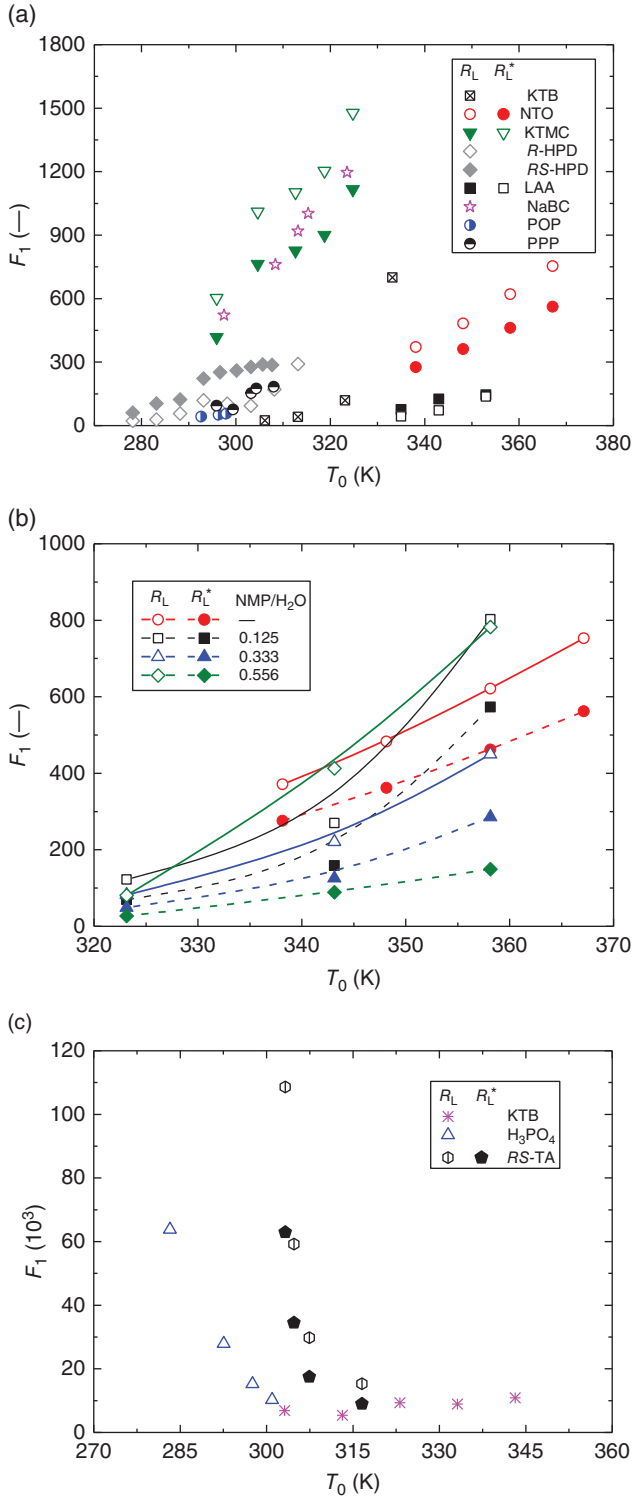

Figure 5.12 Plots of F_1 against T_0 for (a) different compounds, (b) NTO in water/NMP mixtures, and (c) aqueous KTB, H_3PO_4 and *RS*-TA solutions. In (b) solid and dashed curves represent $F_1(T_0)$ data for uncorrected R_L and corrected R_L^*, respectively.

5.2.5 Dependence of Parameters Φ and *F* on Saturation Temperature T_0

It was observed (Sangwal, 2009a, b, 2010) that the experimental data of Φ and $-\ln(F^{1/2})$ for different solute–solution systems as a function of saturation temperature T_0 may be described by an Arrhenius-type relation:

$$C = C_0 - \frac{E_{sat}}{R_G T_0}, \tag{5.55}$$

where C represents both $-\ln(F^{1/2})$ and Φ, C_0 represents the extrapolated value of $-\ln(F^{1/2})$ and Φ corresponding to $T_0 = \infty$, and E_{sat} is the activation energy associated with the diffusion of solute molecules in the solution. Figure 5.13a and b shows examples of the dependence of Φ and $-\ln(F^{1/2})$ on $1/T_0$ for some solute –solution systems according to Eq. (5.55). The linear plots represent the best fit of the data. In Figure 5.13b, the best-fit plots are drawn with cooling rates R_L^* corrected with different values of threshold cooling rate ΔR_L corresponding to various T_0.

While analyzing the $\ln \Phi(1/T_0)$ data in Figure 5.13a, the points for borax at 295 K and for ASF (without seeds) at 333.15 K were excluded in view of relatively high values of the corresponding β. The high values of β, and hence low values of the nucleation constant m, suggest that maximum supercooling ΔT_{max} in these cases is determined by secondary nucleation (see below). The mean values of β for different systems are included in Table 5.5. The values of the intercept Φ_0 and $[-\ln(F^{1/2})]_0$ and the activation energy E_{sat} collected for different systems are given in Table 5.5.

It may be noted from Table 5.5 that the $\Phi(1/T_0)$ plots predict somewhat different values of the intercept Φ_0 and the activation energy E_{sat} from the values of the intercept $[-\ln(F^{1/2})]_0$ and the activation energy E_{sat} obtained from the plots of $-\ln(F^{1/2})$ against $1/T_0$. The value of the intercept Φ_0 is much higher than that of $[-\ln(F^{1/2})]_0$. However, the value of $[-\ln(F^{1/2})]_0$ calculated for the uncorrected $\ln R$ data is higher than that calculated for the corrected $\ln R_L^*$, but the value of E_{sat} obtained from both uncorrected $\ln R_L$ and corrected $\ln R_L^*$ remains essentially unaltered. The values of Φ obtained from the fit of the experimental $u_{max}(R)$ data by Eq. (5.20) is expected to be equal to the values of $-\ln(F^{1/2})$ obtained by using Eq. (5.27).

It should be mentioned that the values of the activation energy E_{sat} for different compounds can be positive (Sangwal, 2009a, b, c, 2011a) as well as negative (Sangwal, 2010). Positive and negative values of the activation energy E_{sat} are observed for systems with $F_1 < 10^4$ and $F_1 > 10^4$, respectively. When E_{sat} is equal to the activation energy E_D for diffusion, $u_{max} = \Delta T_{max}/T_0$ is independent of T_0. When $E_{sat} > E_D$, $\Delta T_{max}/T_0$ decreases with an increase in T_0. However, when $E_{sat} < E_D$, $u_{max} = \Delta T_{max}/T_0$ increases with an increase in T_0.

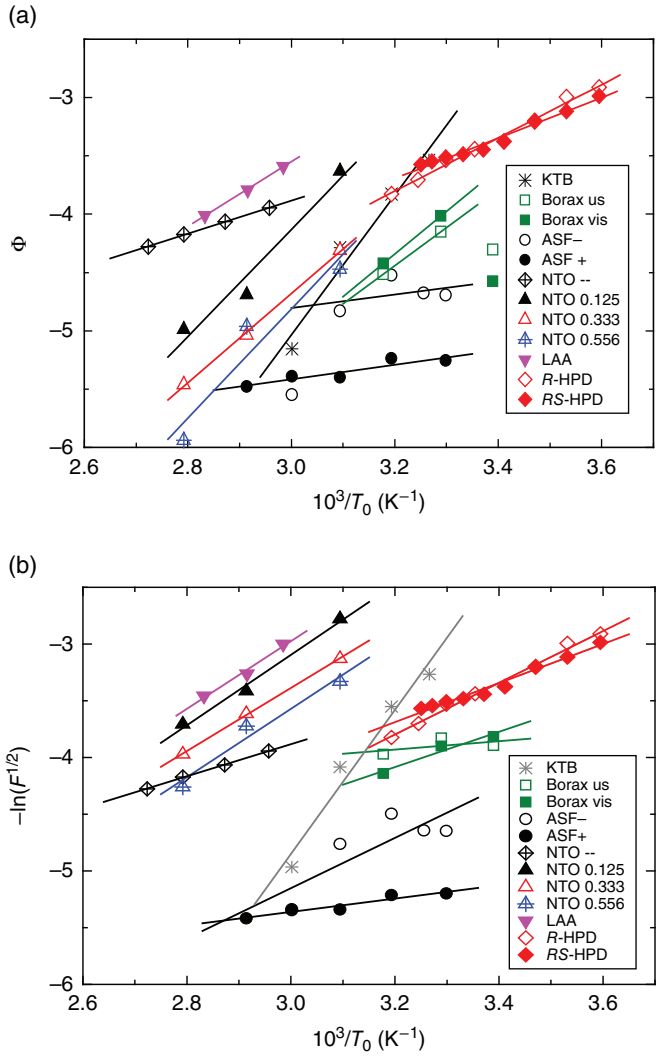

Figure 5.13 Plots of (a) Φ and (b) $-\ln(F^{1/2})$ against $1/T_0$ for different solute–solvent systems. In (b) data for corrected R_L^* are presented. *Source:* Original data from references listed in Section 5.2.

Sangwal (2009a, b) suggested that nucleation of solute during metastability may be interpreted in terms of diffusion of solute molecules in the solution when the quantity $(u_{max})_0 = [\Delta T_{max}/T_0]_0$ corresponding to $\exp\Phi_0$ or $[(F^{-1/2})]_0$ at $\ln R_L = 0$ in Eq. (5.55) is considered as a dimensionless quantity connected with the diffusion of solute molecules in the solution with reference to the saturation

Table 5.5 Calculated values of Φ_0 $[-\ln F^{1/2}]_0$, and E_{sat}, and β for some systems.

	$\Phi(T^{-1})$ data			$\ln F^{1/2}(T^{-1})$ data	
Solute	Φ_0	E_{sat} (kJ·mol^{-1})	β	$[-\ln F^{1/2}]_0$	E_{sat} (kJ·mol^{-1})
Borax–water (us)[a]	−14.9	27.2	0.274		
Borax–water (vis)[a]	−16.0	30.3	0.227		
ASF–water (–)[b]	−6.5	4.8	0.153		
ASF–water (+)[b]	−7.28	5.2	0.168	−5.12	3.88
KTB–water	−23.0	49.9	0.454	−23.90	52.81
LAA–water[c]	−11.88	23.07	0.324	−11.93 (−13.82)[d]	24.83 (30.81)
NTO–water	−8.13	11.8	0.099	−8.13 (−7.98)	11.77 (11.52)
NTO–water/NMP 0.125[e]	−18.86	38.9	0.488	−13.03 (−11.96)	26.21 (23.96)
NTO–water/NMP 0.333	−17.93	38.2	0.491	−11.74 (−11.53)	23.11 (23.24)
NTO–water/NMP 0.556	−16.16	31.8	0.427	−11.96 (−11.27)	24.50 (23.24)
H_3PO_4–water	10.34	−38.47	0.324	10.07	−37.87
KTMC–acetone	−9.73	12.71	0.410	−7.64 (−7.13)	8.70 (7.34)
POP–acetone (TBT)	−10.14	17.0	0.062 ± 0.008	−9.15	14.7
POP–acetone (CRY)	−14.15	26.8	0.069 ± 0.016	−12.09	21.9
PPP–acetone (TBT)	−14.55	27.5	0.123 ± 0.010	−15.19	29.5

Source: Adapted from Sangwal (2011a).

[a] Us and vis indicate detection of onset of crystallization by ultrasound and naked eye.
[b] – and + signs indicate initial absence and presence of seeds, respectively.
[c] Also contains methanol and ethanol.
[d] Values in parentheses correspond to corrected R_L.
[e] NMP content in water-NMP mixture.

solution. If τ is the mean jump time for an ion/molecule in solution to cover the mean diffusion distance l, the jump frequency ν^* of the ion/molecule (i.e. the mean number of jumps made by an ion/molecule per second; $\nu^* = 1/\tau$) may be given by (for example, see Chap. 4, Bockris and Reddy, 1970)

$$\nu^* = \nu_0^* \exp\left(-\frac{E}{R_G T}\right), \tag{5.56}$$

where E is the activation energy for the process and ν_0^* is the vibration frequency of the ion/molecule at its saddle point before diffusion. From Eq. (5.56), the ratio of jump frequencies ν_{sat}^* and ν_{met}^* of ions/molecules in solutions corresponding to saturation and metastable states, respectively, may be given by

$$\nu_{met}^* = \nu_{sat}^* \exp\left[\frac{E_{sat} - E_{met}}{R_G T_0}\right], \tag{5.57}$$

from which one obtains

$$\frac{\Delta \nu^*_{\max}}{\nu^*_{\text{sat}}} = \frac{\exp\{(E_{\text{sat}} - E_{\text{met}})/R_G T_0)\} - 1}{\exp(-E_{\text{sat}}/R_G T_0)} = \left[\exp\left\{\frac{(E_{\text{sat}} - E_{\text{met}})}{R_G T}\right\} - 1\right] \cdot \exp\left(\frac{E_{\text{sat}}}{R_G T_0}\right), \tag{5.58}$$

where the jump frequency difference $\Delta\nu^*_{\max} = \left(\nu^*_{\text{met}} - \nu^*_{\text{sat}}\right)$. In the above equations, E_{sat} and E_{met} are the activation energies corresponding to saturation and metastable states, respectively. Upon replacing $\Delta\nu^*_{\max}/\Delta\nu^*_{\text{sat}}$ by $[\Delta T_{\max}/T_0]_0 = (u_{\max})_0$ in Eq. (5.57) and taking logarithm on both sides, one obtains Eq. (5.55) with C_0 given by

$$C_0 = \ln\left\{\left[\exp\left(\frac{E_{\text{sat}} - E_{\text{met}}}{R_G T_0}\right)\right] - 1\right\}, \tag{5.59}$$

where C denotes Φ and $-\ln(F^{1/2})$ determined by Eqs. (5.20) and (5.27), respectively.

Finally, it should be mentioned that relation (5.55) does not follow directly from the definition of F (see Eq. (5.28)). However, since it is related to the temperature-dependent quantity F_1 and practically temperature-independent quantity Z, one may speculate that its temperature dependence originates from the solid–medium interfacial energy γ because the heat of solution ΔH_s, the other parameter appearing in Eq. (5.28), is essentially a constant quantity for a solute–solution system. Using the approximation $\ln x \approx (1 + x)$ and $T_{\text{lim}} \approx T_0$, from Eq. (5.58), one may write

$$-\frac{1}{2}\ln F = \frac{1}{2}(\ln Z - \ln F_1) \approx \frac{1}{2}\ln Z + \frac{1}{2} + \left[\frac{\kappa\left(\gamma\Omega^{2/3}\right)^3}{2k_B(\Delta H_s)^2}\frac{1}{T_0}\right]. \tag{5.60}$$

This implies that $C_0 = (\ln Z + 1)/2$ and $E_{\text{sat}} = \kappa(\gamma\Omega^{2/3})^3/2k_B(\Delta H_s)^2$.

5.2.6 Physical Significance of E_{sat} and Its Relationship with ΔH_s

If one assumes that Eq. (5.55) is a consequence of diffusion of solute ions/molecules in the solution, it is natural to expect a relationship between the activation energy E_{sat} and the nature of diffusing ions/molecules. According to the hole theory of liquids, for simple liquids in which the size of the holes is similar to that of ions/molecules, which jump into them (see Bockris and Reddy, 1970; section 6.5.6), the activation energy E_D for self-diffusion in pure liquid electrolytes (e.g. Na in NaCl) is usually a constant, independent of temperature, and follows the relation (Bockris and Reddy, 1970; section 6.4.2):

$$\frac{E_D}{R_G} = 3.7T_m, \tag{5.61}$$

where T_m is the melting point of the electrolyte. For example, in the case of acetone (T_m = 178 K), water (T_m = 273 K), and NMP (T_m = 547.9 K; cf. Kim, 2000) as solvents, from Eq. (5.61), one obtains E_D = 5.5, 8.4 and 16.9 kJ·mol^{-1}, respectively. These values of E_D are expected when the diffusing ions/molecules in solutions show ideal behavior. As seen from Table 5.5, the observed values of E_{sat} for KTMC–acetone and NTO–water systems alone are comparable with the predicted values of E_D. In all other cases, E_{sat} is much higher than E_D, implying that the diffusing ions/molecules in these solutions do not show ideal behavior.

An ideal behavior of diffusing ions/molecules is expected at very low solute concentrations when solute ions/molecules do not associate with solvent molecules forming large-sized solvated entities and with themselves forming large-sized complexes. However, except for the NTO–water system, all solutes of Table 5.5 have relatively high solubility in the solvents used in the measurement of MSZW of their solutions. The high solubility of these solutes indeed suggests strong solute–solvent interactions, leading to the formation of large clusters. It should be noted that potassium tetraborate and NTO molecules dissolved in water and molecules of all other solutes dissolved in acetone are indeed much larger than the solvent molecules. The participation of these large-sized entities in diffusion during the cooling of their solutions is responsible for the observation that $E_{sat} > E_D$.

Figure 5.14 shows the dependence of E_{sat}/E_D ratio on volume fraction X of NMP in water for NTO–water/NMP systems. The values of E_D for water –NMP mixtures of different compositions were calculated from the values of

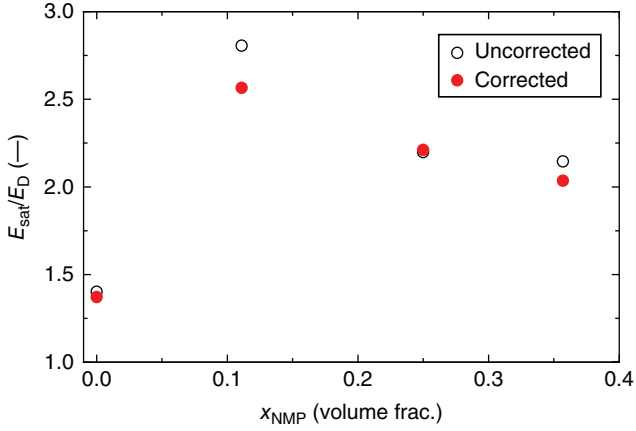

Figure 5.14 Dependence of E_{sat}/E_D on volume fraction X of NMP in water for NTO–water/NMP systems. *Source:* Adapted from Sangwal (2011a). Copyright (2011), with permission from Royal Chemical Society.

E_D given above for water and NMP solvents using the additive rule. It may be seen from the figure that addition of even a small amount of NMP solvent abruptly leads to an increase in the E_{sat}/E_D ratio, but the E_{sat}/E_D ratio subsequently decreases with an increase in NMP content in water. The abrupt increase followed by a decrease in the E_{sat}/E_D ratio is a consequence of a strong NTO–NMP interaction than NTO–water interaction.

The activation energy E_{sat} for different solute–solvent systems does not show any well-defined relationship with their corresponding ΔH_s. This behavior may be observed from Figure 5.15, which shows the data of E_{sat} against ΔH_s for

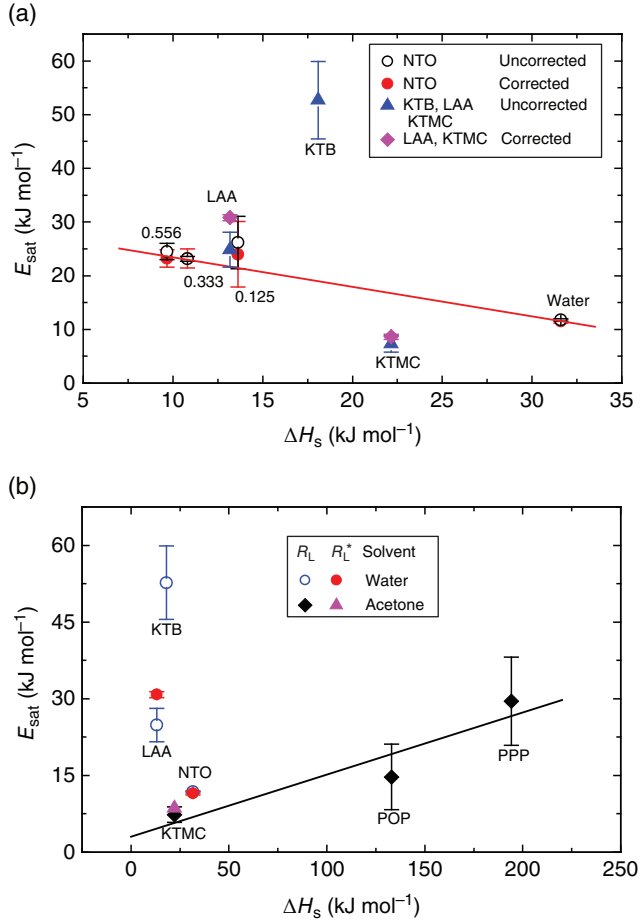

Figure 5.15 Plot of E_{sat} against ΔH_s for different compounds. Compounds are indicated. See text for details. *Source:* Adapted from Sangwal (2011a). Copyright (2011), with permission from Royal Chemical Society.

various systems. The absence of intimate relationship between E_{sat} and ΔH_s for the systems analyzed here is a consequence of the nature of the processes involved. The value of ΔH_s is associated with the establishment of equilibrium between solute and solvent molecules and reflects solute–solvent interactions leading to the formation of large clusters. In contrast to this, the value of E_{sat} is connected with the diffusion of species involved in the formation of 3D nuclei.

The ratio $E_{sat}/\Delta H_s$ lies between 0.12 and 0.39 for NTO–water, KTMC–acetone, PPP–acetone, and POP–acetone systems, but it lies between 1.7 and 2.5 for all other systems. If one considers the solvent acetone alone with KTMC, PPP, and POP solutes (Figure 5.15b), and NTO solute in water/NMP solvents of various composition (Figure 5.15a), E_{sat} and ΔH_s follow the linear relation:

$$E_{sat} = E_0 + \zeta \Delta H_s, \tag{5.62}$$

where E_0 and ζ are empirical constants, given in Table 5.6. In the case of NTO –water/NMP systems, the best-fit correlation is presented for E_{sat} values obtained from the plots of $\ln(F^{-1/2})$ against $1/T_0$ for as-applied R_L and corrected cooling rate R_L^*. Obviously, there are no significant differences in the values of E_0 and ζ obtained from the uncorrected and corrected data.

For a real solute–solvent system, the enthalpy of dissolution ΔH_s is related to the enthalpy of melting ΔH_m by the relation:

$$\Delta H_s = \Delta H_m + \Delta H_{mix}, \tag{5.63}$$

where ΔH_{mix} is a measure of solute–solvent interaction. For an ideal solution, $\Delta H_{mix} = 0$. The negative value of the slope ζ of the linear dependence of E_{sat} on ΔH_s for NTO–water/NMP systems may be attributed to increasing solute –solvent interaction with increasing addition of NMP to water. In this case, the solvent composition determines the strength of solute–solvent interaction. This is also the situation in KTB–water and LAA–water/methanol/ethanol systems, which involve strong solute–solvent interactions. However, the positive value of the slope ζ in the case of acetone solvent containing KTMC, PPP, and POP may be explained in terms of decreasing solute–solvent interactions involved in these solutes.

Table 5.6 Constants E_0 and ζ of Eq. (5.62).

System	Figure	Data	E_0 (kJ·mol^{-1})	ζ (–)	R^2
NTO–water/NMP	5.15a	Uncorrected	29.15 ± 0.49	–0.550 ± 0.017	0.9990
		Corrected	28.92 ± 0.61	–0.550 ± 0.020	0.9986
KTMC and others/ acetone	5.15b	Uncorrected	3.06 ± 0.12	0.121 ± 0.045	0.9371

Source: Adapted from Sangwal (2011a).

From Table 5.5, one observes that the preexponential term Φ_0 or $[\ln F^{-1/2}]_0$ and the activation energy E_{sat} are mutually related. The higher the value of the activation energy E_{sat} for a system, the higher are the values of the corresponding preexponential terms Φ_0 and $[\ln F^{-1/2}]_0$. Figure 5.16a and b shows the dependence of Φ_0 and $[\ln F^{-1/2}]_0$ on E_{sat} for the different systems, respectively. The data for the H_3PO_4–water system were used for the analysis but these data

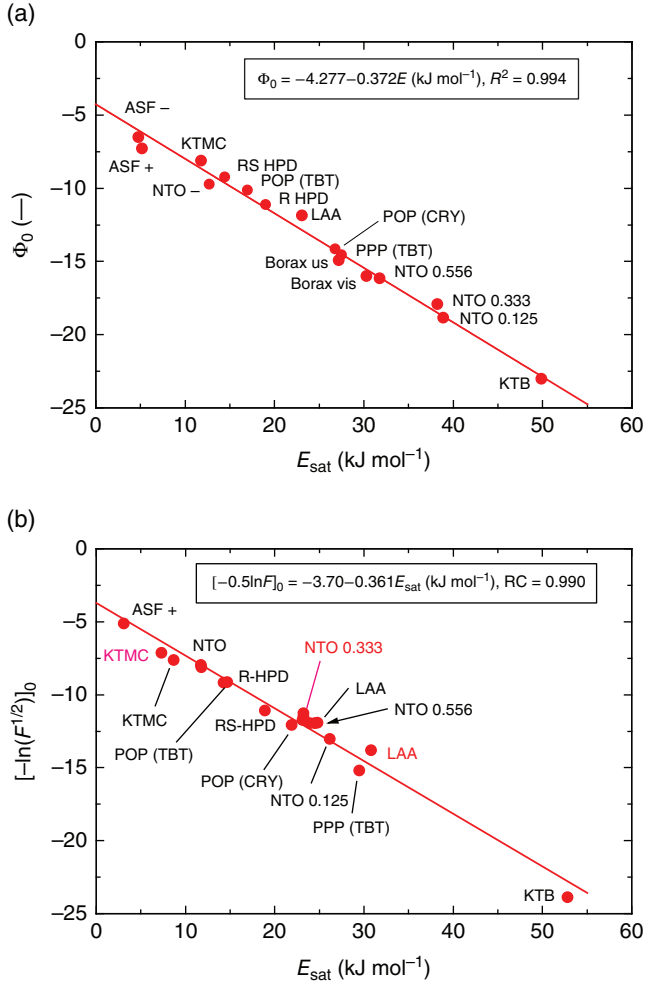

Figure 5.16 Relationship between (a) Φ_0 and (b) $[\ln(F^{-1/2})]_0$ and E_{sat} for various solute –solvent systems. Data for the H_3PO_4–water system were used for the analysis, but these data are not shown in the above plots.

are not shown in the above plots. It may be seen that Φ_0 and $[\ln F^{-1/2}]_0$, denoted by C_0, decrease with increasing E_{sat}, following the relation:

$$C_0 = A_1 - A_2 E_{sat}, \tag{5.64}$$

where A_1 and A_2 are empirical constants. As seen from the plots of Figure 5.16, the dependence of both Φ_0 and $[\ln F^{-1/2}]_0$ on E_{sat} for different solute–solvent systems may be described by universal linear plots with intercept $A_1 = -4.277$ and -3.70, and slope $A_2 = 0.372$ and 0.361 mol·kJ^{-1} for the plots of Figure 5.16a and b, respectively.

To understand the physical sense of relation (5.64), we draw an analogy of the dependences of cooling-rate independent $(u_{max})_0$, represented by Φ_0 and $(\ln F^{-1/2})_0$ on saturation temperature T_0 with the transition-state theory of chemical reactions involving the formation of activated complexes (Atkins, 1998; Eggers et al., 1964). According to the transition-state theory of reaction rates, the rate constant k of a reaction at temperature T is given by the relation:

$$\ln k = \left[\ln\left(\frac{k_B T}{h_P}\right) + \frac{\Delta S^*}{R_G}\right] - \frac{\Delta H^*}{R_G T}, \tag{5.65}$$

where h_P is the Planck constant, and ΔH^* and ΔS^* are the standard changes in heat content and entropy of the system, respectively. From a comparison of Eq. (5.55) with (5.65), one finds that the term contained in the square brackets is equal to C_0 and $\Delta H^* = E_{sat}$ and relation (5.64) is a consequence of interdependence between ΔH^* and ΔS^*.

From the mean value of $A_1 \approx -4.0$ corresponding to $E_{sat} = 0$, one obtains the relative jump frequency $(u_{max})_0 = \exp A_1 = 1.8 \cdot 10^{-2}$ s^{-1}, which from Eq. (5.65) gives a critical value of $E_{met} = 45.7$ J·mol^{-1}. This critical value of E_{met} may be associated with a threshold jump frequency $\nu^*_{met}/\nu^*_{sat} \approx 0.9817$ above which diffusion of ions/molecules in the solution is possible (see Eq. (5.57)). However, when $C_0 = 0$, the corresponding activation energy $E_{sat0} = A_1/A_2 \approx 10$ kJ·mol^{-1}. Physically, the condition $C_0 = 0$ implies that the system corresponds to the saturation state (see Eq. (5.58)).

5.2.7 The Nucleation Order *m*

Nývlt et al. (1985) have collected data on m for aqueous solutions of various solutes at different temperatures for unseeded and seeded systems without and with intentionally added foreign substances (i.e. additives). The values of m vary in a wide range lying generally between 2.06 for KNO_3 and 13.64 for $Ca(NO_3)_2 \cdot 4H_2O$ aqueous solutions, but a value as low as 1.41 for $(NH_4)_2HPO_4$ and as high as 20.05 for unfiltered KH_2PO_4 solutions are also found. Moreover, no specific trend in the values of m for a solute at a given T_0 for unseeded and seeded systems or at different T_0 for seeded or unseeded

systems can be discerned. Since the experimentally determined values of nucleation order m reported for different systems in the literature represent the statistical behavior of different systems regarding the values of m, Sangwal (2011b) analyzed the frequency of occurrence of m from the standpoint of the theoretical predictions of progressive and instantaneous nucleation approaches with the experimental results

Figure 5.17 presents the frequency of occurrence of different values of m in increments of 1 (for example, between 2.00 and 2.99, 3.00 and 3.99, etc.) for aqueous solutions of various solutes at different temperatures T_0. The total number of points is 138 and includes, among others, data for unseeded and seeded systems without and with additives. If the average value of m in an increment is considered in this figure, one finds that: (i) $1.5 < m < 20.5$, (ii) if the extreme points for $m > 12$ are omitted, $1.5 < m < 10.5$, and (iii) the frequency of occurrence is 51% for $2.5 < m < 3.5$. Obviously, the values of m exceeding about 3 suggests that crystallization in aqueous solutions takes place by progressive nucleation during MSZW measurements, whereas the observation $m \geq 7.5$ for progressive nucleation is expected when crystallites grow by 2D nucleation mechanism.

We note here that enormously different values of m even for the same solute have been reported (Nývlt et al., 1985). For example, for the unseeded $(NH_4)_2SO_4$ system, the value of m equal to 8.26 and 2.45 at 40 and 60 °C, respectively, and for the unseeded $Ca(NO_3)_2{\cdot}4H_2O$ system, the value of m equal to 2.29 and 13.64 at 19.5 and 38.7 °C, respectively, have been reported. These enormously different values of m even for the same system by progressive nucleation are also possible when crystallites grow by different growth mechanisms.

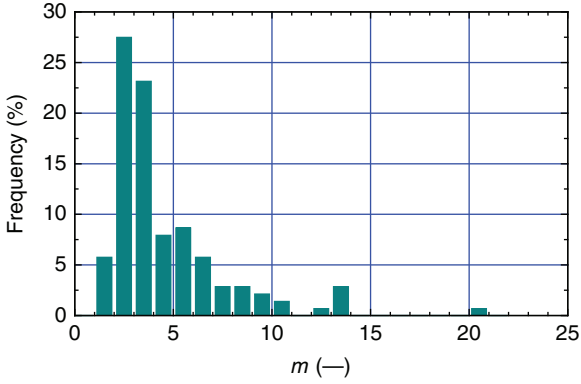

Figure 5.17 Frequency of occurrence of different values of m for aqueous solutions of various solutes at different temperatures. Data also include unseeded and seeded systems as well as additives. Total number of points 138. *Source:* Data from Nývlt et al. (1985). Reproduced from Sangwal (2011b). Copyright (2011), with permission from Elsevier.

As seen from Table 5.5, the mean value of β for different solutes in water decreases in the order: KTB, borax, ASF, and NTO. Since the nucleation order $m = 1/\beta$, one finds m equal to about 10, 6, 4, and 2 for NTO, ASF, borax, and KTB, respectively. This suggests that in the NTO–water system, metastability is achieved by primary nucleation, in the KTB–water system mainly by secondary nucleation, while in ASF–water and borax–water systems by combined primary and secondary nucleation. Among the four solutes analyzed here, NTO has the lowest solubility in water. This suggests, among others, that the solubility of a solute is an important factor that determines the value of nucleation order m. The lower the solubility of a solute in a given solvent, the higher is the value of m.

5.3 Isothermal Crystallization

Equation (5.27) can equally be adapted for the determination of MSZW by the isothermal method, which is based on cooling down of a solution saturated at a particular temperature T_0 to a predefined temperature T_1 as fast as possible to obtain a desired supersaturation. The method usually involves measurement of the induction period for various supersaturations defined as $\ln S$, but one can also determine MSZW of a supersaturated solution simply from observation of spontaneous nucleation as soon as the predefined supersaturation is attained. Then the MSZW is taken as $\ln S_{\max}$, and is defined by Eq. (5.14).

In the isothermal method, the cooling rate R_L in an experiment usually does not exceed 500 $K{\cdot}h^{-1}$ (i.e. about 0.14 $K{\cdot}s^{-1}$), and the limiting cooling rate $R_{L\lim}$ is probably its lowest value. Thus, the term $\ln R_L$ is a constant equal to 6.2 and −2.0 when $R_{L\lim}$ is taken in $K{\cdot}h^{-1}$ and $K{\cdot}s^{-1}$ units, respectively, and is insensitive to the chosen value of $R_{L\lim}$. Then, from Eq. (5.27), one obtains

$$u_{\max}^{-2} = F - F_1 \ln R_{L\lim} = F(1 - Z \ln R_{L\lim}). \tag{5.66}$$

When the maximum supersaturation is defined as $\ln S_{\max} = \ln(c_0/c_{\lim})$, upon substituting the value of $u_{\max}$ in Eq. (5.66) from Eq. (5.13), one obtains

$$S_{\max} = \exp\left\{\left(\frac{ZB}{1 - Z \ln R_{L\lim}}\right)^{1/2}\right\}, \tag{5.67}$$

where B and Z are given by Eqs. (5.23) and (5.29), respectively.

5.4 Effect of Additives on MSZW of Solutions

There are several papers devoted to the investigation of the effect of impurities on the MSZW of various substances. It is observed that an impurity frequently enhances the MSZW (Dhanaraj et al., 2008a, b; Gürbüz and Özdemir, 2003;

Haja Hameed et al., 2007; Omar and Ulrich, 2003; Poornachary et al., 2008; Qu et al., 2006; Rajesh et al., 2001; Sahin et al., 2007; Sangwal and Mielniczek-Brzóska, 2004; Sangwal and Wójcik, 2009; Shimamura and Suzuki, 1989), but there are solute–solvent systems where an impurity leads to a reduction in the MSZW (Omar and Ulrich, 2006; Qu et al., 2006; Sayan and Ulrich, 2001). There are also solute–solvent systems in which the MSZW either first increases and then decreases or first decreases and then increases with increasing concentration c_i of an impurity, showing a maximum or minimum at some concentration c_{im} of the impurity (Ceyhan and Bulutcu, 2005; Haja Hameed et al., 2007; Titiz-Sargut and Ulrich, 2002). Addition of impurities to solute–solvent systems also leads to a change in the solute solubility, thereby changing the saturation temperature T_0 (Anandha Babu and Ramasamy, 2008; Ceyhan and Bulutcu, 2005; Dhanaraj et al., 2008a, b; Omar and Ulrich, 2003, 2006; Qu et al., 2006; Sangwal and Mielniczek-Brzóska, 2004; Sayan and Ulrich, 2001; Shimamura and Suzuki, 1989; Titiz-Sargut and Ulrich, 2002), but there is no predictable trend for the effect of an impurity and its concentration in the variation of T_0 of a given solute–solvent system (Ceyhan and Bulutcu, 2005; Omar and Ulrich, 2006; Titiz-Sargut and Ulrich, 2002). For the determination of the MSZWs of several solute–solvent systems, the effect of an impurity and its concentration on the variation of T_0 has not been studied (Dhanaraj et al., 2008a, b; Gürbüz and Özdemir, 2003; Haja Hameed et al., 2007; Poornachary et al., 2008; Sahin et al., 2007). In the case of potash alum aqueous solutions containing Cu(II), Mg(II), and Cr(III) ions and KCl aqueous solutions containing Cr(III) ions, Titiz-Sargut and Ulrich (2002) reported that the MSZW ΔT_{max} can increase as well as decrease even for the same impurity, depending on its concentration, and is related with changes in T_0 by the impurity. However, in their investigation of common ion effect on the MSZW of KCl, Ceyhan and Bulutcu (2005) found no relationship between ΔT_{max} and T_0.

In this section the main problems associated with MSZW of various systems in the presence of impurities are described and discussed using extensions of theoretical approaches presented above. For the analysis, representative examples of experimental $\Delta T_{max}(R,c_i)$ data obtained by the polythermal method and $\ln S_{max}(c_i)$ data obtained by the isothermal method are considered. The contents of the section are based on the author's work published before (Sangwal, 2009c, 2010; Sangwal and Smith, 2010).

5.4.1 Some General Features

It was mentioned before that for pure solute–solvent systems the maximum supercooling ΔT_{max} increases with increasing cooling rate R_L either linearly or nonlinearly following a power-law relation. For a given concentration c_i of an impurity, plots of ΔT_{max} against R_L also show trends similar to those observed in pure systems. Figure 5.18a presents a typical example, from the

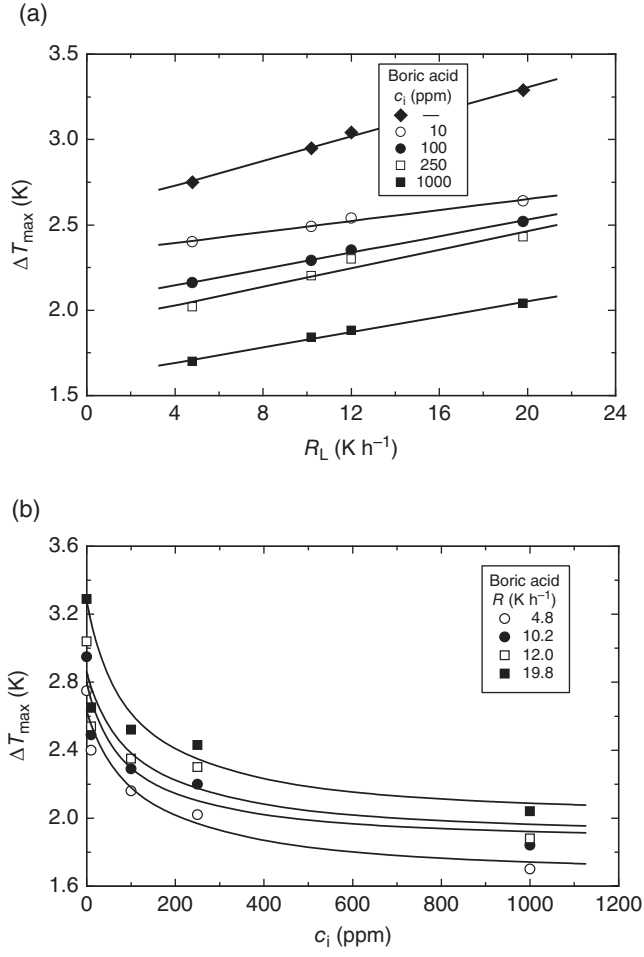

Figure 5.18 (a) Typical examples of dependence of ΔT_{max} on R_L for aqueous boric acid solutions containing different concentrations c_i of Cr(III) additive. (b) Data of ΔT_{max} plotted against Cr(III) additive concentrations c_i for different cooling rates R_L. *Source:* Original data from Sayan and Ulrich (2001).

work of Sayan and Ulrich (2001), of the linear dependence of ΔT_{max} on R_L for boric acid aqueous solutions containing different concentrations c_i of Cr(III) additive.

It may be seen that the maximum supercooling ΔT_{max} corresponding to a given cooling rate R_L decreases with an increase in impurity concentration c_i. For different values of R_L, this behavior of the decrease in ΔT_{max} of boric acid aqueous solutions with increasing concentration of Cr(III) impurity is shown in

Figure 5.18b. The $\Delta T_{max}(c_i)$ data of Figure 5.18b for different R_L can be represented by the following empirical relation:

$$\Delta T_{max} = \Delta T_{max0}(1 - \alpha\theta), \tag{5.68}$$

where α is an empirical constant and the fractional surface coverage θ is given by the Langmuir adsorption isotherm and is related to the Langmuir constant K_L and the differential heat of adsorption Q_{diff} (see Eqs. (5.77) and (5.79)). The values of constants of Eq. (5.68) for Cr(III) impurity in boric acid aqueous solutions are listed in Table 5.7. One finds that the values of constant α and differential heat of adsorption Q_{diff} for Cr(III) impurity obtained from Eq. (5.68) are independent of cooling rate R_L.

It is sometimes found that for constant values of R_L the plots of ΔT_{max} against c_i of various impurities in a solid–solvent system exhibit poor fit. For example, this behavior was noted in the case of Ca(II) impurity contained in the boric acid–water system. One of the main reasons of this poor fit is that addition of an impurity leads to a marked increase in the solubility of the solute, thereby increasing the saturation temperature T_0 with an increase in the impurity concentration c_i, but this increase in T_0 with an increasing c_i of the impurity is not linear. In the case of boric acid–water system, Ca(II) impurity indeed shows a significant increase in T_0, but Cr(III), Mg(II), and Fe(II) impurities, irrespective of their concentration c_i in the solution, lead to a relatively poor change in T_0. The values of T_0 of the boric acid–water system recovered from the plots of T_0 as a function of c_i of different impurities reported by Sayan and Ulrich (2001) are given in Table 5.8 for different concentrations c_i.

The above observations suggest that, for constant values of R_L, Eq. (5.68) describes the plots of ΔT_{max} against c_i of an impurity in a system reliably only when the impurity has insignificant effect on T_0 or when T_0 changes with c_i of the impurity monotonically. However, irrespective of the fact that Eq. (5.68) describes the data satisfactorily or not, this equation is empirical.

Table 5.7 Constants ΔT_{max0}, α, K_L, and Q_{diff} for Cr(III) impurity in boric acid aqueous solutions.

R (K·h^{-1})	ΔT_{max0} (K)	α (–)	K_L (10^3)	Q_{diff} (kJ·mol^{-1})
4.8	2.63 ± 0.12	0.376 ± 0.081	9.0 ± 7.7	23.0 ± 1.6
10.2	2.80 ± 0.17	0.339 ± 0.096	12.3 ± 15.4	23.8 ± 2.0
12.0	2.86 ± 0.19	0.344 ± 0.115	10.1 ± 13.9	23.3 ± 2.2
19.8	3.28 ± 0.23	0.305 ± 0.067	13.9 ± 16.1	24.1 ± 2.7

Source: Adapted from Sangwal (2009c).

Table 5.8 Saturation temperature T_0 (K) of boric acid aqueous solutions in different additives.

c_i (ppm)	Cr(III)	Ca(II)	Mg(II)	Fe(II)
—	304.15	304.15	304.15	304.15
10	304.06	—	—	—
100	—	304.5	304.09	304.13
250	303.96	304.75	304.09	304.13
500	303.89	305.28	304.09	304.14
1000	303.88	306.19	304.09	304.14

Source: Adapted from Sangwal (2009c).

5.4.2 Theoretical Considerations

5.4.2.1 Approach Based on Classical Nucleation Theory

Equation (5.27) of the approach proposed based on the classical theory of 3D nucleation can be extended to explain the effect of impurities contained in a solute–solvent system on its MSZW. The parameters that account for the effect of an impurity on the value of MSZW of a system according to Eq. (5.27) are: (i) the interfacial energy γ, (ii) the heat of dissolution ΔH_s, (iii) the kinetic factor J_0 associated with the integration of growth units to the growing nuclei, and (iv) the factor f determined by aggregation and diffusion processes in the solution. Since the heat of dissolution ΔH_s is intimately connected with the interfacial energy γ and the factor f is connected with the kinetic factor J_0, the effect of an impurity on MSZW may be considered in terms of γ and J_0 contained in Eq. (5.22) of the nucleation rate J (Sangwal, 2009c, 2010).

When impurity particles are present in the solution, they reach the surface of the forming nuclei by diffusion in the bulk and, if adsorbed on them, lead to a decrease in the value of γ. Therefore, the adsorption of an impurity either promotes the nucleation rate or has no effect on it. The other effect of the impurity particles adsorbed on the nucleus surface is to physically block the existing active sites for the attachment of growth units on them, thereby leading to a decrease in the kinetic constant J_0. Thus, an impurity present in the solution has opposing effect on nucleation rate J.

If θ is the fraction of active sites of growing nuclei affected by impurity particles, the kinetic factor may be expressed in the form:

$$J_0 = J_0^0(1-\theta) + J_0^i\theta = J_0^0(1-\alpha_{\text{eff}}\theta), \tag{5.69}$$

where J_0^0 and J_0^i denote the kinetic factors in the absence and presence of the impurity, respectively, and the impurity effectiveness factor α_{eff} is given by

$$\alpha_{\text{eff}} = \frac{\left(J_0^0 - J_0^i\right)}{J_0^0}. \tag{5.70}$$

Obviously, when impurity particles inhibit the integration of growth units to growing nuclei by physically blocking the active sites, $0 < \alpha_{\text{eff}} \leq 1$ $\left(\text{i.e. } 0 \leq J_0^{\text{i}} \leq J_0^0\right)$ and $J_0^{\text{i}} < J_0$. However, when impurity particles favor the integration of growth units to growing nuclei such that $J_0^{\text{i}} > J_0^0$, $\alpha_{\text{eff}} < 0$ and $J_0 > J_0^0$.

Introduction of the above effects of an impurity on the interfacial energy γ and the kinetic factor J_0 in Eq. (5.22) of the 3D nucleation rate J gives an equation of the form of Eq. (5.27) with F_1 given by Eq. (5.28) and

$$Z = \frac{F_1}{F} = \ln\left\{\frac{f}{J_0^0 T_0 (1-\alpha_{\text{eff}}\theta)} \frac{\lambda_{\text{s}}}{(1-u_{\max})}\right\}, \tag{5.71}$$

where $J_0^0(1-\alpha_{\text{eff}}\theta)$ is the new preexponential factor in the presence of the impurity. Obviously, an impurity affects both F_1 and Z, implying that the effect of the impurity on the parameter F may be described through F_1 and Z.

The constant Z is usually less than 0.2 for different solute–water systems without intentionally added impurities (i.e. $Z < 0.2$). Therefore, when $\alpha_{\text{eff}}\theta \ll 1$, Eq. (5.71) may be rewritten in the simplified form:

$$Z = \frac{Z_0}{1-\alpha_{\text{eff}}\theta} \approx Z_0(1+\alpha_{\text{eff}}\theta), \tag{5.72}$$

where Z_0 is the value of Z when $\theta = 0$ (see Eq. (5.29)). Now we assume that the interfacial energy γ decreases with an increase in the surface coverage θ of an impurity following the empirical relation (Kubota et al., 2000; Ościk, 1982; Sangwal, 2007):

$$\gamma = \gamma_0(1-b\theta), \tag{5.73}$$

for $b\theta \ll 1$, with b as an empirical constant. Then from Eq. (5.25), ω^3 may be given by

$$\omega^3 = \omega_0^3(1-3b\theta), \tag{5.74}$$

where ω_0 is the dimensionless interfacial energy in the absence of impurity. Substituting the value of ω^3 from Eq. (5.74) in Eq. (5.28) and neglecting the θ^2 term, one obtains

$$F_1 = F_{10}(1+b_1\theta), \tag{5.75}$$

with

$$b_1 = (3b - \alpha_{\text{eff}}). \tag{5.76}$$

In the above expressions, γ_0, F_{10}, and ω_0 are the values of γ, F_1, and ω for impurity-free systems (i.e. when $\theta = 0$), and the constant $b \approx 1$ (cf. Ościk, 1982). In fact, when $\theta = 0$, Eq. (5.27) describes the dependence of MSZW on the cooling rate for pure solute–solvent systems. The surface coverage θ by an impurity is described by the usual adsorption isotherms (see below).

5.4.2.2 Final Expressions for Analysis of Experimental Data

When the fractional surface coverage θ is given by the Langmuir adsorption isotherm (Eggers et al., 1964; Ościk, 1982; Sangwal, 2007)

$$\theta = \frac{K_{\mathrm{L}} c_{\mathrm{i}}}{(1 + K_{\mathrm{L}} c_{\mathrm{i}})}, \tag{5.77}$$

Eq. (5.75) may be written in the form:

$$F_1 = F_{10}\left[1 + \frac{b_1 K_{\mathrm{L}} c_{\mathrm{i}}}{1 + K_{\mathrm{L}} c_{\mathrm{i}}}\right], \tag{5.78}$$

where K_{L} is the Langmuir constant given by (Eggers et al., 1964; Ościk, 1982)

$$K_{\mathrm{L}} = \frac{Q_{\mathrm{diff}}}{R_{\mathrm{G}} T}, \tag{5.79}$$

with the differential heat of adsorption Q_{diff}. In the case of Freundlich isotherm (Eggers et al., 1964; Ościk, 1982; Sangwal, 2007) when

$$\theta = K_1 c_{\mathrm{i}}^{n}, \tag{5.80}$$

from Eq. (5.75), one has

$$F_1 = F_{10}\left(1 + b_1 K_1 c_{\mathrm{i}}^{n}\right), \tag{5.81}$$

where the constant

$$K_1 = \frac{n}{c_{\mathrm{i}}^{*n}}, \tag{5.82}$$

the exponent n is related to the differential heat of adsorption and c_{i}^{*} is the impurity concentration when $\theta = 1$. When $K_{\mathrm{L}} c_{\mathrm{i}} \ll 1$ and $n = 1$, Eqs. (5.78) and (5.81) reduce to Henry's linear adsorption isotherm, i.e. $\theta = K_{\mathrm{L}} c_{\mathrm{i}}$. Then Eq. (5.75) takes the form:

$$F_1 = F_{10}(1 + b_1 K_{\mathrm{L}} c_{\mathrm{i}}), \tag{5.83}$$

where $K_{\mathrm{L}} = K_1 = 1/c_i^{*}$. Using Eqs. (5.78), (5.81), and (5.83), one can analyze the effect of impurities on quantity F. Obviously, F increases or decreases with an increase in c_{i} when $b_1 > 0$ or $b_1 < 0$ (i.e. when $3b > \alpha_{\mathrm{eff}}$ or $3b < \alpha_{\mathrm{eff}}$).

Equation (5.72) can be used to analyze the effect of impurities on Z. According to Eq. (5.72), the value of Z increases or decreases linearly with increasing surface coverage θ when the impurity effectiveness parameter α_{eff} remains constant in a certain concentration of the impurity. When an impurity suppresses nucleation by physically blocking the available growth sites of the growing embryo (i.e. $0 < \alpha_{\mathrm{eff}} < 1$), Z increases with increasing θ ($Z > Z_0$). However, when an impurity promotes nucleation (i.e. $\alpha_{\mathrm{eff}} < 0$), Z decreases with increasing θ ($Z < Z_0$). Obviously, when an impurity is ineffective for nucleation, $\alpha_{\mathrm{eff}} = 0$ and $Z = Z_0$.

In order to analyze the effect of an impurity on ΔT_{max} corresponding to a constant value of cooling rate R, one has to consider the effect resulting from both thermodynamic and kinetic factors. Upon substituting for F_1 and Z from Eqs. (5.75) and (5.72) in Eq. (5.27), one obtains the relation:

$$\left(\frac{T_0}{\Delta T_{max}}\right)^2 = \left[\left(\frac{T_0}{\Delta T_{max}}\right)^2\right]_0 (1 + b_2\theta), \tag{5.84}$$

with

$$b_2 = \left(3b - \frac{\alpha_{eff}}{1 - Z_0 \ln R_L}\right), \tag{5.85}$$

and

$$\left[\left(\frac{T_0}{\Delta T_{max}}\right)^2\right]_0 = F_0(1 - Z_0 \ln R_L), \tag{5.86}$$

where F_0 and Z_0 are the values of F and Z of Eqs. (5.28) and (5.29), respectively, in the absence of an impurity.

It may be seen that in Eq. (5.85) the value of the constant b_2 of the plot of $(T_0/\Delta T_{max})^2$ against θ can be positive as well as negative, depending on whether $b_2 > 0$ or $b_2 < 0$. As seen from Eq. (5.85), when $b_2 > 0$, $3b > \alpha_{eff}/(1 - Z_0 \ln R_L)$, and the thermodynamic effect prevails. However, when $b_2 < 0$, $3b < \alpha_{eff}/(1 - Z_0 \ln R_L)$, and the kinetic effect dominates over the thermodynamic effect.

5.4.3 Some Examples of Effect of Impurities on MSZW

5.4.3.1 Boric Acid Aqueous Solutions

As observed for pure solute–solvent systems, the value of $(T_0/\Delta T_{max})^2$ decreases linearly with increasing $\ln R_L$ for different concentrations c_i of various impurities contained in the boric acid–water system. As an example, Figure 5.19a presents the data of Figure 5.18a in the form of the dependence of $(T_0/\Delta T_{max})^2$ on $\ln R_L$ for different concentrations c_i of Cr(III), predicted by Eq. (5.27). The calculated values of constants F and Z of Eq. (5.27) for different impurities are illustrated in Figure 5.19b and c as a function of c_i as predicted by Eqs. (5.75) and (5.72), respectively.

It may be seen from Figure 5.19b that the quantity F increases practically linearly with the concentrations c_i of Ca(II), Mg(II), and Fe(II) impurities, while the dependence of F on c_i of Cr(III) impurity may be described by both Langmuir and Freundlich adsorption isotherms. For Cr(III) impurity, Langmuir isotherm describes the $F(c_i)$ data better than Freundlich isotherm. The values of constants F_0, K_L, and Q_{diff} for different impurities are given in Table 5.9. While calculating the value of Langmuir constant for Ca(II), Mg(II), and Fe(II) impurities from the

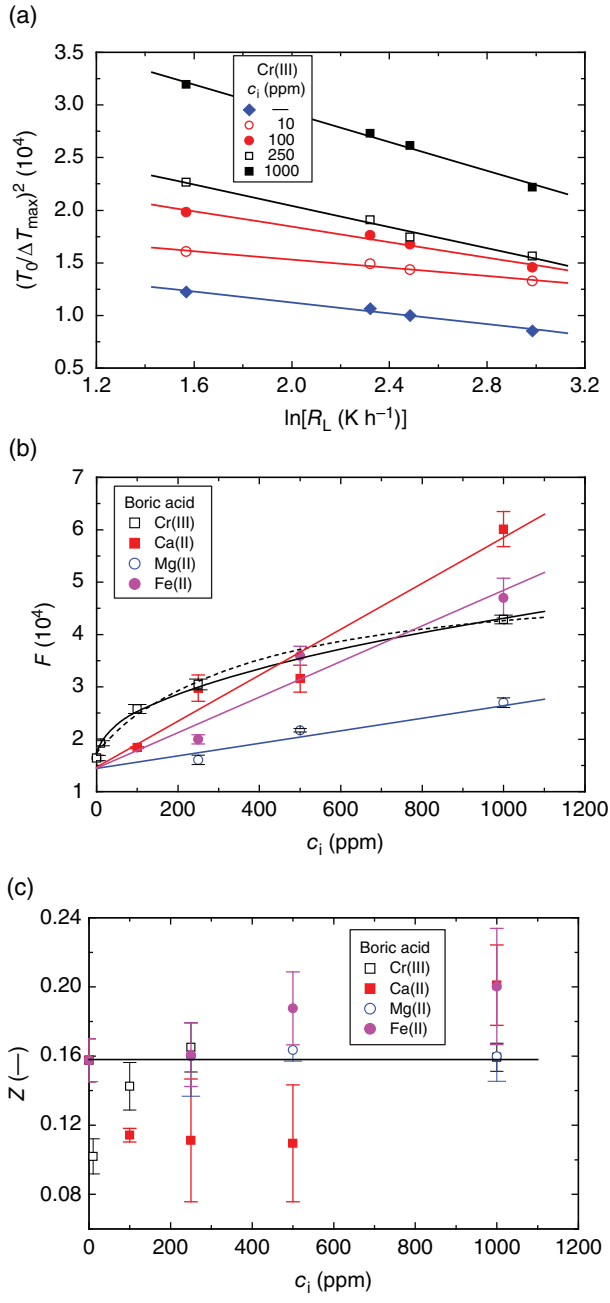

Figure 5.19 Dependence of (a) $(T_0/\Delta T_{max})^2$ on ln R_L for boric acid aqueous solutions containing different concentrations c_i of Cr(III) additive. Plots of (b) F and (c) Z against c_i of Eq. (5.27) for different additives contained in boric acid aqueous solutions as a function of c_i as predicted by Eqs. (5.75) and (5.72), respectively. In (b) dotted and continuous curves for Cr(III) are best-fit plots according to Eq. (5.75) with θ given by Langmuir and Freundlich adsorption isotherms, respectively. In (c) continuous line represents impurity-independent Z_0. *Source:* Original data from Sayan and Ulrich (2001). Adapted from Sangwal (2009c). Copyright (2009), with permission from Elsevier.

Table 5.9 Constants F_0, K_L, and Q_{diff} for different impurities in boric acid aqueous solutions.

Impurity	Isotherm	F_0 (10^4)	b_1	n	K_L or K_1 (10^3)	Q_{diff} (kJ·mol^{-1})
Cr(III)	Langmuir	1.75 ± 0.10	1.97 ± 0.24	—	2.7 ± 0.8	20.0 ± 0.7
	Freundlich	1.72 ± 0.05	2	0.5	23.9 ± 0.8	—
Ca(II)	Henry	1.47 ± 0.40	2	1	1.5 ± 0.24	18.5 ± 0.4
Mg(II)	Henry	1.34 ± 0.19	2	1	0.52 ± 0.11	15.8 ± 0.5
Fe(II)	Henry	1.45 ± 0.68	2	1	1.17 ± 0.36	17.9 ± 0.7

Source: Adapted from Sangwal (2009c).

linear dependence in Figure 5.19b, it was assumed that b_1 for all the impurities is the same as that found for the Cr(III) impurity from the best fit of the data according to Eq. (5.78) based on Langmuir adsorption isotherm.

From Figure 5.19c, the following features may be noted:

1) The value of Z practically remains unchanged in the presence of Mg(II) and Cr(III) impurities.
2) The value of Z somewhat increases with increasing c_i of Fe(II) impurity.
3) In the case of Ca(II) impurity, Z first decreases attaining a value of about 0.1 between 250 and 500 ppm and subsequently increases to about 0.2 at 1000 ppm.

The above features may be explained mainly in terms of the impurity effectiveness parameter α_{eff} associated with the kinetic term $(1 + \alpha_{eff}\theta)$ in Eq. (5.72) relating Z with θ. In the presence of an impurity, the value of this term increases with surface coverage θ for $\alpha_{eff} > 0$, thereby increasing the value of Z. However, when $\alpha_{eff} < 0$ for an impurity, the impurity leads to a decrease in the value of Z. Thus, the decrease in Z for Cr(III) and Ca(II) impurities at relatively low c_i may be attributed to $\alpha_{eff} < 0$, the steady increase in Z with increasing c_i of Fe(II), and the increased value of Z at 1000 ppm Ca(II) to $\alpha_{eff} > 0$, while the practically constant value of Z in the case of all concentrations of Mg(II) and for $c_i > 100$ ppm of Cr(III) to $\alpha_{eff} = 0$. Obviously, the value of the parameter α_{eff} is determined by the chemical properties of impurity cations added to a solute–solvent system and the nature of complexes formed in the solution. It is these complexes that ultimately determine the chemical activity of impurities during nucleation.

As in the case of pure solute–solvent systems, the value of $\ln(\Delta T_{max}/T_0)$ increases linearly with increasing $\ln R_L$ for different concentrations c_i of various impurities contained in the boric acid–water system. Figure 5.20a shows the data of Figure 5.18a in the form of the dependence of $\ln(\Delta T_{max}/T_0)$ on $\ln R_L$ for different c_i of Cr(III), predicted by Eq. (5.20). The calculated values of

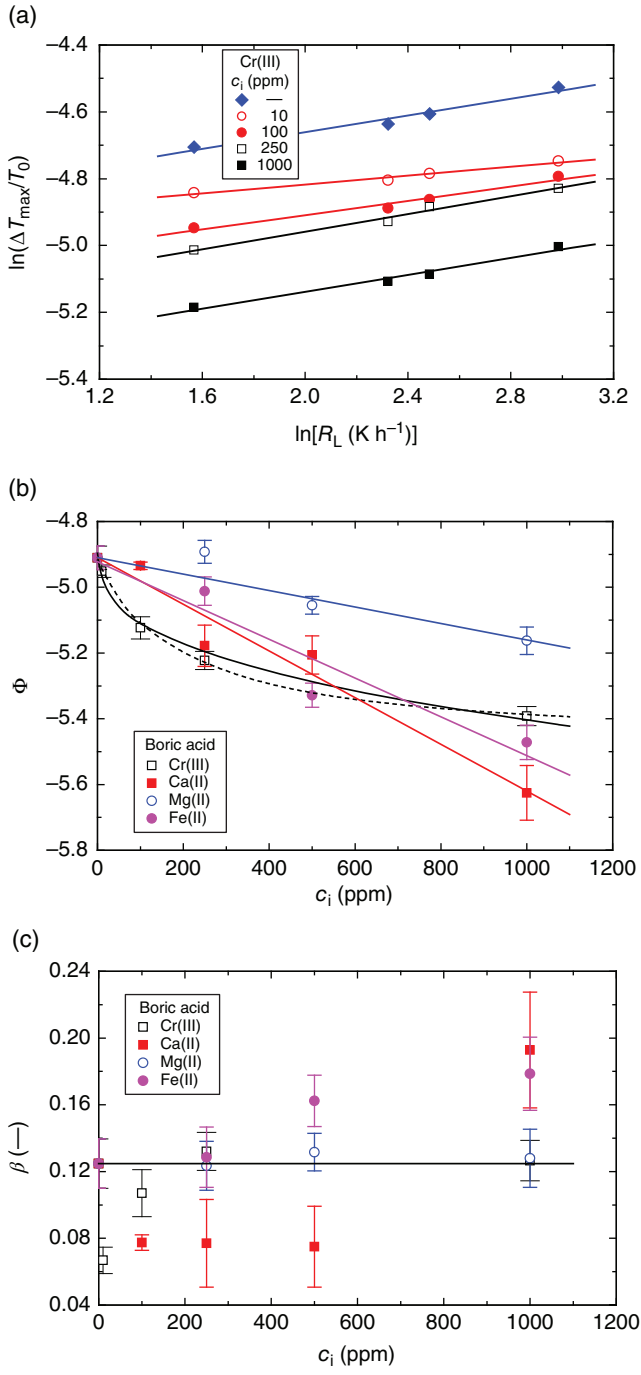

Figure 5.20 Dependence of (a) $\ln(\Delta T_{max}/T_0)$ on $\ln R_L$ for boric acid aqueous solutions containing different concentrations c_i of Cr(III) additive. Plots of (b) Φ and (c) β against c_i of Eq. (5.28) for different additives contained in boric acid aqueous solutions. In (b) dotted and continuous curves for Cr(III) are best-fit plots according to Eq. (5.75) with θ represented by Langmuir and Freundlich adsorption isotherms, respectively. In (c) continuous line represents impurity-independent β_0. *Source:* Original data from Sayan and Ulrich (2001). Adapted from Sangwal (2009c). Copyright (2009), with permission from Elsevier.

quantities Φ and β of Eq. (5.20) for different impurities are presented in Figure 5.20b and c, respectively.

The quantity Φ decreases with an increase in the concentrations c_i of different impurities, following the empirical relation:

$$\Phi = \Phi_0(1 - b_3\theta), \tag{5.87}$$

where b_3 is a constant and θ is the surface coverage. The best-fit constants of the data of Figure 5.20b are given in Table 5.10. While calculating the values of Langmuir constant K_L from the best fit, it was assumed that $b_3 = 0.113$ for all impurities. This value of b_3 was obtained from the best fit of the $\Phi(c_i)$ data for Cr(III) when Langmuir isotherm was used. As in the case of $F(c_i)$ data of Figure 5.19b, for Cr(III) the fit was better for Langmuir isotherm than that for Freundlich isotherm.

It may be noted that, for different impurities, the values of Langmuir constant K_L and differential heat of adsorption Q_{diff} obtained by fitting the $\Phi(c_i)$ data by empirical relation (5.87) are in good agreement with those obtained from fitting the $F(c_i)$ data according to Eq. (5.75). This observation means the analysis of the $\Phi(c_i)$ data by using empirical relation (5.87) gives essentially the same information as does Eq. (5.75), which has sound physical basis. As seen from Tables 5.9 and 5.10, the constants b_1 and b_3 of Eqs. (5.76) and (5.87) are related: $b_1 \approx 2\exp b_3$.

It is interesting to note that the trends of the plots of β against c_i of different impurities seen in Figure 5.20c are exactly the same as those of Z against c_i of these impurities observed in Figure 5.19c. This implies that the effect of impurities on the value of β in a system is essentially kinetic and is associated with their chemical nature. In contrast to this, the effect of impurities on the values of F and Φ is thermodynamic and is associated with the ability of their adsorption on the developing embryos into critically-sized stable nuclei. If one considers the differential heat of adsorption Q_{diff} as a measure of the adsorption ability

Table 5.10 Values of Φ_0 and other constants for different impurities in boric acid aqueous solutions.

Impurity	Isotherm	$-\Phi_0$	b_3	n	K_L or K_1 (10^3)	Q_{diff} (kJ·mol^{-1})
Cr(III)	Langmuir	4.918 ± 0.011	0.113 ± 0.005	—	5.4 ± 0.8	21.7 ± 0.4
	Freundlich	4.896 ± 0.033	0.113	0.372	7.9 ± 4.0	—
Ca(II)	Henry	4.910 ± 0.044	0.113	1	1.28 ± 0.16	18.1 ± 0.3
Mg(II)	Henry	4.882 ± 0.041	0.113	1	0.51 ± 0.13	15.7 ± 0.6
Fe(II)	Henry	4.922 ± 0.072	0.113	1	1.06 ± 0.23	17.6 ± 0.5

Source: Adapted from Sangwal (2009c).

of an impurity, this ability for the investigated impurities decreases in the sequence (see Tables 5.9 and 5.10): Cr(III), Ca(II), Fe(II), and Mg(II). However, as seen from Tables 5.9 and 5.10, the values of Q_{diff} calculated from the best fit of the data for Cr(III) impurity by using Eqs. (5.75) and (5.87) are comparable with those obtained in Table 5.7 from the empirical relation (5.68).

5.4.3.2 KDP Aqueous Solutions

Shimamura and Suzuki (1989) reported the experimental data of maximum supercooling $\Delta T_{\max}$ for different saturation temperatures T_0 of KDP obtained by the polythermal method at a cooling rate of about 0.33 K·h^{-1} and found that addition of Cr(III) ions does not change the saturation temperature T_0 of KDP solutions. These authors observed that, at a given saturation temperature T_0 for KDP aqueous solutions, the maximum supercooling $\Delta T_{\max}$ increases with increasing impurity concentration c_i of Cr(III) impurity. Figure 5.21a shows the experimental data as plots of $\Delta T_{\max}/T_0$ against concentration c_i of Cr(III) contained in KDP aqueous solutions corresponding to various saturation temperatures T_0. As seen from the plots, the effect of the impurity on the relative maximum supercooling $\Delta T_{\max}/T_0$ decreases with increasing T_0.

Figure 5.21b shows the data of Figure 5.21a as the dependence of $(T_0/\Delta T_{\max})^2$ on c_i of Cr(III), according to Eq. (5.85). It was found that the data of Figure 5.21a can equally be presented as plots of $\ln(\Delta T_{\max}/T_0)$ against c_i of Cr(III), as shown in Figure 5.21c, using the empirical relation:

$$\ln\left(\frac{\Delta T_{\max}}{T_0}\right) = \left[\ln\left(\frac{\Delta T_{\max}}{T_0}\right)\right]_0 (1 - b_4\theta), \tag{5.88}$$

where $[\ln(\Delta T_{\max}/T_0)]_0$ is the value of $\ln(\Delta T_{\max}/T_0)$ for impurity-free solution (i.e. when $\theta = 0$) and b_4 is an empirical constant. The values of constants of Eqs. (5.84) and (5.88) obtained by using Langmuir adsorption isotherm are listed in Table 5.11 for different saturation temperatures T_0.

From Table 5.11, one finds that the values of Q_{diff} obtained at a particular saturation temperature T_0 by analyzing the $\Delta T_{\max}(c_i)$ data for KDP solutions in the presence of Cr(III) impurity using Eqs. (5.84) and (5.88) are in good agreement with each other. However, the value of Q_{diff} somewhat decreases while that of b_2 or b_4 increases with an increase in saturation temperature T_0. Moreover, the constants b_2 and b_4 are mutually related: $b_2 \approx 1.3\exp b_4$. These observations are associated with an increase in the value of the constant $b_2 = [3b - \alpha_{\text{eff}}/(1 - Z_0 \ln R_L)]$ of Eq. (5.85) with an increase in T_0. In other words, the impurity effectiveness parameter α_{eff} involved in the kinetic factor increases with an increase in T_0 (cf. Eq. (5.70)).

As seen from Table 5.11, the quantities $\ln\left\{\left[(T_0/\Delta T_{\max})^2\right]_0^{1/2}\right\}$ or $[\ln(\Delta T_{\max}/T_0)]_0$ and Langmuir constant K_L depend on T_0, as shown in Figure 5.22a and b, respectively. In fact, the dependence of $[(T_0/\Delta T_{\max})^2]_0$ on T_0 follows an

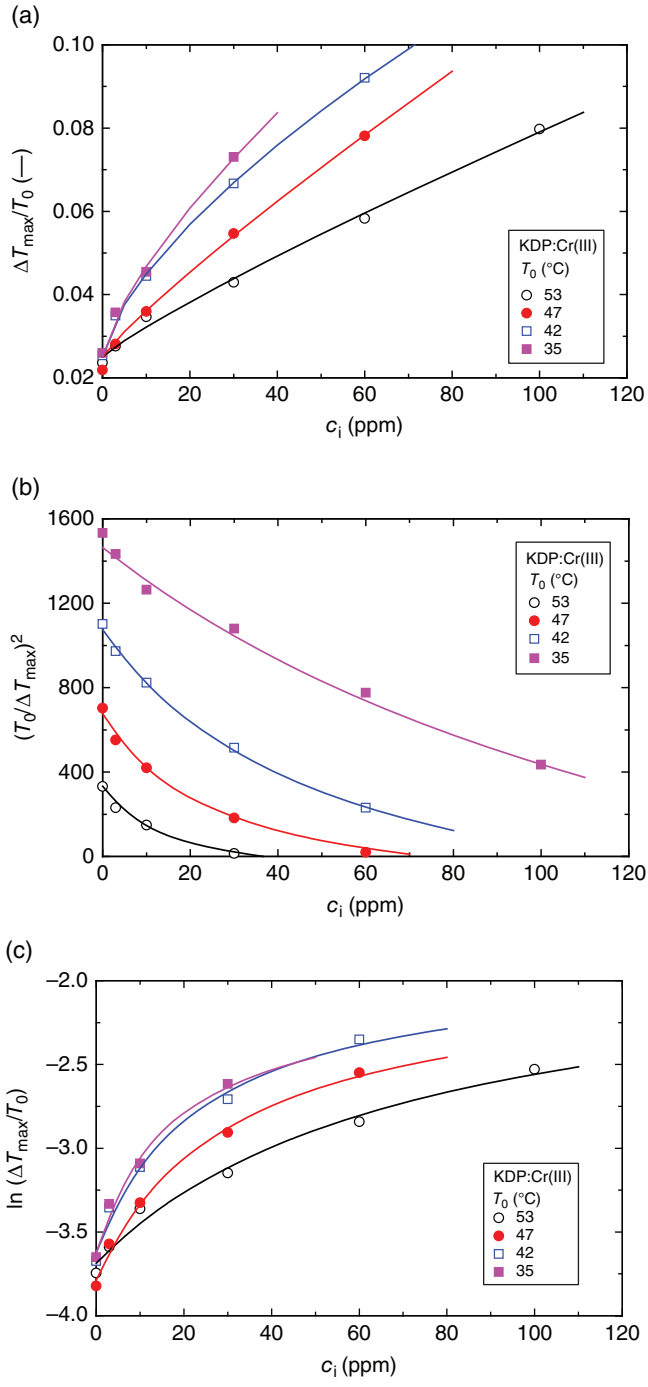

Figure 5.21 Plots of (a) $\Delta T_{max}/T_0$ against c_i, (b) $(T_0/\Delta T_{max})^2$ against c_i, and (c) $\ln(\Delta T_{max}/T_0)$ against c_i of Cr(III) in aqueous KDP solutions at different saturation temperatures T_0. Best-fit plots in (a), (b), and (c) are drawn according to Eqs. (5.68), (5.84), and (5.88), respectively. *Source:* Original data from Shimamura and Suzuki (1989). Adapted from Sangwal (2009c). Copyright (2009), with permission from Elsevier.

Table 5.11 Constants $[(T_0/\Delta T_{max})^2]_0$, K_L, and Q_{diff} for Cr(III) in KDP aqueous solutions.

Relation	T_0 (°C)	$[(T_0/\Delta T_{max})^2]_0$ or $-[\ln(\Delta T_{max}/T_0)]_0$	b_2 or b_4	K_L (10^4)	Q_{diff} (kJ·mol^{-1})
(5.84)	53	1464 ± 35	1.84 ± 0.65	0.62 ± 0.33	23.7 ± 1.1
	46	1075 ± 19	1.45 ± 0.17	1.98 ± 0.46	26.2 ± 0.6
	41	677 ± 23	1.33 ± 0.13	4.03 ± 1.11	27.7 ± 0.6
	36	333 ± 19	1.40 ± 0.25	6.95 ± 3.08	28.7 ± 0.9
(5.88)	53	3.687 ± 0.053	0.142 ± 0.031	1.42 ± 0.66	25.9 ± 1.0
	46	3.787 ± 0.044	0.127 ± 0.014	3.35 ± 0.98	27.6 ± 0.7
	41	3.624 ± 0.0067	0.132 ± 0.018	4.22 ± 1.68	27.8 ± 0.9
	36	3.624 ± 0.074	0.119 ± 0.028	5.81 ± 3.34	28.2 ± 1.1

Source: Adapted from Sangwal (2009c).

Arrhenius-type relationship, with an activation energy $E_a = (34.6 \pm 5.0)$ kJ·mol^{-1}, but $[\ln(\Delta T_{max}/T_0)]_0$ is relatively insensitive to T_0. The Langmuir constant K_L, on the other hand, decreases practically linearly with an increase in T_0. The observed relationship between K_L and saturation temperature T_0 follows from Eq. (5.79).

5.4.3.3 POP-Acetone Solutions Containing PPP Additive

Figure 5.23 presents the plots of experimental F and $\exp(-2\Phi)$ against concentration c_i of PPP in POP solutions, while the curves are drawn according to the theoretical relation (5.84) with the best-fit parameters given in Table 5.12. The values of the experimental F and $\exp(-2\Phi)$ corresponding to $\ln R_L = 0$ were calculated from the plots of $\ln u_{max}$ and u_{max}^{-2} against $\ln R_L$ according to Eqs. (5.20) and (5.27) based on self-consistent Nývlt-like approach (SCA) and CNT, respectively, for the data of the temperature difference ΔT_{max} obtained by turbidimetry [i.e. $\Delta T_{max} = (T_0 - T_c)$] and growth exotherms (i.e. $\Delta T_{max} = (T_0 - T_g)$), denoted by TBT and CRY, respectively.

It may be seen from Table 5.12 that $b_2 = (3b - \alpha_{eff}) \approx 2$ and -1 for turbidity and growth exotherm data, respectively, which means that α_{eff} is equal to about 1 and 4, respectively. These values of α_{eff} imply that PPP impurity in POP solutions does not inhibit the development of POP crystal nuclei by physically blocking the available growth sites, because $0 < \alpha_{eff} < 1$ for this inhibition. Thus, it may be concluded that, because of its lower solubility, PPP impurity molecules act as centers for heterogeneous nucleation for the integration of POP molecules. This conclusion is corroborated by the observation that PPP impurity leads to the crystallization of a PPP-like POP phase (Smith et al., 2005). It is also consistent with the fact that the PPP–POP binary mixture exhibits the

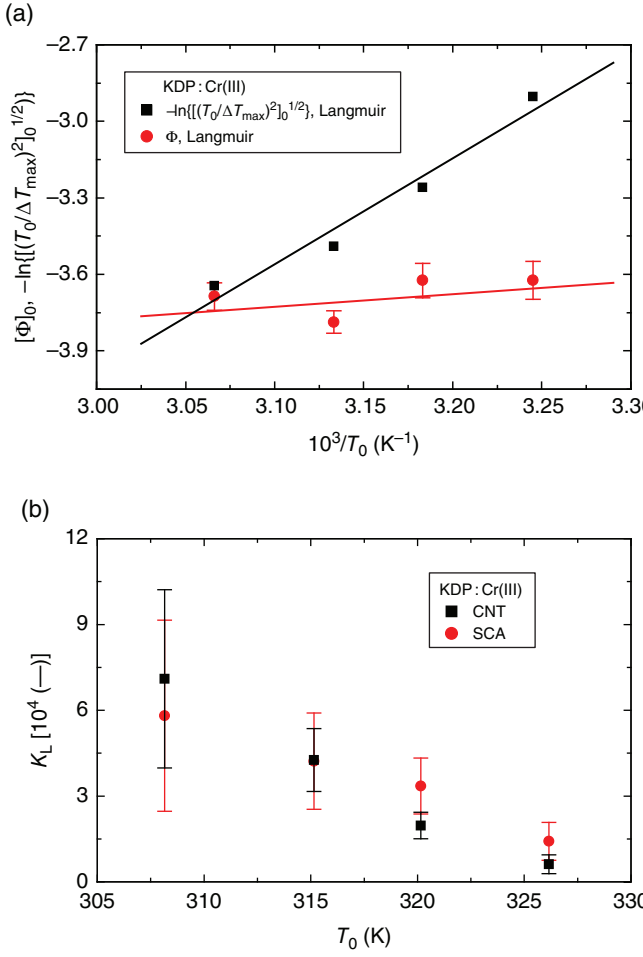

Figure 5.22 Dependence of (a) $\ln\left\{\left[\left(T_0/\Delta T_{max}\right)^2\right]_0^{1/2}\right\}$ and $[\ln(\Delta T_{max}/T_0)]_0$ on $1/T_0$ according to CNT-based Eq. (5.84) and SCA-based empirical equal (5.88), and (b) corresponding Langmuir constant K_L on T_0 for aqueous KDP solutions containing Cr(III) additive. *Source:* Adapted from Sangwal (2009c). Copyright (2009), with permission from Elsevier.

formation of eutectic phases for α, β′, and β polymorphs induced by steric hindrance between the saturated and oleic acid moieties (Minato et al., 1996; Sato, 2001).

An experimental technique for the measurement of MSZW records the temperature of formation of crystallites at 3D nuclei, which have grown only to sizes detectable by the technique. Therefore, it can be assumed that turbidimetry

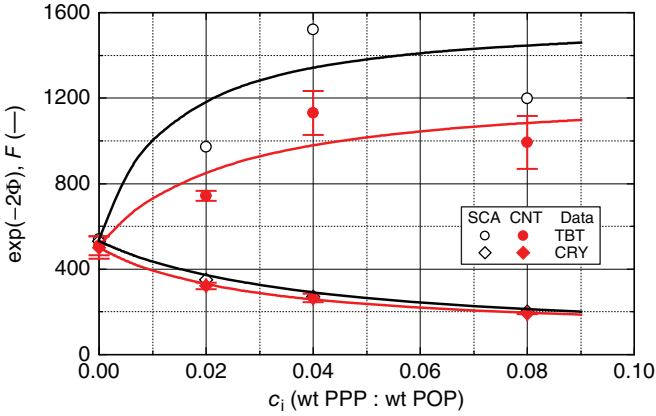

Figure 5.23 Plots of exp(−2Φ) and F against c_i of PPP in POP solutions. Curves represent fit for the data according to Eqs. (5.88) and (5.84). See text for details. *Source:* Adapted from Sangwal and Smith (2010). Copyright (2010), with permission from American Chemical Society.

Table 5.12 Values of constants of Eq. (5.75).

Data	Technique	$[(T_0/\Delta T_{max})^2]_0$	b_2 (—)	K_L (—)	Q_{diff} (kJ·mol^{-1})
F	TBT	508	1.44 ± 0.76	46 ± 71	9.3 ± 2.2
	CRY	500	−0.81 ± 0.04	37 ± 5	8.8 ± 0.3
Φ	TBT	541	1.92 ± 0.91	86 ± 174	10.8 ± 2.7
	CRY	530	−0.89 ± 0.17	26 ± 12	7.9 ± 0.9

Source: Adapted from Sangwal and Smith (2010).

measures maximum supercooling ΔT_{max} mainly for 3D nucleation with negligible contribution due to subsequent growth of stable nuclei. This means that the value of b_2 obtained from turbidity data corresponds to the nucleation event alone, but that obtained from growth exotherm data also represents some contribution of growth of stable nuclei after nucleation.

Figure 5.24 shows the dependence of β and Z on c_i of POP in PPP solutions, while the plots are drawn according to Eq. (5.72) of the theoretical dependence of Z on c_i with two sets of constants given in Table 5.13. Figure 5.24 reveals that the nature of curves of the dependence of Z on c_i for the data obtained from turbidity is very sensitive to the value of α_{eff} (see Curves 1 and 3). In this case, the correct trend of the $Z(c_i)$ data can be predicted with different values of α_{eff} lying between 1 and 4. However, the nature of the curves representing the data obtained from growth exotherms is relatively insensitive to the chosen value of

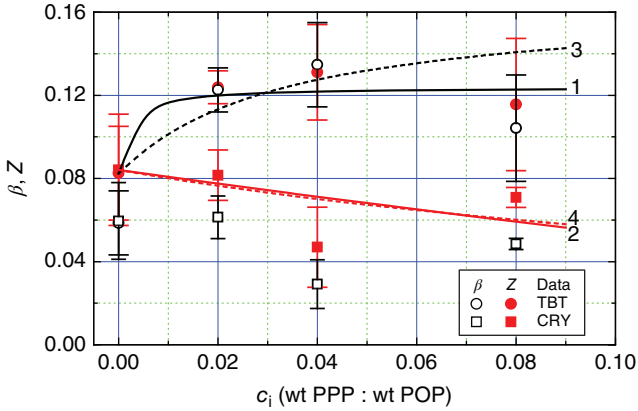

Figure 5.24 Plots of β and Z against c_i of POP in PPP solutions. Dashed curves 3 and 4 are drawn with $|\alpha_{eff}| = 1$, while solid curves 1 and 2 for $|\alpha_{eff}| = 4$ and 0.5 corresponding to data obtained from turbidimetry and growth exotherms, respectively. *Source:* Adapted from Sangwal and Smith (2010). Copyright (2010), with permission from American Chemical Society.

Table 5.13 Values of constants of Eq. (5.72).

Data	Curve	Z_0 (—)	α_{eff} (—)	K_L (—)	Q_{diff} (kJ·mol^{-1})
TBT	1 (solid)	0.0825	4.0	1	0
	3 (dash)	0.0825	1.0	5	3.9
CRY	2 (solid)	0.0841	−0.5	500	15.0
	4 (dash)	0.0841	−1.0	30	8.2

Source: Adapted from Sangwal and Smith (2010).

α_{eff} and may be represented with both $\alpha_{eff} = -0.5$ and -1 (see Curves 2 and 4). Obviously, the scatter in the calculated values of Z and the technique used for the detection of nucleation event in the polythermal method play a decisive role in the theoretical fit according to Eq. (5.75).

It may be noted that the values of Langmuir constant K_L and differential heat of adsorption Q_{diff} corresponding to $Z(c_i)$ data from turbidimetry are very low in comparison with those obtained from data obtained from growth exotherms. This implies that, in the case of data obtained from growth exotherms, the value of Q_{diff} is essentially determined by the growth of stable nuclei to detectable dimensions. The fact that $\alpha_{eff} \geq 1$ for nucleation implies that the impurity particles favor the integration of growth units to the growing nuclei.

5.4.4 Dependence of Maximum Supersaturation Ratio on Impurity Concentration

Equation (5.84) can be employed to analyze the effect of impurities on the MSZW determined by the isothermal method when a solution is rapidly cooled. Using Eq. (5.13), one may write Eq. (5.84) in the form:

$$\frac{1}{\ln^2 S_{max}} = \frac{1}{\ln^2 S_{max0}}(1 - b_2\theta), \tag{5.89}$$

where S_{max} and S_{max0} denote the values of supersaturation ratio of a solute –solvent system in the presence and absence of a particular impurity, respectively, and b_2 is given in Eq. (5.85).

Sangwal and Mielniczek-Brzóska (2004) investigated the effect of several bi- and trivalent cations on the MSZW of aqueous ammonium oxalate (AO) solutions measured as maximum supersaturation ratio S_{max} at a saturation temperature $T_0 \approx 30\,^{\circ}C$ by the isothermal method. The data were obtained for seeded solutions. It was also observed that all these impurities lead to an increase in the solubility of AO. Therefore, the authors took into account the change in the solubility of AO in the calculation of S_{max} data in the presence of these impurities. The dependence of maximum supersaturation ratio S_{max} of AO aqueous solutions on concentration c_i of different cationic impurities at saturation temperature $T_0 \approx 30\,^{\circ}C$ is shown in Figure 5.25a.

It may be noted that S_{max} does not depend on c_i of Cu(II), Fe(III), and Cr(III), while it increases with concentration c_i of all other impurities. Figure 5.25b presents the data of Figure 5.25a as plots of σ_{max}^{-2} against c_i for the effective cationic impurities Mn(II), Co(II), and Ni(II). Here, the supersaturation $\sigma_{max} = S_{max} - 1$. In the figure the curves are drawn according to Eq. (5.89), with the best-fit constants given in Table 5.14.

Taking the differential heat of adsorption Q_{diff} as a measure of the adsorption ability of an impurity, from Table 5.14, one finds that this ability for the three impurities decreases in the sequence: Co(II), Ni(II), and Mn(II). This is precisely the sequence in which the value of b_2 increases for these impurities, the lowest and the highest values of b_2 corresponding to Co(II) and Mn(II) impurities. Since the value of b_2 is determined by the relative contributions of thermodynamic term $3b$ related to solute–solvent interfacial energy γ and kinetic term $[\alpha_{eff}/(1 - Z_0 \ln R_L)]$ associated with the integration of growth entities to the growing embryos (see Eq. (5.85)), one may conclude that the differential heat of adsorption Q_{diff} of an impurity also decreases for a solute–solvent system when the relative contribution of the kinetic term $[\alpha_{eff}/(1 - Z_0 \ln R_L)]$ decreases.

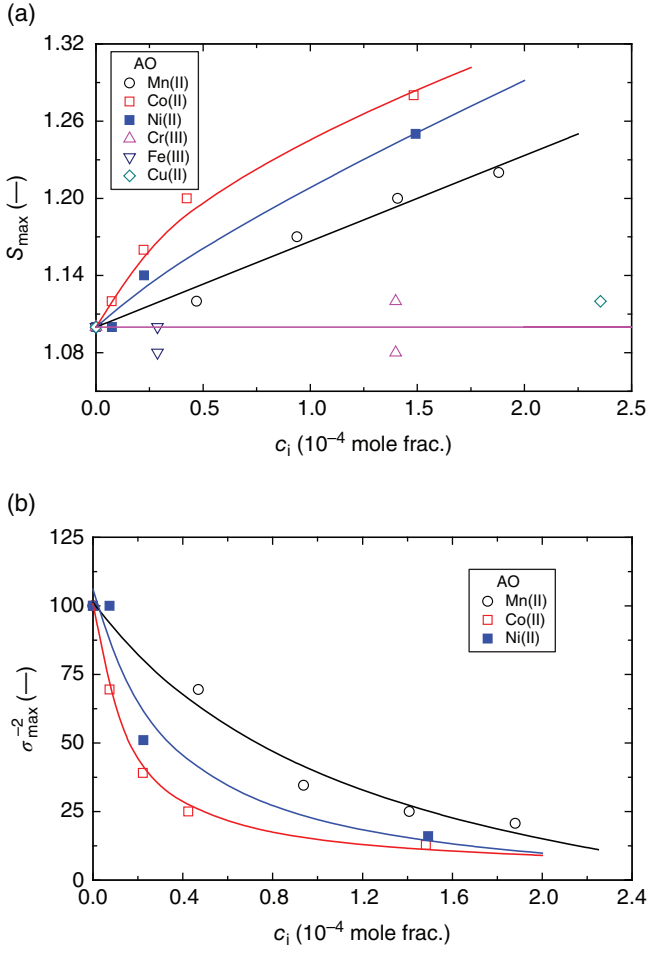

Figure 5.25 (a) Dependence of maximum supersaturation ratio S_{max} on concentration c_i of different cationic impurities in aqueous ammonium oxalate solutions at saturation temperature $T_0 \approx 30\,^{\circ}C$. (b) Plots of σ^{-2}_{max} against c_i for effective cationic impurities. Best-fit curves are drawn according to Eq. (5.89) with constants given in Table 5.14. *Source:* Adapted from Sangwal (2009c). Copyright (2009), with permission from Elsevier.

Table 5.14 Constants of Eq. (5.89) for different impurities in AO solutions.

Impurity	σ_0^{-2}	b_2	K_L (10^4)	Q_{diff} (kJ·mol^{-1})
Mn(II)	101.3 ± 7.2	1.39 ± 0.41	0.79 ± 0.50	22.6 ± 1.2
Co(II)	100.8 ± 2.8	0.97 ± 0.04	7.13 ± 1.10	28.2 ± 0.4
Ni(II)	106.1 ± 17.6	1.06 ± 0.35	2.99 ± 3.42	26.0 ± 1.9

Source: Adapted from Sangwal (2009c).

5.4.5 Solute-Additive Binding Energies and MSZW of Systems

Intentionally added or inherently present foreign component, frequently referred to as additive, in supersaturated solutions is known to modify crystal habits, stabilize the formation of a metastable polymorph, crystallize stable polymorph, and control solution–medium phase transformation. These effects of additives are associated with selective interaction of their molecules stereochemically with the molecules of the nucleating and growing crystallites, thereby influencing nucleation and growth kinetics. Investigations of habit modification and nucleation control in molecular crystals from their solutions containing "tailor-made" additives have shown that the specific interaction of additive molecules occurs preferentially on selective faces of crystalline materials.

As mentioned above in Section 5.4.2, adsorption of an additive on the surface of 3D nuclei forming in a supersaturated medium can lead to a decrease in the solid–medium interfacial energy γ (thermodynamic effect) and a decrease in their surface area, thereby decreasing the preexponential factor J_0 (kinetic effect), by physically blocking the available sites for the integration of growth units. Consequently, an additive is expected to increase the nucleation rate J in the former case and decrease it in the latter case. Equation (5.84) describes the combined effect of the interfacial energy and the attachment frequency on the MSZW. As concluded from Eq. (5.84), MSZW, as measured by $(\Delta T_{\max}/T_0)$, of a system containing an additive decreases when thermodynamic effect prevails over kinetic effect, and it increases when kinetic effect prevails over thermodynamic effect. Moreover, the effect of the additive depends on its concentration in the supersaturated medium. More the additive concentration c_i in the solution, the higher is the change in MSZW.

In a systematic investigation of the binding energy of nine alkanoic acids to the major crystal faces of adipic acid employing molecular modeling techniques, Myerson and Jang (1995) observed the following:

1) The binding energy between different straight-chain alkanoic acids and main low-index faces of the crystal increases with the number of carbon atoms to a maximum of 14 carbon atoms (myristic acid), decreases until 16 carbon atoms (palmitic acid), and then increases again above 16 carbon atoms.
2) The binding forces between additives and the crystal surface are basically electrostatic interactions, hydrogen bonds, and van der Waals forces, which tend to increase with the molecular weight of the additive. However, the stable conformation of the alkanoic acids with less than 14 carbon atoms is a long straight-chain on the crystal surface, whereas that of the acids with more than 16 carbon atoms is more like a coil or helix. Consequently, the binding energy drops from 14 carbon atoms to 16, and then increases again with molecular weight.

3) The binding energy for different faces is associated with their surface structure, with the highest binding energy corresponding to the {100} face. The high values of the binding energies for the {100} and {011} faces are due to carboxylic oxygen and hydrogen atoms (hydrophilic sites) exposed on the above faces for easy access of carboxylic acid groups of alkanoic acids for their adsorption. On the faces such as {110}, where only carboxylic acid groups are exposed, the binding energies are low. However, the faces where both hydrophobic and hydrophilic sites are exposed have intermediate binding energies.

The above authors obtained MSZW data, from measurements of the maximum temperature decrease ΔT_{max}, of adipic acid solution in ethanol saturated at 302.15 K with and without alkanoic acid additives by cooling at a constant cooling rate of 1 K·min^{-1}. The temperature of onset of crystallization was detected by employing a differential scanning calorimeter. Figure 5.26 shows the plot of the calculated binding energy against the MSZW ΔT_{max}. The concentration of each additive in the solution for measurements was 0.7 mol%. The results show that all alkanoic acids increase the MSZW of adipic acid in ethanol solution, and that the higher the binding energy, the larger is the value of ΔT_{max}. The inhibitive effect increases with the number of carbon atoms in alkanoic acids until a maximum is obtained at carbon atom 14 (myristic acid). Thereafter, the MSZW decreases up to carbon atom 16 (palmitic acid), and then it increases again with increasing carbon number.

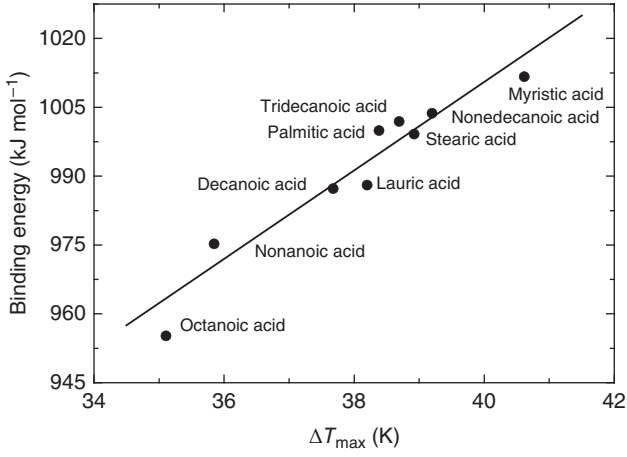

Figure 5.26 Relationship between binding energy of different alkanoic acids on the {100} faces of adipic acid and its MSZW in ethanol solutions saturated at 302.15 K. Additive concentration for MSZW measurements was 0.7 mol%. *Source:* Adapted from Myerson and Jang (1995). Copyright (1995), with permission from Elsevier.

Another example of the effect of additives on the MSZW of a solute–solvent system is due to Poornachary et al. (2008), who studied the effect of different L-amino acids on the MSZW of aqueous saturated glycine solutions. Glycine ($^{+}H_3NCH_2CO_2^{-}$) is the simplest amino acid and exhibits polymorphism with α, β, and γ crystal structures, whereas the amino acids used as additives were: Aspartic, glutamic, alanine, valine, leucine, isoleucine, and phenylalanine acids. The additives studied belonged to two categories: (i) Neutral L-amino acids such as alanine, valine, leucine, isoleucine, and phenylalanine, and (ii) acidic L-amino acids like aspartic and glutamic acids. The additives were added at different concentrations up to 4 wt% to the solution saturated at 303.15 K. The authors observed that addition of the above impurities does not affect the glycine solubility. A saturated solution was initially heated at 313.15 K for 30 min to ensure complete dissolution and then cooled at a rate of 0.5 K·min^{-1} until the onset of sudden nucleation detected by a sharp decrease in the solution transmittance.

Measurements of the MSZW of aqueous glycine solutions showed that neutral amino acids do not affect the value of MSZW irrespective of their concentration, but acidic amino acids lead to an increase in MSZW in proportion with the additive concentration, resulting in about 49 and 39% increase at L-aspartic and L-glutamic acid concentrations of 4 wt%, respectively. Under the experimental conditions used above with L-aspartic and L-glutamic acids, metastable α-glycine was observed to be crystallized only at low supersaturations, as from pure solutions, but the habit of the crystals was modified. However, at higher supersaturations, a mixture of both unstable α and stable γ forms of glycine is crystallized. In contrast to L-amino acids, trace amounts of D- and DL-amino acids were found to favor the crystallization of stable γ form of glycine. The authors interpreted the preferred crystallization of the γ form of glycine from consideration of inhibition of nucleation of unstable α polymorph involving interactions between charged molecular species, formed at the experimental conditions from dissociation of aspartic and glutamic acids in glycine solution, and the developing crystal nuclei of the two phases of glycine in the supersaturated solution.

From the above results it may be concluded that different alkanoic acid impurities contained in saturated adipic acid solution in ethanol and L-aspartic and L-glutamic acid impurities contained in saturated aqueous glycine solutions lead to a decrease in the 3D nucleation rate by the adsorption of impurity molecules on the surfaces of the developing nuclei. The results of the effect of impurities on the crystallization of solute from its saturated solution are also consistent with the idea that the strength of the intermolecular bonds involved during adsorption determines the MSZW and with the predictions of Eq. (5.84) based on the classical theory of 3D nucleation.

5.5 Effects of Some Other Factors on MSZW of Solutions

5.5.1 Effect of Stirring and Ultrasound on MSZW

The value of MSZW of a supersaturated solute–solvent system depends on the level of agitation (Akrap et al., 2010; Kubota, 2008; Liang et al., 2004; Mitchell and Frawley, 2010; Nývlt et al., 1985) and ultrasound applied during cooling crystallization of a supersaturated solution in its metastable zone (Lyczko et al., 2002; Kordylla et al., 2008; Wohlgemuth et al., 2010). Both agitation and ultrasound reduce its value and it is generally accepted that they induce new nuclei by different mechanisms.

According to Kubota (2008), agitation leads to an increase in secondary nucleation from the grown crystals nucleated by primary nucleation, causing an increased number density N_{det}/V of detectable nuclei by a detection technique (see Section 5.1.2). An alternative interpretation involves washing-away of surface-induced nuclei from the stirrer surface to the bulk solution due to strong fluid shear forces (Liang et al., 2004). The effect of ultrasound power is also similar and is associated with the formation of additional nucleation centers. It is generally accepted that ultrasonic waves produce cavitation bubbles whose surface acts as centers of formation of heterogeneous nuclei (Wohlgemuth et al., 2010).

5.5.2 Effect of Solution Volume on MSZW

The MSZW is traditionally considered independent of the crystallizer working volume V as long as the same detection technique is employed for its measurement. However, it is observed that the value of MSZW of a solute–solvent system depends on the solution volume (Kadam et al., 2011, 2012; Mielniczek-Brzóska, 2014; Mitchell and Frawley, 2010). Figure 5.27 shows, as an example, the data of maximum supercooling ΔT_{max} for isonicotinamide –ethanol of concentration $0.1619\ g{\cdot}ml^{-1}$ obtained at cooling rate $R_L = 0.5$ $K{\cdot}min^{-1}$ in different solution volumes V.

As seen from the figure, the experimental ΔT_{max} data is a distribution of values differing by about 25 K. This large volume-dependent deviation implies that MSZW of a system is not a fixed (deterministic) quantity caused as a result of multiple nucleation in the volume and their subsequent growth to detectable dimension. If this large volume is divided into smaller compartments, one can assume that the rate of nucleation per compartment remains the same in all compartments comprising a large solution volume and ensures reproducibility of the MSZW (i.e. MSZW is deterministic). However, when the sample volume is reduced, the nucleation in a compartment begins to occur randomly and takes

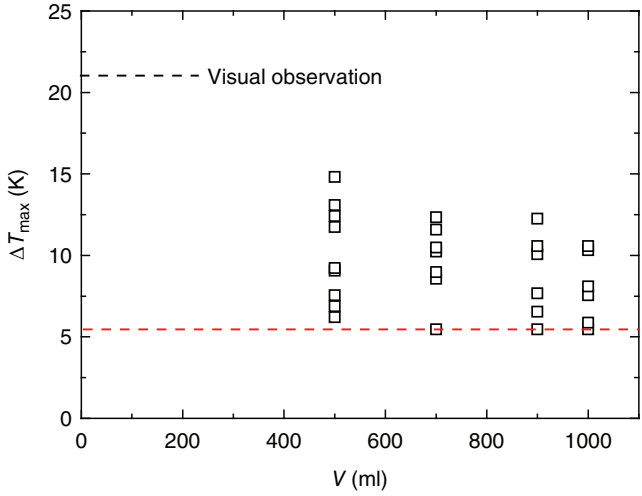

Figure 5.27 Example of stochastic distribution of maximum supercooling ΔT_{max} for isonicotinamide–ethanol of concentration 0.1619 g·ml^{-1} obtained at cooling rate $R_L = 0.5$ K·min^{-1} in different solution volumes *V*. *Source:* Adapted from Kadam et al. (2012). Copyright (2012), with permission from Elsevier.

a stochastic nature. This means that the variations in the MSZW gradually disappear when the solution volume is increased. Since the nucleation rate increases with increasing supersaturation, one also expects that the transition volume of the solution decreases with increasing cooling rate R_L when the deterministic MSZW becomes stochastic.

Different stochastic models describing the effect of working solution volume on the MSZW of a system are given by Kadam et al. (2012) and Kubota (2012). In their considerations, Kadam et al. (2012) assumed that in a saturated solution of volume V a single nucleus is initially formed by heterogeneous and then this nucleus, after its growth to a minimum size, leads to a secondary nucleation event sufficient to generate spontaneously detectable crystal volume fraction by processes such as attrition by crystallizer impeller. To derive an equation of the probability of detection of crystals in the MSZW, these authors considered three functions: (i) Poisson's law to describe stochastic behavior of nucleation in volume V, (ii) equation of rate of 3D nucleation, and (iii) power-law growth kinetics. From their analysis the authors concluded that: (i) the reduction in the spread occurs exponentially with an increase in volume, implying that the MSZW will be deterministic when the volume approaches infinity and (ii) for the stochastic model there is a transition volume above which the MSZW is reproducible within 0.5 °C.

In his approach to describe the volume dependence of MSZW, Kubota (2012) followed a procedure similar to that used in Section 5.1.2 and used power law to describe the dependence of nucleation rate and temperature difference ΔT, but splitted the total sample size into smaller sizes. Finally, he derived the relation of the stochastic MSZW in the form:

$$\Delta T_{\mathrm{maxS}} = \Gamma\left(\frac{2+m^*}{1+m^*}\right)\left[\frac{1+m^*}{k_1 V}\right]^{1/(1+m*)} R_{\mathrm{L}}^{1/(1+m*)}, \tag{5.90}$$

where $\Gamma[(m^*+2)/(m^*+1)]$ is the gamma function defined as

$$\Gamma(x) = \int_0^\infty t^{x-1}\exp(-t)\mathrm{d}t, \tag{5.91}$$

V is the solution volume, and, as defined in Section 5.1.2, k_1 and m^* are constants of Eq. (5.8). In order to compare stochastic MSZW (ΔT_{maxS}) with deterministic MSZW (ΔT_{maxD}) for a system, Kubota derived the relation for the ratio r_{MSZW} of these two MSZWs in the form:

$$r_{\mathrm{MSZW}} = \frac{\Delta T_{\mathrm{maxS}}}{\Delta T_{\mathrm{maxD}}} = \Gamma\left(\frac{m^*+2}{m^*+1}\right)\left[\frac{1/V}{(N/V)_{\mathrm{det}}}\right]^{1/(1+m^*)}, \tag{5.92}$$

where $1/V$ and $(N/V)_{\mathrm{det}}$ are the number densities of crystals at the moments when deterministic and stochastic MSZWs are reached, respectively, and m^* is the primary nucleation order. Both $1/V$ and $(N/V)_{\mathrm{det}}$ are determined by the detection technique but the ratio r_{MSZW} does not reach unity unless the term contained in the square term is unity.

Kashchiev (2011) pointed out that the dependence of the maximum supersaturation ΔT_{max} for nucleation on the volume V of a solute–solution system can be explained by the CNT. According to the nucleation theory, in single component nucleation the stationary number of N_i of critically-sized nuclei of i molecules is approximately given by $N_i = k_i C^* V$ and $N_i = k_i C^* S_{\mathrm{A}}$ corresponding to homogeneous and heterogeneous nucleation, respectively. In these relations k_i is an i-dependent factor, C^* (in m^{-3} or m^{-2}) is the equilibrium concentration of critically-sized nuclei, and $S_{\mathrm{A}} = \kappa V^{2/3}$, where κ is a shape factor. The equilibrium concentration C^* is given by: $C^* = C_0\exp[-B/(\Delta T/T_0)^2]$, where C_0 is the concentration of monomers, and B is given by Eq. (5.23)). Assuming that $\Delta T_{\mathrm{max}}/T_0$ defines the value of temperature difference $\Delta T/T_0$ when one critically-sized nucleus of i^* monomers is formed and $N_i(\Delta T_{\mathrm{max}}/T_0) = 1$, one obtains the relations (Kashchiev, 2011):

$$\frac{\Delta T_{\mathrm{max}}}{T_0} = \left[\frac{B}{\ln(k_i C_0 V)}\right]^{1/2}, \quad \text{homogeneous nucleation}, \tag{5.93}$$

$$\frac{\Delta T_{\mathrm{max}}}{T_0} = \left[\frac{B}{\ln(\kappa k_i C_0 V^{2/3})}\right]^{1/2}, \quad \text{heterogeneous nucleation}. \tag{5.94}$$

Obviously, the relative supercooling u_{max} decreases with increasing solution volume V.

The above treatment does not include the effect of cooling rate R_L on u_{max}. To account for this we may use the approach advanced in Section 5.1.4 based on the CNT. As in the derivation of Eq. (5.90) by Kubota (2012), we assume that the relationship between nucleation rate J and cooling rate R_L is given by Eq. (5.15). Then, under the assumption that the number N_i of critically-sized nuclei induced by cooling is volume independent, with the definition of N_i given above, from Eqs. (5.27) and (5.93) one obtains

$$u_{max} = \frac{\Delta T_{max}}{T_0} \approx \frac{\omega^{3/2}}{\lambda_s} \left[\frac{\kappa Z}{(1 - Z \ln R_L)} \right]^{1/2}, \tag{5.95}$$

where

$$Z \approx \ln \left[\frac{f_s \lambda_s}{k_i C_0 T_0 V} \right], \tag{5.96}$$

with f_s as a new constant. For a particular system with constant f_s, λ, and ω, Eq. (5.95) predicts that, corresponding to a given value of R_L, u_{max} decreases with an increase in V, and corresponding to a given volume V, u_{max} increases with an increase in R_L. As seen from Figure 5.28, the experimental results are consistent with these predictions.

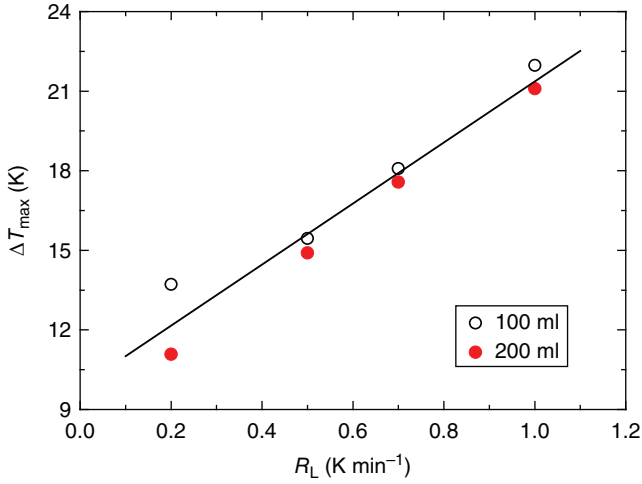

Figure 5.28 Dependence of ΔT_{max} on cooling rate R_L for two volumes of 100 and 200 ml paracetamol–ethanol solutions saturated at 307.15 K. *Source:* Adapted from Mitchell and Frawley (2010). Copyright (2010), with permission from Elsevier.

It should be mentioned that in order to examine the effect of solution volume on MSZW, identical experimental conditions for measurements should be maintained. For example, during a study of the MSZW of 4 and 100 ml KNO_3 aqueous solutions, Mielniczek-Brzóska (2014) observed similar maximum dispersion of about 20% in the value of ΔT_{max} for the two volumes in the studied range of cooling rate R_L and saturation temperature T_0, which did not appear to be significantly related to the solution volume V. For all solutions saturated at different T_0, this author also observed that the average value of ΔT_{max} measured in 100 ml solutions at a given R_L is higher than that measured in 4 ml solutions. The former observation of large dispersion both in 4 and 100 ml solutions suggests that the nucleation process in these solution volumes is essentially stochastic. The latter observation of a higher value of MSZW in larger volume is, however, contrary to the prediction of CNT and stochastic model. One possible explanation of this discrepancy is associated with differences in the diffusion processes in the two volumes.

5.6 Nonisothermal Crystallization Kinetics in Melts

We recall here that nonisothermal crystallization is based on the cooling of a liquid at a particular cooling rate R_L from the equilibrium state at temperature T_0 to a lower temperature T_c where crystallization takes place and that this notion is used in the derivation of all of the theoretical relationships, described above, between normalized temperature difference $\Delta T/T_0$ and cooling rate R_L. Therefore, so far as the understanding of the MSZW is concerned, all of the equations are equally applicable in the case of melts, with essentially the same physical quantities and parameters.

It is observed that the evolution of overall nonisothermal crystallization kinetics from melts at different cooling rates R_L is similar to isothermal crystallization kinetics. At a given cooling rate R_L, the time dependence of the overall crystallization curve shows an initial period t_{in} without observable crystallized mass and then there is a sudden increase in the crystallized mass, which subsequently approaches a constant value. It is also observed that the induction period t_{in} and the duration of the overall crystallization y for a crystallizing phase decrease with increasing cooling rate R_L, whereas an increase in R_L induces the formation of more metastable phases such that the crystallization of the stable phase occurring at low R_L is completely replaced by the crystallization of the metastable phase with an increasing R_L. Therefore, basically the mechanisms proposed by isothermal crystallization are also valid here but the effect of cooling rate has to be included in the explanation of nonisothermal crystallization (for example, see: Narine et al., 2006; Rousset, 2002; Rousset and Rappaz, 1996; Rousset et al., 1998; Smith et al., 2005). Analysis of the time dependence of volume fraction of

crystallized masses of individual components and mixtures of components is carried out by splitting cooling curves into small time steps of constant temperature and fitting the data with Avrami equation (4.5) considering k and q as temperature-dependent parameters, time–temperature–transformation diagrams, and fictitious times between two successive time steps. This procedure also enables to calculate time t_{in} of start and time t_f of finish of crystallization as a function of cooling rate R_L (see Figure 5.2). Some of these aspects are discussed in Section 7.4.3.

References

Akrap, M., Kuzmanić, N., and Prlić-Kardum, J. (2010). Effect of mixing on the crystal size distribution of borax decahydrate in a batch cooling crystallizer. *J. Cryst. Growth* 312: 3603–3608.

Ananda Babu, G. and Ramasamy, P. (2008). Effect of additives in supersaturated binary and ternary solutions on cluster growth by gravity driven concentration gradient studies. *Cryst. Res. Technol.* 43: 626–633.

Anuar, N., Doud, W.R.W., Roberts, K.J. et al. (2009). An examination of solution chemistry, nucleation kinetics, crystal morphology, and polymorphic behavior of aqueous phase batch crystallized L-isoleucine at the 250 mL scale size. *Cryst. Growth Des.* 9: 2853–2862.

Atkins, P.W. (1998). *Physical Chemistry*, 6. Oxford: Oxford University Press.

Barrett, P. and Glennon, B. (2002). Characterizing the metastable zone width and solubility curve using Lasentec FBRM and PVM. *Trans. Inst. Chem. Eng. A* 80: 799–805.

Barrett, M., McNamara, M., Hao, H.-X. et al. (2010). Supersaturation tracking for the development, optimization and control of crystallization processes. *Chem. Eng. Res. Des.* 88: 1108–1119.

Bockris, J.O.'.M. and Reddy, A.K.N. (1970). *Modern Electrochemistry*, vol. 1. New York: Plenum.

Ceyhan, A. and Bulutcu, A.N. (2005). The commom ion effect on the metastable zone width of KCl. *VDI Ber.* 1901: 229–234.

Correla, P., Lopes, C., Piedade, M.E.M. et al. (2006). Solubility and metastable zone width of 1-keto-1,2,3,4-tetrahydro-6-methylcarbozole in acetone. *J. Chem. Eng. Data* 51: 1306–1309.

Dang, L., Wei, H., Zhu, Z., and Wang, J. (2007). The influence of impurities on phosphoric acid hemihydrate crystallization. *J. Cryst. Growth* 307: 104–111.

Danuwila, D.D., Carrol, L.B., and Berglund, K.A. (1994). An investigation of the applicability of attenuated total reflection infrared spectroscopy for measurement of solubility and supersaturation of aqueous citric acid solutions. *J. Cryst. Growth* 137: 561–568.

Danuwila, D.D., Carrol, L.B., and Berglund, K.A. (1997). ATR FTIR spectroscopy for in-situ measurement of supersaturation. *J. Cryst. Growth* 179: 185–193.

Dhanaraj, P.V., Bhagavannarayana, G., and Rajesh, N.P. (2008a). Effect of amino acid additives on crystal growth parameters and properties of ammonium dihydrogen orthophosphate crystals. *Mater. Chem. Phys.* 112: 490–495.

Dhanaraj, P.V., Mahadevan, C.K., Bhagavannarayana, G. et al. (2008b). Growth and characterization of KDP crystals with potassium carbonate as additive. *J. Cryst. Growth* 310: 5341–5346.

Eggers, D.F., Gregory, N.W., Halsey, G.D., and Rabinovitch, B.S. (1964). *Physical Chemistry*. New York: Wiley.

Graber, T.A., Taboada, M.E., Alvarez, M.N., and Schmidt, E.H. (1999). Determination of mass transfer coefficient for crystal growth of nitrate salts. *Cryst. Res. Technol.* 34: 1269–1277.

Groen, H. and Roberts, K.J. (2004). An examination of the crystallization of urea from supersaturated aqueous and aqueous-methanol solutions monitored in-process using ATR FTIR spectroscopy. *Cryst. Growth Des.* 5: 929–936.

Gürbüz, H. and Özdemir, B. (2003). Experimental determination of the metastable zone width of borax decahydrate by ultrasonic velocity measurement. *J. Cryst. Growth* 252: 343–349.

Haja Hameed, A.S., Ravi, G., Nixon Azariah, A. et al. (2003). Growth and characterization of organic nonlinear optical crystal: indole-3-aldehyde. *J. Phys. Chem. Solids* 64: 147–153.

Haja Hameed, A.S., Rohani, S., Yu, W.C. et al. (2007). Growth and characterization of a new chelating agent added 4-dimethylamino-*N*-methyl-4-stilbazolium tosylate (DAST) single crystals. *Mater. Chem. Phys.* 102: 60–66.

Kadam, S.S., Kramer, H.J.M., and ter Horst, J.H. (2011). Combination of a single primary nucleation event and secondary nucleation in crystallization processes. *Cryst. Growth Des.* 11: 1271–1277.

Kadam, S.S., Kulkarni, S.A., Ribera, R.C. et al. (2012). A new view on the metastable zone width during cooling crystallization. *Chem. Eng. Sci.* 72: 10–19.

Kashchiev, D. (2000). *Nucleation: Basic Theory with Applications*. Oxford: Butterworth-Heinemann.

Kashchiev, D. (2011). Note: on the critical supersaturation for nucleation. *J. Chem. Phys.* 134: 196102.

Kashchiev, D., Borissova, A., Hammond, R.B., and Roberts, K.J. (2010a). Effect of cooling rate on the critical undercooling for crystallization. *J. Cryst. Growth* 312: 698–705.

Kashchiev, D., Borissova, A., Hammond, R.B., and Roberts, K.J. (2010b). Dependence of the critical undercooling for crystallization on the cooling rate. *J. Phys. Chem.* 114: 5441–5446.

Kim, K.-J. (2000). Spherulitic crystallization of 3-nitro-1,2,4-triazol-5-one in water +*N*-methyl-2-pyrrolidone. *J. Cryst. Growth* 208: 569–578.

Kim, K.-J. and Kim, K.-M. (2001). Nucleation kinetics in spherulitic crystallization of explosive compound: 3-nitro-1,2,4-triazol-5-one. *Powder Technol.* 119: 109–116.

Kim, K.-J. and Mersmann, A. (2001). Estimation of metastable zone width in different nucleation processes. *Chem. Eng. Sci.* 56: 2315–2324.

Kordylla, A., Koch, S., Tumakaka, F., and Schembecker, G. (2008). Towards an optimized crystallization with ultrasound: effect of solvent properties and ultrasonic process parameters. *J. Cryst. Growth* 310: 4177–4184.

Kubota, N. (2008). A new interpretation of metastable zone widths measured for unseeded solutions. *J. Cryst. Growth* 310: 629–634.

Kubota, N. (2012). Effect of sample volume on metastable zone width and induction time. *J. Cryst. Growth* 345: 27–33.

Kubota, N., Yukota, M., and Mullin, W. (2000). The combined influence of supersaturation and impurity concentration on crystal growth. *J. Cryst. Growth* 212: 480–488.

Lewiner, F., Klein, J.P., Puel, F., and Fevotte, G. (2001). On-line ATR FTIR measurement of supersaturation during solution crystallization processes. Calibration and applications on three solute/solvent systems. *Chem. Eng. Sci.* 56: 2069–2084.

Li, G., Xue, L., Su, G. et al. (2005). Rapid growth of KDP crystal from aqueous solutions with additives and its optical studies. *Cryst. Res. Technol.* 40: 867–870.

Liang, K., White, G., Wilkinson, D. et al. (2004). Examination of the process scale dependence of L-glutamic acid batch crystallized from supersaturated aqueous solutions in relation to reactor hydrodynamics. *Ind. Eng. Chem. Res.* 43: 1227–1234.

Lyczko, N., Espitalier, F., Louisnard, O., and Schwartzentruber, J. (2002). Effect of ultrasound on the induction time and the metastable zone widths of potassium sulphate. *Chem. Eng. J.* 86: 233–241.

Ma, Y., Zhu, J., Ren, H., and Chen, K. (2009). Effect of impurity ions on solubility and metastable zone width of phosphoric acid. *Cryst. Res. Technol.* 44: 1313–1318.

Marangoni, A.G. (2005). Crystallization kinetics. In: *Fat Crystal Networks* (ed. A.G. Marangoni), 21–82. New York: Marcel Dekker.

Marciniak, B. (2002). Density and ultrasonic velocity of undersaturated and supersaturated solutions of fluoranthene in trichloroethylene, and study of their metastable zone width. *J. Cryst. Growth* 236: 347–356.

Mielniczek-Brzóska, E. (2014). Effect of sample volume on the metastable zone width of potassium nitrate aqueous solutions. *J. Cryst. Growth* 271: 271–274.

Minato, A., Ueno, S., Yano, J. et al. (1996). Synchrotron radiation X-ray diffraction study on phase behavior of PPP-POP binary mixture. *J. Am. Oil Chem. Soc.* 73: 1567–1572.

Mitchell, N.A. and Frawley, P.J. (2010). Nucleation kinetics of paracetamol-ethanol solutions from metastable zone widths. *J. Cryst. Growth* 312: 2740–2746.

Myerson, A.S. and Jang, S.M. (1995). A comparison of binding energy and metastable zone width for adipic acid with various additives. *J. Cryst. Growth* 156: 459–466.

Narine, S.S., Humphrey, K.L., and Bouzidi, L. (2006). Modification of the Avrami model for application of the melt crystallization of lipids. *J. Am. Oil Chem. Soc.* 83: 913–921.

Nývlt, J. (1968). Kinetics of nucleation from solutions. *J. Cryst. Growth* 3–4: 377–383.

Nývlt, J., Söhnel, O., Matuchova, M., and Broul, M. (1985). *The Kinetics of Industrial Crystallization*. Prague: Academia.

Omar, W. and Ulrich, J. (2003). Influence of crystallization conditions on the mechanism and rate of crystal growth of potassium sulphate. *Cryst. Res. Technol.* 38: 34–41.

Omar, W. and Ulrich, J. (2006). Solid liquid equilibrium, metastable zone, and nucleation parameters of the oxalic acid–water system. *Cryst. Growth Des.* 6: 1927–1930.

Omar, W. and Ulrich, J. (2007). Determination of nucleation parameters and the solid liquid interfacial energy of the KCl-ethanol-water system. *Cryst. Res. Technol.* 42: 432–439.

Ościk, J. (1982). *Adsorption*. Warsaw: PWN.

Poornachary, S.K., Chow, P.S., and Tan, R.B.H. (2008). Influence of solution speciation of impurities on polymeric nucleation in glycine. *Cryst. Growth Des.* 8: 179–185.

Qu, H., Louhi-Kultanen, M., and Kallas, J. (2006). In-line image analysis on the effects of additives in batch cooling crystallization. *J. Cryst. Growth* 289: 286–294.

Rajesh, N.P., Lakshmana Perumal, C.K., Santhana Raghavan, P., and Ramasamy, P. (2001). Effect of urea on metastable zone width, induction time and nucleation parameters of ammonium dihydrogen orthophosphate. *Cryst. Res. Technol.* 36: 55–61.

Rousset, P. (2002). Modeling crystallization kinetics of triacylglycerols. In: *Physical Properties of Lipids* (ed. A.G. Marangoni and S.S. Narine), 1–36. New York: Marcel Dekker.

Rousset, P. and Rappaz, M. (1996). Crystallization kinetics of the pure triacylglycerols glycerol-1,3-dipalmitate-2-oleate, glycerol-1-palmitate-2-oleate-3-stearate, and glycerol-3,3-distearate-2-oleate. *J. Am. Oil Chem. Soc.* 73: 1051–1057.

Rousset, P., Rappaz, M., and Minner, E. (1998). Polymorphism and solidification kinetics of the binary system POS-SOS. *J. Am. Oil Chem. Soc.* 75: 857–864.

Sahin, O., Dolas, H., and Demir, H. (2007). Determination of nucleation kinetics of potassium tetraborate tetrahydrate. *Cryst. Res. Technol.* 42: 766–772.

Sangwal, K. (2007). *Additives and Crystallization Processes: From Fundamentals to Applications*. Chichester: Wiley.

Sangwal, K. (2009a). Novel approach to analyze metastable zone width determined by the polythermal method: physical interpretation of various parameters. *Cryst. Growth Des.* 9: 942–950.

Sangwal, K. (2009b). A novel self-consistent Nývlt-like equation for metastable zone width determined by the polythermal method. *Cryst. Res. Technol.* 44: 231–247.

Sangwal, K. (2009c). Effect of impurities on the metastable zone width of solute-solvent systems. *J. Cryst. Growth* 311: 4050–4061.

Sangwal, K. (2010). On the effect of impurities on the metastable zone width of phosphoric acid. *J. Cryst. Growth* 312: 3316–3325.

Sangwal, K. (2011a). Some features of metastable zone width of various systems determined by polythermal method. *Cryst. Eng. Comm.* 13: 489–501.

Sangwal, K. (2011b). Recent developments in understanding of the metastable zone width of different solute–solvent systems. *J. Cryst. Growth* 318: 103–109.

Sangwal, K. and Mielniczek-Brzóska, E. (2004). Effect of impurities on metastable zone width for the growth of ammonium oxalate monohydrate crystals from aqueous solutions. *J. Cryst. Growth* 267: 662–675.

Sangwal, K. and Sato, K. (2012). Nucleation and crystallization kinetics of fats. In: *Structure-Function Analysis of Edible Fats* (ed. A.G. Marangoni), 25–78. Urbana: AOCS Press.

Sangwal, K. and Smith, K.W. (2010). On the metastable zone width of 1,3-dipalmitoyl-2-oleoylglycerol, tripalmitoylglycerol and their mixtures in acetone solutions. *Cryst. Growth Des.* 10: 640–647.

Sangwal, K. and Wójcik, K. (2009). Investigation of metastable zone width of ammonium oxalate aqueous solutions. *Cryst. Res. Technol.* 44: 363–372.

Sato, K. (2001). Crystallization behaviour of fats and lipids – a review. *Chem. Eng. Sci.* 56: 2255–2265.

Sayan, P. and Ulrich, J. (2001). Effect of various impurities on the metastable zone width of boric acid. *Cryst. Res. Technol.* 36: 411–417.

Shimamura, O. and Suzuki, M. (1989). The increase of temperature range in the region of supersaturation of KDP solution by addition of impurity. *J. Cryst. Growth* 98: 850–852.

Smith, K.W., Cain, F.W., and Talbot, G. (2005). Crystallisation of 1,3-dipalmitoyl-2-oleoylglycerol and tripalmitoylglycerol and their mixtures from acetone. *Eur. J. Lipid Sci. Technol.* 107: 583–593.

Taboada, M.E., Palma, P.A., and Graber, T.A. (2003). Crystallization of potassium sulfate by cooling and salting-out using 1-propanol in a calorimetric reactor. *Cryst. Res. Technol.* 38: 21–29.

Titiz-Sargut, S. and Ulrich, J. (2002). Influence of additives on the width of the metastable zone. *Cryst. Growth Des.* 2: 371–374.

Wang, L., Feng, H., Dong, Y. et al. (2016). Solubility and metastable zone width of aqueous sodium dichromate hydrate solutions in the presence of sodium chromate additive. *J. Cryst. Growth* 454: 105–110.

Wang, X.J. and Ching, C.B. (2006). A systematic approach for preferential crystallization of 4-hydroxy-2-pyrrolidone: thermodynamic, kinetics, optimal operation and in-situ monitoring aspects. *Chem. Eng. Sci.* 61: 2406–2417.

Wang, X.J., Yang, X., Liu, Y.X., and Ching, C.B. (2008). Intrinsic MSZW characteristics of racemic species: implication for chiral crystallization. *AIChE J.* 54: 2281–2292.

Wierzbowska, B., Matynia, A., Piotrowski, K., and Koralewska, J. (2007). Solubility and nucleation in l(+)-ascorbic acid–methanol–ethanol–water system. *Chem. Eng. Process.* 46: 351–359.

Wohlgemuth, K., Ruether, F., and Schembecker, G. (2010). Sonocrystallization and crystallization with gassing of adipic acid. *Chem. Eng. Sci.* 65: 1016–1027.

Zhang, X.-Y., Wang, X., Hao, L. et al. (2012). Solubility and metastable zone width of DL-tartaric acid in aqueous solution. *Cryst. Res. Technol.* 47: 1153–1163.

6

Antisolvent Crystallization and the Metastable Zone Width

Antisolvent crystallization is widely used in chemical and pharmaceutical industries for different materials. Antisolvent crystallization is traditionally carried out at a predefined constant temperature by feeding an antisolvent at a constant rate to a saturated solution of a solute in a solvent in which it is fairly soluble. Supersaturation for crystallization of the solute at the constant temperature is created by the antisolvent because of the solubility difference of the solute in the two solvents. The maximum antisolvent content added continuously to the solution of a solute saturated in a suitable solvent at a given temperature defines the metastable zone width (MSZW) of the solution and is a measure of the maximum value of supersaturation necessary for spontaneous occurrence of three-dimensional (3D) nucleation generated by the antisolvent (Kubota, 2008; O'Ciardha et al., 2011; O'Grady et al., 2007; Sangwal, 2010). Experimental measurements of the value of MSZW in antisolvent crystallization involving antisolvent feeding to saturated solutions at predefined temperature have shown that its value depends on initial solution concentration, type of antisolvent, antisolvent addition rate, location of addition of antisolvent, and solution stirring rate (Chaitanya and Sarkar, 2014; O'Grady et al., 2007). For the precise measurements of MSZW in antisolvent crystallization techniques such as focused-beam reflectance measurements (FBRM) (Nowee et al., 2008; O'Ciardha et al., 2011; O'Grady et al., 2007), and monitoring of solute concentration in the solution by ATR-FTIR spectroscopy (O'Grady et al., 2007), turbidity probe (Zhang et al., 2015; Zhu et al., 2003), ultrasound probe (Jim and Kim, 2012; Park and Yeo, 2012), and transmission of laser light through the solution (Chaitanya and Sarkar, 2014; Guo et al., 2005; Sangwal and Mielniczek-Brzóska, 2016a, b, 2017) have been used. Apart from antisolvent crystallization, combined antisolvent/cooling crystallization (Knox et al., 2009; Lindenberg et al., 2009; Trifkovic et al., 2009), appearance of different polymorphs of crystallizing compounds of industrial importance during antisolvent crystallization (Kitamura and Sugimoto, 2003), and drown-out crystallization (Holmbäck and Rasmuson,

Nucleation and Crystal Growth: Metastability of Solutions and Melts, First Edition.
Keshra Sangwal.
© 2018 John Wiley & Sons, Inc. Published 2018 by John Wiley & Sons, Inc.

1999; Jim and Kim, 2012) have been investigated. Studies have also been devoted to the theoretical explanation of the relationship between MSZW in antisolvent crystallization, antisolvent feeding rate, and solution stirring (Kubota, 2008; O'Grady et al., 2007; Sangwal, 2010).

In this chapter an overview of different aspects of antisolvent and combined antisolvent/cooling crystallization is presented with emphasis on processes involved. Drowning-out crystallization is not discussed here because the literature on it is confined to induction period measurements and particle size distribution. The appearance of different polymorphs of crystallizing compounds by antisolvent and combined antisolvent/cooling crystallization are also not discussed. Induction period measurements, and crystal size distribution and formation of different polymorphs in these crystallizations are discussed in Chapters 7 and 8, respectively.

6.1 Observation Techniques for Antisolvent Crystallization

O'Grady et al. (2007) carried out measurements of MSZW for antisolvent crystallization of benzoic acid in a water–ethanol mixture, with water as an antisolvent, using FBRM and ATR-FTIR spectroscopy and compared the results obtained by the two methods. The authors found that: (i) FBRM detects crystals in the system whereas ATR-FTIR indicates the formation of crystals when the solute concentration decreases by a detectable amount and (ii) FBRM detects the onset of nucleation before ATR-FTIR spectroscopy. FBRM is a probe-based instrument that measures *in situ* the time duration for a part of a monochromatic laser beam reflected back up the probe to a detector by change in the size, shape, and population of particles. With increasing antisolvent feeding time, the FBRM count rate shows an abrupt increase after remaining constant over a certain time and finally approaches a maximum value (O'Grady et al., 2007). Simple optical probe, applied by Chaitanya and Sarkar (2014), also gives the variation of output voltage during a typical antisolvent crystallization run from aqueous glycine solution with feeding duration of ethanol similar to that of FBRM counts mentioned above. However, ATR-FTIR spectroscopy measures solution concentration by irradiating the solution with infrared light to produce an infrared spectrum, which is a characteristic of the vibrational structure of the substance in contact with the ATR probe. As a consequence of absorption of light by the substance concentration, the relative absorption of light initially shows a slow decrease from a constant value, followed by a practically exponential decrease with antisolvent feeding duration (O'Grady et al., 2007).

Technique based on recording laser light transmitted through saturated solutions of different compounds for the measurements of MSZW of solutions by

polythermal crystallization has been used in several studies (Dang et al., 2007; Nong et al., 2014; Sun et al., 2009; Wang et al., 2006), but neither these measurements were carried out for long durations nor details of laser wavelength are given in these publications. In the studies on antisolvent crystallization, the experimental setups for the measurement of MSZW of solutions have provision of control of temperature of solution (for example, see Chaitanya and Sarkar, 2014; Lindenberg et al., 2009), but changes in solution temperature, if any, occurring during crystallization are not mentioned and discussed.

It is interesting to note that the trends of the evolution of FBRM counts (O'Grady et al., 2007) and output voltage with time (Chaitanya and Sarkar, 2014) are similar to the trend described by the fraction y of overall crystallization of mass m of solute from solution involving 3D nucleation according to the treatment of the Kolmogorov–Johnson–Mehl–Avrami (KJMA) theory (Kashchiev, 2000; see Section 3.9) given by the relation:

$$y = \frac{m}{m_{\max}} = 1 - \exp\left[-\left(\frac{t}{\Theta}\right)^{q}\right], \tag{6.1}$$

where Θ is a time constant, the exponent q is an indicator of the type of nucleation and diffusion processes, and $m_{\max}$ is the maximum value of the crystallized mass m of the solute when $t \gg \Theta$ (i.e. $y = m/m_{\max} \rightarrow 1$). The overall crystallization fraction y increases from zero to unity with increasing t. Equation (6.1) can equally be used to define the fraction $(1 - y)$ of the uncrystallized solute mass. Then, $(1 - y)$ is an exponential function and its value decreases from unity to zero with increasing t. This is the trend shown by the relative absorption of solute concentration in the solution by ATR-FTIR spectroscopy.

An indigenously designed experimental setup, used recently by Sangwal and Mielniczek-Brzóska (2016a, b), for the investigation of processes of antisolvent crystallization occurring in aqueous ammonium dihydrogen phosphate (ADP) solutions saturated at 30 °C by *in situ* measurements of their temperature T and laser-beam intensity I transmitted through them during feeding of acetone and methanol antisolvents at different rates is shown in Figure 6.1. This setup is somewhat similar to that used by Guo et al. (2005) for the investigation of the effect of ultrasound on antisolvent crystallization of roxithromycin, an organic pharmaceutical ingredient. It consists of a double-walled crystallizer of 300 ml capacity, a thermostating arrangement, a temperature meter (accuracy 0.01 °C), an antisolvent feeding arrangement, a magnetic stirrer with predefined rotation rate, and a mechanical stirrer. Antisolvents were fed at predefined rates R_A to 220 ml of aqueous ADP solutions saturated at 30 °C, and the temperature T_s of the solution in the crystallizer as a function of antisolvent feeding time t of antisolvents was recorded *in situ* every second. The results presented below in Sections 6.2 and 6.3 are mainly from the investigations published recently using this experimental setup.

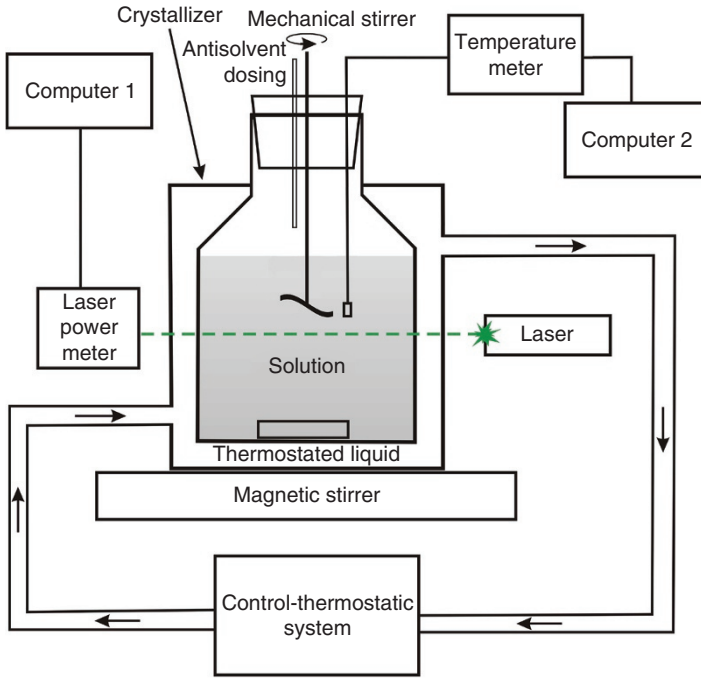

Figure 6.1 Schematic illustration of experiment arrangement of measurements of transmitted laser-beam intensity *I* and temperature *T* of solution during antisolvent crystallization. Different parts are indicated. Crystallizer dimensions are not drawn according to scale. *Source:* Reproduced from Sangwal and Mielniczek-Brzóska (2016a). Copyright (2016), with permission from Wiley.

6.2 Light Intensity Measurements

The recorded data of laser-beam intensity I transmitted through the volume of pure water and solution as a function of feeding time t of an antisolvent at the selected rates R_A frequently reveal small differences in the initial values of their laser-beam intensity I for antisolvent feeding durations before t_0 due to somewhat different alignment of the laser beam through the crystallizer and due to the source of distilled water. To suppress the effect of these differences during the analysis, the original $I(t)$ data were normalized by dividing them by the initial transmitted beam intensity I_0 (i.e. normalized beam intensity $I_n(t) = I(t)/I_0$).

6.2.1 Some Experimental Data

Figure 6.2 shows typical examples of dependence of normalized transmitted laser-beam intensity I_n on feeding time t of methanol at different rates R_A to

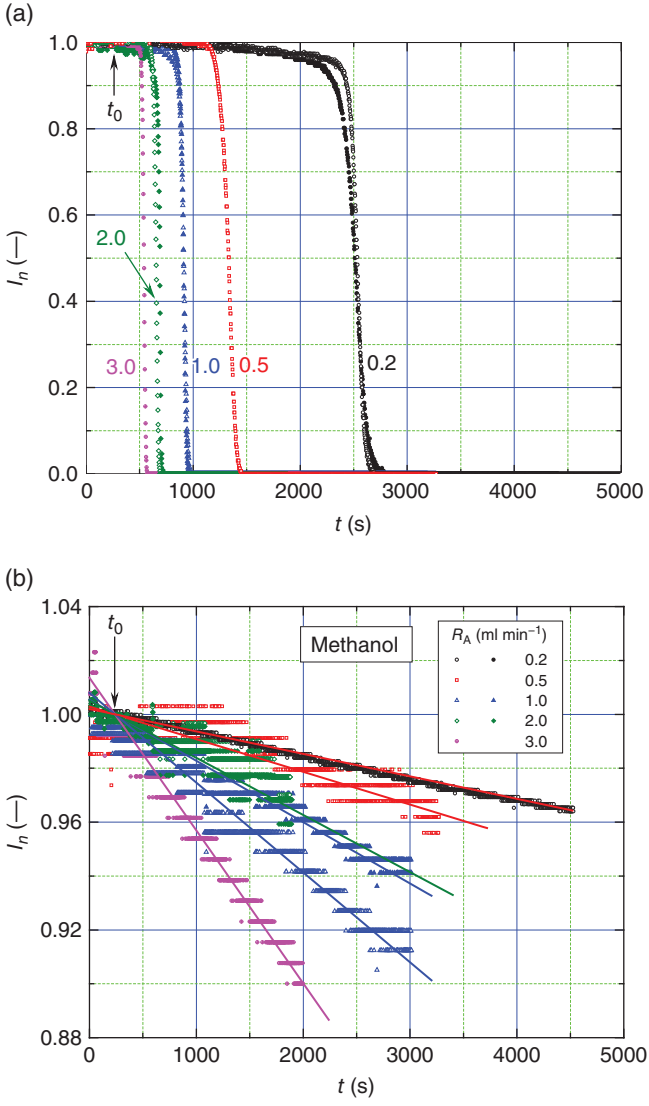

Figure 6.2 Typical examples of dependence of normalized transmitted laser-beam intensity I_n on feeding time t of methanol at different rates R_A to (a) saturated ADP solution and (b) water. *Source:* Adapted from Sangwal (2017). Copyright (2016), with permission from Elsevier.

saturated ADP solution and pure water. Plots of the normalized intensity I_n with methanol, seen in Figure 6.2a, show an initial sluggish decrease with a concave curvature, followed by a subsequent steep fall. These observations are similar to that of the variation of ATR-FTIR absorption with addition of water to saturated

benzoic acid solutions in water–ethanol systems. In contrast to the trends of I_n for solutions mentioned above, Figure 6.2b shows that the intensity I_n of water decreases practically linearly with increasing methanol feeding time t and the decrease is higher with increasing value of feeding rate R_A. The relative changes ΔI_{rel} in the normalized laser-beam intensities, associated with the effect of solute ADP on its crystallization by the addition of antisolvent methanol, calculated by subtracting the data of normalized laser intensity I_n of water as a function of methanol addition time t (Figure 6.2b) from the corresponding data of I_n for aqueous saturated ADP solution (Figure 6.2a), are shown in Figure 6.3.

It may be noted from Figure 6.3 that $\Delta I_{rel}(t)$ curves for different feeding rates R_A of methanol are essentially similar to those of Figure 6.2a in the ΔI_{rel} range between −0.2 and −0.8, but the curvatures of the curves are somewhat increased for ΔI_{rel} above about −0.1 and below about −0.9. Moreover, irrespective of different methanol feeding rates R_A to the ADP solutions, in the case of $\Delta I_{rel} <$ −0.9, for all curves the intensity change ΔI_{rel} approaches a lowest value, followed by its subsequent linear increase with time t.

It was observed (Sangwal, 2017) that the trend of the plots of I_n of aqueous ADP solutions and water as a function of feeding time t of ethanol at different rates R_A are similar to those observed in the case of methanol but the effect of ethanol to water is relatively poor, especially at R_A exceeding 2 ml·min^{-1} when I_n practically remains unchanged with feeding time t. However, the normalized

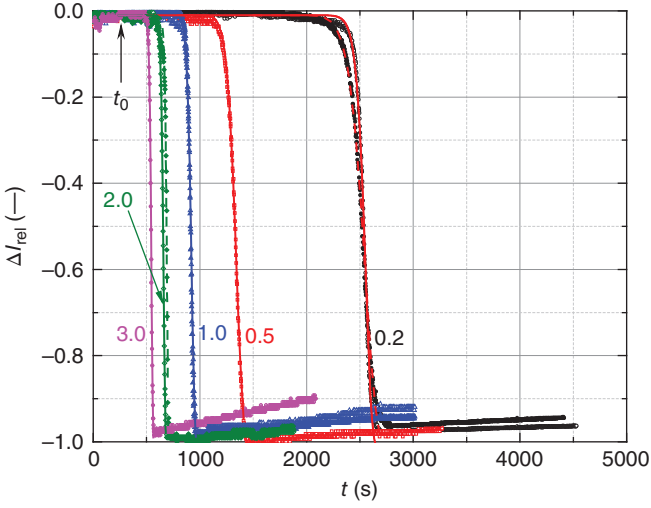

Figure 6.3 Change in relative normalized transmitted laser-beam intensity ΔI_{rel} of ADP solutions saturated at 30 °C with methanol feeding duration t at different rates R_A. *Source:* Adapted from Sangwal and Mielniczek-Brzóska (2016b). Copyright (2016), with permission from Elsevier.

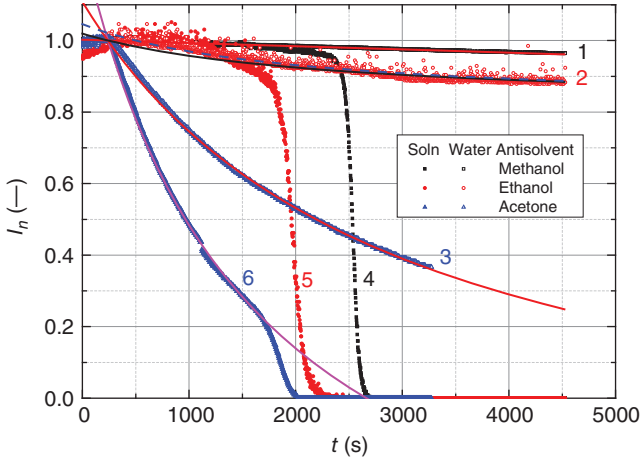

Figure 6.4 Examples of dependence of normalized transmitted laser-beam intensity I_n on feeding time t of different antisolvents to (1–3) water and (4–6) saturated ADP solution at rate $R_A = 0.2$ ml·min^{-1}; curves (1,4) methanol, (2,5) ethanol, and (3,6) acetone. *Source:* Adapted from Sangwal (2017). Copyright (2016), with permission from Elsevier.

transmitted laser-beam intensity I_n of aqueous ADP solution against the feeding time t of acetone for various feeding rates R_A showed (Sangwal and Mielniczek-Brzóska, 2016a) that, after the initial duration t_0 without antisolvent feeding, the normalized intensity I_n with acetone initially decreases exponentially with a convex curvature, followed by a sudden short steep decrease up to t_{min} when finally the intensity approaches zero. The $I_n(t)$ plots for acetone show a somewhat different trend from that observed for methanol and ethanol and is due to a different behavior of the $I_n(t)$ plots, which exhibit a sudden, practically exponential, decrease in I_n with t after the addition of acetone. Figure 6.4 shows examples of dependence of normalized transmitted laser-beam intensity I_n on feeding time t of different antisolvents to water (Curves 1–3) and saturated ADP solutions (Curves 4–6) at rate $R_A = 0.2$ ml·min^{-1}. The plots are drawn according to an equation based on adsorption of antisolvent molecules (Sangwal, 2017).

The trend of the plots of I_n for aqueous ADP solutions against feeding time t of methanol and ethanol obviously differs from that of acetone. However, in all $I_n(t)$ plots for different feeding rates R_A of these antisolvents there are long linear steep parts of slope $\Delta I_n/\Delta t$ occurring at time t_1, which corresponds to the onset of 3D nucleation. The slope $\Delta I_n/\Delta t$ of the $I_n(t)$ plots increases, whereas the feeding duration $(t_1 - t_0)$ decreases with increasing feeding rate R_A. As mentioned above, convex curvatures for acetone and concave curvatures for methanol in the initial parts of the $I_n(t)$ plots of aqueous ADP solutions increase with increasing antisolvent feeding rate R_A. The above observations of different

curvatures in the $I_n(t)$ plots of aqueous ADP solutions in the initial stage and trends of sudden steep decrease after the onset of 3D nucleation are important findings in antisolvent crystallization.

6.2.2 Processes Involved in Antisolvent Crystallization

Measurements of normalized light intensity I_n of aqueous solutions as a function of antisolvent provide useful information about the processes involved in antisolvent crystallization. Here, we consider the $I_n(t)$ data for the feeding of methanol to aqueous ADP solution and solvent water at different rates R_A (Sangwal and Mielniczek-Brzóska, 2016b). The choice of methanol as an antisolvent is justified for the reason that addition of methanol gives linear dependence of I_n in water on feeding time t. For the analysis, the data of change ΔI_{rel} in the normalized intensities I_{ns} and I_{nw} in aqueous solution and water, respectively, as a function of methanol feeding time t at different rates R_A were considered. From the $\Delta I_{rel}(t)$ data rates $R_{\Delta I(rel)} = \Delta I_{rel}/\Delta t$ of linear steep decrease in the relative normalized transmitted intensities ΔI_{rel} in the interval between –0.3 and –0.7 and slow increase beyond the lowest ΔI_{rel} were calculated as functions of methanol feeding rates R_A.

The experimental data of $R_{\Delta I(rel)}(R_A)$ may be analyzed according to the following relations (Sangwal and Mielniczek-Brzóska, 2016b):

$$R_{\Delta I(rel)} = R^* + LR_A, \quad \text{linear relation}, \tag{6.2}$$

$$R_{\Delta I(rel)} = R_0 R_A^p, \quad \text{power-law relation}. \tag{6.3}$$

In Eq (6.2) the intercept R^* represents the extrapolated value of $R_{\Delta I(rel)}$ corresponding to $R_A = 0$ and L is the slope of the $R_{\Delta I(rel)}(R_A)$ plots, whereas in Eq. (6.3) R_0 and p are empirical constants. Note that the units of $R_{\Delta I(rel)}$ are s^{-1} whereas that of L are m^{-3}. The $R_{\Delta I(rel)}(R_A)$ data are shown in Figure 6.5a and b according to Eqs. (6.2) and (6.3), respectively. In Figure 6.5b the $R_{\Delta I(rel)}(R_A)$ data are shown in the form of plots of $\ln(R_{\Delta I(rel)})$ against $\ln R_A$. The best-fit values of the constants of the two relations are given in Table 6.1.

The values of the parameters of Eqs. (6.2) and (6.3) are related to the processes of growth of crystallites and correspond to the regions of linear decrease and linear increase in the change in the relative normalized intensity $R_{\Delta I(rel)}$, denoted as decreasing and increasing trends, respectively, with increasing R_A. The decrease in $R_{\Delta I(rel)}$ with increasing R_A is a consequence of increasing dimensions of growing crystallites nucleated progressively with increasing antisolvent content in the solution. This aspect is discussed below. However, the increase in $R_{\Delta I(rel)}$ after reaching its minimum value with an increase in R_A is likely to be associated with the reorganization of the size distribution of the already grown crystallites by Ostwald ripening. This topic is discussed in Chapter 8.

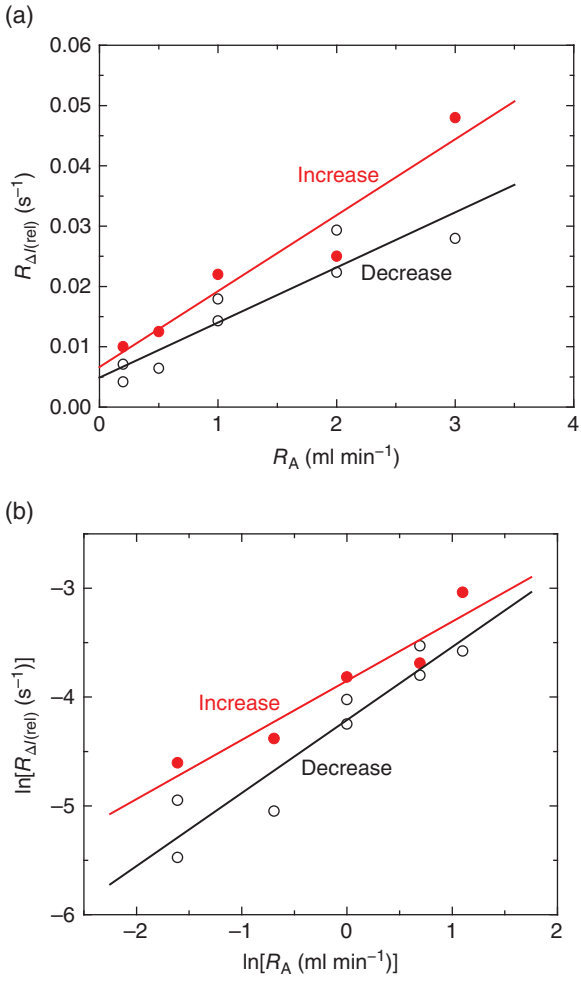

Figure 6.5 The $R_{\Delta I(\mathrm{rel})}(R_A)$ data for aqueous ADP solutions saturated at 30 °C with antisolvent methanol shown as plots of (a) $R_{\Delta I(\mathrm{rel})}$ against R_A and (b) $\ln(R_{\Delta I(\mathrm{rel})})$ against $\ln R_A$, according to Eqs. (6.2) and (6.3), respectively. Best-fit values of the constants of the two relations are given in Table 6.1. *Source:* Original data from Sangwal and Mielniczek-Brzóska (2016b).

Table 6.1 Parameters of Eqs. (6.2) and (6.3).

	Eq. (6.2)			Eq. (6.3)			
Trend	10^3R^* (s^{-1})	10^3L (m^{-3})	R^2	$\ln[R_0$ (s^{-1})]	R_0 (s^{-1})	p	R^2
Decrease	4.9	9.1	0.848	−4.21	$1.48{\cdot}10^{-2}$	0.671	0.881
Increase	6.7	12.6	0.900	−10.7	$2.12{\cdot}10^{-5}$	0.544	0.884

6.3 Temperature Measurements

6.3.1 Some Experimental Data

Trends of plots of changes in the temperatures $T_s(t)$ of ADP solutions saturated at 30 °C and pure solvent $T_w(t)$ from the initial temperature of 30 °C with the time t of feeding of three antisolvents (i.e. methanol, ethanol, and acetone) at different rates R_A are similar (Sangwal and Mielniczek-Brzóska, 2017). An example of plots of $T_s(t)$ and $T_w(t)$ for ethanol is shown in Figure 6.6. Here, we describe the general features following from the plots of this figure.

As seen from the example of Figure 6.6a for ADP solution, after the initial stage up to $t_0 = 240$ s without feeding of antisolvent when the temperature remains constant, with antisolvent feeding time t at a particular rate R_A there is an initial slight increase in T up to t_1, but after t_1 the solution temperature T_s increases abruptly and approaches a maximum temperature T_{max} at t_{max}. Beyond t_{max} the solution temperature decreases and approaches the starting saturation temperature of 30 °C. The curvature of the decrease in a $T_s(t)$ plot is different before and after the interruption of feeding, denoted by t_{int}. Figure 6.6b shows the plots of change in the temperature T_w of water as a function of antisolvent feeding duration t for different feeding rates R_A. It should be noted that each $T_s(t)$ plot reveals an initial practically linear increase and then a decrease after going through a maximum at temperature T_{max} at feeding time t_{max}. Before and after T_{max}, the curvature of the $T_w(t)$ plot increases with increasing antisolvent feeding rate R_A.

The plots of the temperature T_s of the solution against antisolvent feeding duration t for the three antisolvent studied by Sangwal and Mielniczek-Brzóska (2016a, b, 2017) reveal that: (i) after the initial feeding-free duration t_0, each $T_s(t)$ plot shows an initial steep increase in T_s, followed by a shoulder at t_1 when the solution temperature T_s again increases abruptly and approaches a maximum temperature T_{max} at t_{max}, and (ii) the increase in solution temperature T_s up to t_1 increases with R_A and can be up to 1 K for $R_A = 3$ ml·min^{-1}, depending on the antisolvent used (Table 6.2). Obviously, according to these studies the temperature T_s of a saturated solution does not remain constant during the feeding of the antisolvent. A change in the solution temperature is accompanied by a change in its density. Therefore, one expects that the concentration of particles serving as transport and scattering centers also changes in the solution involving antisolvent crystallization.

It is interesting to note that the value of the maximum temperature difference ΔT_{max} in the initial stage of feeding of an antisolvent to saturated solution and water decreases in the order: methanol, ethanol, and acetone, but the value of ΔT_{max} corresponding to the time t_{max} is practically independent of the antisolvent. As seen from Table 6.2, the former observation is directly connected with the dielectric constant ε of the solvent and is associated with the solute–solvent

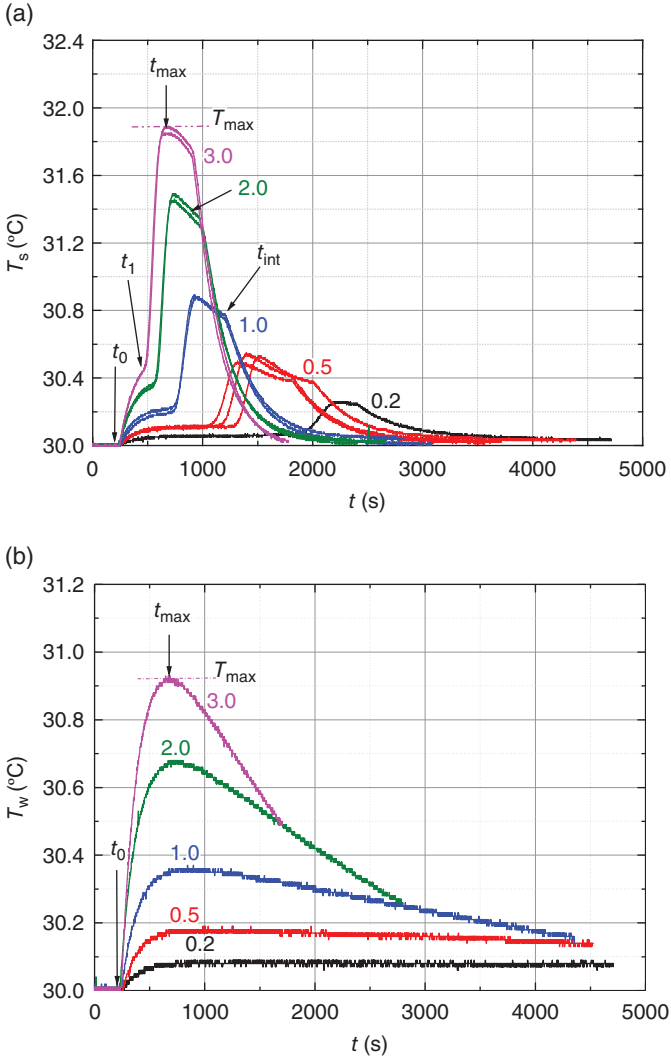

Figure 6.6 Change in temperature T of (a) aqueous ADP solution saturated at 30 °C and (b) pure water at 30 °C with feeding of ethanol at different rates R_A. In (a) time t_0 indicates beginning of ethanol feeding whereas t_1, t_{max}, and t_{int} represent onset of 3D nucleation, the maximum temperature T_{max}, and interruption of methanol feeding, respectively. *Source:* Reproduced from Sangwal and Mielniczek-Brzóska (2017). Copyright (2017), with permission from Wiley.

Table 6.2 Values of different ΔT_{max} of solution temperature and water in different antisolvents.

		ADP solution		Water
Antisolvent[a]	ε (—)	ΔT_{max} at t_1 (K)	ΔT_{max} at t_{max} (K)	ΔT_{max} at t_{max} (K)
Methanol	33.0	0.70	1.9	1.05
Ethanol	25.3	0.45	1.8	0.93
Acetone	21.0	0.42	2.0	0.80

[a] Dielectric constant ε at 20 °C (Lide, 1996/1997).

and solute–antisolvent interactions. However, the latter observation of the temperature change ΔT_{max} corresponding to the time t_{max} is associated with the evolution of heat involved during crystallization due to these interactions.

In order to examine the effect of antisolvent on the crystallization of ADP from its aqueous solutions as a function of antisolvent feeding time t, it is necessary to consider relative changes $\Delta T = T_s - T_w$ due to the solute ADP at different feeding rates R_A in the temperature T_s of solutions and temperature T_w of water as the function of antisolvent feeding duration t. Figure 6.7 shows, as an example, plots of the temperature difference ΔT against feeding rate t of ethanol for different feeding rates R_A. A characteristic feature of the plots of ΔT against t for a particular feeding rate R_A is the appearance of three well-defined regions. Two of them lying between t_0 and t_1 and beyond t_2 are connected with $\Delta T < 0$, with maximum temperature drops in these regions marked as ΔT_{min1} and ΔT_{min2} (see Figure 6.7). However, the region between t_1 and t_2 is associated with $\Delta T > 0$. In this region, initially ΔT steeply increases and then decreases, after going through a maximum temperature change ΔT_{max} at time t_{max}. Region I between t_0 and t_1 is associated with the creation of supersaturation necessary for 3D nucleation, region II between t_1 and t_2 involves processes of formation of 3D nuclei and their subsequent growth, whereas region III beyond t_2 is associated with processes like Ostwald ripening. The origin of different temperature differences is discussed later.

It should be noted that the time t_1 corresponds to the equilibrium temperature T_0 of the solution containing antisolvent content Δx_{max} necessary for the creation of supersaturation for 3D nucleation, but the time t_{min1} when the lowest temperature ΔT_{min1} is attained is always somewhat lower than t_1 (i.e. $t_{min1} < t_1$). This feature may be seen from Figure 6.7. As discussed below (Sangwal and Mielniczek-Brzóska, 2016a, b), for the determination of MSZW the values of $\Delta t = t_1 - t_0$ are more reliable than those of $\Delta t^* = t_{min1} - t_0$.

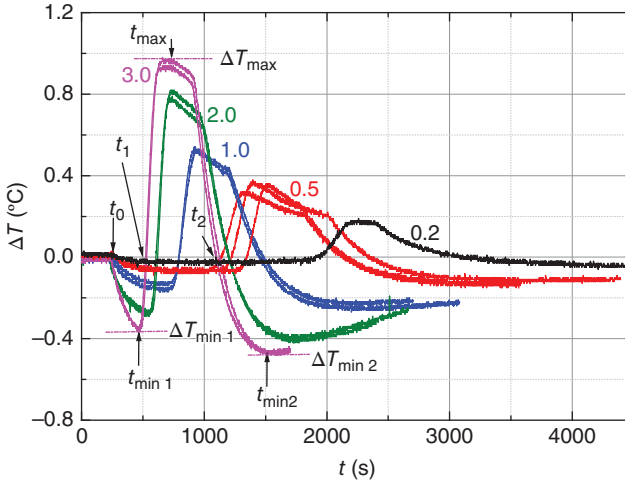

Figure 6.7 Change in temperature difference ΔT of ADP solutions saturated at 30 °C with ethanol feeding duration t at different rates R_A. *Source:* Reproduced from Sangwal and Mielniczek-Brzóska (2017). Copyright (2017), with permission from Wiley.

6.3.2 Kinetics of Temperature Increase

As mentioned above, the temperature T_s of aqueous ADP solution saturated at 30 °C increases with an increase in the duration t of feeding of an antisolvent at different rates R_A in regions between t_0 and t_1 and between t_1 and t_{max} (Figure 6.6a). A similar increase in the temperature T_w of pure water is observed with increasing duration of feeding of the antisolvent at different rates R_A up to t_{max} (Figure 6.6b). In all these cases there are antisolvent feeding durations Δt when the temperature increases linearly with increasing antisolvent feeding duration t, but this duration is relatively short in the region immediately after t_0. We denote these linear increases in temperature T_s and T_w with time by rates $R_T = \Delta T_s/\Delta t$ and $R_T = \Delta T_w/\Delta t$. Similarly, data of the rate R_T, defined as $R_T = \Delta(\Delta T)/\Delta t$, of temperature increase in the region between t_1 and t_{max} in the plots of difference ΔT in temperatures T_s and T_w of aqueous ADP solutions and water, respectively, in antisolvent feeding duration Δt against rate R_A may also be considered (see Figure 6.7). However, since this rate is practically the same as the linear rate between t_1 and t_{max}, it is sufficient to consider the linear rate calculated from the $T_s(t)$ plots. Following Sangwal and Mielniczek-Brzóska (2016a, b, 2017), we discuss here the above $R_T(R_A)$ data for aqueous ADP solution and pure water in different antisolvents.

The rates R_T of linear increase in temperature T of aqueous ADP solutions in antisolvent feeding regions between $t_1 - t_0$ and $t_{max} - t_1$ are associated with the creation of supersaturation for 3D nucleation and growth of crystallites,

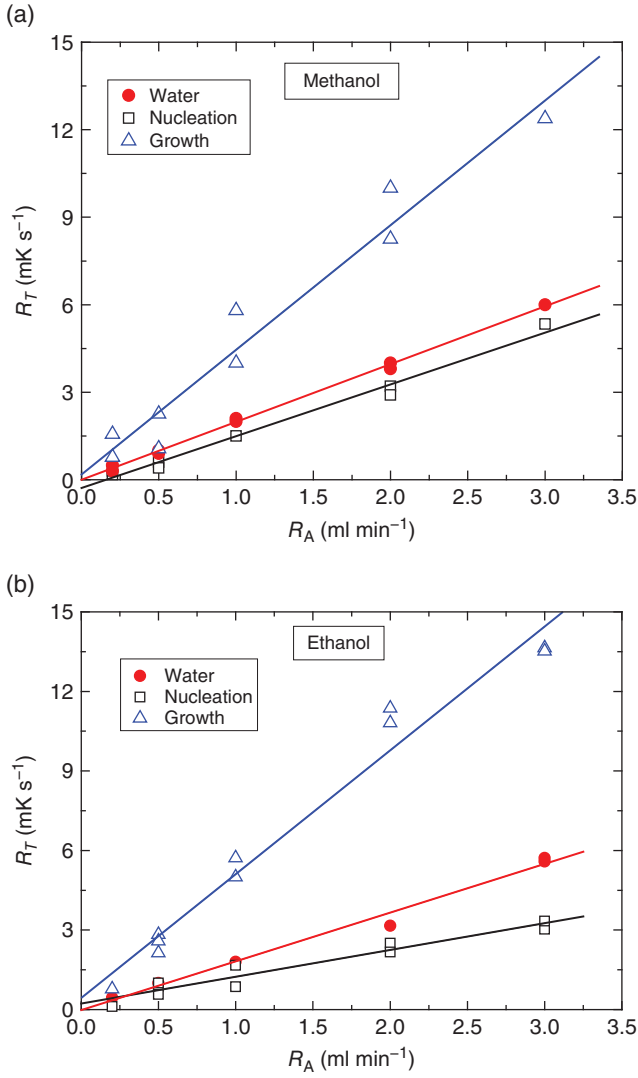

Figure 6.8 Plot of rates R_T for 3D nucleation close to t_0 and in the long linear range between t_1 and t_{max} from solutions and linear increase of temperature of water with feeding duration t of different antisolvents as functions of rates R_A: (a) methanol, (b) ethanol, and (c) acetone. Linear plots are drawn according to Eq. (6.4) with values of parameters listed in Table 6.3. *Source:* Original data from Sangwal and Mielniczek-Brzóska (2016a, b, 2017).

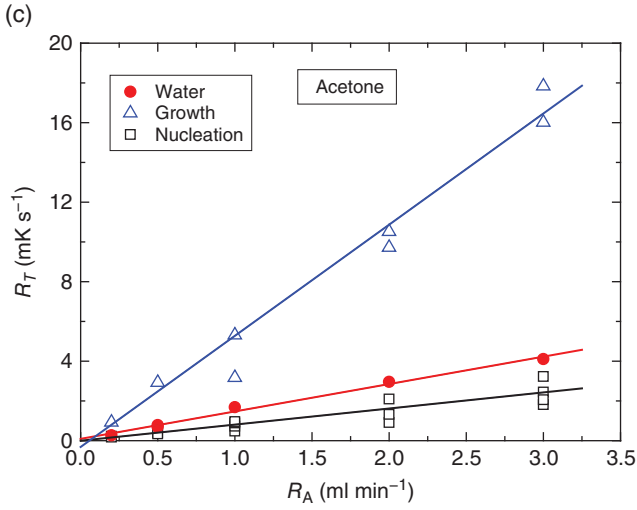

Figure 6.8 (Continued)

respectively, and with the mixing of an antisolvent in pure water with time t. The experimental data of different rates R_T for the three solvents are presented in Figure 6.8 as a function of antisolvent feeding rate R_A. The data follow the linear relation:

$$R_T = R_T^* + LR_A, \tag{6.4}$$

where R_T^* and L are empirical constants. In the figure the linear plots are drawn according to Eq. (6.4) with the best-fit values of the parameters listed in Table 6.3.

From Table 6.3 it follows that $R_T^* \approx 0$ and the parameter L has units representing volumetric temperature of transition (i.e. K·m^{-3}). This means that for a comparison of the nature of processes involved in nucleation and growth induced by feeding antisolvents, it is sufficient to consider the values of L for nucleation and growth.

Following Sangwal and Mielniczek-Brzóska (2016a, b), we consider first the interpretation of linear relation (6.4) between the rate R_T and R_A observed above in terms of chemical reactions. Since the rate $R_T = \Delta T/\Delta t$ and $R_A = \Delta V_a/\Delta t$, in the case of temperature increase ΔT, Eq. (6.4) gives

$$\Delta T = L\Delta V_a. \tag{6.5}$$

Since $\Delta V_a = V_s \Delta x$ (see Eq. (6.14)), where Δx is an increase in the antisolvent content in the solution volume V_s, and a change in temperature ΔT, whether by endothermic or exothermic reactions, during each stage of antisolvent

Table 6.3 Parameters of Eq. (6.4) for different antisolvents.

Antisolvent	System	Process	R_T^* (mK·s^{-1})	L (mK·ml^{-1}·[min·s^{-1}])	L (kK·m^{-3})	R^2 [a]	$10^3 L/\Delta T_{max}$ (m^{-3})
Methanol	Solution	Nucleation	−0.282 ± 0.046	1.774 ± 0.079	106.4 ± 4.7	0.9844	152
		Growth	0.182 ± 0.504	4.273 ± 0.341	256.4 ± 20.5	0.9510	214
Ethanol	Solution	Nucleation	−0.228 ± 0.156	1.010 ± 0.092	60.4 ± 5.5	0.9302	134
		Growth	0.439 ± 0.476	4.669 ± 0.280	280.6 ± 16.8	0.9684	208
Acetone	Solution	Nucleation	$-5.2 \cdot 10^{-4} \pm 0.21$	0.809 ± 0.113	48.5 ± 6.8	0.7700	115
		Growth	−0.317 ± 0.613	5.594 ± 0.311	335.6 ± 18.7	0.9817	212
Methanol	Water	Increase	−0.004 ± 0.055	1.984 ± 0.037	119.1 ± 2.2	0.9972	113
Ethanol	Water	Increase	−0.022 ± 0.204	1.839 ± 0.103	110.3 ± 6.2	0.9844	118
Acetone	Water	Increase	0.094 ± 0.097	1.378 ± 0.062	82.7 ± 3.7	0.9899	103

[a] R-square fit.

crystallization is associated with a change ΔQ in heat in the solution of volume V_s, given by (for example, see Barrow, 1973; Hamil et al., 1966)

$$\Delta Q = C_V \Delta T, \tag{6.6}$$

where C_V is the heat capacity (units: $J \cdot K^{-1}$) of solution of volume V, from Eqs. (6.5) and (6.6), one obtains

$$\Delta Q = \lambda \Delta x, \tag{6.7}$$

where the new constant $\lambda = LC_V \Delta V_a$. This relation shows that an increase in the change ΔQ of a system linearly increases with the addition of volume fraction Δx of an antisolvent. This inference is a consequence of the fact that addition of an antisolvent to a saturated solution or solvent involves chemical reactions with evolution of heat during 3D nucleation and growth of 3D nuclei into crystallites and during mixing of an antisolvent with solvent water.

The linear dependence of R_T on R_A can equally be explained from the standpoint of crystallization processes. For this purpose we refer to Eq. (6.35) relating 3D nucleation rate J with R_A. In relation (6.35) the dimensionality of nucleation is determined by the proportionality constant f, which is the number of ions/molecules in the initial solution with the addition of antisolvent. However, a similar proportionality constant can also be used to obtain an expression relating growth of these 3D nuclei with R_A (cf. Eq. (6.35)), where this new proportionality constant represents the number of ions/molecules adsorbed on the two-dimensional (2D) surfaces of growing crystallites. Since both 3D and 2D nucleations involve chemical reactions associated with the attachment of ions/molecules to unstable 3D nuclei and to evolving 2D surfaces of stable 3D nuclei, respectively, it can be argued that R_T is related to these processes in regions between t_0 and t_1 and between t_1 and t_{max}. In the case of feeding of acetone to pure solvent water, the linear relation between R_T and R_A is due to their enthalpy of mixing.

The linear dependence of rate R_T of temperature increase on antisolvent feeding rate R_A may be given by a more general Avrami-type equation relating ΔT with antisolvent feeding time t (see Eq. (6.1)), for example, from t_1 to t_{max} in the form (see Figure 6.6):

$$\Delta T = \Delta T_{max} \left\{ 1 - \exp\left[-\left(\frac{t - t_0}{\Theta} \right)^q \right] \right\}, \tag{6.8}$$

where Θ is a time constant, the feeding time $\Delta t = t_{max} - t_1$, and the exponent $q \geq 1$. Here, $\Delta T = (T - T_s)$ and $\Delta T_{max} = (T_{max} - T_s)$ denote increases in temperatures T and T_{max}, respectively, from the initial solution temperature T_s. Obviously, $\Delta T = 0$ when $\Delta t = 0$. Equation (6.8) predicts an S-shaped $\Delta T(t)$ curve with an initial convex curvature, followed by practically a linear dependence in a wide range of Δt and later exhibiting a concave curvature, such that finally the

solution temperature $T_s \rightarrow T_{max}$ at a relatively high Δt when $\Delta t/\Theta \rightarrow \infty$. The convex curvature of the S-shaped curve in the initial stage increases with increasing q. A long linear $\Delta T(t)$ dependence is expected when $(\Delta t/\Theta)^q \ll 1$ and the exponent $q = 1$. Then one gets

$$R_T = \frac{\Delta T}{\Delta t} = \frac{\Delta T_{max}}{\Theta} = \frac{\Delta T_{max}}{\Delta x_\Theta}\frac{\Delta x_\Theta}{\Theta} = LR_A, \tag{6.9}$$

where Δx_Θ is the antisolvent content in solution volume V_s at antisolvent feeding time Θ corresponding to maximum temperature difference ΔT_{max}, $L = \Delta T_{max}/\Delta x_\Theta$ and $R_A = \Delta x_\Theta/\Theta = \Delta x/\Delta t$ (cf. Figure 6.6b).

The relationship between R_T on R_A for 3D nucleation and growth of 3D nuclei according to Avrami equation (6.8) is based on the assumption that: (i) 3D nuclei in the solution volume V_s are formed progressively, (ii) the overall crystallized mass m is proportional to the antisolvent content x, and (iii) the increase in solution temperature T is proportional to the overall crystallized mass m. The former two assumptions are in agreement with the theoretical basis of overall crystallization from solutions and molten phases (Kashchiev, 2000), but the last assumption is a result of heats ΔQ of chemical reactions involved during 3D nucleation and growth (cf. Eq. (6.7)). Difference in the values of the constant L for the rate R_T of temperature increase in the regions of formation of 3D nuclei and their subsequent growth is due to difference in the overall masses involved in these processes. An explanation, similar to that used above, based on the formation of nuclei of water–antisolvent phase in pure water by the feeding of an antisolvent may also be given for the dependence of R_T on R_A for antisolvent-fed water system.

From Table 6.3, the following trends may be noted:

1) The value of L for the growth of ADP crystallites by feeding an antisolvent to ADP solution is much higher than that for 3D nucleation of ADP and increases with the dielectric constant ε_a of the antisolvent.
2) The value of L for nucleation of ADP from aqueous solutions and for mixing with solvent water by feeding an antisolvent decreases with an increase in the dielectric constant ε_a of the antisolvent. However, the decrease in the value of L for nucleation of ADP from aqueous solutions becomes increasingly pronounced with increasing dielectric constant ε_a of the antisolvent.

To understand the above trends, we consider the ratio $L/\Delta T_{max}$, where L was defined above and ΔT_{max} is the maximum increase in the temperature caused by the addition of volume fraction Δx_c of a given antisolvent during 3D nucleation and growth of 3D nuclei into crystallites in the solution volume V_s and mixing of the antisolvent with solvent in the solvent–antisolvent mixture volume V_s. The values of ΔT_{max} involved during nucleation, overall crystallization, and solvent–antisolvent mixing from initial temperature of 30 °C are listed in Table 6.2. For the analysis, we rewrite Eq. (6.7) in the form:

$$\frac{L}{\Delta T_{\max}} = \frac{1}{\Delta V_a} = \frac{1}{V_s \Delta x_c}, \tag{6.10}$$

and take the values of $\Delta T_{\max}$ from Table 6.2 for the 3D nucleation and growth of 3D nuclei into ADP crystallites from aqueous solutions and mixing of antisolvent with solvent water of volume V_s at feeding rates of 3 ml·min^{-1} for different antisolvents. Since the maximum temperature increase $\Delta T_{\max}$ corresponding to $t_{\max}$ in column 4 of Table 6.2 is due to overall crystallization of ADP, the temperature increase $\Delta T_{\max}$ only due to the growth of 3D nuclei into ADP crystallites was calculated by subtracting $\Delta T_{\max}$ for nucleation (column 3) from $\Delta T_{\max}$ for overall crystallization (column 4). From the values of L and $\Delta T_{\max}$ given in Tables 6.3 and 6.2, the calculated values of the ratio $L/\Delta T_{\max}$ are listed in the last column of Table 6.3.

From Table 6.3 it may be noted that the quantity $L/\Delta T_{\max}$ for 3D nucleation decreases with an increase in the dielectric constant ε of the antisolvent (cf. Table 6.2). This trend follows from Eq. (6.10). According to this relation a higher volume fraction Δx_c in the solution during nucleation is necessary to achieve a particular value of the maximum temperature increase $\Delta T_{\max}$ by the addition of an antisolvent of a lower dielectric constant ε. This observation is associated with processes involved during the desolvation of solute during its nucleation (see Section 6.6). In contrast to the importance of desolvation during 3D nucleation, this process does not play a major role in the growth of 3D ADP nuclei into large crystallites. As seen from Table 6.3, the quantity $L/\Delta T_{\max}$ for the growth of 3D nuclei into ADP crystallites and for the mixing of the antisolvent with the solvent is practically constant, equal to about 210 and 110 m^{-1}, respectively, and are independent of the added antisolvent.

Change in the temperature of a solution and a solvent by addition of an antisolvent involves solute–solvent (w_{CS}), solute–antisolvent (w_{CA}), solvent–antisolvent (w_{SA}), and solute–solute interactions (w_{CC}), and is associated with the work w_m and w_c required for these processes, given by

$$w_m = [(w_{SS} + w_{AA}) - 2w_{AS})], \tag{6.11}$$

$$w_c = [(w_{CS} + w_{AA}) - (w_{CA} + w_{AS})], \tag{6.12}$$

respectively. These interactions result in solute crystallites during solvent–antisolvent mixing (miscibility) and crystallization. The rates of these processes are determined by the values of w (i.e. w_m and w_c) because the rate is proportional to exp $(-w/R_G T)$. This means the lower the value of w, the higher is the rate of the process. Since the value of w increases with increasing w_{AS}, it is expected that the rates of solvent–antisolvent mixing (miscibility) and crystallization increase with increasing solvent–antisolvent interactions. The trends of the ratio $L/\Delta T_{\max}$ with the dielectric constant ε of different antisolvents is consistent with this concept. However, crystallization is accompanied not only by an

increase in the volumes of the solution by the addition of an antisolvent, but also involves diffusion of solvent molecules released from solvated ions/molecules of solute, and agglomeration of solute molecules into 3D nuclei and diffusion of solute molecules in the solution volume. The increase in the ratio $L/\Delta T_{max}$ with decreasing dielectric constant ε of the antisolvents may be attributed to the diffusion of antisolvent molecules in the solution during growth.

6.3.3 Physical Interpretation of Temperature Changes of ADP Solutions with Antisolvent Feeding Time at Different Rates

We consider here changes ΔT in the temperature T of a solution saturated at a given temperature, say T_0 such that $\Delta T = (T - T_0)$, caused in solvent water containing solute ADP and in water by the addition of antisolvent methanol as chemical reactions. For this purpose, we describe the dependence of different ΔT's on antisolvent feeding time t at a constant feeding rate R_A by KJMA relation (6.1), written in the form of Eq. (6.8), with reference to T_0, for example, with temperature changes ΔT and ΔT_{max}, and, depending on the chemical reaction, each $\Delta T(t)$ dependence is characterized by its own Θ and q (Sangwal and Mielniczek-Brzóska, 2016b). Note that each of the $T(t)$ plots for solutions is composed of two independent plots below and above feeding time t_1, whereas every $T(t)$ plot for water covers the entire feeding range up to T_{max}. Figure 6.9

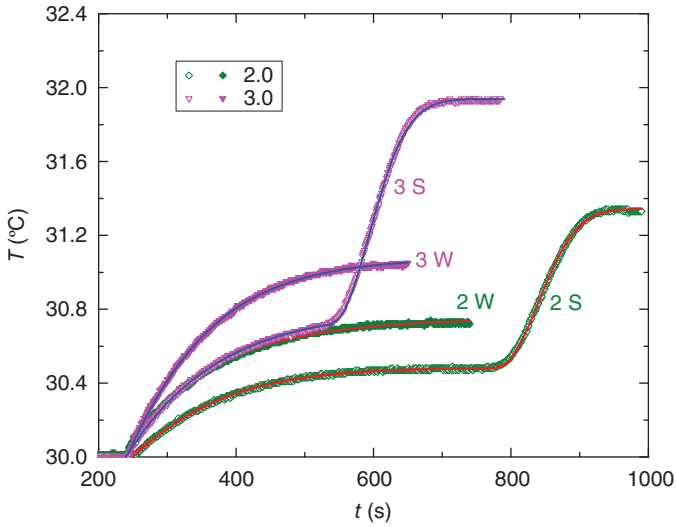

Figure 6.9 Examples of best-fit plots of the $\Delta T(t)$ data for two feeding rates R_A. S and W denote ADP solution and water, respectively. *Source:* Adapted from Sangwal and Mielniczek-Brzóska (2016b). Copyright (2016), with permission from Elsevier.

shows examples of the experimental $T(t)$ data for two feeding rates R_A for ADP solutions and water, with best-fit plots for the data according to Eq. (6.8).

Sangwal and Mielniczek-Brzóska (2016b) analyzed the data of time constant Θ and exponent q as functions of methanol feeding rate R_A for all measurements of temperature T against methanol feeding time t. It was found that Θ decreases with increasing R_A but the decrease is very pronounced for growth than for nucleation and is insignificant for water. However, for growth the exponent q decreases from about 4 to 2 with increasing R_A but it remains unchanged at 1 for nucleation as well as water.

To understand the above trends of variations of q with R_A, one assumes that Eq. (6.1) of the KJMA theory involving progressive nucleation holds for the processes of mixing of methanol with water, the formation of 3D nuclei and growth of nuclei into crystallites in antisolvent crystallization, the observed value of $q = 1$ for nucleation and antisolvent mixing with water is expected because stable 3D nuclei formed in these processes do not grow (i.e. $d = 0$). However, during growth beyond the time t_1 of methanol addition, one expects q between 1 and 4, depending on the dimensionality d of growing 3D nuclei. This behavior of the exponent q is a consequence of two factors: (i) differences in the kinetics of 3D nucleation and kinetics of growth of faces appearing in the crystal morphology with increasing supersaturation σ due to increasing antisolvent feeding rate R_A and (ii) anisotropy in the growth kinetics of different faces. It is well known that growth kinetics dominate nucleation kinetics at low supersaturation σ but 3D nucleation kinetics dominate growth kinetics at high supersaturation σ. This implies that the growth of 3D nuclei into crystallites with well-developed morphology (where $d = 3$) is possible at low feeding rates R_A, but the morphology becomes platy, needle-shaped, and finally granular due to decreasing dimensionality d of growing crystallites from 2 to 0 with increasing methanol feeding rate R_A.

Sangwal and Mielniczek-Brzóska (2016b) observed that the $\Theta(R_A)$ data may be described by an empirical relation similar to that used to describe retardation of growth rates in the presence of additives in terms of adsorption isotherms (Ościk, 1982; Sangwal, 2007). This means that the dependence of time constant Θ on R_A can be explained from consideration of adsorption (solvation–desolvation) processes involving replacement of solvent molecules adhering to the forming 3D nuclei and growing crystallites by antisolvent molecules. A similar line of argument may also be used to explain the dependence of q on R_A.

6.3.4 Origin of Two Minima and Maximum in Temperature Change ΔT During Antisolvent Crystallization

The first minimum ΔT_{min1} and the maximum ΔT_{max} appear upon the addition of the antisolvent, whereas the second minimum ΔT_{min2} appears even in the absence of antisolvent feeding (see Figure 6.7). This means that the former minimum ΔT_{min1} is a result of generation of solute concentration difference

$\Delta c = c_1 - c_0$ with respect to the solute concentration c_1 corresponding to the feeding duration $\Delta t_1 = t_1 - t_0$ of the antisolvent (cf. Figure 6.15) and the corresponding supersaturation $\sigma = \Delta c/c_2$ (see Eq. (6.34)). This supersaturation is necessary for the occurrence of 3D nucleation at time t_1 associated with the antisolvent feeding time Δt at a given rate R_A. As shown in Section 6.6.1, the origin of ΔT_{min1} is associated with the energy change ΔQ_1 due to desolvation processes by the addition of the antisolvent.

The 3D nuclei in the solution can form in two ways (see Section 3.9): (i) all nuclei are formed instantaneously at time t_1 (instantaneous nucleation) and (ii) the nuclei are formed progressively before and after time t_1 (progressive nucleation). Trends of $T(t)$ and $\Delta T(t)$ plots (see Figures 6.6b and 6.7) show that nucleation usually occurs progressively but high antisolvent feeding rate favors instantaneous nucleation. Thus, addition of more antisolvent beyond t_1 up to t_{max} ensures subsequent increase in supersaturation in the crystallizer followed by the growth of the already formed and newly forming 3D nuclei. This stage of growth of the 3D nuclei is accompanied by the heat of crystallization, which is always a positive quantity.

It is expected that antisolvent crystallization between t_1 and t_{max} occurs at high supersaturations and the crystal size is small. Moreover, as expected from the formation of 3D nuclei by progressive nucleation, the crystallites grown in the solution have a particular crystal size distribution (for example, see: Kashchiev, 2000; Söhnel and Garside, 1992). However, beyond t_{max} (and beyond t_{int}) after the cessation of addition of the antisolvent, the supersaturation σ available in the crystallizer decreases steadily with ultimate cessation of growth of the crystallites of a particular crystal size distribution. Then the crystallites in contact with the saturated solution undergo a change in their crystal size distribution with time because the system tends to achieve the minimum energy state by processes such as Ostwald ripening (Kashchiev, 2000; Nývlt et al., 1985; Söhnel and Garside, 1992). This results in the second minimum ΔT_{min2}. Obviously, the origin of ΔT_{min2} differs from that of the first minimum ΔT_{min1} because it occurs even in the absence of addition of the antisolvent and the amount of heat ΔQ involved in the two minima is different.

6.3.5 Relationship Between Different Temperature Changes, Antisolvent Feeding Rate, and Antisolvent Content

The $\Delta T(t)$ plots of aqueous ADP solutions for different antisolvents show (Sangwal and Mielniczek-Brzóska, 2016a, b, 2017) that the values of ΔT_{min1} and ΔT_{min2} of endothermic minima 1 and 2 and ΔT_{max} of the endotherm maximum increase, whereas those of the time differences $\Delta t_{10} = t_1 - t_0$, $\Delta t_{21} = t_2 - t_1$, and $\Delta t_{max1} = t_{max} - t_1$ decrease with increasing antisolvent feeding rate R_A (see Figure 6.7). Similarly, the $T(t)$ plots of water for different antisolvents show that the values of maximum temperature increase ΔT_{maxW} observed at t_{max}

increase (see Figure 6.6b), but those of the time difference $\Delta t_{maxW} = t_{max} - t_0$ exhibit general decrease with the feeding rate R_A. These observations mean that the time differences are inversely related to the temperature differences ΔT_{min1} and ΔT_{min2} in the two endothermic minima and ΔT_{max} in the exothermic maximum of solutions and to ΔT_{maxW} in the exothermic maximum of water. The

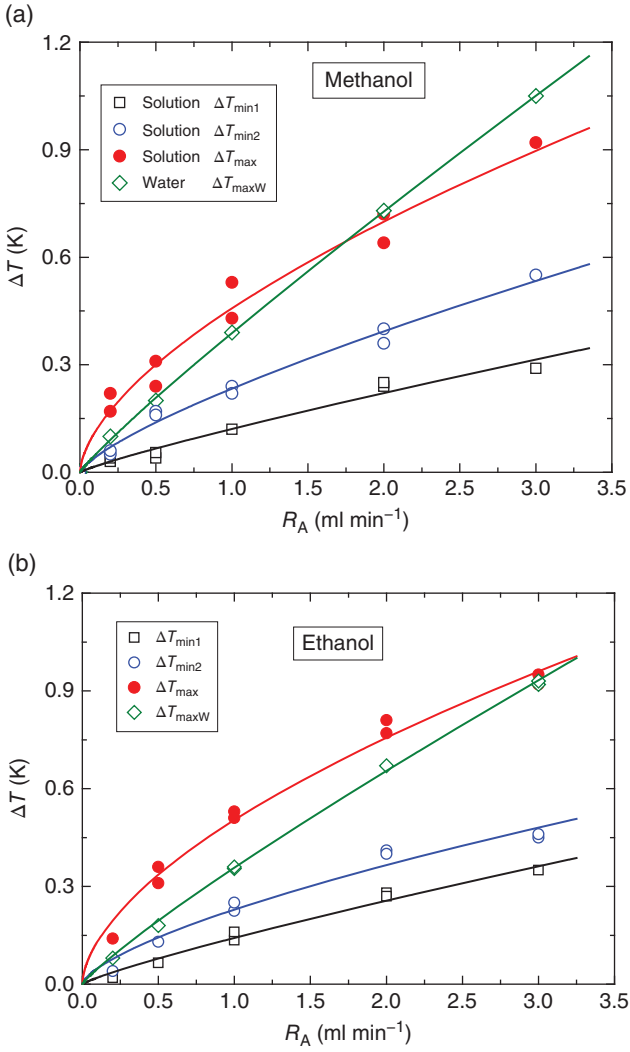

Figure 6.10 Dependence of different temperature changes ΔT_{min1}, ΔT_{min2}, and ΔT_{max} of ADP solutions and ΔT_{maxW} of water on (a) methanol, (b) ethanol, and (c) acetone feeding rates R_A. Plots are drawn according to Eq. (6.13) with the parameters given in Table 6.4.

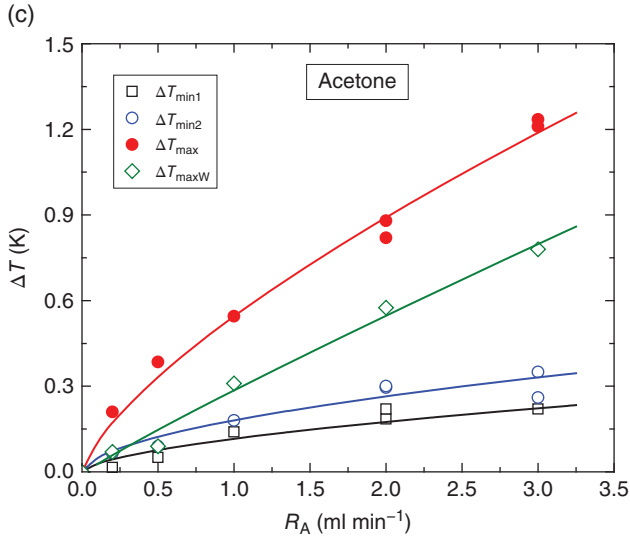

Figure 6.10 (Continued)

data of temperature differences ΔT_{min1} and ΔT_{min2}, ΔT_{max} and ΔT_{maxW} as functions of feeding rate R_A of methanol, ethanol, and acetone obtained from the original computer files are presented in Figure 6.10, whereas the plots are drawn according to the empirical relation:

$$\Delta T_{min,max} = AR_A^n, \tag{6.13}$$

with the values of the empirical constants A and n listed in Table 6.4. Note that ΔT_{max} represents the enthalpy change involved in the growth of crystallites alone and corresponds to the time difference $\Delta t_{max1} = t_{max} - t_1$ in the $T(t)$ plots (cf. Figure 6.7).

Using the values of different time differences Δt between various time intervals from the $\Delta T_s(t)$ plots of solutions and those of the $T_w(t)$ of water for the corresponding antisolvent feeding rate R_A for different antisolvents, values of the volume fraction Δx corresponding to different time intervals in the initial solution were calculated using the relation:

$$\Delta x = \frac{V_a}{V_s + V_a}, \tag{6.14}$$

where the antisolvent volume $V_a = R_A \Delta t$ and the solution volume $V_s = 220$ ml. Figure 6.11 shows the values of ΔT_{min1}, ΔT_{max} and ΔT_{min2} as a function of calculated volume fraction Δx of different solvents. The data follow the linear dependence

$$\Delta T = b(\Delta x - \Delta x^*), \tag{6.15}$$

Table 6.4 Values of parameters of Eqs. (6.13) and (6.15).[a,b]

			Eq. (6.13)			Eq. (6.15)		
Antisolvent	**System**	**Data**	A (K[ml·min^{-1}]$^{-n}$)	n	R^2	Δx^* (vol%)	b (K)	R^2
Methanol	Solution	ΔT_{min1}	0.122	0.866	0.9694	2.52	5.82	0.8785
		ΔT_{min2}	0.235	0.749	0.9852			
		ΔT_{max}	0.460	0.609	0.9743	−0.60	21.89	0.7880
	Water	ΔT_{maxW}	0.389	0.904	0.9997	1.30	14.54	0.9640
Ethanol	Solution	ΔT_{min1}	0.142	0.849	0.9858	2.29	12.07	0.9603
		ΔT_{min2}	0.230	0.672	0.9718			
		ΔT_{max}	0.506	0.583	0.9887	−0.37	36.57	0.9230
	Water	ΔT_{maxW}	0.358	0.872	0.9989	0.45	11.54	0.9702
Acetone	Solution	ΔT_{min1}	0.076	0.642	0.9250	2.05	7.3	0.8683
		ΔT_{min2}	0.123	0.595	0.9058			
		ΔT_{max}	0.336	0.755	0.9890	1.63	16.49	0.9461
	Water	ΔT_{maxW}	0.414	0.734	0.9967	−0.40	6.77	0.9981

[a] Original data from Sangwal and Mielniczek-Brzóska (2016a, b, 2017).
[b] R^2 denotes R-square fit.

where ΔT denotes ΔT_{min1} and ΔT_{min2}, ΔT_{max} and Δx^* and b are empirical constants listed in Table 6.4. The parameter Δx^* in relation (6.15) defines the antisolvent concentration beyond which the above linear relation holds.

It is well known (for example, see: Barrow, 1973; Hamil et al., 1966) that the rates of many chemical reactions at a particular temperature are proportional to the concentration of one, two, or more components and the rate of the evolved heat of a reaction is related to the reaction rate. Since the heat ΔQ of the reaction in a system is proportional to the temperature change ΔT associated with it (cf. Eq. (6.6)), Eq. (6.15) suggests that the chemical reactions involved in the generation of temperature change ΔT are of the first order. According to Eq. (6.15), $\Delta Q < 0$ means that the temperature change ΔT caused by antisolvent content Δx in aqueous ADP solution is also negative (i.e. the reaction is endothermic), but when $\Delta Q > 0$ the change ΔT caused by the antisolvent content Δx is positive (i.e. the reaction is exothermic).

6.3.6 Comparison of Light-intensity and Temperature Measurements

It was mentioned above that, apart from a difference in the curvatures of $I_{ns}(t)$ plots of feeding of saturated aqueous ADP solutions by methanol and ethanol from those of acetone, the effect of acetone on the transmitted light intensity I_{ns}

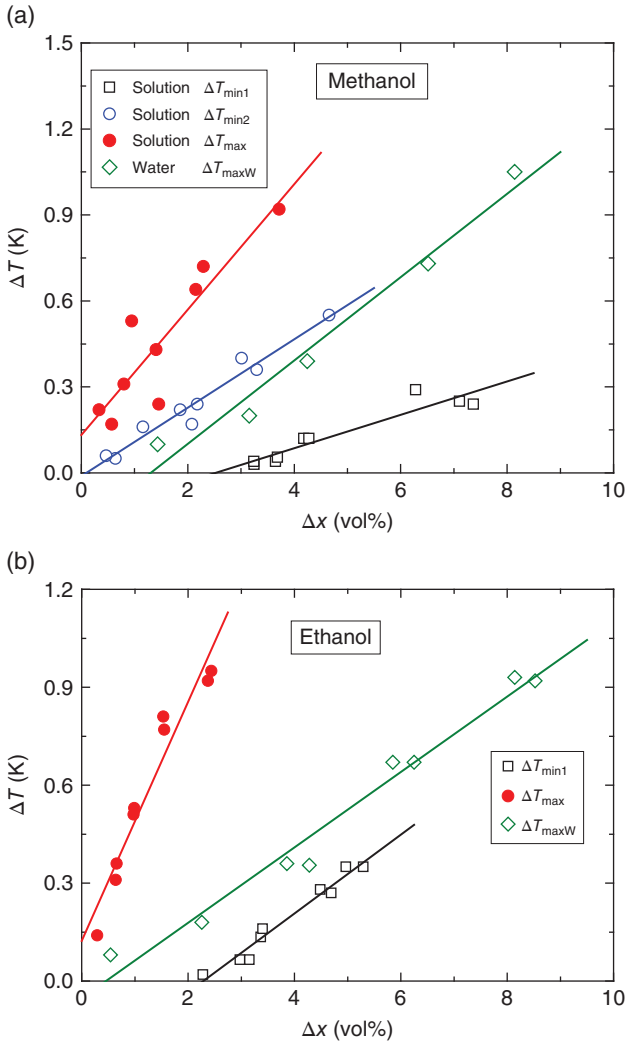

Figure 6.11 Dependence of different temperature changes ΔT_{min1}, ΔT_{min2}, and ΔT_{max} of ADP solutions and ΔT_{maxW} of water on (a) methanol, (b) ethanol, and (c) acetone content Δx_{max} in solution. Plots are drawn according to Eq. (6.15) with the parameters given in Table 6.4.

is more pronounced than methanol and ethanol. The $T_s(t)$ plots of feeding of solutions by the three antisolvents also reveal similar trends. Therefore, we compare, as an illustration, the effect of antisolvent acetone on the normalized transmitted laser-beam intensity I_{ns} and the temperature T_s of aqueous ADP

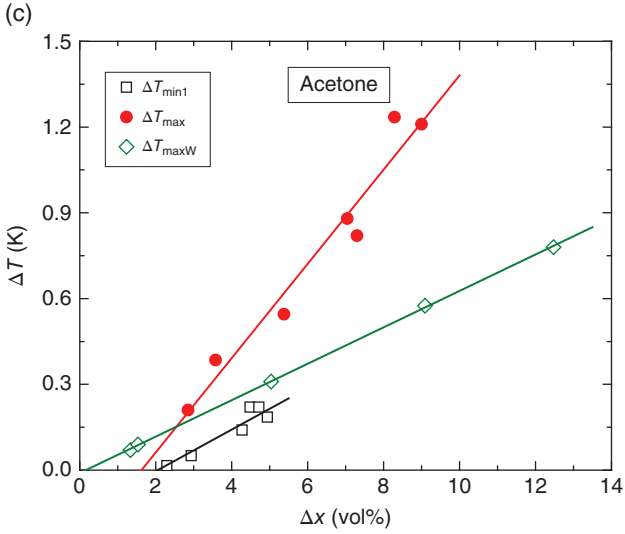

Figure 6.11 (Continued)

solution saturated at 30 °C as a function of feeding duration t. Figure 6.12a and b presents the change in I_{ns} and T_s of aqueous ADP solution saturated at 30 °C with acetone feeding at different rates R_A. Times t_0 and t_1 are indicated in both figures, but the values of t_1 for the $I_n(t)$ plots of different feeding rates R_A are indicated by arrows in Figure 6.12a. In Figure 6.12b, t_{max} and t_{int} represent the maximum temperature and interruption of acetone feeding at rate R_A = 3.0 ml·min^{-1}. Different notations are indicated in Figure 6.12b.

It may be seen from Figure 6.12a that, after the initial duration t_0, with antisolvent feeding time t in the saturated solution the normalized intensity I_{ns} initially decreases exponentially up to t_1, followed by a sudden short steep decrease up to t_{lim} when finally the intensity approaches zero. A general feature of the two parts of these plots is that, with increasing antisolvent feeding rate R_A, the curvature of their initial parts increases whereas the feeding durations ($t_1 - t_0$) and ($t_{lim} - t_1$) decrease. The plots of Figure 6.12b of temperature T_s of the solution against antisolvent feeding time t after the initial duration t_0 show three distinct regions. Initially, with an increase in acetone feeding time t the solution temperature T_s slowly increases up to t_1, and with increasing feeding rate R_A the rate of rise in T_s increases and the feeding duration difference ($t_1 - t_0$) decreases. Later, after t_1 the temperature T_s steeply increases and approaches the maximum value t_{max}, and between t_1 and t_{max} there is a region when T_s increases linearly with antisolvent feeding time t. At higher feeding durations beyond t_{max}, the solution temperature T_s slowly decreases with increasing time t and finally tends to approach the thermostated temperature 30 °C. In this region, after t_{int} the

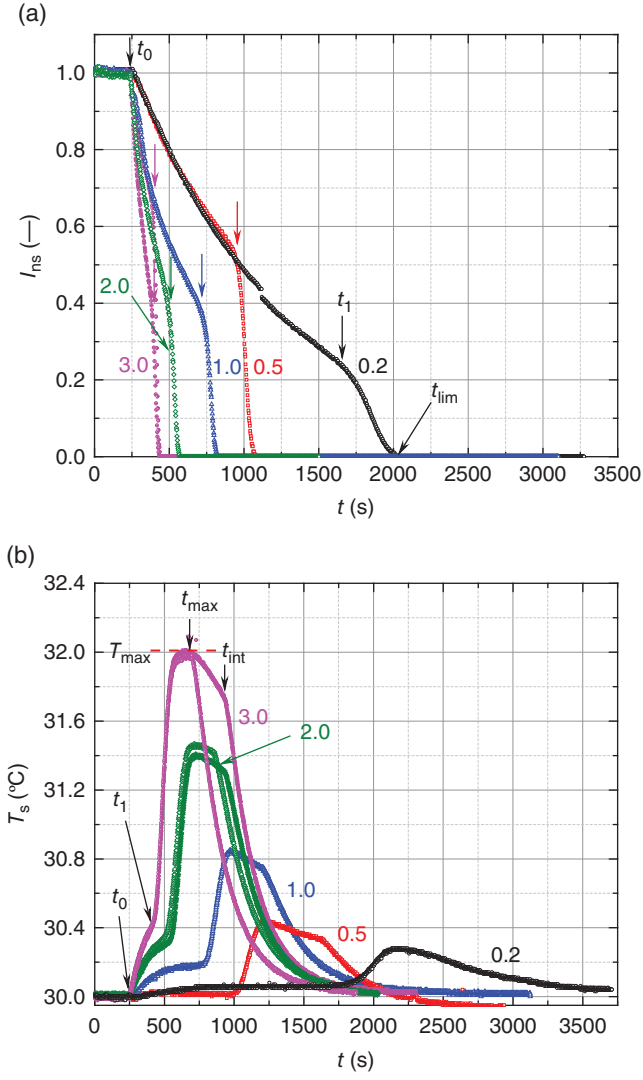

Figure 6.12 Change in (a) normalized transmitted laser-beam intensity I_{ns} and (b) temperature T_s of aqueous ADP solution saturated at 30 °C with acetone feeding at different rates R_A. Times t_0 and t_1 are indicated in both figures whereas t_{max} and t_{int} in (b) represent the maximum temperature and interruption of acetone feeding at rate $R_A = 3.0$ ml·min^{-1}. *Source:* After Sangwal and Mielniczek-Brzóska (2016a). Copyright (2016), with permission from Wiley.

curvature of the $T_s(t)$ plot increases with increasing values of the initial acetone feeding rate R_A but acetone feeding reduces their curvature between t_{max} and t_{int}.

As discussed above, the region between t_0 and t_1 is associated with the onset of 3D nucleation and the time t_1 defines the MSZW when 3D nucleation occurs instantaneously, the region between t_1 and t_{max} is associated with complex crystal growth processes including the growth of 3D nuclei, whereas in the region beyond t_{max} the size distribution of crystallites formed before undergoes reorganization. The time t_{max}, when the temperature reaches a maximum value of T_{max} of aqueous ADP solution at a particular acetone feeding rate R_A, decreases with increasing feeding rate R_A.

From Figure 6.12, it may be noted that the trends in changes in laser-beam intensity I_{ns} and solution temperature T_s show similar characteristics in the range of antisolvent feeding time below t_{lim}. Both techniques detect the onset of nucleation of ADP by antisolvent crystallization in terms of antisolvent feeding time t_1 at a given rate R_A. However, the value of time t_1, say t_I^*, when the curvature of an $I_{ns}(t)$ plot begins to change, noted from the $I_{ns}(t)$ plots of Figure 6.12a is lower than t_1 from the $T_s(t)$ plots of Figure 6.12b. For example, for the feeding rate $R_A = 0.2\ ml{\cdot}min^{-1}$, the value of $t_I^* \approx 1700$ s from the $I_n(t)$ plot whereas $t_1 = 1800$ s from the $T_s(t)$ plot. However, the value of t_1 is practically the same at time t_I^{**} when I_{ns} in the $I_{ns}(t)$ plot begins to decrease linearly with feeding time t. The feeding time t_{lim} in the $I_{ns}(t)$ plots when I_{ns} approaches zero usually lies between t_1 and t_{max} in the $T_s(t)$ plots.

The intensity I_{ns} of laser beam transmitted through a solution and solvent is a result of diffraction of light by various types of particles present in them, whereas the decrease in I_{ns} of laser beam transmitted through the supersaturated solution with antisolvent feeding time t is associated with the scattering of light by crystallized solute particles (i.e. crystallites) forming in it. The latter process essentially involves the formation of 3D nuclei progressively and their growth in the solution volume with time t. During the time interval of antisolvent feeding for the creation of supersaturation for 3D nucleation, the temperature of aqueous ADP solutions does not remain constant but increases more than 1 K. The relative decrease in the densities of water and saturated solutions of compounds like ADP from 303.15 to 308.15 K does not exceed $2{\cdot}10^{-3}$ (Sangwal, 2017). This means that changes in the densities of water and saturated solutions due to the increase in their temperature during 3D nucleation by the addition of an antisolvent may be considered insignificant in the determination of MSZW by light-intensity measurements during the antisolvent feeding.

Finally, it may be concluded that the values of time t_1 when the $I_n(t)$ plots of different antisolvents show steep linear parts and when the $T_s(t)$ plots show steep linear increase may be taken to represent the occurrence of 3D nucleation during MSZW measurements. However, as seen from observation of different temperature changes described and discussed above, temperature

measurements are more informative than transmitted light-intensity measurements because they provide insight into the processes involved in kinetics of crystallization.

6.4 Effect of Antisolvent Composition on Nucleation Rate

It is well known that interfacial tension γ and solubility c of different compounds are related (see Section 2.5). Therefore, to discuss the effect of addition of an antisolvent on the solubility c of solute in a given solvent on 3D nucleation rate J at a temperature T, we should first consider the general relationship between interfacial tension γ of different compounds and their solubility c in water. However, since the solubility c has been expressed in different units in the relationships proposed in the literature (Bennema and Söhnel, 1990; Mersmann, 1990; Nielsen and Söhnel, 1971; Sangwal, 1989; Söhnel, 1982), expressing c in mole fraction we use relation (2.86); see Section 2.5:

$$\frac{\gamma\Omega^{2/3}}{k_B T} = -\frac{\ln c}{\zeta}, \tag{6.16}$$

where the parameter ζ is equal to 8 and Ω is the molecular volume ($\Omega \approx a^3$, with a as the atomic/molecular size). We consider the example of a solute dissolved in solvent S and antisolvent A used to create supersaturation for the occurrence of antisolvent crystallization. We take the solubility c_S of our solute equal to 0.3 mole fraction. This value of solubility c is close to $c_S = 0.29$ mole fraction for NTO in NMP at 323 K and decreases with the addition of water in which c_A is about 0.007 mole fraction (Kim and Kim, 2001), where c_S and c_A denote the solubility of the solute in the solvent and the antisolvent, respectively. Antisolvent crystallization usually occurs at $S = c_S/c_A < 1.8$. Using Eq. (6.16), the values of $\gamma\Omega^{2/3}/k_B T$ may be calculated for different solvent–antisolvent proportions $1 : X$, values of antisolvent content $x_m = (1 - X)c_S + Xc_A$ with reference to the solubility c_A, which subsequently enables one to calculate the solubility-dependent parameter B and the nucleation rate J according to the classical theory of 3D nucleation (see Section 2.2)

$$J = J_0 \exp\left[\left(-\frac{B}{\ln S}\right)^2\right], \tag{6.17}$$

where the preexponential factor J_0 is determined by the kinetics of association and dissociation of monomers to developing nuclei and the parameter B is given by

$$B = \kappa\left(\frac{\gamma\Omega^{2/3}}{k_B T}\right)^3, \tag{6.18}$$

and $\ln S = \ln(c_S/c_A)$, with $c_S = 0.3$ and $c_A = 0.007$ mole fraction, given by Eq. (6.34). In Eq. (6.18), κ is the shape factor for the nuclei ($\kappa = 16\pi/3$ for spherical nuclei), γ is the solid–medium interfacial energy at temperature T, and k_B is the Boltzmann constant.

Figure 6.13 shows the dependence of J/J_0 for solubility-dependent and solubility-independent B and the ratio of J/J_0 for solubility-dependent and solubility-independent B on solvent–antisolvent composition x_m. It may be seen from this figure that the ratio of J/J_0 for solubility-dependent and solubility-independent B is essentially constant at 0.893 ± 0.045 in the x_m range of pronounced nucleation rate (i.e. for $x_m \geq 0.4$). In the range of low x_m (e.g. for $x_m < 0.2$) corresponding to relatively low nucleation rate, even small decreases in antisolvent composition x_m lead to significant reduction in the nucleation rate.

From the above, it may be concluded that, as far as the effect of solvent–antisolvent composition on nucleation rate is concerned, in the range of low antisolvent content x_m the nucleation rate during antisolvent crystallization is strongly suppressed due to reduction in the interfacial tension γ of the crystallizing system, but at relatively high x_m it is immaterial whether or not one takes into account the effect of solubility on the nucleation rate J. It should also be noted that, if one takes $\gamma_{eff}\Omega^{2/3}/k_BT$ instead of $\gamma\Omega^{2/3}/k_BT$, the value of $\gamma_{eff}\Omega^{2/3}/k_BT$ can account for homogeneous as well as heterogeneous nucleation. A lower value of $\gamma_{eff}\Omega^{2/3}/k_BT$ is also expected for seeded systems.

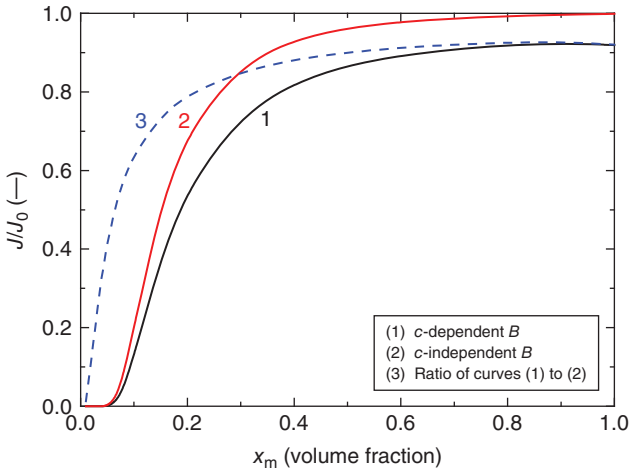

Figure 6.13 Dependence of calculated J/J_0 for solubility-dependent (curve 2) and solubility-independent B (curve 1) and the ratio of J/J_0 for solubility-dependent and solubility-independent B (curve 3) on solvent–antisolvent composition x_m.

6.5 Different Approaches of MSZW

6.5.1 Modified Nývlt-like Approach

Following the classical approach of Nývlt for crystallization from solution by cooling at a constant rate (Nývlt, 1968; Nývlt et al., 1985), O'Grady et al. (2007) derived a relation between MSZW, defined as the maximum antisolvent composition Δx_{max} added to a solution saturated at a given temperature T, and rate of addition of the antisolvent R_A. O'Grady et al. (2007) assumed that the nucleation rate is related to the excess solute concentration Δc according to the empirical power-law dependence

$$J = k(\Delta c)^m, \tag{6.19}$$

and the excess concentration Δc of the solute during addition of antisolvent to the solution volume V_s follows the linear dependence on antisolvent content Δx according to the relation:

$$\Delta c = \frac{dc_0}{dx}\Delta x, \tag{6.20}$$

where the value of the excessive antisolvent content Δx corresponds to Δc and dc_0/dx is the slope of the $c(x)$ dependence. From Eq. (6.20), the rate of generation of excess solute concentration Δc may be given by

$$\frac{d\Delta c}{dt} = R_A \frac{dc_0}{dx}, \tag{6.21}$$

where c_0 is the initial saturation solute concentration, and the antisolvent addition rate R_A is given by

$$R_A = \frac{d(\Delta x)}{dt}. \tag{6.22}$$

In the above equations, the excessive antisolvent composition $\Delta x = x_1 - x_2$, where x_1 and x_2 are the antisolvent compositions at time t_1 and t_2, respectively, c_1 and c_2 are the solute concentrations corresponding to t_1 and t_2, respectively, k is the so-called nucleation constant, and m is the nucleation order. The rate of generation of excess solute concentration Δc and the rate of nucleation with antisolvent addition time at a constant rate R_A are schematically shown in Figure 6.14. Since the nucleation rate J increases with Δc according to Eq. (6.19) with $m > 1$, intense nucleation occurs in the vicinity of metastability.

At the point of crystallization, the rate of supersaturation generation, defined by Eq. (6.21), is equal to the rate J of formation of new crystals. Therefore, on substituting for Δc from Eq. (6.20) in Eq. (6.19) and equating Eq. (6.19) and (6.21), for $\Delta c = \Delta c_{max}$ one obtains

$$\ln(\Delta x_{max}) = \frac{(m-1)}{m}\ln\frac{dc_0}{dx} + \frac{1}{m}\ln k + \frac{1}{m}\ln R_A. \tag{6.23}$$

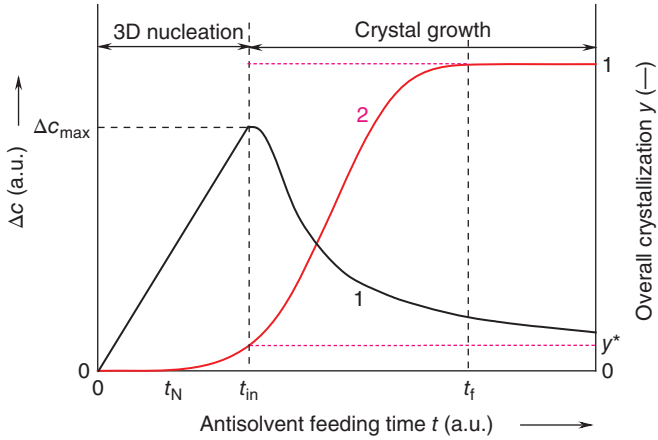

Figure 6.14 Schematic presentation of generation of excess solute concentration Δc (curve 1) and 3D nucleation rate (curve 2) in original solution volume V_s with antisolvent addition time t at a constant rate R_A.

According to Eq. (6.23), the maximum antisolvent content Δx_{max}, which represents the MSZW, depends on nucleation parameters k and m, and the antisolvent addition rate R_A.

6.5.2 Kubota's Approach

Kubota (2008) considered the excessive antisolvent composition Δx in terms of the number density of nuclei $(N/V)_{max}$, defined as the number of nuclei N per unit volume V, that have reached a certain value for detection. He calculated the value of $(N/V)_{max}$ by integrating the nucleation rate $J = \mathrm{d}(N/V)/\mathrm{d}t$ with respect to time from 0 to t_{max}:

$$\left(\frac{N}{V}\right)_{max} = \int_0^{(N/V)_{max}} \mathrm{d}\left(\frac{N}{V}\right) = \int_0^{t_{max}} J\,\mathrm{d}t, \tag{6.24}$$

where J is given by Eq. (6.19) and it is assumed that nucleation occurs instantaneously during the measurement of MSZW. When the antisolvent is added at a constant rate R_A, using Eq. (6.22) such that $\mathrm{d}t = \mathrm{d}(\Delta x)/R_A$, Eq. (6.24) may be written in the form:

$$\left(\frac{N}{V}\right)_{max} = \int_0^{\Delta x_{max}} \left(\frac{J}{R_A}\right) \mathrm{d}(\Delta x), \tag{6.25}$$

where Δx_{max} refers to the MSZW and corresponds to t_{max}. After substituting the value of the nucleation rate J from Eq. (6.19) with Δc_{max} given by Eq. (6.22), Eq. (6.25) yields

$$\left(\frac{N}{V}\right)_{max} = \left[\frac{k_m}{(m+1)R_A}\right](\Delta x_{max})^{m+1}, \tag{6.26}$$

where $k_m = k(dc_0/dx)^m$. Upon rearrangement, Eq. (6.26) takes the form:

$$\Delta x_{max} = \left[(m+1)\frac{(N/V)_{max}}{k_m}\right]^{1/(m+1)} R_A^{1/(m+1)}. \tag{6.27}$$

Upon taking logarithm on both sides, Eq. (6.27) may be rewritten in the form:

$$\ln(\Delta x_{max}) = \frac{1}{m+1}\ln\left[(m+1)\frac{(N/V)_{max}}{k_m}\right] + \frac{1}{m+1}\ln R_A. \tag{6.28}$$

According to Eq. (6.28), Δx_{max} depends on nucleation parameters k_m and m, antisolvent addition rate R_A, and the method of detection of the nucleation event.

6.5.3 Another Derivation of Nývlt-like Equation

Relations (6.23) and (6.28) between Δx_{max} and R_A are derived on the assumption that the solubility c of the crystalline solute linearly decreases with an increase in antisolvent composition (i.e. dc_0/dx = constant). However, plots of the solubility c of different solutes as a function of antisolvent composition x reveal that the dependence of c of a solute on x is not linear but follows the relation (Sangwal, 2010), see Section 2.4:

$$\ln(c+\delta) = a_1 - a_2 x, \tag{6.29}$$

where a_1 and a_2 are constants and δ is a small correction term in the solubility c such that the effective or corrected solute concentration $c^* = c + \delta$. Equation (6.29) may be derived from the theory of regular solutions, where the solubility c of the solute in a solvent is given by the relation:

$$\ln c = C - \frac{\Delta H_s}{R_G T}, \tag{6.30}$$

where C is a constant, R_G is the gas constant, and ΔH_s is the enthalpy of dissolution of the solute in the solvent. When Eq. (6.30) is applied for solutions of a solute in solvent S and antisolvent A, one obtains

$$a_1 = \ln c_A + (C_S - C_A), \tag{6.31}$$

$$a_2 = \frac{\Delta H_{sS} - \Delta H_{sA}}{R_G T}, \tag{6.32}$$

where the subscripts S and A with c, C, and ΔH_s denote solvent S and antisolvent A, respectively, and x is the antisolvent content in the solvent–antisolvent mixture. Figure 6.15 presents schematically the dependence of saturation concentration c of solute on volume fraction x of antisolvent to solvent, expressed by Eq. (6.29), for situations when the correction term $\delta = 0$. Using this concept, Sangwal (2010) derived another Nývlt-like equation.

We consider a solution of initial concentration c_1 corresponding to solvent –antisolvent composition x_1, and add the antisolvent at a constant rate R_A until the concentration c_2 corresponding to the composition x_2 is reached. Then the nucleation rate J at x_2 due to the generating supersaturation may be given by (cf. Figures 6.14 and 6.15)

$$J = f\frac{\Delta}{c_2 \Delta t} = f\frac{\Delta c}{c_2 \Delta x}\frac{\Delta x}{\Delta t} = fR_A\frac{\Delta c}{c_2 \Delta x}, \tag{6.33}$$

where f is the number of molecules/ions in the initial solution of concentration c_1 of antisolvent, the excess concentration difference $\Delta c = c_1 - c_2$, the composition difference $\Delta x = x_1 - x_2$, and the antisolvent addition rate $R_A = \Delta x/\Delta t$. Equation (6.33) here defines nucleation rate J in terms of the number of nuclei rather than nucleating mass as in the modified Nývlt-like approach described above in Section 6.5.1. Using Eq. (6.29) to express the saturation concentration c, for $c_2 \gg \delta$, one obtains

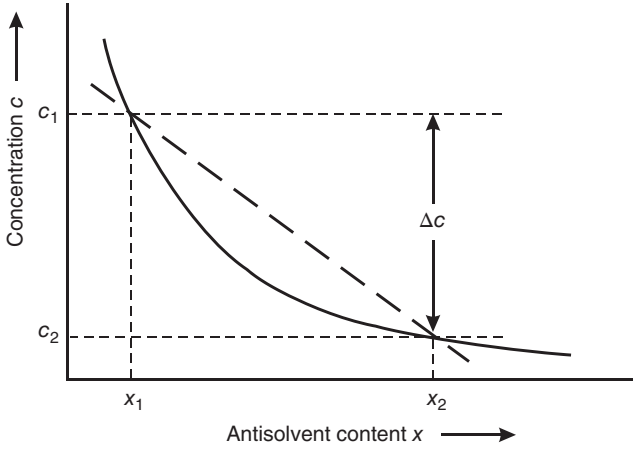

Figure 6.15 Schematic illustration of dependence of saturation concentration c of solute on volume fraction x of antisolvent to solvent according to Eq. (6.29). Dashed line shows constant gradient dc_1/dx.

$$\ln S \approx \frac{\Delta c}{c_2} = a_2 \Delta x, \tag{6.34}$$

where the supersaturation ratio $S = (1 + \Delta c/c_2)$. Using Eq. (6.34) in (6.33), one obtains the nucleation rate in the form:

$$J = f a_2 R_A. \tag{6.35}$$

It should be mentioned that Eq. (6.35) simply denotes the number of nuclei forming per unit volume per unit time in the solution bulk and does not give any information on the size of 3D nuclei forming in the solution.

As in the approaches of O'Grady et al. (2007) and Kubota (2008), during the derivation of the final relationship between Δx_{max} and R_A, Sangwal (2010) also assumed that the nucleation rate J at concentration c_2 during antisolvent crystallization may be described by a power-law equation of the form:

$$J = K\left(\frac{\Delta c}{c_2}\right)^m = K(a_2 \Delta x)^2, \tag{6.36}$$

where K and m are empirical constants but the dimensionless supersaturation $\Delta c/c_2$ is given by Eq. (6.34). Note that K has the dimensions of nucleation rate J. From Eqs. (6.35) and (6.36) to eliminate J and taking $\Delta x = \Delta x_{max}$ for MSZW, upon rearrangement one obtains

$$\Delta x_{max} = \left(\frac{f R_A}{K}\right)^{1/m} a_2^{(1-m)/m} = \left[\left(\frac{f}{K}\right)^{1/m} a_2^{(1-m)/m}\right] R_A^{1/m}, \tag{6.37}$$

which, upon taking logarithm on both sides, gives

$$\ln(\Delta x_{max}) = \Phi + \frac{1}{m} \ln R_A, \tag{6.38}$$

where

$$\Phi = \frac{1}{m} \ln\left(\frac{f}{K}\right) + \frac{1-m}{m} \ln a_2. \tag{6.39}$$

The form of Eq. (6.38) is the same as that of modified Nývlt equation (6.23) and Kubota's equation (6.28). Equation (6.38) also predicts a linear dependence of $\ln(\Delta x_{max})$ on $\ln R_A$, with intercept Φ and slope $1/m$. The two new parameters a_2 and f have physical interpretation, but K and m are still empirical.

6.5.4 Approach Based on Classical Theory of 3D Nucleation

The drawback of Eqs. (6.23), (6.28), and (6.38) involving empirical constants k, k_m, and K can be eliminated when the nucleation rate J is described by the classical theory of 3D nucleation and the real dependence of solubility of a solute on

the composition of solvent mixtures. Sangwal (2010) used this approach to derive another relationship between Δx_{max} and R_A. The approach described below is based on these considerations.

According to the classical theory of 3D nucleation, Eq. (6.17) describes the dependence of nucleation rate J on supersaturation $\ln S$. On substituting $\ln S$ from Eq. (6.34) in Eq. (6.17), one obtains

$$J = J_0 \exp\left[-\frac{B}{(a_2 \Delta x)^2}\right]. \tag{6.40}$$

Equating J from Eqs. (6.35) and (6.40), for $\Delta x = \Delta x_{max}$, one finds

$$(\Delta x_{max})^{-2} = F(1 - Z \ln R_A), \tag{6.41}$$

where

$$F = \frac{a_2^2}{B} \ln\left(\frac{J_0}{f a_2}\right), \tag{6.42}$$

$$Z = \ln\left(\frac{f a_2}{J_0}\right). \tag{6.43}$$

According to Eq. (6.41), a plot of $(\Delta x_{max})^{-2}$ against $\ln R_A$ is a straight line with intercept F and slope FZ, where F and Z are given by Eqs. (6.42) and (6.43), respectively.

It may be seen that all of the quantities contained in the parameters F and Z have well-defined physical meaning, and characterize the antisolvent crystallization of a system. The parameter Z is essentially temperature independent because all quantities are contained in the logarithmic term, but its value is related with f and a_2. The quantity f is associated with the solubility of a solute in the solvent while the quantity a_2 is related to the resultant solute–solvent and solute–antisolvent interactions (cf. Eq. (6.32)). In contrast to Z, F strongly depends on a_2 and B, both of which are determined by the resultant solute –solvent and solute–antisolvent interactions. Both a_2 and B depend on temperature T (see Eqs. (6.32) and (6.18)), and, according to Eq. (6.42), F increases linearly with T, because the logarithm term is practically temperature independent.

6.6 Experimental Data of MSZW in Antisolvent Crystallization

In this section experimental data of antisolvent content Δx_{max}, representing MSZW of aqueous ADP solutions from measurements of solution temperature T_s by feeding of three antisolvents (methanol, ethanol, and acetone), and

MSZW of ethanolic benzoic acid solutions from FBRM and ATR-FTIR measurements by feeding antisolvent water as a function of feeding rate R_A are presented and discussed. For the analysis, Eqs. (6.38) and (6.41) were used. The contents of this section are based on recent publications by Sangwal (2010) and Sangwal and Mielniczek-Brzóska (2016a, b, 2017).

6.6.1 Analysis of Experimental $\Delta x_{max}(R_A)$ Data[1]

In order to obtain experimental data of antisolvent content Δx_{max} necessary for the creation of supersaturation necessary for 3D nucleation in measurements of temperature T_s of ADP solutions saturated at 30 °C as a function of rates R_A of feeding of three antisolvents (methanol, ethanol, and acetone), the values of Δx_{max} were calculated for the antisolvent feeding duration Δt from t_0 to t_1 (i.e. $\Delta t = t_1 - t_0$) corresponding to the equilibrium temperature T_0 of the solution in the plots of ΔT against t (see Figure 6.7). In the $T_s(t)$ plots the time t_1 represents a slightly higher temperature associated with solute–antisolvent interaction (see Figure 6.6a). As pointed out above, for the determination of MSZW the values of $\Delta t = t_1 - t_0$ are more reliable than those of $\Delta t^* = t_{min1} - t_0$ (cf. Figure 6.7). The antisolvent content Δx_{max} for a given antisolvent feeding rate R_A in a saturated solution of volume V_s was calculated using relation (6.14) where the antisolvent volume $V_a = R_A \cdot (t - t_0)$ and the solution volume $V_s = 220$ ml. Figure 6.16 shows the data of Δx_{max} calculated from antisolvent feeding durations $(t - t_0)$ for different antisolvents as a function of their feeding rate R_A. The $\Delta x_{max}(R_A)$ data may be represented by a power-law relation $\Delta x_{max} = AR_{Am}$, with $A = \exp\Phi$ and m listed in Table 6.5.

The experimental $\Delta x_{max}(R_A)$ data for the crystallization of ADP crystals from aqueous solutions with different antisolvents are shown in Figure 6.17a and b as plots of $\ln(\Delta x_{max})$ and $(\Delta x_{max})^{-2}$ against $\ln R_A$ according to Eqs. (6.38) and (6.41), respectively, with the best-fit values of their parameters, including the values of m and $2/Z$, listed in Table 6.5. From Table 6.5, it may be seen that Eq. (6.41) describes the $\Delta x_{max}(R_A)$ data somewhat better than Eq. (6.38) for methanol, but Eq. (6.38) describes the data better than Eq. (6.41) for ethanol and acetone. However, in the case of Eq. (6.41), the best fit of the data improves significantly when a small correction $\Delta R_A = 0.15$ ml·min^{-1}, such that $R_A^* = R_A - \Delta R_A$, is used in the feeding rate R_A.

From Table 6.5 and Figure 6.17, the following trends of the different parameters of Eqs. (6.38) and (6.41) may be noted:

1) The values of $-\Phi$ and m of Eq. (6.38) increase with decreasing dielectric constants ε_a of different antisolvents. The values of the dielectric constant ε_a are

[1] Based on Sangwal and Mielniczek-Brzóska (2017).

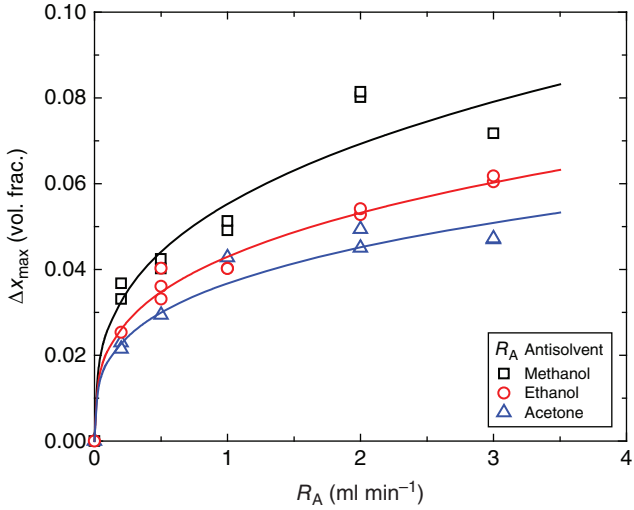

Figure 6.16 Dependence of antisolvent composition Δx_{max} on feeding rate R_A of different antisolvents to aqueous ADP solutions. Plots are drawn according to power-law relation $\Delta x_{max} = AR_A^m$, with $A = \exp\Phi$ and m listed in Table 6.5. *Source:* Adapted from Sangwal and Mielniczek-Brzóska (2017). Copyright (2017), with permission from Wiley.

Table 6.5 Best-fit parameters of Eqs. (6.38) and (6.41) for $\Delta x_{max}(R_A)$ data.

	Eq. (6.38)				Eq. (6.41)				
Antisolvent	**Φ**	**$1/m$**	**m**	**R^2**	**F**	**$-FZ$**	**$-2Z^{-1}$**	**R^2**	**[a]**
Methanol	2.894 ± 0.041	0.325 ± 0.043	3.078	0.8765	395.1 ± 23.46	265.6 ± 24.4	2.975 ± 0.180	0.9361	a
Ethanol	3.145 ± 0.021	0.307 ± 0.025	3.258	0.9442	627.8 ± 49.4	398.9 ± 57.4	3.148 ± 0248	0.8400	a
					537.6 ± 34.0	300.1 ± 27.5	3.583 ± 0.226	0.9292	a, b
Acetone	3.302 ± 0.031	0.295 ± 0.029	3.388	0.9346	921.7 ± 83.1	600.0 ± 78.2	3.072 ± 0.277	0.8921	a
					746.5 ± 59.6	412.2 ± 35.9	3.622 ± 0.289	0.9492	a, b

Source: After Sangwal and Mielniczek-Brzóska (2017).
[a] Comments: (a) $\Delta T = 0$ and (b) $\Delta R_A = 0.15$ ml min^{-1}.

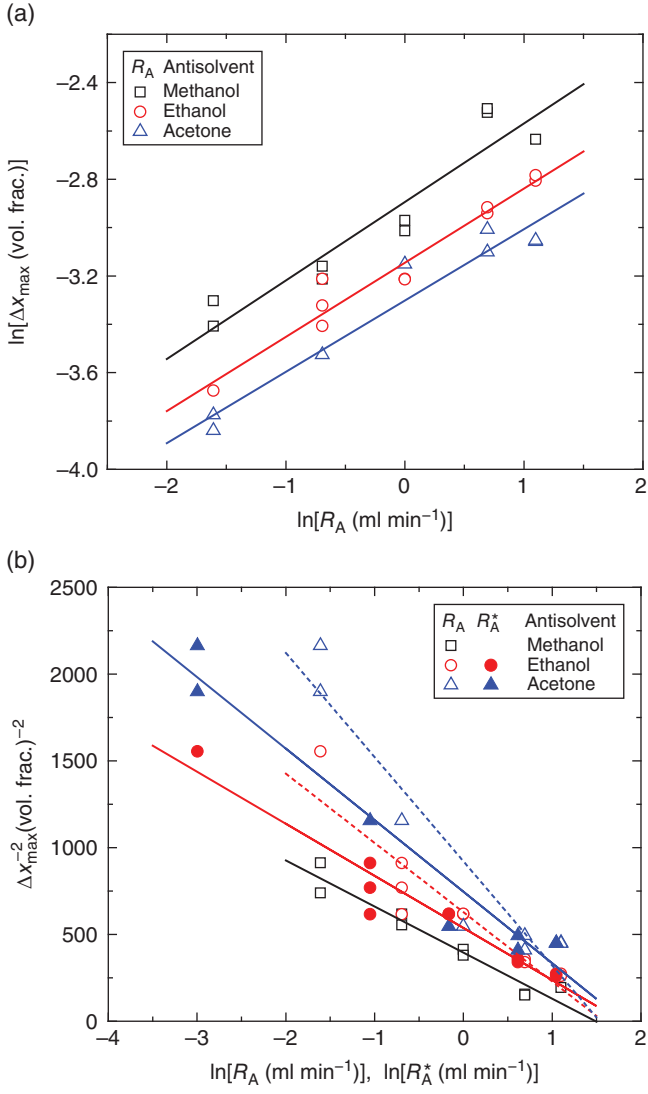

Figure 6.17 Dependence of (a) ln Δx_{max} and (b) Δx_{max}^{-2} on ln R_A for different antisolvents added to aqueous ADP solutions according to Eqs. (6.38) and (6.41), respectively. Plots are drawn with the best-fit parameters given in Table 6.5. *Source:* Adapted from Sangwal and Mielniczek-Brzóska (2017). Copyright (2017), with permission from Wiley.

33.0, 25.3, and 21.0 for methanol, ethanol, and acetone at 293.2 K, respectively, and that of ε_s for solvent water is 80.1 at 293.2 K (Lide, 1996/1997).

2) For the $\Delta x_{max}(R_A)$ data of different antisolvents with $\Delta T = 0$, the following relationships are observed: $\Phi = -\ln F/2$ and $m = -2/Z$. These relations mainly hold for methanol but $\Phi < -\ln F/2$ and $m > -2/Z$ for ethanol and acetone. However, the equalities $\Phi = -\ln F/2$ and $m = -2/Z$ improve when the antisolvent feeding rate is corrected by ΔR_A.
3) The equalities $\Phi = -\ln F/2$ and $m = -2/Z$ may be understood upon taking logarithm on both sides of Eq. (6.41), which gives Eq. (4.38) for $\ln(1 - Z\ln R_A) \approx Z\ln R_A$.

Figure 6.18a and b shows the plots of Φ and $-\ln F/2$, and m and $-2/Z$ against the dielectric constant ε_a of the three antisolvents, respectively. From the figures, one observes that the dependence of calculated values of Φ and m for different antisolvents on their dielectric constant ε_a may be represented by the following empirical relation:

$$\Phi, m = \Phi_1, m_1 - \frac{z_1}{\varepsilon_a} = \Phi_1, m_1 \left\{ 1 - \frac{z_1}{(\Phi_1, m_1)\varepsilon_a} \right\}, \tag{6.44}$$

where Φ_1, m_1 is the value of Φ, m when $1/\varepsilon_a \to 0$ and z_1 is the slope of the plot. The best-fit parameters for the linear plots of the $\Phi(1/\varepsilon_a)$ and $m(1/\varepsilon_a)$ data are listed in Table 6.6. It was observed that the $\Phi(\varepsilon_a)$ and $m(\varepsilon_a)$ data may also be described by the linear relation:

$$\Phi, m = \Phi_2, m_2 - z_2\varepsilon_a, \tag{6.45}$$

with the intercept Φ_2, m_2 and slope z_2 listed in Table 6.6. Here Φ_2, m_2 are the values of Φ, m when $\varepsilon_a \to 0$. Since the constants Φ and m in Eq. (6.38) are empirical, no physical interpretation can be given for the dependences of Eqs. (6.44) and (6.45). However, the equalities $\Phi = -\ln F/2$ and $m = -2/Z$ suggest that the constants Φ and m and their dependencies on the dielectric constant ε_a of antisolvents have physical basis.

The parameters F and Z are essentially determined by four parameters a_2, B, f, and J_0 (see Eqs. (6.42) and (6.43)). The parameter B is related to the interfacial energy γ (Eq. (6.18)), f is determined by the solute concentration in the solution, and a_2 is related to the difference in the dissolution enthalpies of solvent and antisolvents (cf. Eq. (6.32)). Since the solubility of an electrolyte in different solvents decreases with their decreasing dielectric constant ε_s (Lide, 1996/1997), it may be argued that the value of the a_2 parameter for our antisolvents is determined by their dielectric constants ε_a. However, the values of F and Z from Eqs. (6.42) and (4.43) lead to the inference that $\Phi = -\ln F/2$ and $m = -2/Z$ do not change linearly with the a_2 parameter of the antisolvents, and hence with their dielectric constants ε_a.

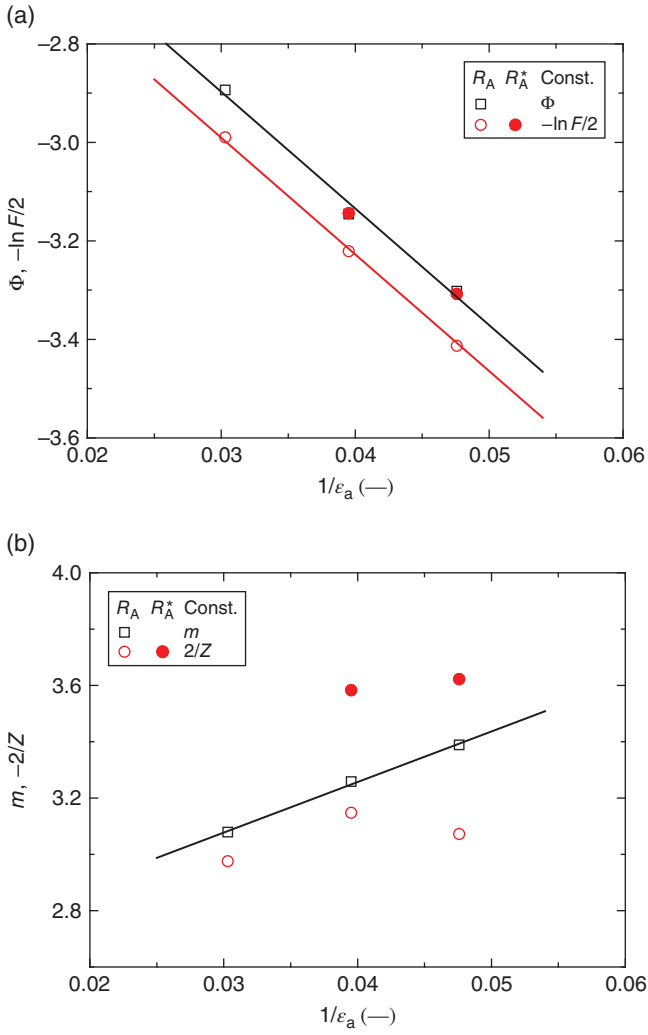

Figure 6.18 Dependence of (a) Φ and −ln *F*/2, and (b) *m* and −2/*Z* on $1/\varepsilon_a$ of antisolvents added to aqueous ADP solutions according to Eq. (6.44). Linear plots are drawn with constants listed in Table 6.6. Filled circles represent −ln *F*/2 data with corrected R_A^*. *Source:* Adapted from Sangwal and Mielniczek-Brzóska (2017). Copyright (2017), with permission from Wiley.

Table 6.6 Best-fit parameters of Eqs. (6.44) and (6.45) for $\Phi(\varepsilon_a)$ and $m(\varepsilon_a)$ data.

	Eq. (6.44)				Eq. (6.45)			
Data	Φ_1,m_1	z_1	$z_1/(\Phi_1,m_1)$	R^2	Φ_2,m_2	$10^{-2}z_2$	$10^{-3}z_2/(\Phi_2,m_2)$	R^2
$\Phi(\varepsilon_a)$	−2.187 ± 0.090	−23.68 ± 2.27	10.83 ± 1.04	0.9817	−4.009 ± 0.026	3.387 ± 0.026	8.45 ± 0.24	0.9983
$m(\varepsilon_a)$	2.539 ± 0.039	17.96 ± 0.99	7.07 ± 0.39	0.9939	3.917 ± 0.048	2.555 ± 0.177	6.52 ± 0.45	0.9905

Source: After Sangwal and Mielniczek-Brzóska (2017).

From the data of $FZ = a_2^2/B$ and $Z = \ln(fa_2/J_0)$, the values of a_2 were calculated arbitrarily assuming that $B = 0.1$ and $J_0/f = 3$ (cf. Table 6.7). The calculated values of the a_2 parameter from the FZ and Z data, with feeding rates R_A and R_A^*, for different antisolvents are shown in Figure 6.19 as a function of their $1/\varepsilon_a$. The best-fit plots for the data from $\Delta T = 0$ follow the empirical relation:

$$a_2 = a_1 + \frac{b_1}{\varepsilon_a} = \frac{b_1}{\varepsilon_s}\left(\frac{\varepsilon_s}{\varepsilon_a} + \frac{a_1\varepsilon_s}{b_1}\right), \tag{6.46}$$

where ε_s is the dielectric constant of solvent water at 293.2 K, and the parameters a_1 and b_1 listed in Table 6.7.

From Figure 6.19, it may be seen that for $\Delta T = 0$ the values of a_2 calculated from the $FZ(\varepsilon_a)$ data both for feeding rates R_A and R_A^* linearly increase with $1/\varepsilon_a$ but those calculated from the $Z(\varepsilon_a)$ data for R_A and R_A^* practically remain independent of $1/\varepsilon_a$, with constant values of 5.76 ± 0.11 and 5.23 ± 0.02, respectively. In the former case, the intercept a_1 and the slope b_1 are different and are included in Table 6.7. The practically ε_a-independent value of a_2 from the $Z(\varepsilon_a)$ data is essentially a consequence of the assumption that the term J_0/f in Eq. (6.43) is a constant quantity independent of the dielectric constant ε_a of the antisolvent. In fact, the values of a_2 calculated from the $Z(\varepsilon_a)$ data increases when J_0/f increases with increasing $1/\varepsilon_a$. This means that, for a constant J_0, the f parameter decreases with decreasing dielectric constant ε_a of the antisolvent used for crystallization. Obviously, the value of f is intimately connected with the solubility of solute in the solvent–antisolvent mixture. This inference is contrary to the assumption that the f parameter is related to the solubility of the solute in the original solution of a solute used for antisolvent crystallization (see Eq. (6.35)).

Creation of supersaturation necessary for 3D nucleation (i.e. MSZW) in saturated aqueous ADP solution at a given temperature by the addition of an antisolvent is associated with the replacement of water molecules surrounding

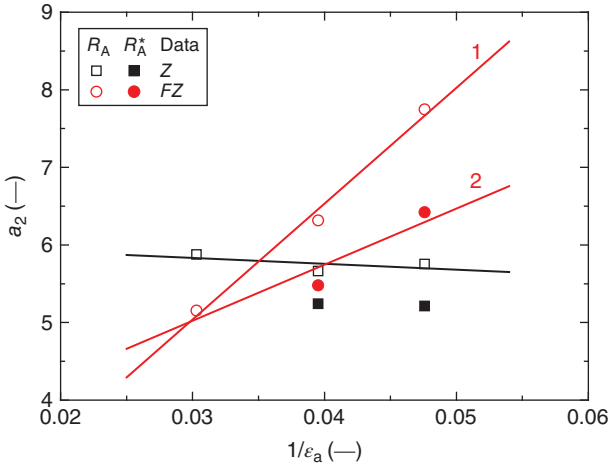

Figure 6.19 Plots of a_2, calculated from $FZ = a_2^2/B$ and $Z = \ln\left(f_a^2/J_0\right)$, against $1/\varepsilon_a$ according to Eq. (6.46) for different antisolvents. Open squares and circles represent values of a_2 calculated from $Z = \ln\left(f_a^2/J_0\right)$ and FZ, respectively, for R_A, whereas filled squares and circles show values of a_2 calculated from $Z = \ln\left(f_a^2/J_0\right)$ and FZ, respectively, with corrected $R_A^* = R_A - \Delta R_A$. Curves are drawn with values of a_2 from (1) $\Delta x_{max}(R_A)$ and (2) $\Delta x_{max}\left(R_A^*\right)$ data for $\Delta T = 0$ with values of a_1 and b_1 listed in Table 6.7. *Source:* Adapted from Sangwal and Mielniczek-Brzóska (2017). Copyright (2017), with permission from Wiley.

solute ions/molecules by antisolvent molecules may be explained qualitatively in terms of change $\Delta(\Delta G_{I-SA})$ in the free energies ΔG_{I-S} and ΔG_{I-A} of ion–solvent and ion–antisolvent interactions, calculated by the Born model, in the form (Sangwal and Mielniczek-Brzóska, 2016a):

$$\Delta(\Delta G_{I-SA}) = \Delta G_{I-S} - \Delta G_{I-A} = -N_A k_0 \frac{q^2}{2r_i}\left(\frac{1}{\varepsilon_a} - \frac{1}{\varepsilon_s}\right), \tag{6.47}$$

where the Avogadro number $N_A = 6{\cdot}10^{23}$ ions per mol, the Coulombian proportionality constant $k_0 = 9{\cdot}10^9\ \mathrm{Nm^2{\cdot}C^{-2}}$, the elementary ionic charge $q = 1.6{\cdot}10^{-19}$ C, and the ionic radius $r_i \approx 1.5{\cdot}10^{-10}$ m. On substituting the values of different quantities, Eq. (6.47) gives

$$\frac{\Delta(\Delta G_{I-SA})}{R_G T} = -\frac{183}{\varepsilon_s}\left(\frac{\varepsilon_s}{\varepsilon_a} - 1\right), \tag{6.48}$$

where we have taken $R_G T = 2.52\ \mathrm{kJ{\cdot}mol^{-1}}$. Equation (6.48) predicts that the free energy change $\Delta(\Delta G_{I-SA})/R_G T$ increases linearly with increasing $1/\varepsilon_a$. It is easy to show that in a relatively narrow range of ε_a of different antisolvents, the free energy change also decreases with increasing ε_a. Equation (6.48) provides a

connection between the parameter $a_2 = (\Delta H_{sA} - \Delta H_{sS})/R_G T$ and the free energy change $\Delta(\Delta G_{I-SA})/R_G T$. However, in contrast to the a_2 parameter, the free energy change $\Delta(\Delta G_{I-SA})/R_G T$ is a negative quantity.

In order to compare Eqs. (6.48) and (6.46), we rewrite Eq. (6.46) in the form:

$$a_2 = \frac{b_1}{\varepsilon_s}\left(\frac{\varepsilon_s}{\varepsilon_a} - 1\right) + \left(\frac{b_1}{\varepsilon_s} + a_1\right), \tag{6.49}$$

where b_1/ε_s and $(a_1 + b_1/\varepsilon_s)$ are constants. Obviously, the a_2 parameter is composed of two energy terms. The first term is equal in magnitude to the free energy change $\Delta(\Delta G_{I-SA})/R_G T$ associated with the addition of antisolvent to the aqueous solution (see Eq. (6.48)) and involves desolvation of solvated solute ions. However, the second term is an additional free energy term necessary for the creation of supersaturation, and is probably associated with the diffusion of some of solvent water molecules, released from solvation sheath around solute ions by antisolvent molecules, away from the partially desolvated ions. Comparison of the first term of Eq. (6.49) with Eq. (6.48) gives the theoretical value of $b_1 = 183$.

As seen from Table 6.7, the calculated value of b_1 from the experiments is lower by a factor of about 1.22 and 2.5 for feeding rates R_A and R_A^*, respectively, than the theoretical value of $b_1 = 183$ predicted by Eq. (6.48). This discrepancy is due to two reasons: (i) low value of $B = 0.1$ used in the calculations of a_2 and (ii) erratic determination of FZ from the original $\Delta x_{max}(R_A)$ data. For example, the values of FZ from the $\Delta x_{max}(R_A)$ and $\Delta x_{max}\left(R_A^*\right)$ data give the above value of $b_1 = 183$ with $B = 0.15$ and 0.625, respectively. The additional energy term $(a_1 + b_1/\varepsilon_s)$, on the other hand, gives the energy Q equal to 6.1 ± 0.6 and 9.5 ± 3.1 kJ·mol^{-1} from the $\Delta x_{max}(R_A)$ and $\Delta x_{max}\left(R_A^*\right)$, respectively.

Using the values of $B = 0.15$ and 0.625 for feeding rates R_A and R_A^*, respectively, one can estimate the value of solute–solvent interfacial energy γ from Eq. (6.18) rewritten in the form:

$$\gamma = \frac{k_B T}{\Omega^{2/3}}\left(\frac{B}{\kappa}\right)^{1/3}, \tag{6.50}$$

with the shape factor $\kappa = 16\pi/3$ for spherical nuclei and the molecular volume $\Omega = (2r_i)^3$, where we assume, as above, that the ionic radius $r_i = 1.5 \cdot 10^{-10}$ m. These calculated values are listed in Table 6.7. It is interesting to note that the calculated values of the interfacial energy γ, listed in Table 6.7, are in good agreement with the values lying between 4 and 12 mJ·m^{-2} for ADP reported in the literature (Söhnel and Garside, 1992).

It is known that the activation energy for self-diffusion of molten electrolytes frequently follows the relation (see Bockris and Reddy, 1970, Chap. 6):

$$E_D = 3.7 R_G T_m, \tag{6.51}$$

Table 6.7 Best-fit parameters of Eq. (6.46) for $a_2(1/\varepsilon_a)$ data.

Data	a_1	b_1	b_1/ε_s	$a_1 + b_1/\varepsilon_s$	Q (kJ·mol^{-1})	γ (mJ·m^{-2})	R^2	[a]
FZ	0.560 ± 0.058	149.3 ± 14.7	1.864 ± 0.183	2.424 ± 0.242	6.1 ± 0.6	9.7	0.9808	a
	2.853 ± 0.931	72.3 ± 23.4	0.903 ± 0.292	3.756 ± 1.223	9.5 ± 3.1	15.6	0.8104	a, b
Z	6.059 ± 0.388	−7.5 ± 9.7	—	—	—	—	0.2543	a

Source: After Sangwal and Mielniczek-Brzóska (2017).

[a] Comments: (a) $\Delta T = 0$ and (b) $\Delta R_A = \mathbf{0.15\ ml\ min^{-1}}$.

where T_m is the melting point of the electrolyte. Assuming that diffusion of water molecules in aqueous solutions follows Eq. (6.51), one obtains $E_D = 8.4$ kJ·mol^{-1} for water solvent ($T_m = 273$ K). This means that the calculated values of Q are comparable with the value of E_D for self-diffusion and suggest that diffusion plays important role in antisolvent crystallization.

Finally, it should be mentioned that the nucleation order $m > 3$ is obtained for crystallization of ADP from aqueous solutions for different antisolvents. Following the ideas of the distribution of m observed for different compounds crystallized by the solution cooling (polythermal) method (Sangwal, 2011) and the trends of steep increase in temperature T_s of aqueous solutions and abrupt decrease in laser-beam intensity I transmitted through them during the crystallization of ADP by addition of antisolvents acetone and methanol (Sangwal and Mielniczek-Brzóska, 2016a, b), these values of m may be attributed to the occurrence of progressive nucleation (see Section 5.2.7).

6.6.2 Effect of Detection Technique on MSZW

The value of MSZW of a particular system can be affected by two types of factors. The first category of factors belongs to measurement techniques, which themselves may induce heterogeneous and secondary nucleation. Even when the system is free of impurities, the probe of certain techniques such as conductivity and ultrasound measurements, which are inserted in the solution, can induce heterogeneous nucleation. Similarly, stirring can induce both heterogeneous and secondary nucleation. The second category of factors belongs to the identification of the moment of occurrence of primary nucleation. All techniques based on recording of transmitted or scattered light intensity and temperature measurements belong to this category. Moreover, two different techniques usually detect the

occurrence of nucleation in a system at different moments. Therefore, some comments on the techniques used for the measurement of MSZW deserve mention.

In this section examples of measurements of MSZW by (i) identification of two different solution temperatures in the plots of temperature T_s of aqueous ADP solution against the antisolvent feeding duration t at different rates R_A (Sangwal and Mielniczek-Brzóska, 2016b) and (ii) identification of occurrence of nucleation event by two different techniques in ethanolic benzoic acid solutions induced by addition of water (O'Grady et al., 2007) are presented. In the next section the effect of stirring rate on MSZW is described.

The values of maximum antisolvent content Δx_{max} for the occurrence of 3D nucleation in aqueous ADP solutions at different feeding rate R_A values of antisolvent feeding durations $(t_1 - t_0)$ and $(t_{min1} - t_0)$ were calculated from the original computer files of the data of $\Delta T = T_s - T_w$ against the feeding duration t of methanol at different rates R_A. Here, the time t_1 corresponds to the equilibrium temperature T_0 of the solution (i.e. $\Delta T = 0$) containing antisolvent content Δx_{max} necessary for the creation of supersaturation for 3D nucleation, but the time t_{min1} when the lowest temperature ΔT_{min1} is attained is always somewhat lower than t_1 (i.e. $t_{min1} < t_1$ and $\Delta T < 0$). The data of Δx_{max} calculated from antisolvent feeding durations $(t_1 - t_0)$ for different antisolvents and, as an example, from $(t_{min1} - t_0)$ for methanol as a function of R_A showed (Sangwal and Mielniczek-Brzóska, 2016b) that for a given R_A the value of Δx_{max} obtained from durations $(t_{min1} - t_0)$ is lower than that from $(t_1 - t_0)$ up to 20% and the value of Δx_{max} from two experimental runs can differ from each other up to 10%.

Figure 6.20a and b shows $\Delta x_{max}(R_A)$ data for $\Delta T = 0$ and $\Delta T < 0$ as plots of $\ln \Delta x_{max}$ and (b) Δx_{max}^{-2} against $\ln R_A$ for methanol added to aqueous ADP solutions according to Eqs. (6.38) and (6.41), respectively. In Figure 6.22b, dashed and solid plots are drawn for the uncorrected R_A and corrected R_A^*, respectively. Plots are drawn with the best-fit parameters given in Table 6.8. From the table it may be noted that the values of $-\Phi$ and m obtained from the $\Delta x_{max}(R_A)$ data for $\Delta T < 0$ are higher than those from the data for $\Delta T = 0$. Similarly, the values of F and Z are higher for the data with $\Delta T < 0$ than those for the data with $\Delta T = 0$.

O'Grady et al. (2007) found that, among the two methods they used for the measurement of MSZW in antisolvent crystallization of benzoic acid in ethanol–water mixture, FBRM detects the onset of nucleation before ATR-FTIR spectroscopy. Their data of MSZW Δx_{max} for benzoic acid determined by the two techniques as a function of antisolvent addition rate R_A are shown in Figure 6.21a and b according to Eqs. (6.38) and (6.41), respectively, while the best-fit constants of these equations are listed in Table 6.8. In Figure 6.21b, the experimental data are fitted without as well as with a small correction term $\Delta R_A = 0.0435\ g{\cdot}s^{-1}$.

From Figure 6.21 and Table 6.8, it may be noted that the fit is better with Nývlt-like equation. (6.38) for data from ATR-FTIR measurements, whereas it is better with classical theory-based Eq. (6.41) for FBRM measurements. However, with the small correction term ΔR_A such that the effective antisolvent

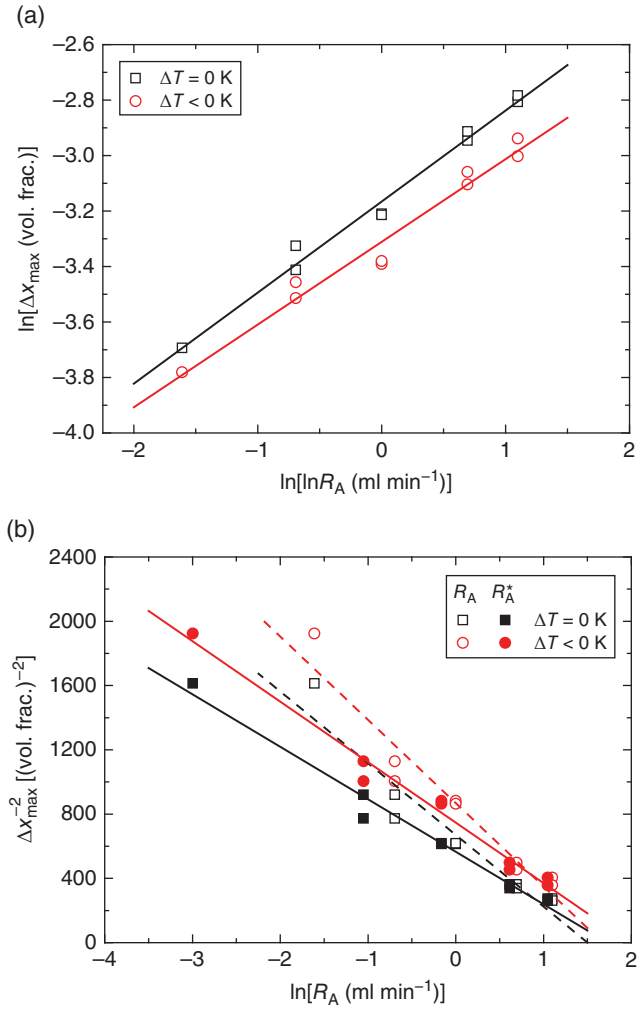

Figure 6.20 Plots of (a) $\ln(\Delta x_{max})$ and (b) $(\Delta x_{max})^{-2}$ against $\ln R_A$ according to Eqs. (6.38) and (6.41), respectively, from $\Delta x_{max}(R_A)$ data obtained for aqueous ADP solutions saturated at 30 °C with temperature difference $\Delta T = 0$ and $\Delta T < 0$ due to solute by feeding ethanol. Linear plots are drawn with the constants given in Table 6.8. *Source:* Original data from Sangwal and Mieniczek-Brzóska (2017).

addition rate $\Delta R_A^* = R_A - \Delta R_A$ in Eq. (6.41), one obtains equally the best fit of the experimental data.

From Table 6.8, it may be noted that the values of the parameters of $-\Phi$ and m of Eq. (6.38) and $-F$ and Z of Eq. (6.41) for the $\Delta x_{max}(R_A)$ data obtained by the FBRM technique are higher than those for the $\Delta x_{max}(R_A)$ data obtained by the ATR-FTIR technique. Recalling that FBRM detects the onset of nucleation

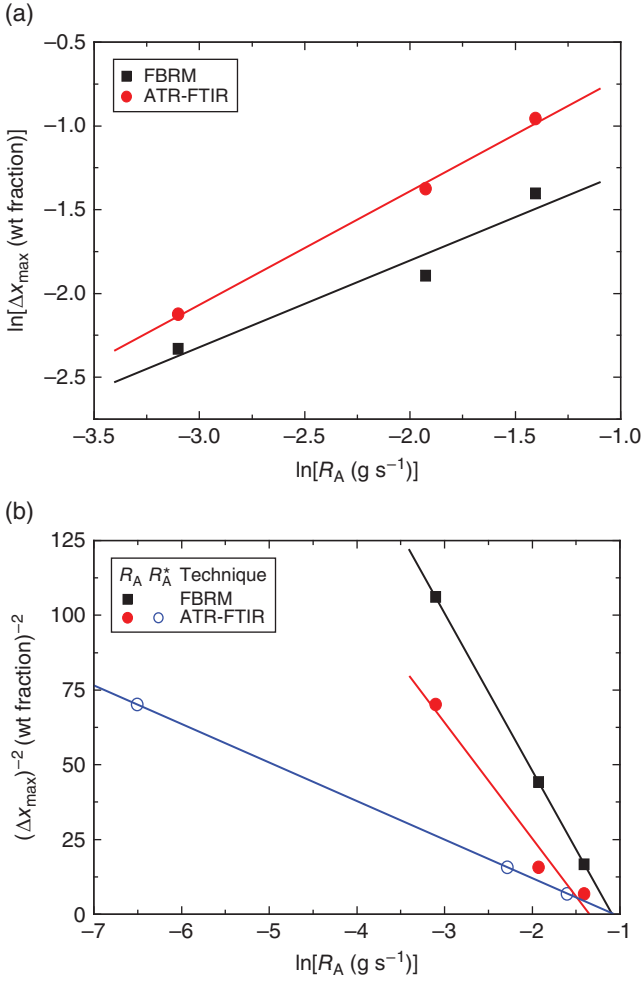

Figure 6.21 Plots of (a) $\ln(\Delta x_{max})$ and (b) $(\Delta x_{max})^{-2}$ against $\ln R_A$ according to Eqs. (6.38) and (6.41), respectively, obtained for benzoic acid at 298.15 K by FBRM and ATR-FTIR. *Source:* Original data from O'Grady et al. (2007).

before ATR-FTIR spectroscopy, these trends are similar to those of the $\Delta x_{max}(R_A)$ data obtained for aqueous ADP solution with $\Delta T < 0$ in comparison with those with $\Delta T = 0$.

6.6.3 Effect of Stirring on MSZW

In order to discuss the effect of stirring on antisolvent crystallization of benzoic acid at 298.15 K, where antisolvent water was added to the saturated ethanol

Table 6.8 Constants Φ and β of Eq. (6.38) and F and Z of Eq. (6.41).

		Eq. (6.38)				Eq. (6.41)				
System	**Data**	**−Φ**	**β**	**m**	**R^2**	**$-F$ (—)**	**$-FZ$**	**Z**	**R^2**	[c]
ADP–water[a]	$\Delta T = 0$	3.166	0.328	3.05	0.9841	670.9	446.2	0.666	0.9090	
						565.7	326.7	0.578	0.9785	(c)
	$\Delta T < 0$	3.311	0.298	3.35	0.9646	868.8	518.2	0.596	0.9269	
						747.4	376.3	0.503	0.9787	
BA–ethanol[b]	ATR-FTIR	0.03112	0.6790	1.47	0.9984	52.4	38.8	0.7413	0.9847	
						13.8	12.9	0.9356	1	(d)
	FBRM	0.7672	0.5175	1.93	0.9687	57.5	52.7	0.9178	1	

[a] Methanol as antisolvent.
[b] Benzoic acid (BA) in water.
[c] Comment: (c) $\Delta R_A = 0.15$ ml·min^{-1} and (d) $\Delta R_A = 0.0435$ g·s^{-1}.

–water solution, the experimental $\Delta x_{max}(R_A)$ data reported by O'Grady et al. (2007) using FBRM are analyzed using theoretical expressions (6.43) and (6.46). The antisolvent was added to a location close to the stirrer shaft and the solution was stirred at 325 and 475 rpm. Figure 6.22a and b shows the original data of Δx_{max} as a function of R_A for benzoic acid, reported by O'Grady et al. (2007), in the form of plots of $\ln(\Delta x_{max})$ and Δx_{max}^{-2} against $\ln R_A$ according to Eqs. (6.38) and (6.41), respectively. In Figure 6.22b, the fit was improved when a corrected antisolvent addition rate $R_A^* = R_A - \Delta R_A$ (where ΔR_A is a small correction term), instead of the as-used feeding rate R_A was used in the analysis. The values of the constants of the equations are listed in Table 6.9.

The effect of stirring may be understood from consideration of the values of the constants of the two equations (Sangwal, 2010). It may be seen from Table 6.9 that the value of m practically does not depend on the solution stirring rate but Φ decreases with an increasing stirring rate. Since the number of ions/molecules f in the initial solution in the two cases is the same and the value of K either increases or remains constant with increasing stirring, the decrease in Φ, given by Eq. (6.39), may be attributed to an increase in the parameter a_2 (see Eqs. (6.39) and (6.32)) with increasing stirring rate because the term $(1 - m)/m$ is about −2/3 in the present case. However, in view of the empirical nature of constants K and m, the above interpretation remains speculative. Therefore, we analyze the effect of stirring from a consideration of changes caused in the values of the constants of Eq. (6.41) and note the following features of the constants from Table 6.9:

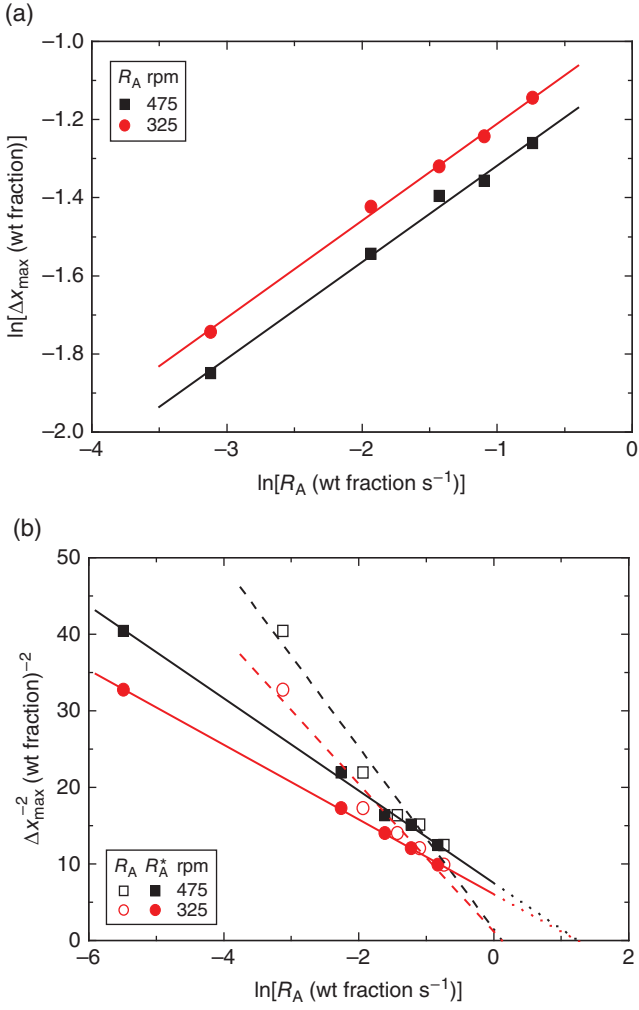

Figure 6.22 Plots of (a) $\ln(\Delta x_{max})$ and (b) $(\Delta x_{max})^{-2}$ against $\ln R_A$ according to Eqs. (6.38) and (6.41), respectively, for benzoic acid–ethanol solution fed with water as antisolvent with two different stirring rates. In (b) dashed and solid curves represent fit of the data without and with corrected feeding rates, respectively. *Source:* Original data from O'Grady et al. (2007).

Table 6.9 Constants Φ and β of Eq. (6.38) and F and Z of Eq. (6.41).

Stirring (rpm)	Φ (—)	β (—)	m	R^2	F (—)	FZ	Z	R^2
325	0.584	0.335	2.99	0.9976	75.20	15.94	0.212	0.9672[a]
					37.90	8.94	0.236	0.9973
475	0.454	0.343	2.92	0.9947	111.52	23.53	0.211	0.9670
					56.46	13.21	0.234	0.9968

[a] Best-fit values of parameters of Eq. (6.41) for a given strring rate are given in upper and lower columns for R_A and R_A^*, respectively.

1) The value of Z is independent of stirring rate R_A, but its value is increased by about 10% when a corrected antisolvent addition rate R_A^* is used for the analysis of the data.
2) The value of ΔR_A is close to the lowest value of antisolvent addition rate R_A.
3) The value of F increases with an increase in stirring rate.

According to Eq. (6.42), the value of F depends on the term a_2^2/B. However, since the parameter B, which is related to the interfacial energy γ (see Eq. (6.18)) for a system, does not depend on solution stirring, it may be inferred that the effect of stirring rate on F is related to the difference in the enthalpy of mixing (cf. Eq. (6.32)). In contrast to this, stirring has poor effect on Z, because all possible variable quantities are contained in the logarithm term.

It should be mentioned that the inference of the effect of stirring on the value of F associated with change in a_2 corroborates the conclusion based on analysis of the experimental data using Nývlt-like equation (6.38). However, the effect of stirring is better explained by the approach based on classical theory of 3D nucleation.

6.6.4 Threshold and Limiting Antisolvent Addition Rates

Analysis of the experimental data according to Eq. (6.41) based on the classical nucleation theory predicts two specific values of antisolvent addition rate: the threshold antisolvent addition rate ΔR_A and the maximum antisolvent addition rate R_{Amax}, which correspond to the lower and the upper limits of the antisolvent addition rate when Eq. (6.41) applies. Physically, ΔR_A and R_{Amax} correspond to situations when an antisolvent crystallization system begins and ceases to respond to the addition of antisolvent. The former antisolvent addition rate is associated with the setting up of an equilibrium between solvent and antisolvent, whereas the latter is connected with the induction period t_{in} for the onset of crystallization.

In analogy with the induction period t_{in} involved in the MSZW measured as the maximum temperature difference ΔT_{max} as a function of solution cooling rate R_L in the traditional nonisothermal (cooling or polythermal) crystallization (Kim and Kim, 2001; Kim and Mersmann, 2001), the induction period t_{in} in antisolvent crystallization may be defined as

$$t_{in} = \frac{\Delta x_{max}}{R_A}, \tag{6.52}$$

where the time when the first crystal is detected in the system is taken as the induction period t_{in}. Note that Δx_{max} is a dimensionless quantity and the induction period t_{in} involves, among others, the initial time t_{reorg} necessary for the reorganization of solute ions/molecules by the addition of Δx_{max} of antisolvent before their integration into the formation of 3D nuclei before reaching a critical

size as well as the time t_g required for their growth into entities detectable in the solution volume V_s by an experimental technique. In the case of aqueous ADP solutions taking a typical value of $\Delta x_{max} = 0.05$ volume fraction of antisolvent ethanol (ml antisolvent in ml solution), $\Delta x_{max} = 0.05 V_s = 11$ ml ($V_s = 220$ ml; see Section 6.1), and the uncorrected data $R_{Amax} = 4.5$ ml·min^{-1} ($\ln R_{Amax} = 1.5$, with antisolvent feeding R_A in ml·min^{-1}; see Figure 6.19b and 6.22b), one finds $t_{in} \approx 147$ s. In this case, corresponding to the threshold $\Delta R_A = 0.15$ ml·min^{-1}, for $\Delta x_{max} = 0.05$ from the value of the corrected feeding rate R_A^*, one finds $t_r \approx 5$ s, implying that $t_r \approx t_{in}/30$.

Finally, it should be mentioned that the value of $\ln R_{Amax}$ is characteristic for a solute–solvent–antisolvent system. Consequently, it is not surprising that its value for different systems is different and is associated with the value of the induction period t_{in} required for the growth of critically-sized nuclei to detectable entities and is directly connected with the parameter Z because $Z = \ln R_{Amax}$ (see Eq. (6.38)).

6.7 Combined Antisolvent/Cooling Crystallization

Crystallization processes are frequently used for obtaining crystals with desired crystal size distribution, shape and purity, and minimum production costs in chemical and pharmaceutical industries. The main requirement to achieve these goals is to carry out crystallization at the optimum supersaturation level which is lower than the maximum supersaturation corresponding to MSZW and is usually generated in the system by adding an antisolvent to it or by cooling it. Most of the experimental and theoretical studies for the determination of MSZW are dedicated to one type of crystallization such as solution cooling or antisolvent feeding. However, some studies of the effect of combined cooling and antisolvent addition on the MSZW have also been published in recent years (Knox et al., 2009; Lindenberg et al., 2009; Saleemi et al., 2012; Trifkovic et al., 2009). This section briefly deals with the MSZW of systems involving combined cooling/antisolvent crystallization.

In combined cooling/antisolvent crystallization solute concentration is changed simultaneously by cooling of the system as well as addition of an antisolvent to it. This means that excess solute concentration Δc during combined cooling/antisolvent crystallization is a result of the sum of two contributions and the MSZW by combined cooling/antisolvent crystallization is determined by a new limiting temperature difference $\Delta T^*_{max} = T_0 - T^*_{lim}$, which is defined by a new solubility curve A and a new metastability curve A* in such that $T_0 > T^*_{lim} > T_{lim}$, as shown schematically in Figure 6.23. Note that simultaneous cooling of a saturated solution during the addition of an antisolvent to it requires lower antisolvent content Δx^*_{max} than Δx_{max} without cooling. In Figure 6.23 we have

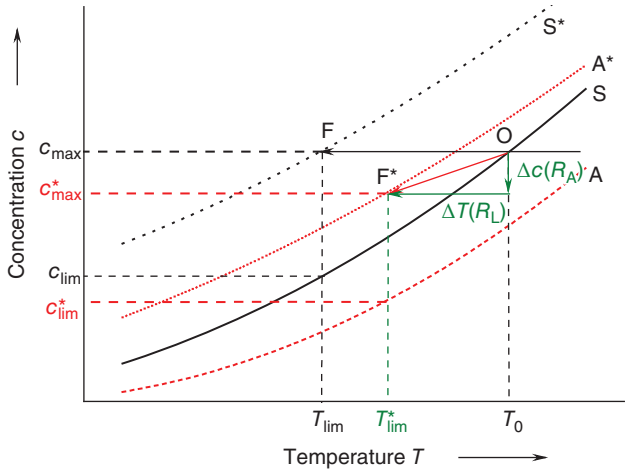

Figure 6.23 Schematic illustration of excess solute concentration Δc and MSZW during combined cooling/antisolvent crystallization as a result of sum of two contributions.

used the same terminology as that used before and Δx_{max} is defined by Eq. (6.14). Assuming that 3D nucleation is primary, two methods have been proposed to describe the MSZW for the system. These methods are based on Nývlt's and Kubota's approaches discussed in Chapter 5 and in this chapter. Both of these approaches assume linear increase in excess solute concentration Δc with a decrease in temperature by ΔT and antisolvent content Δx_A (Trifkovic et al., 2009).

MSZW measurements for cooling/antisolvent crystallization of solutions may be carried out by using the same techniques as those used for MSZW measurements for cooling and antisolvent crystallizations. Trifkovic et al. (2009) and Knox et al. (2009) used ATR-FTIR and FBRM for measurements of MSZW, induction time, and primary nucleation kinetics of paracetamol in isopropanol/water solutions, whereas Saleemi et al. (2012) used ATR-uv/vis spectroscopy and FBRM for monitoring of crystallization of mixtures of aminobenzoic acid isomers. Lindenberg et al. (2009) employed ATR-FTIR and FBRM for *in situ* monitoring of solubility and particle size distribution during combined cooling/antisolvent crystallization of acetylsalicylic acid (ASA) in water/ethanol mixtures and population balance modeling. The main finding of this study was that combined cooling/antisolvent crystallization enables both to improve crystalline productivity and to reduce the formation of fines and that process parameters, derived from nucleation and growth kinetics, and population balance modeling are effective in crystallization processes where solvent composition and temperature are changed simultaneously.

References

Barrow, G.M. (1973). *Physical Chemistry*, 3e. New York: McGraw-Hill.

Bennema, P. and Söhnel, O. (1990). Interfacial surface tension for crystallization and precipitation from aqueous solutions. *J. Cryst. Growth* 102: 547–556.

Bockris, J.O.'.M. and Reddy, A.K. (1970). *Modern Electochemistry*, vol. 1. New York: Plenum.

Chaitanya, K.K. and Sarkar, D. (2014). Determination of the metastable zone width by a simple optical probe. *Chem. Eng. Technol.* 37: 1037–1042.

Dang, L.-P., Wang, Z.-Z., and Liu, P.-B. (2007). Measurement of the metastable zone width of phosphoric acid hemihydrate in the presence of impurity ions. *J. Chem. Eng. Data* 52: 1545–1547.

Guo, Z., Zhang, M., Li, H. et al. (2005). Effect of ultrasound on anti-solvent crystallization process. *J. Cryst. Growth* 273: 555–563.

Hamil, W.H., Williams, R.R., and MacKay, C. (1966). *Principles of Physical Chemistry*, 2e. Upper Saddle River: Prentice-Hall.

Holmbäck, X. and Rasmuson, A.C. (1999). Size and morphology of benzoic acid crystals produced by drowning-out crystallization. *J. Cryst. Growth* 198/199: 780–788.

Kashchiev, D. (2000). *Nucleation: Basic Theory with Applications*. Oxford: Butterworth-Heinemann.

Jim, J. and Kim, K.-J. (2012). Effect of supersaturation on polymorphs of clopidogrel hydrogen sulfate in browning-out crystallization. *Chem. Eng. Technol.* 35: 995–1002.

Kim, K.-J. and Kim, K.-M. (2001). Nucleation kinetics in spherulitic crystallization of explosive compound: 3-nitro-1,2,4-triazol-5-one. *Powder Technol.* 119: 109–116.

Kim, K.-J. and Mersmann, A. (2001). Estimation of metastable zone width in different nucleation processes. *Chem. Eng. Sci.* 56: 2315–2324.

Kitamura, M. and Sugimoto, M. (2003). Anti-solvent crystallization and transformation of thiazole-derivative polymorphs I. Effect of addition rate and initial concentration. *J. Cryst. Growth* 257: 177–184.

Knox, M., Trifkovic, M., and Rohani, S. (2009). Combining anti-solvent and cooling crystallization: effect of solvent composition on yield and metastable zone width. *Chem. Eng. Sci.* 64: 3555–3563.

Kubota, N. (2008). An interpretation of the metastable zone width concerning primary nucleation in anti-solvent crystallization. *J. Cryst. Growth* 310: 4647–4651.

Lide, D.R. (1996/1997). *Handbook of Chemistry and Physics*, 77e. Boca Raton, FL: CRC Press.

Lindenberg, C., Krättli, M., Cornel, J. et al. (2009). Design and optimization of a combined cooling/antisolvent crystallization process. *Cryst. Growth Des.* 9: 1124–1136.

Mersmann, A. (1990). Calculation of interfacial tensions. *J. Cryst. Growth* 102: 841–847.

Nielsen, A.E. and Söhnel, O. (1971). Interfacial tensions electrolyte crystal-aqueous solution, from nucleation data. *J. Cryst. Growth* 11: 233–242.

Nong, W.-J., Chen, X.-P., Wang, L.-L. et al. (2014). Measurement and correlation of solubility of abietic acid in ethanol + water mixtures. *J. Chem. Thermodyn.* 68: 199–204.

Nowee, S.M., Abbas, A., and Romagnoli, J.A. (2008). Antisolvent crystallization: model identification, experimental validation and dynamic simulation. *Chem. Eng. Sci.* 63: 5457–5467.

Nývlt, J. (1968). Kinetics of nucleation from solutions. *J. Cryst. Growth* 3/4: 377–383.

Nývlt, J., Söhnel, O., Matuchova, M., and Broul, M. (1985). *The Kinetics of Industrial Crystallization*. Prague: Academia.

O'Ciardha, C.T., Frawley, P.J., and Mitchel, N.A. (2011). Estimation of the nucleation kinetics for the anti-solvent crystallisation of paracetamol in metanol/water solutions. *J. Cryst. Growth* 328: 50–57.

O'Grady, D., Barret, M., Casey, E., and Glennon, B. (2007). The effect of mixing on the metastable zone width and nucleation kinetics in the anti-solvent crystallization of benzoic acid. *Chem. Eng. Res. Des.* 85: 945–952.

Ościk, J. (1982). *Adsorption*. Warsaw: PWN.

Park, M.-W. and Yeo, S.-D. (2012). Antisolvent crystallization of carbamazepine from organic solutions. *Chem. Eng. Res. Des.* 90: 2202–2208.

Saleemi, A.N., Rielly, D.D., and Nagy, Z.K. (2012). Monitoring of the combined cooling and antisolvent crystallisation of mixtures of aminobenzoic acid isomers using ATR-UV/vis spectroscopy and FBRM. *Chem. Eng. Sci.* 77: 122–129.

Sangwal, K. (1989). On the estimation of surface entropy factor, interfacial-tension, dissolution enthalpy and metastable zone-width for substances crystallizing from solution. *J. Cryst. Growth* 97: 393–405.

Sangwal, K. (2007). *Additives and Crystallization Processes: From Fundamentals to Applications*. Chichester: Wiley.

Sangwal, K. (2010). On the interpretation of metastable zone width in anti-solvent crystallization. *Cryst. Res. Technol.* 44: 909–919.

Sangwal, K. (2011). Recent developments in understanding of the metastable zone width of different solute–solvent systems. *J. Cryst. Growth* 318: 103–109.

Sangwal, K. (2017). On the light intensity transmitted through water and aqueous supersaturated ammonium dihydrogen phosphate solutions containing different antisolvents. *J. Cryst. Growth* 460: 67–77.

Sangwal, K. and Mielniczek-Brzóska, E. (2016a). Antisolvent crystallization of aqueous ammonium dihydrogen phosphate solutions by addition of acetone at different rates. *Cryst. Res. Technol.* 51: 475–490.

Sangwal, K. and Mielniczek-Brzóska, E. (2016b). Antisolvent crystallization of aqueous ammonium dihydrogen phosphate solutions by addition of methanol. *J. Cryst. Growth* 451: 139–149.

Sangwal, K. and Mielniczek-Brzóska, E. (2017). Effect of addition of different antisolvents on the crystallization of aqueous ammonium dihydrogen phosphate solutions. *Cryst. Res. Technol.* 52: 1600361.

Söhnel, O. (1982). Electrolyte crystal-aqueous solution interfacial tensions from crystallization data. *J. Cryst. Growth* 57: 101–108.

Söhnel, O. and Garside, J. (1992). *Precipitation: Basic Principles and Industrial Applications*. London: Butterworth-Heinemann.

Sun, Y.-Z., Song, X.-F., Wang, J. et al. (2009). Unseeded supersolubility of lithium carbonate: experimental measurement and simulation with mathematical models. *J. Cryst. Growth* 311: 4714–4719.

Trifkovic, M., Sheikhzadeh, M., and Rohani, S. (2009). Determination of metastable zone width for combined anti-solvent/cooling crystallization. *J. Cryst. Growth* 311: 3640–3650.

Wang, Z.-Z., Wang, J.-K., Zhang, M.-J., and Dang, L.-P. (2006). Solubility of erythromycin A dihydrate in different pure solvents and acetone + water binary mixtures between 293 K and 323 K. *J. Chem. Eng. Data* 51: 1062–1065.

Zhang, Y., Jiang, Y., Zhang, D. et al. (2015). Metastable zone width, crystal nucleation and growth kinetics measurement in anti-solvent crystallization of β-artemether in the mixture of ethanol and water. *Chem. Eng. Res. Des.* 95: 187–194.

Zhu, Y., Youssef, D., Porte, C. et al. (2003). Study of the solubility and the metastable zone of 1,3-dihydrozyacetone for the drowning-out process. *J. Cryst. Growth* 257: 370–377.

7

Induction Period for Crystallization

Crystallization of a solute from its saturated solution dissolved in a given solvent can be carried out by cooling it or by adding another solvent, usually called antisolvent, in which it has a solubility lower than that in the first solvent of the solution. This excess solute concentration created in the solution, which is related to supersaturation, leads to the formation of three-dimensional (3D) nucleation and their subsequent growth into larger, visible entities detectable by different techniques. Cooling of the solution at a known rate R_L and addition of antisolvent at a known rate R_A are the basis of determination of metastable zone width (MSZW) by polythermal and antisolvent crystallization, respectively. Figure 7.1 shows schematically these two types of MSZWs with reference to the solute solubility curve S in a solvent, whereas the values of the MSZW for cooling crystallization and antisolvent crystallization are indicated by supersolubility curves S^* and M^*, respectively. Note that, corresponding to the reference temperature T_c for crystallization, the supersolubility curve S^* during cooling crystallization is above the solubility curve S such that the equilibrium solubility $c_0 < c_{max}$, but the supersolubility curve M^* in the antisolvent mixture during antisolvent crystallization is below it such that $c_0 > c^A_{max}$.

As seen from Figure 7.1, a decrease in the temperature by ΔT from a saturation temperature T_0^* (where $\Delta T = T_0^* - T$ such that $T_0^* < T_0$) of concentration c (see Point D) results in an excess solute concentration $\Delta c = (c - c_0)$ created in cooling crystallization when T_c is taken as the reference temperature. Similarly, a certain value of the antisolvent content Δx in the solution of concentration c_0 saturated at temperature T_c to reduce the concentration down to c^A (see Point D^A) defines the excess solute concentration $\Delta c_A = (c_0 - c^A)$ created in antisolvent crystallization. These values of the excess solute concentrations Δc and Δc_A with respect to equilibrium concentrations c_0 and c^A, respectively, are measures of supersaturations ln S in the two methods. Different aspects of cooling and antisolvent crystallizations, including measurement and interpretation of MSZW by them, are presented in Chapters 5 and 6, respectively.

Nucleation and Crystal Growth: Metastability of Solutions and Melts, First Edition.
Keshra Sangwal.
© 2018 John Wiley & Sons, Inc. Published 2018 by John Wiley & Sons, Inc.

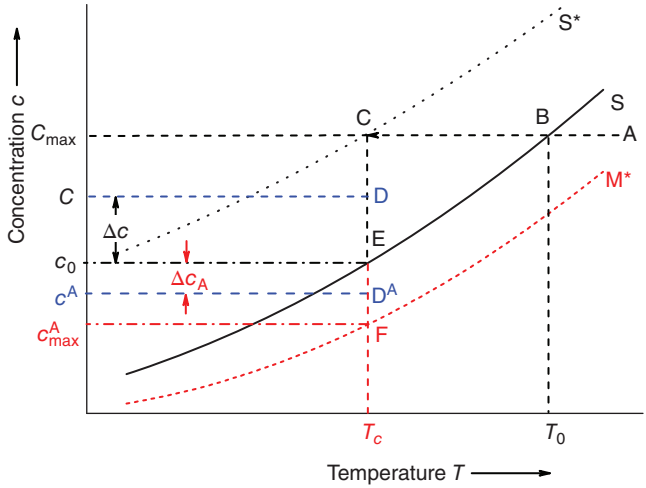

Figure 7.1 Schematic presentation of the creation of excess solute concentration by cooling of solution of initial concentration c_{max} below its saturation temperature T_0 down to T_c corresponding to equilibrium concentration c_0 and by addition of antisolvent at constant temperature T_c to the saturated solution of concentration c_0 down to c^A_{max} in the solution. Solubility and supersolubility curves for pure solvent S and solvent/antisolvent mixture M are denoted by S and S*, and M and M*, respectively.

In cooling and antisolvent crystallizations the creation of excess solute concentration, which defines supersaturation to describe these processes, begins as soon as cooling and antisolvent feeding are commenced at constant rates, and the supersaturation in the solution increases with the duration of solution cooling and antisolvent feeding. According to the classical theory for 3D nucleation the nucleation rate J depends on supersaturation $\ln S$ (see Eq. (2.27)). Therefore, the rate of nucleation becomes increasingly high with increasing supersaturation such that most of the 3D nuclei are formed in the vicinity of metastable zone boundary, which is always reached after some time t from the moment of beginning of cooling and antisolvent feeding. This duration t between the beginning of cooling or antisolvent feeding and the occurrence of spontaneous 3D nucleation in the solution is the induction period t_{in} for nucleation in these two methods. The threshold value of supersaturation $\ln S_{max}$ when intense 3D nucleation occurs in the supersaturated solution is related to the maximum temperature difference ΔT_{max} and the maximum antisolvent content Δx_{max} in the solution corresponding to the crystallization temperature T_c (see Figure 7.1).

Supersaturation $\ln S$ for the formation of 3D nuclei and their subsequent growth can also be created by rapidly cooling the solution to a predefined temperature T to obtain a temperature difference ΔT ($\Delta T < \Delta T_{max}$) in the

polythermal method and by rapidly mixing a known amount of the antisolvent with the saturated solution to obtain antisolvent content Δx ($\Delta x < \Delta x_{max}$) in the solution in antisolvent crystallization, and then determine the time, called the induction period or induction time t_{in}, required for the formation of detectable crystallites. The latter method is also known as drowning-out crystallization. Since crystallization in this latter method is carried out at a predefined temperature, the induction period is usually referred to occur isothermally. This time is an experimentally measurable quantity and is a measure of the ability of the system to remain in the metastable state. The induction time t_{in} is usually measured by visual observation of appearance of first nuclei in the solution and by recording changes in the solution properties, such as turbidity, conductivity, refractive index, density, and ultrasound velocity, over a period of time. Many studies show that one or a few crystallites frequently appear in the solution before noticeable changes in the solution properties. It has also been observed that the value of induction period for a given system is affected, among others, by the level of supersaturation, the temperature, the stirring rate, the presence of impurities, and the viscosity of the system.

The present chapter gives an overview of different aspects of the induction period for crystallization carried out at predefined supersaturation created in the system at the crystallization temperature T_c (isothermal crystallization), at increasing supersaturation attained in the system by continuous addition of antisolvent (antisolvent crystallization), and at increasing supersaturations achieved by cooling the system from saturation temperature T (nonisothermal crystallization). In view of similarity in the basic concepts and equations of induction period for crystallization from supersaturated solutions and supercooled melts, the theoretical relationships of the induction period t_{in} are presented in terms of the chemical potential difference $\Delta\mu$.

7.1 Theoretical Background

The concept of induction period assumes ideal steady-state conditions such that 3D nucleation occurs immediately when the supersaturation is achieved in the system. However, its value is composed of three parts (see Eq. (4.53)): (i) the time t_{reorg} required to attain a uniform distribution of molecular clusters by diffusion of monomers in the solution volume, (ii) the time t_N required by these molecular clusters to evolve into stable 3D nuclei, and (iii) the time t_g required for the subsequent growth of the stable nuclei to observable size. For the analysis of the induction period data, it is usually assumed that t_N is the largest but it may not be so in some cases. For example, excessively long t_{reorg} caused by sluggish diffusion in a viscous system may entirely suppress nucleation and the system acquires glassy state. However, it is easy to verify that $t_g \ll t_N$. The situation in the case of 3D nucleation from melts is also similar.

7.1.1 Theoretical Interpretation of Induction Period

As described in Section 3.9, crystallization of a solid phase in the mother phase is possible by mononuclear (MN) and polynuclear (PN) mechanisms. These two mechanisms describe two extreme cases of formation of detectable nuclei. According to these mechanisms, crystallization always occurs after a time lag τ given by Eqs. (3.59) and (3.60). In Section 4.1, this time lag τ was defined by extrapolating a linear part of the plot of overall crystallization y of a closed system of fixed volume of crystallizing solute as a function of crystallization time t when the overall crystallization y approaches zero. As shown in Figure 4.7, this time lag τ lies between the so-called induction period t_{in} when overall crystallization curve leaves the crystallization time axis and the final period t_f, referred to as the average crystallization duration t_{av} in Section 3.9, when the overall crystallization is complete, i.e. $t_{in} < \tau < t_f$; see Figure 5.2. The fact that $t_{in} < \tau$ is associated with the fact that, strictly speaking, t_{in} represents the time period required for the onset of 3D nucleation, whereas time lag τ comprises a time period t_{in} for the occurrence of 3D nucleation and an addition time for the formation of more 3D nuclei and growth of all nuclei formed until the linear crystallization rate $R = \Delta y/\Delta t$ is reached. This is the amount y^* of crystallites detectable by a technique and is related to the mean duration t_{av} for the overall crystallization and the time constant Θ.

Following Kashchiev (2000), by combining the values of the time constant Θ from Eqs. (3.79) and (3.86) for stationary nucleation according to the MN and PN mechanisms, the induction period t_{in} may be represented by the single expression:

$$t_{in} = t_{MN} + t_{PN} = \frac{1}{J_s V} + \left(\frac{q y^*}{\kappa J_s R_g^{q-1}} \right)^{1/q}, \tag{7.1}$$

where y^* is the smallest experimentally detectable fraction of overall crystallization, κ is the shape factor ($\kappa = 16\pi/3$ for a spherical nucleus), V is the volume of the parent phase, the exponent $q = 1 + \nu d$, the growth rate R of the growing crystallites is related to the available driving force $\Delta\mu/k_B T_c$ by: $R = R_g(\Delta\mu/k_B T_c)^n$, with the exponent n lying between 1 and 2 and R_g as the growth rate constant (see Section 3.6), and the rate of stationary nucleation J_s is given by (see Eq. (2.27))

$$J_s = J_0 \exp\left(- \frac{B}{(\Delta\mu/k_B T_c)^2} \right), \tag{7.2}$$

with the thermodynamic constant

$$B = \kappa \left(\frac{\gamma \Omega^{2/3}}{k_B T_c} \right)^3. \tag{7.3}$$

In Eq. (7.1), the definition of induction time t_{in} includes the additional period for the growth of nuclei into a detectable entity. In the above equations, γ is the solid–liquid interfacial energy, Ω is the molecular volume ($\Omega \approx a^3$, with a as the size of the molecule or atom/ion), k_B is the Boltzmann constant, T_c is the temperature of crystallization, and the chemical potential difference $\Delta\mu/k_BT_c$ for crystallization from the melt and supersaturated solution is given by

$$\frac{\Delta\mu}{k_BT_c} = \lambda_m \frac{\Delta T}{T_c}, \tag{7.4}$$

$$\frac{\Delta\mu}{k_BT_c} = \lambda_s \frac{\Delta T}{T_c} = \ln S, \tag{7.5}$$

with the dimensionless heat of melting and solution, denoted as λ_m and λ_s, respectively, given by

$$\lambda_m = \frac{\Delta H_m}{k_BT_m}, \quad \lambda_s = \frac{\Delta H_s}{k_BT_s}. \tag{7.6}$$

In the above equations, ΔH_m is the enthalpy of melting of the solute, ΔH_s is the enthalpy of solution of the solute, T_m is the melting point of the solute, the temperature difference $\Delta T = T_m - T_c$ during cooling of melt from T_m, $\Delta T = T_s - T_c$ during cooling of solution from the saturation temperature T_s, and S is the supersaturation ratio ($S = c/c_c$, with c_c as the concentration at the crystallization temperature and c as the initial concentration; $c/c_c > 1$).

When

$$V < \left[\frac{\kappa}{qy}\left(\frac{R_g}{J_s}\right)^{q-1}\right]^{1/q}, \tag{7.7}$$

the MN mechanism holds, which applies to supersaturated phases involving sufficiently small volumes. Then

$$t_{in} = t_{MN} = \frac{1}{J_0V}\exp\left(\frac{B}{\lambda^2(\Delta T/T_c)^2}\right), \tag{7.8}$$

where J_0 is the kinetic factor related to the attachment of monomers to the nucleus and λ denotes both λ_m and λ_s given by Eq. (7.6). In the other case involving a large volume, the PN mechanism is applicable. Then

$$t_{in} = t_{PN} = \left(\frac{qy^*}{\kappa J_0 R_g^{q-1}}\right)^{1/q}\exp\left(\frac{B}{q\lambda^2(\Delta T/T_c)^2}\right). \tag{7.9}$$

Upon taking logarithm on both sides, the above equations may be expressed in the form:

$$\ln t_{\text{in}} = -\ln(J_0 V) + \frac{B}{\lambda^2 (\Delta T/T_c)^2}, \tag{7.10}$$

$$\ln t_{\text{in}} = \frac{1}{q} \ln\left(\frac{qy^*}{\kappa J_0 (R_g J_0)^{q-1}}\right) + \frac{B}{q\lambda^2 (\Delta T/T_c)^2}. \tag{7.11}$$

It may be noted that Eq. (7.9) reduces to Eq. (7.8) of the MN mechanism when $q = 1$. Then $y^* = 1$ and $\kappa = V$. According to these dependencies, the plots of $\ln t_{\text{in}}$ against $(\Delta T/T_c)^{-2}$ are straight lines with slopes B/λ^2 and $B/q\lambda^2$, respectively. One may also analyze the experimental $t_{\text{in}}(\Delta T)$ data from plots of $\ln t_{\text{in}}$ against $1/T_c(\Delta T)^2$ with slope $B' = BT_c^3/\lambda^2$ and $B' = BT_c^3/q\lambda^2$, respectively.

When the atomistic model of nucleation applies (see Chapter 2), from Eq. (2.35), one obtains

$$\ln t_{\text{in}} = \left[-\ln J_0 + \frac{\Phi^*}{k_B T}\right] - i^* \lambda \left(\frac{\Delta T}{T_c}\right). \tag{7.12}$$

A plot of $\ln t_{\text{in}}$ against $\Delta T/T_c$ gives a slope equal to $i^*\lambda$ from which one can obtain the number i^* of molecules in the critical nucleus.

From the experimental data on the induction period t_{in} for nucleation as a function of relative supersaturation $\ln S$ or temperature difference ΔT for systems with or without an additive, one can verify the validity of the above models. These equations apply to both 3D homogeneous and heterogeneous nucleations. However, it should be noted that the value of the interfacial energy γ predicted by Eq. (7.11) of the PN model depends on the value of q, and increases as $q^{1/3}$. If the dimensionality d of the nuclei is ignored (i.e. when $d = 0$ such that $q = 1$), Eq. (7.11) takes the same form of the dependence following from the inverse relationship between nucleation rate J and t_{in}. Equation (7.11) then represents the traditional Fisher–Turnbull relationship given by Eq. (7.1), where $t_{\text{in}} \propto 1/J$.

It may be noted that the induction period t_{in} in the PN mechanism is related to both the nucleation rate J and the linear growth rate R_g (see Eq. (7.9)), and may be given by

$$t_{\text{in}} = \left(\frac{qy^*}{\kappa J R_g^{q-1}}\right)^{1/q}. \tag{7.13}$$

According to this relation, when the growth rate R_g and the exponent q are constant for the growing crystallites, $t_{\text{in}} \propto 1/J^{1/q}$.

There are many studies where experimental data of induction period t_{in} as a function of supersaturation $\ln S$ (where $\ln S = \lambda \Delta T/T_c$; see Eq. (7.5)) have been analyzed using the above inverse relationship between induction period t_{in} and

3D nucleation rate J. It is known (Roelands et al., 2006) that this relationship between J and t_{in} indeed holds in the case of rapidly decreasing supersaturation due to the growth of N_p nuclei (m^{-3}) over the length of a tube reactor divided by the half-life t_t for which the solution is depleted (i.e. $S/S_0 = 1$). From the estimated growth rate, the half-life t_t is approximated as the induction period t_{in} (s) and the time when the nucleation rate becomes negligible is $t_{in}/3$, resulting in the definition of nucleation rate as $J = 3N_p/t_{in}$. When desupersaturation proceeds slowly, the supersaturation is approximately constant over the length of the tube, the density of nuclei N present in the solution is related to the residence time t_r (s), and the nucleation rate J by $J = N/t_r$. Since t_r is related to t_{in}, the relationship $J \propto 1/t_{in}$ applies here as well.

The nucleation may be homogeneous as well as heterogeneous, depending on the value of relative supersaturation $\ln S$ or temperature difference ΔT for systems as well as solvent/melt composition. In heterogeneous nucleation, the induction period corresponding to a given value of relative supersaturation $\ln S$ or temperature difference ΔT of a system is reduced due to a decrease in the interfacial energy as well as kinetics of attachment of growth entities (see Eq. (2.40)).

7.1.2 Some Other Relations

As mentioned above, the induction period can be measured in different situations. The commonly used procedure is to create a known supersaturation as quick as possible at a particular temperature followed by observation of the initial stages of formation of 3D nuclei and visible crystallites. The desired supersaturation can be achieved by abrupt cooling of saturated solution as well as by mixing the saturated solution with a known amount of some antisolvent. The above equations describe this situation. In the case of addition of an antisolvent, the level of supersaturation is related to the antisolvent content in the solution volume and may be given by (see Eq. (6.34))

$$\ln S \approx \frac{\Delta c}{c_2} = a_2 \Delta x, \tag{7.14}$$

where Δc is the excess solute concentration created by antisolvent addition, c_2 is the solubility of the solute in the solvent–antisolvent mixture of antisolvent content, and the constant a_2 is defined as

$$a_2 = \frac{\Delta H_{sS} - \Delta H_{sA}}{R_G T}, \tag{7.15}$$

where ΔH_s is the heat of solution and the subscripts S and A denote solvent S and antisolvent A, respectively. Induction period data for such systems may be analyzed using Eqs. (7.8), (7.9), and (7.12) described above with the

values of directly calculated concentrations in the solvent and solvent–antisolvent mixture or antisolvent content Δx.

Supersaturation $\ln S$ can also be created by adding an antisolvent to the saturated solution at a particular temperature or by cooling the saturated solution by cooling it from the saturation temperature T_s to the moment of abrupt crystallization, which defines the MSZW characterized by the maximum antisolvent volume $V_{a(max)}$ added to the solution of volume V_s during antisolvent crystallization and the maximum temperature difference ΔT_{max} during cooling crystallization. In these cases the induction period is defined in terms of antisolvent feeding rate R_A and cooling rate R_L according to the relations:

$$t_{in} = \frac{V_{a(max)}(R_A)}{R_A}, \quad \text{antisolvent crystallization}, \tag{7.16}$$

$$t_{in} = \frac{\Delta T_{max}(R_L)}{R_L}, \quad \text{cooling crystallization}, \tag{7.17}$$

where the added antisolvent volume V_a is related to the dimensionless antisolvent content Δx by (see Section 6.3.5).

$$\Delta x = \frac{V_a}{V_s + V_a}, \tag{7.18}$$

where the antisolvent volume $V_a = R_A \Delta t$ is added to the solution volume V_s. In Eqs. (7.16) and (7.17), we have denoted V_a and ΔT_{max} as functions of R_A and R_L because in these experiments from a given equilibrium concentration c_0 and temperature T_0, the values of $V_{a(max)}$ and ΔT_{max} are affected by R_A and R_L, respectively. Then analysis of the data may be carried out using Eq. (7.2) of the classical nucleation (CN) theory and the assumed inverse relationship between t_{in} and J. This approach has been used in studies of cooling crystallization (Kim and Kim, 2001; Kim and Mersman, 2001).

Starting from the first description of MSZW for cooling crystallization by Nývlt (1968), several theoretical approaches of MSZW for cooling and antisolvent crystallizations are based on the assumption that 3D nucleation rate J is related to excess solute concentration Δc developed in the solution during cooling and antisolvent feeding according to the power law (PL), given by

$$J = K(\ln S)^m, \tag{7.19}$$

where K and m are constants, and the supersaturation $\ln S$ is related to the temperature difference ΔT by Eqs. (7.4) and (7.5) and to the antisolvent content Δx by Eq. (7.14). The assumed inverse relation between J and t_{in} can also be used for the analysis of the $t_{in}(\ln S)$ data for different systems.

According to Eq. (7.17), the induction period t_{in} is related to the MSZW. The lower the MSZW for a solute–solvent system, the lower is the induction period t_{in}. For comparable values of R_L for different solute–solvent systems of different

MSZWs, one also expects that t_{in} increases with the MSZW of the system. Gharsallaoui et al. (2008) indeed observed this trend in the case of saturated aqueous solutions of three disaccharides: Sucrose, maltitol, and trehalose. These authors explained their observation from a consideration of the physico-chemical properties of disaccharide saturated solutions and argued that the trend is associated with the sugar chemical structure and molecular mobility due to the number of unbound hydroxyl groups.

7.1.3 Basic Equations

Different equations of nucleation rate J relating driving force $\Delta\mu/k_B T_c$ expressed by $\ln S$, $\Delta T/T_c$, and Δx, based on three approaches: (i) CN theory, (ii) atomistic theory (AT), and (iii) empirical PL, given above, may be expressed as the following linear relationships:

$$\ln t_{in} = I_{CN} + \frac{B}{\lambda^2 (\Delta T/T_c)^2}, \quad \text{classical nucleation (CN) theory,} \tag{7.20}$$

$$\ln t_{in} = I_{AT} - i^* \lambda \left(\frac{\Delta T}{T_c}\right), \quad \text{atomistic (AT) theory,} \tag{7.21}$$

$$\ln t_{in} = I_{PL} - m \left(\frac{\Delta T}{T_c}\right), \quad \text{power-law (PL) relation,} \tag{7.22}$$

where $\Delta T/T_c$ is related to supersaturation $\ln S$ of the solution and antisolvent content Δx in the solution by Eqs. (7.5) and (7.14), and λ denotes heat of solution or melting, depending on whether crystallization is carried out from solutions or melts. All of the above equations predict linear dependence with an intercept, denoted above by I with the subscript CN, AT, and PL referring to CN theory, AT, and power-law relation, respectively, and a slope of values equal to B/λ^2, $i^*\lambda$ and m.

Experimental data of induction period t_{in} as a function of driving force observed for different systems involving solutions and melts are presented and discussed below according to the above relationships using some specific examples.

7.2 Induction Period for Isothermal Crystallization

7.2.1 Crystallization from Solutions

Figure 7.2a and b shows the experimental data of induction period t_{in} as a function of supersaturation $\ln S$ for aqueous sodium perborate solutions at 18 °C in the form of plots of $\ln t_{in}$ against $(\ln S)^{-2}$ and $\ln S$ according to CN and AT theories, respectively, with the corresponding best-fit values of

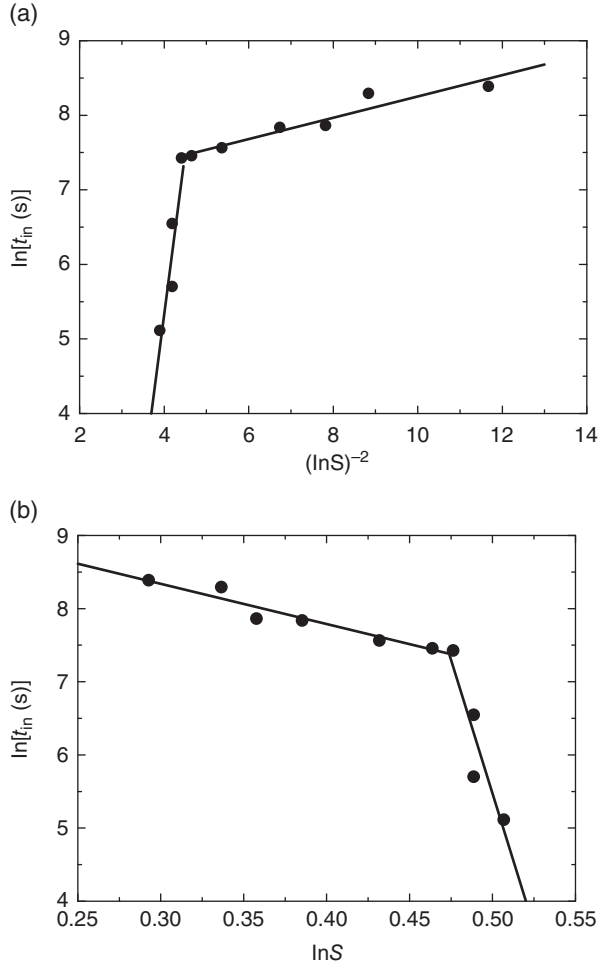

Figure 7.2 Plots of data of induction period t_{in} as a function of supersaturation S for sodium perborate from aqueous solutions according to different models: (a) ln t_{in} against $(\ln S)^{-2}$ (CNT) and (b) ln t_{in} against ln S (AT.). *Source:* Original data from Dugua and Simon (1978).

intercepts I_{CN} and I_{AT} and slopes B and i^* listed in Table 7.1. As seen from the figure, in both cases the linear dependence, with essentially the same correlation coefficient R^2, follows below and above a transition value of supersaturation ln S equal to about 0.47. With a value of $\lambda \approx 7$, one may calculate the values of interfacial energy γ and i^* in the range of low and high supersaturation. From Table 7.1, it follows that the number i^* of molecules constituting the critically-sized nuclei is about 1 and 10 and that the value of the interfacial

Table 7.1 Constants of Eqs. (7.20) and (7.21) for aqueous sodium perborate solutions.[a]

	Eq. (7.20)				Eq. (7.21)			
ln *S* range	I_{CN}	B/λ^2	γ (mJ·m^{-2})	R^2	I_{AT}	$i^*\lambda$	i^*	R^2
<0.47	7.395	0.117	0.6	0.8891	9.985	5.488	1	0.9248
>0.47	11.363	4.329	22.0	0.7753	42.11	73.28	10	0.7585

[a] R^2 fit of the data.

energy γ at low supersaturations is very low, but it is similar to the values for different compounds soluble in water at high supersaturations. These differences in the values of i^* and γ at low and high supersaturations are associated with a transition of heterogeneous nucleation occurring at low supersaturations ln S to homogeneous nucleation at high ln S (see Eq. (2.38)). However, the value of i^* equal to about 1 and 10 at low and high ln S are very low and suggests that for these sizes of the critically-sized nuclei the concept of interfacial energy is only formal.

Figure 7.3a shows another example of the plots of $\ln t_{in}$ against $(\ln S)^{-2}$ according to Eq. (7.20) for dexamethasone sodium phosphate in aqueous solutions containing different acetone contents. It may be seen that the slope of the plot increases steeply with an increase in the acetone content. As in the case of Figure 7.2a for aqueous sodium perborate solutions, the slope is smaller for $(\ln S)^{-2} > 1$ (i.e. $S > 1$) than for $(\ln S)^{-2} < 1$, implying that at low supersaturations nucleation is probably predominantly heterogeneous in comparison with that at $S > 1$. This is due to an increase in the interfacial energy γ with increasing acetone content, and is directly connected with the solubility of the compound in the solution (see Section 2.3). Figure 7.3b shows the dependence of the experimentally determined γ for dexamethasone sodium phosphate from aqueous solutions on acetone content. In the figure are also shown two values of γ obtained for $(\ln S)^{-2} < 1$ and $(\ln S)^{-2} > 1$ in the case of solvent containing 68.8% acetone. In the two supersaturation intervals, the experimentally determined values of γ differ by about 40%, the higher value corresponding to the high supersaturation interval. However, at both low and high supersaturations, these values of γ are lower than those predicted by Mersmann's relation (Mersmann, 1990) for $(\ln S)^{-2} > 1$ (i.e. $S > 1$) than that for $(\ln S)^{-2} < 1$, implying that at low supersaturations, nucleation is probably heterogeneous predominantly in comparison with the nucleation at $S > 1$.

Roelands et al. (2006) carried out an analysis of experimentally determined 3D nucleation rates on different ionic and molecular precipitating compounds to derive the probable nucleation mechanism and compare with the theoretically expected mechanism. The authors concluded that the measurements indicated

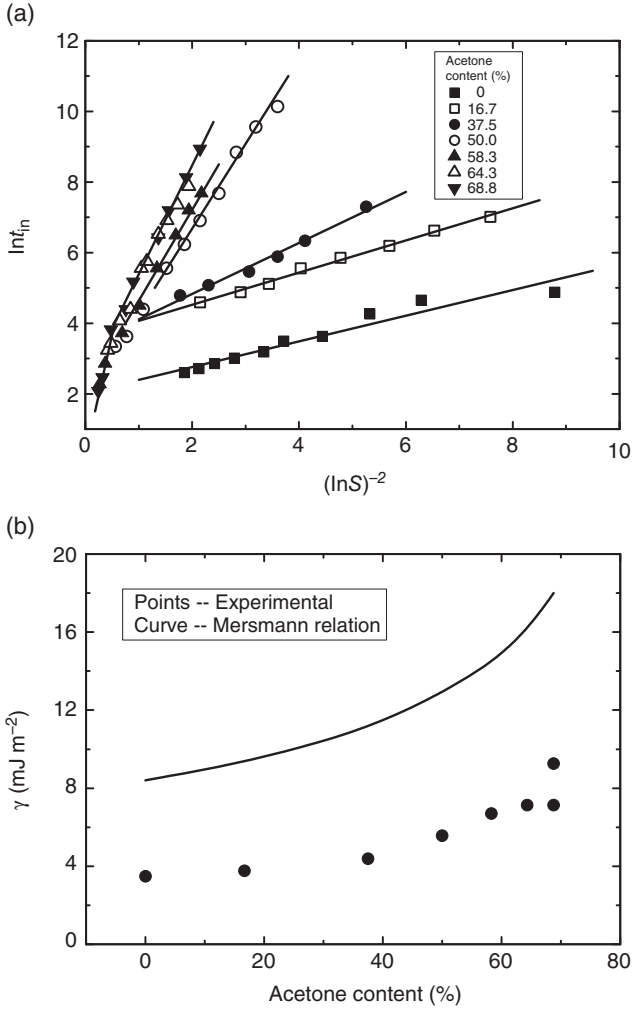

Figure 7.3 (a) Plots of ln t_{in} against $(\ln S)^{-2}$ according to Eq. (7.5) for dexamethasone sodium phosphate in aqueous solutions containing different acetone contents. Note that for $(\ln S)^{-2} < 1$ the slope is higher than that for $(\ln S)^{-2} > 1$. (b) Dependence of interfacial energy γ on acetone content. Note that γ increases with an increase in acetone content. *Source:* Original data from Hao et al. (2005).

the homogeneous nucleation mechanism only for two ionic compounds, barium sulfate and boehmite, and the heterogeneous nucleation mechanism was likely for all molecular compounds. The authors attributed the difference between the experimentally observed and theoretically predicted mechanism

to the use of less suitable experimental methods and techniques as well as to secondary processes, such as agglomeration and phase transformation, occurring in the precipitated suspension.

As mentioned above, 3D nucleation rate J is related to induction period t_{in} and residence time t_r in an experimental setup; the experimental data, summarized by Roelands et al. (2006) from different studies, of the dependence of nucleation rate J of barium sulfate on the applied supersaturation ln S are presented, as an example, in the form of plots of $-\ln J$ against $(\ln S)^{-2}$ in Figure 7.4. The dotted line represents the theoretically predicted dependence for homogeneous nucleation with $J_0 = 10^{35}\ m^{-2}{\cdot}s^{-1}$ and slope $B = 6000$ (cf. Roelands et al., 2006), whereas the solid line covering most of the data of Nielsen and Mohanty in the high ln S range is drawn with a lower $J_0 = 3.4{\cdot}10^{29}\ m^{-2}{\cdot}s^{-1}$ but with the same slope. The data obtained both by Nielsen and Angerhöfer show a change in the slope indicating a change in the nucleation mechanism at $(\ln S)^{-2} \approx 0.006$ (i.e. ln $S \approx 13$) from heterogeneous to homogeneous with increasing supersaturation, but the transition occurs at higher nucleation rate J (lower induction period) in the measurements made by Nielsen than those by Angerhöfer. In the low ln S range corresponding to heterogeneous nucleation, the slope $B \approx 180$ is for measurements both by Nielsen and Angerhöfer. The calculated values of the interfacial energy γ corresponding to homogeneous and heterogeneous nucleation in the range of low and high ln S are 180 and 5 $mJ{\cdot}m^{-2}$, respectively.

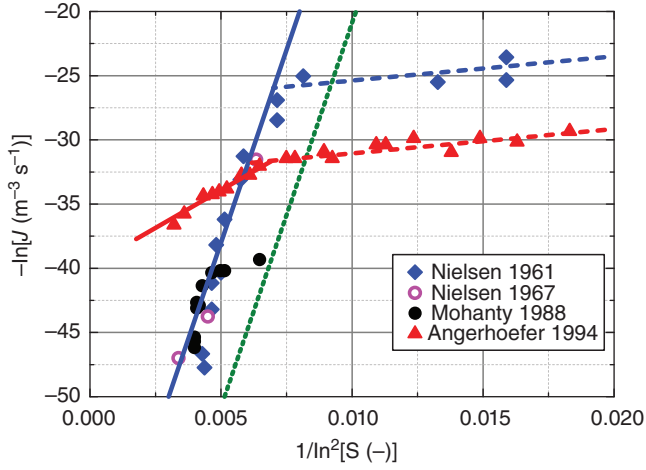

Figure 7.4 Experimental data of $-\ln J$ against $(\ln S)^{-2}$ for the nucleation of barium sulfate. Dotted line represents the theoretically predicted dependence with $J_0 = 10^{35}\ m^{-2}{\cdot}s^{-1}$ and parameter $B = 6000$, whereas solid line covering most of the data by Nielsen and Mohanty is drawn with a lower $J_0 = 10^{30}\ m^{-2}{\cdot}s^{-1}$. In the low ln S range corresponding to heterogeneous nucleation, dashed lines are drawn with slope $B \approx 180$ for data by Nielsen and Angerhöfer. *Source:* Original data from Roelands et al. (2006).

It may be noted that, although the measurements were made in the same supersaturation range, in the high $\ln S$ range the nucleation rates measured by Nielsen and Mohanty are much higher than those obtained by Angerhöfer. In this $\ln S$ range, the slope B of the plot for measurements by Angerhöfer is about 1200 in contrast to 6000 for the data of Nielsen and Mohanty. This lower slope is associated with a decrease in the measured nucleation rate by the agglomeration of nanocrystallites followed by recrystallization in the solution (Roelands et al., 2006). The estimated value of γ from Angerhöfer's data is about 36 $mJ \cdot m^{-2}$. This value is certainly too low.

It should be mentioned here that estimation of interfacial energy γ from the dependence of induction period t_{in} on supersaturation $\ln S$ using the above approach based on the CN theory may be misleading when two or more phases are crystallized under certain experimental conditions. For example, Jim and Kim (2012) investigated the crystallization of metastable I and stable II phase of clopidogrel hydrogen sulfate in drowning-out crystallization from mixtures of formic acid and isopropyl alcohol using polymorph I seeds. The authors observed that the induction period t_{in} for the crystallization of form I is lower than that of form II at the same ln S levels. In contrast to a lower value of γ for the occurrence of metastable form I than that for stable form II, analysis of the experimental $t_{in}(\ln S)$ data gave the values of γ equal to 1.17 and 0.42 $mJ \cdot m^{-2}$ for metastable I and stable II forms, respectively. The value of γ for the stable form II is indeed very low. The possible reasons of this low value are heterogeneous nucleation of phase II and solution-mediated transformation of the metastable phase I.

Finally, it should be noted that, once the value of the interfacial energy γ for a solute–solvent system is known from the experimental $t_{in}(\ln S)$ data, one can calculate the radius r^*_{3D} of 3D stable nucleus and the activation energy ΔG^*_{3D} for 3D nucleation using equations given in Chapter 2 for different values of $\ln S$ applied for measurements of the induction period t_{in}. However, such calculations do not provide any insight into the nucleation process.

7.2.2 Crystallization from the Melt

Here, some features of the dependence of induction period t_{in} on ΔT are described using examples of different polymorphs of tripalmitoylglycerol (PPP) and cocoa butter (CB). The data on the measurement of induction period t_{in} for different polymorphs of PPP were made by Sato and Kuroda (1987) as the time when the occurrence of a crystal was detected optically after attaining a predefined temperature T_c of the melt during isothermal crystallization between 35 and 65 °C. These authors reported that t_{in} is the shortest for the α form, intermediate for the β′ form, and the longest for the β form. The data on t_{in} as a function of crystallization temperature T_c in the range between 19 and 23 °C for the α and β′ polymorphs of CB were reported by Foubert et al. (2005). These $t_{in}(T_c)$ data were obtained by analysis of the isothermal crystallization kinetics using the model of Foubert et al. (2003); see Section 4.2. The reported

melting point T_m of CB is 36 °C, whereas the starting CB materials for the crystallization of the β′ polymorphs were from two different sources and are indicated as CB-A and CB-B. In both cases, supercooling $\Delta T = T_m - T_c$ was calculated by taking into account their corresponding T_m.

Figure 7.5a shows the experimental $t_{in}(T_c)$ data on the crystallization of different PPP polymorphs, reported by Sato and Kuroda (1987), in the form of plots of $\ln t_{in}$ on $1/T_c(\Delta T)^2$, with slope $B' = BT_c^3/\lambda_m^2$, according to Eq. (7.20)

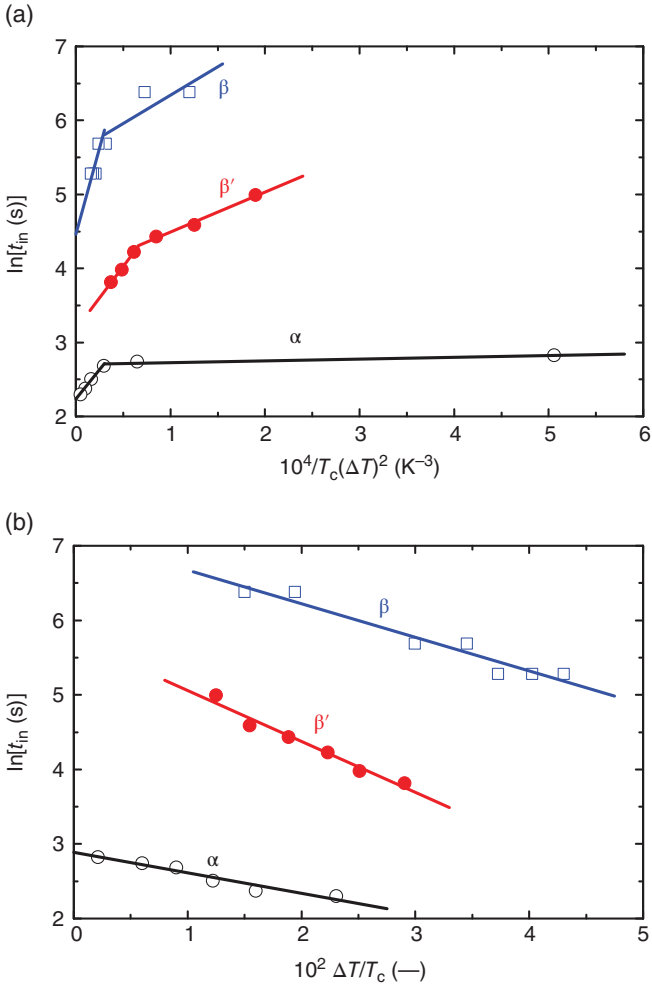

Figure 7.5 Experimental $t_{in}(T_c)$ data for different polymorphs of PPP plotted as dependences of: (a) ln t_{in} on $1/T_c(\Delta T)^2$, with slope $B' = BT_c^3/\lambda_m^2$, according to Eq. (7.20) of classical nucleation theory and (b) ln t_i on $\Delta T/T_c$ according to Eq. (7.21) of atomistic theory. *Source:* Original data from Sato and Kuroda (1987).

based on the CN theory. While plotting the data, the melting points T_m of α, β′, and β forms, as read off from the plots of original $t_{in}(T_c)$ data reported by Sato and Kuroda (1987), were taken as 44, 53, and 64 °C, respectively. It may be seen that the plots for all of the three polymorphs can be represented by two straight lines with transitions values of $1/T_c(\Delta T)^2$ corresponding to T_c equal to about 42, 53, and 55 °C for the α, β′, and β forms, respectively. Figure 7.5b presents the above experimental $t_{in}(T)$ data as plots of ln t_{in} against $\Delta T/T_c$, according to Eq. (7.21) based on the AT. Here, there are linear dependencies of the ln $t_{in}(\Delta T)$ data in the entire range of $\Delta T/T_c$ for different polymorphs.

Figure 7.6a and b shows another example of plots of ln t_{in} against $1/T_c(\Delta T)^2$ for the $t_{in}(T_c)$ data for the α and β′ polymorphs of CB according to Eq. (7.20) of

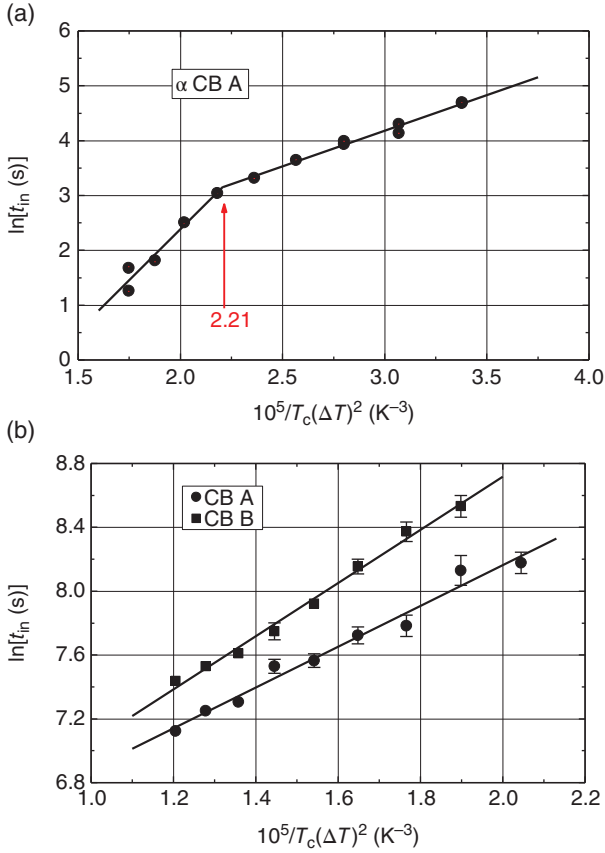

Figure 7.6 Plots of ln t_{in} against $1/T_c(\Delta T)^2$ for the $t_{in}(T_c)$ data for (a) α and (b) β′ polymorphs of cocoa butter according to Eq. (7.20). Note that there are two different slopes B' for the data in (a). *Source:* Original data from Foubert et al. (2005).

the CN theory. In the calculations of supercooling $\Delta T = T - T_m$, $T_m = 36\ ^\circ C$, as reported by Foubert et al. (2005), was taken. It may be seen from the plots that the data in the entire investigated temperature interval for the two polymorphs follow different trends. The plots of $\ln t_{in}$ against $1/T_c(\Delta T)^2$ for the β′ form of two different samples CB-A and CB-B exhibit linear dependences in the entire T_c range. In contrast to the β′ form, the slope of the plot of the data of $\ln t_{in}$ against $1/T_c(\Delta T)^2$ for the α form consists of at least two parts below and above $1/T_c(\Delta T)^2$ equal to $2.21 \cdot 10^{-5}\ K^{-3}$. This transition temperature corresponds to $T_c = 293.5$ K.

It should be mentioned that two different linear regions of different slopes in the plots of $\ln t_{in}$ against $1/T_c(\Delta T)^2$ for the $t_{in}(T_c)$ data from melts and $\ln t_{in}$ against $1/\ln^2 S$ from solutions are frequently encountered in isothermal crystallization of a variety of compounds. This difference is associated with different types of nucleation occurring at low and high driving force as defined by ΔT or $\ln S$, and the transition occurring at particular values of the driving force. A lower slope of the plot of $\ln t_{in}$ against $1/T_c(\Delta T)^2$ or $1/\ln^2 S$ above the transition value of the driving force than a higher slope of the plot below this transition value of the driving force implies that nucleation is heterogeneous predominantly at low driving force ΔT in comparison with that at high ΔT when homogeneous nucleation occurs. The trends of the $\ln t_{in}[1/T_c(\Delta T)^2]$ plots of Figures 7.5 and 7.6 suggest that heterogeneous and homogeneous nucleation mechanisms occur during the crystallization of the three polymorphs of PPP and the α form of CB in the range of small and high supercooling ΔT, respectively. The occurrence of heterogeneous nucleation at low values of the driving force is associated with a decrease in the interfacial energy γ of a solute–solvent system due to the presence of impurities inherently present in them.

It is of interest to note from Figure 7.6 that for CB polymorphs the slopes of the plots of $\ln t_{in}$ against $1/T_c(\Delta T)^2$ in the region of high $1/T_c(\Delta T)^2$ (i.e. at $T_c <$ 293.5 °C corresponding to low driving force) for the α form and in the entire range of $1/T_c(\Delta T)^2$ for the β′ form of different two samples are comparable. This means that the values of the interfacial tension γ in these cases are comparable and the nucleation is mainly heterogeneous in the three cases.

The linear dependencies of the plots of $\ln t_{in}$ against $\Delta T/T_c$ in Figure 7.5b according to Eq. (7.21) based on the atomistic theory in the entire range of $\Delta T/T_c$ for the different polymorphs of PPP suggest that the AT of nucleation is applicable. The slopes of the plots are 27.5, 68.4, and 45.1 for the α, β′,and β forms, respectively. Since the slope is equal to $i^*\lambda$, the molecules in the critical nucleus i^* are about 4, 10, and 7 for the α, β′, and β forms, respectively, for a typical value of dimensionless melting enthalpy $\lambda = 6$. A small number of molecules in the critical nuclei is indeed expected according to the AT.

The data of Figure 7.6a and b for CB polymorphs were also examined using Eq. (7.21) based on the AT. Figure 7.7a and b shows that the plots of $\ln t_{in}$ against $\Delta T/T_c$ for the sample of α form and the two samples of the β′ form. It may be

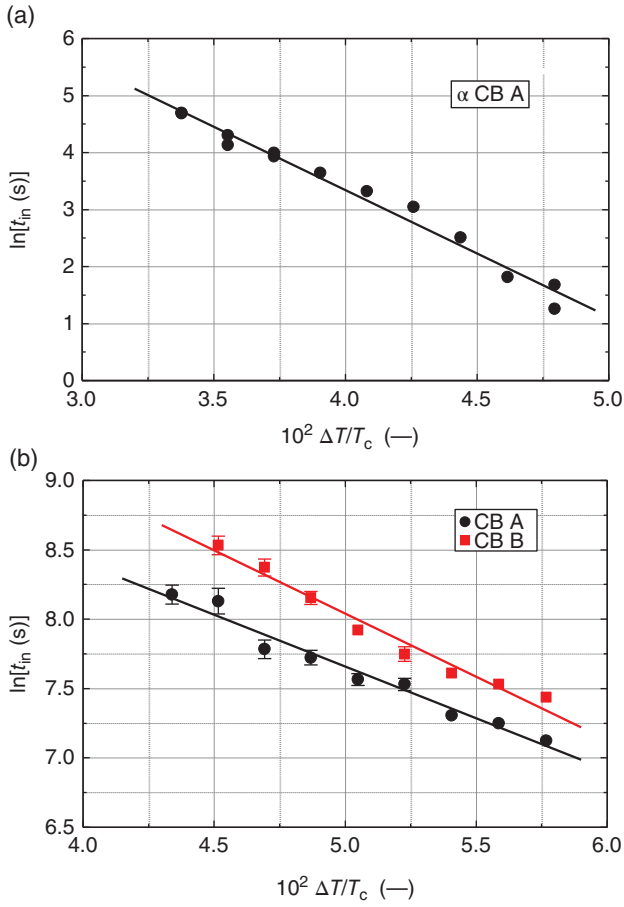

Figure 7.7 Plots of ln t_{in} against $\Delta T/T_c$ according to AT relation (7.21) for samples of different cocoa butter polymorphs: (a) one sample of α form and (b) two samples of β′ form.

seen that the plots of ln t_{in} against $\Delta T/T_c$ for the α form as well as for the β′ form of the two samples are practically linear in the entire T_c range and that the slope $i^*\lambda$ is 222 ± 9 for the α form and 75 ± 5 and 91 ± 6, respectively, for the β′ form of CB-A and CB-B samples. Assuming that $\lambda = 6$ for different polymorphs, one finds that the critical nuclei of the α form contain i^* equal to about 37 molecules, whereas those of the β′ form of CB-A and CB-B samples about 12 and 15 molecules, respectively. However, a careful examination of Figure 7.7a for the α form shows two slightly different slopes below and above $\Delta T/T_c \approx 4.25 \cdot 10^{-2}$. This behavior is similar to that observed in Figure 7.6a, where the slopes are clearly different.

Finally, it should be mentioned that the nuclei in the above cases are relatively large and the linear dependence between ln t_{in} against $\Delta T/Tc$ does not guarantee that the AT represented in the form of Eq. (7.21) is always valid because the effective excess energy Φ^* of the nucleus is also a function of the driving force (cf. Eq. (7.12); see Section 2.2).

7.3 Induction Period in Antisolvent Crystallization

During the last decade, several papers have been devoted to the investigation of measurement of MSZW in antisolvent crystallization of different systems in terms of maximum antisolvent content Δx_{max} necessary for the detection of 3D nucleation by feeding an antisolvent to a known volume of saturated solutions of solute at controlled rates R_A and confrontation of different theoretical approaches advanced to explain the dependence of Δx_{max} on antisolvent feeding rate R_A (see Chapter 6). Since the duration of occurrence of crystallization in this case is determined by the feeding rate, one may define this feeding duration for the onset of crystallization as the induction period t_{in} for this process (see Eq. (7.16)).

In this section the dependence of this duration t_{in} on antisolvent content Δx_{max} is examined using relation (7.20) based on classical theory of 3D nucleation. For the analysis, the experimental data of antisolvent feeding duration Δt as a function of antisolvent feeding rate R_A for the crystallization of ADP from its aqueous solution using three different antisolvents (viz. methanol, ethanol, and acetone) as a function of antisolvent content Δx_{max}, published recently by Sangwal and Mielniczek-Brzóska (2016a, b, 2017), are considered. The values of antisolvent feeding duration Δt, representing the induction period t_{in}, were determined from the plots of the difference $\Delta T = (T_s - T_w)$, where T_s and T_w are the temperatures of solution and water, respectively, for different feeding rates R_A, whereas the antisolvent content Δx_{max} was calculated using relation (7.18).

Figure 7.8 shows the dependence of ln t_{in} on $(\Delta x_{max})^{-2}$ based on the $t_{in}(\Delta x_{max})$ data according to Eq. (7.20) for crystallization of aqueous ammonium dihydrogen phosphate solutions by feeding three antisolvents, whereas the plots are drawn with constants listed in Table 7.2. From the figure, one observed one slope B/a_2^2 of the plot for methanol, but two different slopes B/a_2^2 for ethanol and acetone below and above particular values of $(\Delta x_{max})^{-2}$ equal to about $7.5 \cdot 10^2$ and $6.0 \cdot 10^2$ for ethanol and acetone, respectively. In the latter case, the slope of the plots at higher Δx_{max} is 3–4 times higher than that at lower Δx_{max}. These trends of the plots suggest that addition of methanol results in homogeneous nucleation in the entire Δx_{max} range, but addition of ethanol and acetone leads to the occurrence of heterogeneous and homogeneous

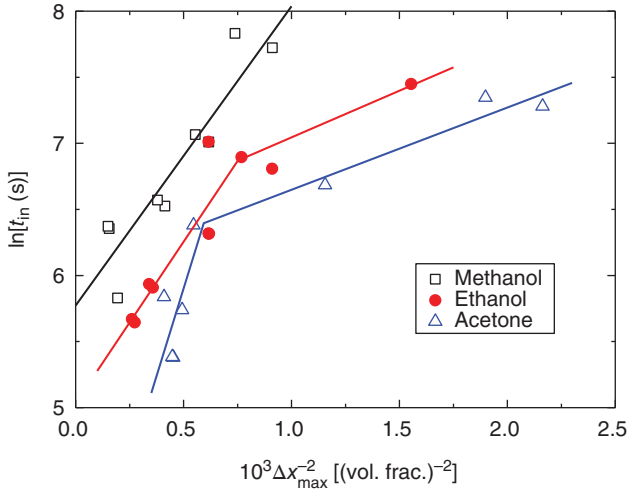

Figure 7.8 Plots of ln t_{in} against $(\Delta x_{max})^{-2}$ from the $t_{in}(\Delta x_{max})$ data according to Eq. (7.20) for crystallization of aqueous ammonium dihydrogen phosphate solutions by feeding three antisolvents. Plots are drawn with constants listed in Table 7.2. *Source:* Original data from Sangwal and Mielniczek-Brzóska (2016a, b, 2017).

Table 7.2 Constants of Eq. (7.20) for aqueous ADP solutions.

Antisolvent	ln t_{in} range	I_{CN}	$10^3 B/a_2^2$	γ (mJ·m^{-2})	R^2
Methanol	Entire	5.77	2.264	10.4	0.8380
Ethanol	<6.9	5.03	2.445	11.3	0.7972
	>6.9	6.40	0.707	3.3	—
Acetone	<6.4	3.27	5.267	24.3	0.2566
	>6.4	6.03	0.623	2.9	0.9277

nucleation below and above the transition value of Δx_{max}. The latter behavior is similar to that observed in isothermal crystallization from solutions (Figures 7.2–7.4) and from melts (Figures 7.5 and 7.6).

From the values of the slope B/a_2^2, the interfacial energy γ of ADP from aqueous solutions were estimated on the assumption that the parameter $a_2 = 10$ and the molecular volume $\Omega = a^3$ with the molecular size $a = 3{\cdot}10^{-10}$ m. These estimated values of γ are included in Table 7.2. The values are reasonable for homogeneous and heterogeneous nucleation.

7.4 Induction Period for Nonisothermal Crystallization

7.4.1 Crystallization from Solutions

Following the concept of a linear increase in supersaturation with increasing duration of cooling of a saturated solution until the occurrence of 3D nucleation, Kim and Mersmann (2001) argued that the maximum temperature difference ΔT_{max} for the onset of 3D nucleation at the cooling rate R_L defines the induction period given by Eq. (7.17). Employing this concept, Kim and Kim (2001) made the first attempt to analyze the dependence of induction time t_{in} for the primary nucleation of 3-nitro-1,2,4-one (NTO) in three different compositions of *N*-methylpyrrolidone + water mixtures using the classical 3D nucleation theory and calculated the solid–solvent interfacial energy γ for different solvent compositions at different temperatures. These authors found that the interfacial energy γ, related to different solvent compositions, varies from 3.1 to 5.8 mJ·m^{-2} in the temperature range of 50–85 °C. Interestingly, this approach of analysis of $\Delta T_{max}(R_L)$ data for different systems provides another procedure to obtain information on interfacial energy γ and related nucleus parameters such as nucleus size and activation energy for 3D nucleation (see Chapter 2).

Cooling crystallization of a variety of solute–solvent systems has been extensively studied and experimental $\Delta T_{max}(R_L)$ data for solutions of several systems saturated at different temperatures have been reported. Two recent examples of cooling crystallization of potassium tetraborate (KTB) from its aqueous solutions (Sahin et al., 2007) and keto-1,2,3,4-tetrahydro-6-methylcarbazole (KTMC) from its solutions in acetone saturated at different temperatures T_0 (Correla et al., 2006) are described and discussed below using Eqs. (7.20)–(7.22).

Figure 7.9 shows the experimental of data of $t_{in}(\Delta T_{max})$ for the cooling crystallization of KTB from its aqueous solutions saturated at different temperatures T_0 as plots of ln t_{in} against $(\Delta T_{max}/T_c)^{-2}$ and $\Delta T_{max}/T_c$ for according to Eqs. (7.20) and (7.21), respectively. It may be noted from Figure 7.9b that, the linear dependence is followed well in the entire range of cooling rates R_L, but in Figure 7.9a, the linear dependence is followed only for the first three cooling rates in the entire R_L range. The linear solid lines are drawn with the parameters given in Table 8.3. Using the value of enthalpy of solution ΔH_s for KTB equal to 18.1 kJ·mol^{-1} to calculate the dimensionless λ_s corresponding to different T_0, from the slopes of the plots of the two dependences the values of the interfacial energy γ and the number i^* of molecules in the critically-sized nucleus were calculated. For the calculations of γ from the values of the thermodynamic constant B, it was assumed that the molecular volume $\Omega = a^3$, with $a = 0.25$ nm. These values of γ and i^* are also listed in Table 8.3.

It may be noted from Figure 7.9a that the plots for 323.15 and 333.15 K indicate much lower values of B/λ_s^2. This suggests that the solid lines for these saturation temperatures represent heterogeneous nucleation. The decreasing

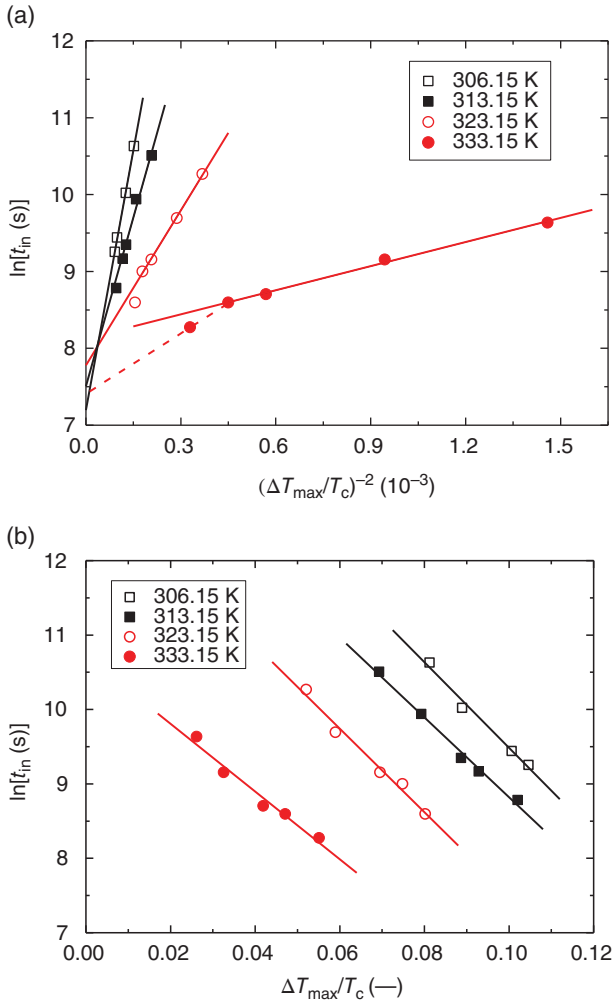

Figure 7.9 Plots of ln t_{in} against (a) $(\Delta T_{max}/T_c)^{-2}$ and (b) $\Delta T_{max}/T_c$ from experimental $t_{in}(\Delta T_{max})$ data according to Eqs. (7.20) and (7.21), respectively, for cooling crystallization of potassium tetraborate from its aqueous solutions saturated at different temperatures T_0 listed in insets. Plots are drawn with the parameters given in Table 8.3. *Source:* Original data from Sahin et al. (2007).

value of γ with increasing saturation temperature T_0 may be attributed to increasing contribution of heterogeneous nucleation with temperature. However, as seen from Table 8.3, the number i^* of molecules constituting critically-sized nucleus in this system is practically temperature independent.

Figure 7.10a and b shows the experimental data of $t_{in}(\Delta T_{max})$ obtained from cooling crystallization of KTMC from its solutions in acetone saturated at different temperatures T_0 in the form of plots of $\ln t_{in}$ against $(\Delta T_{max}/T_c)^{-2}$ and $\Delta T_{max}/T_c$ according to Eqs. (7.20) and (7.21), respectively. The behavior of plots

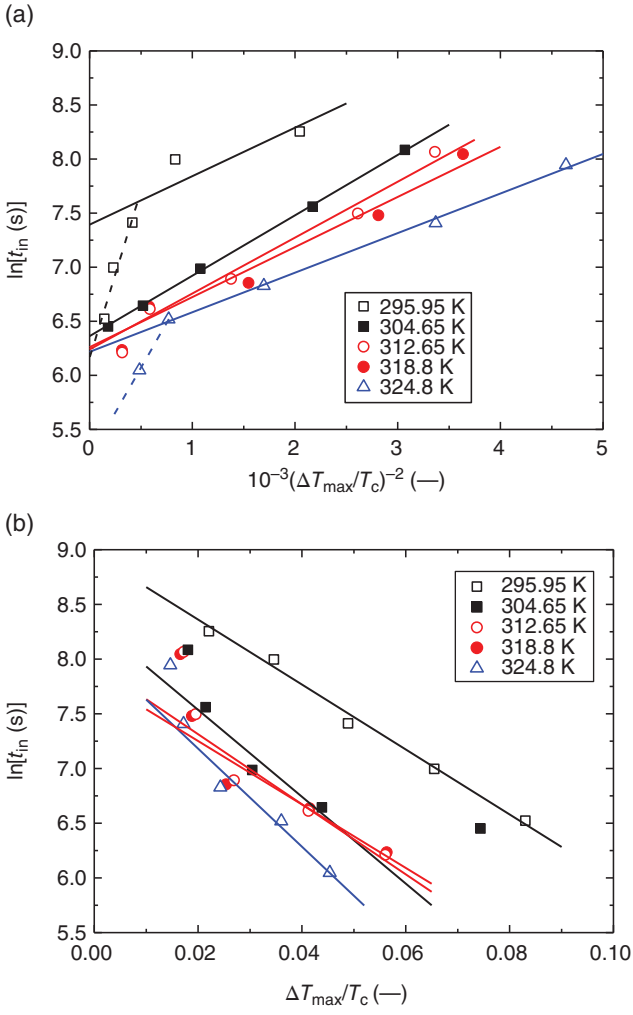

Figure 7.10 Plots of $\ln t_{in}$ against (a) $(\Delta T_{max}/T_c)^{-2}$ and (b) $\Delta T_{max}/T_c$ from experimental $t_{in}(\Delta T_{max})$ data according to Eqs. (7.20) and (7.21), respectively, for cooling crystallization of KTMC from its solutions in acetone saturated at different temperatures T_0 listed in insets. Plots are drawn with the parameters given in Table 8.3. *Source:* Original data from Correla et al. (2006).

of Figure 7.10a is similar to that observed in Figure 7.9a for cooling crystallization of KTB from its aqueous solutions, but the difference lies, irrespective of the saturation temperature T_0, in the value of slope B/λ_s^2, which is lower for $(\Delta T_{max}/T_c)^{-2}$ exceeding about $0.8{\cdot}10^3$ than that for $(\Delta T_{max}/T_c)^{-2} < 0.8{\cdot}10^3$.

In contrast to the plots of Figure 7.10a, according to Eq. (7.20), the linear dependence of $\ln t_{in}$ on $\Delta T_{max}/T_c$ is poorly followed for the $t_{in}(\Delta T_{max}/T_c)$ data corresponding to different saturation temperatures T_0 other than 295.95 K. While analyzing these data, according to Eq. (7.21), the outlier at $\Delta T_{max}/T_c = 0.073$ for $T_0 = 304.65$ K and the data for $R_L = 6\ \mathrm{K{\cdot}h^{-1}}$ (represented by the points at the lowest $\Delta T_{max}/T_c$ for all of the T_0's) were excluded. The plots in Figure 7.10b are drawn with the best-fit parameters listed in Table 7.3.

From the solubility data reported by Correla et al. (2006), one finds that $\Delta H_s = 22.4\ \mathrm{kJ{\cdot}mol^{-1}}$. This value of ΔH_s enables to calculate λ_s and then, from the values of B/λ_s^2 and $i^*\lambda_s$, the interfacial energy γ and the number i^* of molecules in the critical nucleus in supersaturated solution of different T_0. For the calculations of γ from the calculated B, it was assumed at the molecular volume $\Omega = a^3$, with $a = 5.0$ nm. These calculated values of γ and i^* are included in Table 7.3.

From Figure 7.10 and Table 7.3, it may be seen that in the KTMC–acetone system cooling crystallization shows regions of heterogeneous and homogeneous nucleations with the transition occurring at $(\Delta T_{max}/T_c)^{-2} \approx 0.8{\cdot}10^3$

Table 7.3 Constants of Eqs. (7.20) and (7.21) for KTB-water and KTMC-acetone systems.

	Eq. (7.20)				Eq. (7.21)			
T_0 (K)	I_{CN}	$10^3 B/\lambda^2$	γ (mJ·m^{-2})	R^2	I_{AT}	$i^*\lambda$	i^*	R^2
KTB–water system								
306.15	7.196	22.57	50.6	0.9982	15.23	57.51	8.1	0.9795
313.15	7.505	14.64	45.2	0.9804	14.18	53.64	7.7	0.9890
323.15	7.778	6.72	37.0	0.9982	13.11	56.07	8.3	0.9768
333.15	8.128	1.045	20.9	0.9952	10.72	45.50	7.0	0.9590
KTMC–acetone system								
295.65	7.124	0.612	12.5	0.6586	8.96	29.70	3.3	0.9816
	6.155	3.099	21.4	0.8881				
304.65	6.363	0.558	12.7	0.9991	8.33	39.70	4.5	0.8673
312.65	6.240	0.517	12.9	0.9703	7.95	32.03	3.7	0.8777
318.8	6.260	0.463	12.8	0.9461	7.83	29.00	3.4	0.8209
324.8	6.217	0.366	12.3	0.9960	8.08	44.81	5.4	0.9391

(i.e. $\Delta T_{max}/T_c \approx 3.5 \cdot 10^{-2}$) and the value of the effective interfacial energy γ, equal to about 12 mJ·m^{-2}, for heterogeneous nucleation is independent of saturation temperature T_0. The number i^* of molecules in the critical nucleus at high cooling rates R_L essentially remains constant at about 4, but its size increases with cooling rate R_L and approaches a value of about 10 molecules in solutions of high saturation temperature T_0.

The experimental $t_{in}(\Delta T_{max})$ data for cooling crystallization of KTB from its aqueous solutions and KTMC from its solutions in acetone saturated at different temperatures T_0 can also be analyzed using power-law relation (7.22). Figure 7.11 shows the $t_{in}(\Delta T_{max})$ data for cooling crystallization of these systems at different temperatures T_0 in the form of plots of $\ln t_{in}$ against $\ln(\Delta T_{max}/T_c)$ for according to Eq. (7.22). It may be observed from the plots of this figure that the $t_{in}(\Delta T_{max})$ data corresponding to a given T_0 for aqueous KTB solutions can be represented reasonably well by Eq. (7.22) in the entire $(\Delta T_{max}/T_c)$ range for all solutions, but the data for KTMC solutions saturated at T_0 = 295.95 K show a slowly decreasing slope, whereas those for the other solutions saturated at all T_0 exceeding 295.95 K show a constantly increasing slope with a decrease in $\ln(\Delta T_{max}/T_c)$. These trends are a consequence of a relatively narrow range of the values of $\Delta T_{max}/T_c$ observed for the KTB–water system at different T_0 than that for the values of $\Delta T_{max}/T_c$ for the KTMC–acetone system at different T_0.

From the above trends it may be concluded that power-law relation (7.22) does not predict a constant value of the kinetic order m in the entire $\Delta T_{max}/T_c$ range for all situations. Moreover, even in cases when Eq. (7.22) holds, the calculated value of m is not independent of T_0 as is usually observed from analysis of dependence of ΔT_{max} or $\Delta T_{max}/T_c$ on cooling rate R_L for a given system composed of solutions saturated at different temperatures T_0 according to Nývlt-like approaches discussed in Chapter 5. One also observes that Eq. (7.21) based on the AT does not hold in a wide range of ΔT_{max} or $\Delta T_{max}/T_c$. From the above considerations, it may be argued that the classical 3D nucleation theory is versatile and more informative than atomistic and power-law approaches for the analysis of dependence of induction period t_{in} on supersaturation or temperature difference as the driving force in the experimental data.

7.4.2 Effect of Impurities on Crystallization from Solutions

It is well known that impurities present in a growth medium show strong influence on the kinetics of nucleation and growth of a crystallizing substance. The effect of impurities on crystallization processes has been surveyed recently (Sangwal, 2007). Different aspects of the effect of impurities on the MSZW of different solute–solvent systems were described in Section 5.4. It was pointed out that in several cases the dependence of MSZW, as determined by the maximum temperature difference ΔT_{max} obtained for constant values of R_L, on the

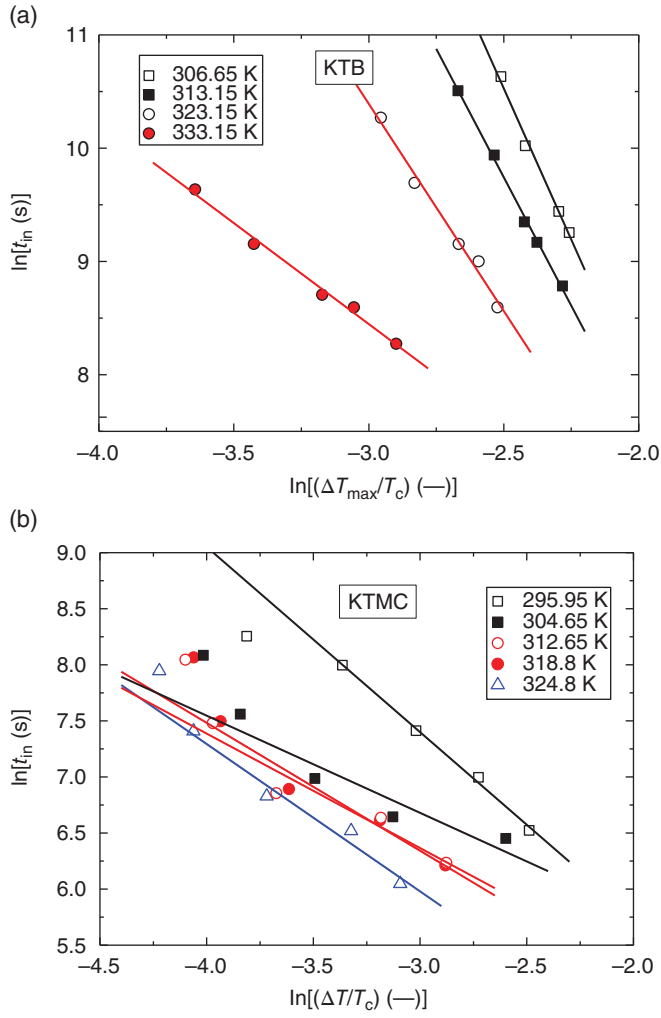

Figure 7.11 Plots of ln t_{in} against ln($\Delta T_{max}/T_c$) from $t_{in}(\Delta T_{max})$ data according to Eq. (7.21) for cooling crystallization of (a) KTB–water and (b) KTMC–acetone systems at different temperatures T_0 listed in the inset. *Source:* Original data from (a) Sahin et al. (2007) and (b) Correla et al. (2006).

concentration c_i of an impurity exhibits poor fit of the theoretical predictions. It was argued that one of the main reasons of this poor fit is that addition of an impurity leads to a marked increase in the solubility of the solute, thereby increasing the saturation temperature T_0 with an increase in the impurity concentration c_i, but this increase in T_0 with an increasing c_i of the impurity is not

linear. A boric acid–water system containing different bi- and trivalent cationic impurities was suggested to be examples showing the above trends. Here, experimental data of induction period t_{in}, calculated from the $\Delta T_{max}(R_L)$ data, reported by Sayan and Ulrich (2001), for the nucleation of boric acid from its aqueous solutions containing different concentrations c_i of Cr(III) impurity are examined. Different features of the MSZW of this system in the presence of some bi- and trivalent cationic impurities are described in Section 5.4.

Figure 7.12a–c presents the experimental $t_{in}(\Delta T_{max})$ data for the cooling crystallization of boric acid from aqueous solutions saturated at 303.8 K containing different concentrations of Cr(III) in the form of plots of ln t_{in} against $(\Delta T_{max}/T_c)^{-2}$, $\Delta T_{max}/T_c$, and $\ln(\Delta T_{max}/T_c)$ according to Eqs. (7.20), (7.21) and (7.22), respectively. In the figure, impurity concentration c_i is listed in the insets, whereas the plots are drawn with the parameters given in Table 7.4.

From Table 7.4, the following features may be noted:

1) The fit of the experimental $t_{in}(\Delta T_{max})$ data is the best according to Eq. (7.20), the worst according to Eq. (7.21), and intermediate between the two according to Eq. (7.22).
2) The values of B/λ_s^2 obtained for the boric acid–water system are comparable with those obtained for the KTMC–acetone system. Taking a value of λ_s equal to 9, one finds that the value of the interfacial energy γ for the boric acid–water system is comparable with that for the KTMC–acetone system. However, the values of $i^*\lambda_s$ for the boric acid–water system is lower by a factor of about 30 than those for the KTMC–acetone system. With the above value of λ_s, one finds that the number i^* of solute molecules in the nucleus is about 0.1. This unrealistic value of i^* implies that the AT of 3D nucleation does not hold in the present case.
3) If the value of m for c_i = 10 ppm is excluded, the value of the nucleation order m is about 7. These values of m are comparable with those determined from the analysis of data of $(\Delta T_{max}/T_0)$ against c_i for this impurity by using self-consistent Nývlt-like equation (5.20); see Figure 5.20c. Recalling that the value of m obtained from the plots of ln t_{in} against $\ln(\Delta T_{max}/T_0)$ holds in a narrow range of constant $(\Delta T_{max}/T_0)$ as observed in the case of KTB–water and KTMC–acetone systems, where the value of m is not independent of T_0, it may be argued that the value of m from the plots of ln t_{in} against $\ln(\Delta T_{max}/T_0)$ is comparable with that obtained from the analysis of data of $(\Delta T_{max}/T_0)$ against R_L according to the power-law relation (7.22) only when the value of $(\Delta T_{max}/T_0)$ at a particular saturation temperature T_0 lies in a narrow range.

From the above discussion, it may be concluded that Eq. (7.20) based on the classical 3D nucleation theory accounts for a satisfactory interpretation of the effect of impurities on the induction period of nucleation for different solute–solvent systems. The main parameter involved in the explanation of

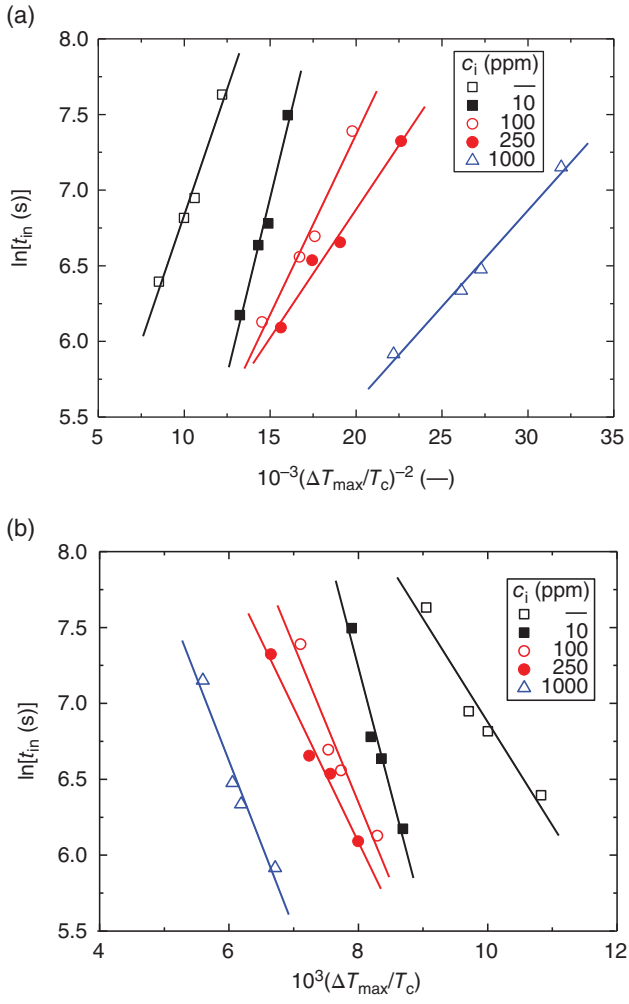

Figure 7.12 Plots of ln t_{in} against (a) $(\Delta T_{max}/T_c)^{-2}$, (b) $\Delta T_{max}/T_c$, and (c) $\ln(\Delta T_{max}/T_c)$ from experimental $t_{in}(\Delta T_{max})$ data according to Eqs. (7.20), (7.21) , and (7.22), respectively, for cooling crystallization of boric acid from aqueous solutions saturated at 303.8 K containing different concentrations of Cr(III) listed in insets. Plots are drawn with the parameters given in Table 7.4. *Source:* Original data from Sayan and Ulrich (2001).

the effect of impurities is the solute–solvent interfacial energy γ in these systems. The dependence of the interfacial energy γ for the boric acid–water system containing Cr(III) impurity, calculated from the values of B/λ_s^2 for the cooling crystallization of this system listed in Table 7.4, on the concentration c_i of Cr(III) impurity is shown in Figure 7.13.

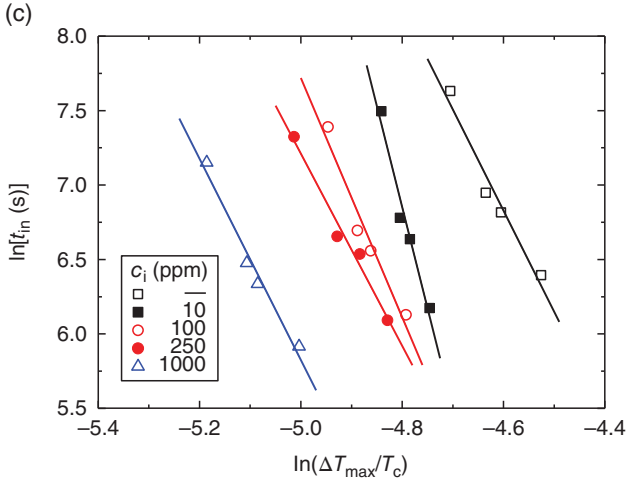

Figure 7.12 (Continued)

Table 7.4 Constants of different relations for the boric acid–water system containing impurity at 303.85 K.

c_i (ppm)	Eq. (7.20)			Eq. (7.21)			Eq. (7.22)		
	I_{CN}	$10^3B/\lambda_s^2$	R^2	I_{AT}	$i^*\lambda_s$	R^2	$-I_{PL}$	m	R^2
—	3.494	0.334	0.9727	13.68	0.68	0.9285	24.42	6.79	0.9457
10	–0.050	0.467	0.9656	20.29	1.63	0.9462	58.24	13.56	0.9533
100	2.605	0.238	0.9631	14.65	1.04	0.9216	32.43	8.03	0.9372
250	3.477	0.170	0.9716	13.17	0.89	0.9668	25.09	6.46	0.9707
1000	3.054	0.127	0.9875	13.19	1.09	0.9488	27.97	6.76	0.9646

As seen from Figure 7.13, except for a sudden increase at Cr(III) concentration c_i of 10 ppm, the interfacial energy γ for the boric acid–water system decreases with an increase in impurity concentration c_i. This dependence may be described by the relation:

$$\gamma = \gamma_0(1-\alpha\theta), \tag{7.23}$$

where θ is the coverage of the surface of the nucleus by the impurity and is described by the usual adsorption isotherms, α is an effectiveness parameter, and γ_0 is the value of the interfacial energy γ when θ approaches zero. When

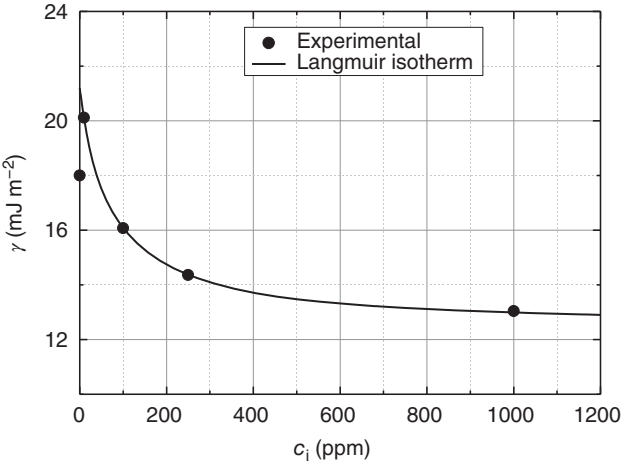

Figure 7.13 Dependence of interfacial energy γ on impurity concentration c_i for cooling crystallization of boric acid from aqueous solutions saturated at 303.8 K. The plot is drawn according to Eq. (7.24) excluding point corresponding to $c_i = 0$.

the surface coverage is described by Langmuir adsorption isotherm, Eq. (7.23) takes the form:

$$\gamma = \gamma_0 \left(1 - \frac{\alpha K_L c_i}{1 + K_L c_i} \right), \tag{7.24}$$

where the Langmuir constant K_L is given by

$$K_L = \exp\left(\frac{Q_{diff}}{R_G T} \right), \tag{7.25}$$

where Q_{diff} is the differential heat of adsorption on the surface. During the analysis, the point corresponding to $c_i = 0$ was excluded. In Figure 7.13, the curve is drawn according to Eq. (7.24) with the following values of the constants: $\alpha = 0.413$ and $K_L = 1.42 \cdot 10^4$. For the saturation temperature $T_0 = 303.85$ K, the value of the Langmuir constant K_L gives $Q_{diff} = 24.1$ kJ·mol^{-1}. This value of Q_{diff} is comparable with that obtained from the analysis of the $\Delta T_{max}(R_L)$ data at different concentrations c_i of Cr(III) ions (see Section 5.4.3).

7.4.3 Crystallization from the Melt

We recall here that nonisothermal crystallization is based on the cooling of a liquid at a particular cooling rate R_L from the equilibrium state at temperature T_0 to a lower temperature T_c where crystallization takes place and that this

notion is used in the derivation of all of the theoretical relationships, described above, between normalized temperature difference $\Delta T/T_0$ and cooling rate R_L. Therefore, so far as the understanding of the MSZW is concerned, all of the equations are equally applicable in the case of melts, with essentially the same physical quantities and parameters.

Evolution of overall nonisothermal crystallization kinetics of fatty acid melts at different cooling rates R_L is similar to isothermal crystallization kinetics. At a given cooling rate R_L, the time dependence of the overall crystallization curve shows an initial period t_{in} without observable crystallized mass and then there is a sudden increase in the crystallized mass, which subsequently approaches a constant value, as shown in Figure 7.14. As in the case of isothermal crystallization, the process of nonisothermal crystallization also comprises three durations: (i) an initial period t_{reorg} required for the evolution of solute clusters in the melt volume by diffusion of solute monomers, (ii) another duration t_N, usually referred to as induction period t_{in}, involving the formation of critically-sized 3D nuclei of a new phase from the distribution of solute clusters, and (iii) subsequent overall crystallization y of the solute during the cooling of supersaturated solution or melt at a constant cooling rate R_L. For a given system, these processes depend on the cooling rate R_L.

It is observed that the induction period t_{in} and the duration of the overall crystallization y for a crystallizing phase decrease with increasing cooling rate R_L (see Figure 7.15), whereas an increase in R_L induces the formation of more metastable phases such that the crystallization of the stable phase occurring at low R_L is completely replaced by the crystallization of the metastable phase with

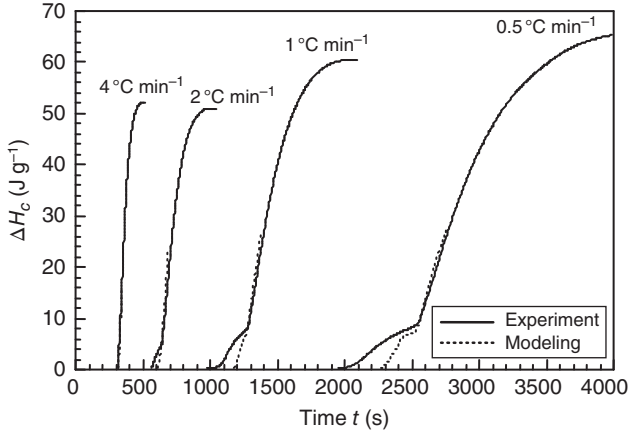

Figure 7.14 Evolution of overall nonisothermal crystallization mass as determined by latent heat ΔH_c released by cocoa butter samples for different cooling rate R_L. *Source:* Adapted from Rousset and Rappaz (2001). Copyright (2001), with permission from AOCS Press.

an increasing R_L (Figure 7.14). The nature of the nonisothermal crystallization curves is similar to that of isothermal crystallization curves. Therefore, basically the mechanisms proposed by isothermal crystallization are also valid here but the effect of cooling rate has to be included in the explanation of nonisothermal crystallization (for example, see: Narine et al., 2006; Rousset and Rappaz, 1996; Rousset et al., 1998; Smith et al., 2005).

Rousset and Rappaz (1996) and Rousset et al. (1998) analyzed the time dependence of volume fraction of crystallized SOS and POS–SOS mixture by splitting the cooling curves into small time steps of constant temperature and fitting the data with Avrami equation (3.88) considering k and q as temperature-dependent parameters, time–temperature–transformation diagrams, and fictitious times between two successive time steps. This procedure enabled to calculate time t_s (denoted here as t_{in}) of start and time t_f of finish of crystallization as a function of cooling rate R_L, as shown in Figure 7.15 by squares and circles, respectively, for the crystallization of SOS by cooling the melt from 100 °C. In the figure, triangles represent data obtained by modeling the process using the additivity principle based on decomposition of the $t_{in}(R_L)$ curve into small steps. The figure also shows the data on t_{in} and t_f for SOS melts initially quenched at 50 to 30 °C and then allowed to cool at cooling rates of 0.8 and 1 K·min^{-1}. These data are presented as open squares, circles, and triangles.

It may be seen from Figure 7.15 that simulation predicts the trend of the curves but gives somewhat lower values of t_{in} and t_f than the experimental data. In any case, these trends of the dependence of t_{in} and t_f on R_L for nonisothermal

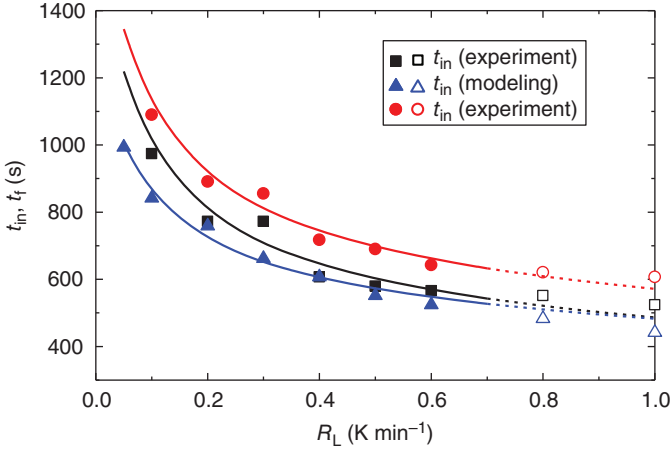

Figure 7.15 Dependence of the times t_{in} and t_f for the nonisothermal crystallization kinetics of SOS on cooling rate R_L. Plots are drawn according to Eq. (7.27) with constants given in Table 7.5. *Source:* Original data from Rousset and Rappaz (1996); Reproduced from Sangwal and Sato (2012). Copyright (2012), with permission from AOCS Press.

crystallization of SOS demonstrate that nonisothermal crystallization can also be described by the Avrami theory. Smith et al. (2005) also found that the KJMA theory best describes the experimental data on the nonisothermal crystallization kinetics of POP, whereas the temperature dependence of the Avrami rate constant k_m is best explained by a Vogel–Fulcher relationship, where the melting point of the crystallizing species is taken as the reference temperature. Narine et al. (2006) extended the Avrami theory to describe the crystallization kinetics of high-volume fraction lipids and suggested that lipids crystallize and grow into networks via very specific growth modes.

Following Kim and Mersman (2001), from the maximum supercooling $\Delta T_{\max}$ attained in the system at a constant cooling rate R_L, we define the induction period t_{in} by relation (7.17). Assuming that $\Delta T_{\max}(R_L)$ increases with R_L following the simple relation:

$$\frac{\Delta T_{\max}(R_L)}{\Delta T_{\max}(R_{Llim})} = \left(\frac{R_L}{R_{Llim}}\right)^p, \tag{7.26}$$

where $\Delta T_{\max}(R_{Llim})$ is the limiting value of $\Delta T_{\max}$ when R_L approaches R_{Llim} and the exponent $p < 1$, Eq. (7.17) may be written as

$$t_{in} = \frac{\Delta T_{\max}(R_{Llim})}{R_{Llim}^{p} R_L^{1-p}}. \tag{7.27}$$

According to Eq. (7.27), t_{in} is strictly not inversely proportional to R_L because of the dependence of $\Delta T_{\max}$ on R_L. The validity of Eq. (7.27) is demonstrated in Figure 7.15, which shows the dependence of the times t_{in} and t_f for the nonisothermal crystallization kinetics of SOS on cooling rate R_L. The continuous and the dashed curves are drawn with the best-fit constants of the data up to 0.6 K·min^{-1} (Table 7.5). The reported values of simulated t_{in} as a function of

Table 7.5 Values of constants of Eq. (7.27) for SOS and POS-SOS mixture.

Sample	Data	$\Delta T_{\max}(R_{Llim})$ (K)	$1/R_{Llim}$ (min·K^{-1})	p
SOS	$t_{in}(R)$[a]	2.397	$4.7\cdot10^{-4}$	0.693
	$t_{in}(R)$[b]	1.478	$4.7\cdot10^{-4}$	0.755
	$t_f(R)$[a]	2.40	$4.7\cdot10^{-4}$	0.714
POS-SOS	$t_{in}(R)$[c]	3.553	$8.09\cdot10^{-7}$	0.393
	$t_f(R)$[c]	3.050	$1.13\cdot10^{-6}$	0.402

[a] Experimental data by Rousset and Rappaz (1996).
[b] Modeling data by Rousset and Rappaz (1996).
[c] Experimental data by Rousset et al. (1998).

R_L, shown in Figure 7.15, are somewhat lower than the experimental values, but they can also be fitted according to Eq. (7.27) with somewhat different values of the constants.

A behavior similar to that of SOS was also observed in the case of nonisothermal crystallization kinetics of a 25 : 75 w/w POS–SOS mixture on cooling rate R_L (Rousset et al., 1998). The values of the constants of Eq. (7.27) for the two samples are listed in Table 7.5.

References

Correla, P., Lopes, C., Piedade, M.E.M. et al. (2006). Solubility and metastable zone width of 1-keto-1,2,3,4-tetrahydro-6-methylcarbazole in acetone. *J. Chem. Eng. Data* 51: 1306–1309.

Dugua, J. and Simon, B. (1978). Crystallization of sodium perborate from aqueous solutions: I. Nucleation rates in pure solution and in presence of a surfactant. *J. Cryst. Growth* 44: 265–279.

Foubert, I., Dewittinck, K., and Vanrolleghem, P.A. (2003). Modelling of the crystallization kinetics of fats. *Trends Food Sci. Technol.* 14: 79–92.

Foubert, I., Vanrolleghem, P.A., and Dewittinck, K. (2005). Insight in model parameters by studying temperature influence on isothermal cocoa butter crystallization. *Eur. J. Lipid Sci. Technol.* 107: 660–672.

Gharsallaoui, A., Rogé, B., and Mathlouthi, M. (2008). Water–disaccharides interactions in saturated solution and the crystallisation conditions. *Food Chem.* 106: 1329–1339.

Hao, H., Wang, J., and Wang, Y. (2005). Determination of induction period and crystal growth mechanism of dexamethasone sodium phosphate in methanol–acetone system. *J. Cryst. Growth* 274: 545–549.

Jim, M. and Kim, K.-J. (2012). Effect of supersaturation on polymorphs of clopidogrel hydrogen sulfate in drowning-out crystallization. *Chem. Eng. Technol.* 35: 995–1002.

Kashchiev, D. (2000). *Nucleation: Basic Theory with Applications*. Oxford: Butterworth-Heinemann.

Kim, K.-J. and Kim, K.-M. (2001). Nucleation kinetics in spherulitic crystallization of explosive compound: 3-nitro-1,2,4-triazol-5-one. *Powder Technol.* 119: 109–116.

Kim, K.-J. and Mersmann, A. (2001). Estimation of metastable zone width in different nucleation processes. *Chem. Eng. Sci.* 56: 2315–2324.

Mersmann, A. (1990). Calculation of interfacial tensions. *J. Cryst. Growth* 102: 841–847.

Narine, S.S., Humphrey, K.L., and Bouzidi, L. (2006). Modification of the Avrami model for application of the melt crystallization of lipids. *J. Am. Oil Chem. Soc.* 83: 913–921.

Nývlt, J. (1968). Kinetics of nucleation from solutions. *J. Cryst. Growth* 3–4: 377–383.

Roelands, C.P.M., ter Horst, J.H., Krammer, H.J.M., and Jensens, P.J. (2006). Analysis of nucleation rate measurements in precipitation process. *Cryst. Growth Des.* 6: 1380–1392.

Rousset, P. and Rappaz, M. (1996). Crystallization kinetics of the pure triacylglycerols glycerol-1,3-dipalmitate-2-oleate, glycerol-1-palmitate-2-oleate-3-stearate, and glycerol-3,3-distearate-2-oleate. *J. Am. Oil Chem. Soc.* 73: 1051–1057.

Rousset, P. and Rappaz, M. (2001). Experimental study and computer modeling of the dynamic and static crystallization of cocoa butter. In: *Crystallization and Solidification Properties of Lipids* (ed. N. Widlak, R. Hartel and S. Narine), 96–109. New York: AOCS Press.

Rousset, P., Rappaz, M., and Minner, E. (1998). Polymorphism and solidification kinetics of the binary system POS-SOS. *J. Am. Oil Chem. Soc.* 75: 857–864.

Sahin, O., Dolas, H., and Demir, H. (2007). Determination of nucleation kinetics of potassium tetraborate tetrahydrate. *Cryst. Res. Technol.* 42: 766–772.

Sangwal, K. (2007). *Additives and Crystallization Processes: From Fundamentals to Applications*. Chichester: Wiley.

Sangwal, K. and Mielniczek-Brzóska, E. (2016a). Antisolvent crystallization of aqueous ammonium dihydrogen phosphate solutions by addition of acetone at different rates. *Cryst. Res. Technol.* 51: 475–490.

Sangwal, K. and Mielniczek-Brzóska, E. (2016b). Antisolvent crystallization of aqueous ammonium dihydrogen phosphate solutions by addition of methanol. *J. Cryst. Growth* 451: 139–149.

Sangwal, K. and Mielniczek-Brzóska, E. (2017). Effect of addition of different antisolvents on the crystallization of aqueous ammonium dihydrogen phosphate solutions. *Cryst. Res. Technol.* 52: 201600361 (1–7).

Sangwal, K. and Sato, K. (2012). Nucleation and crystallization kinetics of fats. In: *Structure-Function Analysis of Edible Fats* (ed. A.G. Marangoni), 25–78. Urbana: AOCS Press.

Sato, K. and Kuroda, T. (1987). Kinetics of melt crystallization and transformation of tripalmitin polymorphs. *J. Am. Oil Chem. Soc.* 64: 124–127.

Sayan, P. and Ulrich, J. (2001). Effect of various impurities on the metastable zone width of boric acid. *Cryst. Res. Technol.* 36: 411–417.

Smith, K.W., Cain, F.W., and Talbot, G. (2005). Kinetic analysis of nonisothermal differential scanning calorimetry of 1,3-dipalmitoyl-2-oleoylglycerol. *J. Agric. Food Chem.* 53: 3031–3040.

8

Ostwald Ripening, Crystal Size Distribution, and Polymorph Selection

During the nucleation stage of a new phase, a large number of stable nuclei are formed either simultaneously or continuously, referred to as instantaneous or progressive nucleation (Chapter 3). When stable three-dimensional (3D) nuclei in a solution of known supersaturation or increasing supersaturation are formed progressively, it is expected that the nuclei formed at different times result in visible crystallites of different sizes. Similarly, when the 3D nuclei in a supersaturated solution are formed instantaneously, they can result in visible crystallites of different sizes due to differences in the defect structure of the growing crystallites and nonuniform growth conditions in the entire volume of the solution. However, after the occurrence of 3D nucleation when crystallites of different sizes grow in a system closed for mass transfer, the supersaturation available for their growth decreases steadily with time and ultimately the system attains an equilibrium state when the supersaturation tends to approach a zero value. In this process of decrease in supersaturation, the initial crystal size distribution (CSD) undergoes a change with time because crystallites of different sizes and different defect structures grow at different rates. Changes in solution temperature and supersaturation and issues related to size distribution of crystals in a crystallization run are the subject of this chapter.

Decay of supersaturation involving polymorphic transformation and CSD are modeled using nucleation and growth kinetic parameters and population balance equations (Cornel et al., 2009; Iggland and Mazzotti, 2012; Lindenberg et al., 2009). For more information on CSD and population balance equations the reader is referred to the literature (Cornel et al., 2009; Iggland and Mazzotti, 2012; Leubner, 2010; Mersmann, 2001; Mullin, 2001; Nývlt et al., 1985; Randolph and Larson, 1988; Söhnel and Garside, 1992; Vetter et al., 2013).

Nucleation and Crystal Growth: Metastability of Solutions and Melts, First Edition.
Keshra Sangwal.
© 2018 John Wiley & Sons, Inc. Published 2018 by John Wiley & Sons, Inc.

8.1 Supersaturation Decay During Antisolvent Crystallization

8.1.1 General Trends

It is well known that, after the onset of 3D nucleation at the induction period t_{in}, the supersaturation available in every closed system results in the formation of new 3D nuclei and the growth of all 3D nuclei into larger entities. Supersaturation $\ln S$, where S is the ratio of actual solute concentration c to the equilibrium concentration c_0, attained at a particular temperature in the closed system begins to decrease with time t and finally approaches the equilibrium state when $\ln S$ attains a limiting value $\ln S_{lim}$. However, external factors such as seeding (Cornel et al., 2009; Jim and Kim, 2012; Lorenz et al., 2006), stirring rate (Akrap et al., 2010; Cornel et al., 2009), and the presence of additives and their concentration (Qu et al., 2006) determine the nature of the desupersaturation curves, which usually show an exponential decay with time after the onset of 3D nucleation. For an unseeded system, intense agitation leads to a reduction in the duration of occurrence of instantaneous 3D nucleation accompanied by an exponential decrease in supersaturation (Akrap et al., 2010). Addition of seeds and foreign substances (i.e. additives) also leads to similar effects. Since such desupersaturation curves are usually observed for different systems, it is interesting to understand processes responsible for their nature.

A common feature of curves of evolution of desupersaturation during unseeded crystallization from a close system of predefined supersaturation $\ln S$ by different experimental techniques is that they mark the event of occurrence of 3D nucleation of the crystallizing phase in the form of a sudden decrease in the supersaturation in the system (Cornel et al., 2009; Jim and Kim, 2012; Lorenz et al., 2006; Qu et al., 2006). Some techniques such as ultrasonic velocity measurements also reveal a sudden peak due to the occurrence of 3D nucleation (Jim and Kim, 2012), but these measurements show large fluctuations with time, thus making observations somewhat difficult. Occurrence of 3D nucleation is also observed in the temperature profile of controlled cooling crystallization as a peak or a break due to the dissipation of heat generated by nucleation (Lorenz et al., 2006; Wohlgemuch et al., 2010).

8.1.2 Kinetics of Supersaturation Decay

The temperature measurement technique used by Sangwal and Mielniczek-Brzóska (2016a, b, 2017b) for the investigation of antisolvent crystallization of ammonium dihydrogen phosphate (ADP) from its aqueous solutions saturated at a well-defined temperature T_0 of 30 °C is based on the generation of heat by processes of 3D nucleation and crystal growth. Since increase in the solution temperature by the addition of an antisolvent is associated with the

generation of solid solute, it may be assumed that the increase ΔT in solution temperature T_s from T_0 (i.e. $\Delta T = T_s - T_0$) is a measure of excess solute concentration Δc created by the addition of the antisolvent.

With the above background of the change in the temperature of solution saturated at a particular temperature with antisolvent feeding, the experimental data of solution temperature T_s as a function of antisolvent feeding duration t at different rates R_A may be analyzed. In order to assess the role of mixing of an antisolvent with the solvent water, the data of change in the temperature T_w of water as a function of antisolvent feeding duration t at different rates R_A should also be analyzed.

Examination of the general behavior of the $T_s(t)$ curves of aqueous ADP solutions observed during feeding of different antisolvents at various rates reveals similar trends (Sangwal and Mielniczek-Brzóska, 2016a, b, 2017b). After the beginning of feeding of an antisolvent to the saturated solution at time t_0, the solution temperature T_s begins to increase initially slowly up to t_1 and then an abrupt increase up to t_{max}, and finally, whether feeding of the antisolvent is continued or interrupted, the temperature T_s decreases slowly and tends to approach the initial temperature of 30 °C. Irrespective of feeding or nonfeeding of an antisolvent, the solution temperature T_s slowly decreases with increasing time t, but the decrease in temperature is faster in the time interval beyond t_{int} than that in the time interval between t_{max} and t_{int}. Figure 8.1 shows, as an

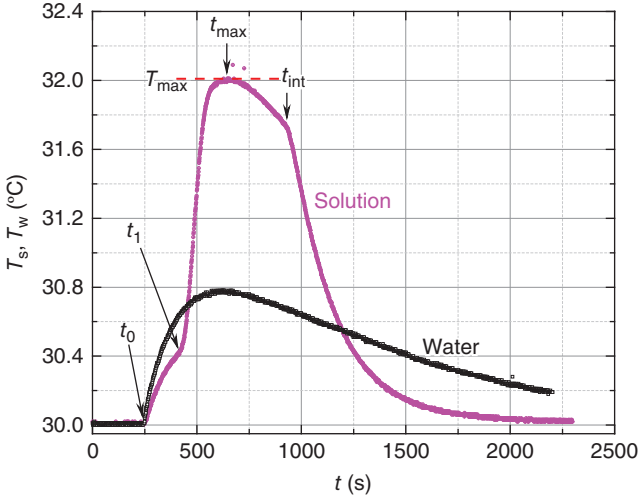

Figure 8.1 Change in (a) temperature T_s of aqueous ADP solution saturated at 30 °C and (b) temperature T_w of pure water at 30 °C with feeding duration t of acetone at rate $R_A = 3.0$ ml·min^{-1}. Different times are indicated. *Source:* Adapted from Sangwal and Mielniczek-Brzóska (2016a).

example, the change in the temperature T_s of 220 ml aqueous ADP solution saturated at 30 °C with feeding duration t of acetone at a rate R_A of 3.0 ml·min^{-1}. In the figure, t_0 denotes the time of beginning of antisolvent feeding, t_1 the time of onset of 3D nucleation, t_{max} the time of appearance of a maximum value of temperature T_{max}, and t_{int} denotes the time of interruption of antisolvent feeding.

The nature of $T_w(t)$ curves for pure water kept at an initial temperature of 30 °C with feeding duration t of an antisolvent at different rates R_A is somewhat similar to that of the $T_s(t)$ curves for solutions, but the temperature T_w abruptly increases from t_0 and then after reaching a maximum temperature T_{max} at time t_{max}, it steadily decreases and tends to approach the initial temperature of 30 °C. This behavior for pure water with feeding duration t of acetone at a rate R_A of 3.0 ml·min^{-1} is also shown in Figure 8.1.

Different aspects of increase in the temperature of solutions and solvent water by addition of antisolvents were discussed in Chapter 6. In this chapter the experimental results of post-crystallization cooling behavior of aqueous supersaturated ADP solutions containing acetone and methanol antisolvents using traditional Newton's law of cooling and diffusion of ions/molecules involved in transporting heat from aqueous ADP solutions contained in the crystallizer to the thermostating system are studied. Following Sangwal and Mielniczek-Brzóska (2017b), these results are described and discussed below.

The steady decrease in the temperature T_s and T_w of aqueous ADP solutions and pure water with increasing time t observed, for example, in Figure 8.1a and b, respectively, may be described by Newton's law of cooling, expressed in the linear form:

$$\frac{dT}{dt} = -K(T - T_0), \tag{8.1}$$

where dT/dt is the instantaneous rate of decrease in temperature T_s or T_w with time t, the constant K is characteristic of the solution composition and the solvent, and T_0 is the temperature of the surroundings.

Figure 8.2 shows, as an example, the dependence of instantaneous rate dT/dt of temperature decrease on temperature T_s of aqueous ADP solution containing acetone added previously up to t_{int} at different feeding rates R_A. This type of aqueous solution systems are referred to as unfed systems. Figure 8.3 presents the data of rate dT/dt of temperature decay as a function of temperature T_w of water with the feeding of acetone for different feeding rates R_A. The plots in these figures are drawn with the best-fit values of the parameters K and T_0 of Eq. (8.1) listed in Table 8.1. In the table, the values of the parameters K and T_0 are also included for methanol antisolvent.

The plots of instantaneous rate dT/dt of temperature decay against temperature T_s of fed aqueous ADP solution in the time interval between t_{max} and t_{int} at different feeding rates R_A of the two antisolvents also reveal linear dependence similar to that observed in Figure 8.2. However, in this case the value of the parameter K is negative, as in Figure 8.2, for plots at R_A below 1.0 ml·min^{-1},

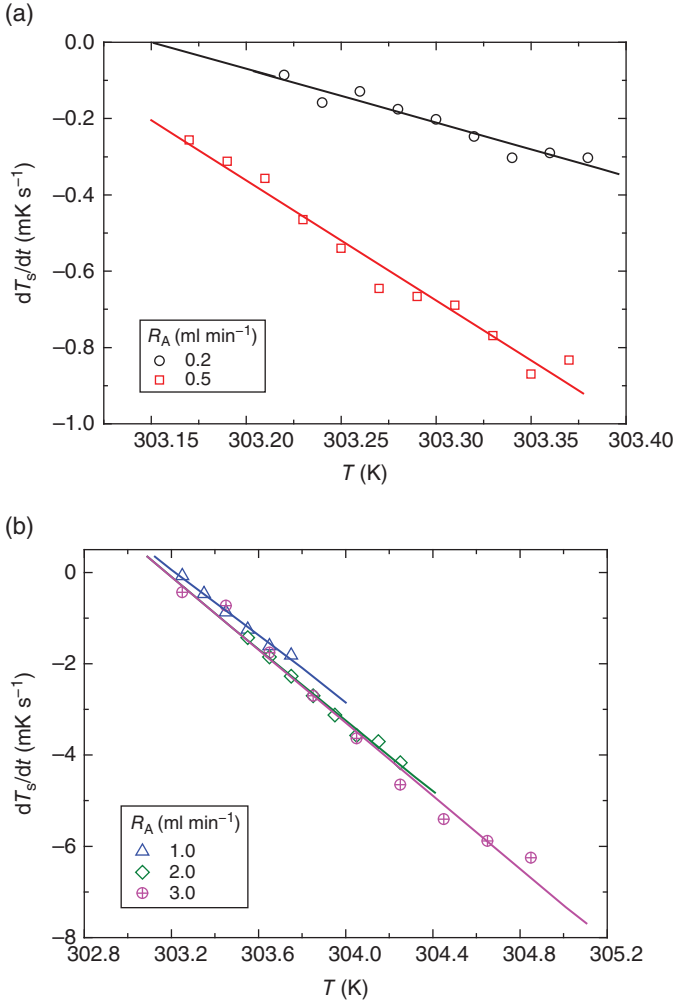

Figure 8.2 Dependence of instantaneous rate dT_s/dt of temperature decrease on temperature T_s of aqueous ADP solution (i.e. unfed aqueous solution system) containing acetone added previously up to t_{int} at different feeding rates R_A: (a) 0.2 and 0.5 ml·min^{-1} and (b) 1.0, 2.0 and 3.0 ml·min^{-1}. Best-fit parameters for the plots are listed in Table 8.1. *Source:* Reproduced from Sangwal and Mielniczek-Brzóska (2017a). Copyright (2017), with permission from Wiley.

whereas it is positive for plots at R_A exceeding 1.0 ml·min^{-1}, such that R_A = 1.0 ml·min^{-1} represents essentially the transition feeding rate when $K \approx 0$. Figure 8.4 shows, as an example, the data of dT/dt against T_s for fed aqueous ADP solutions, with the plots drawn with the best-fit parameters given in Table 8.1.

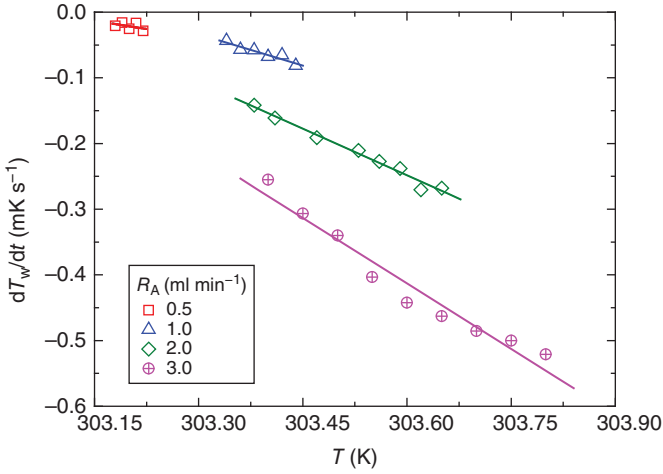

Figure 8.3 Dependence of instantaneous rate dT_w/dt of temperature decrease on temperature T_w of water with the feeding of acetone for different feeding rates R_A. Best-fit parameters for the plots are listed in Table 8.1. *Source:* Reproduced from Sangwal and Mielniczek-Brzóska (2017a). Copyright (2017), with permission from Wiley.

Table 8.1 Values of constants K and T_0 for different systems.

System	Parameter	R_A (ml·min^{-1})				
		0.2	0.5	1.0	2.0	3.0
Acetone						
Unfed solution	10^3K (s^{-1})	1.53	3.15	3.58	3.90	4.00
	T_0 (K)	303.19	302.84	302.94	303.00	303.00
Fed water	10^4K (s^{-1})	—	1.67	3.19	4.74	6.65
	T_0 (K)	—	303.07	303.15	303.07	302.98
Fed solution	10^3K (s^{-1})	—	0.47	−4.36	−4.69	−4.02
	T_0 (K)	—	302.95	304.06	304.61	305.33
Methanol						
Unfed solution	10^3K (s^{-1})	2.80	2.82	3.44	3.85	3.94
	T_0 (K)	303.19	303.19	303.18	303.17	303.17
	10^3K (s^{-1})	2.09	2.76	3.35	3.91	
	T_0 (K)	303.17	303.19	303.19	303.17	
Fed water	10^4K (s^{-1})	—	0.33	2.0	3.75	6.50

Source: Adapted from Sangwal and Mielniczek-Brzóska (2017b).

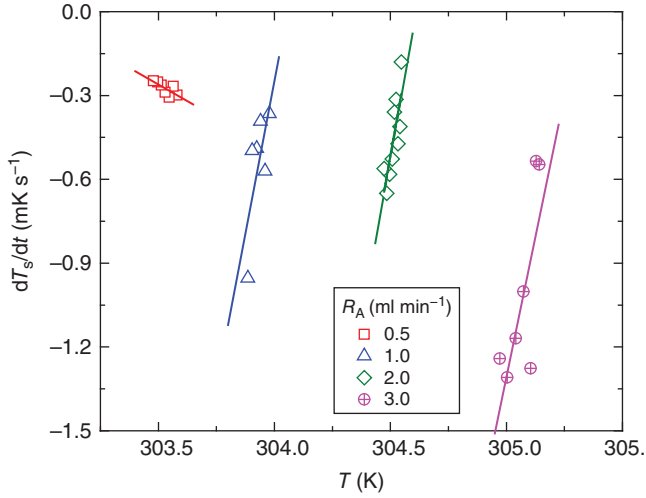

Figure 8.4 Dependence of instantaneous rate dT_s/dt of temperature decrease on temperature T_s of aqueous ADP solution (i.e. fed aqueous solution system) between t_{max} and t_{int} at different feeding rates R_A of acetone. Best-fit parameters for the plots are listed in Table 8.1. *Source:* Reproduced from Sangwal and Mielniczek-Brzóska (2017a). Copyright (2017), with permission from Wiley.

As seen from Table 8.1, the calculated values of the thermostated temperature T_0 for both acetone and methanol are in good agreement with the actual value of 303.15 K for fed water and unfed KDP solution systems, but the value of K depends on whether the system is fed or unfed by the antisolvent. For example, the value of K for fed water and unfed aqueous ADP solution systems increases with an increase in R_A, but the value of K for unfed aqueous ADP solution system is much higher than that for the fed water system. In contrast to a constant value of T_0 for the fed water and unfed aqueous ADP solutions, its value somewhat increases with increasing feeding rate R_A for the fed aqueous ADP solutions with acetone and methanol. Moreover, as mentioned above, for the fed aqueous solution system the value of K decreases and even becomes negative with increasing antisolvent feeding rates R_A. These observations of the relationship between K and R_A are discussed below.

8.1.3 Relationship between Constant *K* and Antisolvent Feeding Rate R_A

The increase in the maximum value ΔT_{max} of solution temperature by feeding with an antisolvent increases with its increasing feeding rate R_A. This means that the excess solute concentration Δc created in the solution at time t_{max} by the

antisolvent increases with its increasing feeding rate R_A. Therefore, it can be argued that, even after the cessation of antisolvent feeding at the antisolvent feeding rate R_A, the values of the excess solute concentration Δc is directly related to initial feeding rates R_A of the antisolvent. The higher the initial feeding rates R_A of an antisolvent, the higher is the excess solute concentration Δc, and hence the supersaturation $\ln S$ associated with it, after the cessation of antisolvent feeding at a particular rate. With this idea, following Sangwal and Mielniczek-Brzóska (2017a), we discuss the relationship between the constant K and the antisolvent feeding rate R_A.

The data of the constant $K > 0$ for fed water and unfed aqueous ADP solution systems as a function of antisolvent feeding rates R_A may be analyzed according to the relations:

$$K = K_1 R_A^p, \quad \text{power law}, \tag{8.2}$$

$$K = K_2 \exp\left(-\frac{\lambda}{R_A}\right), \quad \text{exponential law}, \tag{8.3}$$

whereas K_1, K_2, p, and λ are empirical constants. The units of K_1 and K_2 are $s^{-1}(\text{min}\cdot\text{ml}^{-1})^q$ and s^{-1}, respectively, but λ has the units of antisolvent feeding rate R_A. Figure 8.5a and b shows the data of Table 8.1 as plots of $\ln K$ against $\ln R_A$ and R_A^{-1} according to Eqs. (8.2) and (8.3), respectively, with the best-fit parameters given in Table 8.2. Since it is expected that $K = 0$ when $R_A = 0$, using Eq. (8.2) in its original power-law form the $K(R_A)$ data of Table 8.1 were also analyzed with $K = 0$ corresponding to $R_A = 0$. For each system the best-fit parameters of this relation are included in the second row.

From Table 8.2 it may be seen that the values of $\ln K_1$ and p obtained from the power-law form of Eq. (8.2) are somewhat different from those obtained from the plots of $\ln K$ against $\ln R_A$ but these values do not differ substantially from each other. The goodness-of-the-fit parameter R^2 for the best fit of the $K(R_A)$ data by Eqs. (8.2) and (8.3) are similar.

Equation (8.2) is similar to the Nývlt-like relation of the dependence of Δx_{max} on R_A in region (1) of $\Delta T(R_A)$ data associated with the onset of 3D nucleation in aqueous ADP solution by addition of an antisolvent (see Section 6.5) and that the value of the exponent p of Eq. (8.2) is equal to that of $1/m$ in the Nývlt-like relation. The possible reason of equality of $1/m = p$ is that both processes of the onset of 3D nucleation from supersaturated solution in region (1) and cooling of supersaturated solution in region (3) are determined by the diffusion of ions/molecules of solute in the solution volume.

According to the Nývlt-like relation, the value of the antisolvent content Δx_{max} associated with the creation of supersaturation necessary for the onset of 3D nucleation in the solution increases with R_A and involves diffusion of solute and solvent molecules (see Chapter 6). However, according to Eq. (8.2), the resultant value of the available antisolvent content Δx_A at time t_{int} achieved by the feeding of the

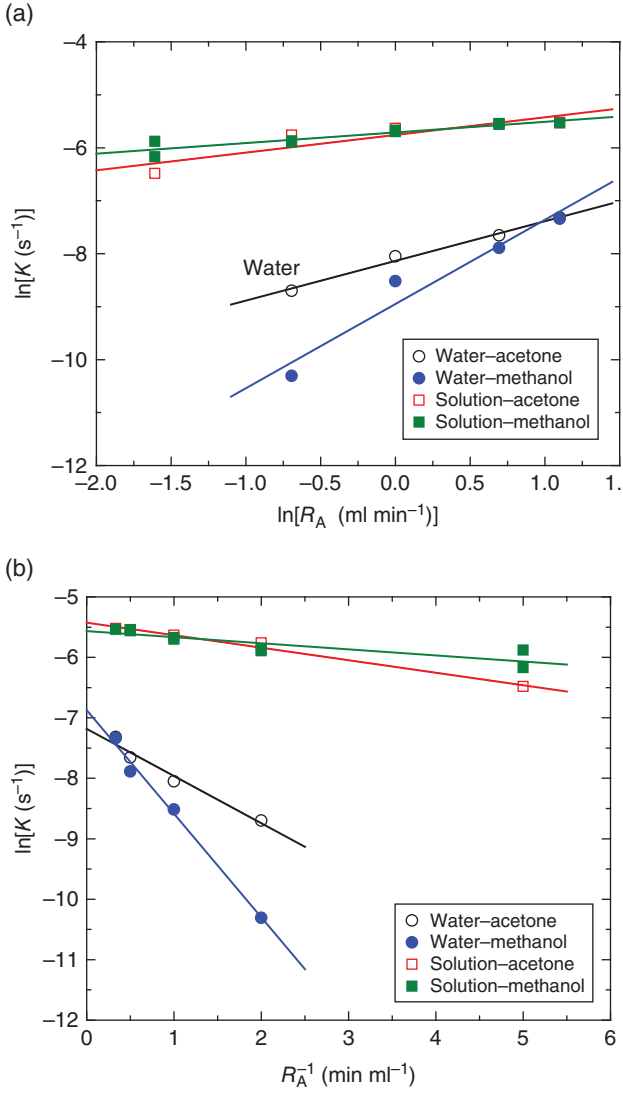

Figure 8.5 Plots of (a) ln K against ln R_A and (b) ln K against R_A^{-1}, according to Eqs. (8.2) and (8.3), respectively, with best-fit parameters given in Table 8.2, for unfed aqueous solution systems containing acetone and methanol. $K(R_A)$ data are from Table 8.1. *Source:* Reproduced from Sangwal and Mielniczek-Brzóska (2017a). Copyright (2017), with permission from Wiley.

Table 8.2 Values of constants of Eqs. (8.2) and (8.3).

	Equation (8.2)			Equation (8.3)				
Sample	$-\ln K_1$	p	R^2	$-\ln[K_2\ (s^{-1})]$	$K_2\ (s^{-1})$	$\lambda\ (ml \cdot min^{-1})$	$E_a\ (kJ \cdot mol^{-1})$	R^2
Solution/ acetone	5.758	0.333	0.7618	5.427	$4.4 \cdot 10^{-3}$	0.207	87.9	0.9884
	5.738	0.261	0.9284					
Solution/ methanol	5.711	0.200	0.8433	5.565	$3.8 \cdot 10^{-3}$	0.100	88.3	0.7257
	5.708	0.195	0.9699					
Water/ acetone	8.136	0.750	0.9846	7.183	$7.6 \cdot 10^{-4}$	0.780	92.3	0.9546
	8.201	0.814	0.9729					
Water/ methanol	8.950	1.591	0.9179	6.871	$1.0 \cdot 10^{-3}$	1.713	91.6	0.9284
	8.720	1.253	0.9870					

Source: Adapted from Sangwal and Mielniczek-Brzóska (2017a).
R^2 denotes R-square fit.

antisolvent at the rate R_A is related to a decrease in the supersaturation created at time t_{int} by diffusion processes. In this case, at time t_{int} the solution has a certain excess solute concentration Δc, and some supersaturation $\Delta c/c_2$ corresponding to it (where c_2 is the equilibrium solute concentration corresponding to a given antisolvent content Δx_A in the solution), which decreases with increasing time t. In fact, this relation between $\Delta c/c_2$ and R_A for time $t > t_{int}$ explains the observed dependence of K on R_A according to Eq. (8.3). This means that K is a jump frequency for the diffusion of ions/molecules in the solution or solvent mixture as defined by the antisolvent feeding rate R_A, whereas λ is the limiting value of the resulting antisolvent feeding rate $R_A \to \infty$ (i.e. $R_A^{-1} \to 0$) when the jump frequency K approaches K_2. Unlike the R_A-dependent jump frequency K, K_2 is independent of R_A. The R_A independence of the limiting jump frequency K_2 implies that the solution or solvent mixture behaves as a homogeneous medium.

If we define an average jump time τ for atoms/molecules to occupy similar positions during their diffusion in a solution or solvent mixture, the jump frequency $K = \tau^{-1}$ and $K_2 = \tau_2^{-1}$, where τ_2 is the limiting jump time for the ions/molecules corresponding to λ. As seen from Table 8.2, τ_2 and λ appear to be mutually related. The higher the value of τ_2, the higher is the value of λ. The difference in the values of K, and the values of limiting jump time τ_2, and the limiting antisolvent feeding rate λ associated with them, for the cooling of solution and solvent is associated with the nature of entities involved in transporting

heat from the solution and the solvent contained in the crystallizer to the thermostating system. These entities are ions and their associates (e.g. pairs, triples, and large ionic clusters) in aqueous ADP solutions, and water and antisolvent molecules in water–antisolvent mixtures (cf. Chapter 3, Bockris and Reddy, 1970).

The antisolvent feeding-rate independent of limiting jump frequency K_2 for the diffusion of ions/molecules in the solution or solvent mixture corresponding to the limiting antisolvent feeding rate λ in Eq. (8.3) on temperature T may be given by (cf. Section 4.4 in Bockris and Reddy, 1970)

$$K_2 = \frac{k_B T}{h_P} \exp\left(- \frac{E_a}{R_G T} \right), \tag{8.4}$$

where h_P is the Planck constant ($h_P = 6.626 \cdot 10^{-34}$ J·s), E_a is the activation energy for the jump, and the gas constant $R_G = k_B N_A$ (the Avogadro number $N_A = 6.0 \cdot 10^{-34}$ mol^{-1}, the Boltzmann constant $k_B = 1.38 \cdot 10^{-23}$ J·K^{-1}, and $R_G = 8.31$ J·mol^{-1}·K^{-1}). With the values of $\ln K_2$ given in Table 8.2 and $\ln(k_B T/h_P) = 29.4737$, one obtains from Eq. (8.4) the corresponding values of the activation energy E_a listed in Table 8.2.

It is found (see Section 6.4 in Bockris and Reddy, 1970) that the activation energy E_D for self-diffusion in molten electrolytes and the activation energy E_η for viscous flow in molecular liquids, molten electrolytes, liquid metals, and liquid inert gases follow the relation:

$$E_{D,\eta} = 3.7 R_G T_m, \tag{8.5}$$

where T_m is their melting point. This relation holds when the diffusion process is controlled by the creation of holes in the liquid due to vibrations of atoms/molecules relative to each other (see Section 6.5 in Bockris and Reddy, 1970). If one assumes that the solvents used here behave as molten salts or molecular liquids, from Eq. (8.5), one expects $E_{D,\eta} \approx 11.5$ kJ·mol^{-1} for solvent water. This value is very low in comparison with those of E_a found from the values of the limiting jump frequency K_2 (cf. Table 8.2). This discrepancy may be attributed to two factors (Section 6.7 in Bockris and Reddy, 1970): (i) our solvent mixtures behave as associated liquids with network structures where diffusion is controlled by the breaking of bonds of the liquid network and (ii) the diffusing entities are not simple ions but their associates.

Finally, it should be mentioned that integration of Eq. (8.1) leads to the general relation:

$$y = y_0[1 - \exp(-kt)], \tag{8.6}$$

where y denotes T, y_0 is the initial value of T_0, k is the rate constant, and dy/dt defines the change in (or production of) y with time t. Equation (8.6) represents first-order reactions in the gas phase and in solution.

8.2 Solvation and Desolvation Processes

After attaining the maximum value of the excess solute concentration Δc by the feeding of an antisolvent at a given rate R_A, as indicated by the maximum temperature T_{max} corresponding to t_{max} (see Figure 8.1), irrespective of feeding or unfeeding of the antisolvent, the excess solute concentration Δc steadily decreases with time. However, beyond t_{max} continuous formation of new 3D nuclei and their growth gives a changing size distribution of crystallites with time. This process continues even in the absence of antisolvent feeding beyond the time t_{int} because these crystallites are endowed with different densities of growth sites (i.e. kinks) and do not represent low-energy growth forms. Beyond $t > t_{int}$ when the solution temperature decreases with the passage of time t, the solution supersaturation steadily decreases with increasing t and finally approaches zero. Under these decreasing supersaturation conditions, different sizes of the crystallites beyond time t_{int} undergo reorganization by dissolution of smaller crystals and transport of ions/molecules by diffusion in the solution from these crystals to deposit on larger crystals. This process leads to a change in the size distribution of crystallites with time as a result of decrease in the free energy of the system. The nature of these free energy decreases is discussed below.

We consider the data of the difference ΔT_{sw} in the solution temperature T_s with respect to the temperature T_w of the solvent water by feeding the antisolvent (i.e. $\Delta T_{sw} = T_s - T_w$) and note that the difference ΔT_{sw} in solution temperature is caused entirely by processes occurring in the solution by the addition of an antisolvent and is associated with solute–antisolvent interactions. An example of typical plots of temperature difference ΔT_{sw} of aqueous ADP solution as a function of feeding duration t of antisolvent acetone at a feeding rate R_A of 3.0 ml·min^{-1} is shown in Figure 8.6.

It may be seen from Figure 8.6 that the $\Delta T_{sw}(t)$ data lie in three regions: Two regions with $\Delta T_{sw} < 0$ (regions of endothermic reactions) and one region with $\Delta T_{sw} > 0$ (region of exothermic reactions). Region 1 lying between t_0 and t_1 is associated with the creation of supersaturation necessary for the onset of 3D nucleation, region 2 lying between t_1 and t_2 is associated with the formation of 3D nuclei and their subsequent growth, whereas region 3 beyond t_2 involves entirely a decrease in the heat energy of the solution. Creation of supersaturation in region 1 and increase in supersaturation by the addition of increasing antisolvent content is responsible for the nucleation and growth of crystallites in region 2. However, growth of larger crystallites at the expense of smaller ones in region 3 is due to the desolvation of solvated solute molecules/ions by antisolvent molecules and, as seen from the nature of the two curves, prolonged feeding of the antisolvent beyond t_{max} leads to an increase in time t_2 and a decrease in the value of ΔT_{min2}. This decrease in ΔT_{min2} with prolonged feeding is associated with a shifted value of t_{int} and, as indicated by a lower value of

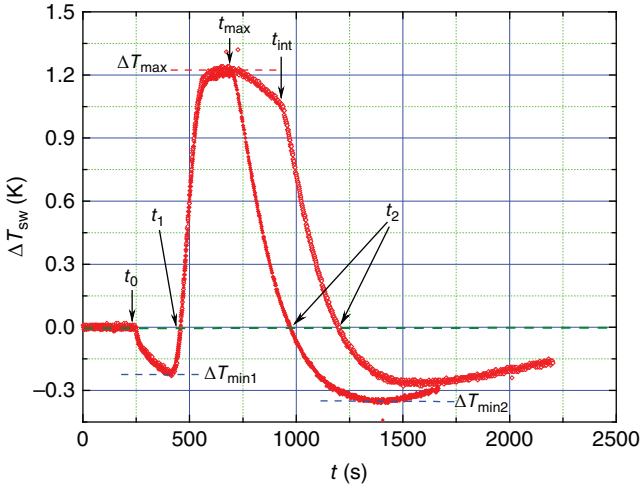

Figure 8.6 Typical plots of temperature difference ΔT_{sw} of aqueous ADP solution as a function of feeding duration t of acetone at feeding rate $R_A = 3.0\ \text{ml·min}^{-1}$. Different times and temperature changes are shown. *Source:* Original data from Sangwal and Mielniczek-Brzóska (2016a).

ΔT_{sw}, with the corresponding initial supersaturation available for the cooling process.

The origin of appearance of minima in the $\Delta T_{sw}(t)$ data of solutions and the kinetics of their evolution are discussed below.

8.2.1 Origin of Minima in $\Delta T_{sw}(t)$ Plots

A change in temperature ΔT_{sw}, whether by endothermic or exothermic reactions, is associated with a change ΔQ_{sw} in heat in the solution of volume V, given by

$$\Delta Q_{sw} = C_V \Delta T_{sw}, \tag{8.7}$$

where C_V is the heat capacity of the solution of volume V. This equation also holds in the case of formation of 3D nuclei and their subsequent growth into crystallites with antisolvent feeding at a particular rate R_A. Then the heat, say ΔQ_{crys}, is evolved and results in the corresponding temperature increase ΔT_{crys} of the solution in the crystallizer. However, in an experimental setup where the crystallizer is thermostated, a certain amount, say ΔQ_{const}, of heat, with a corresponding temperature decrease ΔT_{const}, is steadily withdrawn by the surrounding thermostated water from the heat ΔQ_{crys} of formation of nuclei and their growth in the solution. This means that a change in the temperature

ΔT_{sw} of the solution with increasing addition Δx of the antisolvent results in the evolution of heat ΔQ in the solution of volume V, and may be given by

$$\Delta Q_{crys} - \Delta Q_{const} = C_V \left(\Delta T_{crys} - \Delta T_{const} \right). \tag{8.8}$$

According to Eq. (8.8), three situations are possible: (i) the solution temperature T_s, defined by $(\Delta T_{crys} - \Delta T_{const})$, increases when $\Delta Q_{crys} > \Delta Q_{const}$; (ii) the solution temperature T_s decreases when $\Delta Q_{crys} < \Delta Q_{const}$; and (iii) the solution temperature $T_s = T_{max}$ when $\Delta Q_{crys} = \Delta Q_{const}$. Obviously, the observed nature of the plot of the time dependence of the increase and the decrease, before and after T_{max}, in the temperature T of aqueous saturated ADP solution and of pure water with antisolvent addition at a given rate R_A, as shown in Figure 8.1, is associated with situations (i) and (ii), respectively. Situation (ii) is also encountered after reaching the maximum temperature T_{max} even when antisolvent feeding is continued in the solution (see Figure 8.1).

The process of cooling of solutions and solvents beyond the peak temperature T_{max} is related to the diffusion of ions/molecules present in them. These ions/molecules act as carriers of heat from the crystallizer away to the cooling arrangement. The differences in the values of K in solutions containing antisolvents added at different rates R_A may be attributed to the nature of the species such as ions and molecules diffusing in the volume V of the investigated solutions and solvents. However, it should be remembered that in the case of cooling of a solution containing an antisolvent, Eq. (8.8) holds when the solution composition is not changed during its cooling. This situation is true for solutions containing a certain amount of antisolvent added before at a particular rate R_A until the time t_{int}. The curvature of the plot of T_s against t for a solution is positive and $K > 0$. In contrast to this, beyond T_{max} when the antisolvent is added to aqueous ADP solution at a given feeding rate R_A, additional solute is crystallized as a result of decrease in its solubility in the solution, with simultaneous increase in its temperature due to heat of crystallization. Consequently, depending on the antisolvent feeding rate R_A, the $T_s(t)$ plot shifts to the right with increasing antisolvent feeding time t and begins to assume a negative curvature beyond T_{max}, resulting in $K < 0$. This qualitatively explains the difference in the values of K observed for unfed and fed aqueous ADP solutions.

8.2.2 Kinetics of Evolution of Minima in $\Delta T_{sw}(t)$ Plots

Evolution of minima in the temperature difference $\Delta T_{sw}(t)$ associated with the solvation of solute ions/molecules for the appearance of the first minimum and with the desolvation of ions/molecules of crystallites in the later state for the appearance of the second minimum may be conceived to occur in two ways. In the case of the first minimum, its evolution may be considered to involve replacement of solvent molecules by antisolvent solvent molecules by adsorbing

on the solvated ions/molecules in the solution and a more general approach of occurrence of chemical reactions involving aggregation of solute ions/molecules into 3D nuclei and attachment of ions/molecules in the solution by the addition of an antisolvent. The addition of the antisolvent results in an overall decrease in the heat of the systems by the above processes. In the case of evolution of the second minimum, the system dissipates its heat and tends to attain a low-energy state by processes opposite to those in the first minimum.

If θ is the coverage of solute ions/molecules by the antisolvent molecules at time t, the relative change ΔT_{sw} associated with the solvation of solute ions/molecules by the antisolvent adsorption/desorption may be given by

$$\Delta T_{sw} = \Delta T_{min}(1 - \alpha\theta), \tag{8.9}$$

where α is a parameter characterizing the effectiveness of adsorption/desorption and the coverage θ is described by the usual adsorption isotherms, given by

$$\theta = \frac{K_L \Delta x}{(1 + K_L \Delta x)}, \quad \text{Langmuir isotherm}, \tag{8.10}$$

$$\theta = m\left(\frac{\Delta x}{\Delta x^*}\right)^m, \quad \text{Freundlich isotherm}. \tag{8.11}$$

In Eqs. (8.10) and (8.11), Δx is the antisolvent content in the solution, K_L is the Langmuir constant, the constant m is related to the energy of distribution of adsorption/desorption sites, and Δx^* is the limiting value of Δx when θ approaches unity. The antisolvent content Δx in the solution is related to the evolution duration Δt by $\Delta x \approx R_A \Delta t / V_s$, where V_s is the solution volume and $\Delta t = t - t_0$ with t_0 as the reference temperature when minimum begins to evolve (see Eq. (6.14)).

As described in Section 6.3, the decrease in ΔT_{sw} with the evolution time $\Delta t = t - t_{0,2}$ for the two minima may also be described by the Avrami-type relation:

$$\Delta T_{sw} = \Delta T_{min}\left\{1 - \exp\left[-\left(\frac{t - t_{0,2}}{\Theta}\right)^q\right]\right\}, \tag{8.12}$$

where Θ is a time constant, the exponent $q \geq 1$, and $t_{0,2}$ denotes the times t_0 and t_2 when $\Delta T_{sw} = 0$. Since the evolution time $\Delta t = t - t_{0,2}$ is related to the antisolvent content Δx in the solution, the decrease in ΔT_{sw} is associated with Δx present in the solution and the time constant

$$\Theta \approx \frac{\Delta x_\Theta (V_s + V_a)}{R_A}, \tag{8.13}$$

where Δx_Θ is the antisolvent content corresponding to Θ. Assuming that $\Delta x_\Theta \propto R_A^{-1/3}$ (cf. Nývlt-like approach), from Eq. (8.13), one finds $\Theta \propto R_A^{-2/3}$.

The experimental $\Delta T_{sw}(t)$ data may be analyzed according to the above relations. Analysis of the data showed (K. Sangwal, Unpublished results, 2017) that the former approach is not satisfactory, but the Avrami-type relation (8.12) describes the data satisfactorily. As an example, best-fit plots of the $\Delta T_{sw}(t)$ data of Figure 8.6 for acetone at feeding rate $R_A = 3.0\ \text{ml}\cdot\text{min}^{-1}$ are shown in Figure 8.7 with the values of constants listed in Table 8.3. The values of constants obtained from the reported $\Delta T_{sw}(t)$ data for different antisolvents added at different rates are included in Table 8.3.

From Table 8.3, it may be noted that the exponent $q \approx 1$ at all R_A for the $\Delta T_{sw2}(t)$ data in the three antisolvents and for the $\Delta T_{sw1}(t)$ data in acetone. However, in the case of the first minimum there are situations when q is either lower or higher than 1 and these situations are frequently encountered in methanol. With the feeding of methanol the value of q was about 0.5 at different rates R_A, especially in view of abrupt increase in ΔT_{sw} from the lowest value. Inclusion of more data in the vicinity of this minimum leads to an increase in q, with simultaneous decrease in the value of ΔT_{sw1}. Some examples of this trend may be noted from Table 8.3, where smaller data are given in successive rows.

Equation (8.12) is a different version of the Kolmogorov–Johnson–Mehl–Avrami theory of overall crystallization (Kashchiev, 2000; see Section 3.9) in which the exponent q is an indicator of the type of nucleation, whether instantaneous or progressive, and diffusion processes, and the time constant Θ is related, among others, to the exponent q and the number of nucleation centers N_m during instantaneous nucleation and the nucleation rate J during progressive nucleation. Although Eq. (8.12) describes $\Delta T_{sw1}(t)$ and $\Delta T_{sw2}(t)$ data in

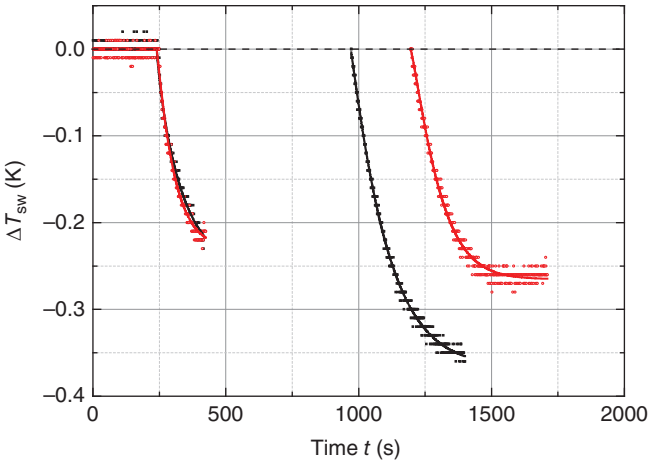

Figure 8.7 Examples of plots of the $\Delta T_{sw}(t)$ data for acetone at feeding rate $R_A = 3.0\ \text{ml}\cdot\text{min}^{-1}$. Values of constants are listed in Table 8.3.

Table 8.3 Constants of Eq. (8.12) for minima 1 and 2 in different antisolvents.

	Minimum 1					Minimum 2				
R_A (ml·min^{-1})	ΔT_{min1} (K)	t_0 (s)	Θ_1 (s)	q (–)	R^2	ΔT_{min2} (K)	t_2 (s)	Θ_2 (s)	q (–)	R^2
Acetone										
3.0	0.265	240	98	0.877	0.992	0.366	970	139	1.077	0.996
	0.229	240	67	1.064	0.991	0.265	1195	114	1.207	0.989
2.0	0.240	240	117	1.163	0.993	0.309	1190	152	1.104	0.993
	0.196	240	113	1.272	0.991	0.298	1133	149	1.095	0.993
1.0	0.132	240	80	0.915	0.977	0.189	1525	202	0.995	0.984
0.5	0.067	240	72	1.559	0.923	0.095	2060	303	0.932	0.920
Ethanol										
3.0	0.409	240	119	1.072	0.996	0.479	1100	131	1.075	0.996
	0.412	240	118	1.004	0.993	0.475	1125	136	1.188	0.996
2.0	0.456	240	323	0.565	0.992	0.408	1203	154	1.149	0.994
	0.377	240	214	0.647	0.993	0.406	1200	164	1.078	0.996
1.0	0.131	240	142	1.275	0.983	0.224	1480	196	1.147	0.984
	0.166	240	131	0.929	0.975	0.249	1445	204	1.189	0.986
0.5	0.073	240	165	1.252	0.955	0.136	2135	312	1.035	0.969
	0.065	240	163	1.327	0.936	0.129	2135	325	1.007	0.965
0.2	0.025	240	171	2.044	0.707	0.048	3070	666	1.099	0.812
Methanol										
3.0	0.324	240	123	1.068	0.996	0.565	977	147	1.094	0.998
2.0	0.297	240	122	0.513	0.995	0.372	1617	173	1.052	0.994
	0.333	240	185	0.474	0.994					
	0.264	240	116	0.623	0.992	0.415	1357	179	1.064	0.996
1.0	0.154	240	209	0.492	0.975	0.237	1770	210	1.087	0.989
	0.126	240	125	0.595	0.962	0.244	1755	201	1.032	0.989
	0.133	240	151	0.566	0.960					
	0.145	240	198	0.539	0.957					
0.5	0.036	240	267	2.317	0.800	0.162	2350	335	0.966	0.974
	0.034	240	246	2.695	0.790					
	0.051	240	135	1.519	0.905	0.153	2460	298	0.981	0.976
	0.051	240	136	1.500	0.909					
0.2	0.027	240	64	1.046	0.698	0.061	3770	419	0.932	0.770
	0.029	240	105	2.062	0.724	0.064	3930	479	0.991	0.646

different antisolvents satisfactorily, it is difficult to attribute the same physical meaning to the exponent q and the time constant Θ in the case of the two data. For example, one finds two different values of q of about 0.5 and 1 for the $\Delta T_{sw1}(t)$ data but a single value of $q = 1$ for the $\Delta T_{sw2}(t)$ data. Similarly, one may attempt to explain the origin of Θ in terms of nucleation centers N_m and nucleation rate J, but the problem of understanding the physical meaning of Θ for the $\Delta T_{min2}(t)$ data remains.

For the $\Delta T_{sw1}(t)$ data, the value of $q = 0.5$ is always accompanied by an abrupt increase in ΔT_{sw} from the lowest value of ΔT_{min1}, but $q = 1$ is observed when ΔT_{min1} occurs for relatively long feeding durations. This means that $q = 1$ and $q = 0.5$ are found from the $\Delta T_{sw1}(t)$ data when 3D nucleation occurs in the system progressively over a long period of feeding of an antisolvent and instantaneously in a short antisolvent feeding span, respectively. For the $\Delta T_{sw2}(t)$ data, however, the value of $q = 1$ indicates the occurrence of progressive growth of larger crystallites at the expense of smaller ones.

With the above information, we discuss the dependence of ΔT_{min1} and ΔT_{min2} and the values of the time constant $\Theta_{1,2}$ on the feeding rate R_A of different antisolvents from consideration of chemical reactions in the aqueous solution involving solute and antisolvent as reactants. Since the exponent q of Eq. (8.12) is unity for the $\Delta T_{sw2}(t)$ data and most of the $\Delta T_{sw1}(t)$, we assume that $q = 1$ in the discussion. Then the form of Eq. (8.12) is similar to that for complex reactions involving decomposition of substance X into two products, say M and N, involving two simultaneous first-order processes, and the formation rate of M is given by (Mortimer, 2008)

$$[M] = \frac{k_M c_{0,X}}{k_M + k_N}[1 - \exp\{-(k_M + k_N)t\}], \tag{8.14}$$

where k_M and k_N are the rate constants of the production of M and N, respectively, and $c_{0,A}$ is the concentration of X at time $t = 0$. Note that the rate of formation of M is related to the initial concentration $c_{0,X}$ of X as well as to the reaction time t. From Eqs. (8.12) and (8.14), one notes that as in Eq. (8.14)

$$\Delta T_{min1,2} = \frac{k_M c_{0,X}}{k_M + k_N}, \tag{8.15}$$

and the time constant

$$\Theta_{1,2} = \frac{1}{(k_M + k_N)}. \tag{8.16}$$

Obviously, the time constant $\Theta_{1,2}$, in reaction kinetics usually called the relaxation time of the process, is related to rate constants k_M and k_N, but $\Delta T_{min1,2}$ depends on rate constants as well as initial concentration $c_{0,X}$ of reactant X. The lower the value of $\Theta_{1,2}$, the faster is the rate of production of M.

Antisolvent crystallization involves the creation of supersaturation as a consequence of replacement (desolvation) of solvated ions/molecules by antisolvent molecules with a change in the heat content of the crystallizing system due to chemical reactions associated with the desolvation processes. Physically, this means that the creation of supersaturation is directly related to the concentration of antisolvent A and the evolution of unsolvated solute ions/molecules and solvent molecules denoted above as M and N, respectively. During the cooling of a supersaturated solution mixture containing crystallites of different sizes, evolution of the size of the crystallites also occurs by desolvation processes and involves the growth of larger crystallites at the expense of smaller ones. Using these concepts the dependence of the two minima and the time constant on the antisolvent feeding rate R_A may be discussed from the standpoint of chemical kinetics.

As seen from Table 8.3, the highest decrease in the values of ΔT_{min1} and ΔT_{min2} increases with an increase in the feeding rate R_A of an antisolvent. The data of ΔT_{min1} and ΔT_{min2} as a function of R_A for different antisolvents are shown as plots of $\ln \Delta T_{min1}$ and $\ln \Delta T_{min2}$ against $\ln R_A$ in Figure 8.8a and b, respectively. Obviously, the data may be represented by the power-law relation:

$$\Delta T_{min1,2} = K_3 R_A^{p^*}, \tag{8.17}$$

where K_3 and p^* are constants. In view of relatively large scatter in the values of ΔT_{min1} for different antisolvents and somewhat small difference in the values of ΔT_{min2} for ethanol from those for methanol and acetone, $\Delta T_{min1}(t)$ data in methanol and $\Delta T_{min2}(t)$ in methanol and acetone were analyzed according to Eq. (8.17). The best-fit constants of the plots for the $\Delta T_{min1}(t)$ and $\Delta T_{min2}(t)$ data shown in Figure 8.8 are listed in Table 8.4.

From Figure 8.8 and Table 8.4, one finds that the exponent $p^* = 1$ for the minimum 1, whereas $p^* \approx 3/4$ for the minimum 2 irrespective of the antisolvent. This suggests that first-order chemical reaction kinetics involving simple desolvation of solute ions/molecules by the antisolvent are followed in the creation of supersaturation involved in the formation of the former minimum 1, but complex chemical reactions involving desolvation and transport processes determine the appearance of the latter minimum 2. However, the value of A is practically independent of the antisolvent in the former case, whereas its value appears to increase in the latter case in the sequence: Acetone, ethanol, and methanol. Since the value of the dielectric constant ε_a of acetone, ethanol, and methanol increases in the above sequence, the above increasing trend of constant A may be attributed to the dielectric constant ε_a of the antisolvent.

The time t_2 corresponding to $\Delta T_{sw2} = 0$ represents the state of a solution composed of crystallites of different sizes immersed in the solvent–antisolvent mixture, but despite $\Delta T_{sw2} = 0$ the solution is not in the minimum energy state. As seen from Table 8.3, the value of t_2 for an antisolvent decreases with

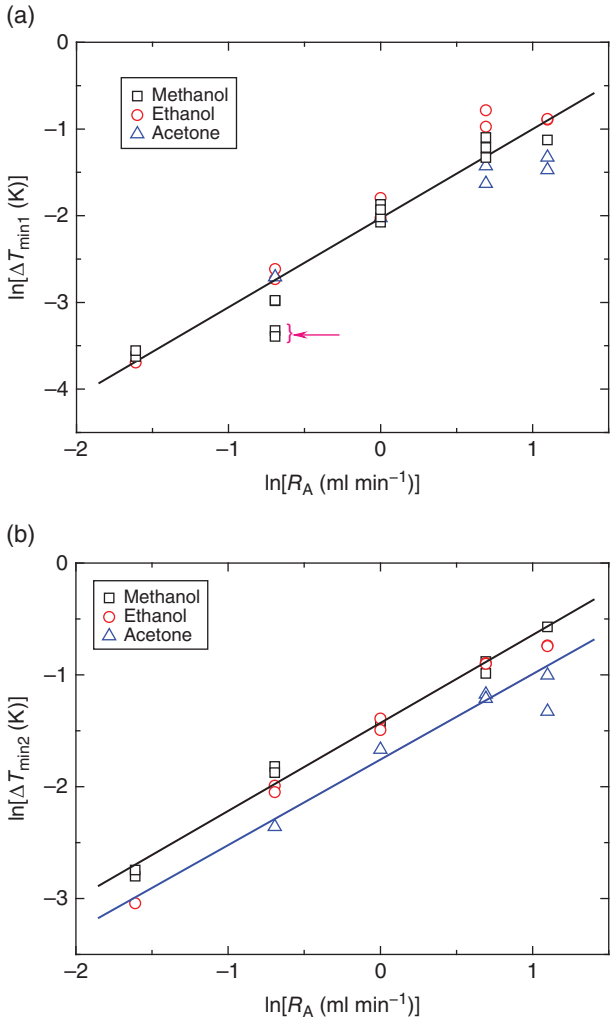

Figure 8.8 Dependence of (a) ln ΔT_{min1} and (b) ln ΔT_{min2} on ln R_A drawn from the $\Delta T_{min1}(R_A)$ and $\Delta T_{min2}(R_A)$ data of Table 8.3. Plots are drawn with the parameters listed in Table 8.4. In (a) two outliers indicated by arrow were excluded from the best fit.

increasing antisolvent feeding rate R_A, whereas for different values of R_A, the value of t_2 increases in the sequence: Acetone, ethanol, and methanol. Physically, these observations mean that the value of t_2 is determined by the antisolvent content Δx in the solution and is associated with the nature of antisolvents used in crystallization. Similarly, the value of the time constant Θ_2 for different antisolvents decreases with an increase in the feeding rate R_A of different

Table 8.4 Constants of Eq. (8.17) for two antisolvents.

	Minimum 1				Minimum 2			
Antisolvent	**lnK_3**	**p^***	**K_3 [K·(min·ml^{-1})^n]**	**R^2**	**lnK_3**	**p^***	**K_3 [K·(min·ml^{-1})^{p*}]**	**R^2**
Acetone					−1.76 ± 0.05	0.77 ± 0.06	0.17	0.973
Methanol	−2.10 ± 0.08	1.094 ± 0.090	0.12	0.9183	−1.43 ± 0.03	0.79 ± 0.03	0.24	0.986

antisolvent and the ratio t_2/Θ_2 for different antisolvents is practically constant equal to 7 for methanol and 6 for ethanol and acetone (see Figure 8.9b). A similarity in the dependence of t_2 and Θ_2 on R_A for different antisolvents is due to the fact that both involve desolvation processes, which are associated with the dielectric constant ε_a of the antisolvents.

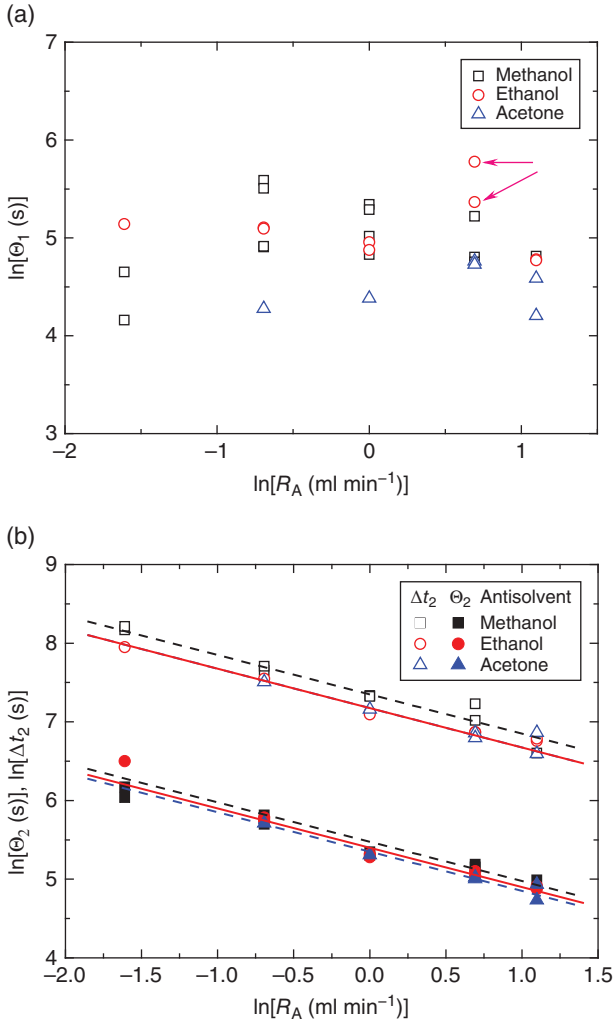

Figure 8.9 Dependence of (a) $\ln\Theta_1$ and (b) $\ln\Theta_2$ and $\ln \Delta t_2$ on $\ln R_A$ drawn from the $\Delta T_{min1}(R_A)$ and $\Delta T_{min2}(R_A)$ data of Table 8.3. In (b) plots for Θ_2 and Δt_2 are drawn with a slope of 0.5, but for Θ_2 with intercepts 5.475, 5.40, and 5.35 for methanol, ethanol, and acetone, respectively, and for Δt_2 with intercepts 7.35 for methanol and 7.175 for both ethanol and acetone.

For the second minima in different antisolvents, the value of time constant Θ_2 decreases with an increase in the feeding rate R_A of different antisolvent, but for the first minima, no clear relationship between Θ_1 and R_A is evident. Figure 8.9a and b shows the experimental $\Theta_1(R_A)$ and $\Theta_2(R_A)$ data from Table 8.3 in the form of plots of $\ln\Theta_1$ and $\ln\Theta_2$ against $\ln R_A$, respectively, according to Eq. (8.13). As predicted by Eq. (8.13), if the data for $R_A = 0.2\ \mathrm{ml{\cdot}min^{-1}}$ are not considered, the time constant Θ decreases with increasing R_A. The slope is about 0.5 for plots of $\ln\Theta_2$ against $\ln R_A$ (Figure 8.9b) and less than 0.1 for plots of $\ln\Theta_1$ against $\ln R_A$ (Figure 8.9a). In contrast to an expected slope of about 2/3 according to Eq. (8.13), the values of the observed slope are low, especially in the case of the $\Theta_1(R_A)$ data. However, the observed values of the slope may be understood in terms of rate constants of Eq. (8.14).

8.3 Evolution of Desupersaturation Curves

In Section 8.1, the evolution of desupersaturation curves of aqueous supersaturated ADP solutions containing acetone and methanol antisolvents was discussed from consideration of their cooling behavior of the solution taking temperature as a measure of solution supersaturation. However, in closed isothermal systems, as in the case of industrial crystallization, different physical methods are used for the measurements of supersaturation involving estimates of solute concentration in the solution. These systems also contain substances other than the crystallizing solute such as inherent impurities (i.e. by-products or foreign compounds) present in them or intentionally added additives, which affect the overall yield of the crystallizing product as well as the shape, size, and polymorphic phase of the crystallites in a crystallization run. However, during a crystallization run the supersaturation of the solution decreases with the duration of crystallization. In this section the evolution of supersaturation of solutions without and with selected additives is described employing the concepts presented above.

Figure 8.10 shows, as an example, desupersaturation data of aqueous KDP solutions without and with ethylene diamine tetraacetic acid (EDTA) and potassium pyrophosphate (KPY) additives. The original data were obtained by Qu et al. (2006) for solutions of three initial supersaturation ratios S_0 equal to 1.103, 1.083, and 1.063 at a temperature of 26 °C without and with additives. Desupersaturation was initiated by adding 1 g seeds of size between 50 and 75 μm to solutions prepared by adding appropriate amounts of additives and KDP mixed with 2500 g water in 3-l crystallizers. The data may be described satisfactorily using the relation:

$$S = S_{\mathrm{lim}} + S_1 \exp\left[-\left(\frac{t}{\Theta}\right)^q\right], \tag{8.18}$$

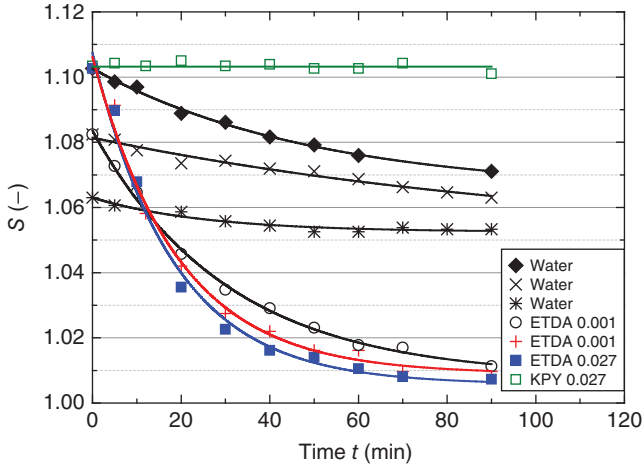

Figure 8.10 Desupersaturation curves of aqueous KDP solutions without and with EDTA and KPY. *Source:* Original data from Qu et al. (2006).

where S_{lim} is the limiting value of S for $t \rightarrow \infty$, the constant $S_1 = S_0 - S_{lim}$, Θ is a time constant, and the exponent $q = 1$. Values of constants of Eq. (8.18) for the plots of the data are given in Table 8.5. In the table S_0 denotes the original supersaturation ratio S.

Figure 8.11 shows another example of desupersaturation curves in cooling crystallization of aqueous borax solutions at different impeller speeds ω. The curves are based on the experimental data of solubility c_0 and excess solute concentration Δc, measured in mmol·l^{-1}, of borax reported by Akrap et al. (2010). The crystallization experiments were carried out in a 2-l flat-bottomed crystallizer at a constant cooling rate of 6 K·h^{-1}. The crystallizer was equipped with a

Table 8.5 Constants of Eq. (8.18) for supersaturated KDP solutions.

S_0 (–)	Additive	c_i (m)	S_{lim} (–)	S_1 (–)	Θ (min)	R^2
1.103			1.065	0.0377	49.7	0.9945
	EDTA	0.001	1.009	0.0973	19.2	0.9884
	EDTA	0.027	1.006	0.1017	18.4	0.9979
	KPY	0.027	1.104	0		
1.083			1.049	0.0326	113	0.9613
	EDTA	0.001	1.008	0.755	30.5	0.9967
1.063			1.052	0.105	25.3	0.9321

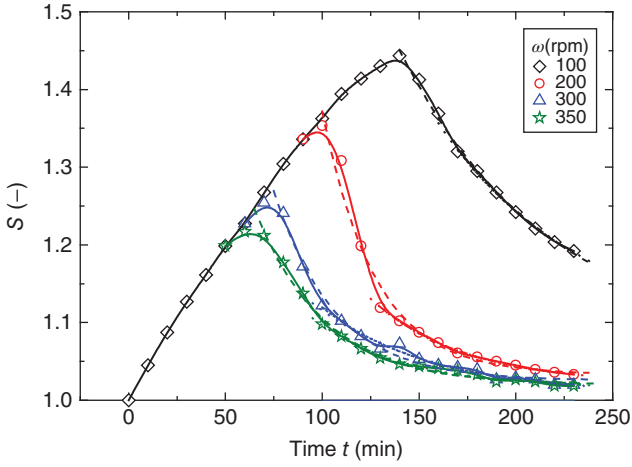

Figure 8.11 Desupersaturation curves of cooling crystallization of aqueous borax solutions at different impeller speeds. Plots of desupersaturation data covering the entire and low S regions according to Eq. (8.18) are shown by dashed and dotted curves. *Source:* Original data from Akrap et al. (2010).

stirrer, a solute concentration monitor, and a programmable temperature controller. At time $t = 0$, the crystallizer is filled with a just-saturated solution, which is supersaturated at the constant cooling rate. With increasing cooling duration, the supersaturation increases and reaches the metastable zone width, defined by S_{max} that corresponds to the induction period t_{in}, when 3D nucleation sets in and crystallites begin to form by the growth of the nuclei. Since the overall surface area of these crystallites increases with time, the supersaturation is consumed by them until it approaches the final value of S_{lim}.

The experimental data of the supersaturation decrease with cooling time for different stirring rates ω were analyzed according to Eq. (8.18) taking t as the effective desupersaturation duration beyond the induction period t_{in} for the occurrence of crystallization. The data of two effective desupersaturation durations were analyzed in the entire desupersaturation duration covering 3D nucleation and growth of crystallites, and in the desupersaturation duration covering only the growth of the crystallites. The topmost point representing the maximum supersaturation ratio S_{max} of occurrence of 3D nucleation and the topmost three points probably still affected significantly by continued nucleation, in the supersaturation interval $S_0 < S < S_{max}$, were omitted in the former and latter cases, respectively. Since the experimental data in the two desupersaturation regions with a variable q and a fixed $q = 1$ gave essentially the same value of the best-fit R^2 parameter, the data were analyzed with $q = 1$. The values of the supersaturations S_{max} and S_0 representing desupersaturation

Table 8.6 Constants of Eq. (8.18) for supersaturated borax solutions.

S_{max} (–)	ω (rpm)	t_{in} (min)	t_{ig} (min)	S_0 (–)	S_{lim} (–)	S_1 (–)	Θ (min)	R^2
1.44	100	140	140	1.44	1.074	0.376	75.4	0.9955
			160	1.37	1.080	0.276	75.7	0.9973
1.35	200	100	100	1.35	1.033	0.339	27.4	0.9754
			130	1.12	1.021	0.099	47.9	0.9978
1.25	300	80	80	1.25	1.025	0.208	31.2	0.9836
			100	1.12	1.007	0.109	60.9	0.9672
1.22	350	60	60	1.22	1.020	0.197	36.1	0.9929
			90	1.14	1.015	0.101	46.4	0.9835

$S(t)$ data for the analysis and the best-fit constants of the plots for different stirring rates ω are listed in Table 8.6. Corresponding to particular stirring rate are the best-fit constants of the plot in the entire and partial desupersaturation regions listed in the table in the first and second rows, respectively. Values of the induction period t_{in} for the occurrence of crystallization and the initial time t_{ig} of desupersaturation duration covering presumably only the growth of the crystallites corresponding to different stirring rates ω are also included in the table.

Desupersaturation curves of Figures 8.10 and 8.11 differ from each other in the manner the maximum supersaturation S_{max} is created in the two cases. The initial supersaturation in KDP solutions was achieved by their rapid cooling to the predefined temperature of 26 °C and their desupersaturation was initiated by adding seeds. The supersaturation in borax solutions was produced by cooling solutions saturated at a predefined temperature at a constant cooling rate and their desupersaturation was initiated by using different stirring speeds ω. Obviously, desupersaturation of the KDP solutions is caused by the growth of seeds, whereas that of the borax solutions by the formation of 3D nuclei and their subsequent growth into crystallites. However, as seen from Tables 8.5 and 8.6, the same value of the exponent $q = 1$ in Eq. (8.18) for different seeded KDP solutions and for unseeded borax solutions suggests that desupersaturation in these solutions is essentially associated with growth. The desupersaturation curves for borax solutions also covers the data of low supersaturation regions of ripening of crystals of different sizes (Ostwald ripening; see Section 3.9), but these low-supersaturation data somewhat deviate from the best-fit plots and lie above them. This low S region is characterized by lower values of S_1 and higher values of Θ than those obtained for the entire desupersaturation regions (see Table 8.6). Stirring of borax solutions leads to the occurrence of 3D nucleation with a lower induction period t_{in} at a lower S_{max}

(Figure 8.11) and is caused by heterogeneous 3D nucleation. However, in the case of desupersaturation of seed systems, stirring is expected to induce secondary nucleation.

The following features may be noted from Tables 8.5 and 8.6:

1) The constant S_1 shows a tendency to decrease with a decrease in the initial solution supersaturation ratio S_0 or S_{max} in pure aqueous solutions of both KDP and borax. The constant S_1 denotes the value of excess solute concentration created in the system by desupersaturation of the solution from S_0 or S_{max}.
2) The value of S_1 increases with an increase in the concentration c_i of EDTA additive but its value decreases in KPY additive.
3) The value of the time constant Θ shows a tendency to decrease with a decrease in S_0 and with an increase in ETDA concentration c_i. This trend is clearly seen from borax solutions, which shows that the time constant Θ is about $t_{in}/2$.

The former two features are associated with the effect of initial supersaturation S_0 and nature and concentration c_i of an additive added to the solution of solute on the metastable zone width of the solution and is directly related to nucleation and growth processes. The last feature is associated with an increased value of the constant k of occurrence of reactions involved and the reactions are facilitated by the stirring of solutions.

It should be mentioned that chelating agents such as EDTA are known to coordinate with cations in solutions of solutes like KDP and ADP or of the surfaces of these crystal, forming complexes and thereby render cationic impurities ineffective as catalysts for heterogeneous nucleation and growth of crystals. This results in the widening of metastable zone width of these systems and promoting their growth. Consequently, additives like EDTA lead to an increase in both growth rate and final yield of KDP crystals in batch crystallization (Qu et al., 2006). In contrast to EDTA, KPY additive acts as a strong inhibitor for crystal growth. Therefore, it shows a poor desupersaturation tendency for KDP solution. Due to the strong inhibiting behavior of KPY, it may be used as a stabilizer of particle size in batch crystallization (Qu et al., 2006).

When $q = 1$, Eq. (8.18) follows from the rate of change of supersaturation, dS/dt, in the form of Eq. (8.1), i.e.

$$\frac{dS}{dt} = -\frac{(S - S_{lim})}{\Theta}, \tag{8.19}$$

where the actual supersaturation S corresponding to time t and the lowest attainable supersaturation S_{lim} now replace T and T_0, respectively, and $1/\Theta$ replaces K. Thus, a relationship between solution temperature T and its supersaturation S is obvious. Both equations may be expressed in the form of relation (8.6).

It may be noted that, if one considers the decrease in supersaturation with time as a chemical process, this process is of the first-order. Relations similar to Eq. (8.19) have been used for the analysis of crystal growth kinetics from desupersaturation data (Nývlt et al., 1985). Desupersaturation curves similar to those of Figure 8.10 have also been reported before for the growth of α polymorph of L-glutamic acid and acetylsalicylic acid (ASA) on previously-prepared seeds added to aqueous and ethanolic solutions, respectively (Cornel et al., 2009; Lindenberg et al., 2009), but similar to those of Figure 8.11 for the nucleation and growth of ASA from cooling crystallization from ethanolic solutions (Lindenberg et al., 2009). In these latter studies, the data of desupersaturation curves were modeled using estimated parameters of known theoretical or semiempirical expressions for nucleation and growth kinetics together with population balance equations. For the description of the overall growth rate R of crystallizing phase, the theoretical expression of birth-and-spread model has been used (see Chapter 3). However, for the 3D nucleation rate J, theoretical expressions of the classical theory of 3D nucleation and simple power law have been employed (Chapter 2). In the case of combined cooling/antisolvent crystallization, the following semiempirical expression for the overall growth rate has been used (Lindenberg et al., 2009):

$$R = k_1 \exp\left(-\frac{k_2}{R_G T}\right)[c_0(S-1)k_3], \tag{8.20}$$

where k_1, k_2, and k_3 are empirical constants that have to be determined from experiments and c_0 is the initial solubility.

Note that the creation of supersaturation in borax solutions with cooling time in Figure 8.11 before the occurrence of nucleation deviates progressively from the initial linear dependence and may be approximated by a power-law dependence: $S = S_2 t^n$, with S_2 and n as empirical constants. The deviation from the expected linear dependence indicates that $n < 1$. A trend similar to that of Figure 8.11 may be noted from the $S(t)$ plots for ASA from ethanol solutions of temperatures 25, 35, and 45 °C, but the exponent $n > 1$ at 25 °C, $n = 1$ at 35 °C, and n is somewhat lower than unity at 45 °C. This implies that the deviation from the expected linear relationship depends on solution temperature and may be caused by processes associated with interactions between solute molecules in the solutions with increasing solute concentration.

8.4 Crystal Morphology

The external form (growth habit or macromorphology, or simply growth morphology) of a freely growing crystal is a polyhedron bound by faces of various surface areas. The rates R of displacement of different faces (called face growth

rates or normal growth rates) determine the final growth morphology. To predict the growth morphology, it is assumed that the growth rates of the faces are proportional to perpendicular distances from the center of the crystal. This also implies that the morphological importance (i.e. surface area) of different faces is proportional to their growth rate. Therefore, slow-growing faces appear in the morphology at the expense of fast-growing faces.

There exists a relationship between morphology and structure of crystals. The first attempts to describe the morphology of crystals were formulated in terms of surface free energy per unit area (see Hartman, 1973; Sunagawa, 1987; Toschev, 1973). The surface free energy is calculated by using Periodic Bond Chains, Connected Nets, or Donnay–Harker analysis of a series of faces likely to be present in the morphology (Grimbergen et al., 1998; Meekes et al., 1998). In these cases, the morphology of a polyhedral crystal is determined on the postulate that the surface free energies per unit area of different faces of the polyhedron are proportional to their perpendicular distances from the center of the crystal.

The equilibrium morphology obtained from relative surface free energies of different faces composing a polyhedral crystal is frequently different from the steady-state growth morphology obtained from relative growth rates of different faces. This difference is due to the fact that the normal growth rate R of a face is determined by the structure of crystal–medium interface where growth entities are incorporated into the crystal and depends on growth kinetics (i.e. on supersaturation, temperature, impurities, and mass and heat transport processes).

Figure 8.12 illustrates two different growth morphologies of a crystal composed of two types of faces, namely F{1} and F{2} faces. Let us consider that

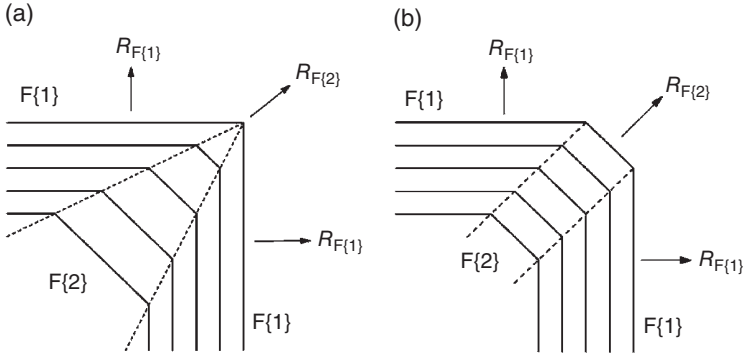

Figure 8.12 Schematic illustration of the difference in the development of F{1} and F{2} faces lying in the same zone in terms of their relative displacement rates under different growth conditions, leading to the (a) elimination and (b) persistence of F{2} face in the growth habit: (a) $R_{F\{1\}} < R_{F\{2\}}$ and (b) $R_{F\{1\}} > R_{F\{2\}}$.

F{2} faces are S faces and F{1} are F faces. In the former case, because of a relatively high density of kinks in comparison with that of the F faces, the S faces are eliminated in the final growth form (Figure 8.12a). In the latter case, the S faces appear when their displacement rate is reduced due to, for example, hindered supply of solute ions/molecules to them from the bulk solution or hindered removal of solvent molecules released from the solvated solute ions/molecules away from the crystal–medium interface into the bulk solution (Figure 8.12b). Consequently, depending on the supersaturation available on the surface of a polyhedral crystal composed of two types of faces for their growth, morphology of the growing crystal can undergo a change. Figure 8.13 shows the change in the morphology of a crystal composed of two types of flat faces F{1} and F{2} growing according to the BCF mechanism. Obviously, the crystal is bounded by F{1} faces below σ_1, by F{2} faces above σ_2, and by both F{1} and F{2} faces for $\sigma_1 < \sigma < \sigma_2$.

While explaining the growth morphology changes in Figure 8.13, it was implicitly understood that the two types of faces remain smooth during the whole supersaturation interval. In fact, in view of this smooth nature of the interface, the BCF parabolic law was used. However, as described in Section 3.3, a smooth interface may become rough with an increase in supersaturation. Thus, depending on the nature of the crystal–medium interface and the corresponding growth mechanisms, different modifications in the growth morphologies of a crystal may be anticipated.

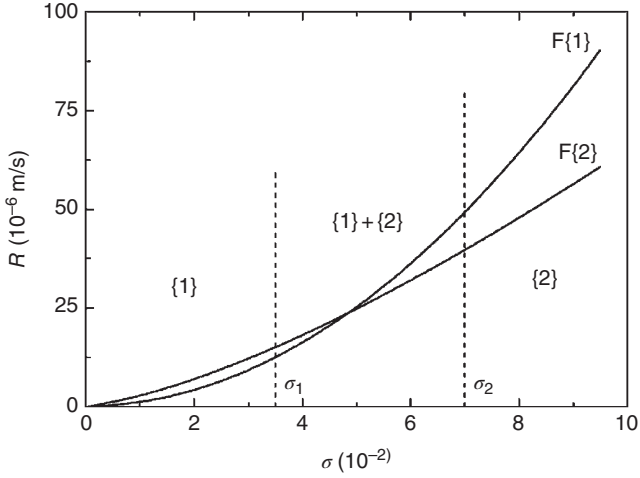

Figure 8.13 Growth morphology of a crystal composed of F{1} and F{2} faces in relation to supersaturation. Polyhedra {1} and {2} composed of F{1} and F{2} faces are formed at low and high supersaturations, respectively.

Evolution of the morphology of individual crystals growing freely from solutions with supersaturation may be correlated with crystal growth processes (Sunagawa, 1981, 2005), as illustrated in Figure 8.14. Above σ^{**}, the interface is rough and continuous (linear) growth occurs. Here, crystals take dendritic to spherulitic morphology with increasing supersaturation. Below σ^{**}, the interface is smooth and growth is possible by BCF or a two-dimensional nucleation mechanism. In the region below σ^{*}, the BCF mechanism predominates and F faces grow by the outward motion of growth layers originating from dislocations. In this case, an individual crystal takes a polyhedral morphology bounded by flat faces. In the supersaturation region $\sigma^{*} < \sigma < \sigma^{**}$, growth by the two-dimensional nucleation mechanism predominates the BCF mechanism. Since the probability of occurrence of two-dimensional nucleation is more near the edges of faces, growth layers will advance inward from edges and a hopper (skeletal) morphology will be produced.

It should be mentioned that growth from solution and vapor phases involves transport of crystallizing entities to the face of a crystal. Consequently, the supersaturation available on the surface may be smaller than that in the bulk of the medium. In growth controlled by reactions and transport on a smooth surface (i.e. surface-diffusion controlled growth), the supersaturation on the surface approaches the bulk supersaturation, while in growth controlled by volume diffusion in the medium the supersaturation on the surface is lower than in the bulk. This supersaturation change also results in a supersaturation difference on the surface such that the supersaturation is the highest at edges and corners of the face, and is the lowest at the center of the face (Berg effect).

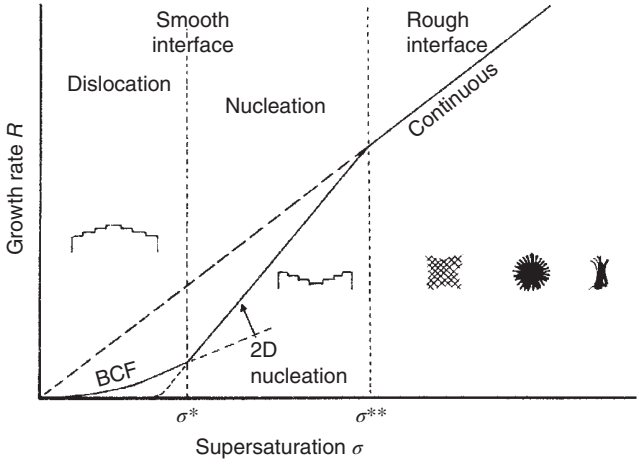

Figure 8.14 Schematic representation of the dependence of growth rate *R* on supersaturation σ for different growth mechanisms. *Source:* After Sunagawa (1981).

Hopper growth of freely developing faces at high supersaturations and on faces in contact with the bottom of a crystallizer in solution growth even at moderate supersaturations is a consequence of this effect.

Experiments on the growth of crystals on self-nucleated seeds always show a large number of faces in the initial stage of growth. On prolonged growth some of the faces disappear while others grow in size, finally resulting in a steady-state growth morphology. It is also observed that, even when the crystals are sufficiently large and the final morphology is close to the steady-state morphology, new faces appear while the already-present faces disappear during their subsequent growth. According to the phenomenological approach of determination of growth morphology from relative growth rates of different faces, this type of changes in the growth morphology of crystals is caused by changes in growth conditions (i.e. on supersaturation, temperature, impurities, and mass and heat transport processes). Therefore, depending on the extent of fluctuations in growth conditions, some faces of the crystal may disappear, some other faces appear, while still others simply remain present in the growth morphology. Conversely, since the evolution of growth morphology of crystals depends on growth rates, the above phenomenological concept that fast-growing faces disappear while slow-growing faces appear in the morphology still applies to predict the growth morphology.

Understanding of the causes of appearance and disappearance of faces during the evolution of crystal morphology has drawn considerable interest (Gadewar and Doherty, 2004; Prywer, 2005; Rohl, 2003). These studies revealed that: (i) the morphological importance of a face A depends not only on its normal growth rate R but also on the growth rates of its neighboring faces 1 and 2 and on the angles that the normal to the face A makes with the normals of faces 1 and 2, and (ii) geometry of the initial seed used has a strong influence on the evolution of the growth morphology of crystals.

Growth morphology of crystals may be determined by using connected net analysis carried out in two steps (Bennema, 1993; Grimbergen et al., 1998; Meekes et al., 1998). First, direct chains are identified from the crystal structure as a sequence of strongly bonded possible growth units on the projection of different faces, and then from the direct chain surface graphs containing connected nets are found in the planes of these projections. In the case when individual growth units do not form direct parallel chains in a plane, one takes pairs of growth units lying in a particular direction to form the basic growth units.

The general trend of the evolution of the morphology of crystals, discussed above, is observed for all crystallizing systems but the difference lies in the transition values of supersaturations σ^* and σ^{**}. The polyhedral morphology of a crystal bounded by flat faces appears at supersaturations below σ^* when the growth rates of different faces are determined by the density of growth sites (kinks) available on them for the integration of growth units. Depending on

the structure of faces of crystals, defect structure, and growth environment (including solvent used for preparing solution for growth), the final morphology can be platy, polyhedral, elongated polyhedral, and needle-like. At high supersaturations, needle-like and elongated polyhedral morphologies are commonly observed for organic compounds, whereas large spherulites formed by the aggregation of smaller spherulites composed of small crystals are formed for inorganic compounds like calcium carbonate. However, platy crystals are produced at low supersaturations. These trends are also observed in several cases when two polymorphs of a compound grow from their saturated solution when supersaturation is created by its rapid cooling (Kitamura et al., 2008; Srinivasan and Dhanasekaran, 2011; Sudha and Srinivasan, 2013), by drowning-out crystallization (Jim and Kim, 2012) or by adding solution of one of the reactants to that of another reactant at a constant rate during reactive crystallization (Andreassen, 2005; Kile et al., 2000; Kitamura, 2001).

Solvents are known to have a strong influence on the growth morphology of crystalline materials (Algra et al., 2005; Boistelle, 1980; Salvalaglio et al., 2013; Weissbuch et al., 2001). The role of solvents is associated with the constitution of their molecules, which affect the growth rates of different faces appearing in the crystal morphology differently. The effect of a solvent on growth rates of different faces is associated with selective adsorption of solvent molecules on them. The effect of solvent on growth rates can be explained by two approaches (Weissbuch et al., 2001). The first approach considers change in the interfacial energy due to interactions between solvent and crystal molecules of the growing crystal face. An increase in the interfacial energy leads to a decrease in the growth rate, while a decrease in the interfacial energy to an increase in the growth rate. In the second approach, it is the difference in the removal of solvent molecules adsorbed on the faces of a crystal, which determines the growth rates of different faces of the crystal and its growth morphology. In this case, the face, where solvent molecules are more strongly adsorbed than on other faces, will grow more slowly than those where the solvent molecules are less strongly adsorbed.

Growth of *n*-alkanes (such as *n*-$C_{36}H_{74}$) from aliphatic solvents such as pentane, heptane, and decane (Boistelle, 1980) is an interesting example of the effect of solvents. The solubility of *n*-alkane in each of these solvents is roughly the same, but the growth rate of the {110} faces of *n*-alkane crystals decreases drastically with increasing chain length of the solvent. The decreasing growth rate with increasing chain length of the solvents is due to the increasing adsorption energy of solvent molecules on the crystal surface as a result of van der Waals interactions.

Another example of the solvent-induced change in growth morphology is the organic compound alizarin (1,2-dihydroxy-9,10-anthraquinone), which crystallizes as long needles from the vapor and organic solvents like acetone, acetonitrile, hexane, toluene, and acetic acid, while flat triangular-shaped crystals are

produced by alcohols like ethanol, methanol, and propanol (Algra et al., 2005). Here, the morphology change is not caused by the direct interaction of solvent molecules with the crystal surface itself, but by the interaction of partially deprotonated alizarin molecules by the solvent. This example demonstrates that a solvent can also play an indirect role in changing the morphology of a crystal. The solvent changes the structure of the solute molecules, which subsequently adsorb on several faces of the crystal, thereby blocking their normal growth.

From an examination of the morphology of urea crystals from solutions in different solvents and from solutions containing biuret additive, Salvalaglio et al. (2013) concluded that the role of solution phase in the growth morphology can be computed from molecular simulations in which solvent, solute, and the presence of an additive are taken into account. These authors demonstrated that for the prediction of crystal morphology, the ratio between the growth rates of different faces can be estimated quantitatively from the surface free energy profiles associated with the growth of successive layers employing the transition state theory and Langmuir adsorption isotherm.

Figure 8.15 shows, as an example, the needle-like morphology of metastable A form and prismatic morphology of stable B form of BPT isobutyl ester (BPT: 2-(3-cyano-4-(2-methylpropoxy)-phenyl)-4-methyl-thiazole-5-caboxylic acid) obtained from cyclohexane solution of initial concentration of 30 mM by rapid cooling crystallization. These polymorphs were identified after crystallization periods of 100 and 900 min, respectively, and involves drop in concentration in two steps associated with the solution-mediated transformation of the metastable A form into the stable B form.

Figure 8.16 shows another example of change in the size and morphology of calcium carbonate particles for two different addition rates of concentration $c = 0.05$ and $0.2\ \text{mol}\cdot\text{l}^{-1}$ of sodium carbonate solutions to calcium chloride solutions of the same concentration. In the photographs, prismatic crystals are stable calcite form while spherulites are metastable vaterite form. From Figure 8.16, the following features may be noted:

1) The larger spherulites of vaterite are formed by the aggregation of smaller spherulites composed of small crystallites.
2) With an increase in solution concentration from 0.05 to $0.2\ \text{mol}\cdot\text{l}^{-1}$, the proportion of vaterite spherulites having relatively smooth surfaces increases while the crystal size decreases (see Figure 8.16a and c).
3) The vaterite spherulites are irregularly shaped at high solution concentration and small addition rate (Figure 8.16d), and their size is smaller than that at small addition rate (see Figure 8.16b and d).

The above features are associated with: (i) Crystallization of metastable form and its subsequent transformation to stable form in accordance with Ostwald rule of stages and (ii) occurrence of secondary nucleation favored by addition of solution of one of the reactants to the other at low rates.

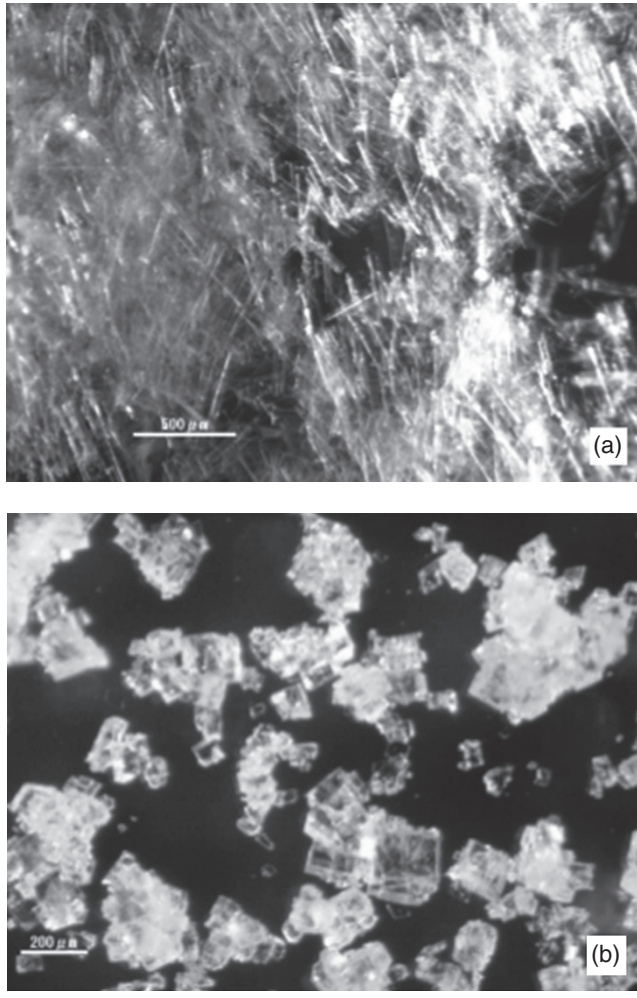

Figure 8.15 (a) Needle-like morphology of metastable A form and (b) prismatic morphology of stable B form of BPT isobutyl ester obtained from cyclohexane solution. *Source:* Reproduced from Kitamura et al. (2008). Copyright (2008), with permission from Elsevier.

The final product in a crystallization run is a resultant of a variety of simultaneously occurring processes involving: (i) formation and growth of stable nuclei of metastable form, (ii) aggregation of nuclei, (iii) transformation of a metastable phase or polymorph into a stable one, and (iv) Ostwald ripening. However, processes of formation of stable nuclei and their subsequent growth may be complex. For example, the presence of trace amounts of unintentional

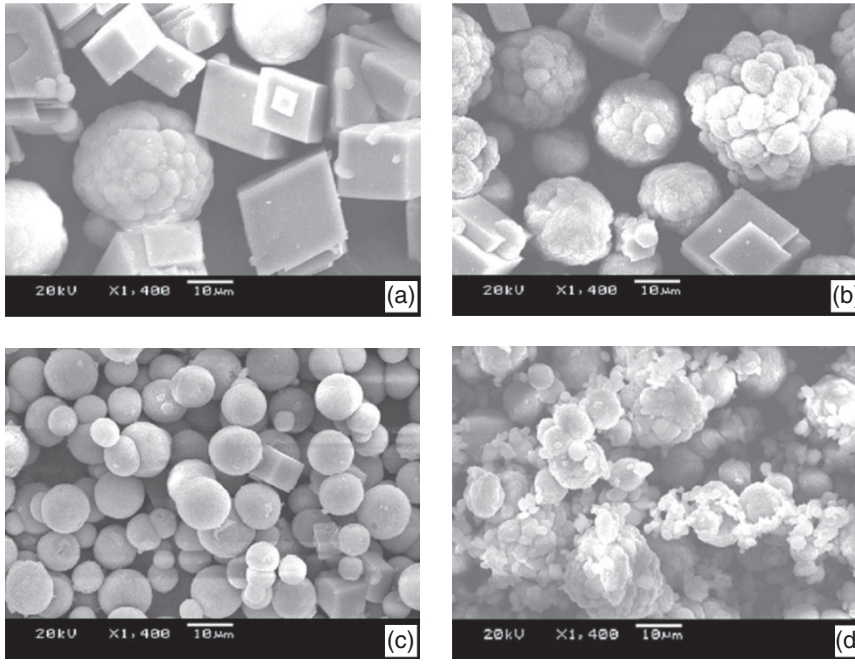

Figure 8.16 SEM photographs of calcium carbonate particles obtained by addition of sodium carbonate solutions to calcium chloride solutions at different addition rates: (a and c) 5 mol·s^{-1} and (b and d) 0.05 mol·s^{-1}. Concentration of reactants: (a and c) 0.05 mol·l^{-1} and (b and d) 0.2 mol·l^{-1}. *Source:* Reproduced from Kitamura (2001). Copyright (2001), with permission from Elsevier.

impurities may lead to heterogeneous nucleation, while the presence of the already growing crystals in a crystallization run may lead to secondary nucleation. Similarly, depending on the growth conditions, the kinetics of growth of the crystals may be controlled by volume diffusion or surface reactions and may determine their shape, average size, and quality.

Distribution of crystal size in terms of crystallization conditions and evolution of CSD with time are important topics in industrial crystallization. Therefore, the processes that determine CSD and its evolution are briefly described below.

8.5 Growth Rate Dispersion

For larger crystals size-dependent growth is possible when the density of dislocations participating in growth increases as the crystal size increases. Thus, larger crystals growing by the BCF surface diffusion mechanism will grow faster

than smaller crystals (see Section 3.6). It is also possible that smaller crystals are devoid of dislocations, but with an increase in their size, dislocations are developed in their growing surface. In this case, smaller crystals growing by two-dimensional nucleation will grow at a lower rate than larger crystals that grow by the BCF surface diffusion mechanism. This results in the final product composed of crystals of different sizes.

Crystals of different sizes are frequently observed in mass crystallization, and this phenomenon is usually referred to as *growth rate dispersion*. By this term, one understands that crystals of the same size and material exposed to identical conditions of supersaturation, temperature, and hydrodynamics do not necessarily grow at the same rate. This is not the same as size-dependent growth in which crystals of different sizes grow at different rates.

Two different mechanisms are known to explain growth rate dispersion. The first mechanism considers a distribution of growth rates for the crystal population for given growth conditions but each individual crystal grows at a constant rate. This means that at steady-state conditions, nuclei are formed with a distribution of growth rates and two nuclei in a crystallizer grow at constant but different rates. Crystal fragments produced by attrition, and secondary nuclei and single crystals produced by primary nucleation show this behavior. According to the second mechanism, all crystals have the same time-averaged growth rate, but the growth rates of individual crystals can fluctuate significantly with time. This means that two different crystals growing under identical conditions can have different growth rates at any time but their time-averaged growth rate over a long time period remains the same.

Growth rate dispersion is usually explained from the standpoint of the BCF theory of crystal growth. According to the BCF theory, the growth rate of a crystal depends on the density of dislocations emerging on the growing surface. A higher density of screw dislocations leads to a higher growth rate. Collisions of growing crystals with the impeller, crystallizer walls, and each other cause damage to them, resulting in new dislocations during growth. This type of behavior is especially expected for crystals grown by secondary nucleation.

The growth rate of a crystal can also increase with an increase in the density of edge dislocations (see Section 3.6). According to Frank (1981), an edge dislocation always has a region compressed on one side and dilated on the other side of the site of its emergence on the surface. This causes compressive and tensile stresses in the vicinity of the edge dislocation. Therefore, irrespective of whether the surface stress is compressive or tensile, the region near the emergence point of a dislocation is always more favorable than the unstrained surface for the formation of a surface nucleus. There are other experimental evidences of changes in the growth rate of crystals due to the inherent presence of internal strain in them or due to the externally applied stresses on them (Bhat et al., 1987). The latter may be introduced in crystals during their grinding to obtain seeds of desired dimensions. In the initial stage of growth of these seeds, lattice strain

is also developed at their newly formed interface. The degree of strain depends on the nature of the original damage and the rate of refacetting. The strain may be released plastically by the formation of dislocations or it may be retained. The dislocations so formed can contribute to the growth process and enhance the growth rate in proportion to the number of dislocations so formed. Elastic strain always leads to a reduction in the growth rate. Thus, differences in the distribution of dislocations and strain in different crystals can lead to growth rate dispersion. A measure of the overall lattice strain, irrespective of its origin, is the mosaic spread of a crystal (van der Heijden and van der Eerden, 1992). Therefore, crystals with large initial size, having smaller mosaic spread, are expected to have a high growth rate R and vice versa. Ristic et al. (1988) observed that the growth rate R of crystals is inversely proportional to their mosaic spread η.

Investigation of the dependence of growth rates R of different crystals on the initial crystal size L shows a general increasing tendency and several empirical functions have been proposed to describe the experimental $R(L)$ data (Mitrović et al., 2000). In the case of constant growth rates of crystals, it seems that their growth rate R increases linearly with crystal size L.

8.6 Ostwald Ripening

Crystallization from supersaturated solutions under isothermal conditions occurs as a result of 3D nucleation and growth of the solid phase. Consequently, the final product is a mixture of solid particles of different sizes contained in the solution. Thermodynamically, this particulate ensemble is not a state of minimum Gibbs free energy because it represents an excess surface energy configuration according to the relation:

$$\mathrm{d}G = -S\mathrm{d}T - V\mathrm{d}p + \sum \mu_{\mathrm{i}}\mathrm{d}n_{\mathrm{i}} + \gamma \mathrm{d}A, \tag{8.21}$$

where S, T, V, and p are the entropy, temperature, volume, and pressure of the system, respectively, n_{i} is the number of i species, μ_{i} is their chemical potential, and γ and A are the surface free energy and the area of the solid particle. At the given T, V, and p conditions, the system tends to achieve the minimum energy state by an increase in the size scale of the crystalline particles, thus decreasing their total interfacial area A. Ideally, this evolution would lead to a single particle (or crystalline aggregate) containing the entire volume fraction of the solid phase. This evolution of the distribution of the size L of solid particles driven by excess surface energy is called *Ostwald ripening* or *coarsening*.

Decrease in the interfacial area A associated with its reaching the thermodynamic equilibrium is accompanied by particle coarsening because the solubility of particles in the system changes as a function of their size

L by the Gibbs–Thomson (also called Ostwald–Freundlich) relation (see Figure 3.8a, and Eq. (3.19a):

$$\ln\left(\frac{c(L)}{c_0}\right) = \left(\frac{4\gamma\Omega}{k_B T}\right)\frac{1}{L} = \frac{\kappa}{L}, \tag{8.22}$$

where $c(L)$ is the solubility of the spherical particle of diameter L, c_0 is the solute concentration at a plane interface in the system in equilibrium with particle of infinite radius (i.e. equilibrium solubility), and Ω is the molecular volume. In Eq. (8.22), the *capillary length* κ combines different parameters of the particles. For crystals of nonspherical shape, one takes into account area and volume shape factors k_A and k_V such that the factor 4 is replaced by $2k_A/3k_V$. Since ripening occurs at low supersaturations S, using the approximation $\ln[c(L)/c_0] \approx [c(L) - c_0]/c_0$, one gets

$$c(L) = c_0\left(1 + \frac{\kappa}{L}\right). \tag{8.23}$$

Obviously, the solubility of crystalline particles depends on their size L and results in a difference in supersaturation as a function of particle size L.

According to Eq. (8.23), smaller particles will be at a lower supersaturation than larger particles. The difference between $c(L)$ and c_0 induces a diffusive flux of ions/molecules from smaller to larger particles. If mass transport between the particles in the ensemble occurs by volume diffusion and the kinetics of transport process are first order, the change in particle size with time is

$$\frac{dL}{dt} = \frac{2D\Omega[c - c(L)]}{L}, \tag{8.24}$$

where c is the average bulk solution concentration; from Eq. (8.23), one has

$$\frac{dL}{dt} = \frac{2D\Omega}{L}\left\{[c - c(L)] - \frac{\kappa c_0}{L}\right\}, \tag{8.25}$$

with $c > c_0$ during crystallization. When the system is in equilibrium, $dL/dt = 0$ and there is a critical size

$$L^* = \frac{\kappa c_0}{c - c(L)}. \tag{8.26}$$

All particles smaller than L^* will dissolve and all particles larger than L^* will grow by the transfer of the dissolved mass. Consequently, not only the total free surface enthalpy decreases with time (see Eq. ((8.21)) but also the average size of the particles increases and their total number decreases with time. However, during decreasing supersaturation in a closed system of an initial supersaturation $S = c/c_0$, larger crystals appear by the growth of critically-sized 3D nuclei formed earlier than the nuclei formed later, i.e. only the former crystals survive at the expense of the latter during the ripening process.

For diffusion-controlled growth kinetics, the linear growth rate is given by (for example, see Mullin, 2001)

$$\frac{dL}{dt} = \frac{8D\Omega\kappa c_0}{3L^2}, \tag{8.27}$$

which, on integration gives

$$L = (8D\Omega\kappa c_0 t)^{1/3}. \tag{8.28}$$

Since ripening occurs at low supersaturation, it is possible that the process is controlled by surface reaction instead of volume diffusion. In this case, the linear growth rate (also see Section 3.7)

$$\frac{dL}{dt} = R_g(c - c_0)^p, \tag{8.29}$$

where R_g is a growth rate constant and the exponent p lies between 1 and 2. When $p = 2$ as in growth occurring at screw dislocations, one finds (Mullin, 2001)

$$L = 2\left(\frac{\kappa c_0 R_g^{1/2}}{4}\right)^{2/3} t^{1/3}. \tag{8.30}$$

Equations (8.28) and (8.30) for the ripening process controlled both by bulk diffusion and surface reaction predict that the smaller the particle size L, or the higher the solubility c_0 and interfacial energy γ, the faster is the ripening process. It should be noted that Ostwald ripening of particles is a case of size-dependent growth, but this mechanism becomes important when the crystal size is smaller than about 1 μm.

It was mentioned above that Ostwald ripening may be attributed to first-order chemical reactions, which are statistical processes described by exponential functions like Eq. (8.14) characterized by reaction constants k and related time constants $\Theta = 1/k$. In fact, Eq. (8.14) represents a distribution function expressing the fraction of M molecules formed by the decomposition of A molecules at time t as $\exp[-(k_M + k_N)t]$. This function gives the average life-time for the survival of a molecule, given by

$$t_{av} = \frac{\int_0^\infty t\exp(-kt)dt}{\int_0^\infty \exp(-kt)dt,} \tag{8.31}$$

where $k = (k_M + k_N)$.

Several theories have been proposed to describe Ostwald ripening where their main aim is to determine how the solid phase particles grow with time. A ripening theory is expected to explain the observations that the average size of the particles in the system increases and their number decreases with time.

Therefore, the quantities of interest in different theories are the particle size distribution function $f(L,t)$, the average particle size $L_{av}(t)$, and the total number $N(t)$ of particles. All of the theories consider the ripening process as first-order phase transition and predict the following growth law:

$$L_{av}(t) = \left[L_{av}^3(0) + K(y)t\right]^{1/3}, \tag{8.32}$$

where $L_{av}(0)$ is the average particle size when $t = 0$ and $K(y)$ is the ripening rate, which is a monotonically increasing function of the volume fraction y. The particle-size distribution function is given by

$$f(L,t) \propto \frac{g(z,y)}{L_{av}^{d+1}}, \tag{8.33}$$

where $z = L/L_{av}$, d is the dimensionality of particles, and the $g(z)$ distribution.

$$\int_0^{z_{max}} zg(z)\mathrm{d}z = 1. \tag{8.34}$$

Equation (8.34) is a consequence of the fact that the variable z defines the value of the average L_{av} (see Eq. (8.31)).

Baldan (2002) has reviewed different theories up through 2001 and compared their predictions with the experimental data for superalloys. According to him, the so-called LSEM theory, advanced by Davies et al. (1980), is superior to other theories in predicting the experimental particle size distribution in metallic alloys. The main postulate of this theory is that, when a significant amount of the solid phase is present during the ripening process, interaction between the diffusion fields around neighboring particles may bring their surfaces closer causing them to coalesce. In this situation the diffusion field of larger particles dominates over that of smaller particles, thus resulting in the rapid dissolution of the latter and their coalescence with the former. The coalescence of particles somewhat increases the growth rate of larger particles and broadens the particle size distribution, but the rate of change of the mean particle size remains proportional to the cube-root of the ripening time.

The main limitation of different theories of ripening is that all of them predict negative skewness of particle size distribution but the experimental results show a positive or a less skewness. This is a result of the role of finite volume fractions of the crystallized solute on the ripening behavior of two-phase systems. This means (Baldan, 2002) that volume fraction effects alone, as considered in the theories of Ostwald ripening, are not sufficient for the interpretation of particle size distribution.

Based on Gibbs–Thomson relation between particle size and solubility to describe size-dependent growth rate, Iggland and Mazzotti (2012) recently presented a population balance model for Ostwald ripening. In this work the effect of parameters, such as average initial particle size, initial width of particle size

distribution, and initial particle mass as well as their solubility in the continuous phase, on the ripening behavior of particles were studied. These authors found that the initial conditions have a strong influence on the initial stages of the ripening process, and that small size of particles, large variation in their size, low mass of particles, and their high solubility in the continuous phase lead to a reduction in the time of ripening of a population of particles.

A general feature of the CSD due to Ostwald ripening is the approaching of a universal steady-state shape having a negatively skewed shape irrespective of its initial shape. A steady-state shape represents a constant shape of the CSD when plotted on reduced axes denoted by normalized density $n_{rel} = n/n_{max}$ of density n of crystals of size L to the maximum density n_{max} and the ratio $L_{rel} = L/L_{av}$ of sizes of crystals (Kile et al., 2000). Figure 8.17 shows the data of normalized density n_{rel} as a function of normalized size L_{rel} for five experiments on calcium carbonate (both calcite and vaterite) crystals obtained by rapidly mixing Ca^{2+} and CO_3^{2-}, resulting in working solutions with supersaturation levels $S > 100$, involving initial S_0 lying between 106 and 3090 and average size L_{av} of crystals lying between 8.5 and 28.1. Experimental data (Sample CCP-4) of continued growth of previously Ostwald ripened crystals obtained by adding seed crystals of another Ostwald ripened crystals to a supersaturated solution (Sample

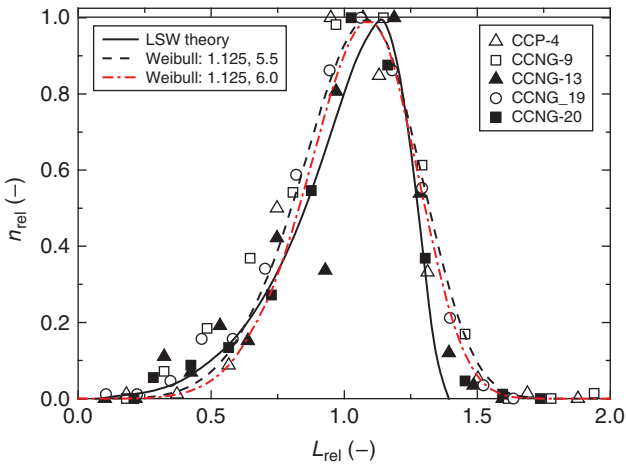

Figure 8.17 Normalized density n_{rel} as a function of normalized size L_{rel} for five experiments on calcium carbonate crystals obtained by rapidly mixing Ca^{2+} and CO_3^{2-}, resulting in working solutions with supersaturation levels $S > 100$. Universal steady-state curve represents the diffusion-controlled Ostwald ripening according to the LSW theory, while dashed and dotted curves are drawn according to Weibull relation (8.43) with $L_\Theta = 1.125$ and $q^* = 5.5$ and 6. *Source:* Original data from Kile et al. (2000).

CCNG-19) are also shown in Figure 8.17. The reduced shape of the CSD for the crystals of Sample CCP-4 remained constant but the mean size increased from 8.5 to 10.6 μm, implying that supply-controlled growth followed Ostwald ripening. The universal steady-state curve represents the diffusion-controlled Ostwald ripening according to the LSW theory (Lifshitz and Slyozov, 1961; Wagner, 1961).

It may be seen from Figure 8.17 that the universal curve representing the diffusion-controlled Ostwald ripening does not cover the data of normalized $L_{rel} > 1.4$. However, the normalized CSD data may equally be described by Weibull relation (8.42) with the normalized average crystal length L_{Θ} equal to 1.125 and the exponent q^* lying between 5.5 and 6. Since the exponent $q^* = q(1 - b)$ and, according to the KJMA theory (see Section 3.8), the maximum value of the constant q is 2.5 and 4 for diffusion and surface-controlled crystallization, respectively, for a typical value of $q^* = 6$, one finds that the parameter b is −1.4 and −0.5, respectively. Obviously, irrespective of the control of crystallization whether by diffusion or surface reactions, the parameter $b < 0$.

8.7 Crystal Size Distribution

The successful crystallization of a material on a large scale is intimately connected with the size, shape, and size distribution of material particles due to various reasons. Small mean size of crystals causes problems of their centrifuge, wash, and package. In some cases, a wide range of the size of product crystals ensures a variation in time for their dissolution. Therefore, understanding of the genesis of size and size distribution of crystals is of scientific and practical importance.

Several approaches have been advanced to model CSD, which may be divided into three categories, namely: (i) size-dependent growth approach, (ii) population balance approach, and (iii) balanced nucleation-growth approach. The former two approaches are described below, but for the balanced nucleation-growth approach, the reader is referred to Leubner (2000, 2002, 2010). For more details on the population balance approach and its modified versions, the reader is referred to Berglund (1993, 2002), Randolph and Larson (1988), and Mersmann (2001).

Different shapes of CSD observed in various experiments carried out under a variety of conditions are shown in Figure 8.18 (Kile et al., 2000). They are:

1) Asymptotic CSD, in which the frequencies of the sizes of crystals in a growth run are greatest in the smallest size range and exponentially decrease with increasing size (Figure 8.18a). This shape has been traditionally discussed in the population balance approach.
2) Log-normal CSD, in which the logarithms of the crystal sizes are normally distributed, but the curve has a positive skew towards larger sizes in the plots of logarithm of frequencies of sizes against crystal size (Figure 8.18a).

3) Ostwald ripened CSD, usually referred to as universal steady-state shape, in which a negative skew in the plots of frequencies of sizes against crystal size is towards smaller sizes (Figure 8.18b).
4) Bimodel CSD, in which two peaks of usually unequal height appear at two crystal sizes (Figure 8.18b).

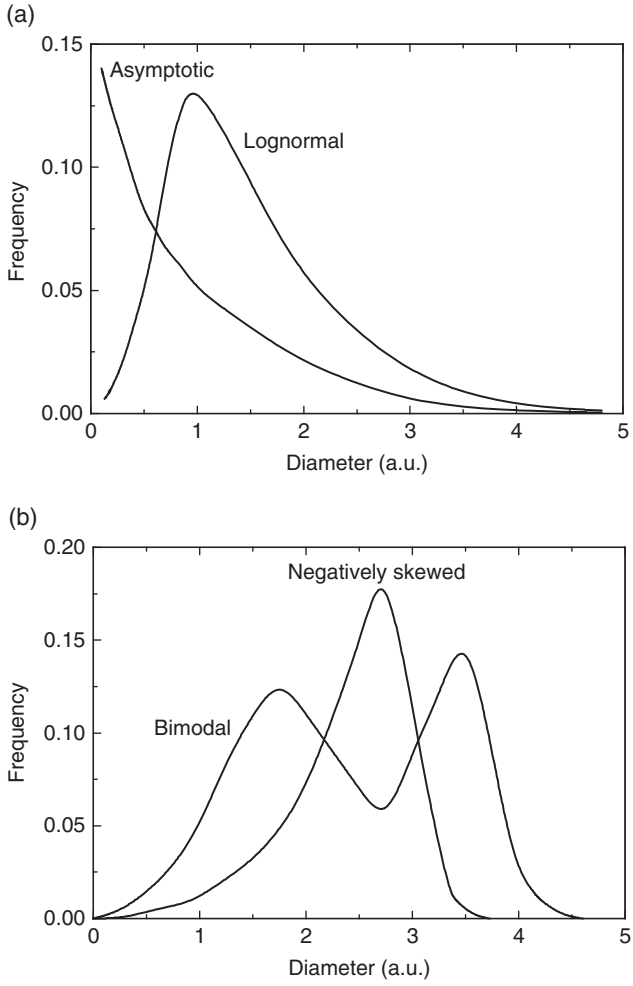

Figure 8.18 Four basic shapes of experimental CSDs observed under a variety of conditions: (a) asymptotic and log-normal CSDs and (b) negatively-skewed and bimodal CSDs. *Source:* Adapted from Kile et al. (2000).

Kile et al. (2000) employed the Law of Proportionate Effect, LPE, to explain different CSDs obtained in the experiments of crystallization of calcium carbonate (both calcite and vaterite) crystals obtained by mixing Ca^{2+} and CO_3^{2-} (reactive crystallization). According to this law, the rate of growth is proportional to linear size times a random number, thereby making growth rate size dependent. LPE leads to size-dependent growth in two regimes: (i) Surface-controlled and (ii) supply-controlled growth. In the former regime, the growth rate is limited by deposition of solid on the crystal surface and not by the rate of reactant supply to the crystal surface. This growth results in an exponential increase in mean crystal size L_{av} and a linear increase in the variation in crystal size L. The growth rate R of individual crystals is governed by its size L_j and a variable ε_j lying between 0 and 1, such that the value of the crystal size is evenly distributed:

$$L_{j+1} = L_j + \varepsilon_j L_j. \tag{8.35}$$

Iteration of growth according to the above equation with time predicts a log-normal CSD, which implies that LPE growth requires an exponentially increasing amount of nutrients as growth is continued.

In the surface-controlled LPE growth, crystals are subjected to size-dependent growth (during which larger crystals tend to grow faster) as well as to crystal size dispersion (during which crystals of the same initial size may grow at different rates). Both of these processes are represented by the $\varepsilon_j L_j$ term in Eq. (8.35), where L_j manifests size dependence whereas the ε_j range manifests size dispersion. In the supply-controlled regime, however, the crystals show a smaller tendency for size dispersion (i.e. a narrower ε_j range). This leads to a decreasing growth rate with increasing mean size and to a constant variation in size. Therefore, though size-dependent growth continues during supply-controlled growth, there is poor tendency for growth size dispersion, and the growth rate $dL/dt \approx kL$.

In contrast to growth by surface- and supply-controlled LPE, according to the growth theories linear growth rate dL/dt = constant. This is corroborated by McCabe's law, which states that geometrically similar crystals in the same solution grow at the same rate. Physically, this means that the absolute differences in the sizes of the crystals are maintained as growth proceeds and the variation in their size diminishes with time.

According to Kile et al. (2000), during the crystallization of calcite/vaterite at 25 °C, asymptotic and log-normal CSDs are developed when the growth rate is proportional to their linear size and growth is surface controlled. An asymptotic CSD develops when there is a decay in the rate of formation of nuclei or new nuclei are added to a growth system at a constant rate. This means that nucleation gradually subsides while previously nucleated crystals continue to grow, and the nature of the CSD curve depends on the duration of growth following nucleation. The authors obtained asymptotic CSD in the calcite growth

experiments when additional reactants were added stepwise to the surface of solutions that were supersaturated with respect to calcite (initial $S = 20$). However, a log-normal CSD results when the amount of reactants increases exponentially but due to their limited supply growth becomes mass transport controlled. This CSD is positively skewed. This CSD occurs when reactants are added continuously below the solution surface, via a submerged tube, to similarly supersaturated solutions (initial supersaturation ratio S between 22 and 41), leading to a single nucleation event followed by surface-controlled growth. In contrast to the above CSDs, negatively skewed shape of CSD is produced by diffusion-controlled Ostwald ripening where smaller crystals dissolve to provide materials for the growth of larger crystals. The Ostwald CSD results when concentrated reactants are rapidly mixed, leading initially to high supersaturation ($S > 100$). The bimodal CSDs are produced as a consequence of two distinct nucleation events, which are possible due to two reasons: (i) Addition of one of the reactants to the initially supersaturated solution is carried out twice and is separated by a time interval, rather than adding continuously (Kile et al., 2000) and (ii) nucleation and ripening of one phase, followed by dissolution of the first phase and nucleation and ripening of another more stable phase.

The population balance approach was proposed by Randolph and Larson (1988) to predict the product CSD from a continuous stirred tank reactor (abbreviated as CSTR; also referred to as continuous mixed-suspension mixed product removal crystallizer; MSMPR) under steady-state conditions. The important assumptions involved in this model are the following:

1) CSD is the same as that found within the crystallizer.
2) The particles are formed only by nucleation and increase in size occurs by growth.
3) There is no breakage, attrition, and agglomeration of growing particles.
4) The growing particles have the same shape.

According to the population balance approach, if the crystallization system under consideration follows McCabe's law that growth rate $R \neq R(L)$, the population density $\mathrm{d}n$ in the size range between L and $L + \mathrm{d}L$ is given by

$$\frac{\mathrm{d}n}{\mathrm{d}L} = \frac{n}{R\tau}, \tag{8.36}$$

where n is the population density at size L and τ is the retention time equal to the reaction volume V divided by the flow rate R_F. Integration of Eq. (8.36) gives

$$n = n_0 \exp\left(-\frac{L}{R\tau}\right), \tag{8.37}$$

where n_0 is the population density for zero-sized crystals. Thus, according to Eq. (8.37), a plot of $\ln n$ against L predicts a straight line with intercept $\ln n_0$

and slope $(1/R\tau)$, from which one can calculate the growth rate R for the known value of τ.

Figure 8.19 illustrates the plots of ln n against L for two different sets of experimental data reported for a sucrose–water system in MSMPR crystallizers by Belter et al. (1988) and Berglund and de Jong (1990). It may be seen that the data of Belter et al. (1988) are well described by Eq. (8.36), but a single growth rate distribution is insufficient to explain the data of Berglund and de Jong (1990). In the latter case, a combination of two growth rates (i.e. the sum of two exponentials) is necessary to describe the data. It is interesting to note that the experimental data obtained in the two studies agree well for L smaller than about 0.4 mm. In fact, a strong upward curvature at smaller sizes of about 0.1 mm is observed in many cases in the plot of ln n against L (Berglund, 1993, 2002).

The strong upward curvature, as seen in curve 2 in Figure 8.19, has been attributed to size-dependent growth, growth rate dispersion, and agglomeration (Berglund, 1993). In the case of size-dependent growth, the following empirical dependence of growth rate R on crystal size L is assumed (Abegg et al., 1968):

$$R = R_0(1 + fL)^b, \tag{8.38}$$

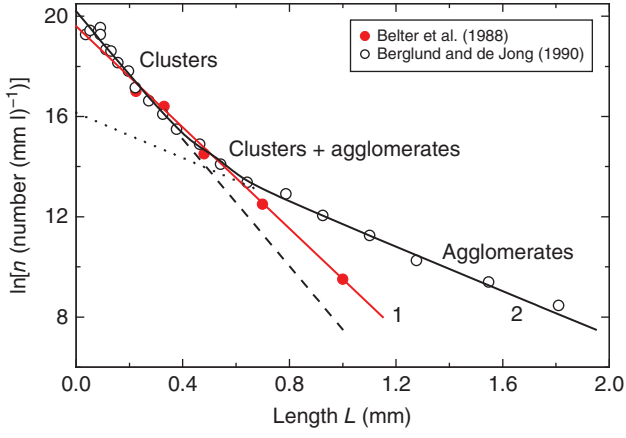

Figure 8.19 Plots of ln n against L for two different sets of experimental data for the sucrose–water system in MSMPR crystallizers. Note that data represented by filled circles (curve 1) can be fitted by a single growth rate distribution (i.e. in Eq. (8.37) one value of R), while data denoted by open circles (curve 2) requires two growth rate distributions (i.e. the sum of two exponentials). *Source:* Adapted from Berglund (1993). Copyright (1993), with permission from Elsevier.

where the empirical constants $f > 0$ and $b < 1$. Then from the population balance, the following $n(L)$ dependence is obtained (Abegg et al., 1968; Berglund, 1993, 2002):

$$n(L) = K_2 n_0 (1 + fL)^{-b} \exp\left\{ -\frac{(1 + fL)^{1-b}}{R_0 \tau f (1-b)} \right\}, \tag{8.39}$$

where $K_2 = \exp[1/R_0 \tau f(1 - b)]$ and $b < 1$. Obviously, when $f = 0$, there is no size-dependent growth and the situation corresponds to that given by Eq. (8.38). Moreover, as expected from Eq. (8.39), the upward curvature is obtained when $0 < b < 1$.

When growth rate dispersion occurs, the overall population balance yields an $n(L)$ relation, which gives a linear plot of $\ln n$ against L with a large mean size than that predicted from the growth rate (Berglund, 1993). Agglomeration also results in a curvature similar to that found in size-dependent growth and growth rate dispersion (Hartel and Randolph, 1986). Agglomeration is commonly observed during the precipitation of proteins without intentionally added impurities and several ionic compounds both without as well as in the presence of additives (see Figure 8.16). According to this approach, a higher slope at smaller size L is due to the growth of isolated clusters, while a smaller slope at larger size is caused by agglomerates. The regions of clusters and agglomerates are shown in Figure 8.19. However, Glatz et al. (1986) reported that agglomeration and breakup can lead to the appearance of a local maximum in the plots of $\ln n$ against L.

Several mathematical functions have been suggested to describe cumulative and differential CSDs, $N(L)$ and $n(L)$, respectively (for example, see: Mullin, 2001; Nývlt et al., 1985). They are: Normal, log-normal, and gamma-function distributions. Merits and demerits of different distribution functions are discussed in the above literature. The main requirement for the use of a universal mathematical function is to explain at least the observed first three CSDs, i.e. asymptotic, negatively skewed, and positively skewed CSDs. The traditional population balance approach does not explain the CSDs.

In recent years, population balance equations in combination with CSD and different process parameters are frequently employed to model different crystallization processes such as transformation of polymorphs (Caillet et al., 2007; Cornel et al., 2009; Fevotte et al., 2007), combined cooling/antisolvent crystallization (Lindenberg et al., 2009), and Ostwald ripening (Iggland and Mazzotti, 2012). However, theoretical models based on population balance equations are unable to describe Ostwald ripening and nucleation simultaneously, because the 3D nucleation models assume a constant critical nucleus size, whereas Ostwald ripening models require supersaturation dependence of the critical nucleus size. A model that takes into account the processes of nucleation, growth, and ripening is based on kinetic rate equation. Vetter et al. (2013)

investigated a comprehensive model of the processes of nucleation, growth, and Ostwald ripening based on kinetic rate equation and compared its findings with the models based on population balance equations.

It a common observation that the dependence of overall crystallization y (expressed in mass of crystallized solid) on time t of a large number of systems can be represented by an Avrami-type relation:

$$F(t) = \frac{y(t)}{y_0} = 1 - \exp\left\{ -\left(\frac{t}{\Theta}\right)^q \right\}, \tag{8.40}$$

where $F(t)$ denotes the fraction of the total crystallizable mass y_0, and q and Θ are constants (see Section 3.8). Assuming that the growth rate $R = \mathrm{d}L/\mathrm{d}t$ follows the relation: $\mathrm{d}L/\mathrm{d}t = R_0 L^b$, one may write the relation between crystal size and t in the form:

$$t = AL^{1-b} \tag{8.41}$$

where A is a constant, $b < 1$, and the initial crystal size $L = 0$ is when $t = 0$. According to Eq. (8.41), growth rate R is time independent when $b = 0$, increases when $b > 0$, and decreases when $b < 0$. The deviation of b from zero indicates whether growth conditions facilitate or inhibit growth. Growth is facilitated when $b > 0$ but it is inhibited when $b < 0$.

Replacing t and Θ in Eq. (8.40) using (8.41), one obtains the Weibull distribution function:

$$F(L) = \frac{N(L)}{N_{\max}} = 1 - \exp\left\{ -\left(\frac{L}{L_\Theta}\right)^{q^*} \right\}, \tag{8.42}$$

and its differential distribution function:

$$\frac{\mathrm{d}F(L)}{\mathrm{d}L} = \frac{1}{N_{\max}} \frac{\mathrm{d}N(L)}{\mathrm{d}L} = \frac{q^*}{L_\Theta^{q^*}} L^{q^*-1} \exp\left\{ -\left(\frac{L}{L_\Theta}\right)^{q^*} \right\} = \frac{q^*}{L_\Theta^{q^*}} L^{q^*-1} [1 - F(L)], \tag{8.43}$$

where $N_{\max}$ is the maximum number of crystals in a crystallization run, $q^* = q(1 - b)$, and L_Θ is the average size of the crystals. When $L = L_0$ at $t = 0$, for example, in the case of added seeds and their regeneration before growth, one takes $(L - L_0)$ instead of L in the above equations and the size constant L_Θ represents the $(L - L_0)$ region of the size distribution.

Note that $N(L)$ function denotes cumulative CSD and $\mathrm{d}N(L)/\mathrm{d}L$ of Eq. (8.43) denotes the differential CSD function $n(L)$. One also notes the form of Eq. (8.42) is similar to that of Eq. (8.40). The main difference between Eqs. (8.40) and (8.42) lies in the values of their exponents in the exponential terms. Since the maximum value of q is 4 and $0 < b < 1$, $0 < q^* < 4$. Depending on the values of q^* and L_Θ, Eq. (8.42) also predicts asymptotic, symmetrical, and negatively and positively skewed CSDs.

Figure 8.20 shows examples of evolution of the cumulative number $N(L)$ of KDP crystals of length L after 40 min from their aqueous solutions with and without 0.027 m EDTA and KPY additive. These data were recovered from the original plots published by Qu et al. (2006), who investigated the length L and width W of KDP crystals, using in-line video microscopy, from their aqueous solutions at evolution durations of 10, 20, and 40 min in the presence of seeds. Best-fit plots for the $N(L)$ data are drawn according to Eq. (8.42) with constants listed in Table 8.7 and the values of L_0 taken from the original data. As an illustration, a best-fit plot is also shown with $q^* = 1$ for seeds.

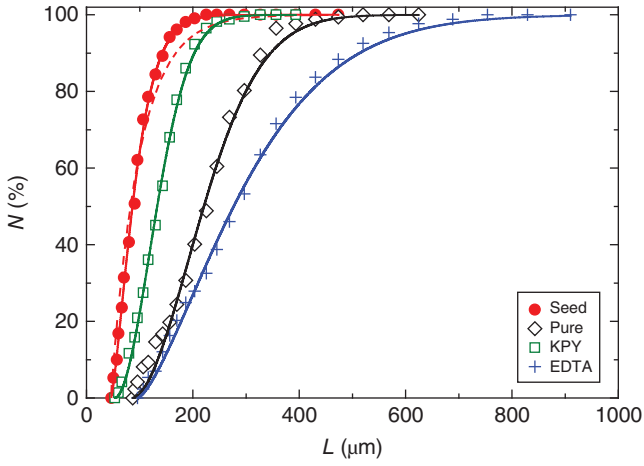

Figure 8.20 Examples of evolution of the distribution $N(L)$ of length L of KDP crystals with and without 0.027 m EDTA and KPY additives. Plots are drawn according to Eq. (8.42) with constants listed in Table 8.7. Dashed curve represents best-fit plot for $q^* = 1$. *Source:* Original data from Qu et al. (2006).

Table 8.7 Constants of Eq. (8.42) for evolution of length L of KDP crystals.

CSD	L_0 (μm)	L_Θ (μm)	q^* (–)	R^2
Seeds	46	52.7 (75)	1.377 (1.85)	0.9985
	46	52.9	1.0	0.9814
KPY	53	96.8 (120)	1.912 (2.5)	0.9983
Pure solution	86	164.7 (220)	1.826 (2.5)	0.9937
EDTA	96	233.3 (325)	1.436 (1.8)	0.9971

It may be seen from Figure 8.20 and Table 8.7 that the entire $N(L)$ data are represented well with $q^* > 1$ and the fit deteriorates when q^* is taken as unity. The $N(L)$ data appear to deviate significantly for low L from the best-fit plot for impurity-free solution, probably due to errors involved in recovering the data. The best-fit plots with the values of q^* given in Table 8.7 predicts somewhat lower N values than the experimental $N(L)$ data in the high L interval. This indicates that the values of initial L_0 are somewhat lower and those of q^* are higher than those listed in the table.

Figure 8.21 shows the above $N(L)$ data in the form of differential $n(L)$ distribution and the plots are drawn according to Eq. (8.42) with the values of q^* and L_Θ given in the parentheses in Table 8.7. It may be seen that, despite large scatter in the $n(L)$ data, the plots reproduce the trends of the $n(L)$ data reasonably well. These curves show the following features:

1) All of them are positively skewed.
2) The average length L_Θ of the crystals grown from pure solutions manifests the trends of the seed but the crystal distribution is widened during growth.
3) KPY additive suppresses the average length L_Θ of the crystals and maintains essentially the seed distribution, but EDTA additive increases the average crystal length L_Θ and widens the CSD.

The positive skewness of the curves is associated with the value of the exponent $q^* > 1$. Since $q^* = q(1 - b)$, one finds that $b \approx -0.3$ for pure KDP solution

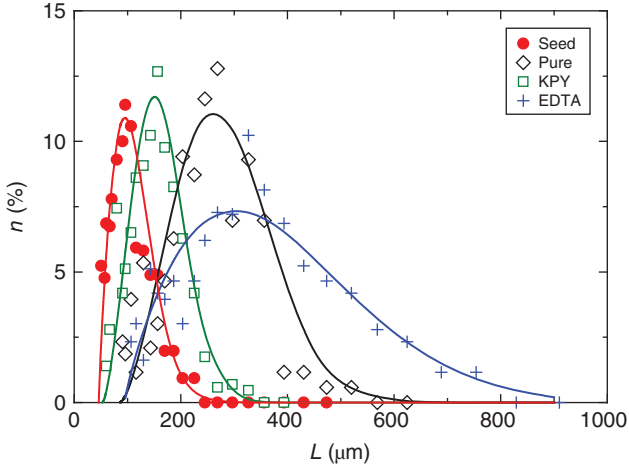

Figure 8.21 Differential $n(L)$ distribution from the $N(L)$ data of Figure 8.20. Plots are drawn according to Eq. (8.43) with the values of q^* and L_Θ given in parentheses in Table 8.7.

and solution containing KPY, whereas $b = 0$ for solution containing EDTA. Physically, this means that the linear growth R, given by Eq. (8.41) as $R = L^b/A$, increases with crystal length in pure KDP solution and solution containing KPY impurity but remain size independent in the case of EDTA. The dependence of R on L is expected in the case of growth rate dispersion (see Section 8.5), but the crystallization behavior of impurities is associated with their kinetic and thermodynamic effects (Qu et al., 2006).

8.8 Control of Phase and Size of Crystallizing Particles

A large number of inorganic and organic compounds exist as polymorphs differing in their physical and chemical properties. Therefore, the study of polymorphism is an important topic in the field of chemical engineering and pharmaceutics. Crystallization of these compounds from solutions and melts usually results in crystals of the thermodynamically most stable form, and thermodynamically unstable forms, if formed in the initial stages of crystallization, ultimately transform to the most stable form by the so-called solution- or melt-mediated transformation following the Ostwald rule of stages. In the pharmaceutical industry, pharmaceuticals of thermodynamically metastable forms are usually desired because of their enhanced biopharmaceutical properties due to higher solubilities and faster dissolution than those of stable forms. However, these metastable forms transform to more stable forms during processing and storage, thereby causing problems of formulation of solid dosage form and change in bioavailability. Therefore, thermodynamically the most stable polymorphic form is usually preferred for marketing purposes.

Among the important parameters that determine the control of crystallization of polymorphs of a compound are selection of suitable solvents for the preparation of solutions for crystallization and the available supersaturation level. In the case of fairly-soluble compounds, supersaturation can be created in the solution by controlled evaporation of the solvent. However, this method does not ensure easy supersaturation control, and ultimately leads to the growth of thermodynamically the most stable form, because all unstable forms produced in the solution undergo solution-mediated transformation. As described in Chapters 4–6, the supersaturation for crystallization can be created in different ways: (i) Controlled cooling of solution (cooling crystallization), (ii) controlled addition of antisolvent to saturated solution (antisolvent crystallization), (iii) addition of solution of known concentration to an antisolvent (drowning-out crystallization), and (iv) controlled addition of a solution of one reactant to that of another (reactive crystallization). Method (iii) enables to produce a predefined supersaturation instantaneously, whereas the other methods ensure the creation of supersaturation at a constant rate. However, fast

cooling of a solution can produce a predefined supersaturation. In methods (ii) and (iv), the supersaturation is created by adding at the surface or in the volume of the solution an antisolvent to the saturated solution or solution of one reactant to a large volume of the solution of the second reactant.

Crystallization of polymorphs of different compounds from solution is determined by the available supersaturation level and the thermodynamic and kinetic factors associated with the 3D nucleation and growth of an individual polymorph. The supersaturation level determines whether crystallization of a compound occurs in kinetically- or diffusion-controlled regime, the former and the latter occurring at low and high supersaturations, respectively.

Traditional cooling and antisolvent crystallizations have limited application for the nucleation and growth of specific polymorphs because the attained supersaturation level leads to the occurrence of spontaneous nucleation of crystals. However, fast cooling and drowning-out crystallizations have been employed to obtain different polymorphs. Here, some basic ideas are presented for the control of polymorphs involving (i) self-seeding by fast cooling of solutions and by mixing of reactant solutions and (ii) seeding of supersaturated solutions.

The main idea of obtaining the desired polymorph of a compound by cooling, called swift cooling (Srinivasan and Dhanasekaran, 2011; Sudha and Srinivasan, 2013), is to cool solution of a particular concentration from temperature T_0 as fast as possible to a predefined crystallization temperature T_c. Figure 8.22 shows schematically the crystallization behavior of stable polymorph S and metastable polymorph M of a compound from its solutions of equilibrium concentrations

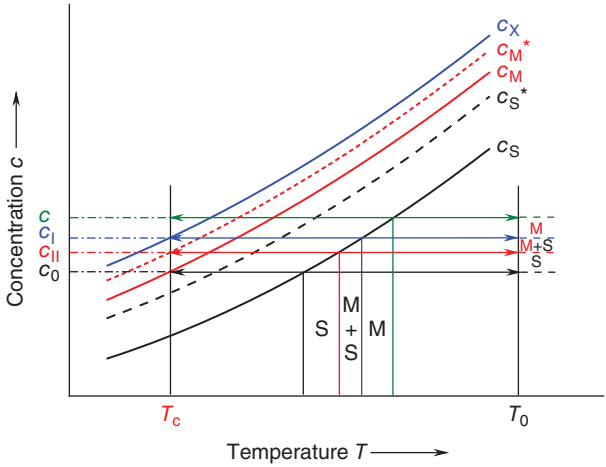

Figure 8.22 Schematic illustration of crystallization of two polymorphs and their solubility and supersolubility curves.

c_0 and c_I with reference to the temperature dependence of the solubility of the stable polymorph of the compound. The figure illustrates the curves of solubility (c_S and c_M) and supersolubility (c_S^* and c_M^*) of stable polymorph S and metastable polymorph M of a compound in a solvent and the solubility curve (c_X) of a hypothetical unstable polymorph X possibly existing in the solution. While constructing the supersolubility curves for the forms, it is assumed that the metastable zone width of a polymorph increases with its stability.

We recall here the fact that the solubility of the polymorphs is related to the level of their stability, which is also intimately related to their interfacial energy γ in the solution. The lower the solubility of polymorph, the higher is its stability and its interfacial energy γ. In the figure, c_0 and c_I denote the equilibrium solubilities of the stable and metastable forms, respectively. Consequently, if the 3D nucleation kinetics of the two polymorphs are controlled by their interfacial energy γ (i.e. thermodynamic factor) alone, one expects the crystallization of stable and metastable forms in the concentration intervals between c_0 and c_{II} and $c > c_I$, respectively, and the crystallization of a mixture of both stable and metastable forms in the concentration interval between c_I and c_{II}.

Several examples of crystallization of polymorphs of different compounds according to the above mechanism are known where their desupersaturation curve from the initial concentration c occurs in steps (for example, see: Kitamura et al., 2008; Kurotani and Hirosawa, 2010); Section 4.1. According to this concept crystallization of polymorphs of different stability of a compound is directly related to their temperature dependence of solubility. Using this approach, Sudha and Srinivasan (2013) explained the crystallization of stable monoclinic form I, metastable orthorhombic form II, and unstable form III of paracetamol (acetaminophen) by the swift cooling crystallization of their aqueous solutions of different saturations temperatures from 305 and 331.5 K. These authors prepared saturated solutions of various concentrations c of the solute in water using the temperature dependence of solubility c, from the most stable polymorph of the compound having the lowest solubility. Different saturation temperatures ensured different initial concentrations of the aqueous solutions of paracetamol, whereas swift cooling of the solutions was carried out from 353 K down to 278 K. Polymorphs were identified by powder X-ray diffraction (PXRD) analysis. The results obtained by these authors are summarized in Table 8.8. Morphology of the observed polymorphs and values of induction period t_{in} for the appearance of the polymorphs are also given. The former and latter values of t_{in} refer to the lower and higher values of supersaturation ratio S.

The trend of the observed morphology of the polymorphs is expected (see Section 8.4). Similarly, a decrease in the induction period t_{in} with an increase in supersaturation S for different polymorphs and a lower value of t_{in} for form II than that for form I are also expected (see Chapter 7). However, relatively high value of t_{in} for form III than that for form II and for form I at high S is

Table 8.8 Crystallization conditions for different paracetamol polymorphs.

c (g/100 ml)	S (–)	Polymorph	Morphology	t_{in} (min)
1.8–2.6	1.84–2.13	I	Polyhedral	25–5
2.7–2.8	2.14–2.19	I + II		
2.9–3.1	2.20–2.26	II	Needle-like	5–4
3.2–3.7	2.27–2.39	III	Fibrous	10–7
>3.7	>2.40	I	Polyhedral	7–3

Source: Data from Sudha and Srinivasan (2013).

probably associated with the role of diffusion processes in controlling their formation.

Another example is the crystallization of different polymorphs of L-glutamic acid from its aqueous solution saturated at a temperature $T_s = 40\,^{\circ}C$ by swift cooling from crystallization temperatures T_c varying from 1 to 34 °C (Srinivasan and Dhanasekaran, 2011). The swift-cooling crystallization experiments on L-glutamic acid showed that the metastable polymorph crystallizes when the temperature difference $\Delta T = T_s - T_c$ lies between 31 and 39 °C, the stable polymorph crystallizes when ΔT lies between 6 and 13 °C, and a mixture of both when ΔT lies between 13 and 30 °C. Since the temperature difference is a measure of driving force in crystallization (i.e. available supersaturation ratio S), a similarity in the trend of crystallization of L-glutamic acid with that of paracetamol described above is evident.

During cooling crystallization, the cooling rate has a strong effect on the distribution of the size of resulting crystals and polymorphs. The common observation that higher cooling rates result in a wider metastable zone width implies that the supersaturation developed at the time of 3D nucleation increases with increasing cooling rate. Consequently, after the onset of nucleation the solute concentration falls leading to a particular size distribution, which is determined by the cooling rate. In general, a wider metastable zone width by a high cooling rate gives smaller crystals because of the higher level of nucleation than a narrower metastable zone by a low cooling rate, which gives larger crystals because of reduced nucleation. This fact has been suggested as a strategy to obtain a desired CSD in which the initial zone width is rapidly established and then the system is held isothermally until nucleation and subsequent crystal growth reduces the solubility to the equilibrium concentration (Barrett et al., 2010).

In the above examples, crystallization of metastable polymorphs followed by their transformation to stable forms was described in terms of supersaturation levels and thermodynamic considerations. However, the above approach of crystallization of polymorphs in proportion to their solubility fails when kinetic

factors prevail over thermodynamic factors. For example, crystallization of L-glutamic acid occurs by reacting aqueous solutions of sodium glutamate and sulfuric acid. L-Glutamic acid exhibits metastable α and stable β polymorphs (Qu et al., 2009). According to Qu et al. (2009), nucleation of metastable α and stable β polymorphs of L-glutamic acid during reactive crystallization requires high supersaturation level and that the feeding manner of the reactant strongly affects the local supersaturation level inside the reactive crystallizer. According to these authors, when the reactant sulfuric acid is fed to a poorly mixed region such as the surface of the sodium glutamate solution in the crystallize, a high local supersaturation level is produced near the feeding point. This high local supersaturation level significantly increases with the increase in the concentrations of the reactants, thereby increasing the fraction of the β polymorph with the concentration of the reactants. However, feeding the reactant to a well-mixed zone near the impeller can avoid the creation of high local supersaturation and this results in the reduction of formation of the β polymorph on the reactant concentration. This type of crystallization involves fast generation rate of supersaturation and high supersaturation levels. Consequently, rapidly occurring processes of nucleation, growth, and agglomeration determine the formation of the resulting solid phase. When the crystallizing solute exists in different polymorphs, the high supersaturation level involved in their crystallization reduces the effect of thermodynamic factor because of reduced difference in the supersaturation level due to insignificant difference in their solubilities. Then the kinetic factor controls the formation of the solid and the nucleation kinetics of the polymorphs mainly determine their crystallization, which might be driven by the solvent, additive, and mixing of crystallizing solution.

According to the classical theory of 3D nucleation, the kinetic and thermodynamic factors in 3D nucleation are the preexponential factor J_0 and the constant B, respectively. The supersaturation ratio S at its sufficiently large values may be taken with reference to the stable form. Then one expects crystallization of metastable and stable polymorphs to occur in the range of low and high supersaturation ratio S, respectively, and crystallization of a mixture of the two forms at intermediate S.

Qu et al. (2009) also studied the effect of impeller type and mixing intensity on the size distribution of crystals of the metastable α polymorph with a concentration of reactants of 0.75 M. The authors found that lower mixing intensity essentially gives a symmetrical distribution of relatively wide size but increased mixing intensity results in positively skewed distribution and smaller crystals lying in a narrow range. These observations are a consequence of enhanced nucleation induced by increased mixing intensity.

Drowning out of solution of known concentration of solute in an antisolvent is another way to produce supersaturation in the bulk solution (for example, see: Hyung et al., 2008; Jim and Kim, 2012; Park and Yeo, 2012) and to monitor the

process of crystallization of the polymorph in the absence and presence of seeds of known polymorphs (Jim and Kim, 2012). These studies showed that particle size and its distribution strongly depend on crystallization parameters such as feeding rate, agitation rate, and solute concentration fed to the antisolvent, whereas seeding facilitates nucleation of new crystals.

In their investigation of the selective crystallization of unstable polymorph I and stable polymorph II of clopidogrel hydrogen sulfate (CHS) in mixed solvents such as formic acid (FA) and isopropyl alcohol (IPA), both without and in the presence of seeds of the two polymorphs, Jim and Kim (2012) monitored the crystallization process by variation in the ultrasonic velocity, solute concentration, and temperature, and identified the CHS polymorphs by PXRD analysis, scanning electron microscopy, and differential scanning calorimetry. This study revealed the following features:

1) In the case of absence of seeding, nucleation of stable polymorph II is observed at the induction point and grows thereafter, but seeding by polymorph II induces nucleation of form I, which subsequently transforms to polymorph II.
2) Addition of various amounts of unstable polymorph I at various seeding points induces an increase in the supersaturation, which leads to an enhanced possibility of obtaining the metastable form. In fact, it was found (Jim and Kim, 2012) that seeding of form I crystals induces a large number of its nuclei in the solution, which favors the formation of polymorph I. However, here also these crystals finally transform to the stable polymorph II by solution-mediated transformation.
3) The induction period for nucleation decreases with increasing the amount of the seed and the final concentration of the seeded system is lower than that of the unseeded system. The latter observation is due to the creation of higher initial supersaturation by seeding, which ultimately results in the nucleation of the unstable polymorph I in the seeded system.

Finally, it should be mentioned that cooling crystallization has been applied to separate individual enantiomers from their mixtures and mathematical description of size distribution of seeded and growing enantiomer particles (Elsner et al., 2005; Lorenz et al., 2006).

References

Abegg, C.F., Stevens, J.D., and Larson, M.A. (1968). Crystal size distributions in continuous crystallizers when growth rate is size dependent. *AIChE J.* 14: 118–122.

Akrap, M., Kuzmanić, N., and Prlić-Kardum, J. (2010). Effect of mixing on the crystal size distribution of borax decahydrate in a batch cooling crystallizer. *J. Cryst. Growth* 312: 3603–3608.

Algra, R.E., Graswinckel, W.S., van Enckevort, W.J.P., and Vlieg, E. (2005). Alizarin crystals: an extreme case of solvent induced morphology change. *J. Cryst. Growth* 285: 168–177.

Andreassen, J.P. (2005). Formation mechanism and morphology in precipitation of vaterite – nano-aggregation or crystal growth? *J. Cryst. Growth* 274, 256–264.

Baldan, A. (2002). Progress in Oswald ripening theories and their application to nickel-base superalloys. *J. Mater. Sci.* 37: 2171–2202.

Barrett, M., McNamara, M., Hao, H.-X. et al. (2010). Supersaturation tracking for the development, optimization and control of crystallization processes. *Chem. Eng. Res. Design* 88: 1108–1119.

Belter, P.A., Cussler, E.L., and Hu, W.-S. (1988). *Bioseparations*. New York: Interscience.

Bennema, P. (1993). Growth and morphology of crystals: integration of theories of roughening and Hartman-Perdok theory. In: *Handbook of Crystal Growth*, vol. 1 (ed. D.T.J. Hurle), 477–583. Amsterdam: Elsevier.

Berglund, K.A. (1993). Analysis and measurement of crystallization utilizing the population balance. In: *Handbook of Industrial Crystallization* (ed. A.S. Myerson), 89. Boston: Butterworth-Heinemann.

Berglund, K.A. (2002). Analysis and measurement of crystallization utilizing the population balance. In: *Handbook of Industrial Crystallization*, 2e (ed. A.S. Myerson), 101–113. Boston: Butterworth-Heinemann.

Berglund, K.A. and de Jong, E.J. (1990). The calculation of growth and nucleation kinetics from MSMPR crystallizer data including growth rate dispersion. *Separations Technol.* 1: 38–45.

Bhat, H.L., Sherwood, J.N., and Shripathi, T. (1987). The influence of stress, strain and fracture of crystals on the crystal growth process. *Chem. Eng. Sci.* 42: 609–618.

Bockris, J.O.'.M. and Reddy, A.K.N. (1970). *Modern Electrochemistry*, vol. 1. New York: Plenum Press.

Boistelle, R. (1980). *Current Topics in Materials Science*, vol. 4 (ed. E. Kaldis), 413. Amsterdam: North-Holland.

Caillet, A., Sheibat-Othman, N., and Fevotte, G. (2007). Crystallization of monohydrate citric acid. 2. Modeling through population balance equations. *Cryst. Growth Des.* 7: 2088–2095.

Cornel, J., Lindenberg, C., and Mazzotti, M. (2009). Experimental characterization and population balance modeling of the polymorph transformation of L-glutamic acid. *Cryst. Growth Des.* 9: 243–252.

Davies, C.K.L., Nash, P., and Stevens, R.N. (1980). The effect of volume fraction of precipitate on Ostwald ripening. *Acta Metallogr.* 28: 179–189.

Elsner, M.P., Fernandez Menendez, D., Alonso Muslera, E., and Seidel-Morgenstern, A. (2005). Experimental study and simplified mathematical description of preferential crystallization. *Chirality* 17: 183–195.

Fevotte, G., Alexandre, C., and Nida, S.O. (2007). A population balance model of the solution-mediated phase transition of citric acid. *AIChE J.* 53: 2578–2589.

Frank, F.C. (1981). Edge dislocations as crystal growth sources. *J. Cryst. Growth* 51: 367–368.

Gadewar, S.B. and Doherty, M.F. (2004). A dynamic model for evolution of crystal shape. *J. Cryst. Growth* 267: 239–250.

Glatz, C.E., Hoare, M., and Landa-Vertz, J. (1986). The formation and growth of protein precipitates in a continuous stirred-tank reactor. *AIChE J.* 32: 1196–1204.

Grimbergen, R.F.P., Meekes, H., Bennema, P. et al. (1998). On the prediction of crystal morphology. I. The Hartman–Perdok theory revisited. *Acta Crystallogr. A* 54: 491–500.

Hartel, R.W. and Randolph, A.D. (1986). Mechanisms and kinetic modeling of calcium oxalate crystal aggregation in a urinelike liquor. Part II: Kinetic modeling. *AIChE J.* 32: 1186–1195.

Hartman, P. (1973). Structure and Morphology. In: *Crystal Growth: An Introduction* (ed. P. Hartman), 367–402. Amsterdam: North-Holland.

Hyung, W., Kim, Y., Chung, C.-H., and Haam, S. (2008). Drowning-out crystallization of L-proline: effect of anti-solvent composition and processing parameters on crystal size and shape. *Powder Technol.* 186: 137–144.

Iggland, C. and Mazzotti, M. (2012). Population balance modeling with size-dependent solubility: Ostwald ripening. *Cryst. Growth Des.* 12: 1489–1500.

Jim, M. and Kim, K.-J. (2012). Effect of supersaturation on polymorphs of clopidogrel hydrogen sulfate in drowning-out crystallization. *Chem. Eng. Technol.* 35: 995–1002.

Kashchiev, D. (2000). *Nucleation: Basic Theory with Applications*. Oxford: Butterworth-Heinemann.

Kile, D.E., Eberl, D.D., Hoch, A.R., and Reddy, M.M. (2000). An assessment of calcite crystal growth mechanisms based on crystal size distributions. *Geochim. Cosmochim. Acta* 64: 2973–2950.

Kitamura, M., Hayashi, Y., and Hara, T. (2008). Effect of solvent and molecular structure on the crystallization of polymorphs of BPT esters. *J. Cryst. Growth* 310: 3067–3071.

Kitamura, M. (2001). Crystallization and Transformation mechanism of calcium carbonate polymorphs and the effect of magnesium Ion. *J. Colloid Interface Sci.* 236: 318–327.

Kurotani, M. and Hirosawa, I. (2010). Effect of ultrsound irradiation on the selective polymorph control in sulfamerazine. *Chem. Eng. Res. Design* 88: 1272–1278.

Leubner, I.H. (2000). Particle nucleation and growth models. *Curr. Opin. Colloid Interface Sci.* 5: 151–159.

Leubner, I.H. (2002). Balanced nucleation and growth model for controlled crystal size distribution. *J. Dispers. Sci. Technol.* 23: 577–590.

Leubner, I.H. (2010). *Precision Crystallization: Theory and Practice of Controlling Crystal Size*. Boca Raton: CRC Press.

Lifshitz, I.M. and Slyozov, V.V. (1961). The kinetics of precipitation from supersaturated solid solutions. *J. Phys. Chem. Solids* 19: 35–50.

Lindenberg, C., Krättli, M., Cornel, J., and Mazzotti, M. (2009). Design and optimization of a combined cooling/antisolvent crystallization process. *Cryst. Growth Des.* 9: 1124–1136.

Lorenz, H., Perlberg, A., Sapoundjiev, D. et al. (2006). Crystallization of enantiomers. *Chem. Eng. Proc.* 45: 863–873.

Meekes, H., Bennema, P., and Grimbergen, R.F.P. (1998). On the prediction of crystal morphology. II. Symmetry roughening of pairs of connected nets. *Acta Crystallogr. A* 54: 501–510.

Mersmann, A. (2001). Particle size distribution and population balance. In: *Crystallization Technology Handbook*, 2e (ed. A. Mersmann), 145–186. New York: Marcel Dekker.

Mitrović, M.M., Žekić, A.A., and Napijalo, M.M. (2000). Correlation between crystal size and crystal growth rate of KDP and Rochelle salt crystals. *J. Cryst. Growth* 216: 437–442.

Mortimer, R.G. (2008). *Physical Chemistry*, 3e. Amsterdam: Elsevier.

Mullin, J.W. (2001). *Crystallization*, 4e. Oxford: Butterworth-Heinemann.

Nývlt, J., Söhnel, O., Matuchova, M., and Broul, M. (1985). *The Kinetics of Industrial Crystallization*. Prague: Academia.

Park, M.-W. and Yeo, S.-D. (2012). Antisolvent crystallization of carbamazepine from organic solutions. *Chem. Eng. Res. Design* 90: 2202–2208.

Prywer, J. (2005). Kinetic and geometric determination of the growth morphology of bulk crystals: recent developments. *Prog. Cryst. Growth Charact. Mater.* 50: 1–38.

Qu, H., Alatalo, H., Hatakka, H. et al. (2009). Raman and ATR FTIR spectroscopy in reactive crystallization: simultaneous monitoring of solute concentration and polymorphic state of the crystals. *J. Cryst. Growth* 311: 3466–3475.

Qu, H., Louhi-Kultanen, M., and Kallas, J. (2006). In-line analysis on the effects of additives in batch cooling crystallization. *J. Cryst. Growth* 289: 286–294.

Randolph, A.D. and Larson, M.A. (1988). *Theory of Particulate Processes*, 2e. San Diego: Academic Press.

Ristic, R.I., Sherwood, J.N., and Wojciechowski, K. (1988). Assessment of the strain in small sodium chlorate crystals and its relation to growth rate dispersion. *J. Cryst. Growth* 91: 163–168.

Rohl, A.I. (2003). Computer prediction of crystal morphology. *Curr. Opin. Solid State Mater. Sci.* 7: 21–26.

Salvalaglio, M., Vetter, T., Mazzotti, M., and Parrinello, M. (2013). Controlling and predicting crystal shapes: The case of urea. *Angew. Chem. Int. Ed.* 52: 13369–13372.

Sangwal, K. and Mielniczek-Brzóska, E. (2016a). Antisolvent crystallization of aqueous ammonium dihydrogen phosphate solutions by addition of acetone at different rates. *Cryst. Res. Technol.* 51: 475–490.

Sangwal, K. and Mielniczek-Brzóska, E. (2016b). Antisolvent crystallization of aqueous ammonium dihydrogen phosphate solutions by addition of methanol. *J. Cryst. Growth* 451: 139–149.

Sangwal, K. and Mielniczek-Brzóska, E. (2017a). Post-crystallization cooling behavior of aqueous supersaturated ammonium dihydrogen phosphate solutions containing acetone and methanol antisolvents added at different rates. *Cryst. Res. Technol.* 52: 201600216 (1–11).

Sangwal, K. and Mielniczek-Brzóska, E. (2017b). Effect of addition of different antisolvents on the crystallization of aqueous ammonium dihydrogen phosphate solutions. *Cryst. Res. Technol.* 52: 201600361 (1–8).

Söhnel, O. and Garside, J. (1992). *Precipitation: Basic Principles and Industrial Applications*. Oxford: Butterworth-Heinemann.

Srinivasan, K. and Dhanasekaran, P. (2011). Nucleation control and crystallization of L-glutamic acid polymorphs by swift cooling process and their characterization. *J. Cryst. Growth* 318: 1080–1084.

Sudha, C. and Srinivasan, K. (2013). Supersaturation dependent nucleation control and separation of mono, ortho and unstable polymorphs of paracetamol by swift cooling crystallization technique. *Cryst. Eng. Comm.* 15: 1914–1921.

Sunagawa, I. (1981). Characteristics of crystal growth in nature as seen from the morphology of mineral crystals. *Bull. Mineral.* 104: 81–87.

Sunagawa, I. ed. (1987). *Morphology of Crystals*. Tokyo: Terrapub.

Sunagawa, I. (2005). *Crystals: Growth, Morphology and Perfection*. Cambridge: Cambridge University Press.

Toschev, S. (1973). Equilibrium forms. In: *Crystal Growth: An Introduction* (ed. P. Hartman), 328–341. Amsterdam: North-Holland.

van der Heijden, A.E.D.M. and van der Eerden, J.P. (1992). Growth rate dispertion: the role of lattice strain. *J. Cryst. Growth* 118: 14–26.

Vetter, T., Iggland, M., Ochsenbein, D.R. et al. (2013). Modeling nucleation, growth, and Ostwald ripening in crystallization processes: a comparison between population balance and kinetic rate equation. *Cryst. Growth Des.* 13: 4890–4905.

Wagner, C. (1961). Theorie der Alterung von Neiderschlägen durch Umlösen (Ostwald Reifung). *Zeitschrift für Elektrochemie* 65: 581–591.

Weissbuch, I., Leiserowitz, L., and Lahav, M. (2001). Tailor-made additives and impurities. In: *Crystallization Technology Handbook*, 2e (ed. A. Mersmann), 563–616. New York: Marcell Dekker.

Wohlgemuch, K., Ruether, F., and Schembecker, G. (2010). Sonocrystallization and crystallization with gassing of adipic acid. *Chem. Eng. Sci.* 65: 1016–1027.

9

Glass Formation and Crystallization Processes

Glasses are disordered solids and are commonly obtained by rapid cooling of melts of different types of substances. Therefore, their properties are intimately related to the properties of metastable liquids cooled below their freezing point (supercooled liquids). At the molecular level, glasses have a liquid-like structure and are devoid of the periodicity of crystals. Mechanically, they behave like solids and exhibit elastic and plastic deformation. The deformation characteristics are determined by external factors such as applied stress and measurement temperature as well as internal factors related to intermolecular bonds involved in glass formation.

There is vast literature on glass formation and glass transition, and several authoritative reviews devoted to the advances in the fundamental understanding of glasses have been published (Angell, 1995; Avramov, 2005; Berthier and Biroli, 2011; Dasgupta, 2005; Debenedetti, 1996; Debenedetti et al., 2001; Ojovan, 2008; Ramachandra Rao et al., 1977; Scherer, 1991; Tropin et al., 2016; Zarzycki, 1991). Main consideration in most of the theories of glass transition is the concept of disorder and voids in the liquid state, which are intimately related to entropy and heat capacity. We note here that the history of voids in disordered systems goes back to the hole theory of the liquid state.

In the field of industrial crystallization from solutions, several approaches have been proposed to describe the relationship between the metastability zone width (MSZW) of saturated solutions, expressed as maximum supercooling ΔT_{max}, and the applied cooling rate R_L (Chapter 5). One of these approaches, advanced by Sangwal (2009a, b), is based on the classical theory of three-dimensional (3D) nucleation, and explains satisfactorily the experimental $\Delta T_{max}(R_L)$ data for various solute–solvent systems in the absence as well as the presence of added impurities.

In this chapter, basic concepts of glass formation and glass transition temperature T_g are briefly described first. Since rapid cooling of melts and viscous solutions leads to glass formation, the approach based on the classical theory of 3D nucleation for the MSZW of solutions by the polythermal method is extended to the solidification of melts and glass formation.

Nucleation and Crystal Growth: Metastability of Solutions and Melts, First Edition.
Keshra Sangwal.
© 2018 John Wiley & Sons, Inc. Published 2018 by John Wiley & Sons, Inc.

9.1 Glass Formation by Cooling of Melts

Solidification of substances, leading to the formation of glasses and crystals, from their melts by cooling at a constant rate R_L may be understood from an analogy with the crystallization of solutions of solute–solvent systems saturated at temperature T_0 during cooling at a constant rate R_L. We assume that the main mechanism involved during solidification by cooling from initial melt temperature T (point A) is a decrease in the melt volume V, as shown in Figure 9.1, from its melting temperature T_m. The figure shows a decrease in the volume V of melt, crystalline solid (1), and glass (2) with decreasing temperature. High and low slopes of plots of V against T for molten and solidified phases correspond to their high and low thermal contraction coefficients α_V, respectively.

Suppose that a melt is in equilibrium at temperature T_m corresponding to the melt volume V_m (point B in Figure 9.1). When the melt is cooled at a constant cooling rate $R_L = \Delta T/\Delta t$ below the melting point, it enters the metastable state by a decrease in its volume V with decreasing temperature T. The melt can enter the metastable state in two ways. At relatively low cooling rates R_L, the volume of the system decreases discontinuously from V_m. Initially, when the melt attains a temperature T_N, 3D nuclei of the solid are formed in the melt (volume V_N, point C). These nuclei subsequently grow in size until the entire melt is crystallized (point E). This process involves a decrease in the melt volume from V_N without a change in the temperature. However, when the cooling rate R_L is sufficiently high (i.e. $R_L \rightarrow R_{Llim}$), solidification occurs in a different way. In this case, the process of nucleation is suppressed, but the melt remains in the

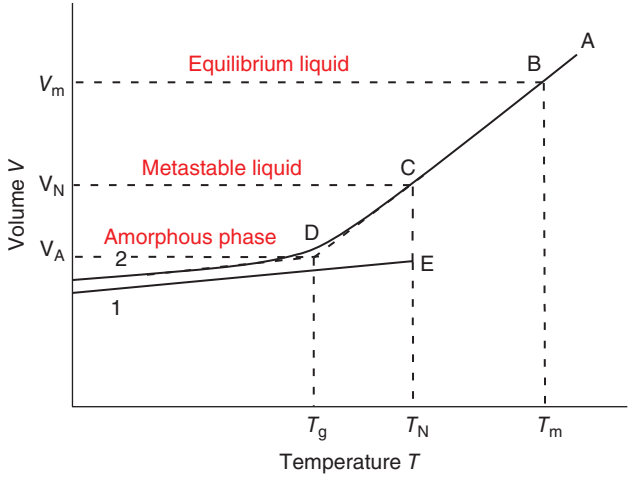

Figure 9.1 Schematic presentation of decrease in the volume V of a melt during its cooling from initial melt temperature T at constant cooling rate R_L. See text for details.

metastable state without the formation of 3D nuclei and continues to contract at the high thermal contraction coefficient of the melt and eventually the molecules/atoms are frozen in fixed positions at a limiting temperature. This limiting temperature, indicated by point D in Figure 9.1, is known as the glass transition temperature T_g, which is defined as the point of intersection of lines of thermal contraction coefficients of melt and glass.

Crystallization from a molten phase or solution is associated with the formation of critical nucleus/nuclei in a certain time (i.e. induction period t_{in}) by the self-assembly of molecules or atoms and by some chance fluctuations involving vibrations of individual molecules/atoms around their average positions and their diffusion in the bulk volume. Cooling slows down this molecular motion. Therefore, a cooling rate R_L can be reached for the cooling of a liquid when the molecular motion in the liquid does not equilibrate in the available time and the liquid structure is frozen on the laboratory scale (e.g. minutes). This failure of reaching equilibrium takes place in a narrow transformation range where the thermal expansion coefficient α_V decreases abruptly to a value lower than that of the liquid and comparable with that of the crystalline solid. The resulting material is a glass.

Glass formation, usually referred to as vitrification, occurs in a narrow temperature range. Consequently, the glass transition temperature T_g is not a precisely-defined, true transition temperature. Moreover, its value for a liquid depends on the cooling rate. The higher the cooling rate, the higher is the value of T_g. This higher T_g with higher cooling rate is associated with the shorter time available for the configuration of molecular bonds in the liquid necessary for the formation of the 3D nuclei. Therefore, the properties of a glass depend on the molecular bonds in the liquid from which it is formed and the cooling rate used. However, since the change in T_g of a material with a change in the cooling rate by an order of magnitude is usually a few K and the transformation range is relatively narrow, T_g is essentially a material characteristic.

Substances known to form glasses are (for example, see: Angell, 1995; Debendetti, 1996; Debendetti et al., 2001): elements like P, S, and Se; oxides like SiO_2, GeO_2, B_2O_3, P_2O_5, As_2O_3, and Sb_2O_3; chalcogenides like As_2S_3; halides like BeF_2 and $ZnCl_2$; mixtures of salts (for example, $KNO_3 + Ca(NO_3)_2$ and $K_2CO_3 + MgCO_3$); aqueous solutions of salts, acids, and bases (for example, H_2SO_4 and LiCl); organic compounds like glycerol, methanol, ethanol, fructose, glucose, and *o*-terphenyl; polymers like polystyrene, poly(vinyl chloride), and poly(ethylene oxide); metal alloys (for example, Ni + Nb and Cu + Zn); and metal–metaloid alloys (for example, Pd + Si and Ni + P). For the vitrification of the melt of a system, the necessary requirement is that the minimum nucleation time (i.e. the duration t_{in}) is longer than the time required to attain T_g from the melting point T_m. Substances with a very low probability of occurrence of nucleation at all temperatures during its cooling between T_m and T_g are good glass formers, but a critical cooling rate has to be exceeded for poorer glass formers. Under processing conditions, the tendency of

formation of glasses (glass-forming ability) and resistance to crystallization (glass stability) is related to structural elements composing the melts of different substances.

The commonly used viscosity equation is that of Vogel–Tamman–Fulcher (VTF). It gives a good description of the temperature dependence of viscosity of supercooled melts near the glass transition temperature. Adam–Gibbs (AG) and Avramov–Milchev (AM) models are also often used to describe the viscosity behavior. These models are briefly described below.

9.2 Temperature Dependence of Viscosity and the Glass Transition Temperature

In the temperature interval of glass transition, the glass-forming ability of a substance from its melt is related to an internal relaxation time τ, which is proportional to the melt viscosity η (see Eq. (9.10)) and changes with temperature T. Data of the dependence of the viscosities η of different glass-forming liquids on their temperature T are collected in Figure 9.2 in the form of Arrhenius plots (Angell, 1991, 1995):

$$\eta = \eta_0 \exp\left(\frac{E}{R_G T}\right), \tag{9.1}$$

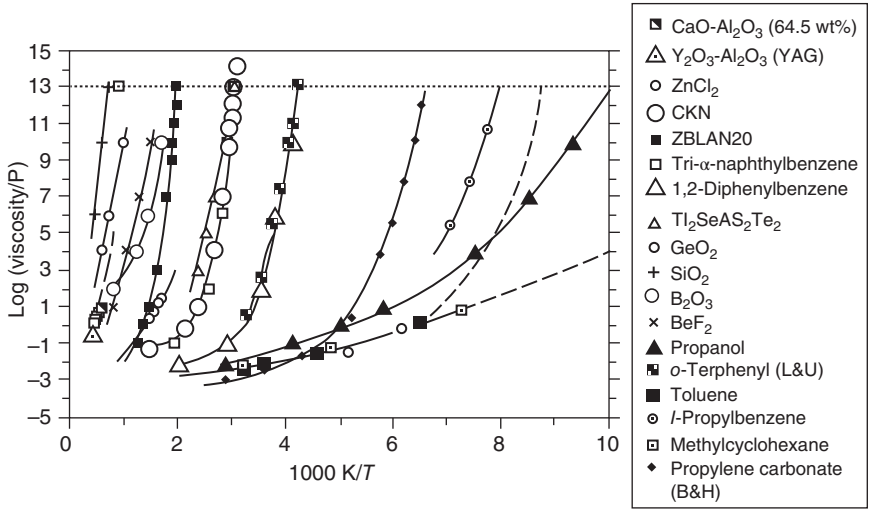

Figure 9.2 Arrhenius plots of viscosity of various supercooled liquids of different types with calorimetric glass transition temperatures. Horizontal dotted line corresponding to 10^{13} P is taken as the glass transition temperature T_g. Dashed lines represent interpolation between T_g and the lowest temperature data point. *Source:* Reproduced from Angell (1995). Copyright (1995), with permission from American Association for the Advancement of Science.

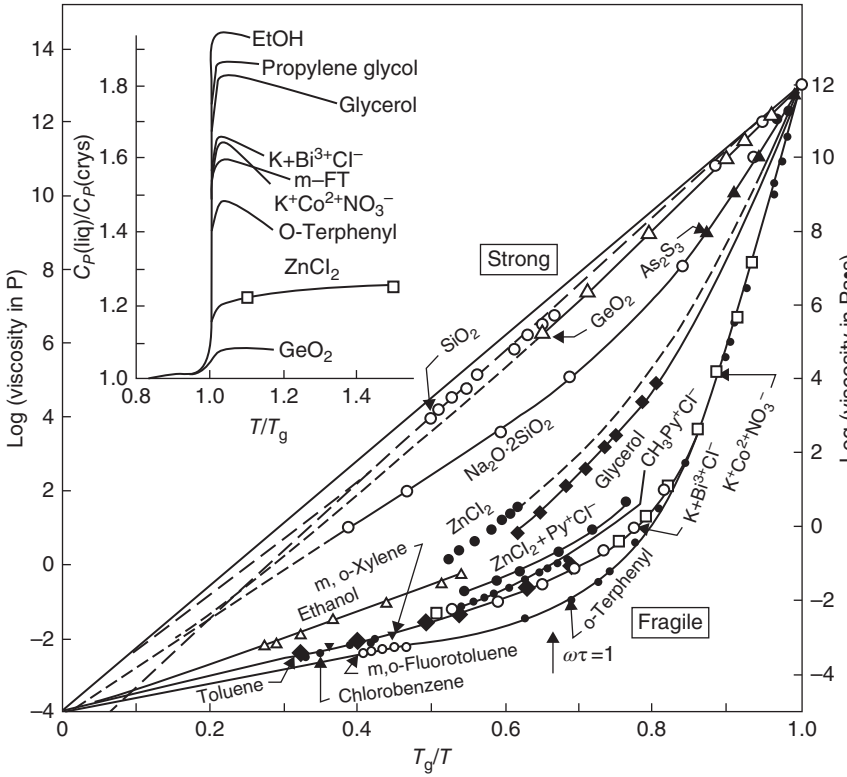

Figure 9.3 Arrhenius plots of viscosity data of Figure 9.2 for various supercooled liquids with temperature scaled by T_g, and classification of liquids into strong and fragile categories. *Source:* Reproduced from Angell (1995). Copyright (1995), with permission from American Association for the Advancement of Science.

where E is the so-called activation energy for viscous flow, η_0 is a preexponential factor at $T \to \infty$, R_G is the gas constant, and T is the temperature in Kelvin. Equation (9.1) reasonably describes the data for some melts such as SiO_2, but it fails to describe the data for most of the substances in the entire range of temperature T. For the latter substances, when the temperature is scaled with the glass temperature T_g (10^{13} P at T_g; 1 P = 0.1 Pa·s), the data give Figure 9.3 (Angell, 1995).

Figure 9.3 shows two extremes in the general behavior of the plots of log η against scaled temperature T_g/T. Open network liquids like SiO_2 and GeO_2 show an Arrhenius-type behavior of the viscosity η between T_g and the high-temperature limit when $\eta = 10^{-2}$ P for many liquids. In these liquids, called *strong liquids*, viscosity follows Arrhenius-type behavior. Liquids, characterized by simple nondirectional Coulomb interactions or weak van der Waals

interactions in substances with many π electrons (usually aromatic substances), form the other extreme of *fragile liquids*. In fragile liquids, viscosity changes in a strongly non-Arrhenius manner between the low and high viscosity limits.

The above classification of strong and fragile liquids is related to the sensitivity of the liquid structure to temperature changes (Angell, 1991, 1995). Strong liquids have a built-in resistance to structural changes with temperature changes. Fragile liquids, on the other hand, form a glassy state structure that easily collapses with little provocation from thermal excitation. As seen from the inset of Figure 9.3, strong liquids are characterized by very small jump ΔC_p in their heat capacity C_p at T_g, whereas fragile liquids show large jumps in ΔC_p.

The $\eta(T_g/T)$ data of Figure 9.3 for different liquids can be well represented by a modified form of the VTF relation (cf. Angell, 1991, 1995):

$$\eta = \eta_0 \exp\left[\frac{B}{(T - T_0)}\right], \tag{9.2}$$

rewritten in the form:

$$\eta = \eta_0 \exp\left[\frac{\Psi T_0}{(T - T_0)}\right], \tag{9.3}$$

where the parameter $\Psi = B/T_0$ is a measure of the strength of mutual interaction between the liquid constituents and $T_g > T_0 > 0$. For a system following the Arrhenius relation, $\Psi = \infty$. The effect of variation in Ψ from 5 to 100 is shown in the inset of Figure 9.3. The parameter Ψ is related to the temperature T_0 according to the simple dependence:

$$\frac{T_g}{T_0} = 1 + \frac{\Psi}{\ln\left(\eta_g/\eta_0\right)}, \tag{9.4}$$

where $\ln(\eta_g/\eta_0) \approx 39$ and the values of the liquid viscosity η at T_g and T_0 are η_g and η_0, respectively. The temperature T_0, called the Vogel temperature, refers the ideal glass transition state when the movement of liquid constituents is totally frozen.

The temperature ratio T_0/T_g has values of 0 and 1 when the parameter Ψ is equal to ∞ and 0, respectively. Therefore, the ratio T_0/T_g may be considered as a measure of fragility of a system. The VTF relation also enables to define a dimensionless fragility index m in the form:

$$m = \frac{\Psi\left(T_0/T_g\right)}{\left[1 - \left(T_0/T_g\right)\right]^2}. \tag{9.5}$$

The value of $m = \log(\eta_g/\eta_0) \approx 17$ for strong liquids follows Arrhenius relation and increases with increasing fragility of the liquids.

As mentioned above, the difference in the fragility of various systems is associated with the excess heat capacity ΔC_p during the cooling of liquids below their melting point T_m. This excess heat capacity ΔC_p of the liquids is due to a slowing down of the motion of the constituent molecules/atoms, which results in a decrease in their entropy from the entropy of fusion ΔS_f at T_m. The process of cooling requires constant reorganization of the constituent molecules/atoms to a low energy configuration, but not all of them are able to reach this stage because of the statistical nature of the local vibrations (cooperative relaxation). Therefore, only a part, say S_{ex}, of this excess entropy ΔS_f is attained by glassy systems at T_g. Since the entropy difference ΔS_f between the entropies S_f and S_g of the melt and the glass in the temperature interval between T_m and T_g can be expressed in terms of the heat capacity C_p according to the relation:

$$\Delta S_f = S_f - S_g = C_p \ln\left(\frac{T_m}{T_g}\right), \tag{9.6}$$

the connection between excess heat capacity ΔC_p at constant pressure p, which is related to the entropy ratio $S_{ex}/\Delta S_f$, during glass formation from a melt and its fragility is evident.

Consideration of cooperative relaxation of their constituent molecules/atoms to describe the non-Arrhenius behavior of viscosities of melts is the basis of the AG equation:

$$\eta = \eta_0 \exp\left[\frac{B}{T\ln(T/T_0)}\right] = \eta_0 \exp\left(\frac{B}{\Delta S_f}\right). \tag{9.7}$$

When the approximation $\ln(T/T_0) \approx (1 + T/T_0)$ holds, Eq. (9.7) transforms to VTF relation (9.2).

The cooperative relaxation motions of constituent molecules/atoms of different melts towards their glass formation ability have a universal behavior, which is described by the Kohlrausch–Williams–Watts (KWW) relaxation function (Angell, 1995; Ikeda and Aniya, 2010):

$$\phi = \phi_0 \exp\left[-\left(\frac{t}{\tau}\right)^{\beta}\right], \tag{9.8}$$

where ϕ_0 is the value of the physical quantity at time $t = 0$, τ is the structural relaxation time, and the exponent $\beta < 1$. This function is frequently called stretched function and the exponent β stretched exponent. The exponent β is an indicator of the degree of interactions between the constituents of liquids, which are structurally disordered. When the constituents exhibit simple relaxation, $\beta = 1$ (called Debye or linear relaxation mode). However, when they exhibit different relaxation modes, $\beta < 1$ (nonlinear relaxation mode).

The exponent β is related to the fragility according to the strength parameter Ψ of the VTF relation and the fragility index m (Ikeda and Aniya, 2010):

$$\beta = 1 - \frac{\left(T_0/T_g\right)}{\Psi^{1/2}} = 1 - \left\{\frac{\left(T_0/T_g\right)^{3/2}}{\left[1-\left(T_0/T_g\right)\right]}\right\}\frac{1}{m^{1/2}}. \tag{9.9}$$

Relationship between the exponent β and the fragility index m has indeed been observed (Ikeda and Aniya, 2010) for various glass-forming oxides when $\eta_g = 10^{12}$ Pa·s and $\eta_0 = 10^{-5}$ Pa·s (i.e. $\log(\eta_g/\eta_0) = 17$).

Examination of the plots of the $\beta(m)$ data for different glass-forming materials, reported by Ikeda and Aniya, 2010, shows that relation (9.9), with the highest value of β, $\beta_0 = 1$, and (T_0/T_g) determined by $\eta_g = 10^{12}$ Pa·s and $\eta_0 = 10^{-5}$ Pa·s (i.e. $\log(\eta_g/\eta_0) = 17$), is obeyed by a large number of glass-forming oxide systems with fragility index m lying between 30 and 160. However, there are glassy systems, such as some oxides (e.g. SiO_2, soda silicates, and borosilicates), polymeric compounds and metal glasses, which do not follow the theoretical curve of Eq. (9.9). In these cases, the values of β for the substances are much lower than those predicted by Eq. (9.9) with the value of $\beta_0 = 1$. These deviations from Eq. (9.9) are mainly associated with the fact that here $\beta_0 < 1$ and $\log(\eta_g/\eta_0) \neq 17$. For example, the $\beta(m)$ data for SiO_2, soda silicates, and borosilicates are reasonably represented by $\beta_0 \approx 0.8$ and $\log(\eta_g/\eta_0) = 17$, but the data for polymeric glasses may be described by $\beta_0 \approx 0.8$ and $\log(\eta_g/\eta_0) \approx 20$.

Theoretical models have also been proposed for the description of the temperature dependence of the viscosity of melts where emphasis has been placed on understanding the microscopic processes in glass formation and the role of chemical composition of the melts. In this context, we mention the bond-strength coordination-number fluctuation (BSCNF) model (Ikeda and Aniya, 2010) and the effective activation-energy barrier model of Avramov and Milchev (Avramov, 1998; Avramov and Milchev, 1988; Avramov et al., 2005). A common feature of these two models is that they describe the temperature dependence of viscosity of liquids in terms of mean bond strength E and mean coordination number Z between the randomly-distributed structural units constituting the melt, whereas thermally-activated viscous flow involves the breaking and formation of bonds between the constituent units. The BSCNF model also takes into account fluctuations ΔE and ΔZ in the mean values of E and Z, respectively, of the structural units. In contrast to the BSCNF model, the AM model considers the coordination number Z in terms of glass network formers.

Ikeda and Aniya (2010) have reviewed and compared the BSCNF model with the VTF theory for description of the viscosity behavior of various materials. It was shown that the BSCNF model shows the same viscosity behavior when fluctuations in the mean bond strength E and coordination number Z are equal.

Avramov (2005) gives a review of the temperature dependence of viscosity using various viscosity models and discusses their merits and demerits. The author demonstrates that the activation energy E of viscous flow is related to the glass transition temperature T_g and the "fragility exponent" α of their AM model is related to the melt composition. An important extension of this model is the description of the effect of secondary phases and their content in the melt on its viscosity (Avramov, 2011a, b, 2013; Avramov et al., 2003, 2005). In view of its success in describing the composition dependence of viscosity and glass transition temperature, the AM model is briefly presented in the next section.

9.3 Composition Dependence of Glass Transition Temperature

Viscosity of solvents strongly depends on the presence of second substance such as another solvent and a solute. This is also true in the case of melts where the presence of the second substance usually leads to enormous changes in its viscosity. For example, the viscosity of $(Me_2O)_x(SiO_2)_{1-x}$, where Me denotes Na and K, decreases by many orders of magnitude from that of SiO_2. A natural consequence of addition of Me_2O is that the glass transition temperature T_g of the melt is decreased enormously. Since these observations are described well by the AM model, this model and its main features are presented below.

The AM model is based on the following postulates (for example, see: Avramov, 1998, 2011b):

1) The viscosity η of a system is proportional to the relaxation time $\langle\tau\rangle$ necessary for the motion of constituent units (molecules/atoms) of the system according to the relation:

$$\eta = G\langle\tau\rangle, \tag{9.10}$$

where G is the high-frequency shear modulus and the average relaxation time $\langle\tau\rangle = 1/\langle\nu\rangle$, with $\langle\nu\rangle$ as the average jump frequency of the constituent units.

2) The relaxation time τ_i of the unit i depends on the activation energy barrier E_i associated with it according to the relation:

$$\tau(E_i) = \tau_0 \exp\left(\frac{E_i}{R_G T}\right), \tag{9.11}$$

where preexponential τ_0 is the value of relaxation time τ when $(E_i/R_G T) \to 0$.

3) The average relaxation time $\langle\tau\rangle$ may be given by the approximation:

$$\langle\tau\rangle = \tau_0 \exp\left(\frac{E_{max}}{\sigma}\right), \tag{9.12}$$

where σ is the dispersion in the activation energy E_i around its maximum value E_{max} in its probability distribution function.

The dispersion σ in the activation energy and the entropy of the system are related:

$$\sigma = \sigma_0 \exp\left\{\frac{2(S-S_0)}{R_G Z}\right\}, \tag{9.13}$$

where σ_0 is the dispersion at the reference state with entropy S_0 and $Z/2$ is the degeneracy of the system. The factor 2 accounts for the possibility of motion of a jumping unit in two directions from its position and Z is the mean coordination number for the units in the liquid network. Upon substituting the value of σ from Eq. (9.13) in Eq. (9.12) and using relation (9.10), one obtains

$$\eta = \eta_0 \exp\left\{\frac{E_{max}}{\sigma_0}\left[\frac{2(S-S_0)}{R_G Z}\right]\right\}, \tag{9.14}$$

where $\eta_0 = G\tau_0$. Using the relation between entropy and heat capacity, given by Eq. (9.6), in Eq. (9.14), the temperature dependence of η may be written in the form:

$$\eta = \eta_0 \exp\left\{\varepsilon\left(\frac{T_g}{T}\right)^{\alpha}\right\}, \tag{9.15}$$

where

$$\varepsilon = \frac{E_{max}}{\sigma_0}, \quad \alpha = \frac{2C_p}{R_G Z}. \tag{9.16}$$

In Eq. (9.16), ε is the dimensionless activation energy at the glass transition, i.e.

$$\varepsilon = 2.3(13.5 - \log\eta_0) \approx 31, \tag{9.17}$$

with

$$\log\eta_0 = \log G + \log\tau_0 \approx 0. \tag{9.18}$$

Note that $\log(\eta_g/\eta_0) = 13.5 - \log\eta_0$ (i.e. $\log\eta_g = 13.5$).

The physical interpretation of the constancy of ε lies in the dispersion σ. Glass transition occurs when the ratio σ/E_{max} is about 3%. In contrast, the parameter α is a measure of fragility, and $\alpha = 1$ represents the strong liquid. The higher its value, the higher is the liquid fragility.

In Eq. (9.5), we defined the fragility index m in terms of the strength parameter Ψ using Eq. (9.3). However, its general definition follows from the slope of the $\eta(T_g/T)$ plot at the glass transition temperature T_g (Angell, 1991):

$$m = \frac{\mathrm{d}\log\eta}{\mathrm{d}\left(T_g/T\right)}. \tag{9.19}$$

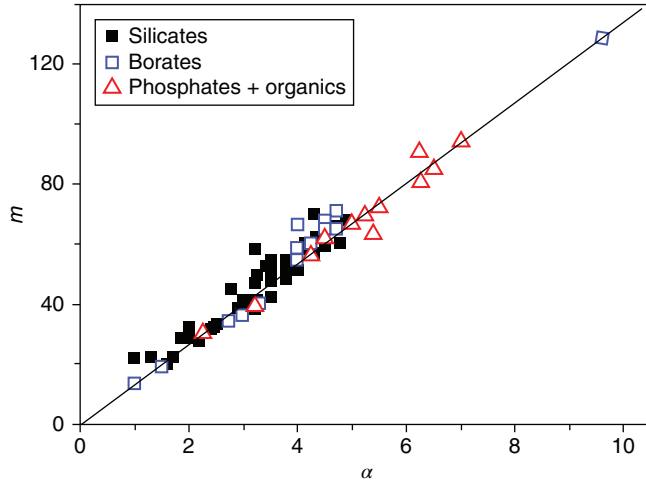

Figure 9.4 Relationship between the fragility parameters m and α for various silicates, borates, phosphates, and organics. Data for silicates, borates, and phosphates and organics are shown by solid squares, open squares, and open triangles, respectively. *Source:* Reproduced from Avramov (2011a). Copyright (2011), with permission from Elsevier.

According to Eq. (9.15), the slope m is

$$m = (13.5 - \log\eta_0)\alpha, \tag{9.20}$$

and the corresponding activation energy

$$E_{\max}(T_g) = \frac{mRT_g}{\alpha}. \tag{9.21}$$

The relationship between the fragility parameters m and α is shown for various silicates, borates, phosphates, and organics in Figure 9.4. The data for silicates, borates, and phosphates and organics are shown by solid squares, open squares, and open triangles, respectively. The straight line represents the dependence $m = 13.5\alpha$, implying that $\log\eta_0 \approx 0$.

From Eq. (9.4) of the VTF theory, one obtains the slope m of $\eta(T_g/T)$ plot at T_g in the form:

$$m = (13.5 - \log\eta_0)\frac{T_g}{T_g - T_0}. \tag{9.22}$$

Comparison of Eqs. (9.20) and (9.22) gives the relation between T_0/T_g and α as (Avramov, 2011a)

$$\frac{T_0}{T_g} = 1 - \frac{A}{\alpha}, \tag{9.23}$$

where $A = (13.5 - \eta_{0VTF})/(13.5 - \eta_{0AM})$ is a dimensionless parameter equal to about 1.2, and the subscripts VTF and AM with η_0 denote its predicted values according to the VTF and AM models, respectively. The constant $A \approx 1.2$ indicates how far below is T_0 from T_g. Replacement of α by $m = 13.5\alpha$ in Eq. (9.23) gives a relation between T_0 and m with a new constant $13.5A \approx 17$. This type of relation between T_0 and m was first given by Böhmer and Angell (1992).

The AM model not only describes the experimental data of the temperature dependence of the viscosity η of various types of glass-forming substances with adjustable parameters $\log\eta_0$, T_0, and α as discussed above but also explains the effect of composition of silicate melts using a melt structure-based approach. The main idea of the approach is that (Avramov et al., 2003, 2011b): (i) the melt is composed of network-forming (NF) oxides such as SiO_2 and network-modifying (NM) oxides such as Na_2O and (ii) there are two different types of bonds in the silicate melt: Rigid bonds like Si–O–Si and "floppy" bonds like Si–O–Na^+ formed by breaking some of the rigid bonds. The role of the modifiers is to reduce the activation energy for shear viscosity of the network formers, thereby decreasing the viscosity of the melt (lubricant effect) and the glass transition temperature T_g.

The concentration dependence of α can be explained by considering the relationship between heat capacity C_p and composition of the melt given in the form (Avramov, 2005):

$$C_p(x) = C_p(0) + 3R_G Z x, \tag{9.24}$$

where x is the molar concentration of the additive and $C_p(0)$ is the heat capacity of the pure network former. Using the relationship between α and heat capacity C_p of a system given by Eq. (9.16), from Eq. (9.24), one obtains

$$\alpha(x) = \frac{2C_p(x)}{R_G Z} = \alpha(0) + 6x. \tag{9.25}$$

This relation is followed by two- and three-component silicates with a slope of 6, but the value of $\alpha(0)$ is either 1 for additives like Na, K, Li, and Pb oxides or greater than 1 for borates (Avramov, 2005, 2011a).

Substitution of α from Eq. (9.25) in Eq. (9.23) gives the dependence of glass transition temperature T_0 on x in the form:

$$T_g = T_0\left[1 - \frac{A}{\alpha(0) + 6x}\right]^{-1} \approx T_0\left[1 + \frac{A}{\alpha(0) + 6x}\right]. \tag{9.26}$$

Obviously, T_g decreases with an increase in x, but this decrease is not linear in the entire x range.

Figure 9.5 shows, as an example, plots of glass transition temperature T_g against mole fraction x of different network modifiers. Open circles, open squares, open triangles pointing up, and open triangles pointing down represent

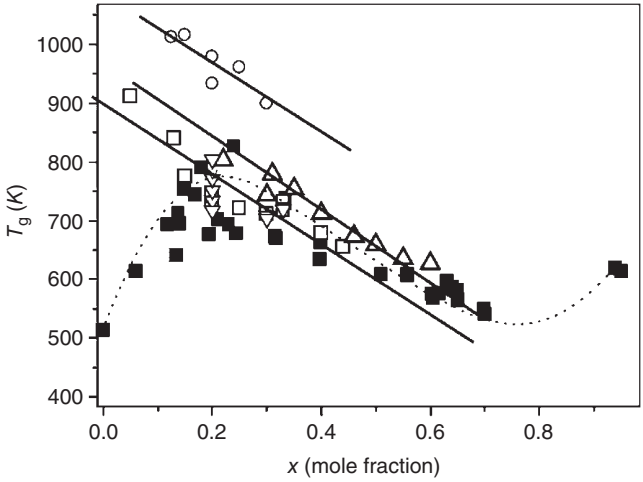

Figure 9.5 Plots of glass transition temperature T_g against mole fraction x of network modifiers. Open circles, open squares, open triangles pointing up, and open triangles pointing down represent alkaline–alumosilicates, sodium silicate, lead silicates, and alkali–metal silicates, respectively; solid squares denote borates. See text for details. *Source:* Adapted from Avramov et al. (2005). Copyright (2005), with permission from Elsevier.

alkaline–alumosilicates, sodium silicate, lead silicates, and alkali–metal silicates, respectively, whereas solid squares denote borates. It may be seen that, except for borates, T_g decreases almost linearly with x in the investigated x range. However, in the case of borates, T_g initially increases up to $x \approx 0.2$, followed by a practically linear decrease up to $x \approx 0.7$ when it increases again. Avramov et al. (2005) attributed the above observations to the participation of different structural units of network-modifying oxides that form strong and floppy bonds with silicate melts. Later, Avramov (2013) discussed the composition dependence of T_g of silicate glasses from entropy considerations and introduced the concept of a composition-related lubricant coefficient L. The author obtained a nonlinear dependence of T_g on L.

9.4 Relationship between Glass Transition Temperature and Metastable Zone Width of Solutions

Crystallization from solutions occurs in the metastable zone width by the association of ions or molecules of the solute diffusing in the bulk solution to form critically-sized stable 3D nuclei. However, in highly concentrated solutions of various substances when the viscosity is high and the mobility of molecules

becomes low, the nucleation may be suppressed and the solution behaves as an amorphous solid (i.e. glass). Aqueous solutions of disaccharides are examples of such amorphous substances. As in the case of melts, these glasses are prepared by rapid cooling of concentrated solutions.

In this section, phase diagrams of three disaccharide–water binary mixtures, studied by Gharsallaoui et al. (2008), are presented to describe the relationship between glass transition temperature and metastable zone width of these solutions. The disaccharides are: Maltitol, sucrose, and trehalose. All the three are nonreducing sugars and are chemically and thermally stable. Solutions (85% by weight) obtained by dissolving in water at a temperature above 85 °C were rapidly cooled and then stored at −18 °C for 24 h.

Phase diagrams of the three systems are shown in Figure 9.6 in the form of plots of temperature against disaccharide mass fraction. The figure also includes equilibrium conditions (i.e. freezing of water and solubility of sugar), metastable zone width, and nucleation conditions for the concentrated amorphous solution (CAS) of each disaccharide. Here, nucleation implies phase transformation of the amorphous state into crystalline form. This process strongly depends on the water content in the amorphous phase and occurs in the labile zone (i.e. beyond the metastable zone width). Values of glass transition T_g, temperature difference ($T_g - T_N$), and growth characteristics are given in Table 9.1.

If one takes the temperature difference ($T_g - T_N$) as a measure of fragility, from Table 9.1, one finds that amorphous trehalose is the most fragile of the three disaccharides, amorphous maltitol is the least fragile, and sucrose lies in between these two. These differences in the fragility of these amorphous saccharides and their crystallization behavior are associated with the viscosity of their solutions. Both are determined by the mobility of molecules, which is related to the sugar–water and sugar–sugar interactions. These interactions also determine the value of T_g of the mixtures, and is related to the suppression of water crystallization. For example, the trehalose–water system has a higher T_g than sucrose–water and maltitol–water solutions because of stronger sugar–water bonds than those in the other systems. Obviously, these processes of fragility and stability of amorphous disaccharide–water systems are of both kinetic and thermodynamic origin.

Kinetic and thermodynamic factors also determine the fragility and stability of glasses formed from their melts. Fragility and stability of glasses from melts are associated with the interactions between different structural units composing the melt. For example, molecular glasses composed of small organic molecules are easily formed and are stable under ambient conditions, but they tend to crystallize over time. However, certain classes of large-molecule organic compounds, such as mexylaminotrazine derivatives, of irregular shapes have strong glass-forming ability and good glass stability above their T_g (for example, see: Laventure et al., 2017). For such compounds, the glass-forming ability and glass stability are determined by competition between two different interactions, namely: hydrogen bonding and directional noncovalent interaction, π–π stacking.

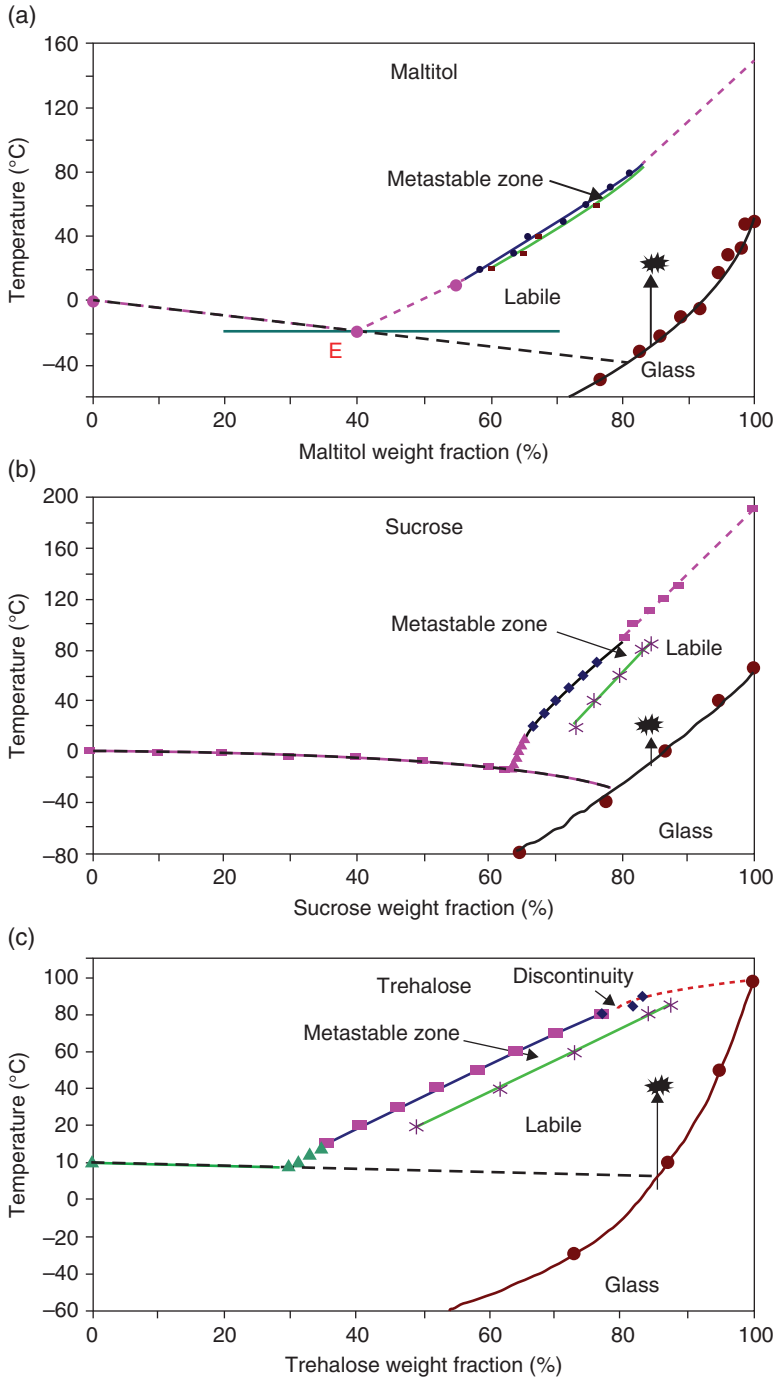

Figure 9.6 Phase diagrams of three disaccharide–water binary systems and temperature of recrystallization of the their amorphous state; systems are (a) maltitol–water, (b) sucrose –water, and (c) trehalose–water. *Source:* Adapted from Gharsallaoui et al. (2008). Copyright (2007), with permission from Elsevier.

Table 9.1 Temperatures T_g and T_N, and growth characteristics of concentrated aqueous solutions of disaccharides.

Disaccharide	T_g (°C)	T_g–T_N (°C)	Growth characteristics
Maltitol	25	29	Very slow (on solution surface)
Sucrose	15	45	Slow (dispersed in sample volume)
Trehalose	45	70	Rapid (middle of sample)

Source: After Gharsallaoui et al. (2008).

The results suggested that π–π stacking promotes crystallization, whereas suppresses it due to high conformational constrains imposed by the π–π stacking (Laventure et al., 2017).

9.5 Metastable Zone Width of Melts and Glass Formation

Estimation of glass formation temperature T_g and corresponding critical cooling rate R_{Lg} during cooling of molten materials of different types is an active field of research (Dasgupta, 2005; Debenedetti, 1996; Scherer, 1991). The commonly used method of predicting the critical cooling rate R_{Lg} for glass formation is based on the construction of a time–temperature–transformation curve (see Scherer, 1991). In practice, this approach is relatively complex because the final expressions used to calculate R_{Lg} involve parameters, which have to be obtained independently. Moreover, in these expressions it is assumed that $T_g \approx 0.77 T_m$. This assumption is based on experimental observation for various materials.

Here, the approach, advanced by Sangwal (2009a, b) for the cooling rate dependence of MSZW of solutions (see Chapter 5), based on the classical theory of 3D nucleation is applied to the prediction of temperature T_g for glass formation and critical cooling rate R_{Lg} for molten elements and alkali halides using volumetric thermal expansion coefficient α_V of molten liquids and density d_m of substances at their melting point T_m.

9.5.1 Derivation of Basic Equations

We consider the change in melt volume $\Delta V = (V_m - V)$ corresponding to the temperature difference $\Delta T = (T_m - T)$ between the melting temperature T_m and the temperature T such that $T_m > T$. Then, one may write the expression for the volumetric thermal contraction coefficient α_V in the form (see Eq. (A.3)):

$$\alpha_V = \frac{\Delta V}{V_m \Delta T} = \frac{\Delta V}{V_m \Delta t} \frac{1}{R_L}, \tag{9.27}$$

where the cooling rate $R_L = \Delta T/\Delta t$. In the vicinity of the onset of nucleation corresponding to temperature T_N when the maximum supercooling $\Delta T_{max} = (T_m - T_N)$ and the maximum decrease in the volume of the melt is $\Delta V_{max} = (V_m - V_N)$, the nucleation rate J is proportional to the rate of change in the relative volume $\Delta V/V_m$ of the melt, given by

$$J = f\frac{\Delta V}{V_m \Delta t}, \tag{9.28}$$

where the proportionality constant f characterizes the number of nuclei forming per unit volume. From Eqs. (9.27) and (9.28), one may write the nucleation rate J in the form:

$$J = f\alpha_V R_L. \tag{9.29}$$

We assume that nucleation occurs according to the classical theory of 3D nucleation, then the nucleation rate J may be expressed as (see Chapter 2)

$$J = J_0 \exp\left[-B\left(\frac{k_B T}{\Delta G_v}\right)^2\right], \tag{9.30}$$

where the thermodynamic parameter

$$B = \frac{16\pi}{3}\left(\frac{\gamma\Omega^{2/3}}{k_B T}\right)^3, \tag{9.31}$$

the free energy change ΔG_v for the transformation of liquid into solid phase per unit volume is given by (see Chapter 2)

$$\Delta G_v = \frac{\Delta H_m \Delta T}{T_m}, \tag{9.32}$$

the preexponential factor J_0 is associated with the processes of integration of growth units to the growing nucleus, γ is the solid–melt interfacial energy, Ω is the molecular volume, k_B is the Boltzmann constant, ΔH_m is the enthalpy of melting, and $\Delta T = (T_m - T)$ is the supercooling. Corresponding to the MSZW at temperature T_N when the maximum supercooling $\Delta T_{max} = (T_m - T_N)$, substitution of the value of ΔG_v from Eq. (9.32) into Eq. (9.30) gives

$$J = J_0 \exp\left[-B\left(\frac{k_B T_m}{\Delta H_m}\right)^2\left(\frac{T_N}{\Delta T_{max}}\right)^2\right]. \tag{9.33}$$

Upon equating the two nucleation rates J given by Eqs. (9.29) and (9.33), one obtains

$$B\left(\frac{k_B T_m}{\Delta H_m}\right)^2\left(\frac{T_N}{\Delta T_{max}}\right)^2 = -\ln\left(\frac{f\alpha_V R_L}{J_0}\right) = -\ln\left(\frac{f\alpha_V}{J_0}\right) - \ln R_L, \tag{9.34}$$

which may be rewritten in the form:

$$\left(\frac{T_N}{\Delta T_{max}}\right)^2 = F(1 - Z\ln R_L), \tag{9.35}$$

where the parameter

$$F = \frac{1}{ZB}\left(\frac{\Delta H_m}{k_B T_m}\right)^2, \tag{9.36}$$

and the constant

$$Z = \ln\left(\frac{f\alpha_V}{J_0}\right). \tag{9.37}$$

Equation (9.35) predicts that $(T_N/\Delta T_{max})^2$ decreases linearly with an increase in $\ln R_L$, with slope FZ and intercept F, where F is given by Eq. (9.36) and Z is given by Eq. (9.37).

The reader should note that Eq. (9.35) is similar to Eq. (5.27) for cooling crystallization from solutions and we have used the same symbols F and Z as in Chapter 5. However, the reader is cautioned not to confuse the constant Z of Eq. (9.35) with the coordination number Z of Section 9.3 because they are completely different quantities.

Following the approach used in the derivation of self-consistent Nývlt-like equation (see Section 5.1.3), one obtains a different relation between $(\Delta T_{max}/T_N)$ and R_L. In this case, one considers that in the vicinity of nucleation temperature T_N the occurrence of 3D nucleation according to the power-law relation:

$$J = k_m\left(\frac{\Delta G_V}{k_B T}\right)^m = \left(\frac{\Delta H_m}{k_B T_m}\frac{\Delta T_{max}}{T_N}\right)^m, \tag{9.38}$$

where k_m is the so-called nucleation constant and m is the nucleation order. Both k_m and m are empirical constants. Here, we have used the same symbols as in Chapter 5 but the nucleation order m should not be confused with the definition of slope m in Sections 9.2 and 9.3. Then, from Eqs. (9.29) and (9.38), one obtains a Nývlt-like equation in the form:

$$\ln\left(\frac{\Delta T_{max}}{T_N}\right) = \Phi + \frac{1}{m}\ln R_L, \tag{9.39}$$

where the constant

$$\Phi = \frac{1}{m}\ln\left(\frac{f\alpha_V}{k_m}\right) - \ln\left(\frac{\Delta H_m}{k_B T_m}\right). \tag{9.40}$$

Note that the constant Φ depends, among others, on the thermal characteristics of a material through $(\Delta H_{max}/T_m)$ and α_V. According to relation (9.39),

a plot of $\ln(\Delta T_{max}/T_N)$ against $\ln R_L$ is expected to give an intercept Φ and slope $1/m$.

Note that usually $\Delta T_{max} \ll T_N$. Therefore, it is convenient to analyze the experimental data of MSZW relating ΔT_{max} with R_L according to Eqs. (9.35) and (9.39) taking T_m instead of T_N. The experimental data, reported by Bouropoulos et al. (1997), on the crystallization of pure and water-containing ε-caprolactam melts are analyzed here as an example. As a raw material this compound is used in the manufacturing of synthetic fibers and various plastics. The authors observed that addition of water to the melt causes a decrease in the melting point T_m and a widening of the MSZW of the samples. In their study of MSZW measurements as a function of cooling rate R_L, the authors used samples of pure caprolactam and caprolactam containing 10% water (by weight) with melting point T_m equal to 341 and 311 K, respectively. Based on the above data, plots of $\ln(\Delta T_{max}/T_m)$ and $(T_m/\Delta T_{max})^2$ against $\ln R_L$ for the above samples are shown in Figure 9.7 according to Eqs. (9.39) and (9.35), respectively, with best-fit constants listed in Table 9.2.

The values of the nucleation order m obtained here for the two samples are similar to those reported by Bouropoulos et al. (1997). As in the case of solutions discussed in Chapter 5, the values of Φ and $1/m$ are related to F and Z, respectively, with $\Phi \approx -(\ln F)/2$. Addition of water to the caprolactam melt leads to an increase in Φ and $1/m$, and the fit of the $\Delta T_{max}(R_L)$ data improves with a small correction ΔR_L but the value of Z is decreased insignificantly.

The parameters F and Z in Eq. (3.35) are related to well-defined physical quantities. Therefore, the effect of addition of water may be explained from consideration of the processes that cause changes in the physical quantities contained in their equations. An increase in Z may be attributed to increases in the thermal expansion (contraction) coefficient α_V and the concentration f of the nuclei forming in the melt (see Eq. (9.37)) as well as a decrease in J_0 when water suppresses nucleation by adsorbing on their surfaces (see Eq. (9.43)). An increase in Z leads to a decrease in F, but this effect of Z alone does not account for the large reduction in F. This indicates that the $(\Delta T_m/k_B T_m)^2/B$ term also decreases with the addition of water.

9.5.2 Effect of Melt Viscosity and Additives on *Z* and *F* Parameters

When mass transport across the nucleus/interface affects the nucleation rate, the nucleation rate may be given by (see Chapter 2)

$$B\left(\frac{k_B T_m}{\Delta H_m}\right)^2 \left(\frac{T_N}{\Delta T_m}\right)^2 - \left(\frac{\Delta G_D}{k_B T}\right) = -\ln\left(\frac{f\alpha_V}{J_0}\right) - \ln R_L, \tag{9.41}$$

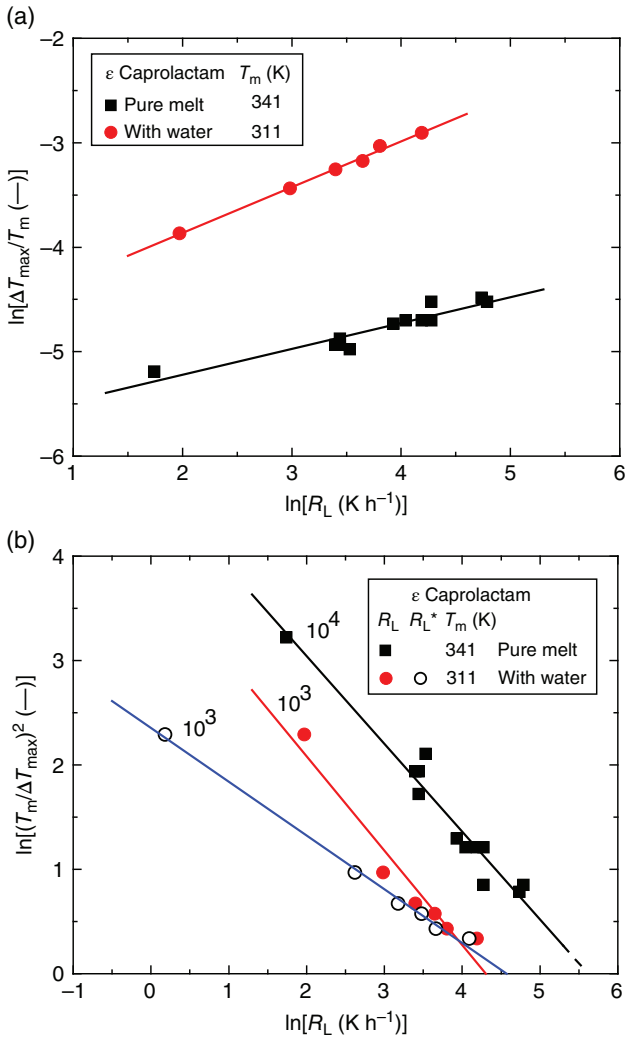

Figure 9.7 Plots of $\ln(\Delta T_{max}/T_m)$ and $(T_m/\Delta T_{max})^2$ against $\ln R_L$ for (a) pure and water-containing caprolactam according to Eqs. (9.39) and (9.35), respectively, with best-fit constants listed in Table 9.2. In (b), plot with open circles is drawn with corrected $R_L^* = R_L - \Delta R_L$, with correction $\Delta R_L = 0.6$ K·h^{-1}. *Source*: Original data from Bouropoulos et al. (1997).

Table 9.2 Values of constants of Eqs. (9.39) and (9.35) for ε-caprolactam samples.

	Equation (9.39)				Equation (9.35)			
Sample	$-\Phi$	$1/m$	m	R^2	10^3F	10^3FZ	Z	R^2
Pure	5.72	0.247	4.04	0.8690	47.27	8.41	0.178	0.9384
+10% water	4.74	0.438	2.28	0.9939	3.89	9.03	0.232	0.9244
+10% water[a]					2.36	5.15	0.219	0.9935

[a] Parameters with corrected R_L^*.

where ΔG_D is the activation energy for material transport by diffusion. Then, from Eqs. (9.29) and (9.41), one obtains Eq. (9.35) with the constant F given by Eq. (9.36) and the constant Z given in the form:

$$Z = \ln\left(\frac{f\alpha_V}{J_0}\right) - \ln\left[\exp\left(\frac{\Delta G_D}{k_B T}\right)\right]. \tag{9.42}$$

Note that for a given R_L an increase in the viscosity leads to a decrease in Z and an increase in F.

The above cases of solidification are valid for one-component systems characterized by well-defined melting points. However, when a one-component melt contains small amounts of another component, appropriate modifications have to be introduced in the above equations.

An additive affects the values of constants F and Z of Eq. (9.35) by changing the values of different quantities. Among the different effects, an additive has pronounced effect on the nucleation rate J by causing changes in the preexponential factor J_0 (kinetic effect) and the interfacial energy γ (thermodynamic effect) of Eq. (9.30). To account for these effects, we follow a procedure similar to that used in Section 5.4.

An additive adsorbing on the nucleus surface can change the value of J_0 by physically occupying (blocking) the existing active sites for the attachment of growth units on the growing nuclei. If θ is the fraction of active sites of growing nuclei affected by additive particles, the effective kinetic factor $J_{0\text{eff}}$ in the presence of the additive may be expressed in the form:

$$J_{0\text{eff}} = J_0(1-\theta) + J_{0\text{i}}\theta = J_0(1-\alpha_{\text{eff}}\theta), \tag{9.43}$$

where J_0 and $J_{0\text{i}}$ denote the kinetic factors in the absence and presence of the additive and the additive effectiveness factor α_{eff} is given by

$$\alpha_{\text{eff}} = \frac{(J_0 - J_{0\text{i}})}{J_0}. \tag{9.44}$$

Obviously, when an additive inhibits nucleation, $0 \le \alpha_{\text{eff}} \le 1$ (i.e. $0 \le J_{0\text{i}} \le J_0$) and $J_{0\text{eff}} < J_0$. However, when additive particles favor nucleations by integration of growth units to growing nuclei such that $J_{0\text{i}} > J_0$, $\alpha_{\text{eff}} < 0$ and $J_{0\text{eff}} > J_0$.

Coverage θ of the surface by an additive causes a decrease in the interfacial energy γ. We assume that the decrease in the interfacial energy γ follows the empirical relation:

$$\gamma = \gamma_0(1 - b\theta). \tag{9.45}$$

Then, from Eq. (9.31), one obtains

$$B = B_0(1 - 3b\theta), \tag{9.46}$$

where B_0 is the value of B when $\theta = 0$, $b\theta \ll 1$, and the constant $b \approx 1$.

When both kinetic and thermodynamic effects of an additive are considered, one obtains Eq. (9.35) with constants F and Z expressed in the form:

$$Z = \frac{Z_0}{(1-\alpha_{\text{eff}}\theta)} \approx Z_0(1+\alpha_{\text{eff}}\theta), \tag{9.47}$$

and

$$F = F_0(1+b_1\theta), \tag{9.48}$$

with

$$b_1 = (3b - \alpha_{\text{eff}}), \tag{9.49}$$

where Z_0 and F_0 are the values of Z and F when $\theta = 0$.

It may be noted from Eq. (9.48) that the value of F is determined by the constant b_1 and the additive content θ. Since $\alpha_{\text{eff}} < 1$, $b_1 > 2$, implying that an additive always leads to an increase in F when the effect of additive on Z is associated with both the thermodynamic and kinetic parameters γ and J_0, respectively.

The limiting cooling rate R_{Llim} is given by the relation: $Z = -\ln R_{\text{Llim}}$. When the solidification of a melt containing an additive is controlled by melt viscosity, from Eq. (9.47), one may write

$$R_{\text{Llim}} = \frac{J_0(1-\alpha_{\text{eff}}\theta)\exp(\Delta G_D/k_{\text{B}}T)}{f\alpha_V}. \tag{9.50}$$

Since the term $\exp(\ldots)(\Delta G_{\text{D}}/k_{\text{B}}T) > 1$, transport by diffusion always leads to an increase in R_{Llim}. However, the value of R_{Llim} decreases when $0 < \alpha_{\text{eff}} < 1$ whereas it increases when $\alpha_{\text{eff}} < 0$. The value of R_{Llim} also depends on the nature of solidifying melt and is reflected by the constant f characterizing the number of nuclei forming per unit volume and the thermal contraction coefficient α_V (see Eq. (9.29)).

9.5.3 Calculations of R_{Llim}, Z, F, and T_{N} for Molten Elements and Electrolytes

The thermal contraction coefficients α_V and $\Delta H_{\text{m}}/R_{\text{G}}T_{\text{m}}$ for most elements and alkali halides are practically constant quantities (see Appendix B). Similarly, the ratios of densities d_{m} of molten elements to their atomic mass M and alkali halides to their averaged atomic mass M_{av} are constant quantities (see Appendix C). The values of different constants are summarized in Table 9.3. In order to calculate R_{Llim}, Z, and F, we take the values of α_{V}, $\Delta H_{\text{m}}/R_{\text{G}}T_{\text{m}}$, and $(d_{\text{m}} - d_{0)}/M$ from Table 9.3, following the hole theory of liquids, the term $(k_{\text{B}}T/\gamma\Omega^{2/3})^{1/2} = 2$ (cf. Chernov, 1984), the preexponential factor $J_0 \approx 10^{26}\ \text{m}^{-3}\cdot\text{s}^{-1}$, and the values of f using the relation:

$$f = \frac{(d_{\text{m}} - d_0)N_{\text{A}}}{M}, \tag{9.51}$$

Table 9.3 Values of different constants used for the calculation of R_{Llim}, Z, and F for molten elements and alkali halides.

Parameter	Elements	Alkali halides
α_V (K^{-1})	$(1.2 \pm 0.3)\cdot 10^{-4}$	$(3.3 \pm 0.6)\cdot 10^{-4}$
$\Delta H_m/R_G T_m$	1.1 ± 0.1	3.7 ± 0.2
$(d_m - d_0)/M$ (cm^{-3})	$6.78\cdot 10^{-2}$	$2.77\cdot 10^{-2}$

Table 9.4 Values of R_{lim}, Z, and F for molten elements and alkali halides and aqueous solutions.

System	State	R_{Llim} ($K\cdot s^{-1}$)	Z	F	$F^{1/2}/(1+F^{1/2})$
Molten elements	No viscosity	20.8	3.04	14.7	0.79
($f = 4\cdot 10^{28}$ m^{-3})	With viscosity	$3.1\cdot 10^{3}$	8.0	38.7	0.86
Molten alkali halides	No viscosity	18.2	2.9	158.8	0.93
($f = 1.66\cdot 10^{28}$ m^{-3})	With viscosity	$2.7\cdot 10^{3}$	7.9	432.6	0.95
KTB–water	No viscosity	$5.3\cdot 10^{-3}$	5.3	14.7	0.79

where N_A is the Avogadro number equal to $6\cdot 10^{26}$ $kmol^{-1}$. In order to understand the effect of melt viscosity, we arbitrarily assume that the term $\Delta G_D/k_B T = 5$. The calculated values of R_{Llim}, Z, and F without and with the effect of viscosity are listed in Table 9.4. Using these values of R_{Llim}, Z, and F, one may obtain plots of $(T_N/\Delta T_{max})^2$ against $\ln R_L$, with slope FZ and intercept F according to Eq. (9.35) without and with the effect of melt viscosity. Figure 9.8 presents the plots of $(T_N/\Delta T_{max})^2$ of a melt against $\ln R_L$ for situations without and with the effect of melt viscosity. The pronounced effect of the viscosity of a melt is clearly seen.

It is interesting to compare the calculated values of R_{Llim}, Z, and F of molten elements and electrolytes, given in Table 9.4, with those of electrolyte aqueous solutions. For this purpose, we consider the values of R_{Llim}, Z, and F obtained by analysis of experimental data of maximum supercooling ΔT_{max} for aqueous solutions, saturated at different temperatures, as a function of cooling rate R_L. These values of R_{Llim} and F are included in Table 9.4. It may be seen from the table that the values of R_{Llim} and F for the melts is over two orders of magnitude higher than those for aqueous solutions.

Finally, it should be noted that the parameter F is directly related to the maximum supercooling ΔT_{max} when $\ln R_L = 0$ (see Eq. (9.35)). Then,

$$T_N = F^{1/2} \Delta T_m. \tag{9.52}$$

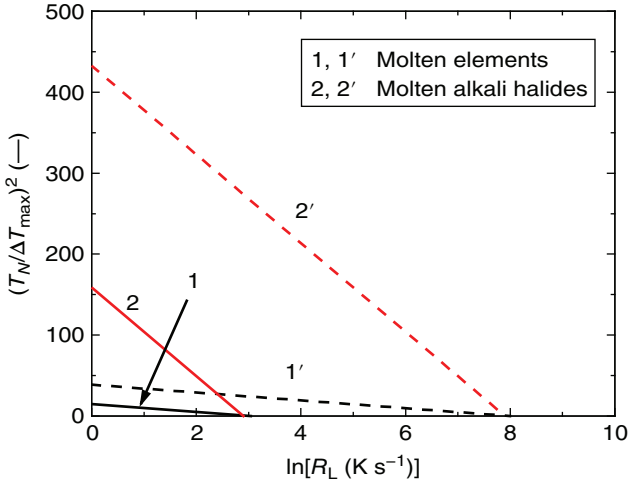

Figure 9.8 Schematic presentation of plots of $(T_N/\Delta T_{max})^2$ against ln R_L, showing the effect of viscosity of (1,1′) metal and (2,2′) alkali halide melts: curves (1,2) without and (1′,2′) with viscosity of the melt. See text for details.

Since $\Delta T_{max} = (T_m - T_N)$, from Eq. (9.52), one obtains

$$T_N = \left(\frac{F^{1/2}}{1+F^{1/2}}\right) T_m. \tag{9.53}$$

This relation shows that the factor $F^{1/2}/(1 + F^{1/2})$ determines the crystallization behavior of different melts under different solidification conditions. The calculated values of the factor $F^{1/2}/(1 + F^{1/2}) = T_N/T_m$ are listed in Table 9.4, whereas the dependence of $F^{1/2}/(1 + F^{1/2})$ on F is illustrated in Figure 9.9. It may be noted that this factor rapidly increases with F in a relatively narrow F interval for materials having a wide MSZW, but increase in its value steadily slows down with decreasing MSZW for large F. A relatively narrow F interval is possible for materials with relatively high values of Z and B. A high value of Z is possible when the preexponential factor J_0 associated with the integration of growth units is slowed down or the value of the proportionality constant f characterizing the concentration of integrating units is high (see Eq. (9.37)). Under these conditions, if one identifies T_N as the glass-forming temperature T_g, it is interesting to examine the relationship between T_g and T_m, as discussed below.

9.5.4 Relationship between T_g and T_m for Various Substances

It is well known that the melting point T_m of various linear long-chain n-alkanes and aliphatic alcohols and acids increases with the number n of carbon atoms in the chain. However, this increase depends on whether the chain has even or odd

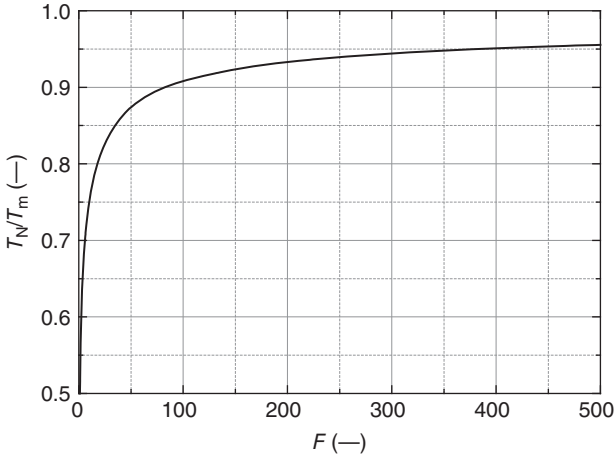

Figure 9.9 Dependence of $F^{1/2}/(1 + F^{1/2}) = T_N/T_m$ on F. See text for details.

number of carbon atoms as well as on the degree of chain branching. These trends are associated with the packing of the molecules in the crystalline state. Compounds with even number of carbon atoms have a higher melting point due to their more effective packing in the crystalline form than those with odd carbon number n in the chain or with chain branching. This trend is also followed by complex ionic compounds composed of cations containing pyridinium, isoquinolinium, pyrrolidinium, or other groups and anions of chemically simple as well as complex radicals. These compounds are ionic liquids at room temperature and most of them show glass transition temperature (Zhang et al., 2006).

Figure 9.10 shows some examples of the dependence of the quotient T_g/T_m on the constitution of the ions of a salt. It may be noted from Figure 9.10a that the value of the quotient T_g/T_m for different salts differs enormously and lies between 0.48 and 0.96. Moreover, its value can differ up to 15% even for the same salt, it is lower for compounds with odd carbon number than that for even n, and its value strongly depends on the chemical constitution of the anion (see Figure 9.10b). However, for even n cations, practically it does not depend on the carbon number n (see Figure 9.10a).

It is well known (Scherer, 1991) that the glass-forming temperature is $T_g \approx 0.77T_m$ for metals that easily attain the glassy state. This value of 0.77 is in good agreement with the value of the factor $F^{1/2}/(1 + F^{1/2})$ for the solidification of molten metals involving a negligible effect of melt viscosity (see Table 9.4). However, as seen from Table 9.4, the calculated value of the factor $F^{1/2}/(1 + F^{1/2})$ for the solidification of molten alkali halides is much higher than that for molten metals. These differences are responsible for the difference in

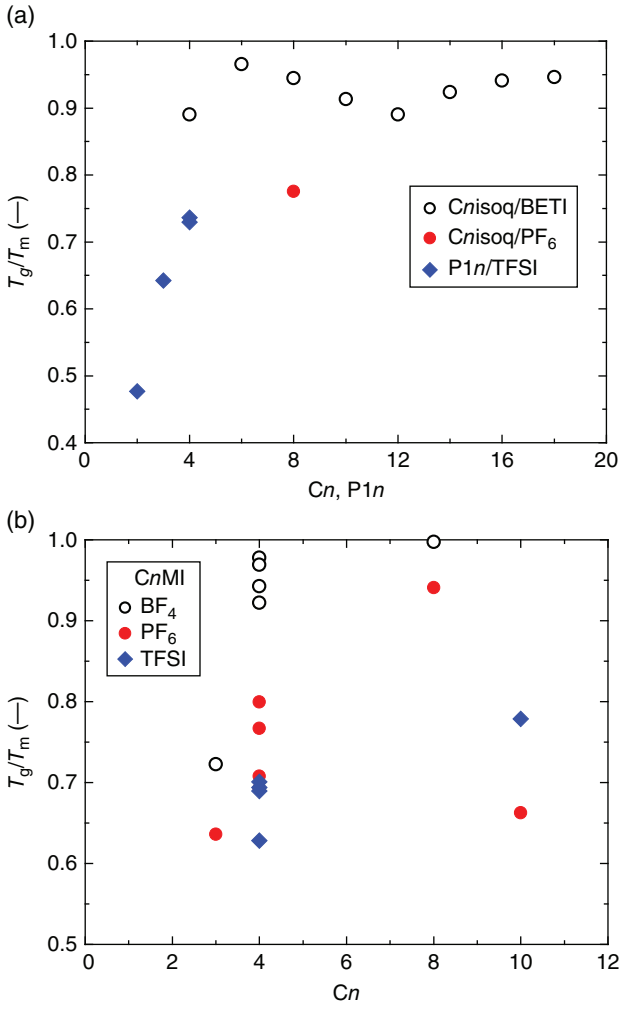

Figure 9.10 Relationship between quotient T_g/T_m on the number *n* of carbon atoms (C*n*) in cations of different salts: (a) *N*-alkyl-isoquinolinium (C*n*isoq) and *N*-methyl-*N*-alkyl-pyrrolidinium (P1*n*) salts and (b) 1-alkyl-3-methylimidazolium (C*n*MI) salts. Anions are: tetrafluoroborate (BF4), hexafluoroborate (PF6), bis((perfluoroethane)sulfonyl)imides (BETI), and bis((trifluoromethyl)sulfonyl)imides (TFSI). *Source:* Data from Zhang et al. (2006).

the observed values of maximum supercooling ΔT_{max} and the cooling rate R_{Llim} in the two cases. The causes of this difference are discussed below.

It may be noted that the calculated values of the limiting cooling rate R_{Llim} for melts are in good agreement with the experiment. For example, $R_{Llim} \approx 3.8\ K{\cdot}s^{-1}$ for the good glass-former lithium disilicate, but it is about $10^4\ K{\cdot}s^{-1}$ for the

relatively poor glass-former $(Au_{85}Cu_{15})_{77}Si_9Ge_{14}$ (Scherer, 1991). This agreement between the predicted and experimental R_{Llim} places confidence in the application of the above approach for the estimation of glass-forming temperature T_g and limiting cooling rate R_{Llim} for a molten material.

In the case of glass transition of ionic liquids composed of cations containing pyridinium, isoquinolinium, pyrrolidinium, or other groups and anions of chemically simple as well as complex radicals, the observed values of T_g/T_m equal to 0.48 and 0.96 imply that F is about 0.85 and 576, respectively. As seen from Eq. (9.36), for an additive-free system the F parameter depends on Z and B, and decrease in the values of Z and B lead to an increase in the value of F. The constant Z decreases with a decrease in f and α_V, and an increase in ΔG_D, whereas B increases with an increase in $\gamma\Omega^{2/3}/k_BT_N$. We consider the effect of these quantities on the value of F parameter taking glass-forming behavior of ionic liquids (see Appendix B).

Assuming that the relationship between the lattice energy U_{latt} and the thermal expansivity α_V is an indicator of the formation of clusters composed of N cation–anion pairs, it may be inferred that this process of clustering leads to a reduction in the value of f by the factor N^3, the maximum value of which is about 200 for ionic salts such as alkali halides (see Table B.1). In contrast to this, the values of α_V for various ionic liquids do not differ by more than by a factor of 10 (see Appendix B.2). Since both f and α_V are contained in the logarithm term, the maximum changes caused in F by changes in them do not exceed by a factor of 4.

The values of the solid–solution interfacial energy γ are 10–40 and 0.1–0.5 $mJ{\cdot}m^{-2}$ for common inorganic and macromolecular crystals, respectively (Malkin et al., 1999; Sangwal, 2007). The low values of the interfacial energy γ of macromolecular crystals than those of inorganic crystals are due to their weak intermolecular interactions per lattice unit. Since ionic liquids undergoing glass transition involve weak intermolecular interactions, following the case of macromolecular crystals, it may be assumed that their interfacial energy is also relatively low. Consequently, since B is proportional to γ^3 (see Eq. (9.31)), even small changes in the values of γ-term can lead to enormous changes in B. Similarly, different values of ΔG_D can result in large changes in Z and hence in F. Thus, it may be concluded that viscosity and interfacial energy mainly determine the values of F.

9.5.5 Comparison of Cooling Behavior of Melts and Electrolyte Solutions

In the case of melt of a metal with melting point $T_m \approx 500$ K, the typical values of ΔT_{max} and R_L are about 100 K and exceeding 20 $K{\cdot}s^{-1}$, respectively. However, in the case of aqueous solutions, the typical values of ΔT_{max} and R_L are about 15 K and less than 100 $K{\cdot}h^{-1}$ (about 0.03 $K{\cdot}s^{-1}$), respectively. Using these values of

Table 9.5 Values of t_{in} and τ for molten melts and electrolyte solutions.

System	t_{in} (s)	τ (s)
Molten metals	<5	10^{-5} to 10^{-1}
Electrolyte solutions	>500	10^{-9}

ΔT_{max} and R_L, one can estimate the induction period for nucleation t_{in} from the relation:

$$t_{in} = \frac{\Delta T_{max}}{R_L}. \tag{9.54}$$

These calculated values of t_{in} are given in Table 9.5. It is interesting to compare these values of t_{in} with the values of relaxation time τ associated with diffusion of atoms, ions, or molecules of the liquid phase during cooling. The relaxation time τ may be calculated from the relation:

$$\tau = \frac{\lambda_D^2}{D}, \tag{9.55}$$

where λ_D is the average jump distance and D is the diffusion coefficient for the atoms, ions, or molecules in the liquid. The value of D for metals lies between 10^{-13} and 10^{-17} $m^2 \cdot s^{-1}$ near the melting point (Bockris and Reddy, 1970; Chernov, 1984), while it is about 10^{-9} $m^2 \cdot s^{-1}$ in solutions (Chernov, 1984). Taking a typical value of λ_D equal to 10^{-9} m, the calculated values of the average jump time from Eq. (9.55) are also listed in Table 9.5.

It may be seen that t_{in} is comparable with the value of τ for molten metals but $t_{in} \gg \tau$ in the case of electrolyte solutions. This implies that diffusion of atoms in molten metals can become the dominating process in the nucleation of molten metals, but diffusion, in general, is unimportant in the formation of nuclei in supersaturated solutions of electrolytes. Consequently, molten metals can be cooled even at very high rates without undergoing nucleation, but electrolyte solutions cannot be cooled at high rates without the occurrence of nucleation in the liquid volume. These differences are associated with the activation energy ΔG_D for the diffusion of atoms, ions, or molecules described by the well-known Frenkel relation:

$$\tau = \tau_0 \exp\left(\frac{\Delta G_D}{R_G T}\right), \tag{9.56}$$

where the jump time $\tau_0 = \nu^{-1}$, where ν is the average atomic jump frequency of the order of 10^{13} s^{-1}. Then, one obtains $\Delta G_D / R_G T$ lying between 18.4 and 27.6 for molten metals and is equal to 9.2 for electrolyte solutions.

References

Angell, C.A. (1991). Relaxation in liquids, polymers and plastic crystals: strong/fragile patterns and problems. *J. Non-Cryst. Solids* 131–133: 13–31.

Angell, C.A. (1995). Formation of glasses from liquids and biopolymers. *Science* 267: 1924–1935.

Avramov, I. (1998). Viscosity of glass-forming melts. *J. Non-Cryst. Solids* 238: 6–10.

Avramov, I. (2005). Viscosity of disordered media. *J. Non-Cryst. Solids* 351: 3163–3173.

Avramov, I. (2011a). Interrelation between the parameters of equations of viscous flow and composition of glassforming. *J. Non-Cryst. Solids* 357: 391–396.

Avramov, I. (2011b). Dependence of the parameters of equations of viscous flow on chemical composition of silicate melts. *J. Non-Cryst. Solids* 357: 3841–3846.

Avramov, I. (2013). The role of entropy on viscosity of silicates. *J. Non-Cryst. Solids* 262: 120–123.

Avramov, I. and Milchev, A. (1988). Effect of disorder on diffusion and viscosity in condensed systems. *J. Non-Cryst. Solids* 104: 253–260.

Avramov, I., Rüssel, C., and Keding, R. (2003). Effect of chemical composition on viscosity of oxide glasses. *J. Non-Cryst. Solids* 324: 29–35.

Avramov, I., Vassilev, T., and Penkov, I. (2005). The glass transition temperature of silicate and borate glasses. *J. Non-Cryst. Solids* 351: 472–476.

Berthier, L. and Biroli, G. (2011). Theoretical perspective on the glass transition and amorphous materials. *Rev. Modern Phys.* 83: 587–646.

Bockris, J.O.'.M., and Reddy, A.K.N. (1970). *Modern Electrochemistry*, vol. 1. New York: Plenum. Chap. 6.

Bouropolous, N.C., Kontoyannis, C.G., and Koutsoukos, P.G. (1997). Influence of operational variables on the crystallization of ε-caprolactam from melts. *J. Cryst. Growth* 177: 119–124.

Böhmer, R. and Angell, C.A. (1992). Correlations of the nonexponentiality and state dependence of mechanical relaxations with bond connectivity in Ge-As-Se supercooled liquids. *Phys. Rev. B* 45: 10091–10094.

Chernov, A.A. (1984). Modern Crystallography III. In: *Crystal Growth*. Berlin: Springer. Chap. 4.

Dasgupta, C. (2005). Theoretical approaches to the glass transition in simple liquids, *Pramana – J. Phys.* 64: 679–694.

Debenedetti, P.G. (1996). *Metastable Liquids*. Princeton: Princeton University Press.

Debenedetti, P.G., Truskett, T.M., Lewis, C.P., and Stillinger, F.H. (2001). Theory of supercooled liquids and glasses: energy landscape and statistical geometry perspectives. *Adv. Chem. Eng.* 28: 21–79.

Gharsallaoui, A., Rogé, B., and Mathlouthi, M. (2008). Water-disaccharides interactions in saturated solution and the crystallisation conditions. *Food Chem.* 106: 1329–1339.

Ikeda, M. and Aniya, M. (2010). Bond strength-coordination number fluctuation model of viscosity: an alternative model for the Vogel-Fulcher-Tammann equation and an application to bulk metallic glass forming liquids. *Materials* 3: 5246–5262.

Laventure, A., Maris, T., Pellerin, C., and Lebel, O. (2017). Glass versus crystal: a balancing act between competing intermolecular interactions. *Cryst. Growth Des.* 17: 2365–2373.

Malkin, A.J., Kuznetsov, Y.G., and McPherson, A. (1999). In situ atomic force microscopy studies of surface morphology, growth kinetics, defect structure and dissolution in macromolecular crystallization. *J. Cryst. Growth* 196: 471–488.

Ojovan, M.I. (2008). Configurons: thermodynamic parameters and symmetry changes at glass transition. *Entropy* 10: 334–364.

Ramachandrarao, P., Cantor, B., and Cahn, R.W. (1977). Free volume theories of the glass transition and the special case of metallic glasses. *J. Mater. Sci.* 12: 2488–2502.

Scherer, G.W. (1991). Glass formation and relaxation. In: *Glasses and Amorphous Materials* (ed. J. Zarzycki), 119–173. Weinheim VCH. Chap. 3.

Sangwal, K. (2009a). Novel approach to analyze metastable zone width determined by the polythermal method: physical interpretation of various parameters. *Cryst. Growth Des.* 9: 942–950.

Sangwal, K. (2009b). Effect of impurities on the metastable zone width of solute–solvent systems. *J. Cryst. Growth* 310: 4050–4061.

Sangwal, K. (2007). *Additives and Crystallization Processes: From Fundamentals to Applications*. Chichester: Wiley. Chap. 4.

Tropin, T.V., Schmelzer, J.W.P., and Aksenov, V.L. (2016). Modern aspects of the kinetic theory of glass transition. *Physics: Uspekhi* 59: 42–66.

Zarzycki, J. (1991). *Glasses and Amorphous Materials*, Materials Science and Technology: A Comprehensive Treatment, vol. 9 (ed. R.W. Cahn, P. Haasen and E.J. Kramer). Weinheim: VCH.

Zhang, S., Sun, N., He, X. et al. (2006). Physical properties of ionic liquids – data base and evaluation. *J. Phys. Chem. Ref. Data* 35: 1475–1517.

Appendix A

Volumetric Thermal Expansion Coefficient of Melts

It is well known that at a given pressure p the density d of a liquid decreases with increasing temperature according to the relation (Lide, 1996/1997):

$$d(T) = d_{\mathrm{m}} - k(T - T_{\mathrm{m}}), \tag{A.1}$$

where T_{m} is the melting point of the material, d_{m} is the density of the liquid at T_{m}, and k is a constant. From Eq. (A.1), one obtains the expression for the coefficient of volumetric thermal expansion:

$$\alpha_V = \frac{k}{d_{\mathrm{m}}} = -\frac{d - d_{\mathrm{m}}}{d_{\mathrm{m}}(T - T_{\mathrm{m}})} = -\frac{1}{d_{\mathrm{m}}}\left(\frac{\Delta d}{\Delta T}\right), \tag{A.2}$$

where $\Delta d = (d - d_{\mathrm{m}})$ and $\Delta T = (T - T_{\mathrm{m}})$. The coefficient α_V is associated with a change in the volume V of the liquid with temperature given by

$$\frac{\Delta V}{V_0} = \alpha_V \Delta T, \tag{A.3}$$

where V_0 is the initial liquid volume V when $\Delta T = 0$. Equation (A.2) may be obtained from Eq. (A.3). From Eq. (A.2), one obtains

$$\alpha_V = \frac{1}{V}\left(\frac{\mathrm{d}V}{\mathrm{d}T}\right) = \frac{1}{V}\left(\frac{\mathrm{d}V}{\mathrm{d}d}\right)_p \left(\frac{\mathrm{d}d}{\mathrm{d}T}\right)_p = \frac{d}{m}\left(-\frac{m}{d^2}\right)\left(\frac{\mathrm{d}d}{\mathrm{d}T}\right) = -\frac{1}{d}\left(\frac{\mathrm{d}d}{\mathrm{d}T}\right). \tag{A.4}$$

From Eq. (A.3), one notes that a change ΔV in the initial liquid volume V_0 is proportional to the change ΔT in the liquid temperature, and the proportionality constant is the volumetric expansion coefficient α_V. Obviously, the coefficient α_V is a constant quantity for a liquid of initial V_0. However, for a given temperature change ΔT for different liquids, the coefficient α_V decreases with an increase in V_0 of a liquid, since V_0 is related to the average distance r_0 between nearest liquid atoms/molecules.

Nucleation and Crystal Growth: Metastability of Solutions and Melts, First Edition.
Keshra Sangwal.
© 2018 John Wiley & Sons, Inc. Published 2018 by John Wiley & Sons, Inc.

In order to give a physical interpretation of Eq. (A.3), we begin with the effect of temperature on crystalline solids, which are composed of atoms/molecules that vibrate about their equilibrium sites of their lattice. The displacement x of the vibrating entities increases with an increase in temperature due to increase in the internal energy E of the lattice. If r_0 is the distance of an atom/molecule from its neighbor at temperature $T = 0$, its displacement x follows an anharmonic behavior with the potential $E_p(x)$ given by (Kittel, 1976)

$$E_p(x) = ax^2 - bx^3 + cx^4, \tag{A.5}$$

where the constants a, b, and c are positive. The ax^2 term represents harmonic contribution, whereas the second and third terms represent anharmonic contribution due to mutual repulsion of atoms/molecules and softening of vibration at large amplitudes, respectively. If $E(r_0)$ is the equilibrium energy of the crystal, corresponding to the distance $r = r_0 + x$ its total energy $E(x)$ is

$$E(x) = E(r_0) + ax^2 - bx^3 + cx^4. \tag{A.6}$$

Change in the average displacement x_{av} during heating of the solid to the temperature T may expressed in the form:

$$x_{av} = \frac{3b}{4a^2} k_B T, \tag{A.7}$$

where the x^4-term has been omitted. Then the relative displacement

$$\frac{x_{av}}{r_0} = \frac{3b}{4r_0 a^2} k_B T, \tag{A.8}$$

which gives the linear thermal expansion coefficient

$$\alpha_l = \frac{dx_{av}}{r_0 dT} = \frac{3bk_B}{4r_0 a^2}, \tag{A.9}$$

and the volumetric thermal expansion coefficient

$$\alpha_V = 3\alpha_l \approx \frac{9bk_B}{4r_0 a^2}. \tag{A.10}$$

According to Eq. (A.10), α_V is independent of solid temperature T but decreases with an increase in the equilibrium distance r_0 between nearest neighbors. The form of this equation is similar to that of Eq. (A.3).

When a crystalline solid is heated, the supplied heat leads to a change in its internal energy, which is composed of the kinetic energy E_k of thermal vibrations of atoms/molecules about their equilibrium sites and the potential energy E_p of their mutual interaction. Heating of the solid causes an increase in the average distance between the lattice sites (linear and volumetric expansion) and the energy of the solid. In this process the amplitude of anharmonic thermal

vibrations of the atoms/molecules in the crystalline lattice increases and the bonds between them become weak. Due to thermal fluctuations involving different amplitudes of vibrations, some of the atoms/molecules are also knocked out of their normal lattice sites, thereby forming point defects. More supply of heat ultimately leads to the dismantling of the bonds between the lattice atoms/molecules and the solid transforms to the liquid state. Heating destroys the long-range lattice order between the atoms/molecules but the short-range order between them is maintained. Consequently, during the melting of a crystalline solid there is insignificant increase in its volume (about 10%). In view of relatively small changes involved during the melting of a solid, the heat of melting ΔH_m at the melting point T_m is also small and is related to the nature of the ruptured bonds.

Thermal fluctuations due to increasing vibrations of the liquid molecules around their temporary equilibrium sites also result in the formation of holes in the liquid. This explains why the volume V of a liquid increases with an increase in temperature. The average hole radius r_h is given by (Bockris and Reddy, 1970)

$$r_h = 0.51\left(\frac{k_B T}{\gamma}\right)^{1/2}, \tag{A.11}$$

where γ is the surface tension of the melt. This average radius r_h of the hole is connected with its volume Ω by the relation: $r_h \approx \Omega^{1/3}$.

Examples illustrating the above predictions are presented in Appendix B.

References

Bockris, J.O'M. and Reddy, A.K.N. (1970). *Modern Electrochemistry*, vol. 1. New York: Plenum. Chap. 6.

Kittel, C. (1976). *Introduction to Solid State Physics*, 5e. New York: Wiley. Chap. 5.

Lide, D.R. ed. (1996/1997). *Handbook of Chemistry and Physics*, 77e. Boca Raton: CRC Press.

Appendix B

Relationship between α_V and Other Physical Properties

B.1 Molten Elements

Data of α_V of different elements as a function of their atomic weight M are shown in Figure B.1a. It may be seen that for most of the elements α_V poorly decreases with an increase in M and follows the relation:

$$\alpha_V\left(\mathrm{K}^{-1}\right) = (1.79 \pm 0.30)\cdot 10^{-4} - (3.7 \pm 2.5)\cdot 10^{-7} M. \tag{B.1}$$

In contrast to the above dependence, for most of the elements α_V does not depend on T_m and is approximately constant (Figure B.1b):

$$\alpha_V\left(\mathrm{K}^{-1}\right) = (1.2 \pm 0.3)\cdot 10^{-4}. \tag{B.2}$$

However, enthalpy of melting ΔH_m and melting point T_m of different elements are related by the following empirical relations (Figure B.2):

$$\Delta H_\mathrm{m}\left(\mathrm{kJ}\cdot\mathrm{mol}^{-1}\right) = -(0.52 \pm 0.87) + (9.3 \pm 0.8)\cdot 10^{-3} T_\mathrm{m}, \tag{B.3}$$

for most of the elements except transition-metal elements, while

$$\Delta H_\mathrm{m}\left(\mathrm{kJ}\cdot\mathrm{mol}^{-1}\right) = -(6.0 \pm 3.0) + (3.3 \pm 0.3)\cdot 10^{-2} T_\mathrm{m}, \tag{B.4}$$

for Si, Ge, Ga, As, Bi, and Th.

B.2 Molten Halite-Type Electrolytes

There is no evident relationship between α_V and T_m of alkali halides (see Figure B.3a). However, except for rubidium halides and CsCl, the data of ΔH_m against T_m for other alkali halides follow the relation (Figure B.3b):

$$\Delta H_\mathrm{m}\left(\mathrm{kJ}\cdot\mathrm{mol}^{-1}\right) = -(6.73 \pm 1.65) + (3.12 \pm 0.18)\cdot 10^{-2} T_\mathrm{m}, \tag{B.5}$$

Nucleation and Crystal Growth: Metastability of Solutions and Melts, First Edition.
Keshra Sangwal.
© 2018 John Wiley & Sons, Inc. Published 2018 by John Wiley & Sons, Inc.

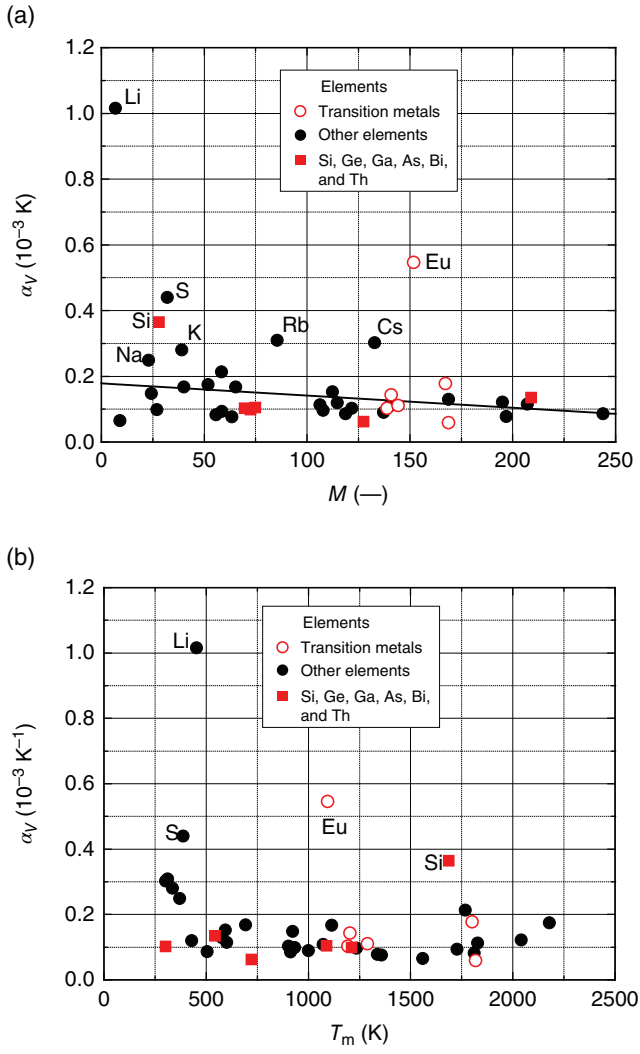

Figure B.1 Dependence of expansion coefficient α_V of different elements as a function of: (a) their atomic weight M and (b) melting point T_m. *Source:* Data from Lide (1996/1997).

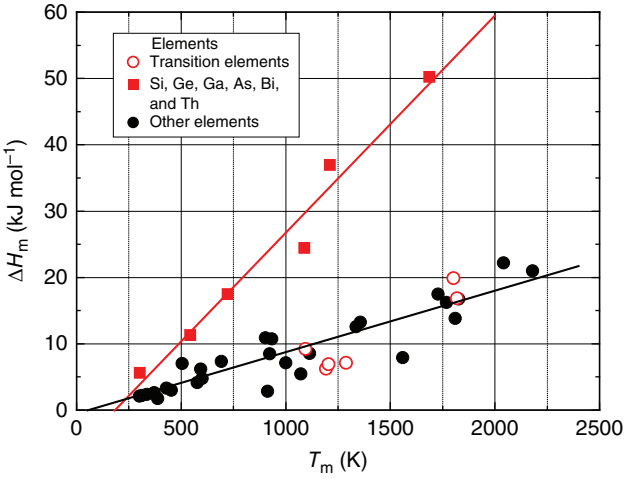

Figure B.2 Relationship between enthalpy of melting ΔH_m and melting point T_m of different elements. *Source:* Data from Lide (1996/1997).

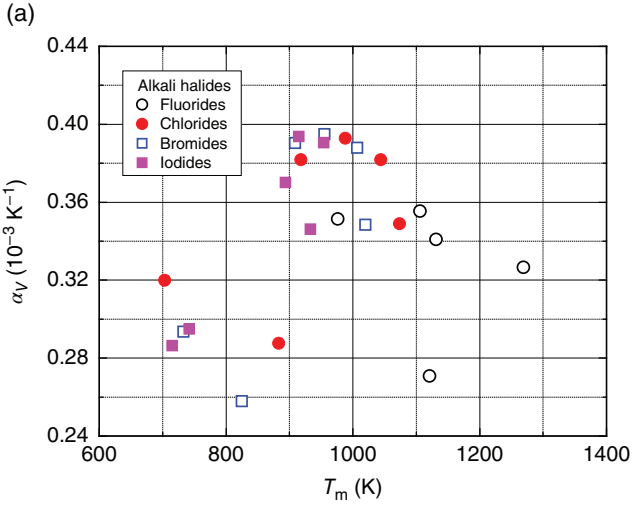

Figure B.3 Relationship between (a) expansion coefficient α_V with melting point T_m, (b) heat of melting ΔH_m and T_m, and (c) lattice energy U_{latt} and α_V for different alkali halides. *Source:* Data from Lide (1996/1997).

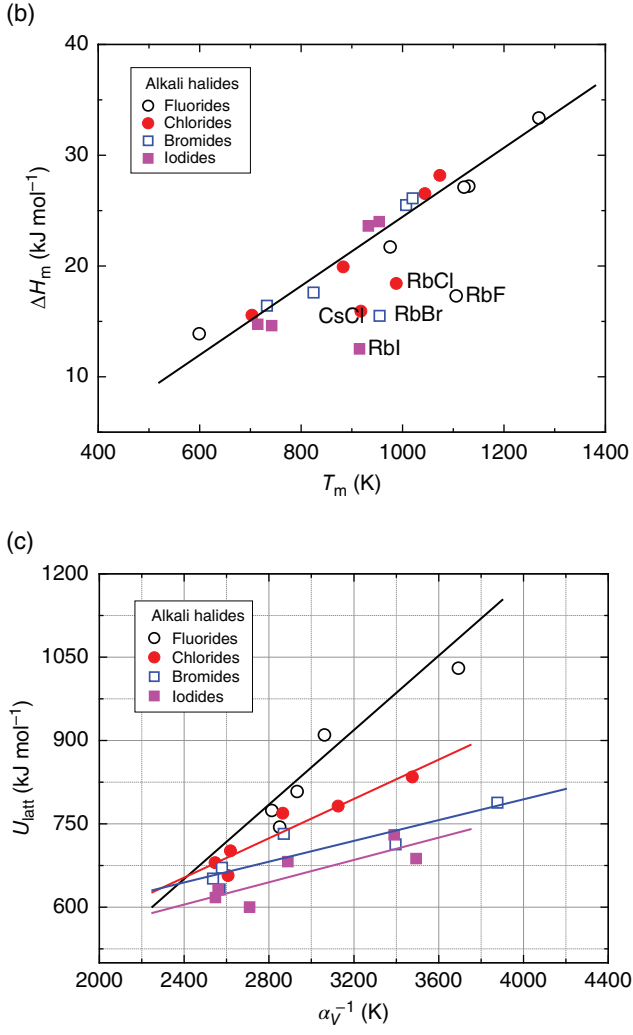

Figure B.3 (Continued)

and α_V increases with the lattice energy U_{latt} of alkali halides (Figure B.3c) following the relation:

$$U_{\text{latt}}\left(\text{kJ}\cdot\text{mol}^{-1}\right) = U_{\text{latt0}} + \frac{\zeta\alpha_V^{-1}}{K}, \tag{B.6}$$

Table B.1 Values of constants U_{latt0} and ζ for alkali halides.

Halide	U_{latt0} (kJ·mol^{-1})	ζ (kJ·mol^{-1}·K^{-1})	Coeff. R	N
Fluorides	−90 ± 182	0.307 ± 0.059	0.948	6 ± 1
Chlorides	228.5 ± 86.1	0.177 ± 0.030	0.947	3.5 ± 0.6
Bromides	419.7 ± 72.1	0.094 ± 0.024	0.891	2 ± 0.5
Iodides	363.9 ± 95.9	0.100 ± 0.032	0.831	2 ± 0.6

where the constants U_{latt0} and ζ and the Pearson coefficient r for the best fit of the data are listed in Table B.1. Since the specific heat of 1 : 1 compounds like alkali halides at ordinary temperatures is about $6R_G \approx 50\,J{\cdot}mol^{-1}{\cdot}K^{-1}$, from the value of ζ, one can infer that clusters composed of N anion–cation pairs participate in the specific heat of the alkali halide melts.

Reference

Lide, D.R. ed. (1996/1997). *Handbook of Chemistry and Physics*, 77e. Boca Raton: CRC Press.

Appendix C

Relationship between Densities d_m of Molten Metals and Electrolytes and Atomic Mass M

The densities d_m of molten metals at their melting point T_m with the atomic mass M and those of molten electrolytes with their average atomic mass M_{av} are illustrated in Figure C.1a and b, respectively. It may be noted that the data for molten metals and various electrolytes follow the linear relation:

$$d_m = d_0 + d_1 M, \tag{C.1}$$

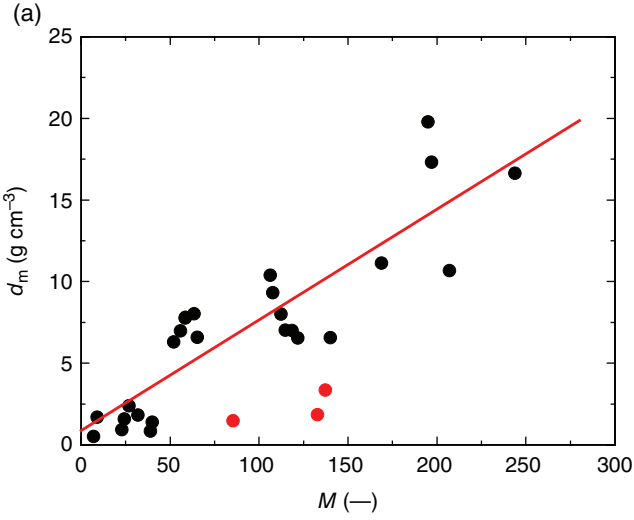

Figure C.1 Dependence of densities d_m of (a) molten metals at their melting point T_m on the atomic mass M and (b) molten electrolytes with their average atomic mass M_{av}.
Source: Data from Lide (1996/1997). The highly deviating points with low d_m for $80 < M < 150$ in (a) were excluded during analysis, whereas most of the data for various electrolytes (dashed line) and alkali halides (solid line) in (b) follow a linear dependence with a large scatter.

Nucleation and Crystal Growth: Metastability of Solutions and Melts, First Edition.
Keshra Sangwal.
© 2018 John Wiley & Sons, Inc. Published 2018 by John Wiley & Sons, Inc.

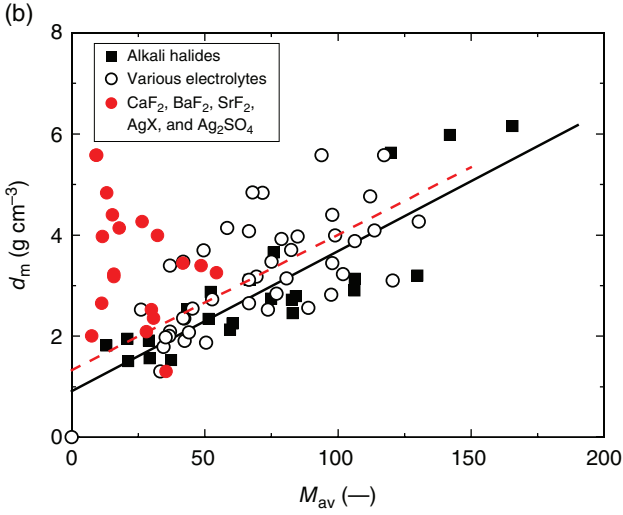

Figure C.1 (Continued)

Table C.1 Best-fit values of constants d_0 and d_1 of Eq. (C.1).

Substance	d_0 (g·cm^{-3})	d_1 (10^{-2} mol·cm^{-3})	Coeff. r
Molten metals	0.878 ± 0.842	6.78 ± 0.74	0.881
Molten alkali halides	0.911 ± 0.292	2.77 ± 0.35	0.863
Various electrolytes	1.330 ± 0.313	2.68 ± 0.42	0.705

where d_0 and d_1 are empirical constants. The constants and the Pearson coefficient r for the best fit are given in Table C.1. The slope of the $d_m(M_{av})$ plots for alkali halides and other electrolytes is practically the same, but its value is about 2.5 times higher for elements.

Reference

Lide, D.R. ed. (1996/1997). *Handbook of Chemistry and Physics*, 77. Boca Raton: CRC Press.

Index

a

Activation barrier in 3D nucleation *see* Three dimensional (3D) nucleation; Two dimensional (2D) nucleation
Activation energy 32, 34
  for diffusion 225–228, 311, 312, 433, 443, 444, 449–450
  dimensionless *see* Avramov and Milchev (AM) model
  for hole formation 31
  for jump in liquid 371
  for self-diffusion in molten electrolytes 371
  for viscous flow 11, 12, 15, 31, 32, 34–36, 59, 371, 427
Activity coefficient 54, 67, 87
Adam–Gibbs (AG) equation 429
Additives, xvi 230, 252, 362, 383, 408, 410, 411, 441, 443–444 *see also* Impurities (additives)
Additivity rule 21, 75, 76, 78, 227
Adsorption isotherms 375
  Freundlich 238–241, 375
  Gibbs 96
  Henry's linear 238, 241, 243
  Langmuir 63, 235, 238–241, 243–246, 354, 375, 394
  Langmuir constant of 63, 235, 238, 239, 241, 243–251, 354, 375
Adsorption (solvation–desolvation) processes 287
Aggregation
  of atoms/molecules 105
  of ions/molecules 286, 375
Adsorption of solvent molecules 393
Agglomeration of crystals/particles/nuclei xiii, 337, 338, 393–395, 407, 408, 416
Amorphous precursor 170–173
Amorphous solids 436 *see also* Glasses
Antisolvent crystallization xiv, xvi, 69, 89, 325–327, 332, 412, 413 *see also* Metastable zone width (MSZW)
  kinetics of temperature increase 279–286
  modified Nývlt relation, xv
    nucleation constants 298–300, 302, 303, 316
    nucleation order 298–300, 302, 312, 316, 317
  supersaturation decay 362–371
    general trends 362

Nucleation and Crystal Growth: Metastability of Solutions and Melts, First Edition.
Keshra Sangwal.
© 2018 John Wiley & Sons, Inc. Published 2018 by John Wiley & Sons, Inc.

Antisolvent crystallization (*cont'd*)
temperature change of solutions during 293–296
origin of minimum and maximum changes 287–288
physical interpretation of 286–287
temperature measurements 270, 276–296
Antisolvent feeding rate
corrected 304–305, 308, 309, 313–317
maximum 318–319
threshold 304, 305, 313–319
Apelblat relation (model) 77
Arrhenius plots 69
Arrhenius-type (Arrhenius) relation 35, 44, 45, 58, 66, 85, 222, 244, 246, 428
Associated liquids 371
Associates of ions 371
Association *see also* Aggregation
of atoms/ions/molecules 67, 68, 198
of ions in alkali halide melts 451
of ions in solutions 18, 29
Atomistic theory of nucleation 330, 341–343 *see also* Three dimensional (3D) nucleation
Average atomic mass 444, 463–464
Average crystallization time 135, 328
Average hole radius 455 *see also* Liquid electrolytes
Average particle size 401, 402
Avrami equation/relation 185, 283–284, 356, 375–376, 409 *see also* Kolmogorov–Johnson–Mehl–Avrami (KJMA) equation
approximate 138, 183, 260
modified 138
precise 182, 183
Avrami kinetic exponent 260 *see also* Kolmogorov–Johnson–Mehl–Avrami (KJMA) equation
Avrami plots 160, 169, 170
Avrami rate constant, 176, 260, 357
Avrami theory 357 *see also* Kolmogorov–Johnson–Mehl–Avrami (KJMA) theory
Avrami-type equation *see* Avrami equation
Avramov and Milchev (AM) model 430–435
dimensionless activation energy 432
fragility exponent 431

b

BCF mechanism 390, 391
BCF parabolic law 390
BCF surface diffusion mechanism 396, 397
BCF theory (model) of crystal growth 119, 120, 124, 397
Berg effect 391
Binding forces between additives and crystal surface 252–254
Birth-and-spread (B+S) model 388 *see also* 2D nucleation models
Born model 310
Bulk diffusion models 119–120
Bulk (volume) diffusion 106, 107, 120, 122

c

Chemical potential difference 53–55, 58–60, 89, 327, 329
Chemical reactions 281, 283, 287, 375, 378
change in heat content 283, 284
complex reactions 378, 379
desolvation processes, associated with 379
endothermic 281, 289–293, 372, 373
exothermic 281, 289–293, 372, 373
first-order reactions 371, 378, 379, 388
heat of 291
rate constant of 378, 383, 387, 400

relaxation time of process 378
time constant 400
Chernov model 120
Classical nucleation theory (CNT)-based approach 186, 197–199, 236–237 *see also* Metastable zone width (MSZW), cooling crystallization
parameter F 198–199, 204, 207–220
temperature dependence of 222–225
parameter F_1 198–199, 204, 207, 220–221
parameter Z 198–199, 204, 207–220
Classical theory of 3D nucleation *see* Three dimensional (3D) nucleation
Cluster formation 56–57, 226
Cluster formation of cation–anion pairs 449
Combined antisolvent/cooling crystallization 267, 268, 319–320, 388, 408
MSZW measurement techniques 320
Compressibility 12, 90
Configurational entropy of nucleus 94
Connected net analysis 392
Connected nets 389
Constant f related to concentration of ions/molecules 196, 199, 236, 283, 301–302, 307, 309, 316, 439–441, 443–446, 449
Continuous (linear) growth 110
Cooling crystallization xiv, xv, xvi, 153, 189, 190, 253, 268, 318, 325–327, 332, 345–348, 362, 394, 412, 413, 415, 417, 423 *see also* Metastable zone width (MSZW), cooling crystallization
swift 413–314
temperature of solution
change by solute in 372
change in 363, 364
measurement
technique 190–191, 362
Cooling rate
corrected 207, 210, 228
threshold 207, 210, 222
Cooperative relaxation 429
Corrected cooling rate 441–442
Coulomb forces 18, 28
Coulomb interactions 121 *see also* Interactions
Coverage of solute ions/molecules 375 *see also* Fractional surface coverage
Creation of supersaturation 219–220, 267, 278, 304, 309, 362, 368, 372–373, 379
Creation of supersaturation for crystallization 412–413
Crystal growth xiii
bulk-(volume-) diffusion-controlled by 123, 132, 138, 200
at edge dislocations 120–121
interface-transfer controlled 132
normal growth mechanism 200–202
simultaneous bulk-diffusion and surface-reaction controlled 121–123
spiral growth mechanism 200–202
surface-reaction controlled 123, 125, 200
two-dimensional (2D) nucleation mechanism 201, 231
Crystal habits 252
Crystalline aggregate 398
Crystallization xiii, xiv
from melt 425
of metastable phases, xvi
Gibbs free energy change 147–150
thermodynamics of 147–151
stability of polymorphs 147
of polymorphs 394, 395, 412–415
of unstable and stable phases 259

Crystallization energy 110
Crystallization period 356, 357
Crystal–medium interface 106–107, 122, 123, 389, 390
  diffuse 108
  kinetic roughening 108, 110, 111
  rough 108, 390
  sharp 108
  smooth 108, 390
  thermodynamic roughening 108–110
Crystal morphology 287, 388–396
Crystal size distribution (CSD) xiii, xiv, xvi, 175, 190, 267, 268, 274, 288, 320, 361, 372, 396, 403–412, 415–416
  cumulative 408, 409
  different approaches of 403
  differential 408, 409
  distribution function 400, 401, 408, 409
  shapes of 403–406
    asymptotic 409
    negatively skewed 401, 402, 409
    positively skewed 409, 411
    skewed 416
    symmetrical 409, 416

d

Density, of crystal, solid, solute 93, 94
  of liquids 438, 444, 445, 453 (*see also* Liquids (solvents))
  of molten metals 463–464 (*see also* Liquids (solvents))
Desolvation of solute molecules/ions 373, 379
Desolvation of solvated solute ions 311
Desolvation processes 379, 382
Desupersaturation curves 362, 383–386, 388, 414
  behavior of 175
  evolution of 383–388
Desupersaturation durations 385–386
Detectable crystallization
  duration 136–137
  limit 192, 193, 201, 255
Detectable fraction of crystallization 328, 343
Dielectric constant of solvent (antisolvent) 167, 168, 278, 284, 285, 304, 306–309, 379, 382
Differential heat of adsorption 235, 238, 241, 243, 244, 246, 248–251, 311, 312
Different positions for growth 106, 107
Diffusion
  of atoms/molecules 222, 425, 450
  coefficient of atoms, ions or molecules 11, 112, 122, 130, 450
  of ions/molecules 223–226, 286, 364, 368, 370–372, 374
    controlled by breaking of bonds of liquid network 371
    controlled by creation of holes in liquid network 371
  of solvent molecules 311
Diffusion processes 376
Dimensionality of growing crystallites 132, 136, 138, 140, 181, 183, 200, 212, 283, 287, 330, 401 *see also* Kolmogorov–Johnson–Mehl–Avrami (KJMA) theory
Dimensionless heat of solution 329
Dimensionless maximum temperature difference 195, 202
Dimensionless melting enthalpy 329, 341
Dipole moment 167, 168
Dirac-delta function 134
Dislocations 105, 107, 108, 110, 112, 128, 396–398
  edge 397
  screw 108, 116, 119, 124, 125, 397, 400
Donnay–Harker analysis 389

Driving force
for crystallization 54, 58, 97, 341, 415
for growth 110
for phase transition 49
Drowning-out crystallization xiv, 267, 268, 327, 338, 412, 413, 416

e

Edge free energy 94
Effectiveness parameter
for adsorption/desorption 375
for impurity adsorption 236, 238, 241, 244, 246, 248, 249, 353, 443
Einstein relation 30, 42
volume fraction of particles 30, 31
Energy
of adsorption of atoms/molecules 115
of dehydration of atoms/molecules 115
of integration of atoms/molecules 114, 115, 125
Enthalpy (heat)
of crystallization 288, 374
of dissolution 53, 66, 75, 94–96, 195, 203, 225, 228, 300, 329, 331, 345
dimensionless 195, 198, 220, 345
of melting 53, 66, 75, 94, 95, 110, 147–148, 195, 228, 329, 439–441, 455, 457, 459–460
dimensionless 195
of mixing 66–68, 70–72, 75, 76, 78, 94, 95, 283, 288
Entropy
difference 429
of fusion/melting 429, 432
of phase 8
of solution 30, 65
of solution/melt 423
Equilibrium morphology 389
Exponential function 400
stretched 429
stretched fragility-related exponent 429–430
Exponential law 368
Extended volume 131–133

f

Faces (classification) 107–108
F (flat) 107
imperfect 108
perfect 108, 112
K (kinked) 107
nonsingular 107, 108
singular 107, 108
S (stepped) 107
vicinal 107, 108
Fisher–Turnbull relationship 330
Foubert equation 185
Foubert model 181 *see also* Model
Fractional surface coverage 235–239, 241–244, 354, 443, 444
Fragile liquids 427, 428, 436 *see also* Glass formation by cooling of melts
Free energy
decrease 372
difference between polymorphs 167
Frenkel relation 450

g

Gamma function 134, 200, 257
Gibbs energy of mixing 90
Gibbs free energy 90, 91, 398 *see also* Free energy
change 51, 52, 55, 65, 87
Gibbs–Helmholtz equation 65
Gibbs–Thomson relation 399, 401
Gibbs–Wulff plot 107
Glasses 423–426, 430, 435, 436
Glass formation by cooling of melts 423–426
estimation of critical cooling rate for 438
estimation of temperature of 438

Glass formation by cooling of melts (*cont'd*)
glass formers 425, 430, 434, 448–449
glass-forming ability 426, 436
glass fragility 436 (*see also* Liquid fragility)
glass stability 426, 436
models of
Adam–Gibbs (AG) model 426
Avramov–Milchev (AM) 426, 434
Vogel, Tamman and Fulcher (VTF) 426, 434
strength parameter 428
Glass transition from melts/solutions
dimensionless activation energy at 432
limiting cooling rate 444, 448, 449
Glass transition temperature 423–426, 432, 447, 449
composition dependence of 431–435
relationship with metastable zone width 435–438
Glassy state 59, 327
Gompertz function 178
Gompertz's equation 178, 181, 185
Gompertz's model 178–179
Growth *see also* Crystal growth
surface-diffusion controlled 391
surface-reaction controlled 396
volume diffusion controlled 391, 396
Growth habit 105 *see also* Crystal morphology
Growth kinetics 93, 106, 107, 120, 126 *see also* Crystal growth
diffusion-controlled 170, 172–174, 177
effect of impurities on 123–127
of stable phase 171
surface-controlled 170, 173, 174
Growth kinetics of imperfect smooth faces 116–121
direct integration model 117–119
linear law (dependence) 118, 119
parabolic law (dependence) 118, 119
surface diffusion model 117–119, 125
Growth kinetics of perfect smooth faces 112–116
two-dimensional nucleation models 112–116, 121, 123
mononuclear model 112, 113, 116
multiple nucleation model 112, 113, 116, 124, 125
polynuclear model 112, 113, 116, 124
Growth kinetics of rough faces 111–112
activation barriers in 111
kinetic coefficient for growth 112
normal growth 112, 126, 127
Wilson–Frenkel law for 112
Growth mechanisms 390 *see also* Crystal growth
Growth morphology 105, 390, 392, 394
Effect of solvents on 393
Growth of 3D nuclei 362, 388
Growth rate constant 131, 132, 134, 135, 139, 140, 174, 328, 330, 400
Growth rate dispersion 396–398, 407, 408, 412
Growth rate distribution 407
Growth spirals 105

h

Habit modification 252 *see also* Crystal morphology
Heat capacity 24, 283, 373
Heat capacity of melt 423, 428, 429, 432, 434
excess heat capacity 429
Heat generation
by crystal growth 362
by 3D nucleation 362
Heat transport 364, 370–371
Hole formation in a liquid 455 *see also* Liquid electrolytes
Hole size 225

Hole theory of liquids 225, 423
Hopper (skeletal) morphology 391, 392
Hydrates *see* Solvates
Hydrates of salts 64–65 *see also* Phase transformation (changes)
Hydration number 93–94

i

Impurities (additives) 62, 63, 341, 349, 362, 383, 387, 389, 394, 396, 423
  immobile 126
  mobile 126
Impurity effectiveness factor *see* Effectiveness parameter
Induction period xvi, 362, 385, 386, 414, 415, 417
  for crystallization (nucleation) xvi, 127, 145, 150, 151, 155, 161, 164, 165, 175, 180, 183, 185, 186, 193, 232, 259, 260, 318–319, 425, 450
Induction period for 3D nucleation xvi, 326–328, 330, 331, 333, 337–340, 351, 355–357
  basic equations based on 333
    atomistic (AT) theory 333
    classical nucleation (CN) theory 333
    power-law (PL) relation 333, 349
  contributions to 355
  effect of impurities on 349–354
    antisolvent crystallization, in 343–344
    atomistic theory approach 340, 343, 349
    classical nucleation theory-based approach 340–341
  for isothermal crystallization 333–343
    crystallization from solutions 333–338
    crystallization from the melt 338–343
  measurements of 267, 268
  for nonisothermal crystallization 345–358
    crystallization from the melt 354
    crystallization from solutions 345–349
  some other relations of 331–333
  theoretical interpretation of 328–331
    mononuclear (MN) mechanism 328–330
    polynuclear (PN) mechanism 328–330
Induction time *see* Induction period
Instantaneous nucleation xv, 140, 362 *see also* Kolmogorov–Johnson–Mehl–Avrami (KJMA) theory
Interactions
  Coulomb 427
  fluid–fluid 67, 76
  free energy changes during 310, 311
  ion–dipole 17, 19, 67
  ion–ion 18, 28, 87
  ion–solvent 17, 28, 87
  solid–fluid 67, 68, 76, 78
  solid–solid 67
  solute–antisolvent 227, 285, 304, 310, 372
  solute–solvent 166, 226, 228, 276, 278, 285, 310, 393
  solute–solvent van der Waals 166, 167
  solute–solute 285
  solvent–antisolvent 285
  sugar–sugar 436
  sugar–water 436
  van der Waals 393, 427
Interfacial energy (tension) 56, 59, 60, 62, 89, 92–96, 115, 121–124, 127, 149, 202, 204, 212, 225, 236, 237, 250, 252, 296–297, 307, 311, 318, 329, 330, 333–335, 337, 338, 341, 343–346, 348, 351–353, 389, 393, 394, 400, 414, 439, 443, 449

Interfacial energy (tension) (*cont'd*)
dimensionless 198, 209, 220, 237
effective 61, 125, 140, 198, 199, 348
solubility and 92–96, 209, 216
Ionic clusters 371
Isothermal crystallization xiv, xvi, 136, 138, 232, 327, 338, 355, 398 *see also* Induction period
induction period for, xvi
Isothermal crystallization curves 356
Isothermal crystallization kinetics 181, 182, 259, 355
some non-KJMA models of 170–181
comparison of different models of 181–186
Isothermal method, xv, xvi 97, 98, 232, 233, 250
Isothermal systems 383

j

Jouyban–Acree model 77
Jump frequency of moving units in a liquid 224–225, 431

k

Kinetic coefficient for step displacement 114, 115, 118, 120, 125
Kinetic exponent *see* Overall crystallization
Kinetic factor in 2D and 3D nucleation rates 57–59, 63, 140, 236, 237, 329, 413, 416
Kirkwood–Buff integrals 90
KJMA equation *see* Kolmogorov–Johnson–Mehl–Avrami (KJMA) equation
Kohlrausch–Williams–Watts relaxation function 429
Kolmogorov–Johnson–Mehl–Avrami (KJMA) equation 134, 135, 157, 160, 166, 173
according to instantaneous nucleation mode 134
according to progressive nucleation mode 135
comments on 138
extended KJMA equation 159
kinetic exponent 157, 159, 165, 166
time constant 139–140, 157, 160, 165–169, 176
unified 135
Kolmogorov–Johnson–Mehl–Avrami (KJMA) theory 129, 136, 156, 157, 175, 179, 181, 269, 287, 357, 376, 402
basic theoretical equations 129–133
kinetic exponent 135–140, 269, 283, 284, 287, 328, 375–378, 383, 384, 386, 387, 409
for instantaneous nucleation 136
for progressive nucleation 136
KJMA formula 131, 132
mononuclear mechanism 133
phase transformation according to 158–160
polynuclear mechanism 133–136
instantaneous nucleation mode 130, 133–136, 140, 376
progressive nucleation mode 130, 133, 135–136, 138, 376
time constant 269, 283, 284, 287, 328, 375–380, 382–384, 386, 387, 409
Kossel crystal 94, 110

l

Lattice energy 449
Lattice energy of alkali halides 460–461
Lattice gas model 109, 110
Law of Mass Action 57, 60
Law of Proportionate Effect 425
Le Chatelier principle 63
Linear free energy of step 109, 111
Linear growth rate 400

Linear relation (dependence) 274, 275, 280, 281, 283, 290, 307
Liquid electrolytes *see also* Network structure
  hole formation (creation) 19
  hole model (theory) 10–12, 15
  hole radius 11
  models, of 8
Liquid fragility 432 *see also* Fragile liquids
  fragility index *m* 428, 430, 432–434
  fragility parameter α 431–434
  strength parameter Ψ 428, 430, 432
Liquid free-volume theory 10–11
Liquid-like structure 423 *see also* Network structure
Liquids (solvents)
  Arrhenius-type relation 15
  associated 8, 12, 15, 35
  density of 2
    temperature dependence of 2, 3, 13
  dielectric constant of 6, 7, 12, 17, 18
  high-temperature 44
  low-temperature 44
  nonassociated 12
  specific volume of 3
    temperature dependence of 3, 4, 13–14
  thermal expansion coefficient of 2
    temperature dependence of 3–5, 12–14
  viscosity of 6, 7, 12, 112
    temperature dependence of 15, 16, 32, 33

m

Macromorphology *see* Crystal morphology
Mass balance equation 177
Mass transfer coefficient
  bulk diffusion 122
  surface reaction 122
Mass transfer rate 122
McCabe's law 405, 406
Maximum temperature difference ΔT_{max} 276–277
Mersmann's relation 335
Metastable region (zone) 96, 129
Metastable zone width (MSZW) xvi, xvii, 325, 343, 349–351, 355, 368, 385, 387, 414, 415, 435–438
Metastable zone width (MSZW), antisolvent crystallization xvi, xvii, 267
  analysis of data 304–308, 313–318
  another Nývlt-like equation 300–302, 313, 318
  CNT-based approach 302–303, 318
  comparison of measurements techniques for 291–296
  effect of detection technique on 312–315
  effect of stirring on 315–318
  modified Nývlt equation 302, 320
  modified Nývlt-like approach 298–299, 301
  Kubota's approach 299–300, 320
  Kubota's equation 302
  observation techniques 268
Metastable zone width (MSZW), cooling crystallization xiv, xvii, 51, 97–99, 145, 189
  CNT-based approach 197–199, 236–237
  effect of additives on 232–251
  effect of detection technique on 210–212
  effect of solution volume on 255–259
    deterministic nucleation 255–257
    stochastic nucleation 255–257
  effect of stirring and ultrasound on 255
  experimental results on 202–232
  instantaneous 3D nucleation-based approach 202

Metastable zone width (MSZW), cooling crystallization (*cont'd*)
Kubota's approach 194, 211
Kubota model 194
Nývlt's approach 192–194, 211
Nývlt model 194
progressive 3D nucleation-based approach 199–202, 211, 212
self-consistent approach (SCA) 195, 211, 246
self-consistent Nývlt-like equation 195–197, 201, 351
theoretical interpretations of 191–202
Metastability zone width (MSZW) of solutions *see* Metastable zone width (MSZW), cooling crystallization
Metastable zone width of melts 423, 424, 438–444 *see also* Metastable zone width (MSZW), cooling crystallization
constant Φ 440–442
constant Z 440–446, 449
derivation of basic equations 438–441
effect of additives 443–444
effect of melt viscosity 441–443
nucleation order m 440–442
parameter F 440–447, 449
self-consistent Nývlt-like equation 440
Model
Foubert 179–181
of Foubert, Dewettinck, Jansen and Vanrolleghem 179–181
Gompertz's 178–179
of Mazzanti, Marangoni and Idziak 175–177
ordinary diffusion equations (ODE) 175
two-step 180
Modified Nývlt equation 195–196 *see also* Nývlt's equation
parameter β 196–197, 204, 207–220
parameter Φ 196–197, 204, 207–220
temperature dependence of 222–225
Mononuclear crystallization 139
Morphological importance 389
Morphology of crystals 414, 415
diffusion processes in controlling their formation 415
growth xiii
Multiple-height growth steps 117
Multiple nucleation model 112, 113, 116, 119, 121

n

Network structure 12
of ice 4, 5
of liquids 7, 432
network formers 434
network modifiers 434–435
of water 4, 5, 35, 92
Newton's law of cooling 364
constant K of 364–370, 374, 387
relationship with antisolvent feeding rate 367–371
temperature decay 364–367
Nonisothermal crystallization 354
Nonisothermal crystallization curves 356
nucleation order m 349
Nonisothermal crystallization kinetics in melts 259–260
Normal face growth 108
Normal face growth rate 113
direct integration mechanism 114, 116
direct integration of growth units 115
surface diffusion mechanism 113, 114, 116

Normal growth *see* Growth kinetics of rough faces
Nucleation order *see* Nývlt's equation
Nývlt-like approaches 349 *see also* Metastable zone width (MSZW), cooling crystallization
Nývlt-like relation *see* Metastable zone width (MSZW); Nývlt's equation
Nývlt's equation xv, 191, 195, 202
  nucleation constant k_m xv, 191
  nucleation order m xv, 191, 192, 196, 201, 202, 204, 207, 209, 211, 212, 219, 220, 222, 230–232, 351, 353, 368
    distribution of 231

o

Ostwald–Freundlich relation 399, 401
Ostwald ripening 274, 278, 284, 288, 386, 395, 398–403, 408
  Diffusion-controlled growth kinetics 399–400, 402
  Surface-reaction controlled growth kinetics 400
Ostwald rule of stages 151, 170, 394, 412
Overall crystallization xv, 106, 127–140, 146, 155, 156, 160, 181, 192, 193, 269, 328, 376, 409 *see also* Kolmogorov–Johnson–Mehl–Avrami (KJMA) theory
  effect of impurities (additives) on 136, 139–140
  evolution of, xvi
  mechanism of
    instantaneous nucleation 192, 202, 220, 231, 288
    progressive nucleation xv, 192, 199, 201, 209, 220, 231, 284, 287, 288, 312
  single-stage 183
  time constant for 134–136, 139, 140
  two-stage 150, 154, 157, 158, 183
Overall crystallization curve(s) 136–137, 181, 184, 259, 355
  two-step 159
Overall crystallization duration 259, 260
Overall growth rate 122
Overall growth coefficient 122
Overall nonisothermal crystallization kinetics from melts 259, 355

p

Packing coefficient of solute 21
Parameter a_2 related to resultant interactions 300–302, 307–311, 318, 331
Particle size distribution *see* Crystal size distribution (CSD)
Periodic Bond Chains (PBCs) 107, 389
Phase transformation
  amorphous to crystalline state 436
  Gibbs free energy change for 439
Phase transformation (changes) xiii, xiv, xvi, 64, 65, 127, 128, 133, 156, 337 *see also* Polymorphic transformation
  diffusion-controlled 156, 173–174
  driving force for 167
  effect of solvent on 160–170
  melt-mediated transformation 149, 150, 153–155, 157, 169
  phase transformation time of 155
  rate of 166
  rate constant of 162, 165–167
  solid-state transformation 149
  solution-mediated 149, 150, 153–155, 157, 161, 167–170, 173, 252, 338
  surface-controlled 173–174
  total transformation time of 161, 165–168
  two-stage 159, 170, 171

Polyhedral morphology 392, 393
Polymorphic modifications 145, 147
Polymorphic phase 383
Polymorphic transformation 156, 361, 394, 408
  melt-mediated 412
  solid-mediated 153
  solution-mediated 394, 412, 417
Polymorphic transformation kinetics 151–158
Polymorphism 254
Polymorphs 338–341
  of crystallizing compounds 267, 268
Polythermal method 97, 99, 145, 189, 233, 244, 249
Polythermal (or nonisothermal) crystallization *see* Cooling crystallization
Population balance approach 403, 406–408
Population balance equation(s) 174, 361, 388
Population balance modeling 320
Post-crystallization cooling behavior 364–371
Power-law equation (relation, function or dependence) xv, xvi, 135, 139, 157, 161–163, 167, 192, 193, 195–197, 233, 257, 274, 275, 298, 302, 304, 305, 332, 349, 351, 368, 379, 388, 440
Power-law growth kinetics 256
Preexponential factor in nucleation rate *see* Kinetic factor in 2D and 3D nucleation rates
Preferential solvation of solute 89–92
Preferential solvation parameter 90–92
Processes involved in antisolvent crystallization 274
Progressive nucleation *see* Kolmogorov–Johnson–Mehl–Avrami (KJMA) theory

r

Reactive crystallization 171–173, 405–406, 412, 413, 416
Relaxation time (structural) 429, 431, 450
Retardation factor *see also* BCF theory (model) of crystal growth
  kink 115, 117, 118
  step 115, 118

s

Saturated solutions *see also* Solutions
  associated 41
  density of 35
    temperature dependence of 35–37
  specific volume 36
    temperature dependence of 36–38
  viscosity of 35
    temperature dependence of 35–43
Shear modulus (high-frequency) of system 431
Size constant 409
Size-dependent growth 405–406, 408
Solid–liquid interfacial energy *see* Interfacial energy (tension)
Solids
  density of 2, 6
    temperature dependence of 2, 3
  specific volume of 3
    temperature dependence of 3, 4
Solubility 49, 89, 93, 94, 96, 97, 149, 155, 165, 166, 168, 174, 209, 233, 254, 296, 300, 325, 350, 374, 384, 399, 400, 412, 414, 436
  curves 96, 98–100, 202, 203, 325, 414
  effect of additives on 250
  factors affecting 68
  ideal 63
  real 63
  solvent mixtures, in 68–76, 89–92
    correction term in 80–87
    mathematical representation of 76

simple practical approach 78–87
temperature coefficient of 65, 110, 192, 195
temperature dependence of xiii, xiv, 35, 63, 64, 68–74, 79, 414
Solubility curve *see* Solubility
Solubility product 54
Solute–additive binding energies 252–254 *see also* Interactions
electrostatic interactions 252
hydrogen bonds 252
van der Waals forces 252
Solute aggregates 169
Solutions
associated 44
Born model 17
compressibility of 22, 24
concentration of 19–21
density of
concentration dependence of 21
temperature dependence of 24–26
high-temperature 44–46
hole radius in 35
ideal 66, 67, 89
low-temperature 44
real 35, 66, 68, 69, 97, 99, 100
regular 66, 68, 72, 94, 96
equation of 203
theory of 195, 197, 300
solvation of ions in 17–19, 24, 30
specific volume of
concentration dependence of 21–23
temperature dependence of 24–26
thermal expansion coefficient of
concentration dependence of 22, 23
temperature dependence of 24, 25
viscosity of 27, 28
concentration dependence of 27–31
temperature dependence of 31–35, 44–46
viscosity *B* coefficient 28–30, 32
Solvated associates 166
Solvated solute ions/molecules 390
Solvates 145, 146, 151, 166
Solvation and desolvation processes 372–383
of solute ions/molecules 374
Solvation of solute ions/molecules 375
Solvation process 21
Solvent–antisolvent composition 296–297
Solvent–antisolvent mixing (miscibility) 285
Solvents
properties of 12
Solvent (water) activity 87–89
Specific heat of compounds 461
Spiral hillock 117
inclination (slope) of 117
Spirals (Growth) 108, 120
Stationary nucleation *see* Three dimensional (3D) nucleation
Step kinetic coefficient *see* Kinetic coefficient for step displacement
Stochastic models 256–257, 259 *see also* MSZW, cooling crystallization
Stokes–Einstein relation 12
Strong liquids 427, 428
Supersaturation *see* Creation of supersaturation
Supersaturation decay 361, 370, 372
kinetics of 362–367
Supersaturation decrease 385, 386
Supersaturation ratio xv, 50, 53–54, 97, 99, 127, 128, 153, 189, 197, 302, 325, 329, 331, 362
maximum 250, 251
dependence on impurity concentration 250–251

Supersolubility curve 96, 98–100, 202, 203, 325, 414
Surface coverage of nucleus *see* Fractional surface coverage
Surface diffusion 106
Surface diffusion layer 121–123
Surface diffusion processes (continuous growth) 111
Surface entropy factor 94, 109, 110
Surface free energy *see* Interfacial energy (tension)
Surface micromorphology 105, 107
Surface reaction 122
Surface relaxation mechanism 121
Surface roughening 94, 123
Surface tension 11, 12 *see also* Interfacial energy (tension)
Surface tension of melts 455

t

Temperature change in solution by solute 372–383
  regions of 372
Thermal expansion (contraction) coefficient
  of liquids and solutions (*see* Liquids (solvents))
  of melts 424, 425, 438–441, 443, 444, 449, 453–454, 457, 458, 460
Thermodynamic parameter 198 *see also* Three-dimensional (3D) nucleation rate
Three-dimensional (3D) nucleation xv, 49, 54–56, 93, 96, 127–128, 145, 167–169, 189, 246, 248, 267, 278, 279, 283, 284, 288, 313, 325, 345, 361, 362, 364, 368, 385, 386
  activation energy barrier for 58, 59, 62, 63, 130, 149, 153, 345
  atomistic theory of 59
  classical 3D nucleation theory (CNT) xv, 58, 89, 192, 194, 196, 197, 199, 202, 204, 236, 246, 257–259, 296, 303, 326, 332, 338, 343, 345, 349, 351, 355, 388, 416, 423, 438, 439
  critically-sized 3D nuclei 57, 62, 89, 94, 127, 128, 186, 192–194, 257, 333–335, 338, 342, 345, 346, 348, 349, 351, 361, 399, 425, 435
  heterogeneous 60–63, 88, 133, 199, 220, 246, 255–257, 297, 312, 330, 331, 334–338, 341, 343, 346, 348, 349, 387, 396
  homogeneous 60, 62, 63, 133, 199, 257, 312, 330, 331, 341, 343, 346, 348
  mechanism 391, 397
    instantaneous nucleation 156, 157, 159, 361
    progressive nucleation 156, 157, 159, 361
  nonstationary 133, 138
    kinetic (pre-exponential) factor 296, 303, 412–416
    kinetics 414
    thermodynamic parameter 296–297, 303, 307, 311, 318, 412–416
  primary nucleation 232, 312, 320, 345
  secondary nucleation 169, 220, 222, 232, 256, 257, 387, 394, 396, 397
  stationary 54–61, 133, 312
Three-dimensional (3D) nucleation rate xv, 49, 57–59, 62, 132, 133, 140, 167, 168, 192, 193, 195–197, 237, 252, 256, 259, 283, 296–303, 326, 330, 331, 337, 376, 378, 388, 438–439, 441, 443
  effect of antisolvent composition on 296–297
  effect of impurities on 60–63, 140
  effect of viscosity 58, 59
  kinetic (pre-exponential) factor J0, 58, 59, 62, 63, 140, 149, 196, 198,

199, 236, 252, 329, 331, 439–441, 443, 444, 446
stationary, time-independent 129, 130, 136, 139, 140, 328
thermodynamic parameter *B* 58, 59, 328, 331, 345, 348, 439, 441, 443, 444, 446, 449
time-dependent 130, 134
Three-dimensional (3D) nuclei 105, 106, 116
Threshold cooling rate 441–442
Time constant *see* Kolmogorov–Johnson–Mehl–Avrami (KJMA) theory
Time lag for growth 179, 183
Time lag for nucleation 130, 135, 136, 138, 328
Total crystallization duration 193, 328
Transition state theory, Eyring's 15, 31, 394
Transition-state theory of chemical reactions 230
Transmitted laser-beam intensity 269, 270
normalized 270–275, 291–296
Transport processes 107, 379, 382, 389
Transport properties
of solutions 19
of solvents/liquids 11, 12
Trouton's rule 8
Two-dimensional (2D) nucleation 60, 108, 111–117, 121, 127–128, 220, 283, 391
activation energy barrier for 111, 115, 117, 124
critical 2D nucleus 111, 115, 117, 124, 125
heterogeneous 124
homogeneous 124
models 123, 124
Two-dimensional (2D) nucleation rate 113, 115, 123–125
kinetic factor in 123, 124, 126
thermodynamic factor in 123, 124, 126

V

van't Hoff relation (model) 77
van't Hoff's equation 65
Viscosity
of liquids (*see* Liquids (solvents); Saturated solutions; Solutions)
of melts 444, 445
Arrhenius plots 426–427
Arrhenius-type behavior 427
non-Arrhenius behavior 428, 429
temperature dependence of 426–431
theoretical models of 430
Vogel–Tammann–Fulcher (VTF) relation 428, 430
theory 433
Vogel temperature 428

W

Weibull distribution function 409, 411
Weibull relation 402
Wetting (contact) angle 60, 61

Z

Zeldovich factor 57, 130

WILEY END USER LICENSE AGREEMENT

Go to www.wiley.com/go/eula to access Wiley’s ebook EULA.